Multiscale approach to assess the DSM-flux capacity to mitigate impacts on the receiving waters : Quantification of overflow rates and interception of particulate pollutants from combined sewer overflows

Ainhoa Mate Marin

N° d'ordre NNT : 2019LYSEI008

THESE de DOCTORAT DE L'UNIVERSITE DE LYON

opérée au sein de

INSTITUT NATIONAL DES SCIENCES APPLIQUEES DE LYON

Ecole Doctorale ED162

MECANIQUE, ENERGETIQUE, GENIE CIVIL, ACOUSTIQUE

Spécialité : GENIE CIVIL

Soutenue publiquement le 12/02/2019, par :

Ainhoa MATE MARIN

MULTISCALE APPROACH TO ASSESS THE DSM-flux CAPACITY TO MITIGATE IMPACTS ON THE RECEIVING WATERS. QUANTIFICATION OF OVERFLOW RATES AND INTERCEPTION OF PARTICULATE POLLUTANTS FROM COMBINED SEWER OVERFLOWS.

Approche multi-échelle pour évaluer la capacité du DSM-flux à protéger les milieux aquatiques. Quantification des flux d'eau rejetés par les déversoirs d'orage et interception des polluants particulaires.

Devant le jury composé de :

GILLOT, Sylvie	Directrice de recherche, IRSTEA Lyon	Présidente
BELLAUD, Gilles	Professeur, Montpellier SupAgro	Rapporteur
DEWALS, Benjamin	Professeur, Université de Liège	Rapporteur
PHILIPPE, Ronan	Responsable autosurveillance Métropole de Lyon	Examinateur
LIPEME KOUYI, Gislain	Maître de conférences, INSA Lyon	Directeur de thèse
RIVIERE, Nicolas	Professeur, INSA Lyon	Co-directeur de thèse
MIGNOT, Emmanuel	Maître de conférences, INSA Lyon	Invité
VISIEDO, Regis	Directeur général EPTB Saône Doubs	Invité

Département FEDORA – INSA Lyon - Ecoles Doctorales – Quinquennal 2016-2020

SIGLE	ECOLE DOCTORALE	NOM ET COORDONNEES DU RESPONSABLE
CHIMIE	**CHIMIE DE LYON** http://www.edchimie-lyon.fr Sec. : Renée EL MELHEM Bât. Blaise PASCAL, 3e étage secretariat@edchimie-lyon.fr INSA : R. GOURDON	M. Stéphane DANIELE Institut de recherches sur la catalyse et l'environnement de Lyon IRCELYON-UMR 5256 Équipe CDFA 2 Avenue Albert EINSTEIN 69 626 Villeurbanne CEDEX directeur@edchimie-lyon.fr
E.E.A.	**ÉLECTRONIQUE, ÉLECTROTECHNIQUE, AUTOMATIQUE** http://edeea.ec-lyon.fr Sec. : M.C. HAVGOUDOUKIAN ecole-doctorale.eea@ec-lyon.fr	M. Gérard SCORLETTI École Centrale de Lyon 36 Avenue Guy DE COLLONGUE 69 134 Écully Tél : 04.72.18.60.97 Fax 04.78.43.37.17 gerard.scorletti@ec-lyon.fr
E2M2	**ÉVOLUTION, ÉCOSYSTÈME, MICROBIOLOGIE, MODÉLISATION** http://e2m2.universite-lyon.fr Sec. : Sylvie ROBERJOT Bât. Atrium, UCB Lyon 1 Tél : 04.72.44.83.62 INSA : H. CHARLES secretariat.e2m2@univ-lyon1.fr	M. Philippe NORMAND UMR 5557 Lab. d'Ecologie Microbienne Université Claude Bernard Lyon 1 Bâtiment Mendel 43, boulevard du 11 Novembre 1918 69 622 Villeurbanne CEDEX philippe.normand@univ-lyon1.fr
EDISS	**INTERDISCIPLINAIRE SCIENCES-SANTÉ** http://www.ediss-lyon.fr Sec. : Sylvie ROBERJOT Bât. Atrium, UCB Lyon 1 Tél : 04.72.44.83.62 INSA : M. LAGARDE secretariat.ediss@univ-lyon1.fr	Mme Emmanuelle CANET-SOULAS INSERM U1060, CarMeN lab, Univ. Lyon 1 Bâtiment IMBL 11 Avenue Jean CAPELLE INSA de Lyon 69 621 Villeurbanne Tél : 04.72.68.49.09 Fax : 04.72.68.49.16 emmanuelle.canet@univ-lyon1.fr
INFOMATHS	**INFORMATIQUE ET MATHÉMATIQUES** http://edinfomaths.universite-lyon.fr Sec. : Renée EL MELHEM Bât. Blaise PASCAL, 3e étage Tél : 04.72.43.80.46 Fax : 04.72.43.16.87 infomaths@univ-lyon1.fr	M. Luca ZAMBONI Bât. Braconnier 43 Boulevard du 11 novembre 1918 69 622 Villeurbanne CEDEX Tél : 04.26.23.45.52 zamboni@maths.univ-lyon1.fr
Matériaux	**MATÉRIAUX DE LYON** http://ed34.universite-lyon.fr Sec. : Marion COMBE Tél : 04.72.43.71.70 Fax : 04.72.43.87.12 Bât. Direction ed.materiaux@insa-lyon.fr	M. Jean-Yves BUFFIÈRE INSA de Lyon MATEIS - Bât. Saint-Exupéry 7 Avenue Jean CAPELLE 69 621 Villeurbanne CEDEX Tél : 04.72.43.71.70 Fax : 04.72.43.85.28 jean-yves.buffiere@insa-lyon.fr
MEGA	**MÉCANIQUE, ÉNERGÉTIQUE, GÉNIE CIVIL, ACOUSTIQUE** http://edmega.universite-lyon.fr Sec. : Marion COMBE Tél : 04.72.43.71.70 Fax : 04.72.43.87.12 Bât. Direction mega@insa-lyon.fr	M. Jocelyn BONJOUR INSA de Lyon Laboratoire CETHIL Bâtiment Sadi-Carnot 9, rue de la Physique 69 621 Villeurbanne CEDEX jocelyn.bonjour@insa-lyon.fr
ScSo	**ScSo*** http://ed483.univ-lyon2.fr Sec. : Viviane POLSINELLI Brigitte DUBOIS INSA : J.Y. TOUSSAINT Tél : 04.78.69.72.76 viviane.polsinelli@univ-lyon2.fr	M. Christian MONTES Université Lyon 2 86 Rue Pasteur 69 365 Lyon CEDEX 07 christian.montes@univ-lyon2.fr

*ScSo : Histoire, Géographie, Aménagement, Urbanisme, Archéologie, Science politique, Sociologie, Anthropologie

To the best teachers in the world, Pilar and José,
who showed me from an early age the importance of
education, knowledge and critical thinking.

AKNOWLEDGEMENTS

First of all, I would like to express my sincere gratitude to my supervisor, Dr. Gislain Lipeme Kouyi, and co-supervisor, Prof. Nicolas Rivière as well as to Dr. Emmanuel Mignot for the continuous support, their patience during the stressful periods, their availability every time I asked for advice or feedback, and for the immense knowledge they have transferred to me.

I would like to thank the rest of my thesis committee, Prof. Gilles Belaud, Prof. Benjamin Dewals, Dr. Sylvie Gillot, Ronan Philippe and Regis Visiedo, for their insightful and encouraging comments about my work which pushed me to delve deeper into my research.

This PhD work was funded by the Auvergne-Rhône-Alpes Region (ADR "Arc Environnement") and the Metropole of Lyon. I gratefully acknowledge Ronan Philippe, Patrick Lucchinacci and their teams from the Metropole of Lyon for their technical insight and support at the field.

A special thank you is to the OTHU and DEEP laboratory technicians, particularly to Stéphane Vacherie, Nicolas Walcker, Serge Naltchayan, Dominique Babaud and Richard Poncet, for their help with the laboratory tests and for the hard work at the field, which was sometimes not easy to deal with, but they always kept the motivation and a positive attitude that pushed all of us to go forward. I also appreciate all the training and tips they gave to me in electricity, DIY, safety at work, etc. which were essential to work properly and achieve the PhD objectives.

Special thanks go also to the PhD students at DEEP laboratory, in particular to my colleagues and friends Xiaoxiao Zhu, Alejandro Claro Bareto, Robin Garnier and Santiago Sandoval, for the hours taken from their work to help me with mine, for their always joyful attitude at the office, their encouragements during the difficult times, all the fun moments inside and outside the laboratory and for their friendship, which I hope it will last in the future. I would also like to thank Adrien Momplot, Pierre Gueroult and Théophile Schouler for their previous work on this project, which was very useful to start the PhD, and their guidance on how to take the baton.

I am also very grateful to all the people working at DEEP laboratory because, even if we didn't work directly together, they all created a very pleasant atmosphere which made the everyday work much easier and nicer. Thank you for all the interesting conversations shared at the coffee machine and all the cheerful moments during the different laboratory activities.

Last but not least, many thanks to my parents, Pilar and José, for their support and inspiration during all my years of education, which allowed me to reach the PhD degree. They have always been a role model to me. And many thanks to Steven and Malu, for their love, patience, greatly wise advices and continuous encouragements during these years.

LIST OF PUBLICATIONS ISSUED FROM THIS WORK

Journal articles

- *Maté Marín A., Rivière N., Lipeme Kouyi G. (2018).* DSM-flux: a new technology for reliable Combined Sewer Overflow discharge monitoring with low uncertainties. *Journal of Environmental Management, 215: 273-282. doi:10.1016/j.jenvman.2018.03.043*

Conference proceedings with oral presentations

- *Maté Marín A., Lipeme Kouyi G., Rivière N. (2016).* Stage-discharge relationship of the DSM-flux to measure overflow rates in combined sewer systems. *8th International Conference on Sewer Processes and Networks, 31 August-2 September 2016, Rotterdam, Netherlands.*
- *Maté Marín A., Lipeme Kouyi G., Rivière N. (2016).* Vérification numérique de la relation hauteur – débit obtenue expérimentalement pour le DSM-flux. *7èmes Journées Doctorales en Hydrologie Urbaine, 11-12 October 2016, Nantes, France.*
- *Maté Marín A., Lipeme Kouyi G., Rivière N. (2017).* Uncertainty analysis of the DSM-flux stage-discharge relationship: comparison of GUM and Monte Carlo approaches. *23rd European Junior Scientist Workshop, 15-20 May 2017, Chichilianne, France.*
- *Maté Marín A., Rivière N., Lipeme Kouyi G. (2017).* Uncertainty analysis of the DSM-flux stage-discharge relationship to measure CSOs: comparison of GUM and Monte Carlo approaches. *14th IWA/IAHR International Conference on Urban Drainage. 10-15 September 2017, Prague, Czech Republic.*
- *Maté Marín A., Lipeme Kouyi G., Rivière N. (2017).* Monitoring CSO volumes and quality with the DSM-flux*. Colombian - French Conference on Urban Water Systems. 30 November – 1 December 2017, Lyon, France.*

Publications in progress

- *Maté Marín A., Rivière N., Philippe R., Lipeme Kouyi G. (accepted).* On site validation of a new CSO monitoring methodology by means of a CFD-based approach*. 10th International Conference Novatech 2019, 1-5 July 2019, Lyon, France.*
- *Maté Marín A., Mignot E., Rivière N., Lipeme Kouyi G. (in progress).* ADV measurements and solid transport tests in physical model for the assessment of the retention capabilities of a new ecotechnology to reduce the particulate pollutants from CSOs.

ABSTRACT

Over the past decade, European Union governments have encouraged to collect data on the volume and quality of all urban water effluents with a significant environmental impact on receiving aquatic environments. Methods for monitoring these flows require improvements, particularly for combined sewer overflows, which are complex flows that contribute in significant proportion to the degradation of the quality of the receiving waters.

The DSM-flux (Device for Stormwater and combined sewer flows Monitoring and the control of pollutant fluxes) is a new pre-calibrated and pre-designed device that guarantees the appropriate hydraulic conditions for measuring discharged flows and volumes as well as the concentrations and mass loads of pollutants carried in suspension by the flow.

In this PhD work, a relationship allowing to measure the flow rates conveying through the DSM-flux was determined thanks to an experimental study on a small-scale physical model, and then validated for several flow configurations upstream of the device. Whatever the upstream hydraulic conditions are, the relative uncertainties are less than 15% and 2% for the flow rates and volumes studied, respectively, which is equivalent to the uncertainties of the most reliable current methods. The monitoring methodology was validated *in situ* in a large-scale device installed at the field and operating in real conditions, which shows the robustness of the method. Moreover, thanks to its original design, the DSM-flux allows the interception of a fraction of particulate pollutants. The hydrodynamics of this monitoring device were analysed as well as the conditions that cause the settling of particulate pollutants. Depending on the flow conditions, this device can retain 50% of the total mass of fine suspended solid matter transiting through the device, but for flows at high discharge rates, this efficiency is significantly reduced. Its retention capacity has also been observed in the field and a methodology has been developed to quantify its retention efficiency in future studies.

Apart from its performance, from an operational point of view, the device has other advantages compared to other current devices: (i) it is pre-calibrated and can be installed downstream from existing combined sewer overflows, (ii) it can be directly installed through a manhole in the discharge channel, (iii) its hydraulic performance is independent from the flow conditions upstream, and (iv) it is an integrated monitoring device, measuring flow rates and their quality simultaneously, in addition to intercepting a part of the particulate pollutants.

RÉSUMÉ

Au cours des dix dernières années, les gouvernements de l'Union Européenne ont été encouragés à collecter des données sur le volume et la qualité de tous les effluents d'eaux urbaines ayant un impact environnemental significatif sur les milieux aquatiques récepteurs. Les méthodes de surveillance de ces flux nécessitent des améliorations, en particulier pour les déversoirs d'orage, structures complexes responsables en grande partie de la dégradation de la qualité des milieux récepteurs.

Le DSM-flux (Dispositif pour la surveillance et maîtrise des flux d'eaux et polluants des réseaux d'eaux pluviales et unitaires) est un nouveau dispositif préfabriqué et pré-étalonné qui garantit les conditions hydrauliques appropriées permettant de mesurer les débits et volumes déversés ainsi que les concentrations et masses de polluants qui y sont transportés.

Dans cette thèse, une relation permettant de mesurer le débit au passage du DSM-flux a été construite grâce à une étude expérimentale sur modèle physique réduit, puis validée pour plusieurs configurations d'écoulement à l'amont du dispositif. Quelles que soient les conditions hydrauliques en amont, les incertitudes relatives sont inférieures à 15% et 2% pour les débits et les volumes étudiés, respectivement, ce qui reste équivalent, voire mieux, par rapport aux incertitudes des méthodes actuelles les plus fiables. La méthode de mesure a été validée *in situ* sur un dispositif à grande échelle construit sur le terrain et fonctionnant en conditions réelles, ce qui montre la robustesse de la méthode. De plus, grâce à sa conception originale, le DSM-flux favorise l'interception d'une fraction des polluants particulaires. L'hydrodynamique de ce dispositif de mesure a été analysée ainsi que les conditions qui engendrent la décantation des polluants particulaires. En fonction des conditions d'écoulement, ce dispositif peut retenir 50% de la masse totale des matières solides fines en suspension transitant par le dispositif, mais pour des écoulements à débits élevés, cette efficacité est significativement réduite. Sa capacité de rétention a été aussi observée sur le terrain et une méthodologie a été élaborée pour quantifier son efficacité de rétention lors d'études futures.

Mise à part sa performance hydraulique, du point de vue opérationnel, le dispositif présente d'autres avantages par rapport à d'autres dispositifs existants : (i) il est pré-étalonné et peut être installé à l'aval de déversoirs d'orage déjà existants, (ii) il peut s'insérer directement au sein du canal de décharge (installation d'un regard de visite équipé d'un DSM-flux), (iii) sa performance hydraulique est indépendante des conditions de l'écoulement à l'amont et (iv) il s'agit d'un dispositif intégré de mesure de débits et de leur qualité simultanément, en plus d'intercepter une partie de polluants particulaires.

TABLE OF CONTENTS

AKNOWLEDGEMENTS i

LIST OF PUBLICATIONS ISSUED FROM THIS WORK iii

ABSTRACT v

RÉSUMÉ vii

TABLE OF CONTENTS ix

LIST OF FIGURES xiii

LIST OF TABLES xxiii

LIST OF ACRONYMS AND ABBREVIATIONS xxv

LIST OF VARIABLES xxvii

1. INTRODUCTION 3

    1.1. CSOs: A PRIORITY WATER POLLUTION CONCERN 5

    1.2. CURRENT SOLUTIONS FOR CSOs POLLUTION QUANTIFICATION 10

    1.3. THE DSM-flux: A NEW ECOTECHNOLOGY FOR CSOs MONITORING 18

    1.4. PhD OBJECTIVES AND STRATEGY 21

    1.5. STRUCTURE OF THE DOCUMENT 26

2. A MULTISCALE APPROACH: THE THREE DSM-FLUX SYSTEMS 29

    2.1. THE SMALL-SCALE PHYSICAL AND NUMERICAL MODELS 30

        2.1.1. The small-scale physical model experimental set-up 30

        2.1.2. The small-scale numerical model 31

    2.2. THE LARGE-SCALE NUMERICAL MODEL AND FIELD PROTOTYPE 52

        2.2.1. The large-scale numerical model 52

        2.2.2. Sathonay-Camp experimental site and field prototype characteristics 56

3. THE DSM-flux: AN ACCURATE MONITORING DEVICE 71

    3.1. THE DSM-flux MONITORING METHODOLOGY 72

        3.1.1. Materials and methods for the establishment of the DSM-flux HQR 72

        3.1.2. The DSM-flux HQR 79

3.1.3. Robustness of the DSM-flux HQR 82
3.1.4. Uncertainty analysis of the DSM-flux HQR 83
3.1.5. Assessment of volumes for typical CSO events and their uncertainties 85
3.1.6. Conclusions of Section 3.1 87
3.2. ASSESSMENT OF THE MONITORING METHODOLOGY AT A LARGER SCALE 89
3.2.1. Materials and methods for the assessment of the DSM-flux HQR at large scale 89
3.2.2. Validation of the small-scale model with the HQR tests data 92
3.2.3. Assessment of the DSM-flux HQR at the large-scale numerical model 95
3.2.4. DSM-flux field prototype optimisation and influence on the DSM-flux HQR . 108
3.2.5. Conclusions of Section 3.2 112
3.3. VALIDATION OF THE MONITORING METHODOLOGY AT THE FIELD SCALE 114
3.3.1. Material and methods for the validation of the DSM-flux HQR at the field ... 114
3.3.2. Comparison of the DSM-flux and the distribution chamber monitored CSOs 122
3.3.3. Conclusions of Section 3.3 129
4. THE DSM-flux: ASSESSMENT OF POLLUTANT RETENTION CAPABILITIES 133
4.1. THE DSM-flux HYDRODYNAMICS AND RETENTION CAPABILITIES 135
4.1.1. The DSM-flux flow patterns and turbulence 136
4.1.2. The DSM-flux retention and erosion efficiencies 154
4.1.3. Conclusions of Section 4.1 179
4.2. NUMERICAL ASSESSMENT OF THE HYDRODYNAMICS AT A LARGER SCALE 181
4.2.1. Materials and methods for the assessment of the hydrodynamics at a larger scale 181
4.2.2. Comparison of the small-scale numerical model hydrodynamics with the VT tests data 184
4.2.3. Application for the large-scale numerical simulation 212
4.2.4. Conclusions of Section 4.2 220
4.3. OBSERVATION OF HYDRODYNAMICS AND RETENTION CAPABILITIES AT THE FIELD 222

4.3.1. Materials and methods for the assessment of the retention capabilities at the field….. 223

4.3.2. Some preliminary data 227

5. CONCLUSIONS AND PERSPECTIVES 233

5.1. CONCLUSIONS 233

5.2. PERSPECTIVES 236

6. REFERENCES 243

7. APPENDICES 257

APPENDICES OF CHAPTER 2 259

7.1.1. The small-scale DSM-flux dimensions 261

7.1.2. The small-scale physical model experimental set-up 262

7.1.3. The small-scale numerical models and computational meshes 263

7.1.4. The initial large-scale DSM-flux dimensions 266

7.1.5. The modified large-scale DSM-flux dimensions 267

7.1.6. The computational mesh of the large-scale numerical models 268

APPENDICES OF CHAPTER 3 271

7.2.1. The Sathonay-Camp experimental site hydrographs 273

APPENDICES OF CHAPTER 4 287

7.3.1. <u'v'> Reynolds stresses at the near-bottom region of the physical model ... 290

7.3.2. <u'v'> Reynolds stresses at the near-surface region of the physical model ... 291

7.3.3. <u'w'> Reynolds stresses at the near-bottom region of the physical model .. 292

7.3.4. <u'w'> Reynolds stresses at the near-surface region of the physical model .. 293

7.3.5. <uv> velocity fields at the near-bottom region of the small-scale numerical model under low flow conditions 294

7.3.6. <uv> velocity fields at the near-surface region of the small-scale numerical model under lower flow conditions 295

7.3.7. <uv> velocity fields at the near-bottom region of the small-scale numerical model under higher flow conditions 296

7.3.8. <uv> velocity fields at the near-surface region of the small-scale numerical model under higher flow conditions 297

7.3.9. Variability and uncertainties of velocity and turbulence data 298

RÉSUMÉ ÉTENDU EN FRANÇAIS 309

LIST OF FIGURES

Figure 1.1. Current methods to measure CSOs volumes. Considered techniques: HQR (stage-discharge relation methods) and VM (velocity-based methods). 11

Figure 1.2. Current methods to measure CSOs pollutant concentrations. 16

Figure 1.3. 3D view of the DSM-flux (a) initial and (b) current designs. 19

Figure 1.4. Schematic of the approach followed in this PhD work. 22

Figure 1.5. Strengths and weaknesses of each of the three systems used in this PhD work. 22

Figure 1.6. Stages of the strategy followed to answer each of the two questions of this PhD work. 24

Figure 2.1. Schematic of the experimental set-up for the small-scale physical model. Zoom views of the DSM-flux with its different zones and of a cross-section of the overflow part that is enclosed in the draining basin. 31

Figure 2.2. 3D view of the small-scale numerical model's domain. Inlet and outlet boundaries in red and blue respectively. The rest are wall boundaries. Zoom of overflow blocks. 34

Figure 2.3. Detail view of the refinement of mesh MS3 done at the dissipation zone and adjacent areas up and downstream. Zoom of the non-conformal interface where the number of nodes upstream is half the number of nodes downstream. 36

Figure 2.4. Instantaneous u velocity time series with decomposition in mean <u> and fluctuating u' components. 39

Figure 2.5. A schematic overview of turbulence modelling (from Andersson et al. (2011)). ... 40

Figure 2.6. The Standard Wall Function implemented in ANSYS Fluent (from ANSYS Fluent Theory Guide (ANSYS, 2015a)). In the figure, points are empirical data and lines correspond to the adjusted laws. ANSYS Fluent Theory Guide (ANSYS, 2015a) variables in this figure correspond to the following: $U/U_T=u^+$ and $y/v=y^+$. The intersection between the viscous layer law and the log law is also indicated in red ($y^+ = 11.125$). 44

Figure 2.7. SIMPLE pressure-velocity coupling algorithm (adapted from Versteeg and Malalasekera (2007)). 50

Figure 2.8. 3D view of the three large-scale numerical models' domain. Inlet and outlet boundaries in red and blue respectively. The rest are wall boundaries. Zoom of overflow blocks. 54

Figure 2.9. Location of the Ravin catchment in Lyon's conurbation, with the six municipalities (partially) covered by the Ravin catchment hatched in black (Sathonay-Camp, Sathonay-Village, Rilieux-La-Pape, Caluire-et-Cuire, Fontaines-Saint-Martin et Fontaines-sur-Saône). Adapted from AU (1998). In the zoom, the DSM-flux experimental site location within the Ravin catchment (image from Google Earth). 57

Figure 2.10. Land uses of the Ravin catchment. Data from the Corin Land Cover database of 2006. 58

Figure 2.11. Sub-catchments of the Ravin hydrological catchment. 58

Figure 2.12. General plan of the Sathonay-Camp site configuration. Adapted from Metropole of Lyon original plans. Dimensions in meters except diameters that are in millimetres. 61

Figure 2.13. Horizontal and profile views of the distribution chamber. Adapted from Metropole of Lyon original plans. Dimensions in meters except diameters that are in millimetres. 62

Figure 2.14. Photos of the connection of the DSM-flux outflow pipe with the Ravin conduit: a) the connection of the outflow pipe and the Ravin conduit before the modification, b) the extension pipe, c) the chamber (looking upstream) where the Ravin conduit and the CSO discharge pipe converge (the DSM-flux outflow pipe extension is observed inside the Ravin's conduit) and d) the system operating during an event the 25th of November of 2017. 63

Figure 2.15. Horizontal and profile views of the DSM-flux chamber. Adapted from Metropole of Lyon original plans. Dimensions in meters except diameters that are in millimetres. DSM-flux prototype dimensions in Appendix 7.1.5..... 64

Figure 2.16. Horizontal and profile views of the DSM-flux chamber with the location of the field instrumentation. 65

Figure 3.1. Methodology for the establishment and validation of the DSM-flux HQR..... 73

Figure 3.2. The DSM-flux geometry: plan (up) and profile (bottom) views – black dots indicating locations where the specified water levels are measured. 76

Figure 3.3. Synthetic hydrographs reproduced for the small-scale DSM-flux physical model unsteady-state tests to compute CSO volumes..... 78

Figure 3.4. (a) Piping piece for additional bends test and (b) asymmetric flow in additional obstacle test. 79

Figure 3.5. Clinging (a), transition (b), and free (c) nappe flow over the right crest of the small-scale DSM-flux physical model. 80

Figure 3.6. DSM-flux HQR (black solid line) represented by Equation 3.8. 81

Figure 3.7. Relative expanded uncertainties of flow rates obtained by the DSM-flux HQR (solid line) and other methods uncertainty values from literature (dashed lines). 85

Figure 3.8. Methodology to assess the HQR at large-scale. 90

Figure 3.9. DSM-flux HQR (solid line) represented by Equation 3.8 and its 95% confidential intervals (dashed lines). Numerical data from simulations at the small-scale models (Table 3.4). 94

Figure 3.10. DSM-flux HQR (solid line) and simulated discharge coefficients for the numerical data of the simulations at the small-scale models (Table 3.4). 94

Figure 3.11. DSM-flux HQR (solid line) represented by Equation 3.8 and its 95% confidential intervals (dashed lines) for different uncertainties of the water level measure. Numerical data from simulations at the large-scale model LM-A (Table 3.5). 97

Figure 3.12. DSM-flux HQR (solid line) and simulated discharge coefficients for the numerical data of the simulations at the small-scale and LM-A models (Table 3.4 and Table 3.5). 98

Figure 3.13. Free surface profile (volume of fluid = 0.5) at the axis of symmetry of the device for the small-scale and large-scale models, for Q=20 l/s and Q=180 l/s respectively. 101

Figure 3.14. Flow pattern for the Reattached Wall Jet regime of a submerged hydraulic jump (adapted from Wu and Rajaratnam (1995)). 102

Figure 3.15. Flow pattern for the Deflecting Surface Jet (above) and Reattached Wall Jet (below) regimes of a submerged hydraulic jump (adapted from Habibzadeh et al. (2011)) 102

Figure 3.16. Free surface profile (volume of fluid = 0.5) at the axis of symmetry of the device for the small-scale and large-scale models, for Q=9 l/s and Q=100 l/s respectively. 102

Figure 3.17. Free surface profile (volume of fluid = 0.5) at cross-sections at the middle of the overflow weir crests for the small-scale and large-scale models, for Q=20 l/s and Q=180 l/s respectively. Views from the upstream, so the weir at the left of the figure is the left weir at the device. 104

Figure 3.18. Free surface profile (volume of fluid = 0.5) at two cross-sections: one at the end of the stabilization area and one at the middle of the overflow area for the small-scale and large-scale models, for Q=9 l/s and Q=100 l/s respectively. Views from the upstream, so the weir at the left of the figure is the left weir at the device. 105

Figure 3.19. Free surface profile (volume of fluid = 0.5) at cross-sections at the middle of the overflow weir crest for the small-scale and large-scale models, for Q=15 l/s, Q=20 l/s and Q=180 l/s, with the mesh lines superposed. Views from the upstream, so the weir at the left of the figure is the left weir at the device. 106

Figure 3.20. Evolution of h_{sim} along the iterations after convergence of the simulation for the large-scale model LM-A at Q=180 l/s (sim LM-A180). 107

Figure 3.21. Evolution of h_{sim} along the iterations after convergence of the simulation for the small-scale model SM-B at Q=20 l/s (sim SM-B20). 108

Figure 3.22. Evolution of h_{sim} along the iterations after convergence of the simulation for the small-scale model SM-B at Q=15 l/s (sim SM-B15). 108

Figure 3.23. DSM-flux HQR (solid line) represented by Equation 3.8 and its 95% confidential intervals (dashed lines) for different uncertainties of the water level measure. Numerical data from simulations at the large-scale model LM-B (Table 3.6)..... 111

Figure 3.24. DSM-flux HQR (solid line) represented by Equation 3.8 and its 95% confidential intervals (dashed lines) for different uncertainties of the water level measure. Numerical data from simulations at the large-scale model LM-C (Table 3.6)..... 111

Figure 3.25. DSM-flux HQR (solid line) and simulated discharge coefficients for the numerical data of the simulations at the small- and large-scale models (Table 3.4 and Table 3.6). 112

Figure 3.26. The distribution chamber geometry: plan (above) and profile (below) views – red dot indicating location where the water level is measured. 116

Figure 3.27. Distribution chamber HQR with numerical data used for its adjustment. 118

Figure 3.28. 3D view of the distribution chamber numerical model's domain. Inlet and outlet boundaries in red and blue respectively. The rest of the indicated parts are wall boundaries. 119

Figure 3.29. Different detail views of the computational mesh of the distribution chamber numerical model. 121

Figure 3.30. Hydrographs registered at Sathonay-Camp the 14th of June of 2018..... 123

Figure 3.31. Relationship between peak flow rates obtained by means of both monitoring methodologies. 125

Figure 3.32. Values of the evaluation coefficients in relation with peak flow rates at the DSM-flux. 126

Figure 3.33. Relationship between CSO volumes obtained by means of both monitoring methodologies. 129

Figure 4.1. ADV measuring points at two different sampling depths. Elevations are in meters (bottom graph). 137

Figure 4.2. Convergence test for the velocity components. 138

Figure 4.3. Convergence test for the Reynolds shear stresses. 139

Figure 4.4. Convergence test for the Reynolds normal stresses. 139

Figure 4.5. Methodology for the assessment of flow patterns and turbulence in the DSM-flux small-scale physical model. 140

Figure 4.6. Energy spectra (in blue) for u velocity component at x/L_d = 0.329, y/B = 0 and z/H_0 = 0.098 and 5/3 slope line (in black) as a reference for Kolmogorov's model. 141

Figure 4.7. <uv> velocity fields at the DSM-flux small-scale physical model for (a) VT2, (b) VT5 and (c) VT9 tests, in the near-bottom region, at depths z/H_0 = 0.125, 0.111 and 0.098, respectively. 146

Figure 4.8. <uv> velocity fields at the DSM-flux small-scale physical model for (a) VT2, (b) VT5 and (c) VT9 tests, in the near-surface region, at depths z/H_0 = 0.694, 0.741 and 0.783 respectively. Grey hatched area corresponds to the hydraulic jump recirculation 147

Figure 4.9. <vw> velocity fields at the cross-section x/L_d = 0.329 of the DSM-flux small-scale physical model for (a) VT2 and (b) VT9 tests. 148

Figure 4.10. TKE values at the DSM-flux small-scale physical model for (a) VT2, (b) VT5 and (c) VT9 tests, in the near-bottom region, at depths z/H_0 of 0.125, 0.111 and 0.098 respectively. Two different markers are used to distinguish data from two consecutive sections. 152

Figure 4.11. TKE values at the DSM-flux small-scale physical model for (a) VT2, (b) VT5 and (c) VT9 tests, in the near-surface region, at depths z/H_0 of 0.694, 0.741 and 0.783 respectively. Grey hatched area corresponds to the hydraulic jump recirculation area. Two different markers are used to distinguish data from two consecutive sections. 153

Figure 4.12. Particle size distribution for Poraver® 100-300 glass beads. 155

Figure 4.13. Methodology for the assessment of the retention and erosion efficiencies and particle segregation in the DSM-flux. 157

Figure 4.14. Event type reproduced at the DSM-flux small-scale physical model for stage 1 of the three SE tests. 158

Figure 4.15. Possible vortex structure formed at the bottom of the end wall of the DSM-flux device that could explain the absence of sediments in that area. 163

Figure 4.16. Photos of the deposition areas (corresponding to MR1 mass load) at the DSM-flux small-scale physical model at the end of stage 1 for (a) SE2_130, (b) SE5_110 and (c) SE2_560 tests. 166

Figure 4.17. Deposition maps at the DSM-flux small-scale physical model at the end of stage 1 (corresponding to MR1 mass load) for (a) SE2_130, (b) SE5_110 and (c) SE2_560 tests. Zones where sediments settled are hatched in red with a grass pattern. Zones hatched in green with a dot pattern represent areas were the deposition layer was finer, so the bottom of the device was visible. This might be either because less settling had taken place there or because some erosion had already occurred. A 5 cm spaced grid, also drawn at the small-scale model, is included in the deposition maps for reference purposes. 167

Figure 4.18. Photos showing the evolution of the material settled in stage 1 for the SE2_130 test. 169

Figure 4.19. Photos showing the evolution of the material settled in stage 1 for the SE5_110 test. 170

Figure 4.20. Photos showing the evolution of the material settled in stage 1 for the SE2_560 test. 171

Figure 4.21. Photos of the deposition areas (corresponding to MR2 mass load) at the DSM-flux small-scale physical model at the end of stage 2 for (a) SE2_130, (b) SE5_110 and (c) SE2_560 tests. 172

Figure 4.22. Deposition maps (corresponding to MR2 mass load) at the DSM-flux small-scale physical model at the end of stage 2 for (a) SE2_130, (b) SE5_110 and (c) SE2_560 tests. The legend for the colors of the hatched zones is the same as for the stage 1 (Figure 4.17) and the 5 cm space grid is also represented for reference. 173

Figure 4.23. Superposition of depositions maps at the end of stage 1 (grey) and stage 2 (purple) for (a) SE2_130, (b) SE5_110 and (c) SE2_560 tests. 174

Figure 4.24. Superposition of deposition maps from Figure 4.23 (grey and violet curves) and TKE values (blue dots and asterisks) from (a) VT2, (b) VT5 and (c) VT2 tests, at depths z/H_0 = 0.125, 0.111 and 0.125 respectively, from Figure 4.10. 175

Figure 4.25. Particle size distribution of samples from test SE2_130. 177

Figure 4.26. Particle size distribution of samples from test SE5_110. 178

Figure 4.27. Particle size distribution of samples from test SE2_560. 178

Figure 4.28. Methodology to assess the hydrodynamics and retention capabilities at large-scale. Parts in red could not be performed within the time of this PhD work. 183

Figure 4.29. <uv> velocity fields (a) at the DSM-flux small-scale physical model for VT2 data (copy from Figure 4.7 (a)), (b) at the numerical model SM-A for Sim SM-A1 data and (c) at the numerical model SM-B for Sim SM-B1 data, in the near-bottom region ($z/H_0 = 0.125$). 188

Figure 4.30. <uv> velocity fields (a) at the DSM-flux small-scale physical model for VT2 data (copy from Figure 4.8 (a), (b) at the numerical model SM-A for Sim SM-A1 data and (c) at the numerical model SM-B for Sim SM-B1 data, in the near-surface region ($z/H_0 = 0.694$). 189

Figure 4.31. <uv> velocity fields (a) at the DSM-flux small-scale physical model for VT9 data (copy from Figure 4.7 (c), (b) at the numerical model SM-A for Sim SM-A5 data and (c) at the numerical model SM-B for Sim SM-B3 data, in the near-bottom region ($z/H_0 = 0.098$). 190

Figure 4.32. <uv> velocity fields (a) at the DSM-flux small-scale physical model for VT9 data (copy from Figure 4.8 (c), (b) at the numerical model SM-A for Sim SM-A5 data and (c) at the numerical model SM-B for Sim SM-B3 data, in the near-surface region ($z/H_0 = 0.783$). 191

Figure 4.33. TKE values (a) at the DSM-flux small-scale physical model for VT2 data (copy from Figure 4.10 (a), (b) at the numerical model SM-A for Sim SM-A1 data and (c) at the numerical model SM-B for Sim SM-B1 data, in the near-bottom region ($z/H_0 = 0.125$). 194

Figure 4.34. TKE values (a) at the DSM-flux small-scale physical model for VT9 data (copy from Figure 4.10 (c), (b) at the numerical model SM-A for Sim SM-A5 data and (c) at the numerical model SM-B for Sim SM-B3 data, in the near-bottom region ($z/H_0 = 0.098$). 195

Figure 4.35. Superposition of deposition maps from test SE2_130 (Figure 4.23 (a)) and TKE values (a) at the DSM-flux small-scale physical model for VT2 data (copy from Figure 4.10 (a)), (b) at the numerical model SM-A for Sim SM-A1 data and (c) at the numerical model SM-B for Sim SM-B1 data, in the near-bottom region ($z/H_0 = 0.125$). 196

Figure 4.36. Superposition of deposition maps from test SE2_560 (Figure 4.23 (c)) and TKE values (a) at the DSM-flux small-scale physical model for VT2 data (copy from Figure 4.10 (a)), (b) at the numerical model SM-A for Sim SM-A1 data and (c) at the numerical model SM-B for Sim SM-B1 data, in the near-bottom region ($z/H_0 = 0.125$). 197

Figure 4.37. Normalized RMSE under the lower flow conditions (VT2, SM-A2, SM-B2) in the near-bottom region ($z/H_0 = 0.125$). 200

Figure 4.38. Normalized RMSE under the lower flow conditions (VT2, SM-A2, SM-B2) in the near-surface region ($z/H_0 = 0.694$). 200

Figure 4.39. Normalized RMSE under the higher flow conditions (VT9, SM-A9, SM-B9) in the near-bottom region ($z/H_0 = 0.098$). 201

Figure 4.40. Normalized RMSE under the higher flow conditions (VT9, SM-A9, SM-B9) in the near-surface region ($z/H_0 = 0.783$). 201

Figure 4.41. Normalized <u>, <v>, <w> and TKE at the DSM-flux small-scale physical model for VT2 data in dots (presented in Figure 4.7 (a)), at the numerical model SM-C for Sim SM-C1 data in asterisks and at the numerical model SM-B for Sim SM-B1 data in crosses, all in the near-bottom region ($z/H_0 = 0.125$). Two different colours are used to distinguish data from two consecutive sections. 204

Figure 4.42. Normalized <u>, <v>, <w> and TKE at the DSM-flux small-scale physical model for VT2 data in dots (presented in Figure 4.8 (a)), at the numerical model SM-C for Sim SM-C1 data in asterisks and at the numerical model SM-B for Sim SM-B1 data in crosses, all in the near-surface region ($z/H_0 = 0.694$). Two different colours are used to distinguish data from two consecutive sections. 205

Figure 4.43. Normalized <u>, <v>, <w> and TKE at the DSM-flux small-scale physical model for VT9 data in dots (presented in Figure 4.7 (c), at the numerical model SM-C for Sim SM-C2 data in asterisks and at the numerical model SM-B for Sim SM-B3 data in crosses, all in the near-bottom region ($z/H_0 = 0.098$). Two different colours are used to distinguish data from two consecutive sections. 206

Figure 4.44. Normalized <u>, <v>, <w> and TKE at the DSM-flux small-scale physical model for VT9 data in dots (presented in Figure 4.8 (c), at the numerical model SM-C for Sim SM-C2 data in asterisks and at the numerical model SM-B for Sim SM-B3 data in crosses, all in the near-surface region ($z/H_0 = 0.783$). Two different colors are used to distinguish data from two consecutive sections. 207

Figure 4.45. Normalized RMSE under the lower flow conditions (VT2, SM-B2, SM-C2) in the near-bottom region ($z/H_0 = 0.125$). 208

Figure 4.46. Normalized RMSE under the lower flow conditions (VT2, SM-B2, SM-C2) in the near-surface region ($z/H_0 = 0.694$). 208

Figure 4.47. Normalized RMSE under the higher flow conditions (VT9, SM-B9, SM-C9) in the near-bottom region ($z/H_0 = 0.098$). 209

Figure 4.48. Normalized RMSE under the higher flow conditions (VT9, SM-B9, SM-C9) in the near-surface region ($z/H_0 = 0.783$). 209

Figure 4.49. Velocity contours in the near-bottom region of the large-scale models, at depth $z/H_0 = 0.2$. 216

Figure 4.50. Velocity contours in the near-bottom region of the large-scale models, at depth $z/H_0 = 0.065$. 217

Figure 4.51. TKE contours in the near-bottom region of the large-scale models, at depth $z/H_0 = 0.2$. 218

Figure 4.52. TKE contours in the near-bottom region of the large-scale models, at depth $z/H_0 = 0.065$. 219

Figure 4.53. Schematic of the design of the support for the upstream suction tube of the automatic samplers. 226

Figure 4.54. Sediments at the DSM-flux field prototype. Photo taken the 14th of June of 2018. 228

LIST OF TABLES

Table 1.1. Strategies to mitigate CSO impacts. 6

Table 1.2. Rules for self-monitoring of CSOs in France established in Ministerial Order DEVL1429608A (MEDDE, 2015a) and detailed in the Technical Comments associated to this Order. TSS stands for total suspended solids, BOD5 stands for biological oxygen demand in 5 days, COD stands for chemical oxygen demand, TKN stands for total Kjeldahl nitrogen, NH4 stands for ammonium and TP stands for total phosphorous. 8

Table 1.3. Conformity criteria for drainage systems concerning CSOs in France, according to Ministerial Order DEVL1429608A (MEDDE, 2015a) and defined in the Technical Note DEVL1519953N (MEDDE, 2015b). 9

Table 1.4. Sampling strategies advantages and drawbacks (adapted from Bertrand-Krajewski et al. (2000). SV stands for Sampling Volume and SF for Sampling Frequency. 13

Table 1.5. Preferable features for current monitoring techniques to control CSOs pollution. .. 17

Table 2.1. Main features of the small-scale numerical models. RNG=ReNormalization group; SCWF=Scalable Wall Function; EWT=Enhanced Wall Treatment; 2UW=Second order upwind; LSCB=Least Squares Cell Based; BFW=Body Force Weighted; MHRIC=Modified High Resolution Interface Capturing; SIMPLE=Semi-Implicit Method for Pressure-Linked Equations; VOF=Volume Of Fluid; VI/MFI=Velocity/Mass Flow Inlet; PO=Pressure Outlet; FX=Fixed Wall; SR=Scaled Residuals; MFB=Mass Flow Balance..... 33

Table 2.2. Characteristics of the computational meshes of the small-scale numerical models. 35

Table 2.3. Characteristics of the computational meshes of the large-scale numerical models. Meshes ML1 and ML2 include a manhole that is not included in the final design and that increases significantly the number of elements of the models. To better compare the size of the meshes, number of elements without the extra cells of the manhole (equivalent configuration to ML3) would be approximately 520.000 and 1.620.000 for ML1 and ML2 respectively..... 55

Table 2.4. Main features of the small-scale numerical models. RNG=ReNormalization group; SCWF=Scalable Wall Function; EWT=Enhanced Wall Treatment; 2UW=Second order upwind; LSCB=Least Squares Cell Based; BFW=Body Force Weighted; MHRIC=Modified High Resolution Interface Capturing; SIMPLE=Semi-Implicit Method for Pressure-Linked Equations; VOF=Volume Of Fluid; MFI=Mass Flow Inlet; PO=Pressure Outlet; FX=Fixed Wall; SR=Scaled Residuals; MFB=Mass Flow Balance. 56

Table 2.5. Characteristics of the urban sub-catchments draining to the CSO structure DO342. Data issued from Metropole of Lyon urban drainage model of the catchment..... 59

Table 3.1. RMSE, MAE, MARE and NS coefficients values for each tested case at the small-scale DSM-flux model. Range of measured discharge rates (Q_{mea}) and total number of measures (N) are also indicated. 81

Table 3.2. Measured reference (Vmea) and estimated (Vest) CSO volume values, relative errors and relative expanded uncertainties for the four synthetic events reproduced at the small-scale DSM-flux model. 86

Table 3.3. Simulations made at the small- and large- scale numerical models. 92

Table 3.4. Numerical results from the simulations at the small-scale numerical models. 93

Table 3.5. Numerical results from the simulations at the large-scale numerical model LM-A... 96

Table 3.6. Numerical results from the simulations at the large-scale numerical models..... 110

Table 3.7. Numerical data for the adjustment of the distribution chamber HQR. 117

Table 3.8. Characteristics and quality indicators for the distribution chamber model computational mesh (MDC1). 120

Table 3.9. CSO events registered at Sathonay-Camp experimental site from February to June 2018. 124

Table 4.1. Hydraulic conditions for the VT tests. Froude (F) and Reynolds (Re) numbers have been estimated based on Manning equation for uniform flow and water depth values were measured at the HQ tests. 140

Table 4.2. Characteristic diameters of granulometric curve of Poraver® 100-300 glass beads. 155

Table 4.3. Hydraulic conditions for stage 1 of the three SE tests. 159

Table 4.4. Results of the SE tests. 161

Table 4.5. Characteristic diameters from granulometric curves of Figure 4.25, Figure 4.26 and Figure 4.27. 177

Table 4.6. Normalized MAE estimated between experimental data from VT tests and numerical data from SM-A and SM-B. 198

LIST OF ACRONYMS AND ABBREVIATIONS

ADV	Acoustic Doppler Velocimeter
ASME	American Society of Mechanical Engineers
BOD	Biological Oxygen Demand
CFD	Computational Fluid Dynamics
COD	Chemical Oxygen Demand
CSO	Combined Sewer Overflow
CSS	Combined Sewer System
DEEP	Déchet Eaux Environment Pollution
DES	Detached Eddie Simulation
DSM-flux	Device for Stormwater and combined sewer flows Monitoring and the control of pollutant fluxes
ENGEES	Ecole Nationale du Génie de l'Eau et l'Environnement de Strasbourg
ENTPE	Ecole Nationale de Travaux Publiques
EPC	European Parliament Council
EU	European Union
HQR	Stage-discharge (H-Q) Relationship
IPCC	Intergovernmental Panel on Climate Change
LES	Large Eddie Simulations
MAE	Mean Absolute Error
MARE	Mean Absolute Relative Error
MDDELCC	Ministère du Développement Durable de l'Environnement et de la Lutte contre les Changements Climatiques
MEDDE	Ministère de l'Ecologie, du Developpement Durable et de l'Energie
MJC	Minister of Justice of Canada
NSE	Nash-Sutcliffe Efficiency index
OME	Ontario Ministry of Environment
OTHU	Observatoire de Terrain en Hydrologie Urbaine
PhD	Philosofiæ Doctor
PISO	Pressure-Implicit with Splitting of Operators
RANS	Reynolds Average Navier Stocks
RMSE	Root Mean Square Error
RNG	ReNormalized Group
RSM	Reynolds Stress Model
SE	Settling-Entrainment tests
SHP	Smoothed Particle Hydrodynamics
SIMPLE	Semi-Implicit Method for Pressure Linked Equations
SUDS	Sustainable Urban Drainage Systems
TKE	Turbulence Kinetic Energy
TKN	Total Kjendal ammonia
TOC	Total Organic Carbon
TSS	Total Suspended Solids
UN	United Nations
URANS	Unsteady Reynolds Average Navier Stocks
US-EPA	United States Environmental Protection Agency
UWWE	Urban Wet Weather Effluents
VOF	Volume Of Fluid
VT	Velocity-Turbulence tests
WWTP	Waste Water Treatment Plant

LIST OF VARIABLES

Q	flow rate
h	water level (from weir crest or from conduit invert)
L	total length of weir crest
L'	length of one weir crest for double weirs
B	channel width
w	weir crest height
S_o	channel slope
θ	flow diversion angle
C_d	discharge coefficient
V	volume
C	concentration
ν	kinematic viscosity
g	gravity
μ	dynamic viscosity
ρ	density
t, T	time
M	mass
u,v,w	instantaneous velocity components
<u>, <v>, <w>	time-averaged velocity components (mean component of u,v,w)
u' , v' , w'	fluctuating component of the velocities u,v,w
<u'v'>, <u'w'>, <v'w'>	time-averaged Reynolds shear stresses
$<u'^2>$, $<v'^2>$, $<w'^2>$	time-averaged Reynolds normal stresses
TKE	turbulent kinetic energy
EMC	event mean concentration
TCM	total collected mass
D50	median diameter
D10	10% percentile diameter
D90	90% percentile diameter
Re	Reynolds number
F	Froude number
We	Weber number

Chapter 1

1. INTRODUCTION

The control of the pollution of aquatic environments due to chemical and biological contaminants carried in urban waters (wastewater and stormwater) is crucial to the protection of water resources, in a context of global changes (increasing water demand, population growth, increasing urbanization, climate change). Indeed, the availability of water resources is strongly related to the water quality: pollution of water sources, like the water bodies receiving urban effluents, may prohibit the use of these and contribute to water scarcity (UN, 2017a). Globally, water demand is predicted to increase significantly over the coming decades, not only due to an increasing demand in the agricultural sector (which represents 70% of the waters abstractions worldwide) but also in other growing sectors like industry and energy production (UN, 2017a). The increase in water demand is also motivated by the growth of the world population: from 7.6 billion in 2017 to 8.6 billion in 2030, 9.8 billion in 2050 and 11.2 billion in 2100, as predicted by the united Nations (UN, 2017b). Accelerated urbanization and the expansion of municipal water supply and sanitation systems contribute to the rising production of urban effluents and their increasing importance within the water cycle. Nowadays, urban population is estimated to 55% of the world population and the United Nations predict that by 2050, urban population will represent 68% of the total world population (UN, 2018). Last prediction on climate change made by the Intergovernmental Panel on Climate Change (IPCC) show that extreme precipitation events over most world regions will very likely become more intense and more frequent as global mean surface temperature increases in the next century (IPCC, 2014). Thus, climate change could further amplify the frequency and magnitude of combined sewer overflows, for example, due to shorter return periods of extreme storm events (Tao *et al.*, 2014) that will exceed easily the sewer capacity.

Urban wet weather effluents (UWWEs) consist of all water flows discharged from drainage systems during a rain event, including untreated combined sewer overflows (CSOs) and stormwater outflows, as well as treated effluents from waste water treatment plants (WWTPs). Pollution coming from UWWEs is, in general, more difficult to control than the urban effluents produced during dry weather, which mainly include the domestic and industrial permanent wastewaters. The reasons are that (i) UWWEs are irregular and challenging predictable flows, (ii) the events that trigger them have a high variability and (iii) there is a lack of knowledge about the source of pollution, as the interest of studying and dealing with this stormwater pollution started later than the interest for the urban dry weather effluents, as the ones from WWTP (Guerber and Tabuchi, 1992). Besides, taking into

consideration the UWWEs pollution needs a global knowledge of the urban catchment (natural environment, climatology, catchment characteristics, urbanism data, etc.) which is not always easy to achieve, as reminded by Guerber and Tabuchi (1992).

The potential impacts of UWWEs on ecosystems and water uses are diverse and their consequences are not negligible (Truchot *et al.*, 1994). Indeed, UWWEs often have a significant impact on the morphology of rivers (bed erosion, solid deposits), on the biochemical composition of aquatic environments (deoxygenation and anoxic shocks, nutrient hyper-eutrophication, micropollutant toxicity, health risks associated with bacteriological pollution), on the perception of these aquatic environments (visual and olfactory pollution) as well as on the uses of this water (drinking water, fish farm, nautical activity) (House *et al.*, 1993; Truchot *et al.*, 1994). The control and minimization of these impacts and their consequences require a better knowledge and control of the pollutant fluxes released by the UWWEs, especially the ones coming from the CSOs.

The next section (Section 1.1) presents the reasons why CSOs water pollution represents a major concern nowadays and the different ways to deal with this source of pollution in both technical and regulatory contexts. In Section 1.2 the current solutions for CSOs pollution monitoring are described, pointing out their main advantages and weaknesses. Section 1.3 presents the DSM-flux as an alternative to the current solutions for CSOs monitoring. Finally, Section 1.4 lists the objectives of this PhD work and explains the general strategy followed to achieve these aims. The general structure of this document is explained at the end of this chapter in Section 1.5.

1.1. CSOs: A PRIORITY WATER POLLUTION CONCERN

During wet weather periods where events with important discharge peaks occur, CSO structures evacuate water surplus that can't be treated by WWTPs and these effluents arrive directly to the natural water bodies without any treatment. CSOs represent a major source of pollution for receiving water bodies as these overflows usually reach the receiving environments with significant pollutant concentrations. Several studies have highlighted the significant role of CSOs as pathways to reach urban receiving waters for various contaminants, such as organic micropollutants (Becouze-Lareure *et al.*, 2016; Launay *et al.*, 2016), especially those highly removed by WWTP (Phillips *et al.*, 2012; Viviano *et al.*, 2017; Weyrauch *et al.*, 2010), inorganic micropollutants (Becouze-Lareure *et al.*, 2016; Weyrauch *et al.*, 2010), nutrients (Becouze-Lareure *et al.*, 2016; Viviano *et al.*, 2017), hormones (Phillips *et al.*, 2012) or bacteria (Passerat *et al.*, 2011; Weyrauch *et al.*, 2010) among others. These studies show the importance of CSOs contribution to both, the annual pollutant loads on the receiving waters and their peak pollutant concentrations during storm events, as well as their impacts on the receiving water bodies. For example, Launay *et al.* (2016) showed that despite the relatively low contribution of CSO to the total annual water discharge (18%), CSO discharges contributed between 30% and 95% of the annual load for 26 pollutants (caffeine, ibuprofen, 16 polycyclic aromatic hydrocarbons (PAHs), phenolic xenoestrogens, and urban pesticides). Phillips *et al.* (2012) also found similar results in their study: composing 10% of the total annual water discharge, CSO discharges contributed between 40% and 90% of the annual load for hormones and organic micropollutants that are otherwise efficiently removed by WWTPs. Phillips *et al.* (2012) also showed that peak concentrations of most of the analyzed pollutants during storm events could reach values up to 10 times higher in CSO than in WWTP effluents. Weyrauch *et al.* (2010) case study at the Spree river in Germany concludes that annual sewage-based substance loads in the river are dominated by CSO for substances with a removal in WWTP higher than 95%. It also showed that during CSO events, some well-removable substances (in the WWTP) like the nitrilotriacetic acid (NTA) can lead to peak concentrations in the receiving river up to 10 times higher than in dry weather conditions. Viviano *et al.* (2017) used caffeine as a marker to identify the CSO contribution of phosphorous to the receiving river during four rain events. For a CSO contribution of around 6.6% of the total river water discharge, 56.5% of the total phosphorous and up to 77% of the total caffeine loads came from CSO. Passerat *et al.* (2011) monitored the changes in the microbiological quality of the river water mass impacted by a CSO in France and they observed that the faecal indicator bacteria (FIB) discharged during the CSO represented between 80 and 100 times the dry weather discharge that the river

receives in that area due to WWTPs. They also observed that during the CSO, concentration of FIB in the receiving waters was between 7 and 9 times higher just downstream the CSO compared to directly upstream, which corresponded to two orders of magnitude higher than the usual dry weather values. Becouze-Lareure *et al.* (2016) studied the spatial-temporal variability of the ecotoxicity in a peri-urban river in France by monitoring different pollutants (total suspended solids (TSS), total organic carbon (TOC), ammonium, 3 metals, and 16 PAHs) and the activity of 4 microorganisms commonly found in aquatic ecosystems. Results highlighted higher concentrations of some pollutants in sections of the river close to the CSO during the storm and significant growth inhibition of the microorganisms especially for the sediment fraction of the samples, downstream of the CSO and during the storm event.

Recovery of receiving water bodies quality requires strategies to mitigate CSO impacts. These strategies can be classified in either preventing actions or corrective actions (Table 1.1), as explained for the UWWEs in general by Chocat *et al.* (2007). Some of the preventing actions to mitigate CSO impacts in particular would involve (i) reducing pollutant emissions at sources conveying to combined sewer systems (CSS) and (ii) reducing the number and magnitude of overflows, for example, (ii-a) by raising the CSO weirs height, (ii-b) by increasing the urban catchment permeability and thereby reducing stormwater runoff volumes (thanks to sustainable urban drainage systems (SUDS), for example)), (ii-c) by improving the CSS management (by integrated modelling or real-time control techniques, for example). Corrective actions mainly imply (i) a better management of CSO quantity and quality (for example, by the construction of devices downstream of the overflow points that will retain part of the pollutants, as CSO retention basins, constructed wetlands or biofilters) and (ii) different remediation measures, like cleaning out campaigns for the removal of contaminated sediments, which are determined according to the importance of the contamination and the sensibility of the ecosystem affected.

Table 1.1. Strategies to mitigate CSO impacts.

Preventing actions (taken before CSO occurs)	**Corrective actions** (taken after CSO occurs)
• Reduce pollutant emissions • Reduce CSOs – Raising CSO weirs height – Increase catchment permeability (reduce stormwater runoff volumes) – Improve CSS management	• Improve CSOs management • Remedial (clean-up) measures

All previous strategies require a better understanding of flow dynamics in the related drainage systems as well as continuous control and reliable monitoring of CSO volumes and pollutant loads. Reliable and accurate CSO data is not only needed before the implementation of these strategies (to assess each case requirements or for design purposes, for example), but they are also needed once these strategies are in operation, in order to assess their performance.

Furthermore, in recent decades, several environmental authorities and governments have encouraged worldwide urban drainage managers to increase the control of CSOs (MDDELCC, 2014; MJC, 2015; OME, 1994; US-EPA, 1994) and to provide reliable data related with CSOs pollution. Since 2006, European Regulation No. 166/2006 (EUPC, 2006) concerning the establishment of a European Pollutant Release and Transfer Register, obliges European Union Member States to report annually the releases to water of any pollutant specified in Annex II of the Regulation for which the applicable threshold value specified in this annex is exceeded. This Regulation obliges the urban drainage managers to implement reliable monitoring methodologies to obtain accurate data of CSO releases, at least for the most important cases. For example, in France, the Ministerial Order DEVL1429608A (MEDDE, 2015a) establishes that urban drainage managers must (i) identify and locate all the discharge points (CSOs) of their sewer systems, (ii) quantify the number of discharges and frequency per year, (iii) self-monitor CSO structures with certain discharge characteristics (specified in Table 1.2), (iv) assess the quality of the receiving waters in some specific cases and (v) transfer all these data to the corresponding national environmental authorities, which will inform annually the European Commission.

Reliable CSOs quantification is also needed to establish appropriate remediation and penalty measures if the levels of pollution exceed the minimum values allowed by law. In these cases, different measures, depending on the pollution level and sensitivity of the receiving waters, are taken by the corresponding authorities. In the European Union, the European Directive 2000/60/EC (EUPC, 2000), known as the Water Framework Directive, presented the first list of priority and hazardous substances to be monitored in surface waters as well as the criteria to maintain a good chemical and ecological status of the surface waters and groundwaters. Following this Directive, the European Directive 2013/39/EU (EUPC, 2013) defines a new list of 45 priority substances, identifying the hazardous ones, and establishes environmental quality standards for most of these compounds, indicated as annual average and maximum allowable concentration values. European Union Member States have environmental regulations including inspection plans to control the pollutant fluxes and to establish the quality standards for the released flows and the receiving water bodies. They also have economic and

administrative instruments to charge effluent discharges and to penalize surplus or unlawful releases. In France, the methods and criteria to assess the status of the surface waters are described in the Ministerial Order DEVL1513989A (MEDDE, 2015a). Ministerial Order DEVL1429608A (MEDDE, 2015a) establishes that monitoring plans of the receiving waters and the quality standards to be guaranteed are defined by the municipal authorities, usually in the Guiding Schemas for the Planning and Management of Waters (GSPMW-SDAGE in French stands for *Schéma directeur d'aménagement et de gestion des eaux*). The same Ministerial Order DEVL1429608A (MEDDE, 2015a) establishes that the Water Police and the Water Agencies are the authorities in charge of the control of the conformity of the drainage systems, including the CSO structures. Conformity criteria for sanitary systems concerning the CSOs are listed in Table 1.3. If the Water Police declare a drainage system as non-compliant, administrative actions are taken in the first place, enforcing the urban drainage manager to elaborate a plan with corrective measures and a schedule for its application. A reduction in the economical aids for water management, called Bonus of Depollution Performance, is also applied. If this plan and its schedule are not followed, legal actions are taken by the corresponding authorities that can lead to fines of 75.000 euros and 2 years of prison for the legal entities responsible of the unlawful releases.

Table 1.2. Rules for self-monitoring of CSOs in France established in Ministerial Order DEVL1429608A (MEDDE, 2015a) and detailed in the Technical Comments associated to this Order. TSS stands for total suspended solids, BOD5 stands for biological oxygen demand in 5 days, COD stands for chemical oxygen demand, TKN stands for total Kjeldahl nitrogen, NH4 stands for ammonium and TP stands for total phosphorous.

CSO POLLUTANT LOAD (PL) (kg of BOD_5/day)	**OBLIGATIONS AT EACH OF THE CSO STRUCTURES**
PL < 120	• No mandatory measures for discharges or pollutant loads.
120 ≤ PL ≤ 600	• Measurement of daily discharge time. • Estimation of the discharged volumes. • Instead of monitoring all the CSO of these characteristics, it can be approved by the municipal authorities to just monitor the CSOs representing at least 70% of the annual volume or fluxes discharged directly to the receiving waters. • No mandatory measures for pollutant loads.
PL > 600	If 10 days of discharge/year: • Continuous measurement and recording of the discharged volumes. • Estimation of pollutant fluxes for TSS, BOD_5, COD, TKN, TP and in some cases NH_4.

Table 1.3. Conformity criteria for drainage systems concerning CSOs in France, according to Ministerial Order DEVL1429608A (MEDDE, 2015a) and defined in the Technical Note DEVL1519953N (MEDDE, 2015b).

DRAINAGE SYSTEMS CONFORMITY CRITERIA CONCERNING CSOs
A drainage system is declared compliant if it guarantees at least one of the following: • Less than 5% of the annual total wastewater volume generated by a conurbation is discharged directly in the natural environment. • Less than 5% of the annual total pollutant fluxes generated by a conurbation is discharged directly in the natural environment. • Less than 20 discharges per year occur for conurbations larger than 2000 equivalent inhabitants. In addition, drainage system releases must also guarantee the minimum quality standards at the receiving waters defined in the GSPMW, based on the Ministerial Order DEVL1513989A (MEDDE, 2015c).

Hence, reliable and accurate CSO data is needed for environmental, technical and legal reasons. The main challenge on the monitoring of CSOs is that overflow structures were not originally built for monitoring purposes. As a result, they often exhibit complex hydrodynamics and the uncertainties associated with the traditional measurement processes, if estimated, usually are considerably high.

1.2. CURRENT SOLUTIONS FOR CSOs POLLUTION QUANTIFICATION

Pollutant fluxes are usually monitored by means of simultaneous measurements of flow rates and pollutant concentrations, which are then integrated in time to obtain volumes and mass loads. A rigorous monitoring implies a continuous measurement of both variables. However, while this is a common practice for the flow rates, the continuous measurements of concentrations are nowadays possible for a limited number of pollutants only (Bertrand-Krajewski *et al.*, 2000).

CSO flow rates are currently estimated by different techniques that can be classified regarding, for example, the CSO structures and surrounding configurations, as shown in Figure 1.1. If hydraulic conditions are favorable in the overflow pipe (uniform flow regime, subcritical flow), CSO flow rates can be measured directly in this conduit, downstream of the CSO structure (measurement location (A)). Two methods are commonly used: stage-discharge relationships (HQRs) or velocity-based methods (VMs). HQRs may be associated with pre-calibrated weirs, pre-designed channels (such as a Venturi or Parshall flume), or any device delivering a rating curve under appropriate flow regimes only needing one water level measurement to obtain CSO measurements, which usually implies low uncertainties for the estimated discharges. However, appropriate hydraulic conditions must be guaranteed and downstream influence must be avoided. Uncertainties in discharges derived from these methodologies are rarely lower than 10% (Joannis *et al.*, 2009). VMs consist in measuring velocities in a selected cross-section of the overflow pipe and the corresponding water level. As for previous water level-based calibrated devices, these methods require specific hydraulic conditions to assume the representativeness of the extracted mean velocities within the selected cross-section. Relative uncertainties in overflow rates obtained by VMs are usually around 20% (Bertrand-Krajewski *et al.*, 2000) and often reach values up to 30% due to *in-situ* factors (Joannis *et al.*, 2009). In addition, flow measurement techniques are intrinsically complicated to deal with as reminded by Melching (2006).

LOCATION	TECHNIQUE	SPECIFIC FEATURES	MAIN DRAWBACKS
(A) Overflow channel	HQR	Pre-designed device	Need specific hydraulic conditions
		On-site calibration	Site-dependent
	VM	-	Representativeness
(B) CSO chamber	HQR	Classical geometry	Need specific hydraulic conditions
		On-site calibration	Site-dependent
			Indirect measurement
(C) Main channel (upstream & downstream from CSO)	HQR	Pre-designed device	Need specific hydraulic conditions
		On-site calibration	Site-dependent
	VM	-	Representativeness
			Double equipment
			Indirect measurement

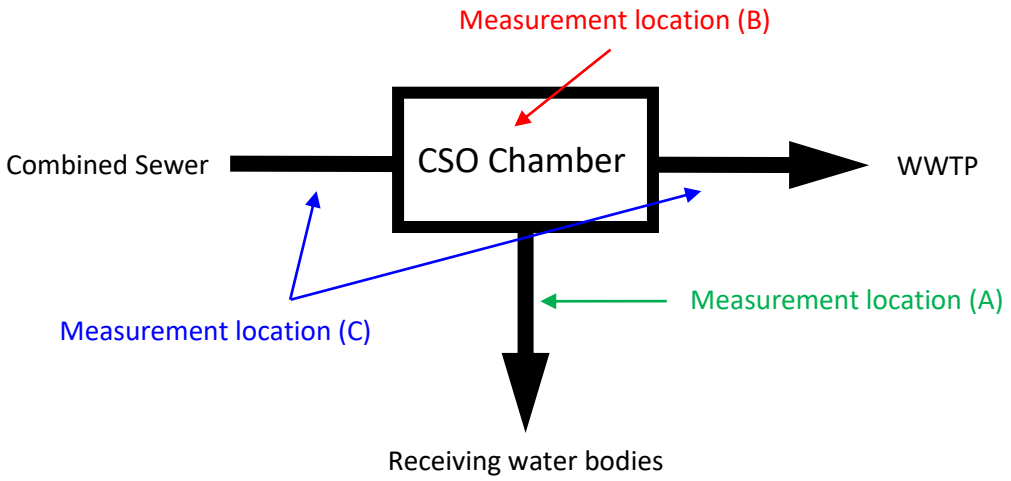

Figure 1.1. Current methods to measure CSOs volumes. Considered techniques: HQR (stage-discharge relation methods) and VM (velocity-based methods).

If it seems difficult to perform measurements in the overflow conduit, two alternatives are usually chosen: either (i) specific HQRs are determined using water levels measured in the CSO chamber (measurement location (B)); or (ii) a balance-based method that enables overflow rates to be obtained by means of the difference between the upstream and downstream flow rates in the main flow pipe is selected (measurement location (C)). The balance-based method has the same limitations as direct measurements in the overflow conduit and it requires double instrumentation, which means that, apart from higher costs particularly related to

maintenance and time needed for the data analysis, uncertainties are also increased because of the double measurement. The specific HQR method is usually more accurate than the balance-based method, particularly if the CSO structure has a geometry that allows the utilization of well-known classical expressions or adapted relations for frontal or lateral weirs. However, in most of the cases, CSO structures have complex geometries, due to maintenance limitations or because they evolve over the years and require a rehabilitation leading to new additional materials such as bricks combined with concrete, new connections with bends or side-walk benches. In these cases, site-specific HQRs must be established. Recent methods use online sensors to estimate overflow rates by means of site-specific HQRs derived from three-dimensional (3D) modelling. Several research groups have applied Computational Fluid Dynamics (CFD)-based methodologies to successfully obtain HQRs for complex CSO structures, defining also the optimal position of the corresponding water level sensors (Fach *et al.*, 2009; Isel *et al.*, 2014; Lipeme Kouyi *et al.*, 2011, 2005). Isel *et al.* (2014) and Lipeme Kouyi *et al.* (2011) estimated relative uncertainty or mean error values around 10% for higher discharges and 30% for smaller overflows obtained by means of these CFD-based methods.

Regarding the monitoring of CSO pollutants concentrations, the most common technique is the analysis of event-based samples at the laboratory following pre-established or normalized protocols to obtain the pollutant concentrations. The reason of its popularity is that this technique can be applied to assess any kind of pollutant, particulate or dissolved, that has a procedure to measure its concentration. Sampling can be manual or automatic and, depending on the time distribution of the samples or sampling frequency (SF) and the sampling volume (SV), Bertrand-Krajewski *et al.* (2000) identify four main sampling strategies (Table 1.4).

One of the main drawbacks of the sampling-based techniques is that the dynamics of the pollutant fluxes are poorly monitored, especially in the case of CSOs, where there is a high and fast variability of the concentrations within the event. Thus, the estimation of the event total mass load is less accurate as the sampling frequency and the total number of samples (for automatic samplers) is limited. Besides, costs of laboratory analysis are significative, and results are obviously lagged, which makes real-time management, automatized control or emergency actions impossible.

Table 1.4. Sampling strategies advantages and drawbacks (adapted from Bertrand-Krajewski et al. (2000). SV stands for Sampling Volume and SF for Sampling Frequency.

STRATEGY	ADVANTAGES	DRAWBACKS
cVcF SV: constant SF: constant	• Simple • Acceptable representation of the flux dynamics if sampling frequency is high enough • Constant sampling frequency • Constant volumes	• Poor representation of the mean pollutant flux
pQVcF SV: proportional to flow rate SF: constant	• Acceptable representation of the mean pollutant flux and flux dynamics if sampling frequency is high enough • Constant sampling frequency	• Needs a flow rate measurement • Variable sampling volume, that can insufficient for analysis or exceed the sampling bottles capacity
pVVcF SV: proportional to flowed volume SF: constant	• Acceptable representation of the mean pollutant flux and flux dynamics if sampling frequency is high enough • Constant sampling frequency	• Needs a flow rate measurement and flowed volume estimation • Variable sampling volume, that can be insufficient for analysis or exceed the sampling bottles capacity
cVpVF SV: constant SF: proportional to flowed volume	• Acceptable representation of the mean pollutant flux • Constant volumes	• Needs a flow rate measurement and flowed volume estimation • Variable sampling frequency, that can be insufficient to represent pollutant flux dynamics during low flow rate periods • Identification of samples in time can be challenging

A preferable option is then a continuous monitoring by means of optical sensors that measure the light scattering or attenuation caused by the matter contained in the water. Two measuring devices are commonly used, according to the measuring principle: (i) the turbidimeters, which measure the reduction of transparency in the water due to the particle or colloidal pollutants suspended in it, and (ii) the spectrometers, which measure the molecular absorption of light by the dissolved pollutants in the water. The pollutant parameters aren't directly measured with any of these optical-based techniques: either turbidity or molecular

absorbance are measured and then these variables are correlated with the pollutant parameters by means of regression methods (some of the most common ones reviewed by Lepot *et al.* (2016). The stability of these relationships depends on the characteristics of the pollutant fluxes that are being measured: if these characteristics (*e.g.*, particles sizes, morphology and distribution, percentage of particulate and dissolved phases of the pollutants, etc) are not constant or stable enough, then the relationships with the optical parameters are not stable neither (Bertrand-Krajewski *et al.*, 2000). Several studies have shown that CSOs pollution is significantly variable in space and even in time (Becouze-Lareure *et al.*, 2016; Launay *et al.*, 2016; Madoux-Humery *et al.*, 2013). Thus, correlations between optical parameters and pollutant concentrations in these cases are site-dependent and temporal variability must be studied at each site (and it should be considered, if significant, in the relationship). This represents the main drawback of this technique, as it introduces an important source of uncertainty and makes this technique difficult to generalize. Besides, to date, only a few parameters (mainly the classical ones: TSS, COD, TOC, DBO_5, nitrates) have been satisfactorily related to optical variables, thus measured accurately by optical sensors: concerning CSO case studies, TSS and COD have been satisfactorily monitored with a turbidimeter by Bertrand-Krajewski *et al.* (2008) as well as with a UV/VIS spectrometer by Gruber *et al.* (2005b). Gruber *et al.* (2005b) also monitored nitrates using the UV/VIS spectrometer, which is a pollutant that presents a well-defined spectrum at a certain wavelength and thus, presents a more stable relationship with absorbance than organic pollutant indicators as COD or BOD, which have a varied molecular composition (Bertrand-Krajewski *et al.*, 2000). Other optical techniques, like fluorescence spectroscopy, have been used to measure organic parameters, including BOD, COD and TOC, for wastewater case studies (Carstea *et al.*, 2016). Fluorescence spectroscopy is similar to absorbance spectrometry but instead of measuring the molecular absorption of light, is the emission of light made by certain components, named fluorophores, that is measured. However, fluorescence spectroscopy doesn't seem to be applied for CSO monitoring as no publications were found in this literature review. This is maybe due to its still relatively low application in sewer systems as wastewater has a complex composition, which might influence and distort the spectra too much to be able to obtain relationships stable enough.

Pollutant concentrations should preferably be monitored at the same point as the flow rates (Figure 1.2). As for the CSO flow rates, the most representative measures are taken at the overflow channel either (i) directly in the channel, when hydraulic conditions are favourable to install the equipment in it and do representative quality measurements; or (ii) indirectly in a

parallel channel, using a by-pass configuration that assures favourable hydraulic conditions and the space needed for the instrumentation. If measurements at the overflow channel are not possible, concentrations are usually measured at the CSO chamber. An interesting technique is to place the sensors on a floating device and submerge their heads at a depth within the water level and the CSO structure crest, so that only the upper water layer is monitored, as done by Gruber *et al.* (2005b) for a CSO monitoring in Graz (Austria). Gruber *et al.* (2005a) explain the advantages and weaknesses of these floating configuration in comparison with the by-pass option. Despite measuring upstream from the CSO structure, the quality of this upper layer is considered to be equivalent to the quality of the overflow. Measuring only the upper layer implies installing a mobile device that can adapt its position according to the water level in the chamber or the main channel. Otherwise, if the sensor is fixed at a lower level (to assure that it is submerged even during dry weather, due to maintenance reasons), measurements might not be representative of the quality of the overflow, as homogeneous mixing conditions are not always met in CSO chambers (there is often a segregation of the pollutants due to the presence of the weir).

Uncertainties associated to pollutant concentration values obtained by sampling-based techniques depend mainly on the sampling strategy and the accuracy of the laboratory analysis whereas the main sources of uncertainty in continuous monitoring with optical sensors are the regression process to transform optical values into pollutant parameters values (which also depends on the sampling-based techniques as a sampling campaign is needed to make these correlations) and the accuracy of the sensor. In both cases, the sampling or measuring location (regarding the sewer system and the cross-section) also influences the level of uncertainty of the data. Bertrand-Krajewski *et al.* (2000) indicate that sampling uncertainties can be of about 20-30% and that laboratory analysis uncertainties for TSS or COD are around 10%. Despite the low uncertainty of optical sensors measurements (1-3% according to Bertrand-Krajewski *et al.* (2000)), Bertrand-Krajewski *et al.* (2000) present a review of different studies that have related TSS or COD concentrations to turbidity or absorbance variables and the estimated uncertainties are between 20 and 35% for cases of different nature of residual waters.

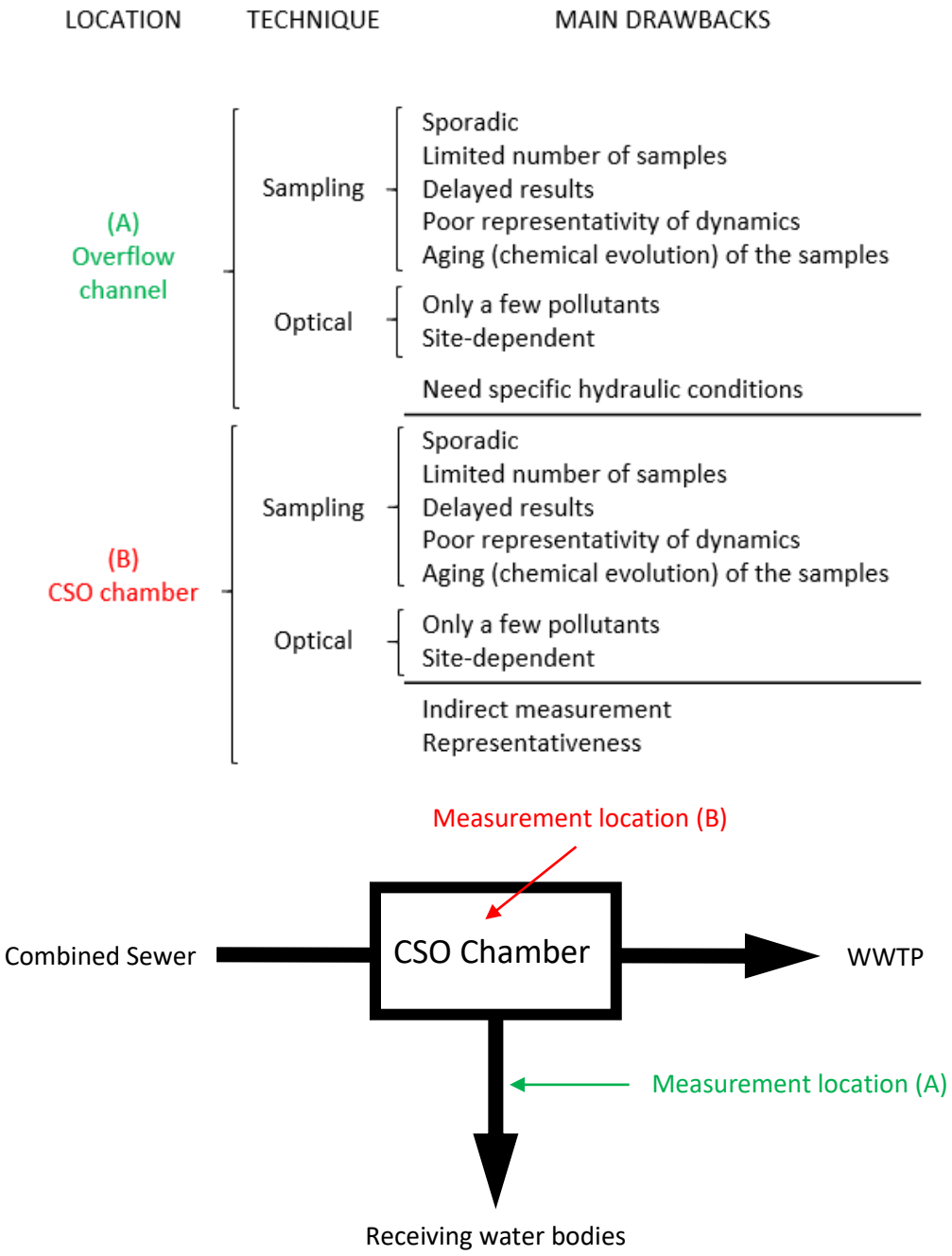

Figure 1.2. Current methods to measure CSOs pollutant concentrations.

Monitoring of pollutant fluxes is done by measuring conjointly CSOs flow rates and pollutant concentrations. From the literature review done in this section, it is observed that HQR methods broadly present lower uncertainties when measuring CSO flow rates. If applied at the CSO structure location, 3D modeling provides very satisfactory results but the obtained HQRs are site-dependent as CSO structures geometries are not standardized. Pre-calibrated devices or available pre-designed channels can be installed in overflow pipes downstream of complex

CSO structures but only under specific hydraulic conditions, *e.g.*, appropriate upstream distance before the implementation of the device or no backwater effect among others. Concerning the pollutant concentrations, the monitoring of CSO quality is more representative if done directly at the overflow conduit, simultaneously with the flow rates, and under hydraulic conditions that assure a homogeneous mixing of the pollutants in the measuring cross-section. Optical-based techniques present the main advantages of providing immediate and continuous results, although establishing relationships between the optical variables and the pollutant parameters needs an on-site calibration with a sampling-based method which can increase considerably the uncertainties on the resulting concentration values. Only a few pollutants have been satisfactory correlated with the optical variables, but researches continue to be able to increase this list. The desirable features for a CSO monitoring device are sum up in Table 1.5.

Table 1.5. Preferable features for current monitoring techniques to control CSOs pollution.

CSO MONITORING DEVICE **Desirable features**
Low uncertainties (HQR)
Continuous (optical sensors)
Generic (pre-design and pre-calibrated)
Representative measures (at discharge channel)
Monitors high number of pollutants

1.3. THE DSM-flux: A NEW ECOTECHNOLOGY FOR CSOs MONITORING

Would it be possible to develop a new technology that regroups some of the best characteristics of the current solutions listed in Table 1.5? What if this monitoring device has retention capabilities to even reduce CSO pollution? Could this new device be pre-design and pre-calibrated, so that it would be easy to install in a wider range of applications?

The **D**evice for **S**tormwater and combined sewer flows **M**onitoring and the control of pollutant **flux**es (DSM-flux), for which the design concept was proposed by Volte *et al.* (2013), represents a new pre-calibrated and pre-designed device to monitor and control the quantity and the quality of CSOs. The DSM-flux has been designed for the purpose of measuring overflow discharges and volumes as well as pollutant concentrations and mass loads. Additionally, thanks to its design, this device also reduces particulate pollutants by sedimentation and mitigates the erosion impacts on the receiving waters by dissipating the flow kinetic energy through turbulence.

The DSM-flux is a rectangular open channel with an original geometry whose dimensions are a function of the internal diameter of the inflow pipe to which the device is connected. Its initial design, shown in Figure 1.3a, was improved by G. Lipeme Kouyi and A. Momplot in the framework of the PhD work of Momplot (2014) et Momplot *et al.* (2014), leading to the current design shown in Figure 1.3b. The DSM-flux is composed by four main zones whose main goal is to allow the device to work properly under various flow regimes at different locations. These zones are, from upstream to downstream: (i) the acceleration and (ii) the energy dissipation areas, which reproduce a geometry based on Smith's stilling basin configuration (Smith, 1988); (iii) the stabilization area, that has a constant cross-section and an optimal length to keep a stable hydraulic jump at the dissipation zone; and (iv) the overflow area, which is formed by an end wall and two converging sidewalls similar to a double sharp-crested oblique weir. Each of the four zones contributes to the principle of operation of the device. First, CSOs entering the DSM-flux accelerate under the supercritical flow regime due to the expansion of the cross-section and the steep slope before the energy dissipation area. Then, the flow experiences a subcritical regime downstream from the hydraulic jump promoted by the blocks of energy dissipation devices. Regarding the one dimensional gradually varied water level, the flow in the DSM-flux is then independent from the upstream hydraulic conditions, which represents one of the main assets of this original design. Besides, this hydraulic jump assures a good mixing of the suspended particles in the flow, which will distribute more homogenously in the cross-section. Velocities decrease progressively in the

stabilization zone and hydraulic conditions become favourable for particle settling. Once the flow reaches the overflow area, the end wall guarantees a downstream control and a stabilized free surface, which creates appropriate conditions for water depth and turbidity measurements. These water depth and turbidity values are related to the discharge rates and total suspended solids (TSS) concentrations respectively, conveyed in the device. As particles are more homogenously distributed after the hydraulic jump, sampling results in this area will also be more representative. Besides, the decrease of velocities makes direct sampling possible.

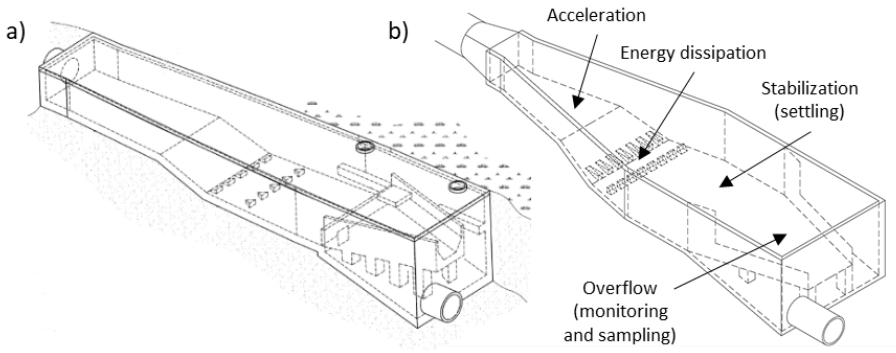

Figure 1.3. 3D view of the DSM-flux (a) initial and (b) current designs.

The design of the DSM-flux is still under development. The optimization process carried out by Momplot (2014) redefined the initial geometry of the DSM-flux according to the following criteria: (i) the water level at the overflow area must be stable and univocally related to the overflow discharge; (ii) the hydraulic jump must be permanently located between the energy dissipation and stabilization zones; and (iii) the stabilization area must allow the settling of particles of similar characteristics to the ones found in combined sewer systems.

This device can be installed at locations where a free flow is guaranteed downstream, including, *e.g.*, overflow conduits, inlets or outlets of WWTPs, or outlet points of separated stormwater drainage system. New constructions and rehabilitated sites are also appropriate as the DSM-flux can be incorporated into a prefabricated manhole that can be inserted in the relating overflow part. Metrology probes as the ones used in this PhD work can also be integrated in the manhole.

The DSM-flux has been designed to meet some of the preferable characteristics for CSO monitoring devices (Table 1.5) and includes additional capabilities as retention or energy dissipation thanks to its original geometry. Furthermore, this new technology is designed to have some advantages compared to other alternatives for monitoring CSO: its measure methodology is independent from the upstream CSOs geometry, it is easy to install on site and

its hydrodynamic characteristics provide appropriate conditions for continuous monitoring and accurate water quality sampling.

1.4. PhD OBJECTIVES AND STRATEGY

The DSM-flux was conceived with the main purpose of monitoring CSOs and pollutant fluxes. Its initial design was optimized in the laboratory by Momplot (2014) by means of experimental tests and numerical simulations but any tests on a field prototype under real operating conditions were carried out. Momplot's work (2014) was mainly focused on the study of the free surface, which determined the current DSM-flux geometry shown in Figure 1.3b as well as a preliminary methodology to measure the overflow discharges from water levels. However, this methodology needed to be refined and validated under different operating conditions. In addition, numerical models used to design the DSM-flux had to be evaluated against experimental data. Only exploratory tests were carried out to assess the retention capabilities of the device, so a detailed analysis of the settling and resuspension mechanisms was suggested to be done in future studies. The present PhD work takes over the baton of Momplot's work (2014) and deals with the aspects that couldn't be addressed, or which needed further evaluation.

The main purpose of this PhD work is to evaluate the DSM-flux capacity to monitor CSOs and thus, to protect the receiving waters by supplying more reliable data as well as by reducing the amount of particulate pollutants discharged. In other words, this study aims to confirm that the DSM-flux performs as it was designed for, and thus answer these two main questions:

(i) Is the DSM-flux a robust monitoring device that provides reliable and accurate flow data?

(ii) Is the DSM-flux capable to efficiently retain particulate pollutants?

A complete answer to these questions would require the analysis of multiple case studies as the performance of the DSM-flux depends on the scale of the device and on the operating conditions specific to the site where it is installed. It is thus understood that this PhD work will only give a partial response to these questions, but it will establish the methodologies and the tools for studying further scenarios in the future. As shown in Figure 1.4, a multiscale approach was considered in order to evaluate the DSM-flux behaviour, where 3 systems from different nature (physical/virtual) were analysed under different operating conditions (laboratory/virtual/real site-specific) at two different scales (small/large).

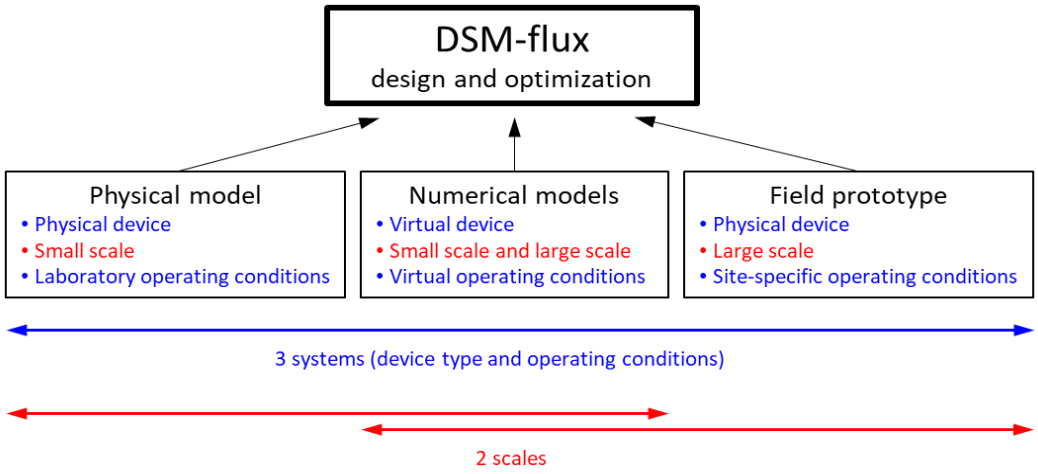

Figure 1.4. Schematic of the approach followed in this PhD work.

The reason for adopting a multiscale approach is that each of the systems has a its strengths and weaknesses to answer the questions, as shown in Figure 1.5, and it is believed that the study of the 3 systems and 2 scales, as well as the relationships among them, will provide the most generic and realistic answer that is possible to obtain within the limits (of time and resources) of this PhD work.

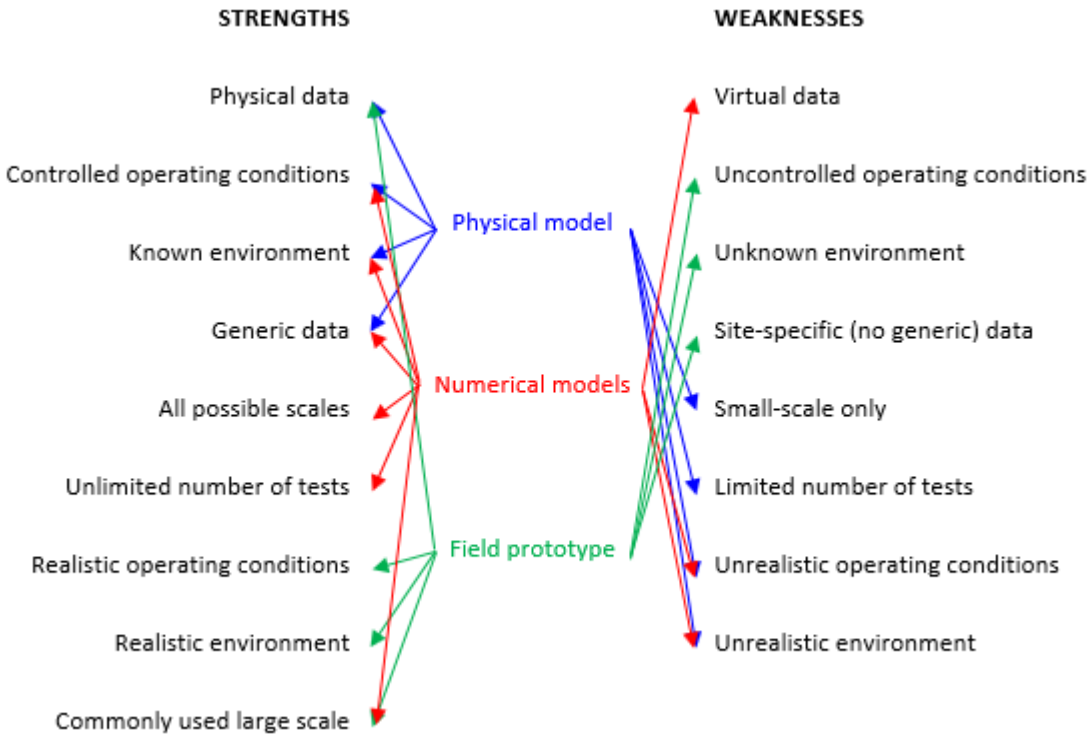

Figure 1.5. Strengths and weaknesses of each of the three systems used in this PhD work.

The strengths and weaknesses that each of the systems has when trying to answer the questions can be explained as follows:

(i) the performance of the field prototype would represent the most realistic results but the access to the device is not possible during the storm events (only autonomous monitoring is possible), the operation conditions are specific to the site (difficult to generalize) and the time of the study (only a few scenarios to be studied) and the system is influenced by multiple factors that can't be controlled or are even unknown (type of pollutants arriving to the device, local hydraulic effects due to the sewer configuration, varying boundary conditions).

(ii) the small-scale physical model provides realistic results because of its physical nature and allows the study of scenarios under controlled operating conditions. However, the scale of the device is smaller than the most commonly used and it is not possible to build other physical models, specially of larger scales, due to obvious space and resources constraints. Besides, the number of scenarios than can be tested is limited according to the laboratory facilities.

(iii) the numerical model provides virtual results that should always be validated, if possible, with experimental data to increase the degree of confidence on the results and confirm that the real physics are represented with the level of accuracy needed. The numerical simulations allow the testing of different device scales under a large variety of scenarios, which will however remain physically unreal.

The final goal being to analyse the performance of the device working under realistic operating conditions at a common scale, each of the questions has been addressed following a common strategy, which can be divided into three major stages, as schematized in Figure 1.6. At first, the small-scale physical model of the DSM-flux was studied in the laboratory under controlled conditions. The experimental data from the tests on this small-scale physical model allowed, on the one hand, a better understanding of the hydrodynamic behaviour of DSM-flux and, on the other hand, an accurately parametrization, testing, improvement and validation of the equivalent 3D numerical model initially used to design the ecotechnology, thanks to the application of Computational Fluid Dynamics (CFD). In a second step, the numerical models evaluated at the small-scale DSM-flux were used to simulate the behaviour of the large-scale field prototype. The analysis of these simulated results enables to assess possible scale effects on the phenomena of interest. In a final step, the field prototype installed *in situ* was equipped and monitored with autonomous devices in order to validate the results derived from the laboratory models by means of the measurement of certain variables under certain operating conditions. Once the scaling methodology will be validated, the large-scale numerical model

(or equivalent models with other scales) could be used to evaluate and predict the ability of DSM-flux to protect aquatic environments under any operating conditions.

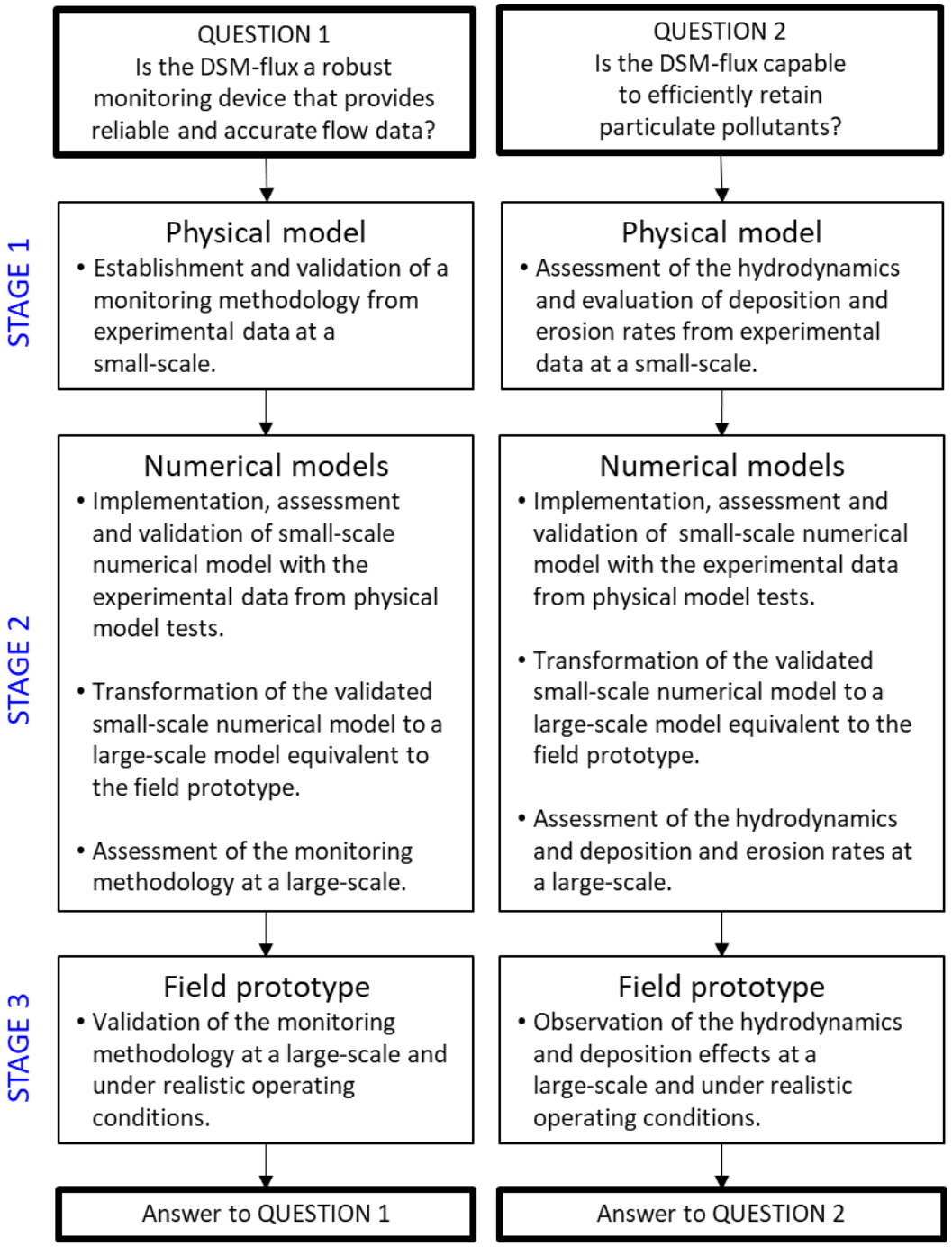

Figure 1.6. Stages of the strategy followed to answer each of the two questions of this PhD work.

In Figure 1.6, it should be noticed that "monitoring methodology" refers to the monitoring of flow rates (and volumes). The DSM-flux is also conceived to monitor pollutant fluxes by means

of turbidity measurements that will be correlated to pollutant concentrations to estimate the pollutant fluxes in combination with the flow rate values. As explained in Section 1.2, these turbidity-pollutant concentration relationships are site-specific and must be calibrated in the field for each case study. Thus, it should be understood that question 1 only deals with flow rates and no generic methodology for pollutant monitoring is presented in this PhD work. Some recommendations to be considered for this turbidity-pollutants calibration can be found in Bertrand-Krajewski *et al.* (2008), which are the guidelines that are planned to be followed for the calibration of the DSM-flux turbidimeter. Furthermore, as it will be observed in Chapter 4, stage 2 of question 2 could not be completed within the time of this PhD work, the reasons being explained in Section 4.2, but it's included in the flowchart for a better understanding of the overall strategy.

The originality of this PhD work is that the questions addressed have been studied following a multiscale approach where results obtained in a device of a certain scale have been reproduced on an equivalent model but of different nature. Then, the device has been scaled and the key hydrodynamic mechanisms have been studied in a larger device, bringing to light not only the relationships between different scales (similarity laws and scale effects) but also the relationships among systems of different nature. All this information will contribute to the knowledge of the DSM-flux behaviour and the improvement and optimization of its design.

1.5. STRUCTURE OF THE DOCUMENT

This PhD thesis has been structured as follows: in **chapter one**, a general introduction to the study is followed by a presentation of the problematic issues addressed in this work and a review of the current solutions. Then, the DSM-flux device is described in detail as a good alternative to current solutions. The main objectives of this PhD work are also presented in chapter one as well as the overall strategy followed to achieve them.

As explained in Section 1.4, two main questions are addressed in this PhD work and to study them, a multiscale approach has been adopted, analysing 3 different systems at 2 to different scales. **Chapter two** describes the main features of each system at the two different scales.

Chapters three and four respond to the questions one and two addressed in this PhD work, respectively. The sections in each chapter correspond to the different steps of the methodology described in Section 1.4 and they present and discuss the results obtained for each of the questions. At the beginning of each chapter's section, the materials used and the specific methodology followed at that part of the study are described. At the end of each section, a final subsection collects the main conclusions issued from that part of the study.

Chapter five presents the main conclusions of this PhD work as well as the perspectives that have been identified, suggesting future lines of research.

Final **chapters six and seven** collect the references and appendices of this work, respectively.

Chapter 2

2. A MULTISCALE APPROACH: THE THREE DSM-FLUX SYSTEMS

In this PhD work, a multiscale approach was considered to answer the scientific questions addressed in the study. As explained in Section 1.4, the DSM-flux was analysed in two different scales: (i) a small-scale, appropriate for experimental tests at the laboratory, and (ii) a large-scale, which is more representative of the device that would be installed in a standard sewer system. Three systems of different nature were used to assess the scaled devices: the small-scale DSM-flux was reproduced with a physical and a numerical model and the large-scale DSM-flux was also reproduced with a numerical model and with an equivalent field prototype.

The following sections describe in detail each of the DSM-flux systems represented in two scales. The small-scale systems are presented in Section 2.1. The first part of this section describes the experimental set-up and instrumentation of the small-scale physical model whereas the second part presents the main characteristics considered to implement the small-scale numerical model as well as the different types of models and numerical options that have been tested. The large-scale systems are presented in Section 2.2. As the large-scale numerical model is adapted from the small-scale numerical model, only the characteristics that differ from the former one are described in detail in the first part of the section. Different large-scale numerical models have also been tested and are described in the first part of Section 2.2. As for the field prototype, the last part of this chapter describes the main features of the hydrological catchment where it is installed, the hydraulic configuration of the site and the instrumentation used to monitor the field prototype.

2.1. THE SMALL-SCALE PHYSICAL AND NUMERICAL MODELS

The small-scale DSM-flux design is issued from Momplot's work (2014) as described in Section 1.3 (Figure 1.3b). A 0.15 m inflow pipe was selected for the physical model of this study and this diameter determined the small-scale device dimensions, which are specified in Appendix 7.1.1. To connect the DSM-flux to the inflow pipe, a 0.21 m transition is used between the end of the inflow pipe and the entry of the DSM-flux which ensures a progressive change from a circular to a rectangular cross-section (2.1). The specific characteristics of the configuration upstream and downstream from the device at the physical and numerical models are described in the following subsections.

2.1.1. The small-scale physical model experimental set-up

A schematic of the experimental set-up of the small-scale physical model of the DSM-flux is shown in 2.1. A detailed plan of the whole system is also included in Appendix 7.1.2. The DSM-flux is made of polyvinyl chloride (PVC), with a transparent lateral wall, and it lays on a stainless-steel water supply basin. A pump sends clean water into a small stilling tank that feeds by gravity the DSM-flux through the inflow conduit of 0.15 m interior diameter. The inflow pipe is made of stainless-steel and has an adjustable slope. At 0.875 m (around 6 pipe diameters) upstream from the DSM-flux entry, there are 0.75 m (5 pipe diameters) of the inflow pipe that are removable so that it is possible to introduce singular elements potentially needed for the tests. These elements, as well as the 0.21 m transition connecting the inflow pipe and the device, are also made of stainless-steel. After passing through the DSM-flux, water flows towards a drainage basin and then, through an outflow 0.1 m diameter pipe, it returns to the water supply basin to refeed the system.

The physical model is instrumented with two electromagnetic flowmeters (Proline Promag 10L from Endress-Hauser; maximum measurement error of ± 2.5% of the measured value decreasing to ± 0.5% for the greatest discharges) located in the inflow and outflow conduits. Only the data from the flowmeter upstream the DSM-flux device was used in this PhD work. The maximum flow rate of the system is 0.01 m^3/s.

The instrumentation and the experimental set-up were adapted according to the type of tests carried out at each stage. A modifiable structure was installed on the water supply basin surrounding the DSM-flux device in order to support, for example, water level radars or other types of probes.

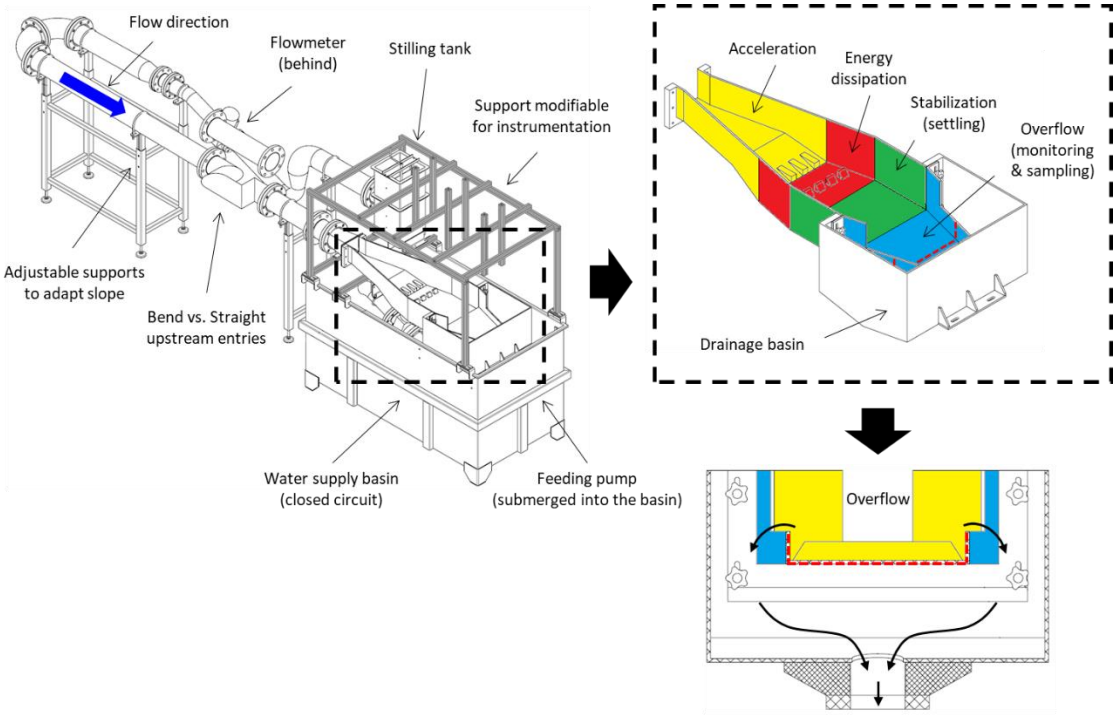

Figure 2.1. Schematic of the experimental set-up for the small-scale physical model. Zoom views of the DSM-flux with its different zones and of a cross-section of the overflow part that is enclosed in the draining basin.

In 2.1 it is observed that the inflow conduit has a 180º curve at the middle of its length. This is because, due to space limitations and to the close-circuit configuration of the experimental set-up, the stilling tank must be located next to the DSM-flux, above the water supply basin. It should be noticed that the section of pipe downstream from the curve is long enough (the equivalent of 25 pipe diameters) to consider that the flow is fully developed and free of the effects from the curve at the entry of the DSM-flux device. The upstream pipe section includes a siphon element so that a full cross-section is ensured for the flowmeter measurements.

2.1.2. The small-scale numerical model

Most of the commercial CFD softwares resolve by means of numerical methods a simplified version of the partial differential equations of transport (convection-diffusion equations) based on the conservation laws of physics: continuity (mass transport) and momentum transport equations, the equations governing flow motion. To solve these equations space (and time) domains are discretized and according to the type of discretization, there are different types of

solvers. In this PhD work, the numerical models have been implemented in the commercial CFD solver ANSYS Fluent. This software is based on a finite volume discretization method and its numerical approach can resolve many different flows including 3D multiphase turbulent flows as the one of the DSM-flux. ANSYS Fluent CFD code has been widely tested in urban hydrology to model different hydraulic flows, also in sewer systems applications (Dufresne *et al.*, 2009; Isel *et al.*, 2014; Jarman *et al.*, 2008; Lipeme Kouyi *et al.*, 2005, 2011; Momplot *et al.*, 2017).

ANSYS Fluent is based on the Reynolds-Averaged Navier-Stokes (RANS) equations, which consists of Navier-Stokes equations defined for viscous flows, averaged in time and whose variables have been decomposed in a mean and a fluctuating component. The continuity equation is also averaged in time and defined with decomposed quantities. Although ANSYS Fluent accounts for density fluctuations, flows studied in this PhD work have been considered incompressible, so density is considered constant. Furthermore, all simulations carried out in this PhD work reproduce steady problems, so the large-scale fluctuations of the variables with time are not modelled neither.

There are different mathematical models to represent the real physics of the simulated flows and the choice for each case study can be somehow subjective, especially when modelling complex flows, where the convenience or performance of the models is more difficult to assess. Apart from the fundamental equations governing the flow motion, numerical results depend on (i) the accuracy of the geometry representing the hydraulic structure conveying the flow, (ii) the type, size and density of the computational mesh, (iii) the boundary conditions, (iv) for turbulent flows, the turbulence model, (v) for bounded flows, the near-wall treatment or the modelling of the flow behaviour near solid boundaries, (vi) for multiphase flows, the modelling of the interaction between the two phases, (vii) numerical option related to the algorithms used in the computations, as the type of algorithm for the pressure-velocity coupling, (viii) the type of discretization schemes to transfer the variable values through the mesh elements and (ix) the convergence criteria, which will determine the end of the iterative computations. As for the mathematical models, there are only very general guidelines about the best way to implement models and to carry out simulations in order to improve accuracy of results as much as possible. In complex flow cases, the only way to determine the most appropriate models and numerical options is by testing different combinations recommended in the literature, comparing the different results with experimental data and validating the one that better represents the real physics. This was the strategy followed in this PhD work, as explained in Section 1.4. Three different small-scale numerical models were implemented with

different combinations of numerical options (near-wall treatment) and types of space discretization (meshes). Table 2.1 presents their main characteristics. In the next subsections, the reasons behind the selection of these three models in particular are discussed and the features of the numerical model settings are broadly explained. Further detail about the models and software algorithms can be found in Versteeg and Malalasekera (2007) and the Fluent Theory Guide (ANSYS, 2015a).

Table 2.1. Main features of the small-scale numerical models. RNG=ReNormalization group; SCWF=Scalable Wall Function; EWT=Enhanced Wall Treatment; 2UW=Second order upwind; LSCB=Least Squares Cell Based; BFW=Body Force Weighted; MHRIC=Modified High Resolution Interface Capturing; SIMPLE=Semi-Implicit Method for Pressure-Linked Equations; VOF=Volume Of Fluid; VI/MFI=Velocity/Mass Flow Inlet; PO=Pressure Outlet; FX=Fixed Wall; SR=Scaled Residuals; MFB=Mass Flow Balance.

MODEL	MESH	TURBULENCE MODEL	NEAR-WAL TREATMENT	DISCRETIZATION SCHEMES	VELOCITY-PRESSURE CLOUPING	FREE SURFACE MODELLING	BOUNDARY CONDITIONS	CONVERGENCE CRITERIA
SM-A	MS1	RNG k-ε	SCWF	2UW LSCB BFW MHRIC	SIMPLE	VOF	VI PO FW	SR < 10^{-3} MFB < 3%
SM-B	MS2	RNG k-ε	EWT	2UW LSCB BFW MHRIC	SIMPLE	VOF	MFI PO FW	SR < 10^{-3} MFB < 3%
SM-C	MS3	RNG k-ε	EWT	2UW LSCB BFW MHRIC	SIMPLE	VOF	MFI PO FW	SR < 10^{-3} MFB < 3%

Computational meshes

Concerning the spatial domain, the DSM-flux numerical model consists of the DSM-flux device, the upstream inflow pipe and the transition that connects the end of the pipe to the entry of the device (Figure 2.2). The geometry and dimensions of the three elements for the numerical models are the same as the ones of the physical model (Appendix 7.1.1. and Appendix 7.1.2),

considering only the section of the inflow pipe downstream the curve. At the outlet of the device, two hexahedral blocks (one for each overflow side) have been added downstream the whole length of the two weir crests, covering from the crest height to the device height (Figure 2.2). This will allow the model to reproduce more accurately the free surface of the flow over the weirs.

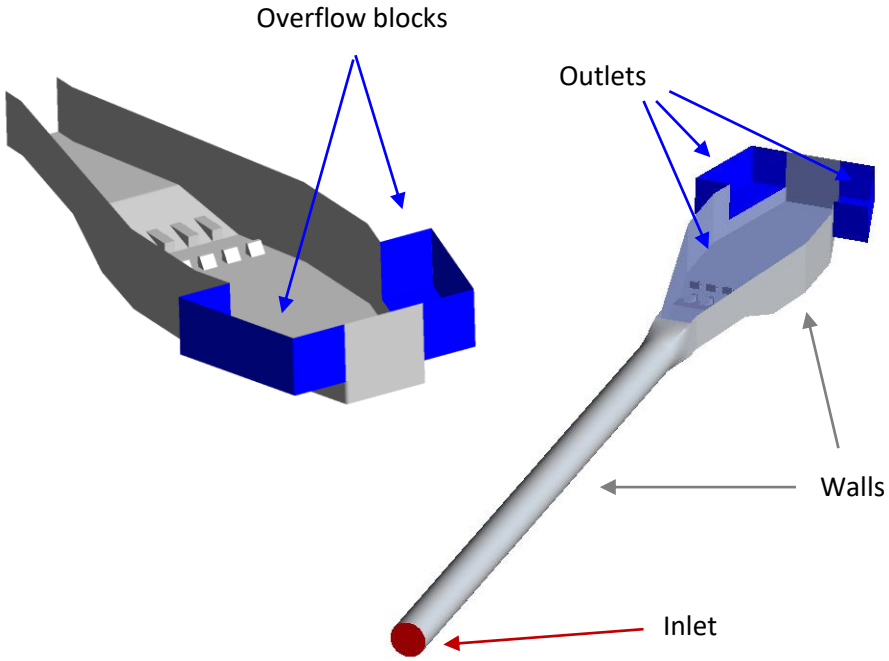

Figure 2.2. 3D view of the small-scale numerical model's domain. Inlet and outlet boundaries in red and blue respectively. The rest are wall boundaries. Zoom of overflow blocks.

Three different structured meshes were used to discretize the domain in hexahedral elements. This type of mesh has several advantages compared to the unstructured one. Firstly, as indexes of the elements are better organized and it is easier to find neighbouring cells, they use less computer memory and compute faster (Andersson *et al.*, 2011). Furthermore, according to Biswas and Strawn (1998) and Hirsch (2007), cited by Bayon *et al.* (2016), structured meshes are generally more accurate than unstructured meshes. Bayon *et al.* (2016) also add that topologically orthogonal meshes tend to cause less numerical issues in multiphase flows, especially when oriented with the main flow's direction. The computational meshes were created according to different meshing strategies. Mesh MS1 followed a simpler meshing strategy leading to a coarser mesh which implies less meshing and computation times. Meshing strategy used for mesh MS2 is slightly more complex and takes more time to implement but it is expected to reproduce physics more accurately as its quality is slightly better and has a higher order of discretization. Mesh MS3 meshing strategy is the same as MS2

but the density of the elements is larger (finer mesh). The characteristics of each of the meshes used as well as some quality parameters are indicated in Table 2.2. Some detail views of the meshes are presented in Appendix 7.1.3.

Table 2.2. Characteristics of the computational meshes of the small-scale numerical models.

MESH CARACTERISTICS	MESH MS1	MESH MS2	MESH MS3
Connectivity	Structured	Structured	Structured
Interior interfaces	No	Yes, non-conformal	Yes, non-conformal
Element shape	Hexahedral	Hexahedral	Hexahedral
Number of elements	585.000	3.800.000	7.500.000
Min side length (m)	$9.3\cdot10^{-4} – 1.0\cdot10^{-2}$	$2.6\cdot10^{-4} – 1.6\cdot10^{-2}$	$2.9\cdot10^{-4} – 5.9\cdot10^{-3}$
Max side length (m)	$5.2\cdot10^{-3} – 3.3\cdot10^{-2}$	$4.9\cdot10^{-4} – 2\cdot10^{-2}$	$5\cdot10^{-4} – 1.6\cdot10^{-2}$
Volume (m^3)	$1.4\cdot10^{-8} – 2.6\cdot10^{-6}$	$3.4\cdot10^{-11} – 3.1\cdot10^{-6}$	$1.8\cdot10^{-10} – 1.8\cdot10^{-7}$
Quality indicators			
Min Ortogonal quality	**0.07** 0.2 (> 99.6%)	0.31	0.31
Max aspect ratio	58 40 (> 99.8%) 20 (> 99.2%) (Mean = 5)	55 40 (> 99.75%) 20 (> 95%) (Mean = 9)	32 20 (> 99.5%) (Mean = 5)
Min angle (°)	**5** 9 (> 99.7%)	18	18
Max Skewness	**0.97** 0.75 (> 98.6%)	0.69	0.69

The main difference among the meshes lies on the number of elements, which is significantly higher for meshes MS2 and MS3, that have 6 and 13 times the number of elements of mesh MS1, respectively. Some mesh size metrics (described in ICEM manual (ANSYS, 2016a)) are indicated in Table 2.2 as a reference for comparison. These differences in the number of elements are the consequence of a progressive refinement made in these two meshes at the dissipation zone that spreads a certain distance to the adjacent upstream and downstream areas (Figure 2.3). In order to keep this refinement local, so that the number of elements doesn't increase too much, these meshes have also 4 (MS2) and 5 (MS3) non-conformal interior interfaces (zoom in Figure 2.3). In this type of interface, the number of computational nodes at one side is a power-of-two times (usually 2) the number of nodes at the other side.

Variable values at the coarser element are a weighted combination of the values of the smaller cell. For MS2 and MS3, the density of mesh elements has been increased close to the weirs crests to try to reproduce more accurately the overflow nappe shape.

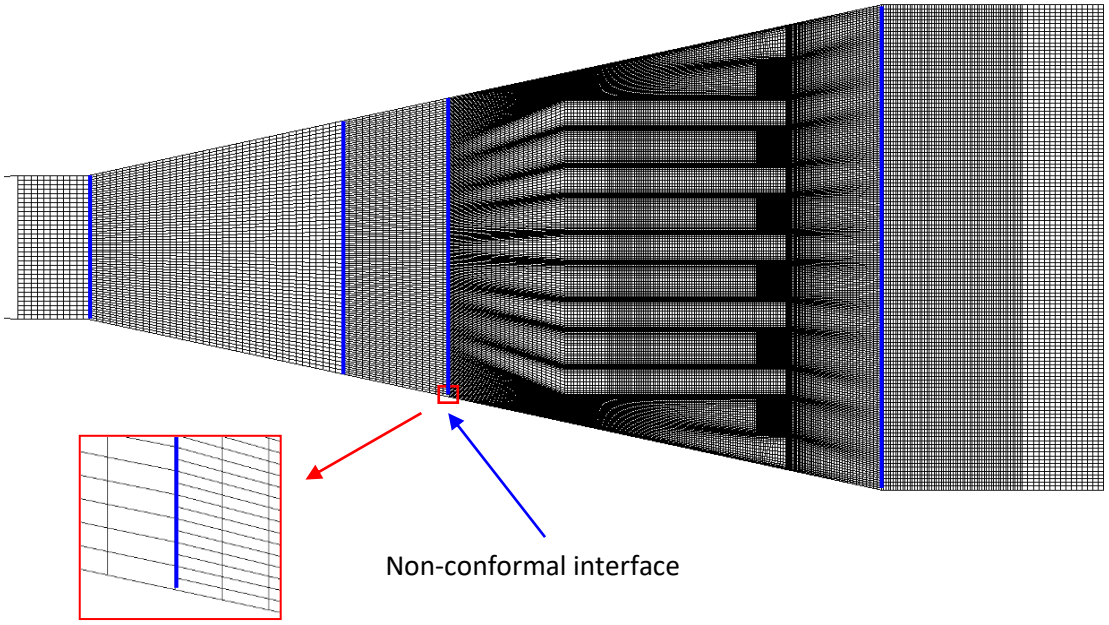

Figure 2.3. Detail view of the refinement of mesh MS3 done at the dissipation zone and adjacent areas up and downstream. Zoom of the non-conformal interface where the number of nodes upstream is half the number of nodes downstream.

Mesh quality is also different among the meshes. Mesh quality indicators as the orthogonal quality (OQ), aspect ratio (AR), elements face angle and skewness are common indicators used by ANSYS to check the quality of the mesh and their definitions are found in the software manual (ANSYS, 2015a). In general, the OQ ranges from 0 (bad) to 1 (good); AR ranges from 0 to infinite, being 1 the ideal value; face angles ranges depend on the type of face elements (0-60 degrees for triangles, 0-90 degrees for quadrilaterals) and usually the higher the values are, the better; and skewness ranges from 0 (good) to 1 (bad). The thresholds to determine if a mesh has a good quality to avoid convergence and numerical diffusion problems are not fixed and depend on the flow characteristics, the location of the bad quality elements and the solvers algorithms. ANSYS Fluent User's Guide (ANSYS, 2015b) recommends a minimal orthogonal quality of 0.01 and a maximum skewness of 0.95. ANSYS Fluent Meshing Guide (ANSYS, 2015c) specifies that meshes with skewness over 0.75 start being considered as poor quality meshes, so it would be recommended to have as few as possible elements over this threshold. Ozen (2014) states in his ANSYS workshops that minimal OQ of 0.15-0.2 should be

considered for the mesh to be acceptable. No indications are given for the minimum angles or AR but in ANSYS CFX Software Guide (ANSYS, 2016b) indicates minimum angles of 10 degrees and maximum AR of 100. Based on these values for the selected indicators, meshes MS2 and MS3 are considered good quality meshes as they respect the previously mentioned quality criteria. Mesh MS3 has a slightly better AR which can help with convergence. Mesh MS1 has minimal and maximal values of quality indicators (highlighted in red in Table 2.2) that don't respect the recommendations from literature. However, as only a low percentage of the elements are of low quality (less than 2%), the mesh has however been tested to analyse if results are influenced by the lower refinement and the few low-quality elements. The maximum AR of the three meshes are far from 1 but their average values for all elements manifest that these relatively high values are not the common tendency. If an AR of 40 is considered as the maximum acceptable AR (a bit less than half the maximum recommended of 100), it is observed that, for the three meshes, only a low percentage of the elements (< 0.3%) exceed this threshold (Table 2.2).

Simulation results depend on the mesh resolution, so a mesh sensitivity analysis should always be done to ensure that further mesh refinement does not modify the results significantly. The optimum mesh size is case specific, but a generic methodology as the Grid Convergence Index (GCI), presented by Roache (1997), can be used to carry out a grid convergence study and determine if a finer mesh would vary the solution. The GCI method is based on generalized Richardson Extrapolation and it basically estimates the discretization error of a converged solution by analysing at least two meshes of different size. The discretization error should decrease as the mesh refinement increase until an asymptote is reached, where further refinement does not improve the solution. If the discretization error of the finer grid of the study is located in that asymptote, it can be considered that the solution won't be sensitive to further mesh refinement. For the study to be significative, the grid refinement rate should be at least of 1.1 (recommended by AIAA (1998)) or 1.3 (recommended by Celik et al, (2008). Celik *et al.* (2008) describes step by step the procedure suggested to American Society of Mechanical Engineers (ASME) journals authors. As it will be observed in the next chapters, in this PhD work, solutions issued from different size meshes were compared to assess the differences, but no generic method as the GCI was applied to study the grid convergence due to different (and opposed) reasons. In the study of the DSM-flux monitoring methodology (chapter 3), numerical results from the three meshes were almost the same and all of them represented accurately enough the experimental data with insignificant divergences. In the study of the DSM-flux hydrodynamics (chapter 4), numerical results diverged more among the

meshes, especially between MS1 and MS2. However, all the solutions were considered too far from the experimental data and, as differences between MS2 and MS3 didn't seem significative, it was concluded that the mismatching was caused by other factors and other numerical options should be tested.

Flow and turbulence equations of the mean flow

Most of the flows in urban hydrology applications are turbulent flows. Turbulent flows can be described as chaotic and random flows where velocity and pressure quantities change continuously in time and space (Versteeg and Malalasekera, 2007). This motion state appears for high Reynolds numbers and it is caused by perturbations on the flow that result in the mixing of the different flow particles and formation of multiple scale eddies. Andersson *et al.* (2011) and Versteeg and Malalasekera (2007) describe in detail the characteristic features of turbulence, which can be summarized as: (i) irregularity (random and chaotic flows that consist of a wide range of length scales, velocity scales and timescales); (ii) diffusivity (faster mixing rates of species, momentum and energy than the rates of molecular diffusion); (iii) instability at large Reynolds numbers (that occurs when the timescale for viscous damping of a velocity fluctuation is much larger than the timescale for convective transport); (iv) three-dimensional structures (as mechanisms such as vortex stretching and vortex tilting cannot occur in two dimensions); (v) dissipation of turbulent kinetic energy (as large eddies are unstable and break up into smaller eddies, thereby transferring the energy to smaller scales, which similar break-up processes and transfer the energy to yet smaller eddies until reaching the smallest scale, where the dissipative eddies energy is dissipated into heat by viscous action due to molecular viscosity. This fact increases the energy losses in turbulent flows); (vi) continuum (even the smallest scales of turbulence are much larger than the molecular length scale); and (vii) anisotropic (for the largest eddies that are highly dependent to the mean flow) and isotropic (for the smallest eddies due to viscosity action).

Properties of turbulent flows, for example the u velocity, can be decomposed into a steady mean value <u> and a fluctuating component u', whose time average value is zero by definition (Figure 2.4). Thus, turbulent flows can be characterised by the mean values of the flow properties and the statistical properties of their fluctuations. Mean values are obtained from Equation 2.1:

$$\Phi = \frac{1}{\Delta t}\int_0^{\Delta t} \varphi(t)dt \qquad \textbf{\textit{Equation 2.1}}$$

where φ is the instantaneous flow property depending on time t and ϕ is the mean of the flow property in the Δt time interval, which must be large enough to represent the slowest variations of the property.

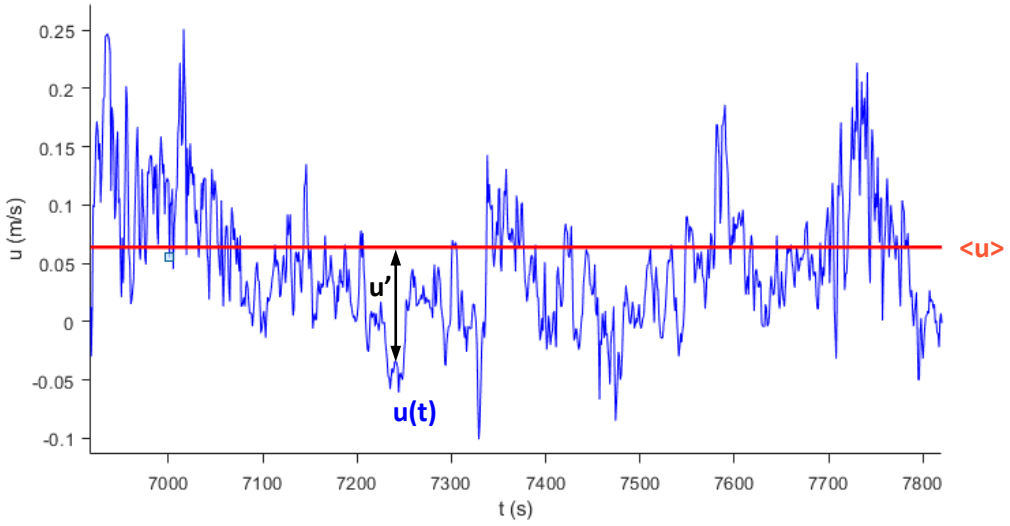

Figure 2.4. Instantaneous u velocity time series with decomposition in mean <u> and fluctuating u' components.

As indicated in the introduction of this section, ANSYS Fluent solves RANS equations, which average in time Navier-Stokes equations. Based on the previous decomposition of the flow properties, this averaging creates new unknowns, the Reynolds stresses, which are different combinations of products of the velocity fluctuations multiplied by the flow's density and averaged in time. As the total number of unknowns exceed the total number of equations and the fluctuating terms are not resolved with RANS, turbulence models are needed to model these terms and close the problem. Versteeg and Malalasekera (2007) describe in detail all the fundamental equations behind this CFD approach.

There are different turbulence models based on time-averaged Reynolds equations and most of them are implemented in ANSYS Fluent. Figure 2.5 (from Andersson *et al.* (2011)) presents a schematic overview of the turbulence modelling, including the ones based on the time-averaged Reynolds equations (RANS-based models in the figure). A detailed description of each of them can also be found in Versteeg and Malalasekera (2007) or Andersson *et al.* (2011) and their implementation in the software is explained in the Fluent Theory Guide

(ANSYS, 2015a). In this PhD thesis, only the turbulence equations considered in the study will be presented.

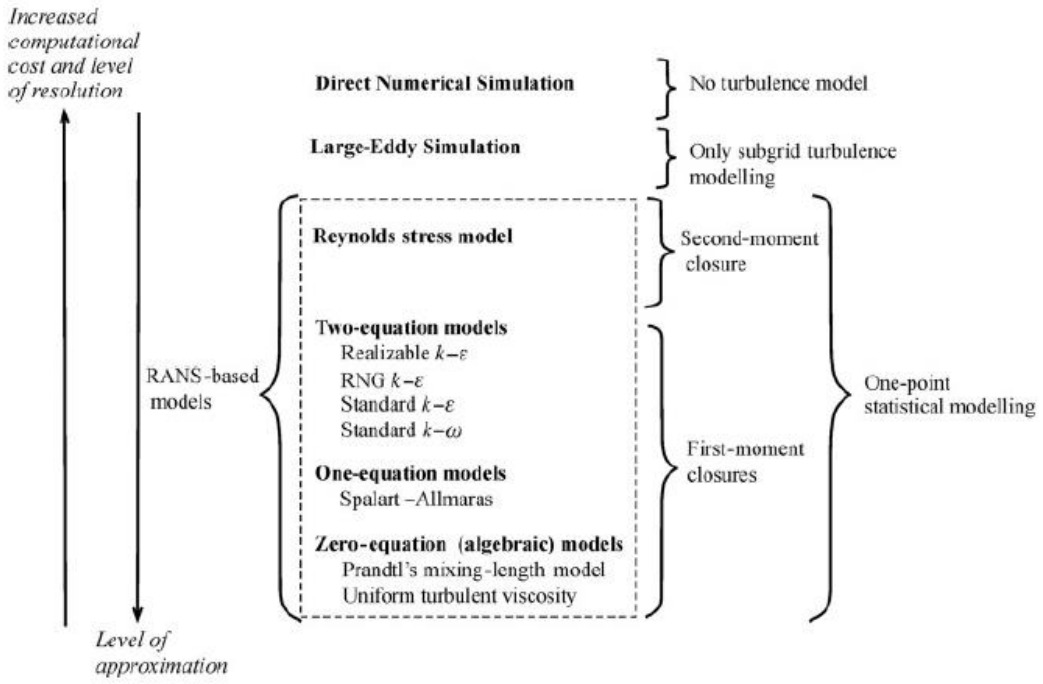

Figure 2.5. A schematic overview of turbulence modelling (from Andersson et al. (2011)).

In general, these time-averaged models can be classified in two main categories: (i) turbulent models based on Boussinesq hypothesis (first-moment closure) and (ii) the Reynolds Stress Model (RSM) (second-moment closure). The Boussinesq hypothesis presumes that there is an analogy between the action of viscous stresses and the Reynolds stresses on the mean flow and, thus, defines the Reynolds stresses as proportional to the mean rates of deformation of the fluid elements (Versteeg and Malalasekera, 2007). For incompressible flows, Equation 2.2 is used:

$$\tau_{ij} = \rho\langle u_i' u_j' \rangle = \mu_t \left(\frac{\partial \langle u_i \rangle}{\partial x_j} + \frac{\partial \langle u_j \rangle}{\partial x_i} \right) - \frac{2}{3}\rho k \delta_{ij} \qquad \textit{Equation 2.2}$$

where $\langle u_i' u_j' \rangle$ is the time-averaged Reynolds stresses, ρ is the fluid density, μ_t is the turbulent viscosity, $\langle u_i \rangle$ is the time-averaged velocity component in x_i direction, k is the turbulent kinetic energy and δ_{ij} is the Kronecker delta. The turbulent kinetic energy is defined as the fluctuating component of the instantaneous kinetic energy: $k=0.5*(\langle u'^2 \rangle+\langle v'^2 \rangle+\langle w'^2 \rangle)$.

Boussinesq-based turbulence models are widely used and validated in engineering applications. From all of them, the k-ε model is one of the more robust, economic and easy to apply and, thus, one of the most popular and validated (Andersson *et al.*, 2011; Versteeg and Malalasekera, 2007), including in hydraulic applications (Rodi, 2017). This turbulence model has been commonly used in case studies similar to the DSM-flux like in the modelling of different types of hydraulic jumps (Bayon *et al.*, 2016; Castillo *et al.*, 2014a; Witt *et al.*, 2015), dissipation basins or flows with baffles (Babaali *et al.*, 2014; Mehdizadeh *et al.*, 2010; Valero *et al.*, 2018) or structures with expansion sections (Dufresne *et al.*, 2009; Yan *et al.*, 2014) among others.

The RNG k-ε variant (Orszag *et al.*, 1993) seems to be appropriate in cases with similar hydrodynamics as the ones taking place in the DSM-flux, as the renormalization group methods are used to derive this model variant to make it more accurate and reliable for a wider class of flows than the standard k-ε model, including swirling flows and flows with separations, like the ones that occur in the DSM-flux due to the expansion of the cross-section and the hydraulic jump. Besides, the RNG theory provides an analytically derived differential formula for effective viscosity that accounts for low-Reynolds number effects, which is effective if an appropriate treatment of the near-wall region is done (ANSYS, 2015a), as it was planned in this PhD work. These are the reasons why the RNG k-ε model was selected for this study.

The k-ε model and its variants are also known as two-equation model because they introduce two additional partial differential equations to the system formed by RANS equations. These models are based on the idea that the turbulent viscosity can be expressed as a proportion of a characteristic velocity and length scales and they focus on developing transport equations for turbulence quantities that might represent these characteristic values, as the turbulent kinetic energy k for the velocity scale and the turbulent dissipation rate ε for the length scale.

The modelling of the turbulent viscosity in the RNG k-ε model is done by:

$$\mu_t = \rho C_\mu \frac{k^2}{\varepsilon} \qquad \textit{Equation 2.3}$$

where C_μ=0.0845 is a constant value derived using RNG theory.

The main mathematical differences with the standard k-ε model are the different model constants and additional terms and functions in the transport equations for k and ε, which are all described in detail in the ANSYS Fluent Theory Guide (ANSYS, 2015a).

Near-wall treatment

Flow behaviour and its characteristics near wall boundaries are different from those at the main stream flow. Indeed, velocities decrease rapidly when approaching the wall as velocity at a fixed and non-slip wall, as the ones of the DSM-flux, is zero. This creates a layer close to the wall, called boundary layer, where velocity gradients are high to the point that there is an area near the wall (viscous sub-layer) where the flow is no longer driven by inertial forces but by viscous forces (low Reynolds number). Thus, flow and turbulence equations presented in the previous subsection, which are conceived for high Reynolds flows, are no longer valid to obtain the flow properties in this near-wall area. There are two approaches to treat the near-wall flow where viscous forces are important: (i) the Wall Functions (WF) approach, where the values of the flow properties in the viscous sublayer are ignored and empirical equations are used to estimate properties at the wall (needed for boundary conditions); and (ii) the Near-wall Modelling (NM) approach, where the high Reynolds turbulence models are adapted (or blended to other low-Reynolds models) so that the equations can be solved at this near-wall area and values of the flow properties at the wall can be calculated for boundary conditions. The use of one approach or the other depends on the objectives of each study: if a precise resolution of the near-wall flow properties including the viscous sub-layer is needed (because either it influences the phenomena of interest or because the phenomena of interest themselves take place in this area), then the second approach should be prioritised. Otherwise, the first approach (less exigent in terms of mesh resolution and computation time) will be accurate enough.

The final objective of the numerical model of the DSM-flux is serve as a tool to study the settling and resuspension mechanisms of particulate pollutants in order to determine the DSM-flux efficiency to retain them from overflowing. Deposition and entrainment of particles settled on the bottom of hydraulic structures depend, among other factors, on the flow properties near the bottom. Thus, it seems reasonable to consider that, in this study, a near-wall modelling approach should be more appropriate, especially if the size of the particles is of the same magnitude than the boundary layer. However, due to the advantages of using the Wall Functions approach and because of its successful results in similar applications (Bayon *et al.*, 2016; Dufresne *et al.*, 2009; Isel *et al.*, 2014; Lipeme Kouyi *et al.*, 2011; Momplot *et al.*, 2017; Yan *et al.*, 2014), both approaches have been tested.

Wall functions approach consists in mathematical expressions obtained empirically which describe the velocity profile of the flow as a function of the distance to the wall. Dimensionless wall variables, like u^+ and y^+, described in Equation 2.4, are usually used for these expressions.

$$u^+ = \frac{\langle u \rangle}{u_\tau} = f\left(\frac{\rho u_\tau y}{\mu}\right) = f(y^+) \qquad \textit{Equation 2.4}$$

In Equation 2.4, u^+ is the dimensionless velocity, y^+ is the dimensionless distance to the wall, <u> is the mean velocity of the flow, u_τ is the friction velocity $u_\tau = \sqrt{\tau_w/\rho}$ depending on the shear stress at the wall, τ_w, and the density of the fluid, and y the distance to the wall.

Among the different wall functions existing in the literature, the Standard Wall Function (STWF) is the most widely used in engineering applications, including hydrology problems, and it is implemented in almost every CFD code (Andersson *et al.*, 2011; Versteeg and Malalasekera, 2007). In ANSYS Fluent, a wall function based on the Launder and Spalding (1972) version of the STWF is implemented. At the viscous sublayer, the velocity profile is considered linear, which is accurate for smooth walls and Equation 2.5 is used to obtain the velocity profile.

$$u^+ = y^+ \qquad \textit{Equation 2.5}$$

At the fully turbulent region of the inner layer, the velocity profile is considered logarithmic and Equation 2.6 is used to represent the velocity profile:

$$u^+ = \frac{1}{\kappa}\ln(y^+) + B \qquad \textit{Equation 2.6}$$

where constants values κ (von Karman constant) and B are considered κ = 0.4 and B = 5.45 in ANSYS fluent.

In between these two regions, there is the buffer region, where there is not a strong consensus of the expression of the velocity profile. Thus, ANSYS Fluent extents the linear and logarithmic profiles until their intersection, at $y^+ = 11.125$. In this case, if $y^+ < 11.125$, Equation 2.5 will be considered and if $y^+ > 11.125$, Equation 2.6 will be used. Figure 2.6 adapted from ANSYS Fluent Theory Guide (ANSYS, 2015a), presents these velocity profiles and the experimental data used to the obtention of these expressions. It is observed that the linear profile is appropriate for $y^+ < 5$ and logarithmic profile for $y^+ > 60$, even 30 as it is commonly considered (Andersson *et al.*, 2011; Versteeg and Malalasekera, 2007), until an upper limit that

depends on the Reynolds number. In the buffer layer, experimental data adjust worse to the expressions, so it is a region to be avoided if possible.

It should be noticed that the obtention of flow properties near the wall is an iterative process, as y^+ depends on the velocity gradient at the wall and the velocity gradient depends on the velocity profile considered, which depends on the y^+ or region where the first node is placed. To avoid this iterative process, which might cost some computation time, ANSYS Fluent suggests the Scalable Wall Function (SCWF), which ignores the viscous sublayer and considers always $y^+ \geq 11.125$. This approximation is convenient when the viscous sublayer is very thin, so that it can be considered that it doesn't exist. Very thin viscous sublayers usually occur if Reynolds numbers are significantly high. In this study, the Scalable Wall Function implemented in ANSYS Fluent code was used to avoid the iterative matching process because the use of a structured mesh made the meshing highly time consuming in order to achieve this y^+ criteria. However, if low Reynolds areas are identified, especially downstream the dissipation zone, the accuracy of results obtained with this near-wall approach could decrease. That is the reason of testing a second near-wall treatment approach.

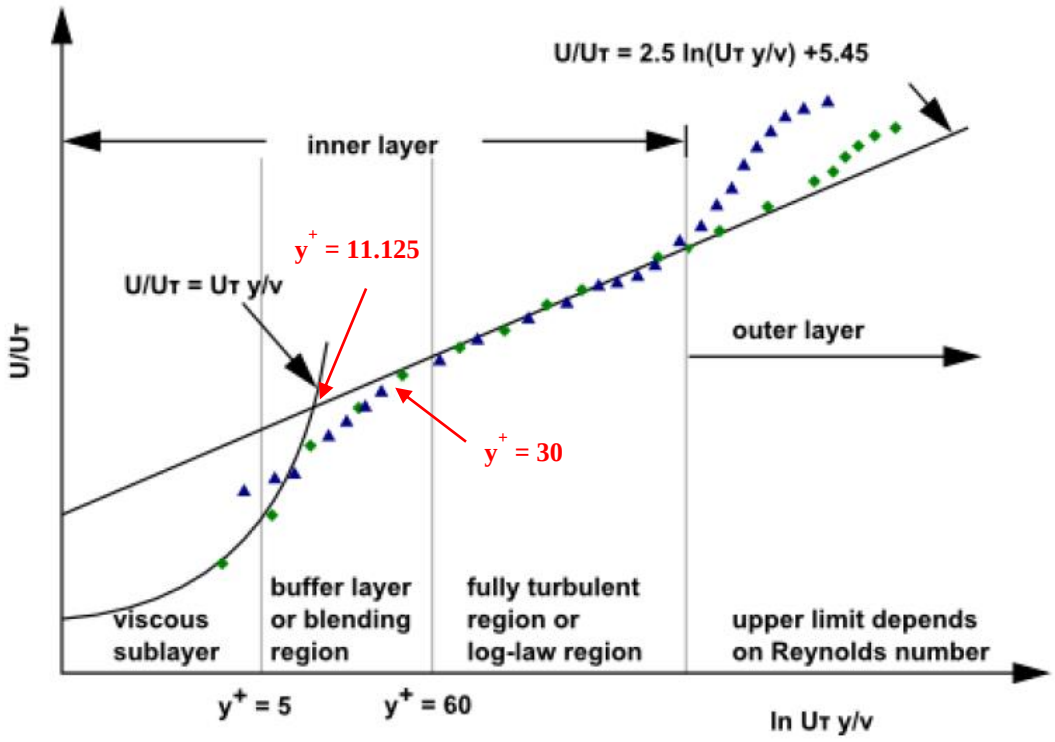

Figure 2.6. The Standard Wall Function implemented in ANSYS Fluent (from ANSYS Fluent Theory Guide (ANSYS, 2015a)). In the figure, points are empirical data and lines correspond to the adjusted laws. ANSYS Fluent Theory Guide (ANSYS, 2015a) variables in this figure correspond to the following: $U/U_T=u^+$ and $y/v=y^+$. The intersection between the viscous layer law and the log law is also indicated in red ($y^+ = 11.125$).

Concerning the near-wall modelling approach, the Enhanced Wall Treatment (EWT) defined in ANSYS Fluent was used in this study. The EWT is based on the concept of the two-layers model where a local Reynolds number (Equation 2.7) is calculated in the near-wall region and depending of its value being greater or lower than a certain threshold Re_y^* (200 in Fluent), different equations are applied to resolve the flow. In the outer region ($Re_y > Re_y^* = 200$), the standard turbulence model equations for the main flow are used (in our case, RNG k-ε), whereas in the inner region ($Re_y < Re_y^* = 200$), different equations are used for the turbulent viscosity and the dissipation rate ε. The turbulent viscosity μ_t in the viscous layer is obtained with the equation of Wolfshtein (1969) (Equation 2.8) and the turbulent dissipation ε calculated algebraically from Equation 2.9.

$$Re_y = \frac{\rho y \sqrt{k}}{\mu} \qquad \textit{Equation 2.7}$$

$$\mu_{t_{viscous}} = \rho C_\mu l_\mu \sqrt{k} \qquad \textit{Equation 2.8}$$

$$\varepsilon = \frac{k^{3/2}}{l_\varepsilon} \qquad \textit{Equation 2.9}$$

In Equation 2.8 and Equation 2.9, constant C_μ and variable k are taken from the RNG k-ε model and l_μ and l_ε length scales are defined by Chen and Patel (1988).

Blending functions are used to smooth the transition of these variables between low and high Reynolds regions. For the turbulent viscosity, the blending function (λ_ε) proposed by Jongen (1992) is used to compute the turbulent viscosity with Equation 2.10:

$$\mu_{t_{enhanced}} = \lambda_\varepsilon \mu_t + (1 - \lambda_\varepsilon)\mu_{t_{viscous}} \qquad \textit{Equation 2.10}$$

where μ_t is the turbulent viscosity in the outer region taken from the turbulent model, RNG k-ε model in this case (Equation 2.3), and $\mu_{tviscous}$ is the turbulent viscosity in the inner region defined by Wolfshtein (1969) (Equation 2.8) . λ_ε is define as follows (Equation 2.11):

$$\lambda_\varepsilon = \frac{1}{2}\left[1 + \tanh\left(\frac{Re_y - Re^*_y}{\frac{|\Delta Re_y|}{artanh(0.98)}}\right)\right] \qquad \textit{Equation 2.11}$$

where ΔRe_y is the width of the bending function, usually considered between 5% and 20% of Re_y*. A similar blending function is used for the dissipation rate (ANSYS, 2015a).

A procedure similar to the STWF combined with a blending approach is followed to obtain the velocities profile at the near-wall region. The logarithmic and linear expressions of u^+ from turbulent and laminar regions respectively are blended as in Equation 2.12 with a function Γ proposed by Kader (1981) (Equation 2.13).

$$u^+ = e^{\Gamma} u^+_{lam} + e^{1/\Gamma} u^+_{turb} \qquad \textit{Equation 2.12}$$

where u^+_{lam} and u^+_{turb} are the dimensionless velocities at the laminar and turbulent regions, respectively. The formulation to obtain the laminar and turbulent velocity profiles, based on the work of different authors, is described in detail in ANSYS Fluent Theory Guide (ANSYS, 2015a).

$$\Gamma = -\frac{0.01 \cdot (y^+)^4}{1 + 5 \cdot y^+} \qquad \textit{Equation 2.13}$$

According to ANSYS Fluent Theory Guide (ANSYS, 2015a), Kader (1981) formula guarantees a reasonable representation of velocity profiles event if the first cell is in the buffer region ($3 < y^+ < 10$).

Free surface modelling

The DSM-flux flow has been considered as a two-phase (air-water) flow, as its standard operation conditions are those of an open channel flow. Despite that, in real operating conditions, the flow will carry solid matter, simulations in this PhD work has been done without considering solid transport.

There are multiple approaches to model multiphase flows (Andersson *et al.*, 2011). For stratified flows where it is important to track the interface between water and air, the Volume of Fluid (VOF) model (Hirt and Nichols, 1981) is recommended (Andersson *et al.*, 2011), especially where the free surface might be complex or transient, like in the hydraulic jump formed in the DSM-flux device. The VOF model is a Euler-Euler model (each phase is treated as continuous) where the interface between them is resolved. This is essential in the DSM-flux case study as water levels are the input for the monitoring methodology of the device being evaluated.

The VOF model is widely used to model free surface flows in urban drainage studies (Bayon *et al.*, 2016; Dufresne *et al.*, 2009; Isel *et al.*, 2014; Jarman *et al.*, 2008; Lipeme Kouyi *et al.*, 2011;

Momplot *et al.*, 2017; Yan *et al.*, 2014). In the model, the different phases are mathematically not interpenetrating, and the concept of volume fraction is introduced into the flow equations for each new phase considered in the problem: a single set of momentum equations is shared by the phases, and the volume fraction of each of the phases in each computational cell is tracked throughout the domain (ANSYS, 2015a). These volume fractions are assumed to be continuous functions of space and time and their sum is equal to one (ANSYS, 2015a). All the formulae are described in ANSYS Fluent Theory Guide (ANSYS, 2015a).

In this PhD work, the Bounded Gradient Maximization (BGM) scheme (Walters and Wolgemuth, 2009) is used as interpolation method for the cells near the free surface. When the interface between two fluid phases begins to curve, surface tension forces appear and will increase with the interface curvature. The surface tension force is included as an additional momentum source term in the model. For large interfaces, such as in stratified flows, but also for interfaces of bubbles or droplets of diameter larger than a few centimetres, the surface-tension force may be negligible (Andersson *et al.*, 2011). However, if the curvature of the flow becomes important, as in flows over weirs, surface tension effects may have more importance. It is considered that surface tension influence is negligible if Weber number is significantly higher than 1 but there is not an agreement about the value from which theses effects can be neglected (Peakall and Warburton, 1996). In this PhD work no surface tension effects were considered because (i) free surface is large in the whole model domain and (ii) in the overflow area, although overflow curvature might be significant for higher flow rates, Weber numbers are considered to be high for most of the operating conditions, as explained in Section 3.1.

Discretization schemes

ANSYS Fluent code is based on the finite volume method to solve the flow by discretization of the domain. Space domain is discretised in control volumes over which the differential equations are integrated and flux conservation in each control volume is guaranteed. The divergence theorem is then applied to convert volume integrals to surface integrals. Thus, derivate terms of the problem equations are evaluated at surfaces of the control volumes. However, the values of the integrands are not available at the faces but at the computational nodes of the control volume which are located in the centroid of the volume. An interpolation is needed in order to obtain the values of all flow properties and its gradients at the faces. Different assumptions can be made about the variation of the flow properties and its gradients between cell centroids, which leads to different types of “numerical schemes” (or discretization schemes) to carry out these interpolations.

There are several numerical schemes implemented in ANSYS fluent. In this PhD work, second-order upwind schemes were used for momentum and turbulence quantities k and ε. This schema is recommended for complex flows solved in hexahedral meshes to improve accuracy (ANSYS, 2015a) and avoid numerical diffusion compared with first-order upwind scheme. Second-order upwind scheme determines the value in a cell face by means of a multidimensional linear reconstruction approach described by Barth and Jespersen (1989), which uses the values from the upstream cells from the face for the calculations. It is considered a second-order accuracy scheme because, when approximating the interpolation function with Taylor series polynomials, it only takes into account first-order derivates but not second-order derivates. The equations used are presented in detail in the ANSYS Fluent Theory Guide (ANSYS, 2015a).

Three methods are available in ANSYS Fluent to compute cell gradients. In this PhD work, the Least Squares Cell-based method was used as it is supposed to be less expensive in computational time, still preserving an accuracy comparable to the other methods (ANSYS, 2015a).

Upwind schemes are less suitable for VOF multiphase model because they are diffusive at the free surface interface. ANSYS Fluent recommends the Modified High Resolution Interface Capturing (HRIC) scheme to transfer the volume of fraction values from cell centres to faces, as it gives more accuracy compare to second-order upwind and other third-order accuracy schemes (ANSYS, 2015a).

Pressure-velocity coupling algorithm

Pressure gradients are needed in momentum equations (Equations 2.3, 2.4, 2.5) but these are usually unknown as the pressure field is usually to be determined from flow equations. If the flow is considered incompressible, there is not an explicit equation to calculate the pressure. A pressure-based approach can then be adopted, where the pressure field is extracted by guessing an initial value and correcting it at each iteration by manipulating continuity and momentum equations. This was the strategy followed in this PhD work, as the flow of interest is considered incompressible.

ANSYS Fluent code has several pressure-velocity coupling algorithms implemented that mainly differ in the convergence speed and stability. As stated by Andersson *et al.* (2011), it is generally not possible to say that a specific scheme is always better than another with respect to efficiency or robustness. Whether a scheme is better than other strongly depends on the flow conditions. The SIMPLE algorithm was the one selected for this study for its simplicity. The

SIMPLE algorithm is a pressure-based algorithm which follows a segregated solution procedure: an initial guess is done for the pressure and velocities field, the momentum equations for the main flow are solved first for all cells, pressure and velocity fields are then corrected thanks to the continuity equation and these updated values are introduced in the rest of equations (turbulence models in this study) to obtain new values of the pressure and velocities field. The process is repeated until convergence is achieved (new and old values are close enough). Figure 2.7 adapted from Versteeg and Malalasekera (2007) shows the sequence of operations followed with the SIMPLE algorithm.

Pressure values are needed in the cell faces, so an interpolation from cell centroids to cell faces is needed. In this study, the body-force-weighted scheme was used as it is the scheme recommended by ANSYS Fluent when using VOF or in problems involving large body forces, as in free surface flows. As indicated in ANSYS (2015a): "*the Body Force Weighted scheme computes the face pressure by assuming that the normal gradient of the difference between pressure and body forces is constant. This works well if the body forces are known a priori in the momentum equations (for example, buoyancy and axisymmetric swirl calculations*)."

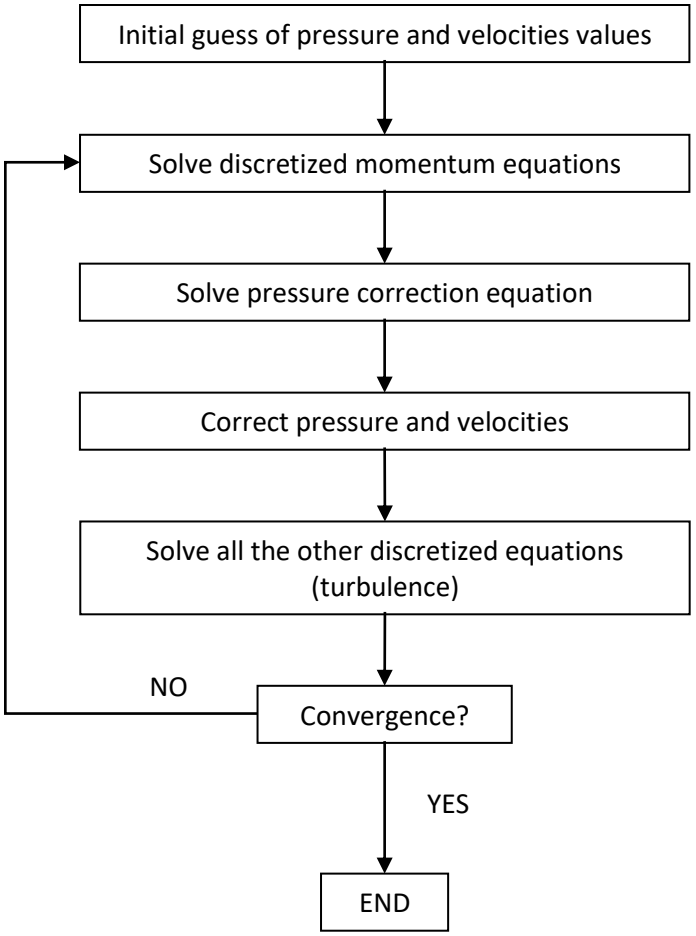

Figure 2.7. SIMPLE pressure-velocity coupling algorithm (adapted from Versteeg and Malalasekera (2007)).

Boundary conditions

The specific solution of a fluid motion problem for a specific case study is defined by the boundary conditions of the problem. The DSM-flux small-scale numerical model domain has three different types of boundaries, indicated already in Figure 2.2: (i) an inlet boundary at the most upstream cross-section of the inflow pipe, where the flow enters the model, (ii) three outlet boundaries, two at the left and right sides of the left and right weir crests respectively and another one at the top of the DSM-flux, as it's an open channel flow, and (iii) several wall boundaries, that correspond to all the solid surfaces which are in contact with the flow (inflow pipe, transition and DSM-flux vertical walls and bottom).

Boundary conditions are used to obtain the values of the problem unknowns (3D velocities, pressure and Reynolds stresses) at the boundary faces of the cells next to the boundaries, which are needed for the numerical calculation schemes detailed in the previous subsection. ANSYS Fluent software allows to define boundary conditions directly from the unknown

variables or by means of other flow variables related to them. In this PhD work, inlet boundary conditions were defined either as velocity-inlet type or mass-flow-inlet type and outlet boundary conditions were defined as pressure-outlet type.

Velocity-inlet or mass-flow-inlet input variables are: (i) velocity (or total flow rate) magnitude and profile distribution and direction and (ii) turbulence quantities. In this study, a constant value of the velocity all over the inlet cross-section and normal to it was considered. Despite this velocity profile is not representative of the fully-turbulent flow velocity profiles, the inflow pipe of the DSM-flux numerical model is considered long enough (25 inflow pipe diameters) to assure a fully-turbulent velocity profile at the end of the pipe. Turbulence quantities have been defined by the turbulent intensity and hydraulic diameter method. The rest of the variables and options have been left with default ANSYS Fluent values.

Pressure-outlet input variable are mainly the static pressure at the outlet and flow variables in case of backflow occurs. In this study, pressure at all the outlets was considered constant and equal to the atmospheric pressure. As no backflow is expected, backflow quantities were mainly left with default ANSYS Fluent values.

Concerning wall boundaries, walls in this study were considered stationary and characterized by a no-slip condition. Some inputs are determined by the near-wall treatment selected for each model. In this study, two different types of near-wall treatment have been tested: (i) Scalable Wall Function and (ii) Enhanced Wall Treatment. Wall function can be modified to take into account effects on turbulence due to the roughness of the wall. In these cases, a wall roughness height and constant must be defined. Roughness heights were taken within 10^{-4} to 10^{-6} m, the range of "equivalent sand-grain" values given by Hager (2010) for concrete, stainless-steel and PVC, the three materials used in the physical model and prototype site. The roughness constant was considered as 0.5, the default value given by ANSYS Fluent. In case of Enhanced Wall Treatment, no additional inputs are needed.

Convergence criteria

Convergence of the solution was evaluated by monitoring the residuals, the mass flow balance between the inlet and the outlets (both sides of the overflow area) and other variables of interest, like the water level at the downstream area of the device. A solution was considered converged when (i) all these monitors clearly tended to an asymptotic line, (ii) scaled residuals were lower than 10^{-3} and (iii) the mass flow balance was lower than 3%.

2.2. THE LARGE-SCALE NUMERICAL MODEL AND FIELD PROTOTYPE

The initial large-scale DSM-flux was designed scaling the small-scale device preserving a geometric similarity with a scale of 2.67. As gravity and inertial forces are dominant in the DSM-flux flow, a Froude similarity is assumed. A 0.4 m inflow pipe was selected for the field prototype because of the site configuration and this diameter determined the initial device dimensions, which are specified in Appendix 7.1.4.

In Section 1.3 it was said that the design of the DSM-flux is still in development.(Momplot, 2014) provided some recommendations to improve the design of the small-scale device which basically consisted in adapting the number and dimensions of the dissipation blocks in order to favour the stabilization of the hydraulic jump downstream from the dissipation. During the assessment of the initial large-scale numerical model (Sections 3.2 and 4.2), some concerns arose about its retention capacity and the stability of the free surface at high flow rates. Thus, two alternative designs were proposed and tested, whose dimensions are specified in Appendix 7.1.5. Although the initial and the alternative designs are presented all together in this section for a better organisation of the document, it should be understood that the alternative designs were conceived taking into account the analysis of Sections 3.2 and 4.2. One of these alternative designs was the selected design for the field prototype, that was built according to the dimensions specified in Appendix 7.1.5.

The specific characteristics of the configuration upstream and downstream from the device for the field prototype and the large-scale numerical models are described in the following subsections.

2.2.1. The large-scale numerical model

The large-scale numerical model is implemented based on the lessons learned with the small-scale model, so it has the same main features and all the literature and reasoning presented in section 2.1.2 for the small-scale model is applicable for the large-scale model, as both flows are 3D multiphase turbulent flows. The DSM-flux flow is a free surface flow, so gravity and inertial forces are dominant, and a Froude similarity is assumed. Thus, the main difference between the small- and large-scale models are related to the Reynolds numbers, which will be higher in the latter. However, this doesn't involve a review of the turbulence models as the model used in this PhD work, the RNG k-ε, was created for highly turbulent flows and it is believed that it will be even more appropriate if the Reynolds are higher.

As for the small-scale numerical models, the large-scale numerical models have been implemented in the commercial CFD solver ANSYS Fluent. Three large-scale numerical models were tested in this PhD work corresponding to the initial (LM-A) and the two alternative designs (LM-B and LM-C). The large-scale numerical model's spatial domain consists of the DSM-flux device, the upstream inflow pipe and either a 1 m wide x 1 m long rectangular chamber or a 0.4 m transition that connects the end of the pipe to the entry of the device, depending if they correspond to the initial (LM-A) and first alternative (LM-B) or the second alternative (LM-C) design, respectively (Figure 2.8). The dimensions of the inflow pipe are those of the experimental site (Figure 2.12) and the rectangular chamber wanted to simulate a manhole that was initially considered for the field but that it was finally discarded. The geometry and dimensions of the DSM-flux device for the three large-scale numerical models are presented in Appendix 7.1.4 for LM-A and in Appendix 7.1.5 for LM-B and LM-C. Similar to the small-scale models, at the outlet of the device, two hexahedral blocks (one for each overflow side) were added downstream the whole length of the two weir crests, covering from the crest height to the device height, in a similar way as the small-scale model (Figure 2.8).

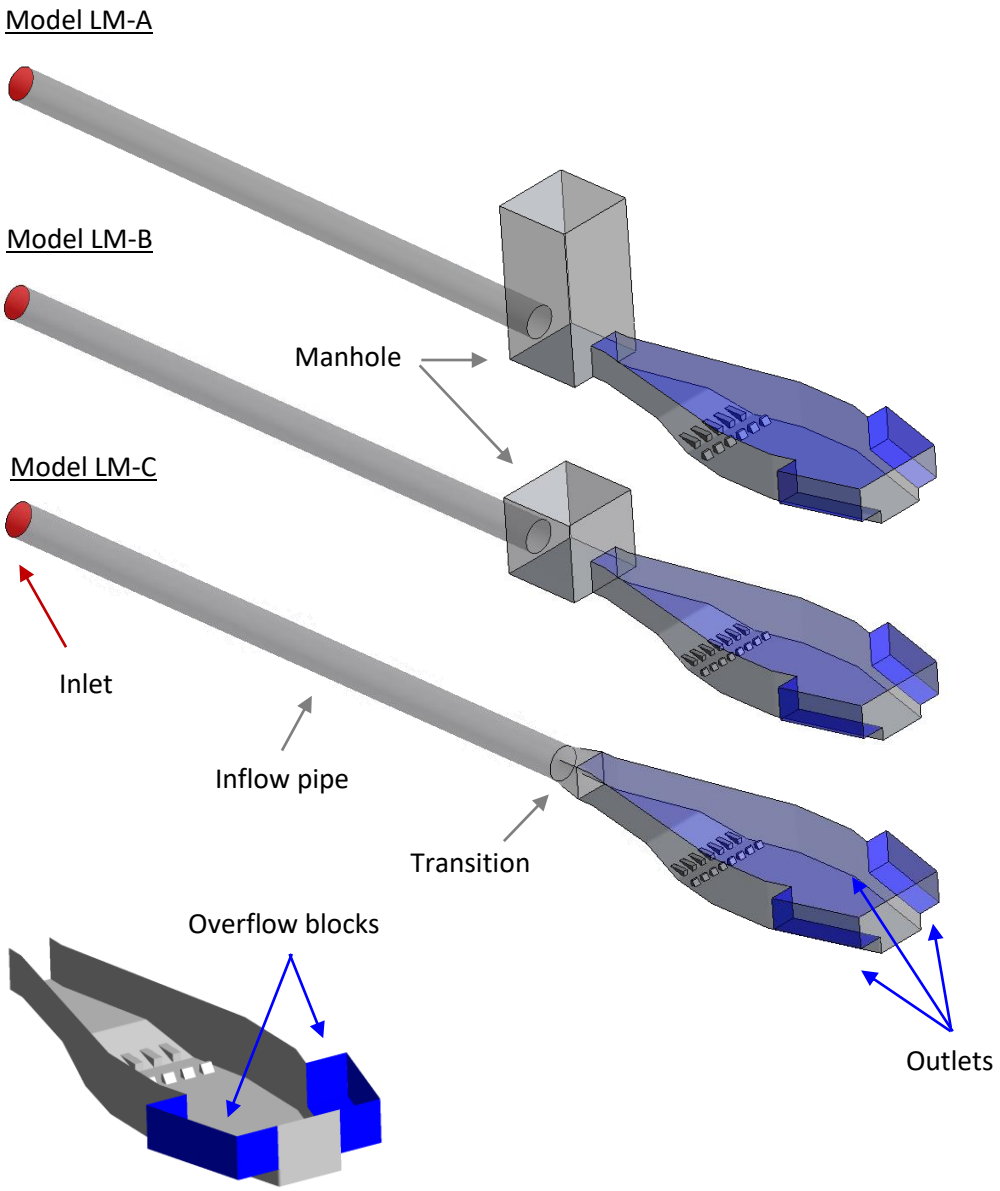

Figure 2.8. 3D view of the three large-scale numerical models' domain. Inlet and outlet boundaries in red and blue respectively. The rest are wall boundaries. Zoom of overflow blocks.

Three different structured meshes, corresponding to each of the designs, were used to discretize the domain in hexahedral elements. The meshes were created according to meshing criteria similar to the ones followed for mesh MS1 of the small-scale model (Table 2.2): they are coarse meshes without any refined areas. So, the differences between the meshes are mainly due to the geometry imposed by each design and a slight difference in the density of elements imposed by these differences in the geometry. For example, the connection between the inflow pipe and the device are different (manhole or transition) and this creates a slightly different organisation of the elements. Some detail views of the meshes are presented in

Appendix 7.1.6. As it is observed, only one of the meshes (MS3) is presented because all the meshes have a similar typology. Differences at the inlets and connections with inflow pipes are indicated for the different meshes. The characteristics of each of the meshes used as well as some quality parameters are indicated in Table 2.3. As for the small-scale models, especially MS1, some values of quality indicators (highlighted in red in Table 2.3) don't respect the recommended quality criteria already described in section 2.1.2, but they usually represent a low percentage of the total elements of the model (< 0.01%). In the case of the large-scale model meshes, bad quality elements are located at the upstream chamber or transition where precision is less critical.

Table 2.3. Characteristics of the computational meshes of the large-scale numerical models. Meshes ML1 and ML2 include a manhole that is not included in the final design and that increases significantly the number of elements of the models. To better compare the size of the meshes, number of elements without the extra cells of the manhole (equivalent configuration to ML3) would be approximately 520.000 and 1.620.000 for ML1 and ML2 respectively.

MESH CARACTERISTICS	MESH ML1	MESH ML2	MESH ML3
Connectivity	Structured	Structured	Structured
Interior interfaces	No	No	No
Element shape	Hexahedral	Hexahedral	Hexahedral
Number of elements	800.000(1)	1.890.000(2)	1.080.000
Min side length (m)	$4.1\cdot10^{-3} – 3.6\cdot10^{-2}$	$4.5\cdot10^{-3} – 4.0\cdot10^{-2}$	$4.7\cdot10^{-3} – 4.0\cdot10^{-2}$
Max size length (m)	$4.1\cdot10^{-3} – 1.5\cdot10^{-1}$	$4.9\cdot10^{-3} – 4.8\cdot10^{-2}$	$5.2\cdot10^{-3} – 9.7\cdot10^{-2}$
Volume (m)	$1.0\cdot10^{-7} – 1.8\cdot10^{-5}$	$1.5\cdot10^{-7} – 3.7\cdot10^{-5}$	$3.0\cdot10^{-7} – 4.9\cdot10^{-5}$
Quality indicators			
Min Ortogonal quality	**0.06** 0.2 (> 99.99%)	**0.07** 0.2 (> 99.99%)	0.31
Max aspect ratio	45 40 (> 99.95%) 20 (> 90%) (Mean = 7)	36 20 (> 99.99%) (Mean = 3)	19 (Mean = 3.5)
Min angle (°)	**6.1** 18 (> 99.99%)	**7.2** 18 (> 99.99%)	18
Max Skewness	**0.97** 0.75 (> 99.95%)	**0.96** 0.75 (> 99.98%)	**0.8** 0.75 (> 99.99%)

Flow and turbulence equations, near-wall treatment, free surface modelling, discretization schemes, pressure-velocity coupling algorithms and boundary conditions tested for the large-scale model are the same as the ones presented in section 2.1.2 for the small-scale model. Table 2.4 presents the three large-scale numerical models analysed in this PhD work.

Table 2.4. Main features of the small-scale numerical models. RNG=ReNormalization group; SCWF=Scalable Wall Function; EWT=Enhanced Wall Treatment; 2UW=Second order upwind; LSCB=Least Squares Cell Based; BFW=Body Force Weighted; MHRIC=Modified High Resolution Interface Capturing; SIMPLE=Semi-Implicit Method for Pressure-Linked Equations; VOF=Volume Of Fluid; MFI=Mass Flow Inlet; PO=Pressure Outlet; FX=Fixed Wall; SR=Scaled Residuals; MFB=Mass Flow Balance.

MODEL	MESH	TURBULENCE MODEL	NEAR-WAL TREATMENT	DISCRETIZATION SCHEMES	VELOCITY-PRESSURE CLOUPING	FREE SURFACE MODELLING	BOUNDARY CONDITIONS	CONVERGENCE CRITERIA
LM-A	ML1	RNG k-ε	SCWF	2UW LSCB BFW MHRIC	SIMPLE	VOF	MFI PO FW	SR < 10^{-3} MFB < 3%
LM-B	ML2	RNG k-ε	SCWF	2UW LSCB BFW MHRIC	SIMPLE	VOF	MFI PO FW	SR < 10^{-3} MFB < 3%
LM-C	ML3	RNG k-ε	SCWF	2UW LSCB BFW MHRIC	SIMPLE	VOF	MFI PO FW	SR < 10^{-3} MFB < 3%

2.2.2. Sathonay-Camp experimental site and field prototype characteristics

The DSM-flux field prototype is installed in an underground experimental site in the sewer system of the municipality of Sathonay-Camp (France), which belongs to Lyon's conurbation. The Sathonay-Camp municipality is located within the drainage basin of the Ravin stream, the water body that receives the outflow from the DSM-flux (Figure 2.9). The Ravin drainage basin has a surface of 9.5 km^2 (Gilard *et al.*, 1997), most of which is urbanized (more than 10000 equivalent inhabitants). The main land use is residential, followed by agricultural,

industrial/commercial and green areas (Figure 2.10). The Ravin stream's source is situated in the south border of the Dombes plateau. The stream has eroded the plateau forming steeped banks and it descends to the downstream part of the catchment with a slope of about 2.5% (Gilard *et al.*, 1997). The areas of the catchment near the downstream section of the Ravin stream are the most urbanised and the stream bed is concreted in some parts, especially at the end, upstream from the confluence with the Saône river, where the stream is completely channelled in an underground tunnel (Gilard *et al.*, 1997). At the Ravin stream confluence with the Saône river, there is the Fontaines-Sur-Saône WWTP (30.000 equivalent inhabitants of capacity), whose treated flows are drained to the Ravin stream before reaching the Saône river.

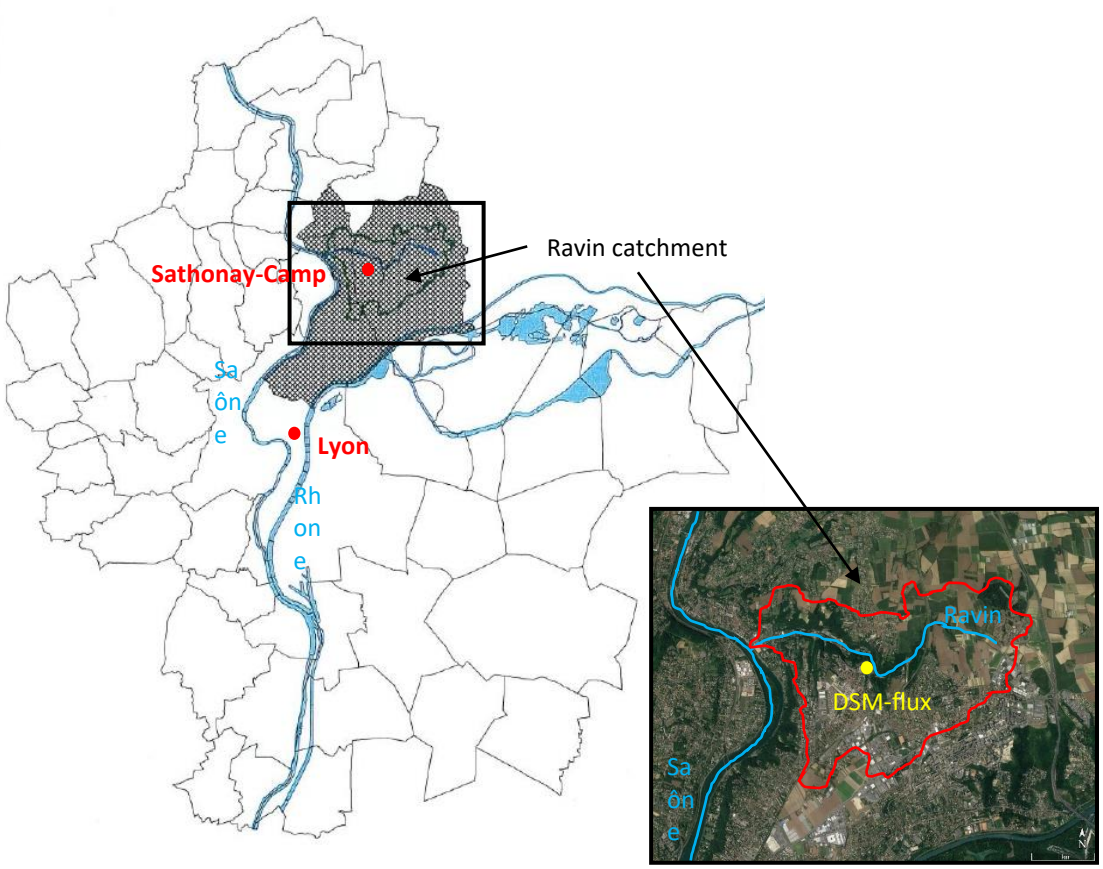

Figure 2.9. Location of the Ravin catchment in Lyon's conurbation, with the six municipalities (partially) covered by the Ravin catchment hatched in black (Sathonay-Camp, Sathonay-Village, Rilieux-La-Pape, Caluire-et-Cuire, Fontaines-Saint-Martin et Fontaines-sur-Saône). Adapted from AU (1998). In the zoom, the DSM-flux experimental site location within the Ravin catchment (image from Google Earth).

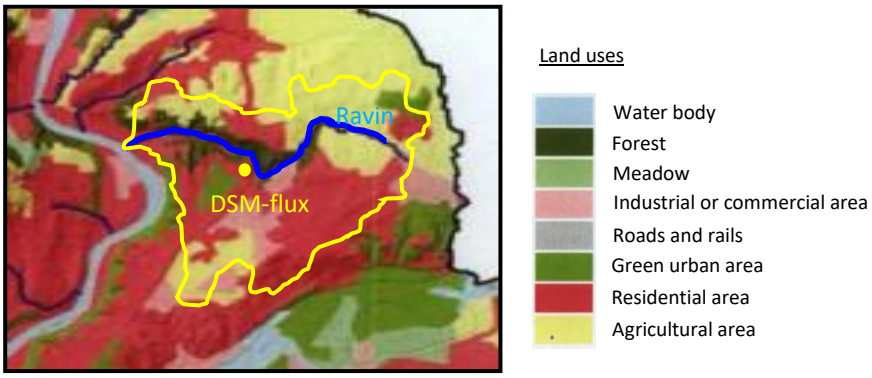

Figure 2.10. Land uses of the Ravin catchment. Data from the Corin Land Cover database of 2006.

The Ravin catchment can be divided into one large rural sub-catchment situated at the north and several urban sub-catchments mainly located at the south. The urban sub-catchments are drained by combined sewer systems which include CSO structures to evacuate water volumes exceeding a certain capacity during wet weather. The DSM-flux experimental site is located between the CSO structure identified as DO342 and the Ravin stream (Figure 2.11). Eleven urban sub-catchments are associated to this point of the sewer system and their main characteristics are indicated in Table 2.5.

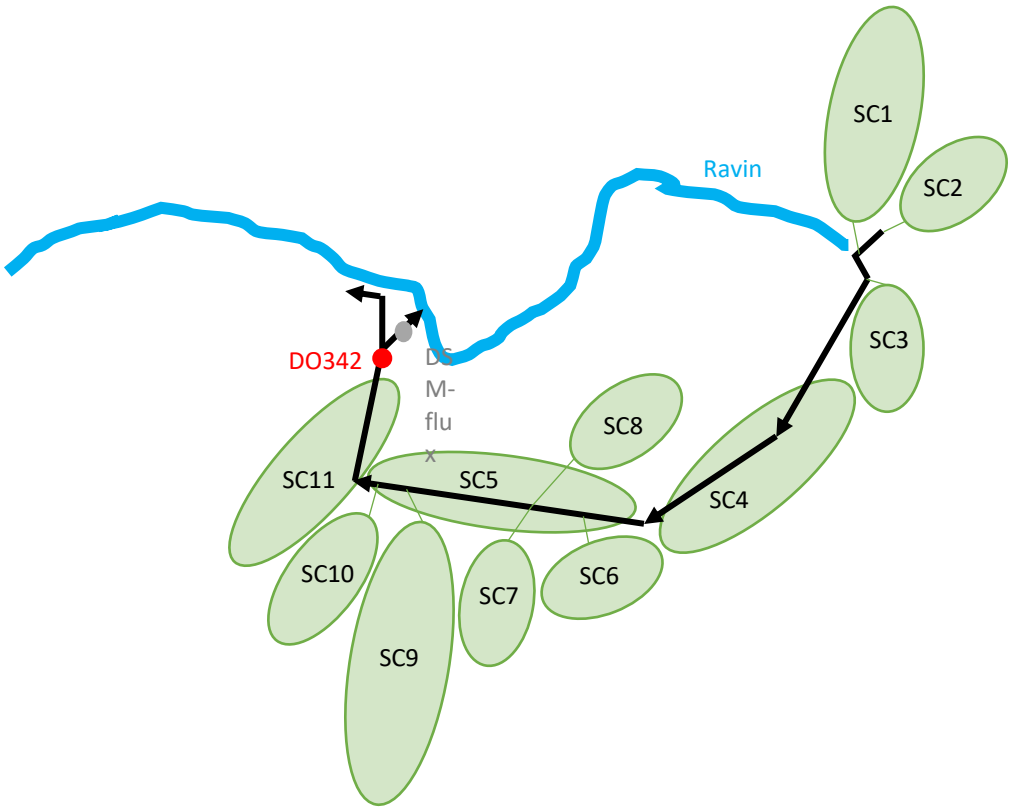

Figure 2.11. Sub-catchments of the Ravin hydrological catchment.

Table 2.5. Characteristics of the urban sub-catchments draining to the CSO structure DO342. Data issued from Metropole of Lyon urban drainage model of the catchment.

SUB-CATCHMENT	SURFACE (ha)	IMPERMEABLE SURFACE (%)	SLOPE (%)	Equivalent inhabitants
SC1	25.7	55	2.1	814
SC2	13.2	66	1.5	333
SC3	11.7	0	0.5	501
SC4	40.6	61	2.4	780
SC5	13.8	55	1.2	700
SC6	17.0	55	3.8	416
SC7	17.1	39	1.2	91
SC8	6.8	57	3.3	354
SC9	55.1	70	1.0	535
SC10	21.9	73	0.9	771
SC11	22.6	51	1.4	569

A general plan of the DSM-flux experimental site is presented in Figure 2.12. The DO342 CSO structure consists of a lateral weir that discharges the CSOs to a 1 m diameter conduit made of concrete. This conduit has a slope of approximately 3% and connects 70 m downstream with the Ravin stream. In order to avoid modifying the existing overflow discharge pipe and due to space limitations, the DSM-flux couldn't be installed directly at the discharge conduit. Hence, it was decided to install the prototype in a smaller pipe, parallel to the existing discharge channel. For that purpose, a distribution chamber was built 25 m downstream from the DO342. Some detailed plans of the distribution chamber are presented in Figure 2.13. This chamber is divided in two sections separated by a 0.69 m height frontal weir. The water entering the chamber firstly fulfils the upstream section and the flow is mainly conveyed to the DSM-flux through a 0.4 m outflow pipe made of PVC. When the entry of this outflow pipe is completely submerged, water starts flowing over the frontal weir, passing through the downstream section of the chamber and reaching the Ravin stream through the downstream section of the 1 m diameter discharge pipe. A 0.2 m diameter drainage gate is located at the invert level of the frontal weir to allow the complete drainage of the upstream part of the chamber after the event. In order to avoid the downstream influence from the Ravin stream, the 0.4 m diameter outflow conduit connecting the distribution chamber with the DSM-flux was raised 0.29 m from the chamber invert. This conduit has a slope of 1% and a length of 10 m. A 0.4 m length transition element connects the end of this conduit to the entry of the DSM-flux, as in the small-scale physical model. This transition as well as the DSM-flux field prototype are made of stainless steel. The water passing through the DSM-flux overflows to a drainage

basin which is connected to a 0.4 m diameter outflow pipe made of PVC. This outflow pipe consisted at first in a 15 m length straight conduit of 1% of slope that conveyed the water to the Ravin stream. Due to the Ravin's configuration upstream and downstream this connexion point, water levels at the Ravin were higher than expected during a few big events and the DSM-flux was influenced by a backflow which caused the complete flooding of the DSM-flux chamber. To avoid this, a 14 m length pipe section was connected to the outflow pipe. This pipe extension, of equivalent cross-section than the outflow pipe, is attached to the interior of the Ravin's pipe, adopting the same slope, and overflows directly into a downstream chamber, where the Ravin converges with the CSO DO342 discharge conduit to continue into a same conduit downstream. In this chamber, water levels are expected to lower as the section is larger than upstream. Figure 2.14 shows some photos of this modification of the outlet of the DSM-flux experimental site.

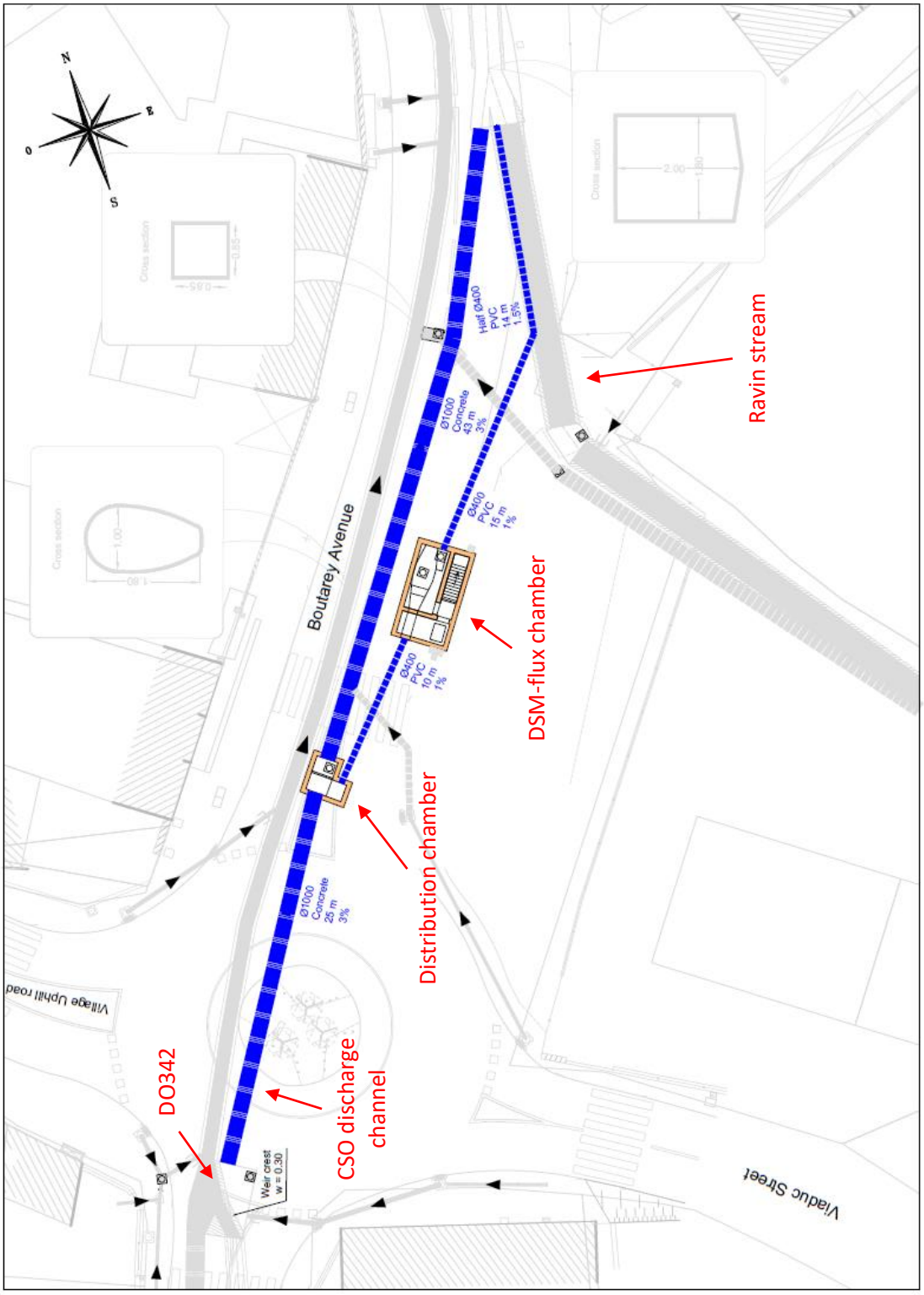

Figure 2.12. General plan of the Sathonay-Camp site configuration. Adapted from Metropole of Lyon original plans. Dimensions in meters except diameters that are in millimetres.

Horizontal view of the distribution chamber

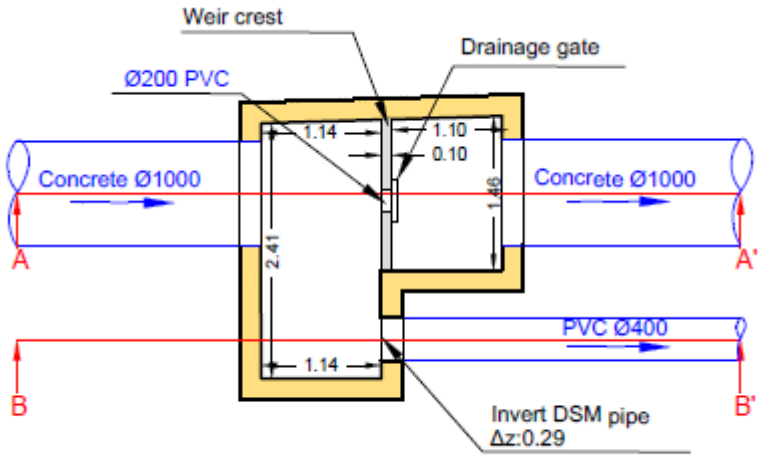

Section AA'

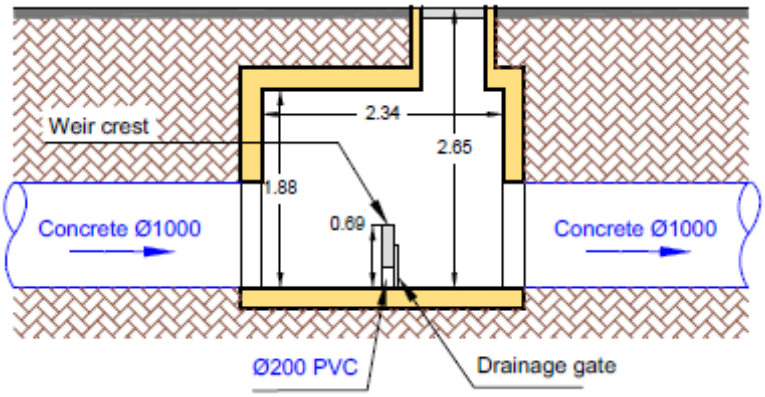

Section BB'

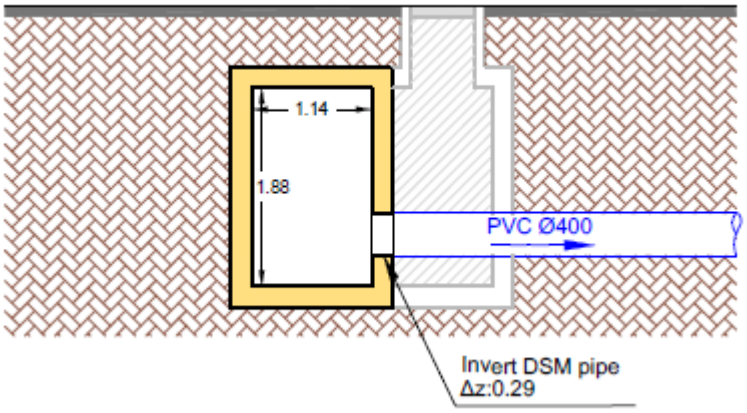

Figure 2.13. Horizontal and profile views of the distribution chamber. Adapted from Metropole of Lyon original plans. Dimensions in meters except diameters that are in millimetres.

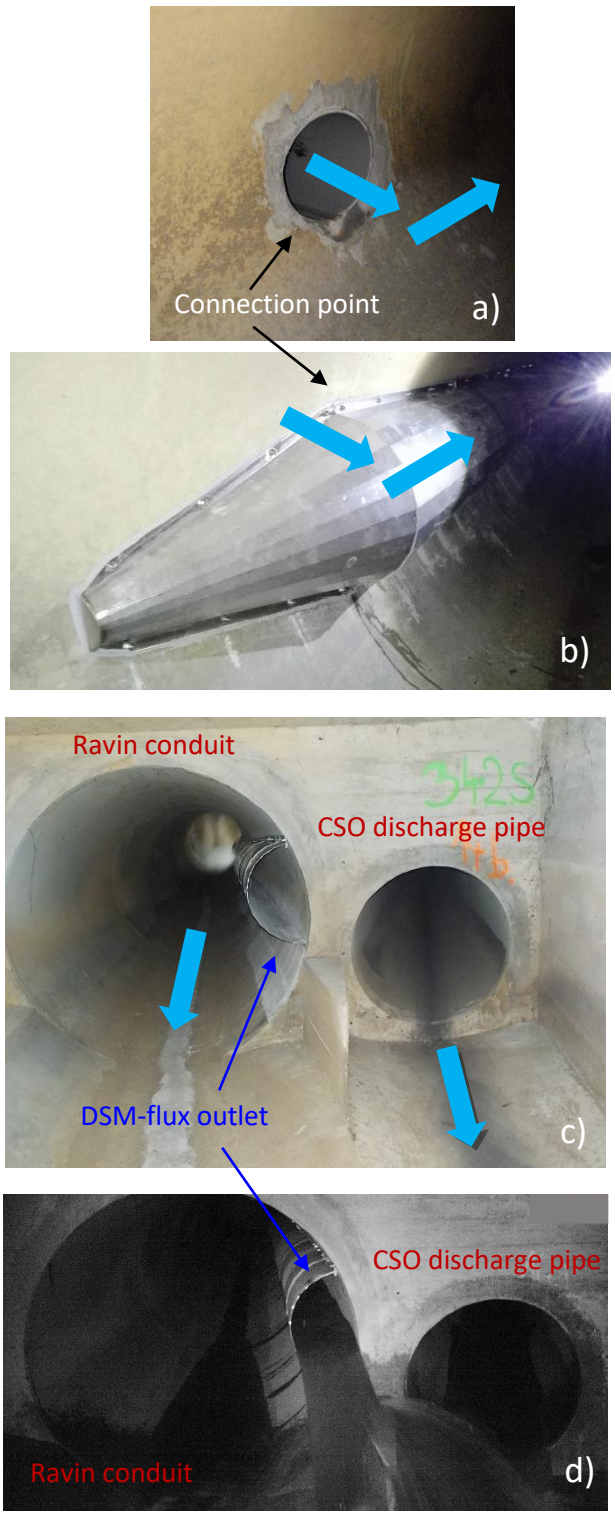

Figure 2.14. Photos of the connection of the DSM-flux outflow pipe with the Ravin conduit: a) the connection of the outflow pipe and the Ravin conduit before the modification, b) the extension pipe, c) the chamber (looking upstream) where the Ravin conduit and the CSO discharge pipe converge (the DSM-flux outflow pipe extension is observed inside the Ravin's conduit) and d) the system operating during an event the 25th of November of 2017.

Horizontal view of the DSM-flux chamber

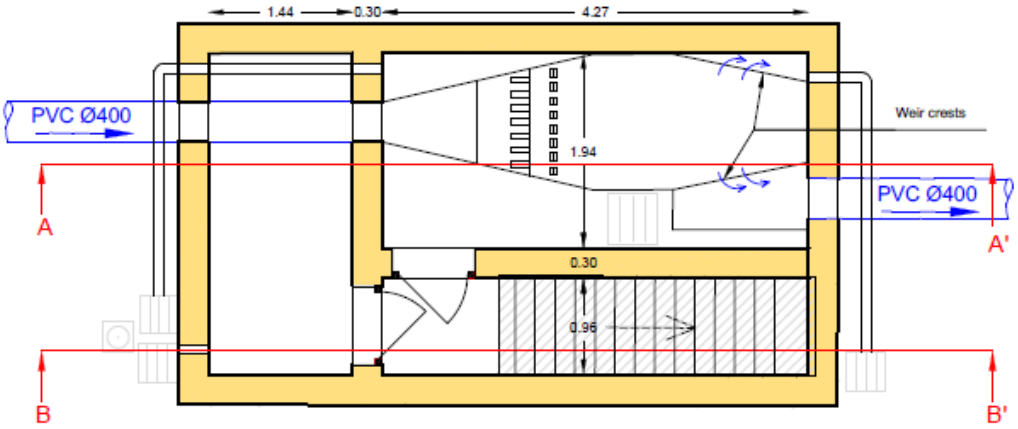

Section AA'

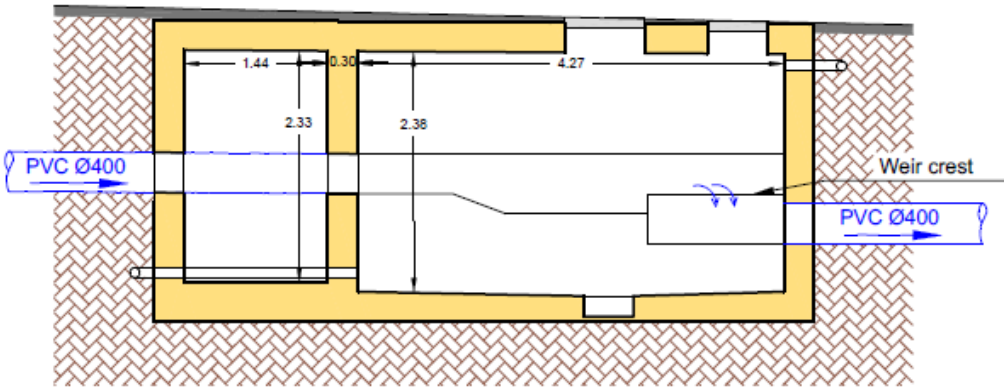

Section BB'

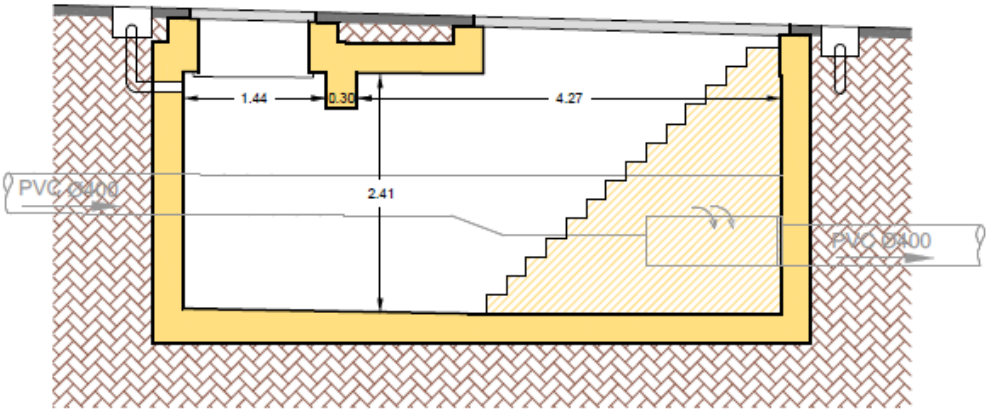

Figure 2.15. Horizontal and profile views of the DSM-flux chamber. Adapted from Metropole of Lyon original plans. Dimensions in meters except diameters that are in millimetres. DSM-flux prototype dimensions in Appendix 7.1.5.

The DSM-flux prototype is installed inside a chamber divided in two rooms: a room where the device is accessible that contains all the instrumentation for monitoring, and a room containing technical equipment that must be isolated from water, like the electricity panels, the electronic material and the automatic samplers. The DSM-flux chamber is reachable from the pavement of Boutarey Avenue. This configuration allows an easy access to the device, the equipment and the data when needed. Some detail plans of the DSM-flux chamber are presented in Figure 2.15 and Figure 2.16 shows a horizontal and profile views of the chamber with the location of all the instrumentation.

Horizontal view of the DSM-flux chamber

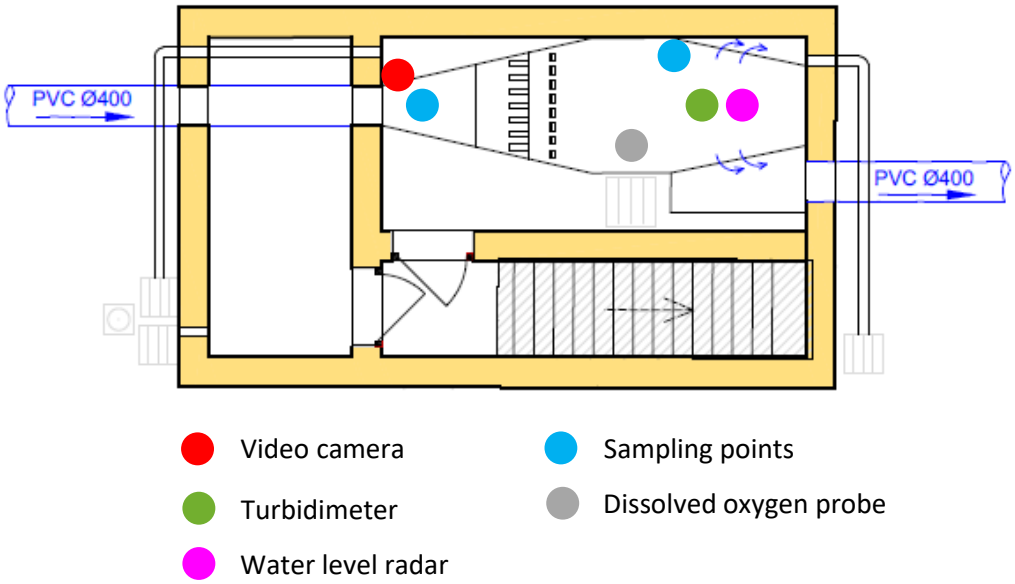

Profile view of the DSM-flux chamber

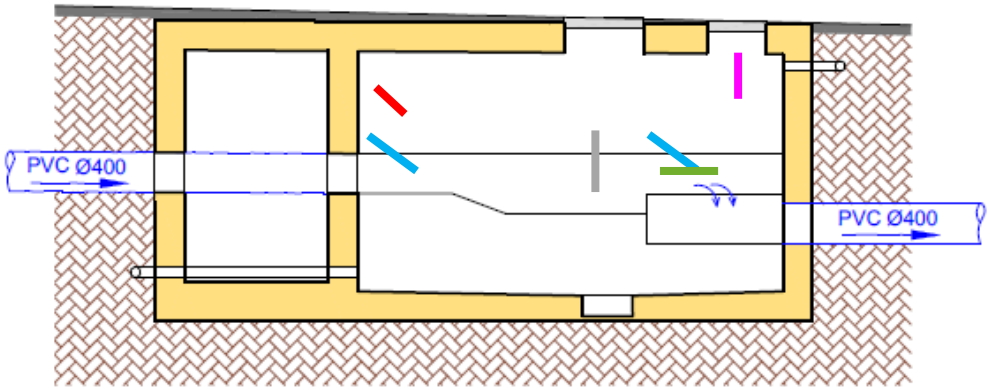

Figure 2.16. Horizontal and profile views of the DSM-flux chamber with the location of the field instrumentation.

The analysis made using the physical and numerical models (results from sections 3.1, 3.2, 4.1 and 4.2) allowed the selection of the most appropriate equipment for the DSM-flux field prototype and the determination of the most appropriate locations for the measurement/sampling points. The DSM-flux field prototype instrumentation has been designed as follows (Figure 2.16): (i) a water level radar (Vegapuls WL61 from VEGA; maximum measurement error of ± 0.002 m) is installed above the overflow area of the device, as in the small-scale physical model; (ii) a turbidimeter (TSS EX1 sc from Hach Lange; accuracy up to 1000 FNU/NTU lower than 5 % of the measured value ± 0.01 FNU/NTU) is located at the symmetry axis of the overflow area, slightly upstream the water level radar position, and submerged below the weir crest level; (iii) there are two automatic samplers (Liquistation CSP44 from Endress+Hauser) with sampling points located (a) at the entry of the device and (b) at the overflow area, near the turbidimeter; (iv) a dissolved oxygen optical probe (VisiPro DO Ex from Hamilton) is installed in the middle length of the stabilization area, at the right side of the device cross-section; and (v) a video camera (ExCam-IPM1145(-L) from Samcon) is placed above the entry of the DSM-flux, with a view angle that covers the whole device. All data is collected with a data logger (Sofrel S550 from Lacroix) and transferred to the laboratory computers via Internet except the videos from the camera, that are stored in a Network-Attached Storage (NAS) at the site and collected manually before its storage limits (controlled via Internet from the laboratory). To complete the monitoring of the CSOs, a second water level radar of the same characteristics is installed in the distribution chamber in order to monitor the flows over the frontal weir by means of a classic frontal weir stage-discharge relationship. The discharge coefficient of this relationship was determined by means of the CFD study carried out at the distribution chamber but the results are not presented as they are out of the scope of this PhD study.

From all this instrumentation, only the water level radar and the video camera data were used in the framework of this PhD work. The rest of the equipment was selected, its locations were determined, and it is being installed for future studies. The water level radar is used to estimate the CSO discharges by means of the DSM-flux HQR established in Chapter 3. The turbidimeter will be used to estimate the TTS and other pollutant fluxes exiting the DSM-flux by means of measurements of turbidity converted into pollutant concentrations. Flow rates measured by means of the DSM-flux HQR are needed to obtain CSO volumes and compute TSS mass loads. In order to correlate the TSS and other pollutant concentrations to the turbidity variables, several samples must be taken with the automatic sampler from the sampling point situated at the overflow area, near the left side-wall of the device, about 20 cm upstream the

cross-section of the turbidity measurements. These samples are taken during an event, and different campaigns must be done to cover a wide variety of events and make the correlation more robust. The automatic samplers are also planned to be used to evaluate the efficiency of the device concerning the removal of particulate pollutants, by means of comparing the concentrations at the entry and at the exit of the device. The dissolved oxygen probe will be used to assess the aeration rate of the flow downstream the hydraulic jump of the dissipation area during the CSO events. This probe is also used to indirectly monitor the production of hydrogen sulphide (H_2S) during the dry weather periods. Indeed, the organic matter settled at the DSM-flux might contain sulphate reducing bacteria which, in the anaerobic conditions that can occur in stagnant water, produce H_2S. The H_2S can gasify and be transferred to the air in the chamber. High concentrations of H_2S in the air are toxic for humans. Thus, a decrease in dissolved oxygen in the stagnant water of the device is an indicator of anaerobic conditions and that these reactions might take place. The probe data is used in this case for security purposes to protect the professionals working in the experimental site. The video camera is activated when water enters the 0.4 m diameter outflow pipe of the distribution chamber and it is used to record the flow passing through the DSM-flux during a CSO event in order to study the real hydrodynamics from visual observations.

Chapter 3

3. THE DSM-flux: AN ACCURATE MONITORING DEVICE

The first question addressed in this PhD work, "Is the DSM-flux a robust monitoring device that provides reliable and accurate flow data?", is analysed in this chapter. As explained in Section 1.4, a multiscale approach was adopted so that the study of this question in three different systems and two different scales, provides the most generic and realistic answer possible. The strategy followed to answer the question is divided in three main stages (Figure 1.6):

- STAGE 1: Establishment and validation of a monitoring methodology from experimental data at a small-scale. As the question asks about an "accurate" device, an uncertainty analysis of the monitoring methodology is also carried out. The methodology is also tested to estimate Combined Sewer Overflow (CSO) volumes.
- STAGE 2: Implementation and validation of a small-scale numerical model with the experimental data from the physical model tests. Transformation of the validated small-scale numerical model to a large-scale model equivalent to the field prototype. Assessment of the monitoring methodology at a large-scale.
- STAGE 3: Validation of the monitoring methodology at a large-scale under realistic operating conditions at the field prototype.

In Sections 3.1, 3.2 and 3.3 of this chapter, the materials and methodologies used at stages 1, 2 and 3, respectively, are described, and the results obtained with each analysis are presented and discussed.

3.1. THE DSM-flux MONITORING METHODOLOGY

The DSM-flux has been conceived with a specific design that allows the monitoring of flow rates, (among other purposes indicated in Section 1.3) by means of a single water level gauge. Thus, the establishment of the monitoring methodology translates into the determination of an appropriate stage-discharge relationship and its uncertainty bounds. In this PhD work, this part of the study was carried out by means of experimental tests (stage-discharge relationship (HQR) tests) using the small-scale physical model. The methodology and results of these analysis are presented in this section, which is an adaptation of the first paper that has been published about this PhD work: "DSM-Flux: A New Technology for Reliable Combined Sewer Overflow Discharge Monitoring with Low Uncertainties" (Maté Marín *et al.*, 2018).

3.1.1. Materials and methods for the establishment of the DSM-flux HQR

Layout and instrumentation of the small-scale physical model for the HQR tests

The experimental set-up of the small-scale DSM-flux physical model was equipped with the necessary instrumentation and adjusted according to the HQR tests characteristics. As presented in Section 2.1, the DSM-flux small-scale physical model is equipped with a flowmeter located at the inflow pipe which measures the flow rate entering the DSM-flux. For the HQR tests, a radar sensor (Vegapuls WL61 from VEGA; maximum measurement error of ± 0.002 m) was installed on a support above the small-scale model in order to measure water level values in the overflow area. The adaptations of the experimental set-up consisted mainly in the adjustment of the inflow pipe slope, which was modified according to the inflow conditions of each of the tests. The purpose of these modifications was to create different inflow regimes.

General methodology for the establishment and validation of the DSM-flux HQR

The methodology followed to establish and validate the DSM-flux HQR consists of four major steps, presented in the flowchart of Figure 3.1.

In addition to the establishment of the DSM-flux HQ relationship and the study of its performance under steady conditions, its capacity to estimate discharged volumes of CSO events was also analysed.

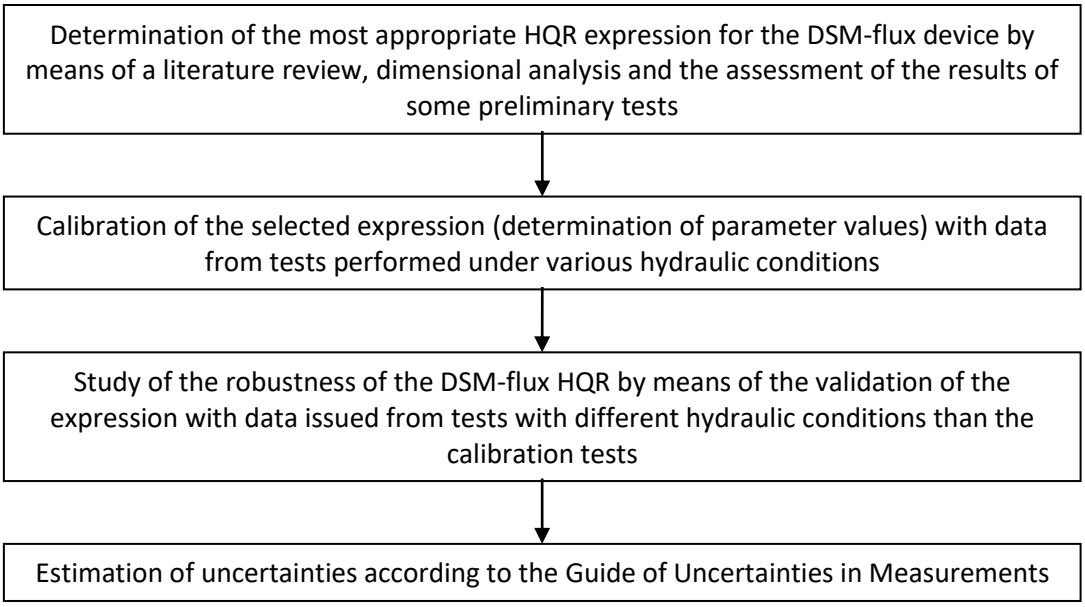

Figure 3.1. Methodology for the establishment and validation of the DSM-flux HQR.

Determination of the DSM-flux HQR expression

Stage-discharge relationships (HQRs) and hydraulic characteristics of flows over pre-calibrated structures such as sharp-crested weirs and Venturi flumes have been widely analyzed. Numerous studies have been done for frontal weirs in rectangular cross-section channels over the last century (*e.g.*, early by Rehbock (1929) or recently by Zhang *et al.* (2015)). Pandey *et al.* (2016) review the most important results. HQRs for this type of structure are commonly defined as (Hager, 2010):

$$Q = C_d \cdot L \cdot \sqrt{2g} \cdot h^{3/2} \qquad \textbf{Equation 3.1}$$

where Q is the discharge over the weir, L is the total weir length ($2L'$ in the case of the DSM-flux, Figure 3.2), g is the gravitational acceleration, and h is the water level above the weir crest, calculated as the difference between the water level upstream of the weir, where the nappe is not curved yet, and the weir crest height (w). C_d is the discharge coefficient that it's usually characterized experimentally. C_d accounts for the nappe curvature and the jet forming downstream of the crest, that both invalidate the hydrostatic pressure assumption and impact the evolution of the velocity profile, as well as the kinetic energy and the head losses. Hence, according to Bagheri *et al.* (2014), Q for sharp-crested weirs is a function of different dominant physical and geometrical quantities. Vaschy-Buckingham's Π-theorem leads to the expression

of C_d in Equation 3.1, but also indicates that C_d relates to a number of dimensionless parameters as follows:

$$C_d = \varphi(F, Re, We, \frac{h}{w}, \frac{h}{L}, \frac{L}{B}, S_0) \qquad \textit{Equation 3.2}$$

where *F*, *Re* and *We* are the Froude, Reynolds, and Weber numbers, respectively, S_o is the channel slope and *B* is the channel width (which, for the DSM-flux device, corresponds to the slope of the part downstream from the energy dissipation chute blocks and the channel width in the stabilization zone, respectively). The φ function, as well as the relevant scales (length, mass, time) that must be used to define *F*, *Re* and *We*, all notably depend on the weir geometry. They also depend on the shape of the nappe: drowned, clinging, or free. In this section the focus is placed on a free nappe. Many authors have studied HQRs for different geometries of sharp-crested weirs using Equation 3.1 and defining specific expressions of C_d from Equation 3.2, according to geometrical characteristics and to hydraulic conditions. Most of the studies done for frontal weirs conclude that C_d depends mainly on *h/w*, or *L/B* if the weir has a contraction (Bagheri *et al.*, 2014). For oblique weirs, Borghei *et al.* (2006) obtained an expression for C_d where the most important dimensionless variables are also *h/w* and *L/B*. Regarding side weirs, Bagheri *et al.* (2014) found that the key dimensionless parameters influencing C_d are *h/w*, *h/L*, *L/B,* and, mainly, *F*, which seems to be a common result for side weirs as velocities remain significant (Borghei and Parvaneh, 2011; Emiroglu *et al.*, 2010; Ramamurthy *et al.*, 2006). Borghei and Parvaneh (2011) and Emiroglu *et al.* (2010) also investigated the influence on C_d of the flow diversion angle (θ) according to the weir crest orientation at oblique and triangular labyrinth weirs, respectively.

Concerning the influence of *Re* and *We*, the common approach is to discard data influenced by viscosity or surface tension effects when calibrating the C_d expression and to limit the application of the resulting HQR to a specific range of hydraulic conditions, including minimum values of *h*, *We*, or *Re*. If a critical regime is considered over the weir crest, the Froude number at the weir crest section (Equation 3.3) will be equal to 1. Thus, velocity over the weir crest (U_{weir}) can be estimated as a function of the water level over the weir crest (h_{weir}) as follows (Equation 3.4):

$$F_{weir} = \sqrt{\frac{(U_{weir})^2}{g \cdot h_{weir}}} \qquad \textit{Equation 3.3}$$

$$U_{weir} = \sqrt{g \cdot h_{weir}} \qquad \textit{Equation 3.4}$$

By applying energy conservation between the weir crest section and the section upstream of the weir where h is known (as defined in Equation 3.1 and Equation 3.2), it can be established that h_{weir} equals $2h/3$.

Reynolds number quantifies turbulence effects, which do not change once the flow regime is fully turbulent, *i.e.* $Re > 10^4$. Considering a wide rectangular cross-section ($L >> h$), the Reynolds number at the weir crest section can be expressed as follows in Equation 3.5:

$$Re_{weir} = \frac{\rho \cdot U_{weir} \cdot 4 \cdot R_h}{\mu} \approx \frac{\rho \cdot U_{weir} \cdot 4 \cdot h_{weir}}{\mu} = \frac{\rho \cdot 4 \cdot \sqrt{g} \cdot {h_{weir}}^{3/2}}{\mu} = \frac{\rho \cdot 4 \cdot \sqrt{g} \cdot \left(\frac{2}{3} h\right)^{3/2}}{\mu} \qquad \textit{Equation 3.5}$$

where U_{weir} is obtained from Equation 3.4, R_h is the hydraulic radius at the weir, ρ is the water density (1000 Kg/m^3) and μ is the water dynamic viscosity ($1.03 \cdot 10^{-3}$ Kg/m·s). For a turbulent flow regime ($Re > 2000$), h is higher than 0.005 m while for a fully turbulent regime ($Re > 10^4$), h is above 0.013 m.

The Weber number accounts for surface tension effects, which can essentially modify the nappe curvature above the weir. By considering the critical water level over the weir crest (h_{weir}) as the scale of the free-surface radius of curvature and its corresponding velocity (U_{weir}), *We* at the weir crest section can be expressed as (Equation 3.6):

$$We = \frac{\rho \cdot g \cdot {U_{weir}}^2 \cdot h_{weir}}{\sigma} = \frac{4 \cdot \rho \cdot g \cdot h^2}{9 \cdot \sigma} \qquad \textit{Equation 3.6}$$

where σ is the surface tension. There is no generally agreed value for the critical Weber number (Peakall and Warburton, 1996). Nevertheless, Erpicum *et al.* (2016) reported that minimal heads (water level above crest weirs) of 0.02 to 0.07 m enable significant size-scale effects to be avoided for free flow over linear weirs, independent of the physical model size.

The DSM-flux has a specific geometry where the parameters w, L, θ, and B are a function of the diameter of the inlet conduit and the part downstream from the energy dissipation devices (which includes the overflow area) is always horizontal ($S_o = 0$) (Figure 3.2). Thus, the geometric ratios will always remain constant as well as the dimensionless parameters L/B, θ, and S_o. Similarly, h/L is known by $(h/w) \cdot (w/L)$, so it will also remain constant. Therefore, C_d is considered in this case as a function of the h/w ratio, which was confirmed by preliminary laboratory tests. These tests also found that the influence of the upstream Froude number, F, was negligible, as expected from the literature review (Borghei *et al.*, 2003; Kabiri-Samani,

2010). The actual geometry, that imposes a flow regime by its initial slope, does not allow the influence of the Reynolds number to be studied independently of *h/w*; however, by setting flow conditions to *Re* > 10^4 and *h* > 0.013 m, which was the case in most of the flows investigated in this study, the effect of *R*e is not considered, neither at the laboratory scale, nor at the field scale where *R*e > 10^5. Similarly, it was not possible to explicitly examine the influence of the Weber number in this study but according to the literature, for *h* > 0.02 m the surface tension effects should be minimal and will decrease with higher *h* in the field.

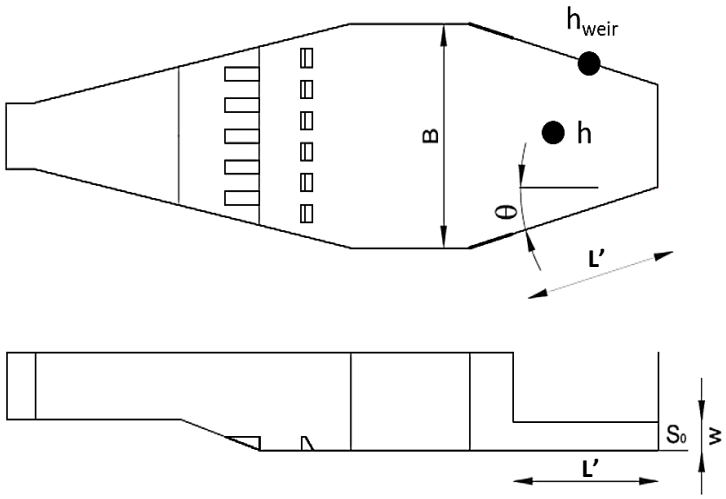

Figure 3.2. The DSM-flux geometry: plan (up) and profile (bottom) views – black dots indicating locations where the specified water levels are measured.

Thus, the C_d expression for the DSM-flux essentially depends on the *h*/*w* dimensionless parameter. According to the literature review and preliminary tests, a power-law seems appropriate, so the DSM-flux HQR is expressed as follows:

$$Q = f(a, b, \frac{h}{w}, L, g, h) = a \cdot \left(\frac{h}{w}\right)^b \cdot L \cdot \sqrt{2g} \cdot h^{3/2} \qquad \textit{Equation 3.7}$$

where *a* and *b* are coefficients to be obtained experimentally by means of a regression method. For this purpose, Equation 3.7 was fitted using 60 *Q*-*h* experimental data and a non-linear regression method based on the Levenberg-Marquardt algorithm implemented in the Matlab® commercial software, as it is presented in Section 3.1.2.

HQR tests characteristics for the calibration and robustness assessment of the DSM-flux HQR

The calibration phase was done with data collected from tests performed for a prismatic open channel and turbulent flow at the inlet pipe with *Re* > 61900. Froude numbers at the inlet pipe

during the calibration tests were lower than 2.5. For all cases, water level measurements were made for flow rate values ranging between 0.0005 m^3/s and 0.01 m^3/s. Inflow was always considered fully-developed as the upstream pipe length was around 25 times the pipe diameter. Tests were computed in steady-state flow conditions with flow rate values which serve to mimic at the physical model scale overflow events with specific hydrograph shapes (Figure 3.3) based on those observed during 15 years in the CSO chamber of the Ecully field site (close to Lyon, France). This site is managed in the frame of a field observatory for water management (www.othu.org). Data associated with high water levels (h > 0.015 m for the DSM-flux, as it was determined in preliminary tests) were used to fit Equation 3.7 whereas data associated with low water levels (h < 0.015 m) served to validate the DSM-flux HQR for this range of low flow rates.

In order to evaluate the robustness of the DSM-flux HQR, two additional tests were done under some inflow conditions that are commonly observed in the field. In the first one, four consecutive 90º bends were installed in the inlet pipe, 6 diameters upstream the DSM-flux entry (Figure 3.4a). In the second test, an obstacle was placed at the DSM-flux entry, blocking half of the cross-section and creating a strong asymmetry in the flow (Figure 3.4b). The objectives of these tests were to create asymmetric flows (from the velocity field point of view) at the entry of the device to evaluate the influence on the HQR and monitoring capacity of the device. These asymmetric flows are commonly found in the field: the 90-degree bends may represent, for example, bad connections to the overflow conduit and the obstacle placed at the entry can simulate a macro-waste, for example, formed by accumulation of solid matter, which are both probable situations in CSO pipes.

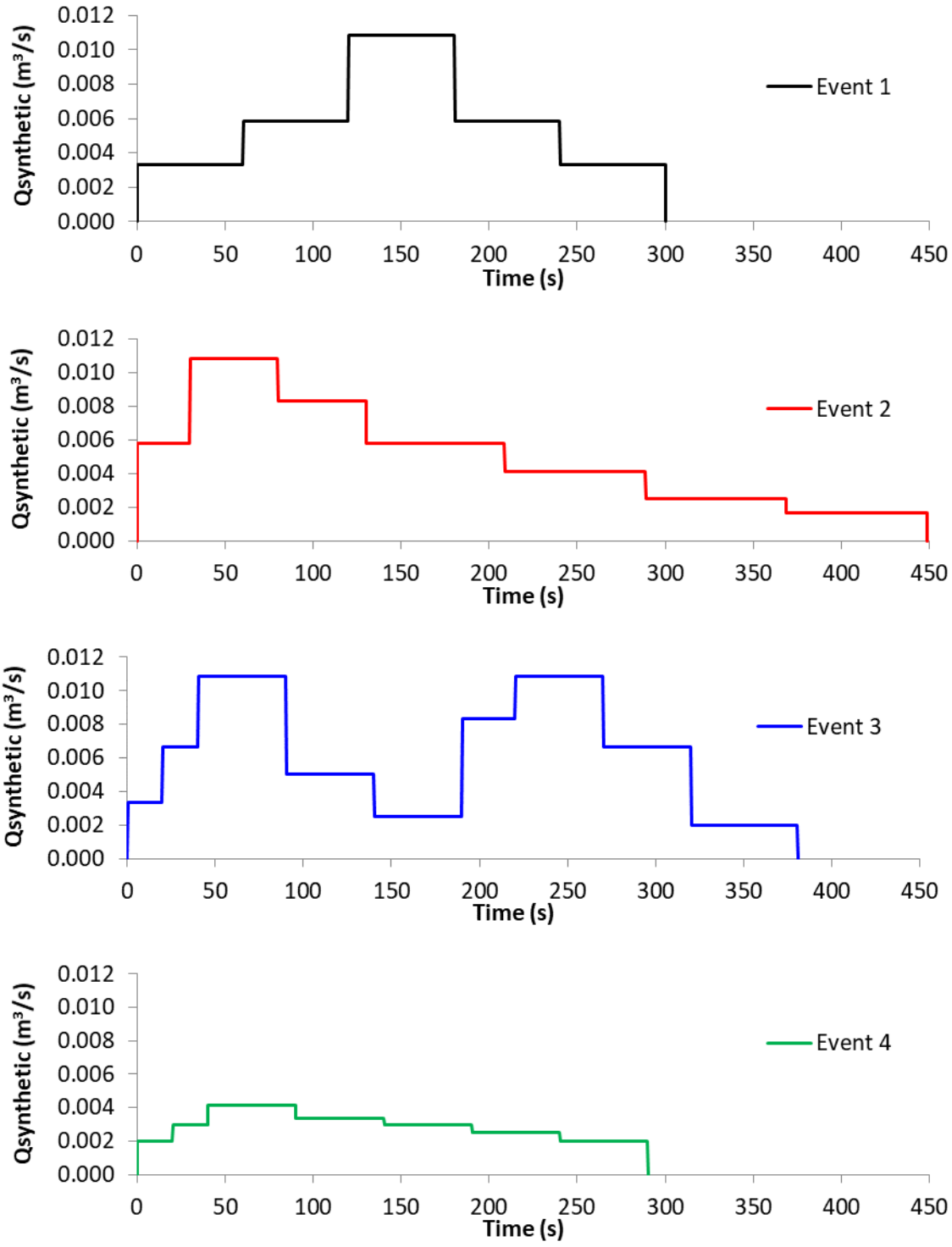

Figure 3.3. Synthetic hydrographs reproduced for the small-scale DSM-flux physical model unsteady-state tests to compute CSO volumes.

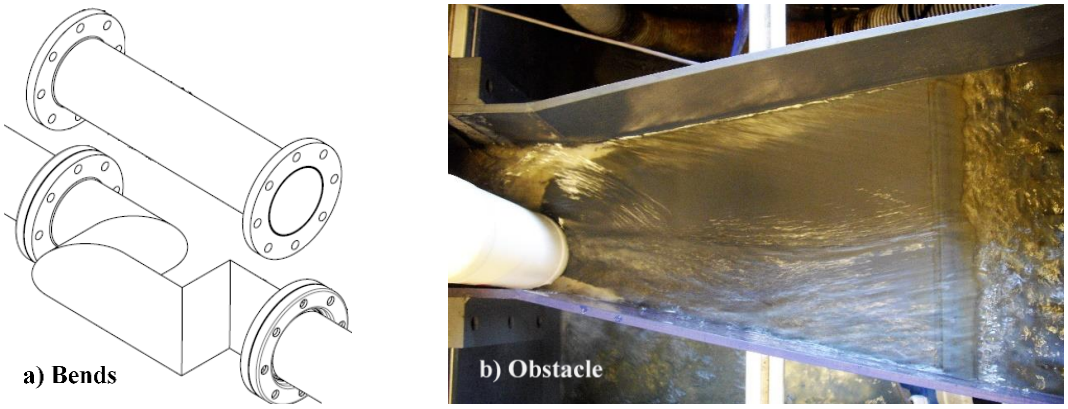

Figure 3.4. (a) Piping piece for additional bends test and (b) asymmetric flow in additional obstacle test.

3.1.2. The DSM-flux HQR

Calibration tests confirmed the existence of three different types of DSM-flux operations according to water level *h* values in the overflow area: for $h < 0.013$ m, a clinging flow appeared over the DSM-flux crests due to local surface tension effects, whereas for greater values of *h* ($h > 0.015$ m), a free flow was established (Figure 3.5). A transition phase was also observed where the nappe flow changed intermittently between clinging and free states at some parts of the DSM-flux weirs before becoming stable along the crests length. Surface tension effects may occur at the beginning of the overflow events. It is assumed that the most common operation is related to free flow. Then the DSM-flux HQR was calibrated using only data with values of water level higher than 0.015 m. The *a* and *b* coefficients values of Equation 3.7 were determined from the regression process based on these calibration data. Equation 3.8 presents the resulting DSM-flux HQR.

$$Q = 0.4639 \cdot \left(\frac{h}{w}\right)^{-0.1350} \cdot L \cdot \sqrt{2g} \cdot h^{3/2} \qquad \textit{Equation 3.8}$$

To assess the goodness of fit related to the calibration process as well as the robustness of the DSM-flux HQR under different flow conditions, four evaluation coefficients were analyzed. The Root Mean Squared Error (RMSE), represented by Equation 3.9, was calculated for each case to evaluate the mean error between measured ($Q_{i\text{-}mea}$) and estimated ($Q_{i\text{-}est}$) flow rates. As this coefficient squares the errors when computing the mean, it causes biases for large flow rates. For this reason, a second indicator, the Mean Absolute Error, labelled MAE (Equation 3.10), was also used, which evaluates absolute errors, and, thus, reduces the bias towards large events. To assess absolute errors in relation with the measured discharges, the Mean Absolute

Relative Error, labelled MARE (Equation 3.11), was calculated as well. Finally, the Nash and Sutcliffe (1970) Efficiency coefficient (NSE) (Equation 3.12), which is widely used as a quality indicator for modeling in hydrology, was the fourth performance parameter analyzed.

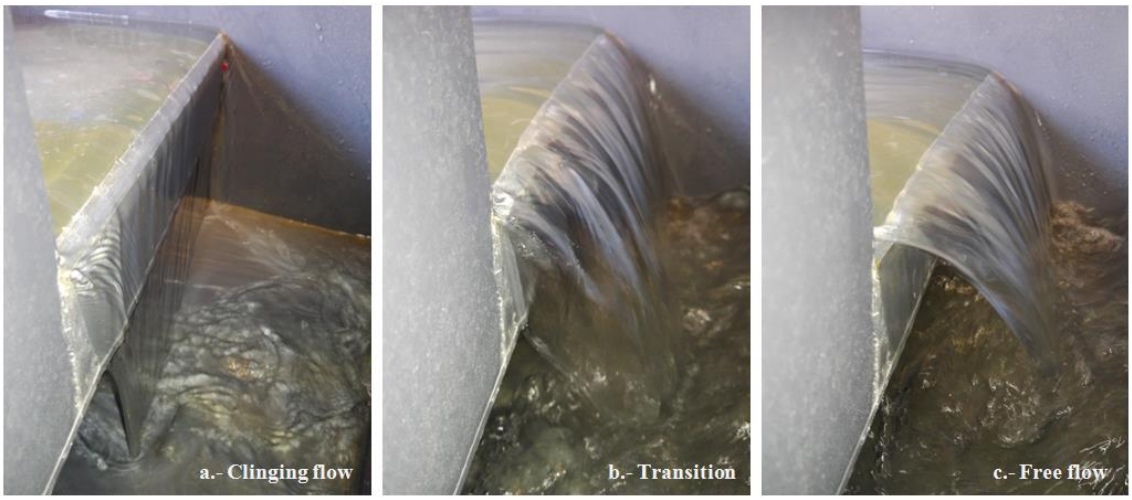

Figure 3.5. Clinging (a), transition (b), and free (c) nappe flow over the right crest of the small-scale DSM-flux physical model.

$$RMSE = \sqrt{\frac{1}{n}\sum_{i=1}^{n}(Q_{i-est} - Q_{i-mea})^2} \qquad \textit{Equation 3.9}$$

$$MAE = \frac{1}{n}\sum_{i=1}^{n}|Q_{i-est} - Q_{i-mea}| \qquad \textit{Equation 3.10}$$

$$MARE = \frac{1}{n}\sum_{i=1}^{n}\left|\frac{Q_{i-est} - Q_{i-mea}}{Q_{i-mea}}\right| \qquad \textit{Equation 3.11}$$

$$NSE = 1 - \frac{\sum_{i=1}^{n}(Q_{i-est} - Q_{i-mea})^2}{\sum_{i=1}^{n}(Q_{i-mea} - \overline{Q_{mea}})^2} \qquad \textit{Equation 3.12}$$

Figure 3.6 shows the DSM-flux HQR (black solid line), represented by Equation 3.8, as well as the calibration data (empty dots) used to determine its coefficients. Values of selected indicators are listed in Table 3.1. The RMSE and MAE coefficients are 0.0004 m^3/s and 0.0003 m^3/s, respectively, for tested values between 0.0041 and 0.0102 m^3/s. MARE is equal to 5% and the NSE is 0.95. Thus, the calibration is considered to be accurate.

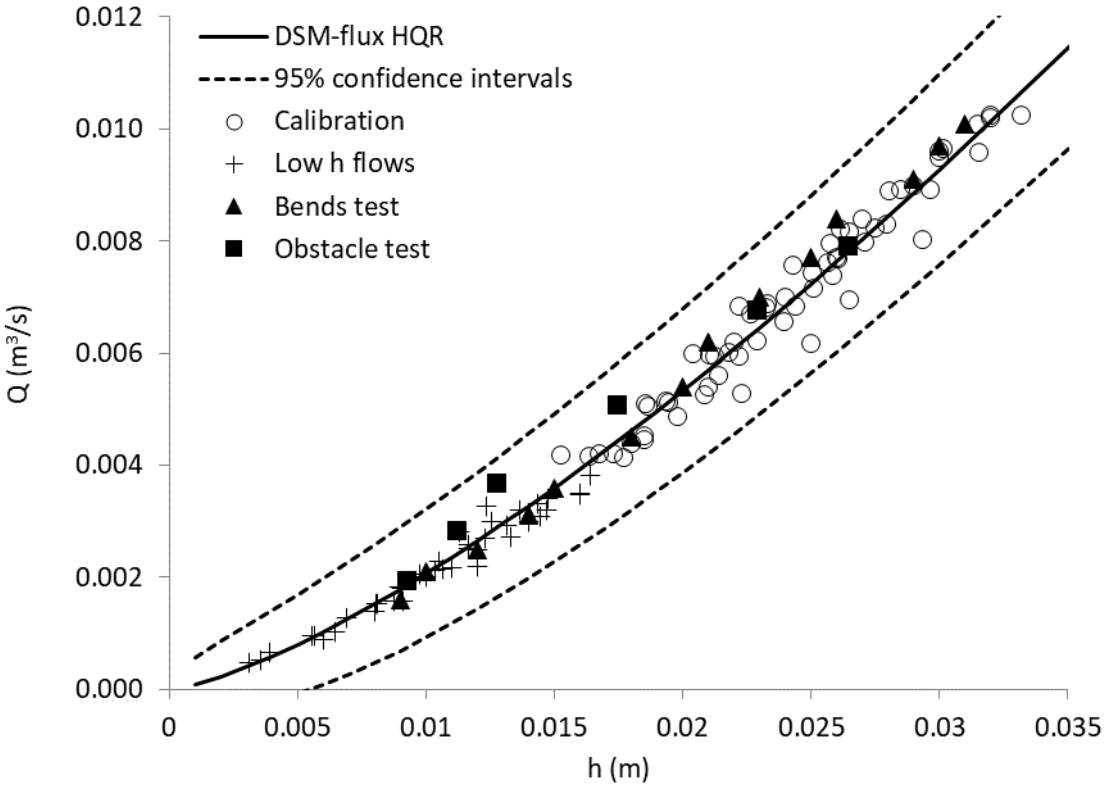

Figure 3.6. DSM-flux HQR (black solid line) represented by Equation 3.8.

Table 3.1. RMSE, MAE, MARE and NS coefficients values for each tested case at the small-scale DSM-flux model. Range of measured discharge rates (Q_{mea}) and total number of measures (N) are also indicated.

Case	RMSE (m^3/s)	MAE (m^3/s)	MARE (%)	NSE (-)	Q_{mea} (m^3/s)	N
Calibration (free)	0.0004	0.0003	5	0.95	0.0041 – 0.0102	60
Clinging	0.0002	0.0002	7	0.95	0.0005 – 0.0038	40
Bends free	0.0004	0.0004	5	0.94	0.0045 – 0.0101	9
Bends clinging	0.0001	0.0001	5	0.95	0.0016 – 0.0036	6
Obstacle free	0.0004	0.0004	7	0.86	0.0051 – 0.0079	3
Obstacle clinging	0.0005	0.0004	13	0.47	0.0019 – 0.0037	3

Data for low water levels (h < 0.015 m) are also represented at Figure 3.6 (crosses). The RMSE and MAE are relatively low, both with values of 0.0002 m^3/s for flow rates between 0.0005 and 0.0038 m^3/s. The MARE increases up to only 7% and the NSE remains equal to 0.95. According to Figure 3.6, flow rates for low water levels estimated by means of the HQR could be slightly overestimated but differences are acceptable, and this is confirmed by the good values of the evaluation coefficients. Thus, the DSM-flux HQR is considered appropriate to determine discharges even under low water level conditions.

3.1.3. Robustness of the DSM-flux HQR

The DSM-flux HQR robustness was analyzed with data obtained from tests where inflow was perturbed to produce an asymmetry in the velocity field either upstream from the entry (bends test) or at the entry of the DSM-flux device (obstacle test). These data are also plotted on Figure 3.6, where filled triangles correspond to data from the bends test and filled squares correspond to data from the obstacle test. Evaluation coefficients are listed in Table 3.1.

Under free flow conditions, the RMSE and MAE associated to the bends test data have values of 0.0004 m^3/s for Q_{mea} between 0.0045 and 0.0101 m^3/s. The MARE is 5% and the NSE is 0.94. For low water levels, the RMSE and MAE are both equal to 0.0001 m^3/s (Q_{mea} between 0.0016 and 0.0036 m^3/s), the MARE remains at 5%, and the NSE equals 0.95. These values are comparable to those obtained from calibration data, which proves the robustness of the global monitoring strategy based on the DSM-flux HQR.

For the extreme case with an obstacle placed at the entry of the device, the RMSE and MAE under free flow conditions are both 0.0004 m^3/s for Q_{mea} between 0.0051 and 0.0079 m^3/s, the MARE is 7% and the NSE is slightly lower than the rest of the cases, reaching 0.86 (see Table 3.1). For low water levels, the RMSE and MAE have values of 0.0005 m^3/s and 0.0004 m^3/s, respectively, for Q_{mea} between 0.0019 and 0.0037 m^3/s but the MARE value increases up to 13% and the NSE decreases down to 0.47. Regarding these extreme flow conditions, the value of MARE is still acceptable and one can consider that the DSM-flux HQR remains robust in the context of CSO monitoring.

The results show that DSM-flux HQR is independent from the inflow hydraulic conditions, whatever the hydraulic conditions occurring at the inlet location are. Indeed, even under a highly asymmetric inflow and any flow regime at the DSM-flux entry, the DSM-flux HQR is a robust method to measure reliable flow rates.

3.1.4. Uncertainty analysis of the DSM-flux HQR

A rigorous uncertainty analysis is conducted in four basic steps (Muste *et al.*, 2012): (i) definition of the measurement process (relation between inputs and outputs) and identification of the error sources; (ii) estimation of uncertainties for each input; (iii) propagation of the input uncertainties to obtain the output uncertainty and (iv) report of the analysis result according to the standards. In the present study, the uncertainty of the flow rate, Q, obtained from Equation 3.7 was evaluated following the Guide to the expression of Uncertainty in Measurement (GUM). The GUM framework is commonly used in the hydrometric field (Bertrand-Krajewski *et al.*, 2000; Muste *et al.*, 2012) particularly for easy measurement processes when inputs follow normal or symmetric probability distributions, as was considered in this case study. The main stages of the GUM methodology for uncertainty evaluation are described in detail in the GUM guidance (JCGM, 2008).

Two main sources of uncertainty were identified within the DSM-flux measurement process: the input data measurements (h) and the determination of the model parameters derived from the calibration process (coefficients a and b in Equation 3.7). The first source of uncertainty is related to the gauge accuracy, which is provided by the manufacturer and depends on the type and model used. Concerning the calibration process, uncertainties in coefficients a and b of Equation 3.7 were derived directly from the regression results (covariance matrix) analyzed with the Matlab® commercial software.

It should be highlighted that uncertainties associated with the data used for calibration (h and Q measurements in the small-scale physical model) were considered negligible as calibration tests were done under well controlled conditions in the laboratory and the instruments used to obtain the data were accurate. During all tests, for each fixed Q, an average of 400 Q-h values was considered in order to reduce random errors.

To propagate the input uncertainties to the final result, standard uncertainties for each input are combined following the propagation law. Further details can be found in the GUM guidance (JCGM, 2008) or in (Muste *et al.*, 2012). By applying the propagation law to the DSM-flux Q measurement model (Equation 3.7), the following expression is obtained:

$$u_c^2(Q) = u^2(a)\left(\frac{\partial f}{\partial a}\right)^2 + u^2(b)\left(\frac{\partial f}{\partial b}\right)^2 + u^2(h)\left(\frac{\partial f}{\partial h}\right)^2 + 2 \cdot u(a,b)\left(\frac{\partial f}{\partial a}\right) \cdot \left(\frac{\partial f}{\partial b}\right) \qquad \textit{Equation 3.13}$$

where $u_c(Q)$ is the combined standard uncertainty of the Q measured by means of the DSM-flux HQR; f is the functional relation representing the measurement process Q = f (a,b,h),

which corresponds to Equation 3.7 with known L, w, and g; u(h), u(a) and u(b) are the standard uncertainties of h, a, and b inputs, respectively, and u(a,b) is the covariance associated with coefficients a and b.

It should be noted that L, w, and g inputs from the measurement process (Equation 3.7) are considered to be well known, so their uncertainties are negligible. Further, the model coefficients a and b and h measurements are not correlated, so their associated covariances were considered equal to zero. However, coefficients a and b are correlated, so their covariance was taken into account when applying the propagation law.

The output discharge quantities can be considered to follow a normal distribution (Muste *et al.*, 2012), so the 95% confidence interval (called coverage intervals in the GUM) was estimated by applying a coverage factor of 2 to $u_c(Q)$, as indicated by Muste *et al.* (2012), in order to obtain the expanded uncertainty of Q, U(Q):

$$U(Q) = 2 \cdot u_c(Q) \qquad \textit{Equation 3.14}$$

In this study, the radar used to measure h values had an accuracy of 0.002 m. The uncertainties related to the coefficients a and b obtained from the covariance matrix had the following values: u(a) = 0.0167, u(b) = 0.0405, and u(a,b) = 0.0007. Equation 3.13 was computed according to these values and the 95% confidence intervals (Equation 3.14) are shown in Figure 3.6 by dashed lines. It would be relevant to include the covariance between h (that may be considered as a random variable) and coefficients a and b in order to see the effect on the confidence intervals of Q. Nevertheless, comparisons were performed against Monte Carlo approach and results on confidence intervals of Q were similar (Maté Marín et al., 2017). It can be observed that all experimental data, either from calibration or validation, are located within the 95% confidence intervals of Q, which means that flow rates obtained by means of the DSM flux HQR for the same water levels as experimental data are known with a level of confidence of 95%. Figure 3.7 illustrates the relative expanded uncertainties, U(Q)/Q as a percentage, for the whole range of discharges of the small-scale DSM-flux physical model analyzed in the present study. Reference values of 10, 15, 20, and 30% corresponding to uncertainty values related to common methods are also represented by dashed horizontal lines for comparison purposes. Relative uncertainties decrease with higher Q and values are lower than 15% for Q above 0.0125 m^3/s, which represents around 60% of the small-scale DSM-flux physical model performance range. As expected, relative uncertainties for low flow rates ($Q < 0.004$ m^3/s) are high, with values above 30%.

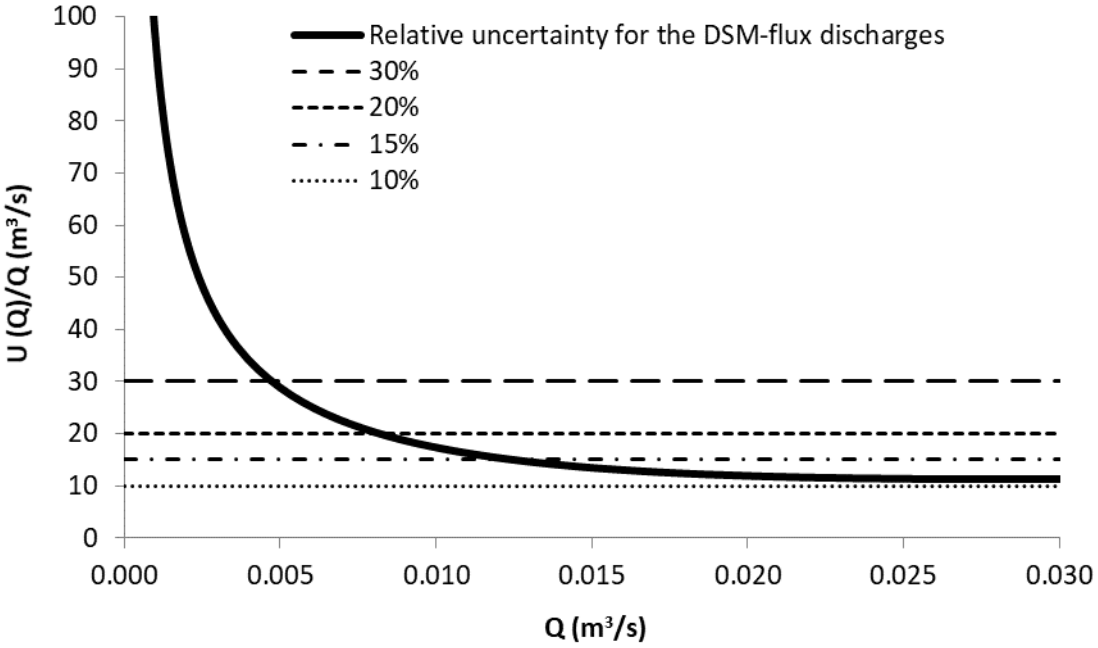

Figure 3.7. Relative expanded uncertainties of flow rates obtained by the DSM-flux HQR (solid line) and other methods uncertainty values from literature (dashed lines).

3.1.5. Assessment of volumes for typical CSO events and their uncertainties

In order to estimate the uncertainties of CSO volumes monitored with the DSM-flux device, the events shown in Figure 3.3 were simulated in the small-scale DSM-flux physical model. Unsteady tests were done to reproduce these hydrographs by means of a flow controller connected to the pump feeding the experimental system. CSO volumes were obtained by means of the trapezes method as computed in the Equation 3.15 proposed by Versini *et al.* (2015):

$$V = z(K_{int}, Q_i) = K_{int} \sum_{i=2}^{m} \frac{Q_{i-1} + Q_i}{2} \cdot \Delta t \qquad \textit{Equation 3.15}$$

Where Δt is the time step of the hydrograph, Q_i is the measured flow rate at time step i, and K_{int} is a coefficient which takes into account the interpolation error between the continuous curve of the real hydrograph and the interpolated curve.

Measured CSO volumes (V_{mea}) obtained via computation of Equation 3.15 with the electromagnetic flowmeter data, were used as reference values for the validation stage. Similarly, estimated CSO volumes (V_{est}) were also obtained in the same way but using

discharges derived from the DSM-flux HQR. As the time step of the overflow events reproduced in the small-scale physical model was short (0.5 s), K_{int} from Equation 3.15 was considered equal to 1. V_{mea} and V_{est} values for each event are listed in Table 3.2. Q_{mea} and the h experimental series were smoothed by applying a simple moving average. Relative errors, $(V_{mea} - V_{est})/V_{mea}$ as a percentage, are lower than 4%, which agrees with values found in other studies using CFD-based methods (see, *e.g.*, Ahm *et al.* (2016)). Event 4 has a higher relative error because flow rates during this event are low ($Q < 0.004$ m^3/s) and, as seen in Figure 3.7, low water level flow rates estimated by the DSM-flux HQR have lower accuracy.

Table 3.2. Measured reference (Vmea) and estimated (Vest) CSO volume values, relative errors and relative expanded uncertainties for the four synthetic events reproduced at the small-scale DSM-flux model.

Event	V_{mea} (m^3)	V_{est} (m^3)	Relative error (%)	Relative uncertainty (%)
1	1.688	1.620	4.0	1.1
2	2.133	2.053	3.7	1.0
3	2.224	2.136	4.0	0.9
4	0.792	0.783	1.1	1.9

Concerning the estimation of the uncertainties associated with these CSO volumes, the GUM approach also was used. In this case, the measurement process consists in integrating the hydrographs obtained from the outputs of the DSM-flux HQR for the whole event duration. No additional sources of error, apart from the ones identified for the flow rates measurements, were considered: *i.e.* the interpolation error represented by K_{int} as well as the error on time measurements were both assumed to be negligible. By applying the propagation law to volumes computed using Equation 3.15, the expression summarized in Equation 3.16 is obtained in order to estimate the uncertainties of CSO volumes measured by means of the DSM-flux device:

$$u_c^2(V) = \sum_{i=1}^{m} u^2(Q_i)\left(\frac{\partial z}{\partial Q_i}\right)^2 \qquad \textit{Equation 3.16}$$

where $u_c(V)$ is the combined standard uncertainty of the volumes measured by integration of the hydrographs obtained from the DSM-flux HQR; z is the functional relation representing the measurement process, and u(Qi) is the standard uncertainty of each Q at time step i of the hydrograph obtained from Equation 3.8 and divided into m time steps. It should be noted that

the covariances between successive discharges have been neglected as these measurements are assumed to be uncorrelated. Indeed, the temporal scale of the measurements is relatively low compared to the event dynamics temporal scale and so successive measurements are considered to be independent.

The output event volume quantities can be considered to follow a normal distribution, so the 95% confidence interval was estimated by applying a coverage factor of 2 to $u_c(V)$, as indicated by Muste *et al.* (2012), in order to obtain the expanded uncertainty of V, U(V):

$$U(V) = 2 \cdot u_c(V) \qquad \textit{Equation 3.17}$$

The uncertainties of Figure 3.7 were used to obtain the standard uncertainties associated with each flow rate of the CSO events shown in Figure 3.3. Equation 3.16 and Equation 3.17 were applied to propagate U(Q) values in order to obtain $u_c(V)$ and to estimate U(V), respectively. Table 3.2 lists the relative uncertainty values for the estimated volumes V_{est}, U(V)/V as a percentage. The maximum value of the four events is 1.9% for Event 4, the rest being around 1%. As expected, the higher the discharges are during the entire event, the lower will be the uncertainty associated with the event volume. These values are relatively low compared to some CSO volumes uncertainties reported in the literature. For example, Isel *et al.* (2014) obtained values that roughly exceed 14% for CFD-based methods.

3.1.6. Conclusions of Section 3.1

The main insights from this section are:

- A simplified HQR has been established specifically for the DSM-flux device by means of investigations on a small-scale physical model.
- It has been proven that the DSM-flux HQR is robust for multiple inflow conditions concerning different flow regimes and velocity fields with different flow symmetry characteristics at the entry of the device. For all tested cases, values of four different indicators (RMSE, MAE, MARE, and NSE) used to assess the goodness and robustness of models calibrated with experimental data have been estimated. Under free flow conditions, the RMSE and MAE values were lower than 0.0004 m^3/s for all cases, for flow rates between 0.0041 and 0.0102 m^3/s. The MARE values were lower than 7% and the NSE exceeded 0.85 in almost all cases. For the case of extreme clinging flow conditions with an

obstacle, the values of statistical indicators are still acceptable in the context of CSO monitoring.

- The GUM framework was applied and for higher flow rates, uncertainties were lower than 15%. Concerning the volumes for the four typical CSO events reproduced in the small-scale physical model, uncertainties were lower than 2%.
- Regarding these results, the DSM-flux appears to be a good alternative compared to current methods in order to reliably monitor CSO structures as the measurement method is independent of the hydraulic conditions upstream from the device and uncertainties associated with the discharge and volume measurements are relatively low, particularly for heavy storm events.

3.2. ASSESSMENT OF THE MONITORING METHODOLOGY AT A LARGER SCALE

The DSM-flux HQR has proven to be a robust methodology to monitor accurately flow rates and CSO event volumes at a small scale. However, the DSM-flux device will probably operate at overflow channels larger than the inflow pipe of the small-scale physical model of this PhD work, as the CSO conduits in the field have usually diameters greater than 0.15 m. The use in a larger device of an HQR obtained at a small-scale model is not always straightforward. When scaling a hydraulic structure considering Froude similarity for the flow (like in this PhD work), Reynolds and Weber numbers are not preserved and this can lead to a different behaviour of the flow at different scales. These differences are commonly known as “scale effects” and, in the case of the DSM-flux monitoring methodology, they could lead to different relationships between flow rates and water levels depending on the scale of the device. In this PhD work, the performance of the DSM-flux HQR at two different scales and the possible scale effects affecting the HQR are assessed numerically by means of CFD simulations. The methodology and results of this assessment are presented in the following subsections.

3.2.1. Materials and methods for the assessment of the DSM-flux HQR at large scale

To assess numerically the performance of the DSM-flux HQR at different scales and the possible scale effects on the flow, it is essential to implement a numerical model that represents as best as possible the real physics. As explained in Section 2.2.1, there are several conceptual models to represent the real physics, for example, for the turbulent phenomena and the flow characteristics near wall boundaries, because these are areas of the fluid dynamics still under research. Also, there are several numerical options to compute the solution differently. And, as said in Chapter 2, the choice of one or another can be somehow subjective, especially for complex flows. Hence, the first step in numerical modelling studies is to determine the most appropriate conceptual model (or mathematical equations) and numerical options according to the physics or phenomena of interest and the specificities of the case that is studied. For that purpose, three different numerical models were tested under similar conditions than the HQR tests and the results were compared to the experimental data for validation. This process was made with the small-scale model because the experimental data are issued from the tests at the small-scale physical model. The most appropriate numerical model (combination of numerical options) was then selected. The HQR was also assessed with a set of data different from the one used for validation corresponding to greater flow rates. Once the HQR had been validated at the small-scale numerical model, the model

was scaled preserving those settings and its performance was analysed for different scenarios to assess the relationship between the flow rates and the water levels. No calibration of equation parameters or unknown input values was performed. Figure 3.8 presents a flowchart with the methodology followed in this section.

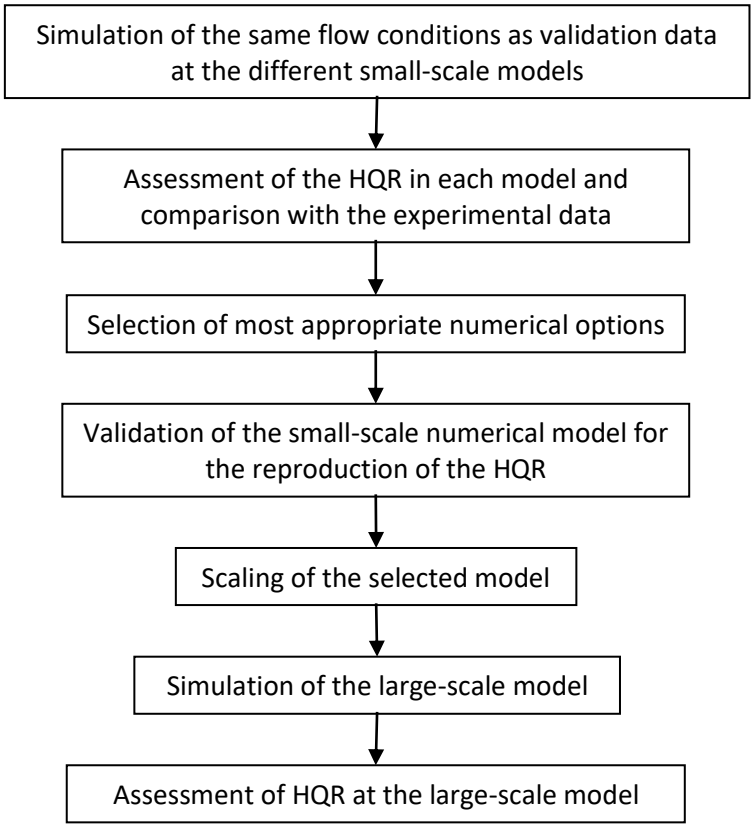

Figure 3.8. Methodology to assess the HQR at large-scale.

Simulations for the assessment of the DSM-flux HQR at different scales

In this PhD work, three different small-scale models were implemented (Table 2.1) in order to identify the numerical options that better represents the real physics of the DSM-flux flow. All the models were simulated under hydraulic conditions within the range of the flow rates tested at the small-scale physical model, which is between 0.002 and 0.009 m^3/s. Additional simulations were done at one of the models (SM-B) for flow rates out of the operating range of the physical model: 0.015 and 0.02 m^3/s. The large-scale models were simulated for five flow rates within the operating range of the field prototype: 0.05, 0.08, 0.1, 0.15 and 0.18 m^3/s. Assuming a Froude similarity between both scaled models, the three lowest flow rates simulated at the large-scale model are within the equivalent range of flow rates tested at the small-scale physical model.

Concerning the inputs of the numerical models, the default values given by ANSYS Fluent code for the parameters of the mathematical equations and the fluid properties were the ones considered in all simulations. Values of variables at the boundary conditions depend on the hydraulic conditions being simulated. As explained in section 2.1.2, the inlet boundary condition was of velocity-inlet or mass-flow-inlet type, so turbulent intensity and hydraulic diameter were determined for each hydraulic condition. At the inlet boundary, turbulent intensity values were considered in between 3% and 10%, as recommended by Andersson *et al.* (2011) and ANSYS Fluent Theory Guide (ANSYS, 2015a), based on Equation 3.18Equation 2.3. It was observed that water levels were not significantly affected by the values of this input probably because of the long inflow pipe.

$$I = 0.16 \cdot Re^{-1/8}$$

Equation 3.18

The hydraulic diameter for an open channel flow is four times the hydraulic radius, which depends on the water level. As the water level at the inlet is variable, it was considered for all simulations that the inlet cross-section was completely fulfilled, and it was let the model develop the flow until the DSM-flux entry. Thus, the hydraulic diameter was considered equal to the inflow pipe diameter.

The outlet boundaries were of pressure-outlet type, so turbulent intensity and hydraulic diameter were also defined. ANSYS Fluent default values or arbitrary values were considered as no backflow is expected to happen.

As introduced in Section 2.1.2, convergence of the solution was evaluated by monitoring the residuals, the mass flow balance between the inlet and the outlets (both sides of the overflow area) and the water level at the downstream zone of the device. A solution was considered converged when (i) all these monitors clearly tended to an asymptotic line, (ii) scaled residuals where lower than 10^{-3} and (iii) the mass flow balance was lower than 3%.

Numerical solutions exhibit some fluctuation even if the preceding criteria defining convergence are fulfilled. Thus, flow rates and water levels values were obtained by averaging data from a long interval of iterations (at least 20000) starting once the convergence criteria are reached. Data within this interval was registered with different frequencies but, in general, mean values of these variables were obtained from, at least, 500 data. Mass-flow imbalance of simulation solutions was taken into account by considering the flow rates as the mean between the inflow and outflow values. Thus, the standard deviation of the mass-balance has been considered as the standard deviation of the flow rate values.

Table 3.3 summarizes all the simulations made at the small and large scales of the numerical models. Values of input variables at the boundary conditions for each simulation are also indicated. For the variables that are not indicated in Table 3.3, default values given by ANSYS Fluent code were considered.

Table 3.3. Simulations made at the small- and large- scale numerical models.

MODEL	SIMULATION	Q_{inlet} (m^3/s)	$I_{turbulent\ inlet}$ (%)
SM-A	Sim SM-A2	0.002	3, 10
	Sim SM-A3	0.0035	3
	Sim SM-A5	0.005	3
	Sim SM-A7	0.007	3
	Sim SM-A9	0.009	3, 10
SM-B	Sim SM-B2	0.002	3, 10
	Sim SM-B5	0.005	4.4
	Sim SM-B9	0.009	4
	Sim SM-B15	0.015	4
	Sim SM-B20	0.02	4
SM-C	Sim SM-C2	0.002	10
	Sim SM-C9	0.009	4
LM-A	Sim LM-A50	0.05	3.6
	Sim LM-A80	0.08	3.4
	Sim LM-A100	0.1	3.3
	Sim LM-A150	0.15	3.1
	Sim LM-A180	0.18	3.1
LM-B	Sim LM-A50	0.05	3.6
	Sim LM-A80	0.08	3.4
	Sim LM-A100	0.1	3.3
	Sim LM-A150	0.15	3.1
	Sim LM-A180	0.18	3.1
LM-C	Sim LM-A50	0.05	3.6
	Sim LM-A80	0.08	3.4
	Sim LM-A100	0.1	3.3
	Sim LM-A150	0.15	3.1
	Sim LM-A180	0.18	3.1

3.2.2. Validation of the small-scale model with the HQR tests data

As explained in section 3.2.1, the three small-scale numerical models considered in this study (Table 2.1) were simulated under hydraulic conditions within the range of the flow rates tested at the small-scale physical model. Table 3.4 presents, for each simulated flow rate (Q_{sim}), the values of the water levels observed at the overflow area of the DSM-flux numerical models

(h_{sim}), as well as the difference between flow rates obtained from simulations and flow rates obtained by means of the DSM-flux HQR (Q_{HQR}) computed with h_{sim} and relative to the DSM-flux HQR values. Water levels at the numerical models are calculated as an area weighted value, equivalent to the area of the radar projection on the water free surface, as it is done at the small-scale physical model. All numerical models reproduce the HQR points with differences lower than 15%, except for the lower flow rates at models SM-B and SM-C, where differences are of 17% and 23% respectively. This was an expected result as the DSM-flux HQR was calibrated for flow rates higher than 0.004 m^3/s and it was accepted that lower discharges could be estimated with a lower accuracy.

Table 3.4. Numerical results from the simulations at the small-scale numerical models.

MODEL	SIMULATION	Q_{sim} (m^3/s)	h_{sim} (m)	Q_{HQR} (m^3/s)	Q_{sim}-Q_{HQR}/Q_{HQR} (%)
SM-A	Sim SM-A2	0.0020	0.010	0.0021	-3%
	Sim SM-A3	0.0035	0.014	0.0033	7%
	Sim SM-A5	0.0070	0.025	0.0072	-3%
	Sim SM-A7	0.0090	0.029	0.0089	2%
	Sim SM-A9	0.0050	0.020	0.0053	-6%
SM-B	Sim SM-B2	0.0020	0.011	0.0024	-17%
	Sim SM-B5	0.0050	0.021	0.0056	-11%
	Sim SM-B9	0.0090	0.030	0.0093	-3%
	Sim SM-B15	0.0151	0.043	0.0153	-2%
	Sim SM-B20	0.0201	0.053	0.0204	-1%
SM-C	Sim SM-C2	0.0020	0.012	0.0025	-23%
	Sim SM-C9	0.0091	0.032	-0.0012	-11%

Figure 3.9 shows the DSM-flux HQR with the corresponding 95% confidence intervals estimated at Section 3.1.4. Numerical data of Table 3.4 have been represented in the same figure with the corresponding standard deviation for the simulated mean flow rates and water levels values. It is observed that all points are located within the uncertainty bounds of the HQR, which means that there is a 95% of probability that the numerical flow rate values correspond to the flow rates obtained by means of the DSM-flux HQR for the same water levels.

Figure 3.10 shows equivalent results to Figure 3.9 in dimensionless terms: the discharge coefficient C_d estimated by the DSM-flux HQR (Equation 3.8) is represented for the whole data range as well as the simulated C_d values corresponding to the numerical data of Table 3.4.

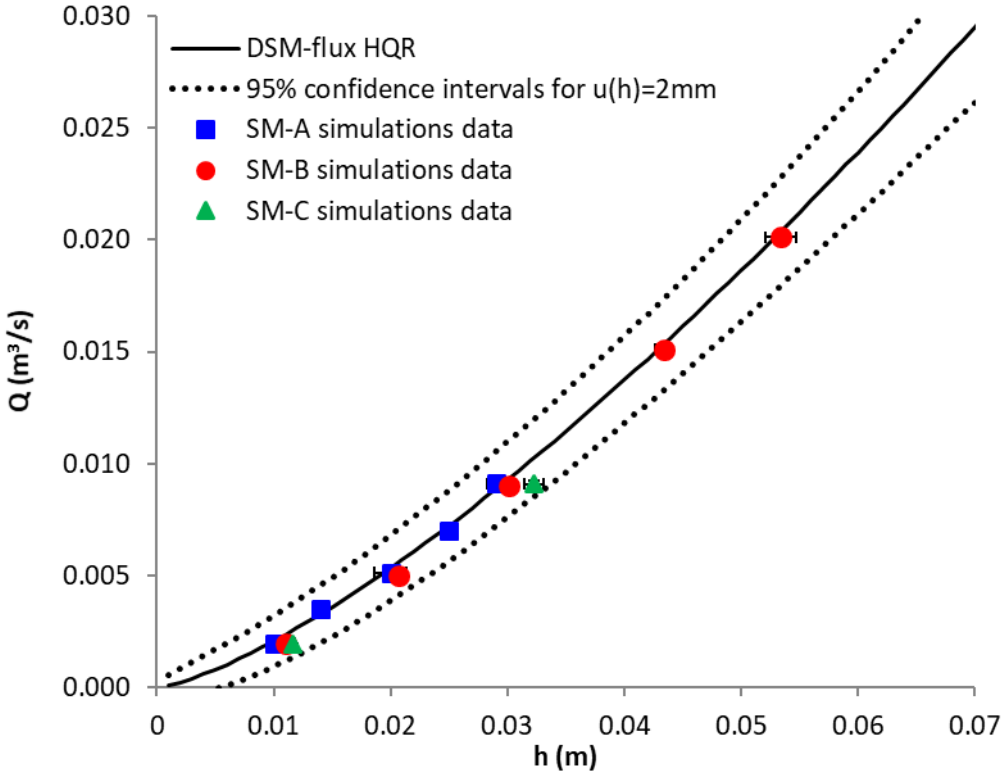

Figure 3.9. DSM-flux HQR (solid line) represented by Equation 3.8 and its 95% confidential intervals (dashed lines). Numerical data from simulations at the small-scale models (Table 3.4).

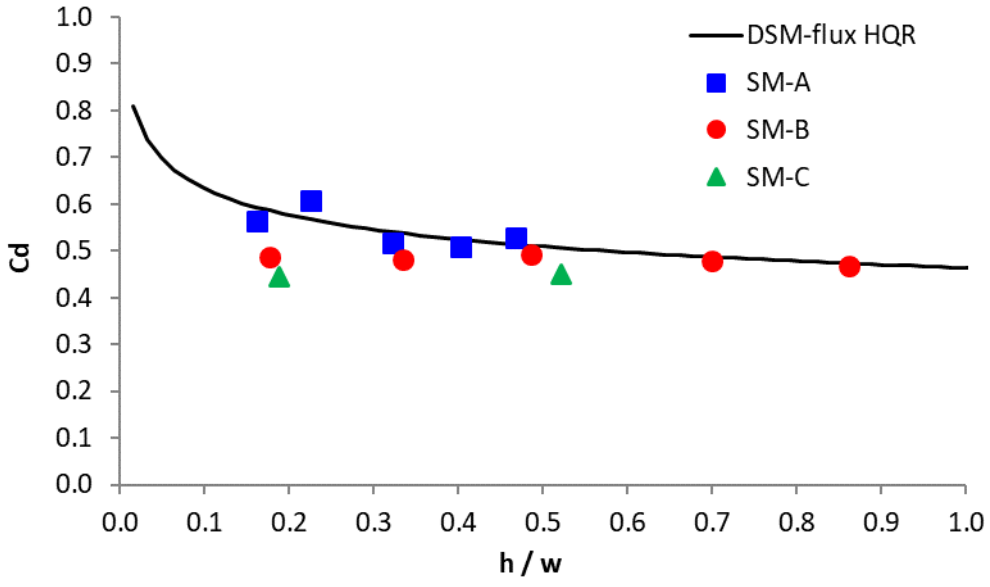

Figure 3.10. DSM-flux HQR (solid line) and simulated discharge coefficients for the numerical data of the simulations at the small-scale models (Table 3.4).

In view of these results, the three models (*i.e.* the combination of mathematical equations and numerical options selected) seem to represent accurately the real flow distribution physics. The VOF model reproduces satisfactorily the experimental data, with independence of the near-wall treatment used. The influence of the type of near-wall treatment on the relationship between the flow rates and the water levels at the DSM-flux seems negligible as results from model SM-A (Scalable Wall Function) and results from models SM-B and SM-C (Enhanced Wall Treatment) are not significantly different. The type of mesh and the level of refinement used in this study don't seem to influence the reproduction of the HQR neither, as the agreement with experimental data is similar for the three models with different sizes of meshes.

Additional simulations were carried out for model SM-B at hydraulic conditions out of the operation range of the small-scale physical model. This model was selected because, regarding the similar results, this model is a good compromise between mesh refinement and computational time compared with the other two models. A very good agreement (1-2% of relative difference) is observed between Q_{sim} and Q_{HQR} for these higher flow rates not tested experimentally, which proves the robustness of the DSM-flux HQR out of its calibration range.

3.2.3. Assessment of the DSM-flux HQR at the large-scale numerical model

The DSM-flux HQR was found to be a robust stage-discharge relationship for the whole operation range of the small-scale device. However, the DSM-flux is probably going to operate at overflow channels larger than the inflow pipe of the small-scale physical model of this PhD work. Thus, the performance of the DSM-flux HQR was evaluated numerically using a large-scale model. As the three small-scale numerical models reproduced the DSM-flux HQR accurately, regardless of the near-wall treatment or mesh refinement, any of the numerical settings combinations seem appropriate to assess the DSM-flux HQR in a larger scale. In order to save computational time, it was decided to use a coarse mesh without any refined zones as in mesh MS1 of model SM-A. For the near-wall treatment, the Scalable Wall Function was used to avoid mesh refinement close to the walls.

As explained in Section 2.2, the initial large-scale numerical model (LM-A) was designed scaling the small-scale device preserving a geometric similarity with a scale of 2.67 and assuming Froude similarity (Table 2.4). Table 3.5 presents, for each simulated flow rate (Q_{sim}), the values of the water levels observed at the overflow area of the DSM-flux numerical model LM-A (h_{sim}), as well as the difference between flow rates obtained from simulations and flow rates obtained by means of the DSM-flux HQR (Q_{HQR}) computed with h_{sim}, and relative to the DSM-

flux HQR values. For the lower flow rates, the LM-A model reproduces the HQR points with differences lower than 15%. However, as the flow rates increase, the relative differences increase as well.

Table 3.5. Numerical results from the simulations at the large-scale numerical model LM-A.

MODEL	SIMULATION	Q_{sim} (m^3/s)	h_{sim} (m)	Q_{HQR} (m^3/s)	$(Q_{sim}-Q_{HQR})/Q_{HQR}$ (%)
LM-A	Sim LM-A50	0.0499	0.046	0.0502	-1%
	Sim LM-A80	0.0806	0.067	0.0846	-5%
	Sim LM-A100	0.1008	0.083	0.1129	-11%
	Sim LM-A150	0.1524	0.119	0.1847	-18%
	Sim LM-A180	0.1830	0.145	0.2426	-25%

Figure 3.11 shows the DSM-flux HQR with the corresponding 95% confidence intervals estimated according to the methodology described in Section 3.1.4 and considering, in this case, different individual uncertainties for the water level measurements, u(h), as these uncertainties might increase up to 0.01 m under field conditions (Bertrand-Krajewski *et al.*, 2000). Numerical data from Table 3.5 have been represented in the same figure with the corresponding standard deviation for the simulated mean flow rates and water levels values. It is observed that all points are located within the uncertainty bounds of the HQR corresponding to a water level measurement uncertainty of 0.01 m, except the higher flow rate point. This means that these numerical flow rate values obtained by CFD simulations have a 95% probability to correspond to the flow rates obtained by means of the DSM-flux HQR for the same water levels if they are measured with at least 0.01 m of uncertainty.

Figure 3.12 presents the simulated C_d values at the small-scale and initial large-scale models, as well as the values issued from the DSM-flux HQR. C_d values have been obtained from Equation 3.8, with w and L depending on the scale of the model.

Lower flow rates of the large-scale model LM-A are estimated accurately with the DSM-flux HQR but differences between the simulated flow rates and the values obtained by means of the HQR increase significantly with higher flow rates and water levels. However, the higher flow rate points are within the range of equivalent values at the small-scale model which already have proven to follow accurately the DSM-flux HQR. The range of flow rates simulated at the small-scale model was from 0.002 to 0.021 m^3/s which, applying Froude similarity, is equivalent to flow rates ranging from 0.023 to 0.233 m^3/s at the large-scale model. Regarding the water levels, the range of the simulated values at the small-scale model was from 0.01 to 0.053 m, which is equivalent to values ranging from 0.027 to 0.141 m at the large-scale model.

So, the large-scale model (h,Q) points are within the range of equivalent values simulated at the small-scale model. Only the higher flow rate point of the large-scale simulations exceeds, but only for a few millimetres, the range tested at the small-scale model.

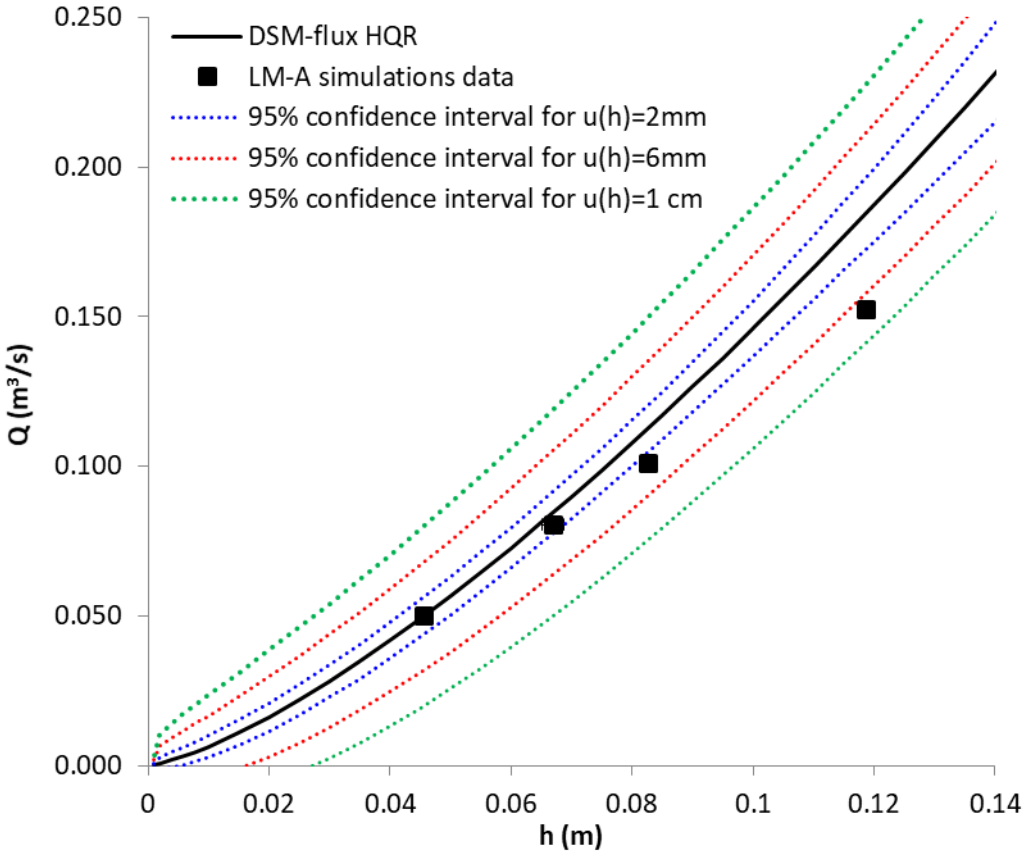

Figure 3.11. DSM-flux HQR (solid line) represented by Equation 3.8 and its 95% confidential intervals (dashed lines) for different uncertainties of the water level measure. Numerical data from simulations at the large-scale model LM-A (Table 3.5).

As flow rates are an input of the numerical model, the answer to this mismatch at higher flow rates is in the free surface behaviour. Five possible reasons could explain these differences at higher flow rates at the large-scale model. The first one is related to the scale effects; the second one is associated to the stabilization of the hydraulic jump downstream from the dissipation area; the third one is related to the curvature of the flow at the overflow area; the fourth one is a consequence of the numerical accuracy of the free surface modelling and the fifth one is related to the modelling of surface waves. In order to study these hypotheses, the solutions of the higher flow rate points of both scale models have been analysed in detail and compared. Equivalent points have been selected for this assessment. From the flow rates point of view, the highest flow rate (h,Q) point of the large-scale model (Q=0.180 m^3/s) is equivalent

to the second highest flow rate (h,Q) point of the small-scale model (Q=0.015 m^3/s). From the water levels point of view, the highest flow rate (h,Q) point of the large-scale model (h=0.145 m) is equivalent to the highest flow rate (h,Q) point of the small-scale model (h=0.053 m). So these three (h,Q) simulations, (0.043,0.015) and (0.053,0.02) for the small-scale model and (0.145,0.183) for the large-scale model, referred to as sim SM-B15, sim SM-B20 and sim LM-A180 respectively from now on, are the ones selected for the detailed analysis.

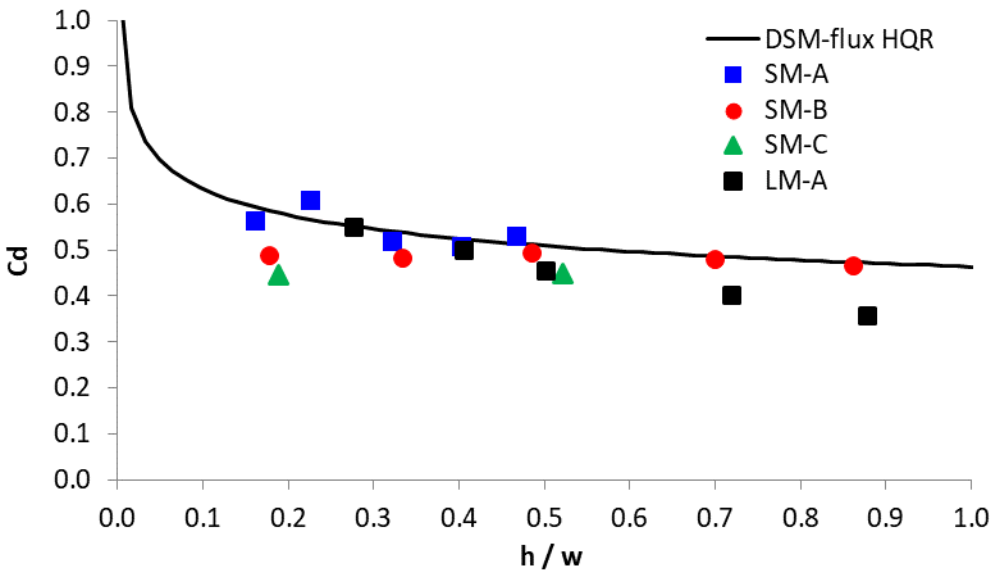

Figure 3.12. DSM-flux HQR (solid line) and simulated discharge coefficients for the numerical data of the simulations at the small-scale and LM-A models (Table 3.4 and Table 3.5).

The scale effects

Scale effects appear when there is a change in the ratio between the different types of forces acting on the flow. Turbulent free surface flows are dominated by gravitational and inertial forces, so Froude number should be more or less the same at the small- and large-scale models for equivalent hydraulic conditions. Froude number has been estimated for the higher flow rate simulations of both scale models at the downstream cross-section of the stabilization area, considering a constant water level equal to $w+h_{sim}$ as the characteristic length (w=0.062 m (small) or w=0.165 m (large), depending on the scale of the model) and an average x-velocity equal to Q_{sim} divided by the cross-section area $Bx(w+h_{sim})$. These Froude number values for the two small-scale and the large-scale simulations are all 0.3, which confirms the conservation of this relation of inertial and gravitational forces in the two scaled models.

When Froude similarity is preserved between two flows of the same fluid, it is not possible to preserve the same Reynolds number at the same time. This difference in the relation between inertial and viscous forces might introduce some scale effects on the flow behaviour. However, these effects tend to decrease with highly turbulent flows ($Re > 10^4$). Reynolds number has been estimated for the higher flow rate simulations of both scale models at the downstream cross-section of the stabilization area, considering the hydraulic diameter of a constant water level cross-section of $w+h_{sim}$ as the characteristic length (w=0.062m (small) or w=0.165m (large), depending on the scale of the model), an average velocity equal to Q_{sim} divided by the cross-section area $Bx(w+h_{sim})$ and a kinematic viscosity of $1.03 \cdot 10^{-6}$ m^2/s for the water. Reynolds values for sim SM-B15 and sim SM-B20 at the small-scale model are of $8 \cdot 10^4$ and 10^5, respectively and for sim LM-A180 of the large-scale models, it is $4 \cdot 10^5$. Although Reynolds number of sim SM-B15 is slightly lower than the other two, all values are greater than 10^4 so it is unlikely that scale effects appear due to different Reynolds numbers.

The third relation of forces that it's not preserved with Froude similarity and that might introduce scale effects on the flow behaviour is the relation between inertial forces and surface tension forces. However, as it was explained in Section 2.1, surface tension forces were not modelled in the CFD simulations because it was considered that their influence was negligible in relation with gravitational, inertial and viscous forces, especially as flow rates increase. So, as numerical models are not affected by surface tension, this can't be the reason for the different behaviour of the flow at the higher flow rates of the different scale models.

In view of these analysis, it is unlikely that the mismatch of the higher flow rate numerical data from the DSM-flux HQR at the large-scale model is due to scale effects. Besides, other case studies that have analysed the scale effects on the HQR of flows over weirs conclude that scale effects decrease with higher water levels (Díaz García, 2015; Erpicum *et al.*, 2016) or that they are even not significative (Sabarots Gerbec *et al.*, 2014).

The stabilization of the hydraulic jump downstream from the dissipation area

The second reason that might explain these differences is associated to the stabilization of the flow downstream from the hydraulic jump. As flow rates (and turbulence) increases (as it is the case with larger scale devices), the stabilization of the hydraulic jump might be more challenging, and this can affect the homogeneity of the free surface at the overflow area introducing some divergences with the DSM-flux HQR (which was obtained under a homogeneous free surface). Figure 3.13 shows the longitudinal profile of the free surface (which is considered the line of volume of fluid values equal to 0.5) along the symmetry axis of

the device, for the sim SM-B15, sim SM-B20 and sim LM-A180 simulations. Velocity vectors have been represented for qualitative analysis and relative comparison only, as velocity field will be discussed in detail in Section 4.2. Starting the analysis by the stabilization area, it is observed that, in both scales, there is a "hollow" in the free surface profile at more or less the middle of the stabilization area. Regarding the flow field, this "hollow" seems to be due to a deflected jet that is formed when the flow impacts the downstream row of dissipators, and that reattaches afterwards to the bottom, plunging into the flow downstream from the downstream row dissipators. In the literature, this flow pattern is called the Reattached Wall Jet (RWJ) regime of a submerged hydraulic jump and is associated with relatively large submergences (Habibzadeh *et al.*, 2012, 2014; Mehdizadeh *et al.*, 2010; Wu and Rajaratnam, 1995). As observed in Figure 3.14 from Wu and Rajaratnam (1995), this plunging jet creates two recirculation zones at different depths: one at the bottom of the channel, immediately downstream from the dissipation blocks, and one at the surface of the flow. If instead of considering the free surface as the iso-surface of volume of fluid values equal to 0.5 it is considered a value of 0.8 (more air than water), it is observed that the "hollows" of Figure 3.13 transform in a recirculating region for sim SM-B20 and sim LM-A180 (sim SM-B15 seems the beginning of the state regime so these recirculation is still not formed), as well as the "hollow" over the slope of the device, that transforms into a recirculating region that appears upstream the dissipation blocks, as observed in the small-scale physical model. The first conclusion issued from this analysis is that the consideration of the iso-surface of volume of fluid values equal to 0.5 as the free surface might entrain some errors when there is air entrainment in the flow. In fact, several authors have highlighted the difficulties and limitations to model air entrainment in hydraulic jumps (Bayon *et al.*, 2016; Javan and Eghbalzadeh, 2013; Valero *et al.*, 2014; Witt *et al.*, 2015) or plunging jets (Castillo *et al.*, 2014b). So careful attention must be taken at the overflow area when determining the free surface of the flow to obtain the water level values. The second conclusion is that no significative differences between scales are observed concerning the free surface profile and the flow field at the stabilization area. Indeed, downstream the plunging jet, the free surface seems to stabilize in both cases. From the longitudinal profile point of view, water levels seem quite homogeneous along the overflow area since the entry to this zone. Certainly, the presence of the end wall seems to create a rise of the free surface at the end of the device. However, this happens at both, the small- and the large-scale models, so the stabilization of the hydraulic jump doesn't seem to be the cause of the differences in the correlation between the DSM-flux HQR and numerical data at different scales.

As it is explained in Section 4.2, it should be highlighted that the Reattached Wall Jet (RWJ) regime doesn't take place at low flow rates (Figure 3.15 from Habibzadeh *et al.* (2011)). Figure 3.16 is equivalent to Figure 3.13 but it corresponds to a case where there are no differences between scales concerning the correlation to the DSM-flux HQR and numerical data. Equivalent (h,Q) simulations, (0.03,0.009) from SM-B small-scale model and (0.083,0.1) from LM-A large-scale model, referred to as sim SM-B9 and sim LM-A100 respectively from now on, have been selected for this comparison. In this case, there is still a deflecting jet at the second row of dissipation blocks, but it doesn't plunge afterwards into the flow: it remains close to the surface. Thus, the recirculating region at the surface disappears. This is called in the literature the Deflecting Surface Jet (DSJ) regime of the submerged hydraulic jumps and it is associated with relatively low downstream levels (Habibzadeh *et al.*, 2014, 2012; Mehdizadeh *et al.*, 2010; Wu and Rajaratnam, 1995). This is the reason why, at low flow rates, no "hollow" in the free surface is observed at the stabilization area.

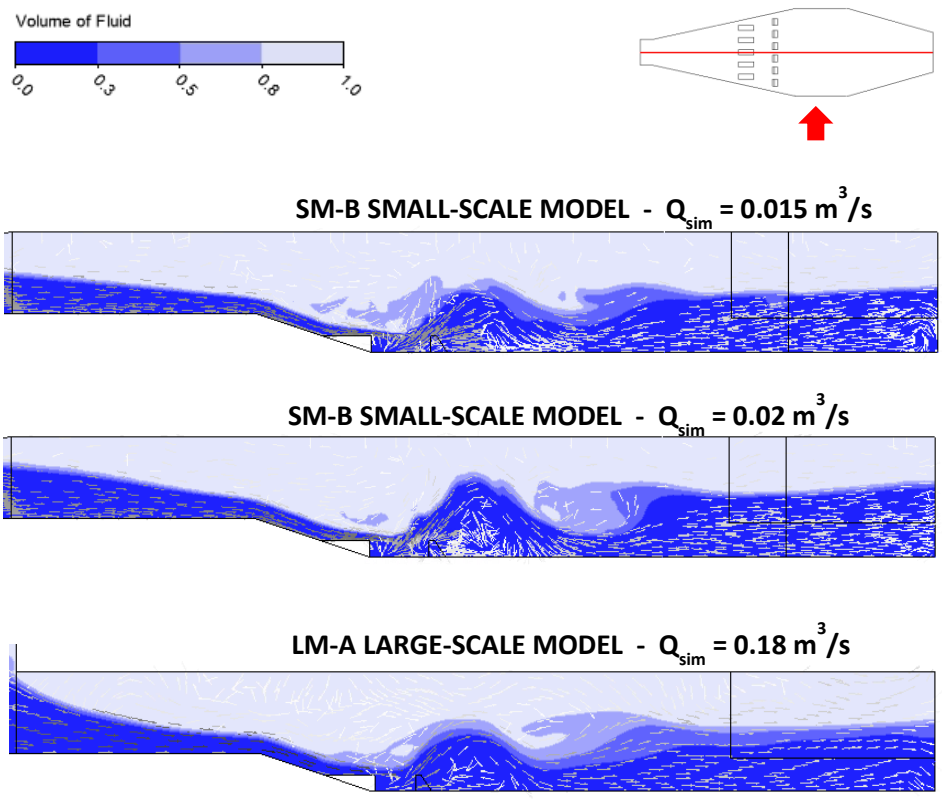

Figure 3.13. Free surface profile (volume of fluid = 0.5) at the axis of symmetry of the device for the small-scale and large-scale models, for Q=20 l/s and Q=180 l/s respectively.

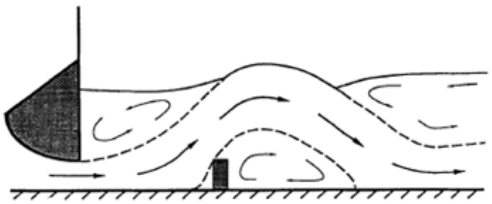

Figure 3.14. Flow pattern for the Reattached Wall Jet regime of a submerged hydraulic jump (adapted from Wu and Rajaratnam (1995)).

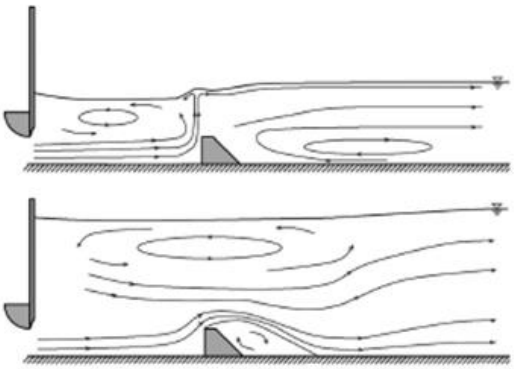

Figure 3.15. Flow pattern for the Deflecting Surface Jet (above) and Reattached Wall Jet (below) regimes of a submerged hydraulic jump (adapted from Habibzadeh et al. (2011)).

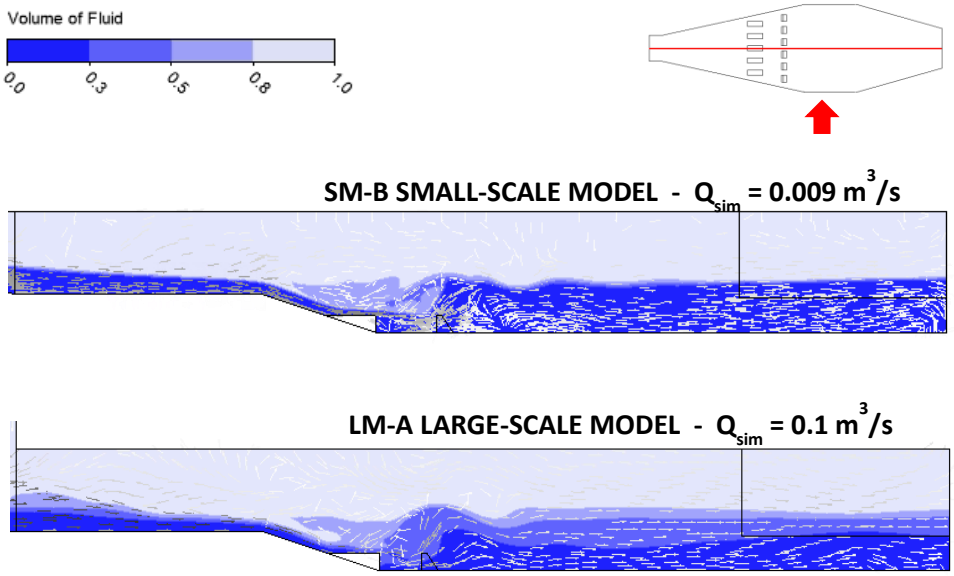

Figure 3.16. Free surface profile (volume of fluid = 0.5) at the axis of symmetry of the device for the small-scale and large-scale models, for Q=9 l/s and Q=100 l/s respectively.

The water level gradient at the overflow area

The third reason that might explain the differences between small- and large-scale results is associated with the curvature of the flow at the overflow area due to the acceleration of the flow when reaching the weir crest. The DSM-flux HQR was calibrated with data issued from hydraulic conditions where the curvature of the free surface at the overflow area was insignificant. As the water levels at the numerical models are calculated as an area weighted value, corresponding to the area of the radar projection on the water free surface, if the cross-section gradient of water levels is significant at higher flow rates at the large-scale simulations, this might entrain a divergence with the DSM-flux HQR values. Figure 3.17 and Figure 3.18 show the free surface profile of the cross-section at the middle of the overflow weir crests, for the same hydraulic conditions and models as the ones presented in Figure 3.13 and Figure 3.16. At the small-scale simulations sim SM-B15 and sim SM-B20, it is observed that the free surface is slightly more homogeneous for a higher flow rate than at the large-scale simulation sim LM-A180, where the gradient of water levels is slightly more important and produces a less homogeneous free surface. This difference between small and large scales is less obvious for lower flow rates at Figure 3.18 issued from sim SM-B9 and sim LM-A100. In this case, the free surface is still quite homogeneous at the larger-scale model. This could help in the divergences with the DSM-flux HQR of the higher flow rate points at the large-scale model, but the order of magnitude of the inaccuracies due to the curvature of the flow seems much lower than the magnitude of the divergences, which is of several centimetres. Further analysis of additional simulation data for higher flow rates at the small-scale model would allow to see (i) if a more important gradient of water levels is formed at the small-scale model and (ii) how the DSM-flux HQR performs in this case. However, this would mean to increase the capacity of the inflow pipe, as the one used in this PhD work is equal to the higher flow rate tested at the small-scale model.

Regarding the concerns about the definition of the free surface as the iso-surface of values of volume of fluid equal to 0.5, it is observed in both Figure 3.17 and Figure 3.18 that at the large-scale simulations there is a wider difference among iso-surface equal to 0.5 and that of 0.8 than in the small-scale simulations. However, this might not explain the divergence with the DSM-flux HQR at large-scale because (i) it happens also at lower flow rates (Figure 3.18) and (ii) the differences of water levels are only of a few millimetres.

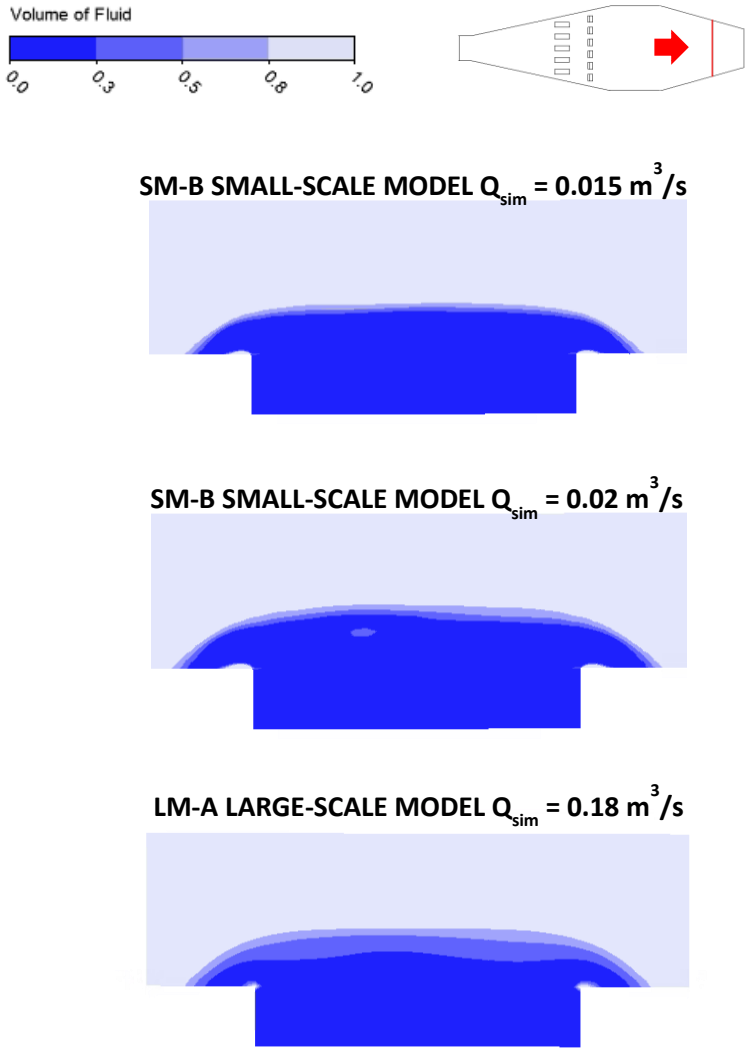

Figure 3.17. Free surface profile (volume of fluid = 0.5) at cross-sections at the middle of the overflow weir crests for the small-scale and large-scale models, for Q=20 l/s and Q=180 l/s respectively. Views from the upstream, so the weir at the left of the figure is the left weir at the device.

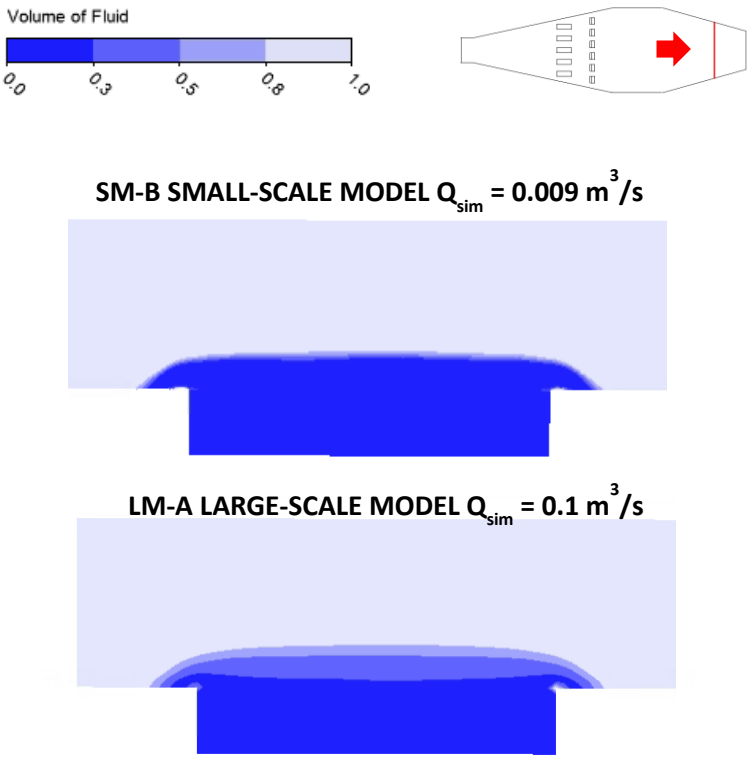

Figure 3.18. Free surface profile (volume of fluid = 0.5) at two cross-sections: one at the end of the stabilization area and one at the middle of the overflow area for the small-scale and large-scale models, for Q=9 l/s and Q=100 l/s respectively. Views from the upstream, so the weir at the left of the figure is the left weir at the device.

The numerical solution accuracy in the free surface modelling

The fourth reason that might explain the differences between small- and large-scale results is associated to the capacity of the numerical model to accurately reproduce the free surface, which is related to the level of discretization of the mesh. Several authors have highlighted the importance of the mesh size when using VOF model (Bayon *et al.*, 2016; Jarman *et al.*, 2008; Witt *et al.*, 2015). It was observed at the small-scale model that the mesh refinement didn't have a significant influence on the reproduction of the DSM-flux HQR, as results from SM-A model, which has a coarse mesh, were as accurate as the results from SM-B or SM-C model, that have a refined mesh at the weir crest level. However, the relative size of the mesh with respect to the water level (Δz/h) at the free surface interface level of the overflow area might be different at the small- and large- scale models. Figure 3.19 presents the three cross-section free surface profiles at the middle of the overflow weir crests presented in Figure 3.17, this time with the mesh lines superposed. Although the small-scale model has a higher discretization, the size of the elements close to the free surface interface relative to the water

level (Δz/h) are equivalent in both scale models: 0.13 and 0.12 for sim SM-B15 and sim SM-B20 respectively at the small-scale model and 0.13 for sim LM-A180 at the large-scale model. So, the local relative size of the elements close to the free surface doesn't seem to be the cause of the divergences between scales but maybe the general higher discretization of model SM-B does. A mesh sensitivity analysis should be carried out for the large-scale model to assess this possibility. However, this analysis couldn't be done in the framework of this PhD work and remains as a pending task.

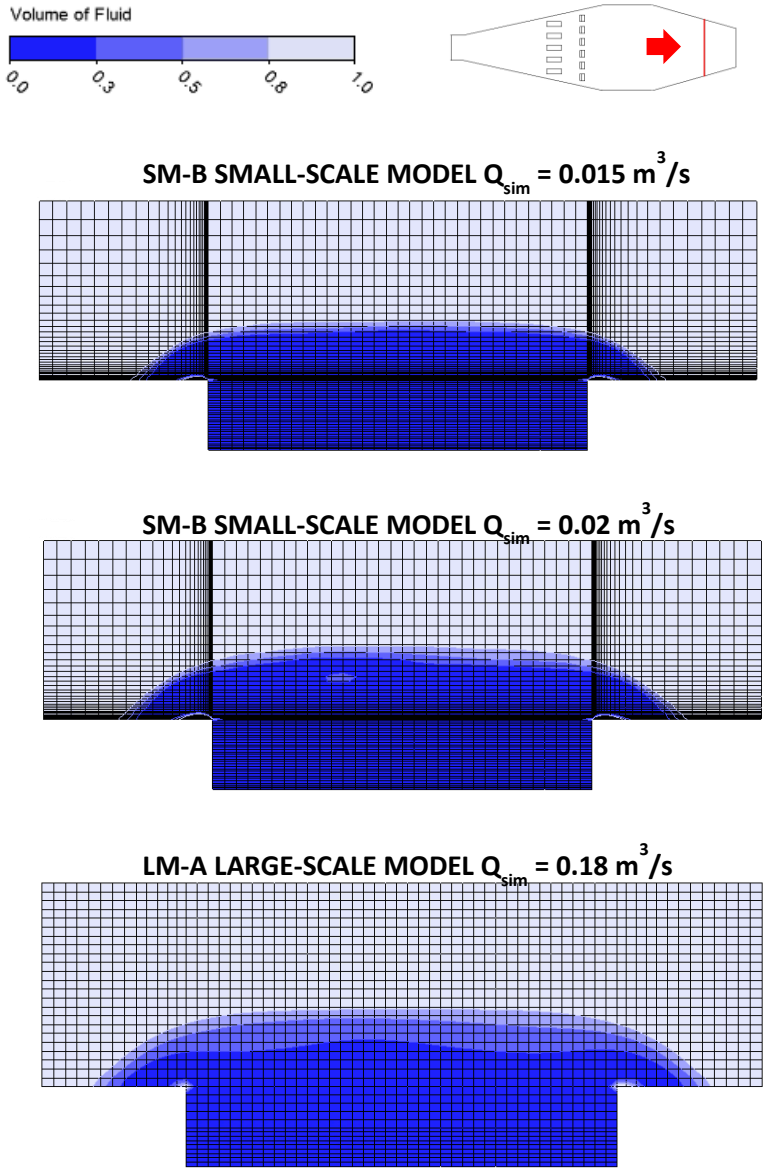

Figure 3.19. Free surface profile (volume of fluid = 0.5) at cross-sections at the middle of the overflow weir crest for the small-scale and large-scale models, for Q=15 l/s, Q=20 l/s and Q=180 l/s, with the mesh lines superposed. Views from the upstream, so the weir at the left of the figure is the left weir at the device.

Free surface waves at high flow rates

The last reason that might explain the differences between small- and large-scale results is associated to the modelling of waves at the free surface interface. The presence of the end wall at the DSM-flux device causes a perturbation in the equilibrium of the free surface interface and leads to gravity waves, whose amplitude increase with higher momentums. Simulations in this PhD work have been carried out for steady conditions, so no transient flow phenomena, as the oscillation of the water levels caused by waves, is reproduced or can be assessed with this simulation results. Indeed, if the flow in this problem is really oscillating, the steady-state solver will not produce an average version of the real transient flow field, but it will cycle between the possible solutions of the transient problem. Thus, a numerically fluctuating solution once convergence is achieved could be associated to the occurrence of an unsteady phenomena. Figure 3.20 presents the evolution of the water level along the iterations of simulation sim LM-A180. It is observed that, although a convergence is achieved, the value of the water level fluctuates with an amplitude of 0.01 m. However, these oscillations also appear at small-scale simulations and they are more or less of the same magnitude, around 0.008 m for sim SM-B20 and lower (0.005) for sim SM-B15 (Figure 3.21 and Figure 3.22). Although a mean value has been considered for the evaluation of the DSM-flux HQR (Table 3.5), these values might not be equivalent to the mean values of the real oscillations, and this could be the cause of the differences between scales. Transient simulations, which unfortunately couldn't be done in this PhD work, will give further insight on this question.

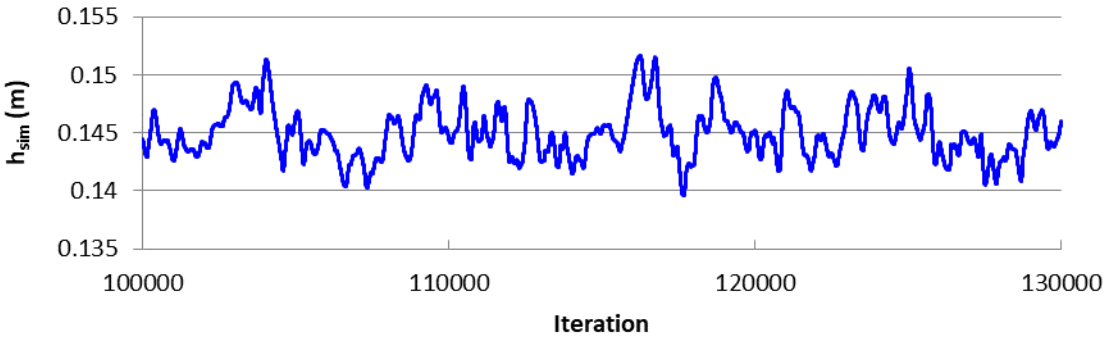

Figure 3.20. Evolution of h_{sim} along the iterations after convergence of the simulation for the large-scale model LM-A at Q=180 l/s (sim LM-A180).

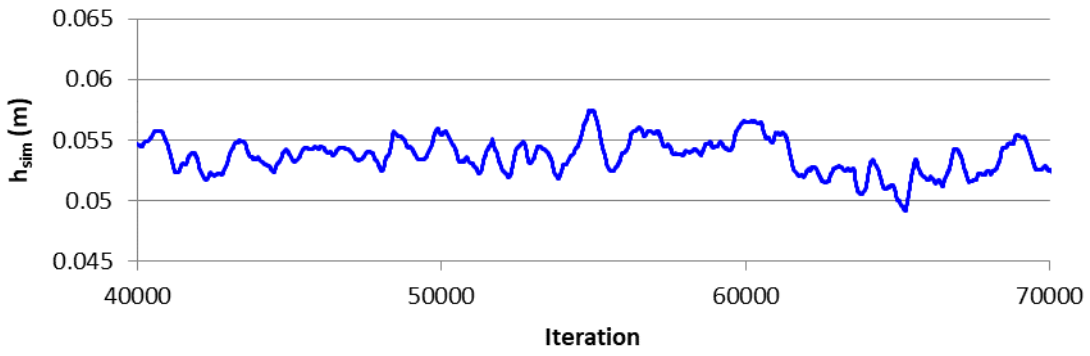

Figure 3.21. Evolution of h_{sim} along the iterations after convergence of the simulation for the small-scale model SM-B at Q=20 l/s (sim SM-B20).

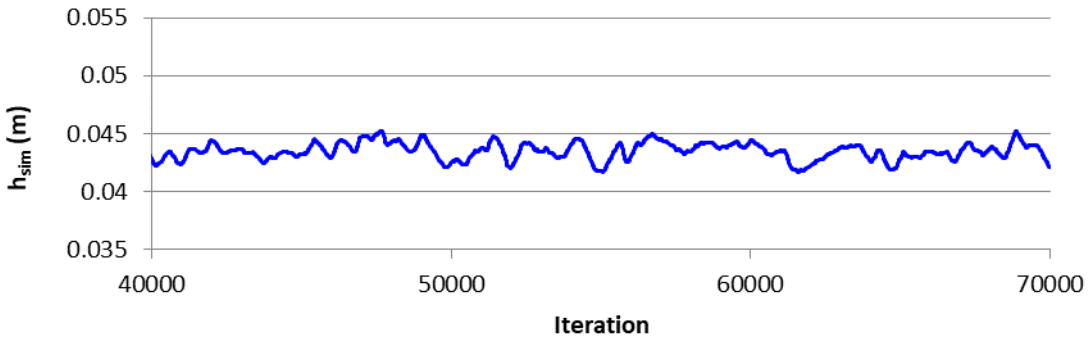

Figure 3.22. Evolution of h_{sim} along the iterations after convergence of the simulation for the small-scale model SM-B at Q=15 l/s (sim SM-B15).

3.2.4. DSM-flux field prototype optimisation and influence on the DSM-flux HQR

Despite the DSM-flux HQR has proven to be an accurate monitoring method for relatively lower flow rates at large scale devices, some divergences appear to occur at higher flow rates that need further investigation. Besides these divergences, some other issues were found when assessing the flow behaviour at the large-scale model LM-A. As explained in Section 4.2.3, a concern arose about the retention capacity of the large-scale device as velocities and TKE observed in the stabilization and overflow areas were considered too high for deposition to happen, based on literature values like the ones given by Yan (2013) and Dufresne (2008) for TKE (figures of section 4.2.3). The construction and operating of the DSM-flux field prototype has two main purposes: (i) to validate the monitoring methodology and (ii) to assess the retention capacity of the device, both under realistic operating conditions. In order to accomplish objective (ii), it is important to ensure that some material will actually settle at the

device. Thus, is was decided to modify the initial design to guarantee a minimum of retention in the field prototype. Further details of this modification process are given in Section 4.3.3. Two modifications are suggested as an alternative to the initial DSM-flux design: (i) to increase the number of dissipation blocks and adapt their height according to some indications given by Momplot (2014) and (ii) to increase the weir crest height. The second modification affects some of the conditions rising from the dimensional analysis carried out when establishing the DSM-flux HQR (Section 3.1.1): h/w and h/L are no longer proportional and thus C_d might also depend on h/L. To evaluate the performance of these to alternative designs and assess the conservation of the DSM-flux HQR, two large-scale numerical models were implemented with the new geometries, LM-B for the design which has increased the number of dissipation blocks and LM-C for the design that not only has more dissipation blocks but also has got higher weir crests (Table 2.4). These models have been simulated for the same operating conditions than LM-A, which are indicated in Section 3.2.1. Table 3.6 presents, for each simulated flow rate (Q_{sim}), the values of the water levels observed at the overflow area of the DSM-flux numerical models LM-B and LM-C (h_{sim}), as well as the difference between flow rates obtained from simulations and flow rates obtained by means of the DSM-flux HQR (Q_{HQR}) computed with h_{sim}, and relative to the DSM-flux HQR values. Values of model LM-A, presented already in Table 3.5, are also included in Table 3.6 for comparison. In general, the models reproduce the HQR points with differences lower than 20% except for the lower flow rate point at model LM-B. The pattern observed at model LM-A, where differences increased as the flow rates increased, is less obvious in models LM-B and LM-C. Differences are slightly lower in model LM-C.

Figure 3.23and Figure 3.24 present, for models LM-B and LM-C respectively, the DSM-flux HQR with the corresponding 95% confidence intervals estimated according to the methodology described in Section 3.1.4 and considering, as in Figure 3.11, different individual uncertainties for the water level measurements, u(h). Numerical data of Table 3.6 have been represented in the same figure with the corresponding standard deviation for the simulated mean flow rates and water levels values. It is observed that all points are located within the uncertainty bounds of the HQR corresponding to a water level measurement uncertainty of 0.01 m. This means that these numerical flow rate values obtained by CFD simulations have a 95% probability to correspond to the flow rates obtained by means of the DSM-flux HQR for the same water levels if they are measured with at least 0.01 m of uncertainty. Simulation data from model LM-C seem closer to the DSM-flux HQR, except for the higher flow rate (h,Q) point. This means that the fact that h/w and h/L are no longer proportional doesn't seem to affect C_d. This statement would need further verification with tests with weir crests at different rates but, in

case this is true, it's a great advantage from an operational point of view as this means that the weir crest could be mobile and thus the weir height could be adapted to favour (or not) retention function of the device without affecting significantly the monitoring function.

Table 3.6. Numerical results from the simulations at the large-scale numerical models.

MODEL	SIMULATION	Q_{sim} (m^3/s)	h_{sim} (m)	Q_{HQR} (m^3/s)	$(Q_{sim}-Q_{HQR})/Q_{HQR}$ (%)
LM-A	Sim LM-A50	0.0499	0.046	0.0502	-1%
	Sim LM-A80	0.0806	0.067	0.0846	-5%
	Sim LM-A100	0.1008	0.083	0.1129	-11%
	Sim LM-A150	0.1524	0.119	0.1847	-18%
	Sim LM-A180	0.1830	0.145	0.2426	-25%
LM-B	Sim LM-B50	0.0493	0.037	0.0379	30%
	Sim LM-B80	0.0797	0.062	0.0762	5%
	Sim LM-B100	0.0995	0.084	0.1157	-14%
	Sim LM-B150	0.1506	0.112	0.1700	-11%
	Sim LM-B180	0.1817	0.135	0.2205	-18%
LM-C	Sim LM-C50	0.0497	0.045	0.0499	0%
	Sim LM-C80	0.0800	0.066	0.0855	-7%
	Sim LM-C100	0.1001	0.074	0.1002	0%
	Sim LM-C150	0.1499	0.106	0.1619	-7%
	Sim LM-C180	0.1801	0.134	0.2236	-19%

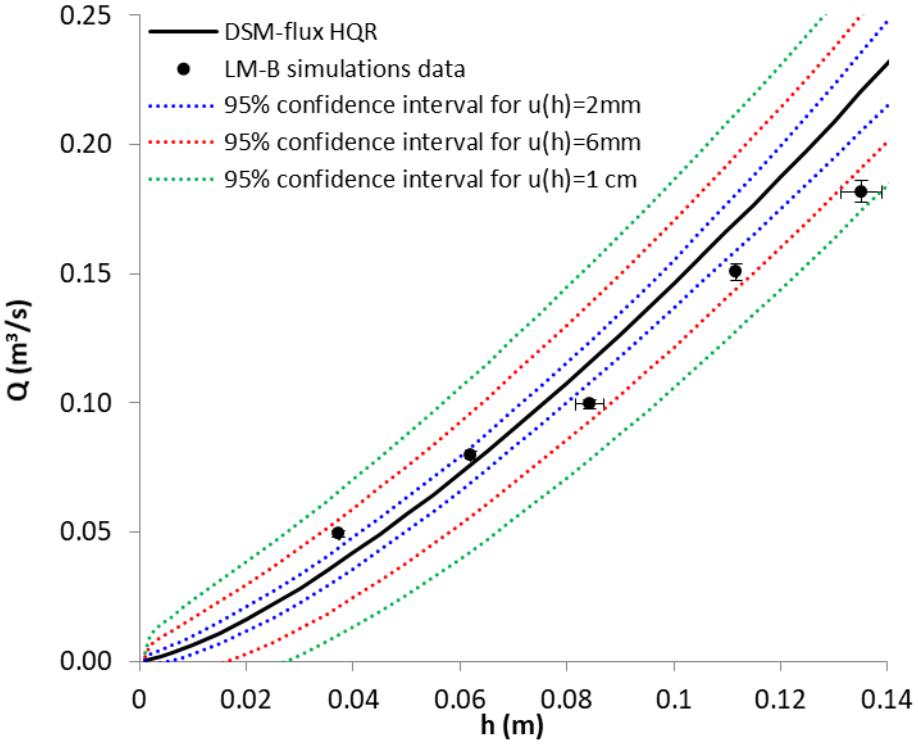

Figure 3.23. DSM-flux HQR (solid line) represented by Equation 3.8 and its 95% confidential intervals (dashed lines) for different uncertainties of the water level measure. Numerical data from simulations at the large-scale model LM-B (Table 3.6).

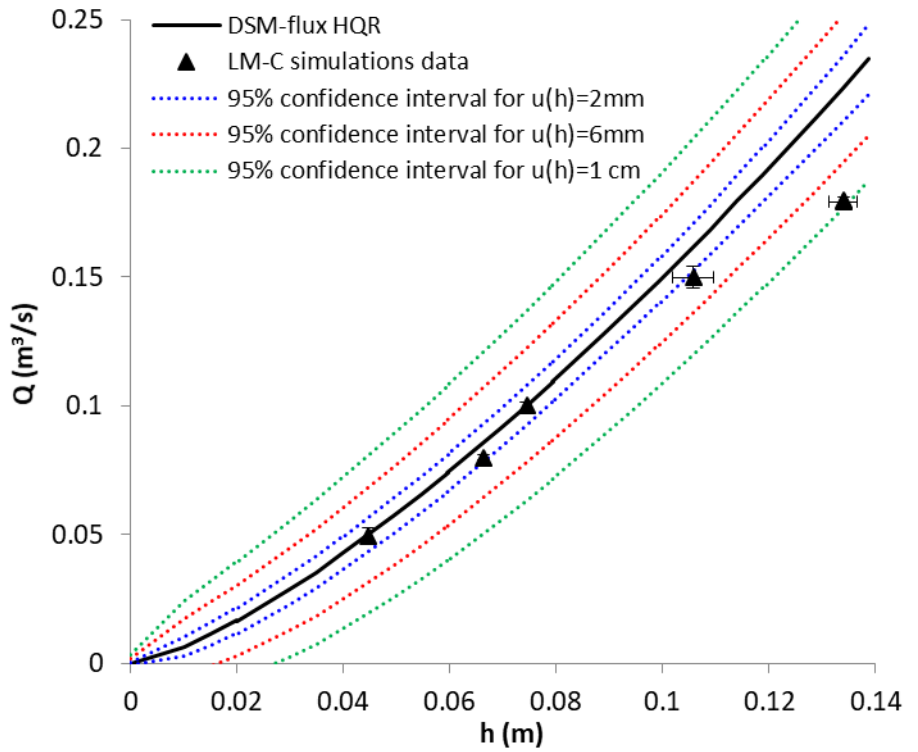

Figure 3.24. DSM-flux HQR (solid line) represented by Equation 3.8 and its 95% confidential intervals (dashed lines) for different uncertainties of the water level measure. Numerical data from simulations at the large-scale model LM-C (Table 3.6).

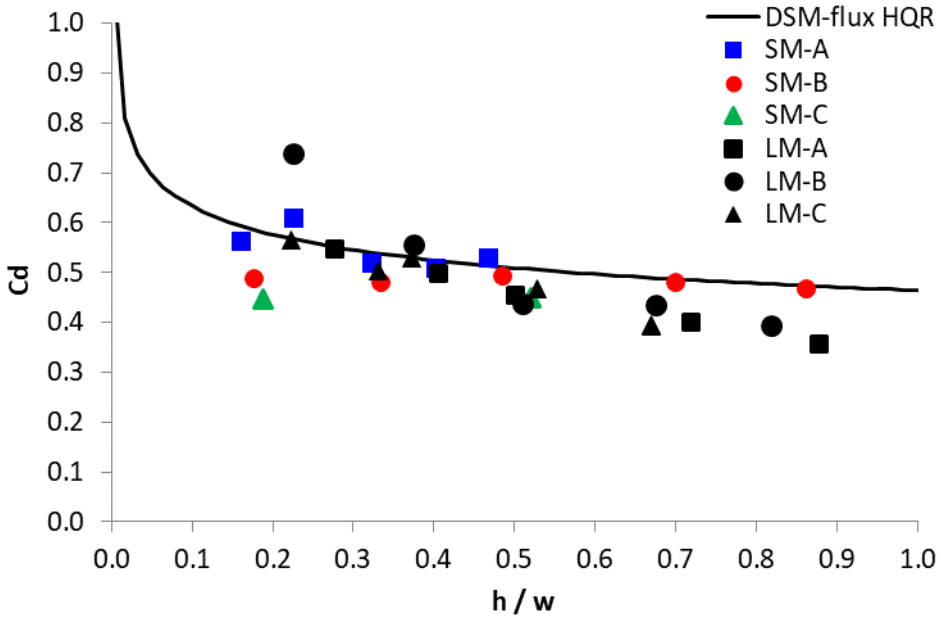

Figure 3.25. DSM-flux HQR (solid line) and simulated discharge coefficients for the numerical data of the simulations at the small- and large-scale models (Table 3.4 and Table 3.6).

Although there are still some divergences concerning the higher flow rates that need further investigation, model LM-C seems to reproduce accurately the DSM-flux HQR, at least for the lower flow rates, with no apparent scale effects. Besides, results from Section 4.2.3 show that velocities are relatively lower and better distributed in this model, which would favour the settling of material. Thus, it was decided to consider this modified design as the design to be reproduced for the field prototype.

3.2.5. Conclusions of Section 3.2

The main insights from this section are:

- the DSM-flux HQR is robust at a small scale, even out of its calibration range.
- the DSM-flux HQR seems robust at a larger scale particularly for the tested flows up to 0.1 m^3/s, with any significant scale effects occurring.
- the DSM-flux HQR doesn't seem to be significantly influenced by smooth modifications of the w/L ratio.
- a scaling of the DSM-flux device preserving a geometric similarity seems to produce velocities and TKE values that, *a priori*, could compromise the settling of material. If this function needs to be assured, it is recommended to increase the number of dissipation

blocks, adapt their height and increase the height of the weir crests of the overflow area. The DSM-flux HQR will continue to be valid for relatively low flow rates and water levels. New design relationships depending, for example, on the size of the device, and the limits of validity of the current DSM-flux HQR should be established for these cases.

- the DSM-flux HQR exhibits higher divergences at a larger scale for relatively high flow rates and water levels. However, these differences are lower than the usual uncertainties found in the field. Further investigations are needed to determine the reasons for these divergences. A modified relationship for high flow rates and water levels should be established to assure the monitoring function of the device within this range of operation conditions at larger scales.

3.3. VALIDATION OF THE MONITORING METHODOLOGY AT THE FIELD SCALE

The DSM-flux HQR has been proven to be a robust monitoring methodology to measure CSO discharges, and volumes, with a relatively low uncertainty and independently of the inflow conditions, at a small scale of the device. At a larger scale, the monitoring methodology is still accurate for the range of lower flow rates, but it seems to have a slightly different behaviour at the higher flow rates, according to numerical simulations. Further investigations are needed to determine the reasons of these divergences. However, for the typical uncertainties of the instruments used in the field to measure water levels, usually not higher than 0.01 m, the DSM-flux HQR is still valid even for the higher flow rates.

Previous conclusions were established by means of laboratory tests, where conditions differ from reality as simplifications are made for the models and, in the field, there are additional factors that can influence the phenomena of interest. In this case, and from the point of view of question 1 of this PhD work, the following factors might influence the reproduction of the DSM-flux HQR in the field: (i) the fact that real fluid is not just clean water as in the laboratory but it also transports solid matter of different sizes and materials, (ii) the fact that the real events to be monitored are unsteady events, that have not been tested at a larger scale, and (iii) the fact that the real devices installed at the field don't have an ideal configuration: there are small constructions defects and other inaccuracies that might cause changes in the flow's behaviour compared to the models. In order to validate the monitoring methodology under realistic operating conditions, and simultaneously assess the possible scale effects at a larger-scale, a field prototype installed in Sathonay-Camp (France) was monitored for 4 months, and its flow rates were compared to an independent monitoring methodology, developed in the framework of this study specifically for this validation. In the next subsections, the methodology followed to carry out this validation at the field is presented, including the description of the independent monitoring methodology used to compare flow rates. Then, the results of the comparison between the DSM-flux and the independent monitoring methodologies are presented and discussed.

3.3.1. Material and methods for the validation of the DSM-flux HQR at the field

As explained in Section 2.2.2, the DSM-flux field prototype was built equivalent to large-scale numerical model LM-C, it was installed in the experimental site of Sathonay-Camp (France) and it was equipped with a water level radar of the same characteristics than the radars used at

the small-scale physical model (Vegapuls WL61 from VEGA; maximum measurement error of ± 0.002 m) which were also located above the overflow area. The recording frequency for the water level data was set to 1 min, which was considered a time step short enough to observe the dynamics of CSOs and long enough to provide an average value getting rid of small waves influence. A post-processing of the water level time series consisting in the replacement of negative values for zeros was done, following the protocols of the Metropole of Lyon, the manager of the site. These negative values, of only a few millimetres, were due to bias in the calibration of the radars so an adjustment of the calibration curve was done when they were detected. Flow rates at the DSM-flux (Q_{dsm}) were calculated by means of the DSM-flux radar water levels (h_{dsm}) computing the DSM-flux HQR (Equation 3.8) with w and L dimensions measured at field prototype after construction, which differed slightly with those of the initial construction plans of the prototype (Appendix 7.1.5):

Equation 3.19

$$Q_{dsm} = 0.4639 \cdot \left(\frac{h_{dsm}}{w}\right)^{-0.135} \cdot L \cdot \sqrt{2g} \cdot {h_{dsm}}^{3/2} = 0.4639 \cdot \left(\frac{h_{dsm}}{0.191}\right)^{-0.135} \cdot 2 \cdot 1.105 \cdot \sqrt{2g} \cdot {h_{dsm}}^{3/2}$$

In order to validate these flow rates, a second flow rate measurement was needed. Several standard methods, as the ones described in Section 1.2.1, were considered and it was finally decided that the most appropriate method was to establish another stage-discharge relationship at the upstream distribution chamber by means of a CFD study. The reasons of this selection were: (i) the existence of favourable conditions to establish a HQR in contrast with the unfavourable conditions for installing a Venturi channel, a doppler or another flowmeter, (ii) the proven high accuracy of the HQRs issued from CFD studies, and (iii) the need (from an operational point of view) to measure also the flows over the weir of the distribution chamber that convey directly to the Ravin stream. The water level radar installed at the distribution chamber is the same as the radars used for the DSM-flux field prototype and the small-scale physical model (Vegapuls WL61 from VEGA; maximum measurement error of ± 0.002 m). Its location is indicated in Figure 3.26. The recording frequency for the water level data was set to 1 min, as for the DSM-flux radar, and the same post-processing was done for the water level time series.

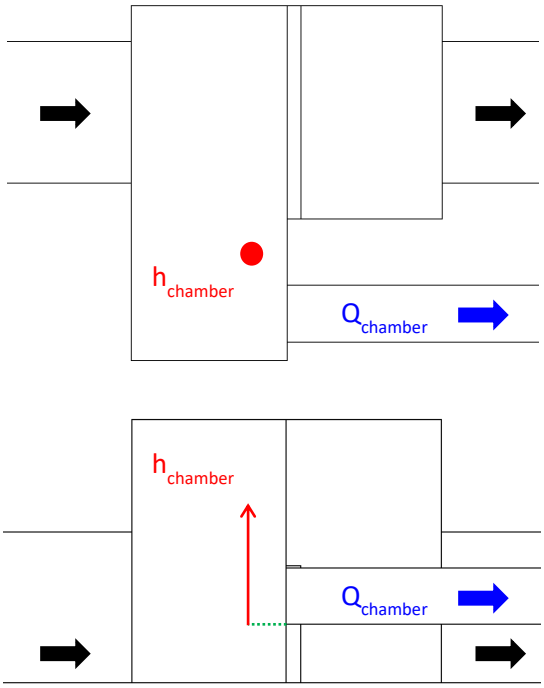

Figure 3.26. The distribution chamber geometry: plan (above) and profile (below) views – red dot indicating location where the water level is measured.

A numerical model representing the distribution chamber was implemented to obtain the distribution chamber HQR. Its main characteristics and numerical settings are explained in the next subsection. For the determination of the distribution chamber HQR, different hydraulic conditions were simulated using the numerical model within the range of the field prototype operating conditions, whose capacity is estimated to 4 m^3/s. Table 3.7 presents, for each inlet flow rate (Q_{inlet}), the values of the water levels observed at the distribution chamber of the numerical model ($h_{chamber}$) and the flow rate at the 0.4m outlet conduit, corresponding to the DSM-flux inflow pipe (Q_{outlet}). As the 0.4m outflow pipe is elevated from the chamber invert, water levels at the chamber presented in this study are considered with respect to the invert level at the entry of the 0.4 m outflow pipe, as indicated in Figure 3.26. Water levels at the numerical model are calculated as an area weighted value, equivalent to the area of the radar projection on the water free surface, equivalent to what is done at the field. The calculation of the numerical mass flow rates is based on the density flux through the outlet wetted cross-section.

Table 3.7. Numerical data for the adjustment of the distribution chamber HQR.

Q_{inlet} (m^3/s)	$h_{chamber}$ (m)	Q_{outlet} (m^3/s)
0.04	0.002	0.0015
0.06	0.104	0.0121
0.08	0.167	0.0267
0.10	0.224	0.0433
0.12	0.28	0.0594
0.14	0.341	0.0742
0.16	0.392	0.0845
0.18	0.424	0.0895
0.20	0.442	0.0934
0.25	0.479	0.0990
0.30	0.508	0.1041
0.50	0.59	0.1165
0.80	0.68	0.1283
1.20	0.79	0.1378

Figure 3.27 presents $h_{chamber}$ and Q_{outlet} data from Table 3.7. It is observed that there are two different relationships according to the submergence of the entry of the 0.4 m outflow pipe of the distribution chamber: a free-surface-entry relationship ($h_{chamber}$ < 0.285 m) and a submerged-entry relationship ($h_{chamber}$ > 0.285 m). Thus, two different HQRs were determined for each of the two operation ranges. These HQRs were obtained by means of ordinary least squares regression method. Several types of functions were tested and their adjustment to the numerical data was evaluated by the coefficient of determination R2 between simulated ($Q_{i\text{-}sim}$) and estimated ($Q_{i\text{-}est}$) outlet flow rate values. Equation 3.20 was found to be the best fit, with R^2 of almost 1 for both parts, and was then selected as the distribution chamber HQR. It should be highlighted that, due to the configuration of the distribution chamber and the position of the radar, the maximal water level $h_{chamber}$ that the radar is able to measure is 1 m.

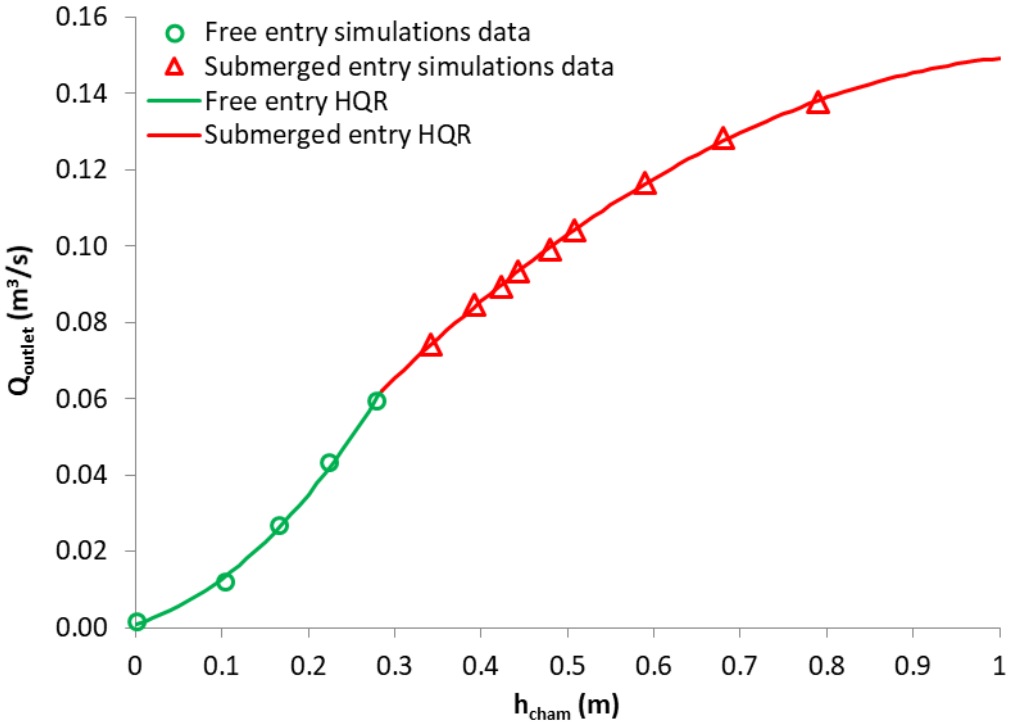

Figure 3.27. Distribution chamber HQR with numerical data used for its adjustment.

Equation 3.20

$$Q_{outlet} = \begin{cases} 0.5229 \cdot {h_{chamber}}^2 + 0.0653 \cdot h_{chamber} + 0.001, & 0 \leq h_{chamber} < 0.285 \\ -0.1365 \cdot {h_{chamber}}^2 + 0.2973 \cdot h_{chamber} - 0.0115, & 0.285 \leq h_{chamber} \leq 1 \end{cases}$$

It should be highlighted that for the cases where the entry of the 0.4 m outflow pipe was submerged, two different operation conditions were observed: if $h_{chamber}$ > 0.45 m, a flow over the distribution chamber weir occurs and this discharge becomes the main outflow of the distribution chamber as the inlet flow rate increases. This implies that the increasing rate of the flow rates at the 0.4 m outflow pipe with $h_{chamber}$ decreases as the inlet flow rate increases, tending to a maximum value of 0.145 m^3/s at $h_{chamber}$ = 1 m.

The distribution chamber numerical model

The numerical model representing the distribution chamber was implemented in ANSYS Fluent commercial code, already used to implement the DSM-flux numerical models, as explained in Sections 2.1.2 and 2.2.1. The model domain consists of the distribution chamber, 20 m of the upstream 1 m diameter inflow conduit and 4 m of the downstream 0.4 m diameter outflow conduit which connects the distribution chamber to the DSM-flux chamber and corresponds to the DSM-flux inflow conduit. The downstream 1 m outflow conduit conveying to the Ravin

stream was not included as part of the model domain because no downstream influence is expected as it has a steep slope, which operates mainly under supercritical regimes, and the outlet arrives to a chamber with a higher capacity which acts as a free outlet condition. Besides, the flow in this conduit wasn't of interest for this study. Figure 3.28 presents a 3D view of the numerical model domain. The upstream 1 m diameter inflow conduit was considered long enough (equivalent length of 20 diameters) to guarantee a fully developed turbulent flow. For security reasons (avoid floods in the DSM-flux chamber downstream caused by extreme events), the entry of the 0.4 m outflow conduit conveying to the DSM-flux was partially closed with a sluice gate. The opening was set to 1/2 for the first months of operation, which correspond to the data used in this study in Section 3.3. In order to avoid stagnant water in the upstream section of the distribution chamber, the 0.2 m diameter drainage gate at the frontal weir is left completely open. Thus, the distribution chamber HQR was established for these specific conditions: a 1/2 opening for the 0.4 m outflow conduit and a complete opening for the 0.2 m diameter drainage gate at the frontal weir, the numerical model geometry being implemented accordingly. The rest of the numerical model dimensions are the ones presented in Figure 2.13.

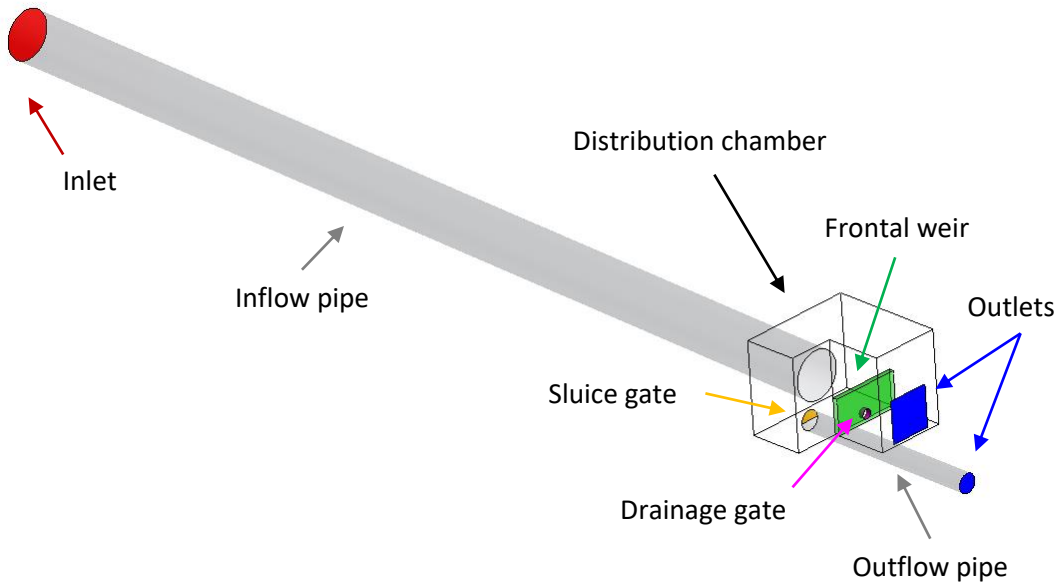

Figure 3.28. 3D view of the distribution chamber numerical model's domain. Inlet and outlet boundaries in red and blue respectively. The rest of the indicated parts are wall boundaries.

As explained in section 2.1.2, all simulations carried out in this PhD work reproduce steady problems. A structured mesh was used to discretize the space domain with hexahedral computational cells, without creating any refinement areas. Different detail views of the mesh

are presented in Figure 3.29. The mesh characteristics as well as some quality parameters are indicated in Table 3.8. The maximal aspect ratio is slightly higher than 100 (value recommended by ANSYS, already described in section 2.1.2), but the average value for all elements manifest that these relatively high value is not the common tendency. It is observed that, for example, only a low percentage of the elements (< 0.9%) exceed 40, which was considered acceptable enough in this PhD work. Similarly, only a low percentage of elements (<0.001%) exceed the recommendations for the skewness indicator. These low-quality elements are located at the upstream of the 1 m diameter inflow pipe and around the 0.2 m diameter drainage gate opening at the frontal weir.

Table 3.8. Characteristics and quality indicators for the distribution chamber model computational mesh (MDC1).

MESH CARACTERISTICS	MESH MDC1
Connectivity	Structured
Interior interfaces	No
Element shape	Hexahedral
Number of elements	800.000
Min side length (m)	$5.0 \cdot 10^{-4} – 5.2 \cdot 10^{-2}$
Max side length (m)	$2.2 \cdot 10^{-2} – 1.8 \cdot 10^{-1}$
Volume (m^3)	$9.5 \cdot 10^{-8} – 1.6 \cdot 10^{-4}$
Quality indicators	
Min Ortogonal quality	0.22
Max aspect ratio	**102** 40 (> 99.1%) 20 (> 94.2%) (Mean = 9)
Min angle (°)	20.8
Max Skewness	**0.79** 0.75 (< 99.99%)

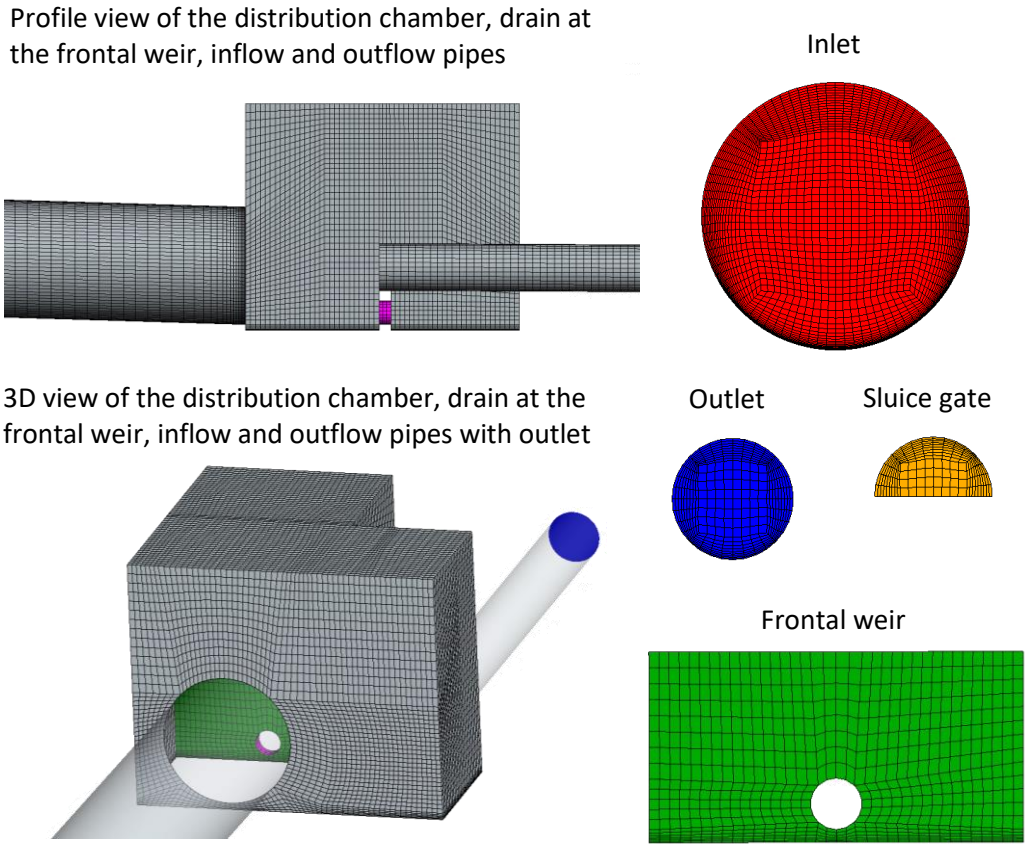

Figure 3.29. Different detail views of the computational mesh of the distribution chamber numerical model.

As the flow expected at the distribution chamber is similar to the flow of the DSM-flux device, flow and turbulence equations, near-wall treatment, free surface modelling, discretization schemes and boundary conditions tested for the distribution chamber model are the same as the ones presented in section 2.1.2 for the small-scale model: RANS equations, RNG k-ε turbulence model, Scalable Wall Function for the near-wall treatment, VOF for the free surface modelling, second order upwind discretization schemes (except for the pressure gradients and the VOF for which the body-force-weighted scheme and the Modified (HRIC) scheme were used respectively as recommended by ANSYS Fluent), mass-flow-inlet and pressure-outlet as boundary types for the inlet (the upstream 1 m diameter inflow conduit) and the two outlets (the downstream of the 0.4 m diameter outflow pipe and downstream outlet of the distribution chamber) respectively and wall type for all the wall boundaries (conduits, frontal weir, sluice gate at the entry of the 0.4 m diameter outflow conduit and all distribution chamber walls and invert). The roughness heights used for wall boundaries of this model were adapted according to the materials of the site: concrete for the 0.1 m diameter inflow pipe,

frontal weir and distribution chamber walls and invert, stainless steel for the sluice gate at the entry of the 0.4 m diameter outflow pipe and PVC for the pipe. The same convergence criteria were also considered: all residuals and monitors must tend to an asymptotic line and (i) scaled residuals be lower than 10^{-3} and (ii) the mass flow balance was lower than 3%. Unlike the rest of numerical models used in this PhD work, in the distribution chamber model the PISO algorithm (Issa, 1986) was used as the pressure-velocity coupling algorithm instead of SIMPLE, to test if it could fasten the computation, as it includes a an additional corrector step that sometimes (but not necessarily always) makes the simulations converge faster/easily than with SIMPLE algorithm.

3.3.2. Comparison of the DSM-flux and the distribution chamber monitored CSOs

The Sathonay-Camp experimental site was monitored for 4 months and water level data of the distribution chamber (h_{cham}) and the DSM-flux (h_{dsm}) radars were recorded every minute. As there is no flow in the system during dry weather, the beginning of a CSO event was easy to identify. The level of the pipe invert at the entry of the 0.4 m outflow pipe of the distribution chamber and the weir crest level at the DSM-flux were considered as reference levels for the beginning of the events at the distribution chamber and the DSM-flux device, respectively. The travel time between the chamber and the DSM-flux varied depending on the velocity of the flow but, in general, the time-lag between the chamber hydrograph and the DSM-flux hydrograph was lower than two minutes.

A total of 41 CSO events were registered during these 4 months. Appendix 7.2.1 shows the hydrographs for each of the events obtained by both monitoring methodologies: Q_{dsm} (in red) and $Q_{chamber}$ (in blue). Figure 3.30 is presented in this section as an example and corresponds to the events 30 and 31 (Table 3.9), registered the 4th June 2018. Some event-based characteristics have been estimated as the duration, the peak flow rate and the total volume, the last two features being obtained for both hydrographs. All these values are presented in Table 3.7. To assess the goodness of fit between both monitoring methodologies, the evaluation coefficients used in Section 3.1.2 (Equation 3.9, Equation 3.10, Equation 3.11 and Equation 3.12, computed with $Q_{i\text{-}dsm}$ and $Q_{i\text{-}chamber}$ instead of $Q_{i\text{-}mea}$ and $Q_{i\text{-}est}$) were calculated for each of the event. Only the RMSE, MAE and Nash coefficients are presented in Figure 3.32, where RMSE and MAE have been normalized by the flow rate peak at the DSM-flux.

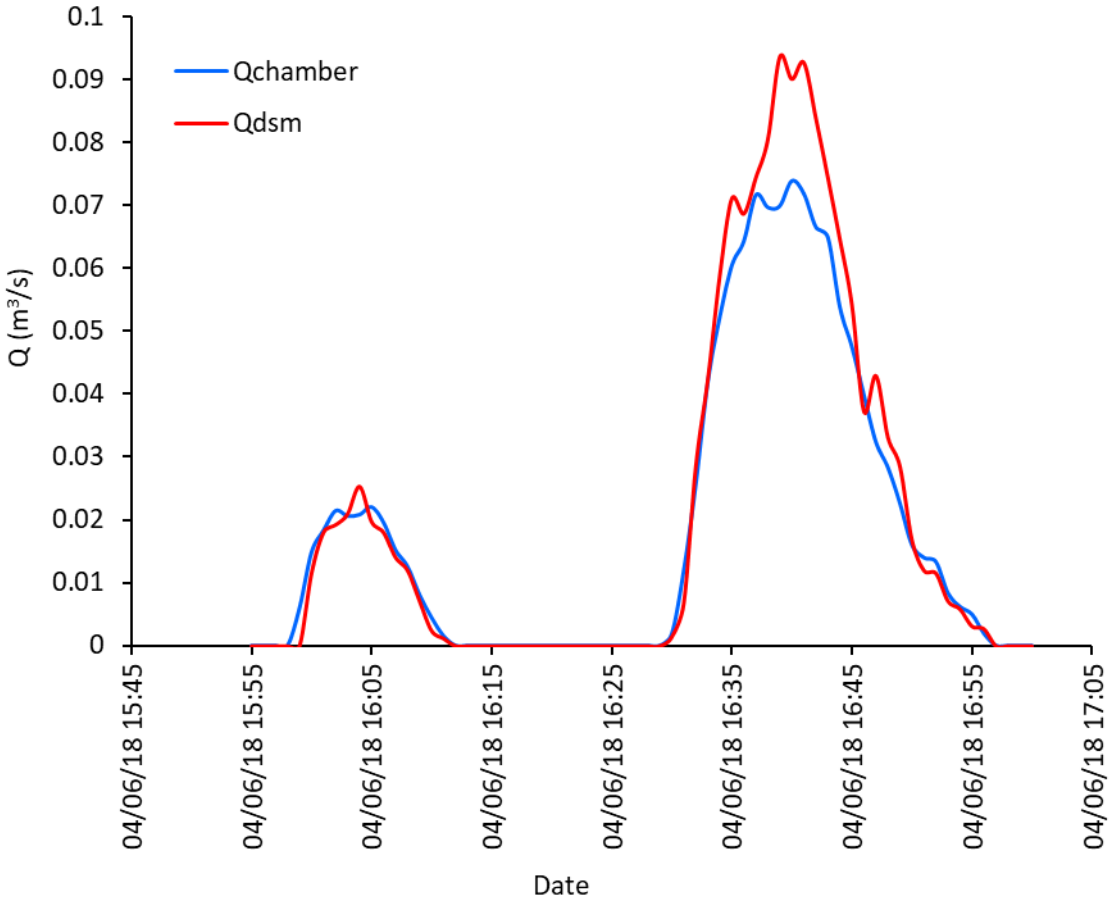

Figure 3.30. Hydrographs registered at Sathonay-Camp the 14th of June of 2018.

Table 3.9. CSO events registered at Sathonay-Camp experimental site from February to June 2018.

Event	Start date	End date	Duration (min)	$Q_{chamber\_max}$ (m^3/s)	Q_{dsm_max} (m^3/s)	$V_{chamber}$ (m^3)	V_{dsm} (m^3)	ΔV (m^3)	$\Delta V/V_{dsm}$ (%)
1	12/02/18 0:11	12/02/18 0:23	12	0.023	0.029	9	10	-1	-12
2	17/02/18 7:54	17/02/18 8:11	17	0.030	0.037	18	21	-3	-15
3	02/03/18 5:48	02/03/18 8:05	137	0.123	0.183	745	989	-244	-25
4	04/03/18 16:34	04/03/18 17:23	49	0.091	0.131	147	192	-45	-23
5	10/03/18 1:56	10/03/18 3:39	103	0.105	0.156	424	586	-163	-28
6	10/03/18 4:06	10/03/18 5:33	87	0.034	0.044	103	121	-19	-15
7	10/03/18 6:07	10/03/18 7:37	90	0.030	0.037	117	136	-18	-13
8	15/03/18 9:16	15/03/18 12:56	220	0.119	0.187	1093	1515	-422	-28
9	15/03/18 13:53	15/03/18 14:11	18	0.025	0.031	16	18	-1	-7
10	16/03/18 21:17	16/03/18 23:26	129	0.092	0.139	344	429	-85	-20
11	17/03/18 9:56	17/03/18 10:04	8	0.003	0.005	1	2	-1	-34
12	28/03/18 19:23	28/03/18 19:50	27	0.037	0.047	33	38	-5	-14
13	30/03/18 10:29	30/03/18 11:35	66	0.123	0.195	344	476	-132	-28
14	04/04/18 9:20	04/04/18 10:29	69	0.126	0.193	377	515	-137	-27
15	04/04/18 10:38	04/04/18 11:35	57	0.078	0.112	149	179	-31	-17
16	04/04/18 17:09	04/04/18 17:46	37	0.131	0.189	192	258	-66	-25
17	10/04/18 4:51	10/04/18 5:25	34	0.030	0.035	31	34	-3	-8
18	29/04/18 22:31	29/04/18 22:56	25	0.068	0.089	63	77	-14	-18
19	13/05/18 1:20	13/05/18 1:31	11	0.017	0.017	6	5	1	16
20	13/05/18 12:31	13/05/18 13:17	46	0.090	0.138	138	182	-43	-24
21	13/05/18 13:48	13/05/18 19:08	316	0.119	0.178	1266	1693	-427	-25
22	14/05/18 5:04	14/05/18 5:49	45	0.099	0.142	150	196	-47	-24
23	14/05/18 7:58	14/05/18 8:18	20	0.019	0.020	14	15	-1	-4
24	15/05/18 1:19	15/05/18 2:37	78	0.098	0.150	284	381	-97	-26
25	22/05/18 18:47	22/05/18 20:05	78	0.150	1.063	467	1195	-728	-61
26	22/05/18 20:49	22/05/18 21:57	68	0.111	0.149	255	320	-65	-20
27	31/05/18 2:49	31/05/18 3:12	23	0.098	0.150	80	106	-26	-25
28	31/05/18 4:15	31/05/18 4:29	14	0.021	0.025	10	10	0	-2
29	31/05/18 5:15	31/05/18 5:41	26	0.064	0.086	54	63	-10	-15
30	04/06/18 15:58	04/06/18 16:12	14	0.022	0.025	11	10	1	9
31	04/06/18 16:29	04/06/18 16:57	28	0.074	0.094	62	71	-9	-13
32	05/06/18 18:44	05/06/18 19:17	33	0.134	0.202	195	266	-71	-27
33	07/06/18 20:23	07/06/18 22:19	116	0.107	0.153	539	713	-174	-24
34	08/06/18 0:15	08/06/18 0:44	29	0.011	0.011	13	11	2	21
35	08/06/18 14:57	08/06/18 15:07	10	0.060	0.070	21	23	-2	-10
36	11/06/18 8:02	11/06/18 8:28	26	0.059	0.079	48	55	-6	-12
37	11/06/18 18:33	11/06/18 20:10	97	0.122	0.187	568	776	-208	-27
38	12/06/18 18:57	12/06/18 19:27	30	0.013	0.014	16	13	3	20
39	12/06/18 19:57	12/06/18 21:47	110	0.144	0.403	625	972	-347	-36
40	12/06/18 21:55	12/06/18 23:15	80	0.142	0.291	446	630	-184	-29
41	13/06/18 3:24	13/06/18 3:49	25	0.059	0.070	49	54	-5	-9

A visual observation of all the events presented in Appendix 7.2.1 reveals that, as for the examples in Figure 3.30, flow rate values from both monitoring methodologies match accurately if flow rates are lower than approximately 0.06 m^3/s. However, for higher flow rates, Q_{dsm} is significantly greater than $Q_{chamber}$, and these divergences seem to increase with the magnitude of the flow rates, being more accentuated at the peak of the hydrographs. In Figure 3.31, which shows the relationship between the peak flow rates for each event obtained by both monitoring methodologies, it is observed that as the peak flow rates are higher, differences between methodologies for peak discharges increase. From Figure 3.31 it is also observed that these divergences increase more or less proportionally to the peak flow rates until the ($Q_{chamber\_peak}$, Q_{dsm_peak}) point of (0.14,0.22), where the divergences shoot up, especially for the three events for higher peak discharges. A more detailed analysis of these events, corresponding to events 25, 39 and 40, has been carried out to determine if these values were realistic. The maximal water levels than can be registered according to the site and prototype configurations are around 1 m for the $h_{chamber}$ and around 0.6 m for the h_{dsm}, which correspond to the highest levels that the radars can measure. Water levels in the distribution chamber and in the DSM-flux device for these three events are below these values so it doesn't seem an error related to incorrect data acquisition.

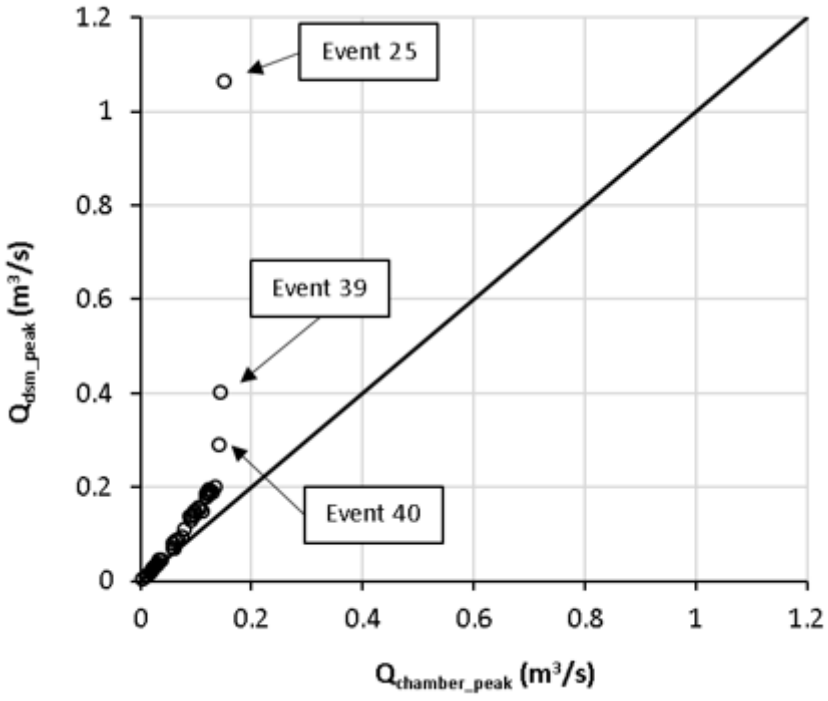

Figure 3.31. Relationship between peak flow rates obtained by means of both monitoring methodologies.

The Sathonay-Camp experimental site is designed to operate under free surface conditions. The capacity of the 0.4 m outflow pipe of the distribution chamber has been estimated to approximately 0.29 m^3/s. Thus, the peak flow rates obtained at the DSM-flux for events 25 and 39 (1.06 m^3/s and 0.4 m^3/s respectively) are above the maximal capacity of the inflow pipe of the device and the peak flow rate of event 40 is in the limit (0.29 m^3/s). It should be reminded that the entry of the inflow pipe is supposed to have an opening of half the section of the pipe which makes the peak flow rates of these three events incoherent. The reasons that could explain these incoherently high values would be that either (ii) there was an extra contribution of water to the DSM-flux, for example, coming from infiltrations through the manhole covers in the chamber or by an opening of the sluice gate, that fails to keep the 1/2 opening; or (ii) an inaccuracy of the DSM-flux HQR, that overestimates the flow rate values. The reliability of these data being doubtful, it was decided to obviate these three events for the rest of the analysis of this section.

The tendency of increasing divergences with peak flow rates is also observed when analysing the MAE (or RSME) values with respect to the peak flow rates, as shown in Figure 3.32. In this figure, it is observed that, for approximately Q_{dsm_peak} > 0.11 m^3/s, the increasing rate of divergences is higher.

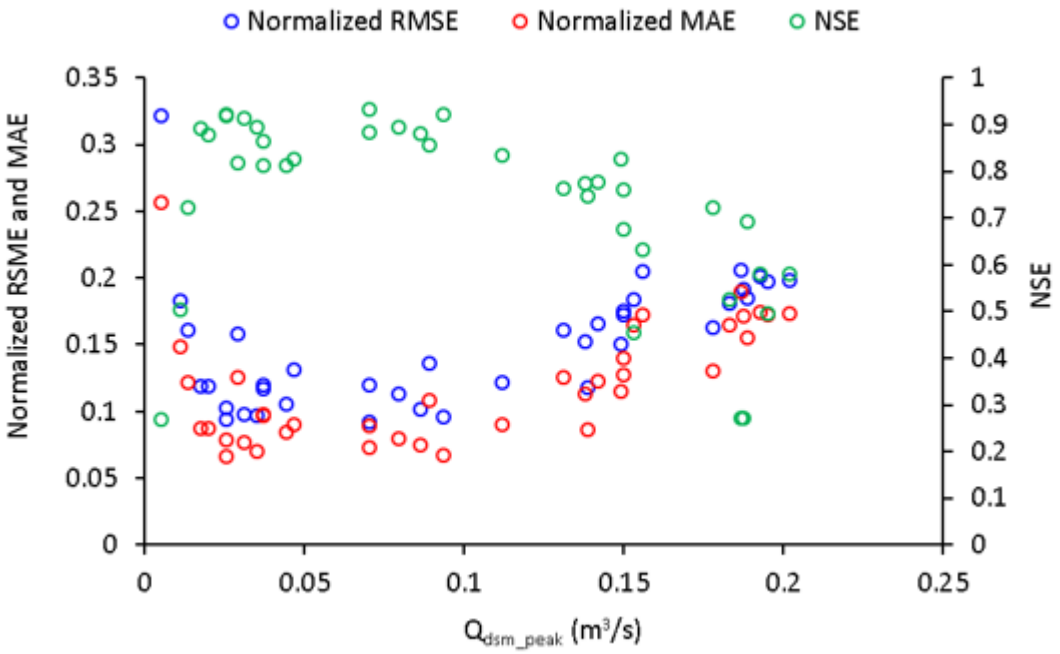

Figure 3.32. Values of the evaluation coefficients in relation with peak flow rates at the DSM-flux.

Concerning NSE values, except for the two events with the lowest peak discharges, the general patterns is that NSE values deteriorate considerably for events where peak discharges are higher than 0.1 m^3/s as well, probably because of the divergences at higher flow rates. According to Moriasi *et al.* (2007), values of Nash higher than 0.5 can be considered satisfactory, depending on the case. Despite the divergences at higher flow rates, 83% of the registered events have NSE values higher than 0.5. Besides, 12% of the events are between 0.5 and 0.6, 7% between 0.6 and 0.7, 17% between 0.7 and 0.8, 34% between 0.8 and 0.9 and 5% higher than 0.9. As for MAE and RMSE, Figure 3.32 shows the decrease of NSE values.

There are two possible reasons to explain the deviations for higher flow rates (particularly for events with peaks higher than 0.15 m^3/s): (i) either there is an inaccuracy with the DSM-flux HQR which creates an overestimation of Q_{dsm} for the higher flow rates, (ii) or there is an inaccuracy with the distribution chamber HQR which causes an underestimation of $Q_{chamber}$ for the higher flow rates. A combination of (i) and (ii) is also possible, which would increase even more these deviations.

Concerning reason (i), it was observed in Section 3.2.3 that flow rates calculated by computing the DSM-flux HQR with h_{sim} values at the large-scale numerical model LM-C were overestimated for the higher flow rates compared to values obtained from simulations. However, the lower flow rates matched accurately enough. The threshold from which these divergences started to be significative seemed to be located above 0.15 m^3/s (Figure 3.24). Thus, even if this overestimation of flow rates with the DSM-flux HQR probably contributes to the flow rate divergences between both monitoring methodologies for higher values at the field, they don't explain the divergences between the flow rates in the range of values 0.06 to 0.15 m^3/s.

The threshold over which deviations between Q_{dsm} and $Q_{chamber}$ become significant (0.06 m^3/s) corresponds more or less with the change of state, from free to submerged, at the entry of the DSM-flux inflow pipe. A field inspection after the analysis of the data and the identification of these divergences revealed that the sluice gate installed to reduce the entry section of the conduit wasn't properly fixed and it wasn't close enough to the wall to assure imperviousness and avoid leaks of water behind the gate. These leaks and the increasing pressure of the water as the level increases could have opened the gate, letting the passage of higher flow rates than expected. In this case, the real configuration of the distribution chamber would differ from the one implemented at the numerical model and this would have affected the HQR obtained numerically for cases where $h_{chamber} > 0.285$ m. A proper fixing of the gate couldn't be done

before the end of this PhD, so the verification of this hypothesis will have to be done in future studies.

Concerning the duration of the CSO events, no clear relationships have been found in line with the evaluation coefficients. The longest event has a duration of almost 5 h 15 min (event 21) but most of the events (95%) have durations lower than 2.5 h and 61% lower than 1 h.

CSO volumes were also estimated for each event from the hydrographs of both monitoring methodologies in order to evaluate the influence of the divergences in the estimation of flow rate values found for the higher values, on an overall CSO event. CSO volumes were obtained via computation of Equation 3.15 with flow rates derived from the DSM-flux HQR (V_{dsm}), represented by Equation 3.19, and from the distribution chamber HQR ($V_{chamber}$), represented by Equation 3.20. As the data recording time step of the overflow events was relatively short for the field dynamics (1 min), K_{int} from Equation 3.15 was considered equal to 1. V_{dsm} and $V_{chamber}$ values for each event are listed in Table 3.9 as well as the relative difference, $(V_{dsm} - V_{chamber})/V_{dsm}$, indicated as a percentage. Results show that most of the events (around 80%) have volumes lower than 500 m^3. As expected, divergences are lower for small magnitude events, as lower flow rates match better. For the lower peak flow rates ($Q_{dsm\_peak} < 0.15$ m^3/s), divergences in volumes are around 100 m^3. Contrary to what was observed for the peak flow rates deviations, the volume divergences rate seems always proportional to peak discharges, even for the events with higher peak flow rates (except for event 25), as it is observed in Figure 3.33. Values of relative differences only exceed 30% for 5% of the events, almost half (48%) of the events have relative differences between 20 and 30%, one third (32%) of the events have differences between 20 and 10% and 15% of the events have relative differences lower than 10%. Considering the deviations at higher flow rates between both monitoring methodologies, these values are rather encouraging. However, CSO volumes from both monitoring methodologies should be closer and this highlights the need to solve the inaccuracies in the estimation of discharges by both HQRs, as previously discussed in this section.

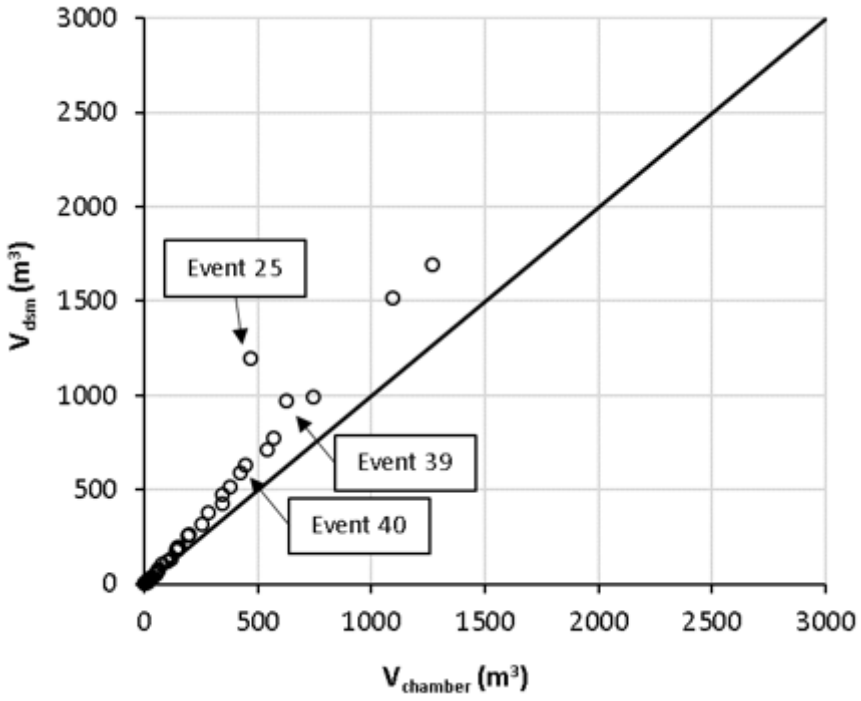

Figure 3.33. Relationship between CSO volumes obtained by means of both monitoring methodologies.

3.3.3. Conclusions of Section 3.3

The main insights from this section are:

- A second monitoring methodology, also based in a stage-discharge relationship but independent from the DSM-flux HQR, was developed at the Sathonay-Camp experimental site to compare these flow rate values to the ones obtained from the DSM-flux HQR, with the objective to validate the DSM-flux monitoring methodology under real operating conditions. The new monitoring methodology was established numerically, and it consisted in a stage-discharge relationship between the water levels registered at the distribution chamber upstream from the DSM-flux and the flow rates conveyed to the DSM-flux through the 0.4 m outflow pipe of the chamber. The resulting distribution chamber HQR had two different operation ranges and its adjustment to the numerical data was very good.
- Discharges measured by means of both monitoring methodologies are similar for the lower flow rates but differ considerably for the higher flow rates, the DSM-flux flow rates being greater than the ones obtained at the distribution chamber. These differences increase as the magnitude of overflow rate of the CSOs increases. Deviations (for both CSO volumes and discharges) are significant particularly for events with discharge peaks higher than 0.15

m^3/s. Either installation mistakes (increasing of the opening of the gate, inflows from streets) or inaccuracies in the monitoring methodologies for higher flow rates, may explain these deviations.

- Despite the differences for the higher flow rate values, evaluation coefficients for most of the registered events are satisfactory, with NSE higher than 0.5 for 83% of the events.
- CSO volumes have also been estimated for both monitoring methodologies and compared. Relative differences are noticeable (only 15% of the events have differences in volumes under 10%) but the above-mentioned technical aspects (sluice gate) cast doubt on their relevance. It is necessary to obtain in the future a sure and accurate second technique to characterize the flow rate and assess the performances of the DSM-flux HQR at the field scale. Due to technical limitations, it was not possible to carry out this second verification in the framework of this PhD work.

Chapter 4

4. THE DSM-flux: ASSESSMENT OF POLLUTANT RETENTION CAPABILITIES

As explained in Section 1.3, due to its design, the DSM-flux has capabilities to retain particulate pollutants by sedimentation. However, the motion of solid matter, especially the finest particles, carried by relatively weakly loaded flows is mainly driven by the forces acting within the fluid. Thus, for the study of solid transport in the DSM-flux, as well as the beginning (entrainment) and the end (settling/deposition) of the motion of solid matter, it is crucial to have a good knowledge of the dynamics of the flow of interest.

Rammal (2016) reviews several studies that show the percentage of particulate phase of pollutant carried in different UWWE, which highlights the importance of particulate pollutants as a significant part of CSOs pollution. Besides, Chebbo (1992) cited by Yan (2013) indicates that a great proportion of particles in combined sewer systems are fine particles with characteristic diameters under 100 µm. As most of the CSO configurations consist of a particular type of weir, it is believed that overflowed particles must be the finest ones, which are mainly carried in suspension. Thus, the retention of fine particles is of major interest in this PhD work and, as their transport is mainly driven by the flow's dynamics, as explained in Section 4.1., the first objective of this chapter is thus to properly describe the flow pattern in the DSM-flux.

The second question addressed in this PhD work, "Is the DSM-flux capable to efficiently retain particulate pollutants?", is analysed in this chapter. It is understood that only the particulate pollutants are considered. In order to have a better knowledge of the particles settling and entrainment mechanisms, and thus study the retention capabilities of the DSM-flux, a detailed analysis of the hydrodynamics of the DSM-flux flow is carried out in combination with tests including solid matter.

Based on a multiscale approach adopted in this PhD work, the study of this question in three different systems and two different scales provides the most generic and realistic answer possible. The strategy followed to answer the question is divided in three main stages (Figure 1.6):

- STAGE 1: Assessment of the hydrodynamics and evaluation of deposition and erosion rates from experimental data at a small-scale. Flow patterns and turbulence quantities potential relationships with the settling and entrainment mechanisms of fine particles are investigated. Particle segregation is also studied by means of granulometry analysis.

- STAGE 2: Implementation of a small-scale numerical model and evaluation of the solutions against the experimental data obtained from physical model tests. The same numerical models already tested in Chapter 3 are used. Then, the aim is to select the most appropriate numerical options (boundary conditions, turbulence models, wall treatment approach, shape of computational meshes and its spatial distribution, convergence criteria, pressure-velocity coupling algorithm, discretization scheme) implemented for small-scale numerical model to simulate flows in the large-scale model representing the field prototype. Simulation results are used to support the assessment of the hydrodynamics and deposition and erosion rates at a large-scale.
- STAGE 3: Observations of the hydrodynamics and deposition effects by means of videos and pictures at a large-scale and under realistic operating conditions in order to check the reliability of conclusions derived from previous stages.

As it will be observed in Section 4.2, stage 2 could not be completed within the time of this PhD work but it's included for a better understanding of the overall strategy.

In Sections 4.1, 4.2 and 4.3 of this chapter, the materials and methodologies used at stages 1, 2 and 3, respectively, are described, and the results obtained with each analysis are presented and discussed.

4.1. THE DSM-flux HYDRODYNAMICS AND RETENTION CAPABILITIES

CSOs consist of a mixture of water and solid matter (sediments) whose composition varies greatly in space and even in time because it depends on what is introduced into the sewage system by the population and on what the stormwater runoff entrains from the urban surfaces. Depending on the concentration of solid matter in the fluid, three types of flows can be considered (Graf, 2000): (i) a Newtonian flow, when the volumetric concentration of particles is very small (<< 1%) and the difference in density between the mixture and the water is also small (<< 16 kg/m^3); (ii) a non-Newtonian flow, if the volumetric concentration (> 8%) and the difference in densities (> 130 kg/m^3) become important; (iii) a quasi-Newtonian fluid, when volumetric concentrations and difference in densities is in between the previous cases. Most of the artificial and natural watercourses are usually considered as Newtonian flows (Graf, 2000) and this includes combined sewer flows.

In Newtonian flows, the motion of a single particle within the fluid occurs when the momentum of the destabilizing forces (*i.e.* drag, lift, buoyancy), with respect to the point of contact, becomes larger than the stabilizing momentum of the gravity force (Chanson, 1999). If a group of particles is considered, inter-granular and cohesion forces also influence the movement. Two types of sediment transport are usually considered (Chanson, 1999; Graf, 2000): bed-load and suspended-load transport. In the first type, sediments stay in close contact with the bed and displace themselves by rolling, sliding or jumping (Chanson, 1999; Graf, 2000). This type of transport usually concerns the relatively large particles (Graf, 2000). In the second type, sediments only have contact with the bed occasionally and they mainly stay in suspension within the water by turbulence (Chanson, 1999). They displace themselves suspended with the fluid motion, by advection-convection and by diffusion.

The thresholds for the start (and the end) of the sediment's motion and the change in type of transport depend on both the flow and the sediments properties. Dey and Papanicolaou (2008) review in detail the different thresholds used to determine the beginning of particles motion. Yan (2013) makes an extensive review of the main criteria that are used to describe the incipient motion of bed load, the transition from bed load and suspension load and the deposition of sediments. According to Yan (2013)'s review, sediment entrainment criteria are mainly based on the definition of either a critical velocity or a critical shear stress value. Yan (2013) indicates that latest researches relate sediments entrainment to turbulence phenomena (bursts) or study it from a probabilistic approach. Criteria for the transition from bed load motion to suspension transport is more complex than those for bed load motion,

according to Bertrand-Krajewski, (2012), cited by Yan (2013). A common approach (Chanson, 1999; Graf, 2000) is to define this threshold by a critical value of the relation between the shear velocity and the particle settling velocity (Yan, 2013). Similar to bed entrainment, criteria for sediments deposition are mainly based on critical values of the flow velocity and shear stress. Some authors have also used the bed turbulent kinetic energy as a criterion for deposition (Dufresne, 2008; Isenmann, 2016; Lipeme Kouyi *et al.*, 2010; Yan, 2013). This last criterion is still under discussion and more studies that evidence (or not) this relationship are needed. Detailed information about formulae and threshold values for sediment motion is found in Yan (2013) and Dey and Papanicolaou (2008) reviews.

The retention capabilities or the efficiency of a retention device is strongly related to the sedimentation or settling and erosion or entrainment of solid matter. Different authors (Dufresne, 2008; Lipeme Kouyi *et al.*, 2010; Yan, 2013) have studied the retention capabilities of retention devices, as for example stormwater detention basins, by means of the study of the hydrodynamics and turbulence quantities, with the hypothesis that quantities like TKE play an important role on the sediment processes. Following these approaches, to better understand the patterns of sediment deposition of the DSM-flux and, particularly, to evaluate the relation with the TKE, instantaneous velocity measurements were carried out in combination with sediment transport tests, which will also allow to evaluate the retention capacity of the DSM-flux.

4.1.1. The DSM-flux flow patterns and turbulence

The velocity field and corresponding turbulence quantities are studied at the small-scale physical model as a function of an incoming constant discharge in order to better understand the flow behaviour in the DSM-flux device under steady conditions. Although the CSOs are unsteady phenomena, these results will give a first insight of the device's hydrodynamics at its simplest hydraulic conditions and they allow to better relate these variables to the depositions patterns. The methodology and results of these analyses are presented in the following subsections.

4.1.1.1. Materials and methods for the Velocity-Turbulence (VT) tests

Layout and instrumentation of the small-scale physical model for the VT tests

For the VT tests, velocity field and turbulence quantities were measured by means of a side-looking Acoustic Doppler Velocimeter (ADV) (Vectrino from Nortek; accuracy of ± 0.5% of the measured value ± 0.001 m/s). ADV probes use the Doppler shift principle to measure local

three-dimension (3D) flow instantaneous velocities at high frequency in a cylindrical control volume of about 6 mm diameter and an adjustable height, that for this study was set to 7 mm. Time averaged and fluctuating velocity components can be derived from these data series and allow to estimate the instantaneous and time-averaged Reynolds stresses. Further information about the operation of the Vectrino ADV can be found in its user manual (Nortek, 2015).

Velocity measurements were carried out in the stabilization and overflow areas of the device, at two different depths, as showed in Figure 4.1. For that, a calibrated support allowing accurate (± 1 mm) displacements in the three spatial axes was installed at the experimental set-up above these areas and was used to place the ADV in the different measuring points. Flow was only characterized downstream from the energy dissipation area because the DSM-flux functions (monitoring, sampling and particle retention) take place at this part of the device. Besides, in the acceleration area, water level wasn't deep enough to fully cover the ADV head and supercritical regime lead to significant flow perturbations when submerging the probe. On the other hand, in the dissipation area, flow was too bubbly to obtain good quality data. As the ADV used in this study is a coherent pulse probe, special attention was taken to avoid pulse interference when measuring near boundaries.

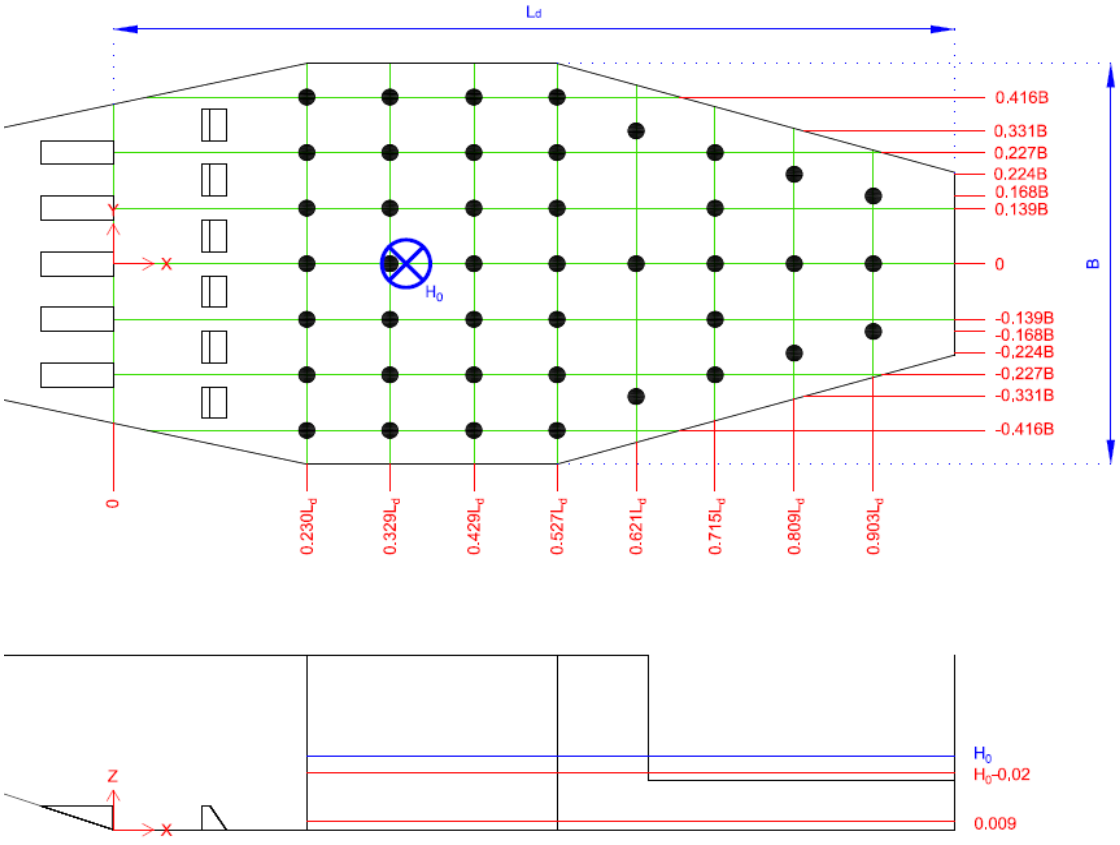

Figure 4.1. ADV measuring points at two different sampling depths. Elevations are in meters (bottom graph).

Methodology and VT tests characteristics for the flow patterns and turbulence assessment

To ensure collecting good enough quality data at the VT tests, the probe parameters were adapted to the flow characteristics and the signal qualities were assessed based on the Kolmogorov turbulence spectra at different locations of the DSM. From preliminary tests, the sampling frequency was established at 50Hz. Nominal velocity range appeared to be one of the most important parameters to obtain good quality data and thus, it was adjusted at each data collection according to the flow conditions. The rest of parameters was left with default values from manufacturer.

A sensitivity analysis was carried out during preliminary tests to determine the required sampling time, which must be large enough to obtain time-converged mean data (time-averaged velocities and Reynolds stresses). Figure 4.2, Figure 4.3 and Figure 4.4 present convergence tests for the time-averaged velocities, tangential Reynolds stresses and normal Reynolds stresses, respectively, for one of the measuring points analysed in the preliminary tests. It is observed that time-averaged velocities converge faster than Reynolds stresses, especially the normal ones. For the conditions tested in this study, a 5 minutes sampling time was selected.

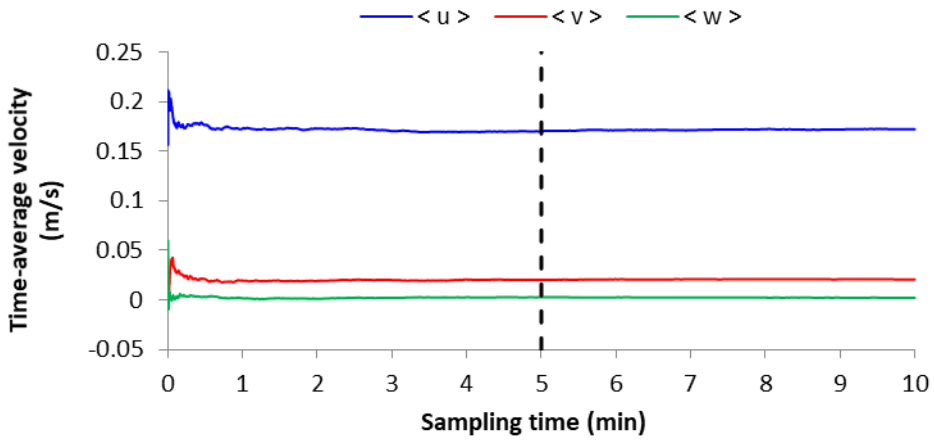

Figure 4.2. Convergence test for the velocity components.

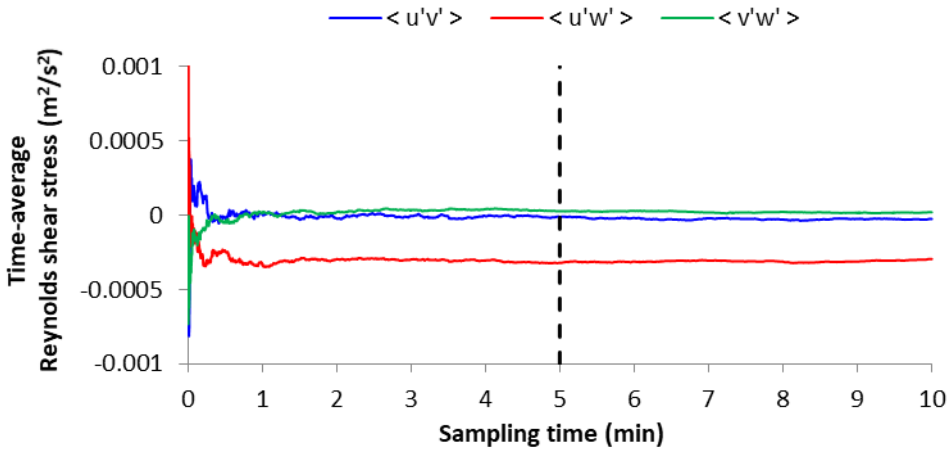

Figure 4.3. Convergence test for the Reynolds shear stresses.

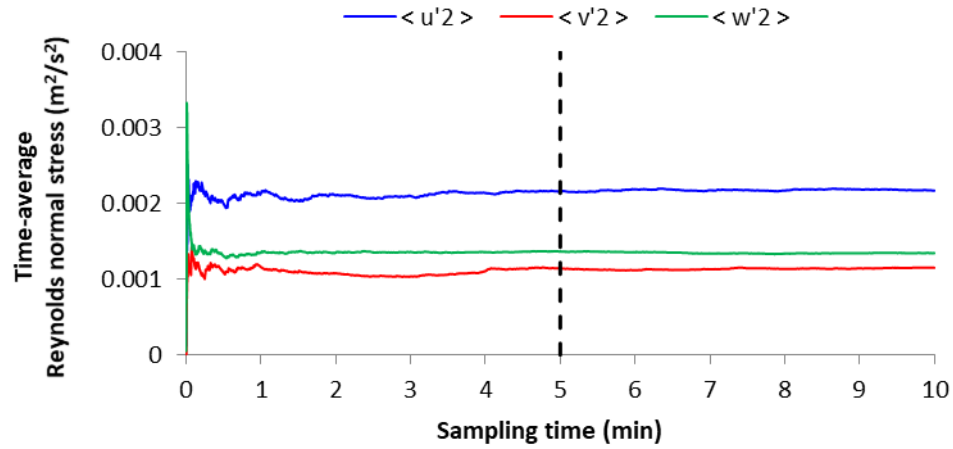

Figure 4.4. Convergence test for the Reynolds normal stresses.

During data collection, signal-to-noise ratio (SNR) and correlation (the normalized correlation, in percentage, of the signals received during one sampling period (1/50 s)) quality indexes were monitored to ensure good quality data. Following the manufacturer requirements, these values were kept over 70% for correlation index and over 15% for the SNR. Note that due to the high aeration of the flow in the hydraulic jump, no additional tracer had to be included in the water, the micro-bubbles acting as acoustic tracers.

Raw data from ADV measurements is usually processed to remove spikes (due, for instance, to the passage of bubbles) and noise from the signals. In this study, the Phase-Space Threshold (PST) despiking algorithm (Goring and Nikora, 2002) was used to remove spikes from the raw

data. The modifications introduced by Wahl *et al.* (2003) concerning the use of the median as location parameter and the median of the absolute median deviation (MAD) as a scale parameter were taken into account as Goring and Nikora (Wahl *et al.*, 2003) agreed on its interest. Replacement of removed spikes was necessary in this study as Reynolds stresses were being calculated based on spectra methods. Despite the weak consensus about which is the most appropriate replacement method of spikes for ADV data, the 12-point third-order polynomial (12PTP) interpolation recommended by Goring and Nikora (2002) for ADV data with sampling frequencies between 25 and 100 Hz was selected. Jesson *et al.* (2013) also obtained good results when applying 12PTP in combination with the PST algorithm to their ADV data. For noise removal, an energy spectra analysis of the signals was carried out.

Three flow configurations with increasing incoming discharges were considered in this study and are specified in Table 4.1.

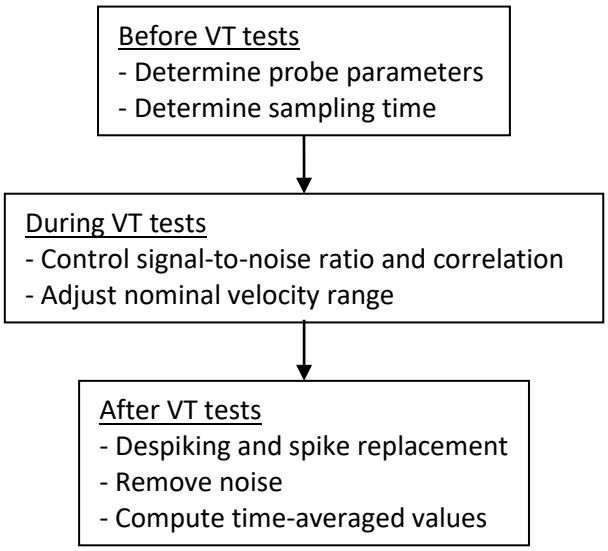

Figure 4.5. Methodology for the assessment of flow patterns and turbulence in the DSM-flux small-scale physical model.

Table 4.1. Hydraulic conditions for the VT tests. Froude (F) and Reynolds (Re) numbers have been estimated based on Manning equation for uniform flow and water depth values were measured at the HQ tests.

TEST ID	Q (m^3/s)	Slope inlet pipe (%)	F inlet pipe	Re inlet pipe	H_0 (m)
VT2	0.002	1	1	16200	0.072
VT5	0.005	1	1.35	35900	0.081
VT9	0.009	1	1.34	58500	0.092

In average, the spikes rate in relation to the total data was between 1 and 4%, which shows that signals weren't too spiky. After despiking the signals and replacing the removed outliers, spectral analysis revealed that noise was negligibly small in most of the signals and that energy spectra corresponded acceptably to Kolmogorov theory, like it is shown in Figure 4.6. For this reason, it was decided not to apply any noise correction filter (such as proposed by Voulgaris and Trowbridge (1998)) to the data and calculate the Reynolds stresses directly as based on each fluctuating velocity component.

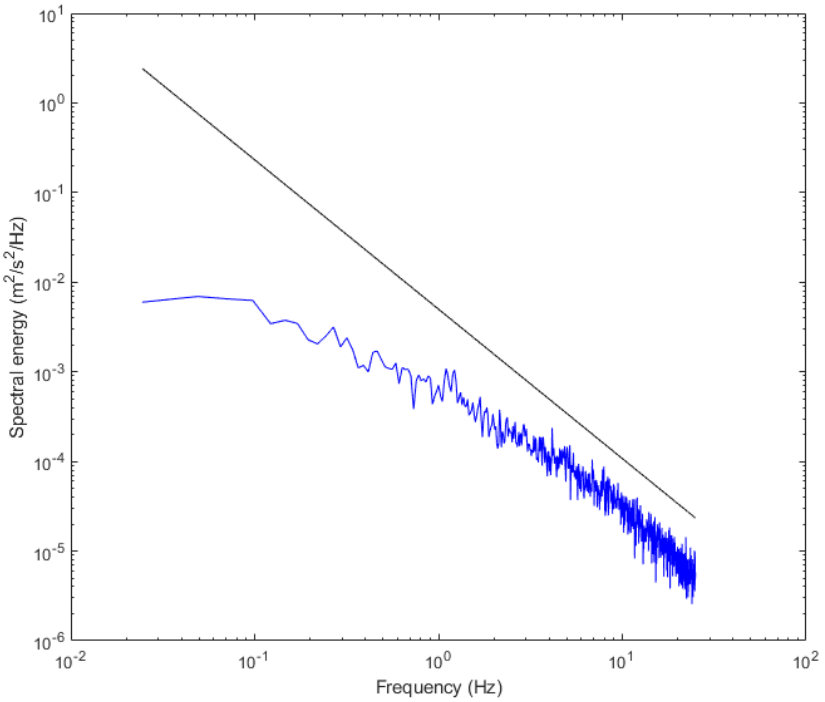

Figure 4.6. Energy spectra (in blue) for u velocity component at x/L_d = 0.329, y/B = 0 and z/H_0 = 0.098 and 5/3 slope line (in black) as a reference for Kolmogorov's model.

4.1.1.2. Flow patterns

In order to determine velocity fields and identify the main flow pattern at the small-scale DSM-flux operating under the flow conditions specified in Table 4.1, time-averaged velocities for each velocity component, noted as <u>, <v> and <w>, were obtained from the pre-processed signals, as well as the horizontal time-averaged <uv> velocities, computed as $\langle uv\rangle=(\langle u\rangle^2+\langle v\rangle^2)^{1/2}$. For the three flow configurations considered in this study, Figure 4.7 and Figure 4.8 show the <uv> velocity fields at the two sampling depths specified in Figure 4.1: approximately 0.9 cm above the bottom (blue vectors), referred as "near-bottom", and 2 cm below the free-surface (red vectors), referred as "near-surface", respectively. Data are normalized by the bulk velocity U_0 at the stabilization zone estimated as the discharge of the

device divided by the cross-section with water depth H_0. The vertical component of these velocity fields didn't show any particular pattern, so it is not presented.

Under the lower flow conditions (Figure 4.7 (a) and Figure 4.8 (a)), normalized magnitudes of <uv> velocities at the downstream area of the small-scale DSM-flux range between $4 \cdot 10^{-2}$ and 1 for the near-bottom, and between $3 \cdot 10^{-1}$ and 2 for the near-surface. In average, <uv> velocities are 10 times (near-surface) and 28 times (near-bottom) lower than the bulk velocity at the inflow pipe under a uniform regime, which highlights the potential of the device to reduce the kinetic energy of CSOs. Considering the velocity components separately, <v> and <w> velocities (not shown here) are in general lower than <u> velocity, especially at the near-surface, even reaching a 10-folds difference for more than half of the points. This manifests that the mean flow pattern is X-dominant, at least at these two sampling depths, and it is particularly visible at the central part of the stabilization area. At the overflow area, <v> velocities increase as flow orientates towards the lateral weir crests. Transversal flow is also relatively noticeable near the walls of the stabilization area. A different pattern is observed in this case between the near-bottom and the near-surface fields: near the bottom, lateral vectors are oriented towards the centre whereas at near the surface, flow conveys towards the walls.

In general, an X-dominant main flow is observed at the centre of the device that spreads towards the weirs crests when reaching the overflow area. If analysed in detail, it can be noticed that this main flow is composed by two parallel streams and that velocities at the symmetry axis of the device are slightly lower. At the stabilization area, flow is much slower close to the lateral walls than in this central area whereas in the overflow zone velocities at the same cross-section are more homogeneous (at the near-bottom) or lower at the central part (at the near-surface) due to the acceleration when reaching the weir crest.

<uv> velocity distributions at both measured depths are about symmetric with regards to the centreline of the DSM-flux. This symmetry is useful because it contributes to a better distribution of the suspended particles along the cross-section of the device. Still, velocities are slightly higher at the right side ($Y < 0$) of the device, but the design of the DSM-flux is symmetric, so it is believed that these small divergences are due to some construction imperfection of the small-scale physical model (as joints jutting out from walls, slightly unlevelled bottom or others) that are not supposed to have an effect in devices of larger scales.

Under the intermediate flow conditions (Figure 4.7 (b) and Figure 4.8 (b)), the main flow patterns are the same as those observed under the lower flow conditions. The only difference concerns the velocity magnitudes: normalized magnitudes of <uv> velocities at the downstream area of the small-scale DSM-flux range between $4 \cdot 10^{-2}$ and 1 for the near-bottom, and between $7 \cdot 10^{-1}$ and 2 for the near-surface. In average, <uv> velocities at the downstream area of the small-scale DSM-flux are 6 times (near-surface) and 10 times (near-bottom) lower than the bulk velocity at the inflow pipe under a uniform regime.

Most of the flow characteristics described for the lower discharge conditions are also valid for the higher discharge flow pattern (Figure 4.7 (c) and Figure 4.8 (c)). However, some differences are observed. Firstly, the transversal flow close to the walls at the stabilization area is less noticeable under a higher discharge, especially at the near-surface, where it is even negligible. Secondly, near the device's bottom, the flow in the stabilization area seems faster close to the walls than in the central part, contrary to what was observed for lower and intermediate discharge conditions. At the near-surface, velocities in each cross-section are more homogeneous and there is not a central stream as observed under lower flow conditions. Another minor difference is that vectors orientation towards the weir crest seems to occur further downstream (one sampling section) at higher discharge conditions. Concerning the velocity magnitudes under higher flow rates, normalized magnitudes of <uv> velocities in the downstream area of the small-scale DSM-flux range between $2 \cdot 10^{-2}$ and 1 for the near-bottom, and between $1 \cdot 10^{-1}$ and 1 for the near-surface. In average, <uv> velocities at the downstream area of the small-scale DSM-flux are 4 times (near-surface) and 9 times (near-bottom) lower than the bulk velocity at the inflow pipe under a uniform regime.

A common trend in the three flow conditions is that <uv> velocities near the surface are around 1.5-2 times higher than the <uv> velocities near the bottom, except for the sections immediately downstream the hydraulic jump and immediately upstream the end wall, where this rate is higher. As these differences are normalized by the bulk velocities, which increase with increasing flow rates, the observed constant rate means that the absolute differences between <uv> velocities at both sampling depths also increase with increasing flow rates.

To better understand the different flow patterns between the near-bottom and the near-surface at the laterals of the stabilization area, additional measurements were carried out along two vertical columns for $X/L_d = 0.329$ and $y/B = \pm 0.416$ (Figure 4.1). Measurements were done for the two extreme flow conditions and resulting <vw> velocity vectors are presented in Figure 4.9, under the lower (Figure 4.9 (a)) and higher (Figure 4.9 (b)) incoming flow

discharges. A switch in transversal flow direction is indeed observed at approximately Z=0.035 m from the bottom (Z/H_0=0.486 for the lower flow rate and Z/H_0=0.380 for the higher flow rate), which is more or less the height of the baffle blocks. These <vw> velocity profiles show the existence of large-scale eddies in the cross-section planes of the stabilization area. These vertical eddies are clockwise in the right part of the flow and anticlockwise in the left, making the flow go towards the walls at the surface and towards the centreline of the device at the bottom.

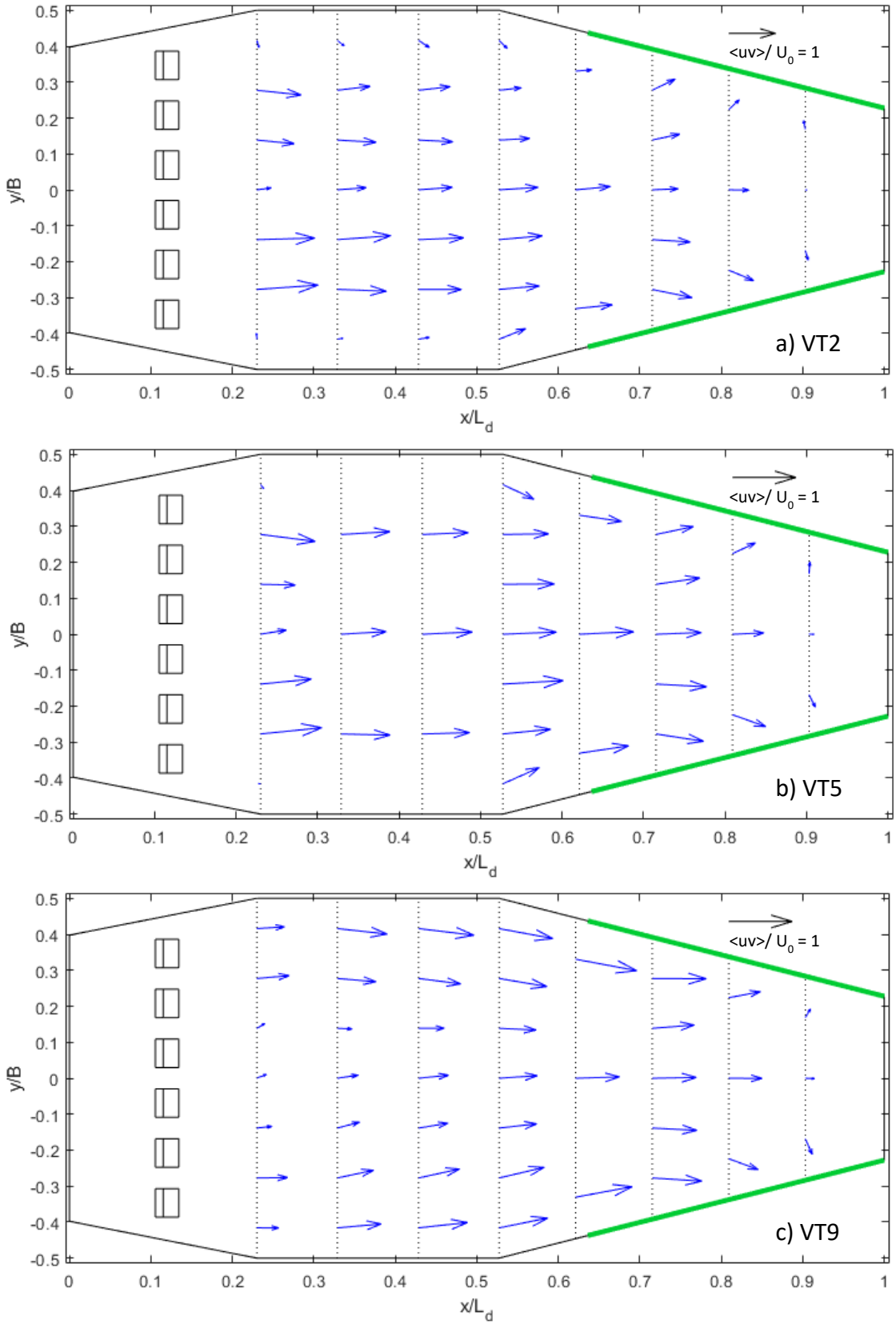

Figure 4.7. <uv> velocity fields at the DSM-flux small-scale physical model for (a) VT2, (b) VT5 and (c) VT9 tests, in the near-bottom region, at depths z/H₀ = 0.125, 0.111 and 0.098, respectively.

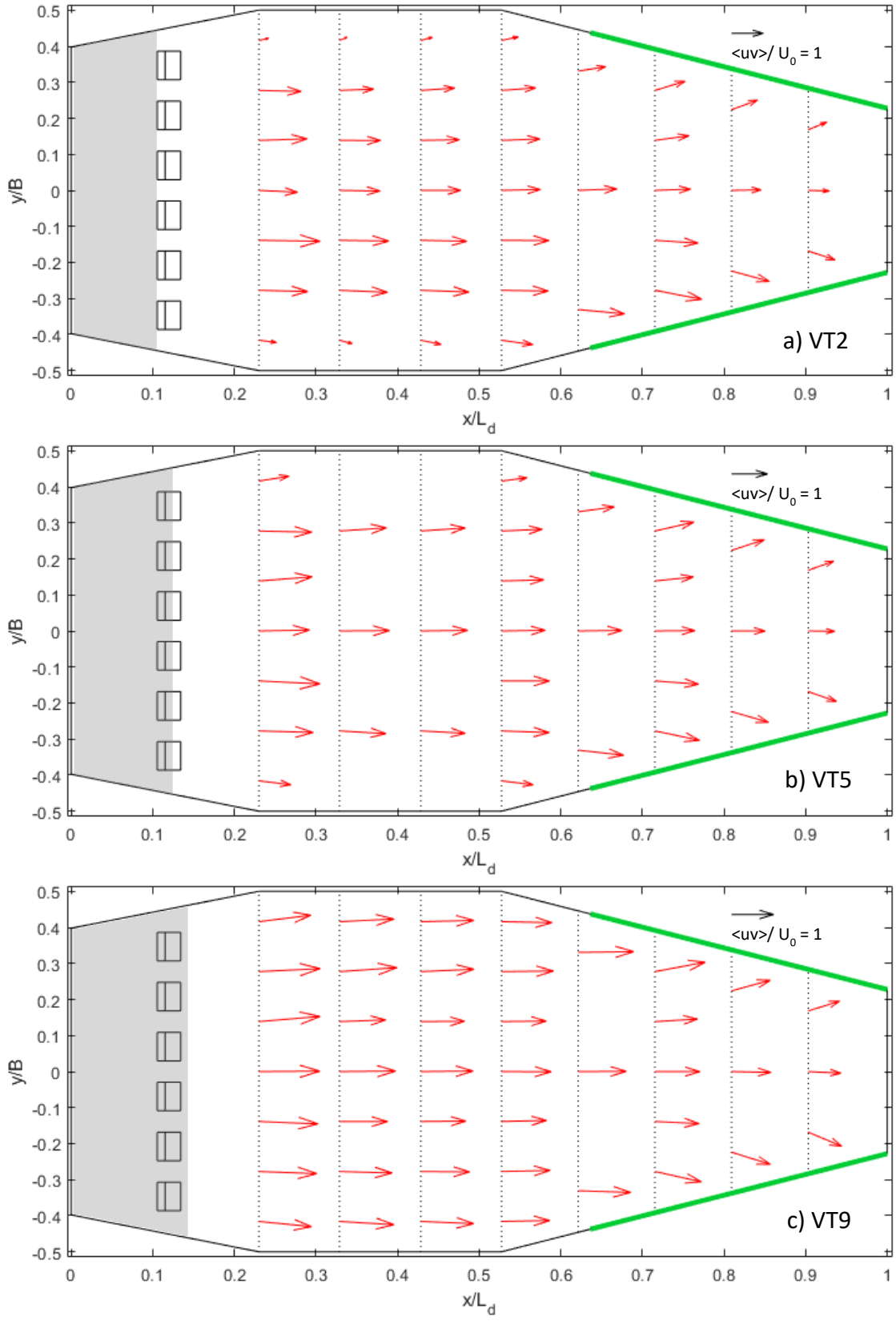

Figure 4.8. <uv> velocity fields at the DSM-flux small-scale physical model for (a) VT2, (b) VT5 and (c) VT9 tests, in the near-surface region, at depths z/H₀ = 0.694, 0.741 and 0.783 respectively. Grey hatched area corresponds to the hydraulic jump recirculation

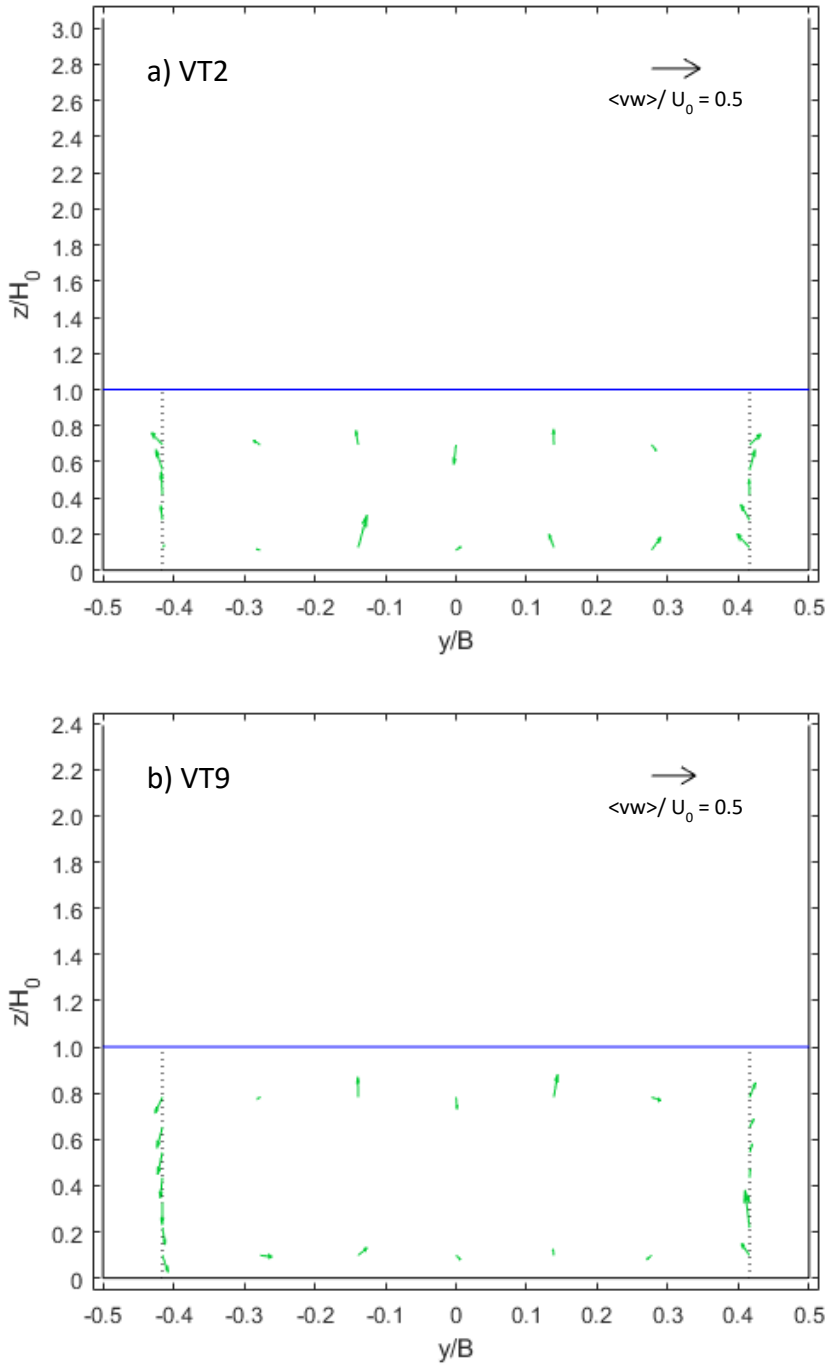

Figure 4.9. <vw> velocity fields at the cross-section x/L_d = 0.329 of the DSM-flux small-scale physical model for (a) VT2 and (b) VT9 tests.

4.1.1.3. Turbulence

Time-averaged turbulent quantities, *i.e.* Reynolds shear stresses and Turbulent Kinetic Energy (TKE) computed as TKE=0.5*(<u'^{2}>+<v'^{2}>+<w'^{2}>), have also been estimated from the velocity data acquired at the small-scale DSM-flux. Reynolds shear stresses are associated with the exchange of momentum due to the velocity gradients and eddies formed within the flow. These exchanges may also entrain solid particles movement. Thus, it is interesting to analyse these quantities for further studies about suspended sediment motion, as resuspension and settling phenomena. Reynolds shear stresses <u'v'> and <u'w'> measured under the flow conditions specified in Table 4.1 are presented in the Appendices for the near-bottom (Appendix 7.3.1 and 7.3.3) and the near-surface (Appendix 7.3.2 and 7.3.4) sampling depths. The <v'w'> shear stress does not show any particular pattern, so it is not presented herein. TKE values are also presented for the three flow conditions specified in Table 4.1, for the near-bottom and the near-surface sampling depths in Figure 4.10 and Figure 4.11 respectively.

Under the lower flow conditions (Appendix 7.3.1 (a), Appendix 7.3.2 (a), Appendix 7.3.3 (a) and Appendix 7.3.4 (a)), normalized <u'v'> and <u'w'> Reynolds shear stresses magnitudes near the bottom (Appendix 7.3.1 (a) and Appendix 7.3.3 (a)) are between 10^{-4} and 10^{-2}. Similar normalized magnitudes are observed near the surface (Appendix 7.3.2 (a) and Appendix 7.3.4 (a)). For both sampling depths, values are relatively higher in the central part of the stabilization area. No general pattern is observed concerning the sign (positive/negative) of the momentum transfers at the near-bottom, except that the <u'w'> stresses seem to be mainly negative, as the mean velocity increases towards the free surface. The same pattern is observed near the surface, where <u'v'> are in general positive in the left area and negative in the right region of the flow. This last pattern is in agreement with the <uv> velocity field gradient presented in Figure 4.8 (a).

Under the intermediate flow conditions (Appendix 7.3.1 (b), Appendix 7.3.2 (b), Appendix 7.3.3 (b) and Appendix 7.3.4 (b)), normalized <u'v'> Reynolds shear stress magnitudes near the bottom (Appendix 7.3.1 (b)) are between 10^{-4} and 10^{-2} and normalized <u'w'> Reynolds shear stress magnitudes (Appendix 7.3.3 (b)) are between 10^{-5} and 10^{-2}. For the near-surface region (Appendix 7.3.2 (b) and Appendix 7.3.4 (b), minimal values are slightly lower: 10^{-3} for <u'v'> and 10^{-4} for <u'w'>. The main difference with the lower flow conditions is that <u'v'> stresses seem mainly negative on the right side and negative on the left side not only at the near-surface as in lower flow conditions, but also near the bottom. This last pattern is in agreement

with the <uv> velocity field gradient presented in Figure 4.7 (b) and Figure 4.8 (b). The other characteristics are similar to the ones observed at the lower flow conditions.

Under the higher flow conditions (Appendix 7.3.1 (c), Appendix 7.3.2 (c), Appendix 7.3.3 (c) and Appendix 7.3.4 (c)), normalized <u'v'> Reynolds shear stress magnitudes at the near-bottom (Appendix 7.3.1 (c)) are between 10^{-5} and 10^{-2} and normalized <u'w'> Reynolds shear stress magnitudes (Appendix 7.3.3 (c)) are between 10^{-3} and 10^{-2}. Similar normalized magnitudes are observed near the surface (Appendix 7.3.2 (c) and Appendix 7.3.4 (c)). At both sampling depths, no clear pattern is observed concerning the location of higher magnitudes for <u'v'> stresses but for <u'w'> stresses, lower values are clearly observed in the overflow region. Concerning the sense of the momentum transfers, near the bottom, <u'v'> stresses seem to be mainly positive on the right side of the stabilisation area and negative on the left side, in agreement agrees with the <uv> velocity field gradient presented in Figure 4.7 (c). This result indicates that eddies in this case turn in the opposite sense of what was observed near the surface for lower flow conditions (Appendix 7.3.1 (a)) and near the bottom and the surface for intermediate flow conditions (Appendix 7.3.1 (b) and Appendix 7.3.2 (b)). Near the surface, no general pattern is observed concerning the sense of the momentum transfers except for <u'w'> stresses that, as for the lower and intermediate flow conditions, are mainly negative.

Concerning TKE values, for the lower flow conditions (Figure 4.10 (a) and Figure 4.11 (a)) normalized values are between 10^{-2} and 10^{-1} at both sampling depths, being in general slightly higher at the surface. TKE values are in general quite homogeneous within the cross-section except for section just downstream from the dissipation zone (x/L_d=0.230), where points at y/B=±0.139 y/B=±0.227 have significant higher TKE, with normalized values closer to 1. This section might still be influenced by the upstream hydraulic jump.

TKE values for the intermediate (Figure 4.10 (b) and Figure 4.11 (b)) and higher (Figure 4.10 (c) and Figure 4.11 (c)) flow conditions have normalized values in the same range of magnitude as for lower flow conditions. The characteristics and trends specified for lower flow conditions are also observed at these higher flow rates.

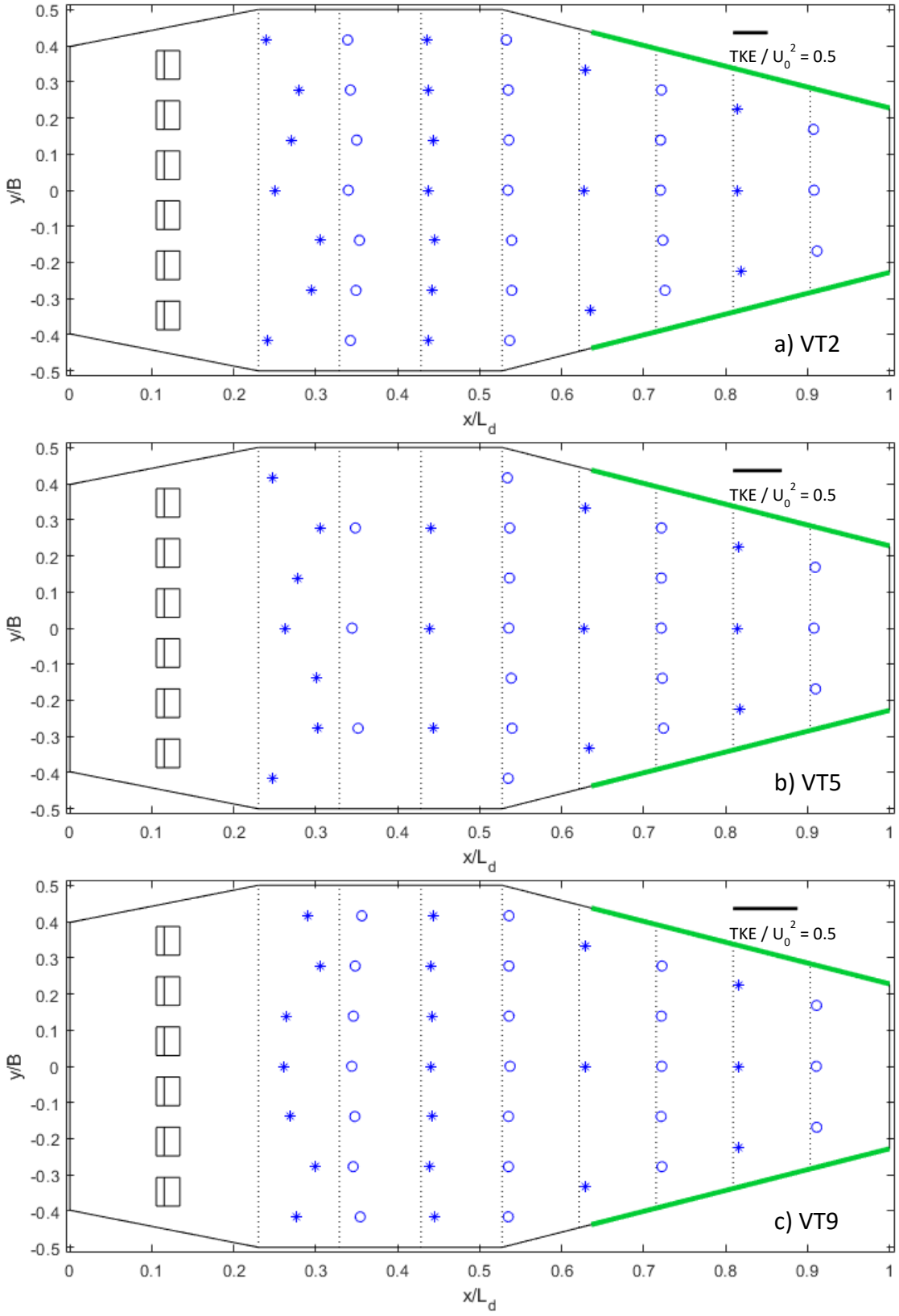

Figure 4.10. TKE values at the DSM-flux small-scale physical model for (a) VT2, (b) VT5 and (c) VT9 tests, in the near-bottom region, at depths z/H_0 of 0.125, 0.111 and 0.098 respectively. Two different markers are used to distinguish data from two consecutive sections.

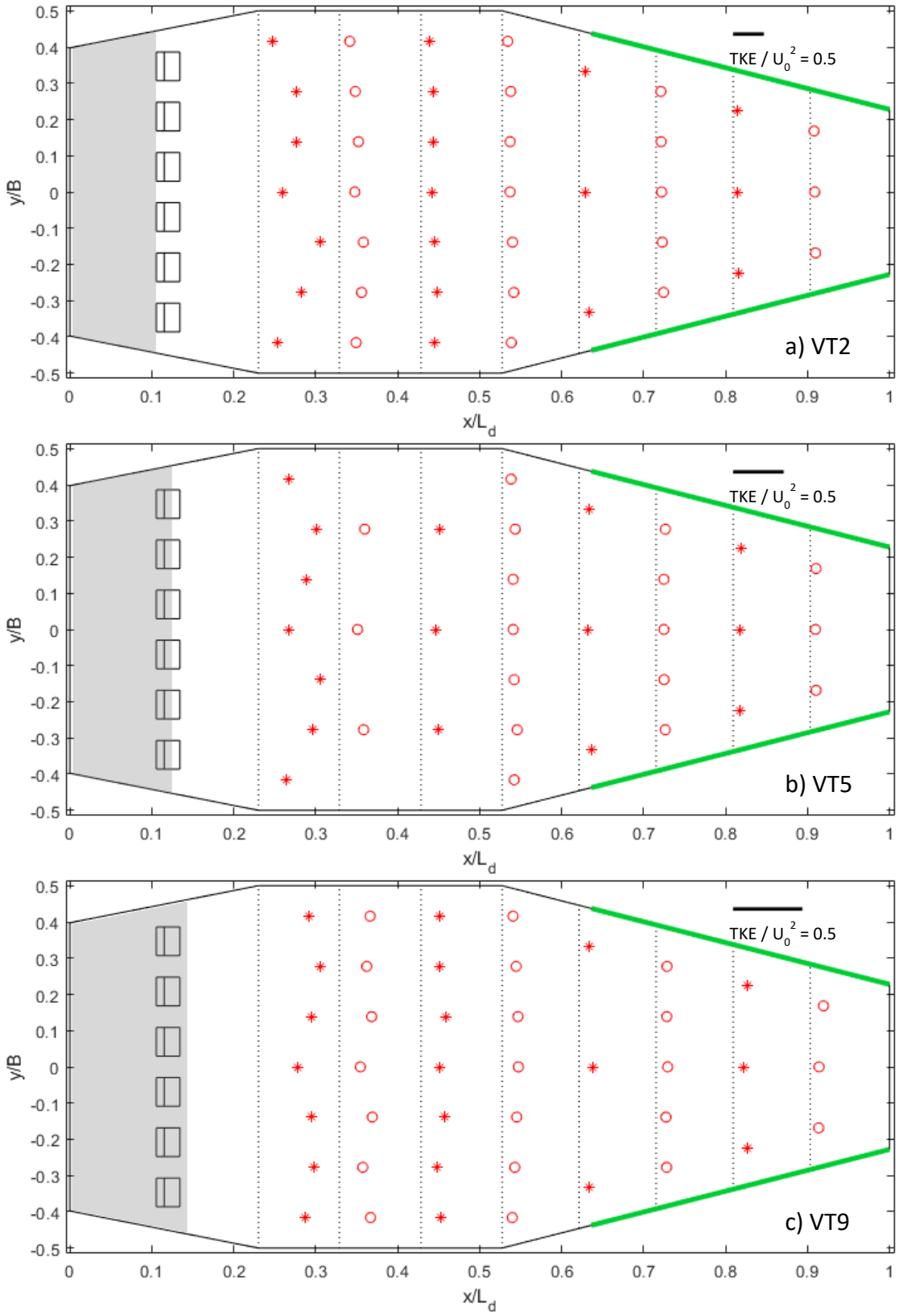

Figure 4.11. TKE values at the DSM-flux small-scale physical model for (a) VT2, (b) VT5 and (c) VT9 tests, in the near-surface region, at depths z/H₀ of 0.694, 0.741 and 0.783 respectively. Grey hatched area corresponds to the hydraulic jump recirculation area. Two different markers are used to distinguish data from two consecutive sections.

4.1.2. The DSM-flux retention and erosion efficiencies

The efficiency of a retention device of specific design depends on the inflow characteristics, pollutant types and particles characteristics among other factors concerning the facility design and management, as for example, the state of the device before the event occurrence. To fully characterize such a device, multiple combinations must be studied and, as explained in Section 1.4, only a few configurations will be addressed in this PhD work. This part of the study is devoted to three objectives: (i) to assess the DSM-flux retention capacity under an event of polluted water and determine the areas of potential deposition; (ii) to estimate the erosion rate of sediments settled at the DSM-flux under a subsequent event of low-polluted water and determine the areas of potential particle entrainment; and (iii) to determine if the DSM-flux contributes to a particle size separation between the retention and overflow mass loads. The same flow configurations as the ones for the assessment of flow patterns and turbulence were selected, in order to investigate potential relationships between the device hydrodynamics and settling and entrainment mechanisms. As explained in Section 4.1.1, even if CSOs are unsteady phenomena, these results will give a first insight of the device's depositions patterns. The methodology and results of these analysis are presented in the following subsections.

4.1.2.1. Materials and methods for the Settling-Entrainment (SE) tests

Layout and instrumentation of the small-scale physical model for the SE tests

For the evaluation of the settling and erosion capacities of the DSM-flux, fine low-density particles had to be injected in the small-scale DSM-flux physical model. For that purpose, the experimental set-up of the small-scale DSM-flux was adapted to be able to inject the particles into the system and collect them once they overflow through the device. A 12 mm interior diameter plastic tube was introduced in the inflow pipe from its outlet, going upstream, so that the injection point was located 3.75 m upstream from the entry of the DSM-flux (the equivalent of 25 inflow pipe diameters). This length was considered enough to reach a good mixing of the particles into the main inflow before entering the device. The injection tube was kept above the flow (in the air) so that no significant perturbations were created into the inflow entering the DSM-flux.

Small light-weighted glass beads were selected for this study in order to represent the finest suspended matter found in the combined sewer systems (Chebbo, 1992). The glass beads used in the SE tests (Poraver® 100-300, Dennert Poraver GmbH) are made from industrially expanded glass granulate from post-consumer recycled glass. According to the manufacturer

technical sheet, granular sizes range from 100 to 300 µm, with an estimated undersize percentage of mass below 15% and an oversize percentage of mass below 10%. These data were verified in the laboratory by optical granulometry. Figure 4.12 shows the granulometric curve obtained and Table 4.2 presents the standard percentile readings from the analysis: characteristic diameters D10, D50 and D90. Particle density is 950 ± 150 kg/m^3 according to DIN EN 1097-6. As these glass beads are porous, they will increase their density when submerged in water. Glass beads were donated by ENGEES laboratory (France) and Isenmann (2016) estimated the wet density to 1240 kg/m^3 by means of a methodology based on their settling velocity.

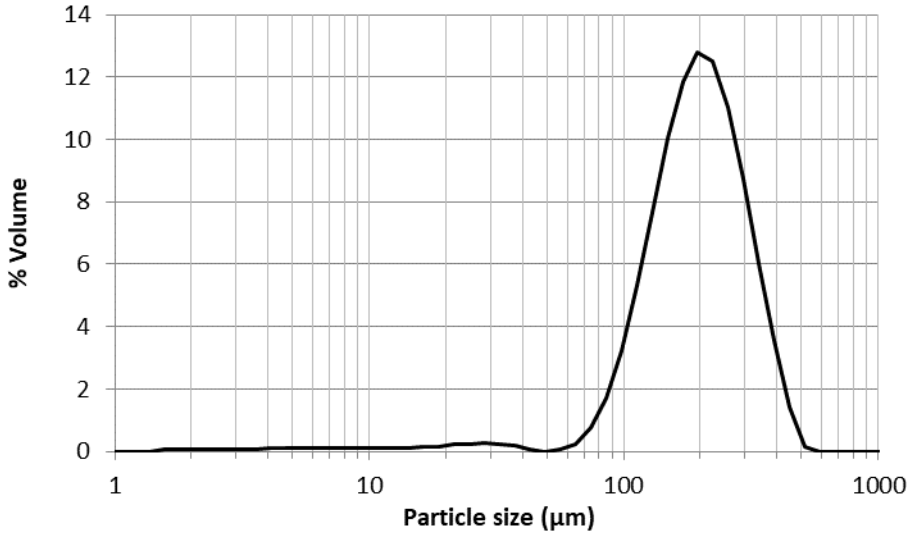

Figure 4.12. Particle size distribution for Poraver® 100-300 glass beads.

Table 4.2. Characteristic diameters of granulometric curve of Poraver® 100-300 glass beads.

Poraver® 100-300		
D10 (µm)	**D50 (µm)**	**D90 (µm)**
108	195	323

Glass beads were mixed with clean water to a certain concentration in a bucket on the side of the experimental device. The mixture was agitated with a mechanical stirrer (Controlab) so that beads were homogeneously distributed in the water before being injected into the system. The glass beads mixture was then pumped into the inflow pipe with a peristaltic pump (7591-07 Analogue Modular I/P Drive System from Masterflex; maximum measurement error of ± 3%) connected to the injection tube and regulated manually with a speed variator. At the outlet of the DSM-flux device, a sieving system was installed to trap all the beads contained in

the DSM-flux overflow. The sieve was made of polyester and had an opening mesh size of 40 µm.

Mass loads of the different samples were measured with digital weighting balances (Adventurer ARA520 and Explorer EOD120 from OHAUS; maximum measurement error of ± 0.01 g). Optical granulometry of the glass beads samples were additionally carried out with a particle size analyser (Mastersizer 2000 from Malvern; maximum measurement error of ± 1% for D50) at the ENTPE laboratory (Lyon, France).

Methodology and SE tests characteristics to assess retention, erosion and particle segregation

The general methodology of this part of the study is presented in Figure 4.13. Before each test, the total mass of particles to be injected was mixed with a certain volume of clean water in a bucket, so that the concentration of this mixture ensures that the mass introduced at the fixed injection flow rate will dilute to the desired concentration in the main flow of the system. The mixture was prepared at least 48h prior to the test to ensure the particles were fully saturated.

In order to assess the retention and the entrainment capacities under the same flow conditions, each SE test (corresponding to certain operating conditions) was divided into two parts or stages, making the final status of stage 1 be the initial status of the device at the beginning of stage 2. Only the lower and the intermediate flow rates tested in the VT tests (Q = 2 l/s and 5 l/s) were selected for the SE tests due to an insufficient capacity of the sieve system to collect the particles at the maximum flow rate (Q = 9 l/s). The details and different steps of each stage of the SE tests are explained in the next subsections.

The particles collected at the DSM-flux and the sieve system were transferred to smaller sieves that were introduced in a stove at 105ºC. Dried particles were then weighted to measure their mass and their granulometry was analysed as explained in the last of the following subsections.

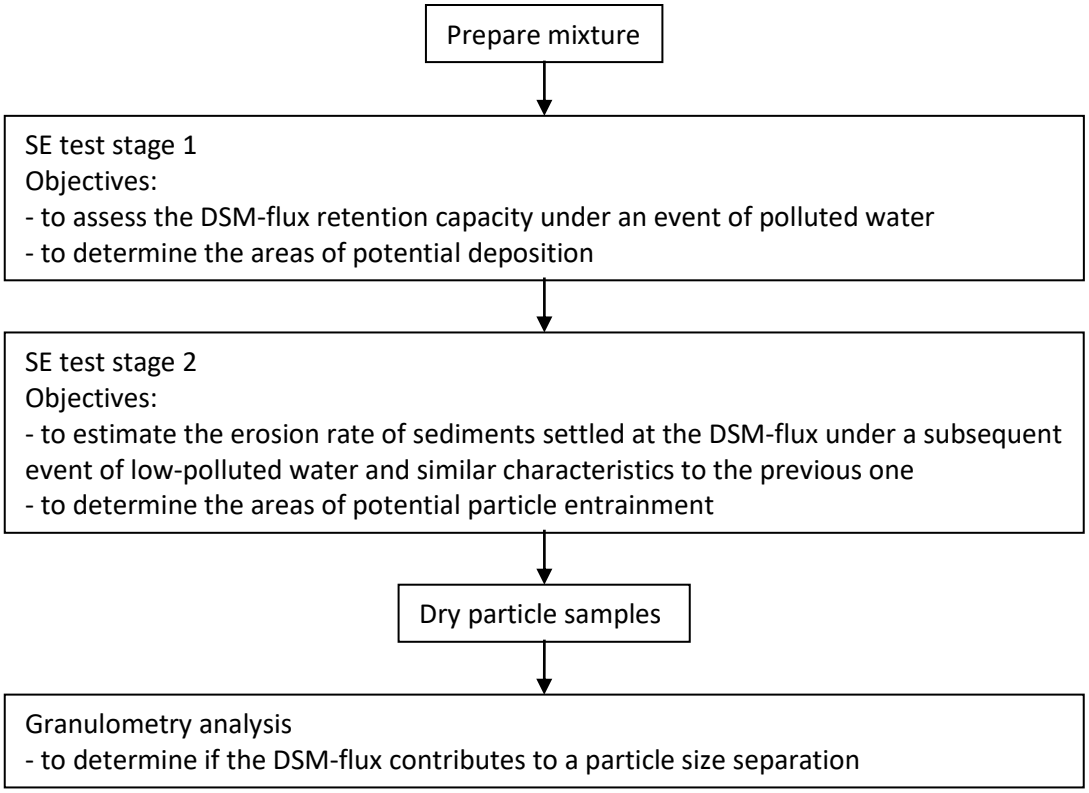

Figure 4.13. Methodology for the assessment of the retention and erosion efficiencies and particle segregation in the DSM-flux.

SE tests stage 1: the retention capacity

The DSM-flux retention capacity depends on the temporal distribution and magnitude of the flow arriving to the device as well as on the temporal distribution and concentration of the pollutants that are transported. CSO events have a high intra- and inter-variability not only in terms of flow rates but also in terms of pollutant concentrations. Being unable to analyse all possible cases in this study, it was decided to start by assessing the simplest case to reproduce in a small-scale physical model: a steady flow event with constant pollutant concentration. This test will give an initial idea of the settling dynamics of the suspended matter in the DSM-flux.

Three different tests were done, one for each of the two flow rates selected (the lower and intermediate flow rates of the VT tests: 2l/s and 5l/s), considering two different concentrations for the lower flow rate Table 4.3. Concentration values were selected according to the range of MES concentrations found in CSO in the literature, which is between 100 mg/l and 2000 mg/l (Becouze-Lareure, 2010; Lipeme Kouyi, 2004).

It was decided to inject the same mass of particles at each test and to do it at the same injection flow rate, in order to make results as comparable as possible. Thus, by fixing the

injected mass of particles (M_{inj}) and the injection flow rate, the duration (T_{inj}) of the injection was automatically determined depending on the concentration (C) and the flow rate (Q) at the system:

$$T_{inj} = \frac{M_{inj}}{C \times Q}$$ ***Equation 4.1***

The total duration of the event (T) for the SE test stage 1 was obtained by adding to the duration of injection the estimated traveling time of the last particle to be injected from the injection point to the outlet of the DSM-flux (T_{travel}), which will vary according to the flow rate of the system:

$$T = T_{inj} + T_{travel}$$ ***Equation 4.2***

The type of hydrograph and pollutograph at the injection point reproduced at this stage 1 of the SE tests is illustrated in Figure 4.14 and the characteristic times of the three tests are specified in Table 4.3.

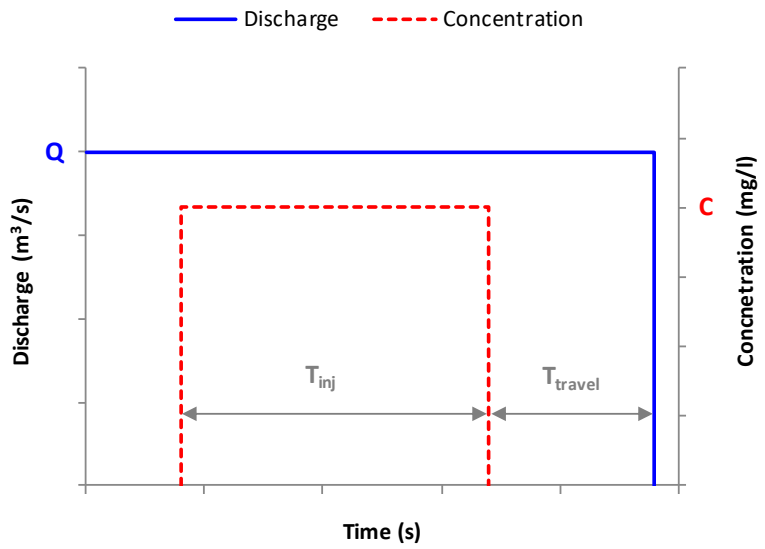

Figure 4.14. Event type reproduced at the DSM-flux small-scale physical model for stage 1 of the three SE tests.

The injection flow rate was set to 0.012 l/s, a value low enough to be negligible compared to the total discharge of the system for all the tested hydraulic conditions. The actual total mass of particles really injected at each test was uncertain because a certain amount of particles remained in the mixture bucket (more mixture than the strictly necessary was prepared to give a certain margin of water depth to the peristaltic pump to perform correctly) and there was a considerable uncertainty on the mass trapped in the inflow pipe. Thus, real mass inflow and

corresponding mean concentrations (C*) were estimated at the end of the tests from the total collected mass (TCM) and the flow rate (Q) of the test.

$$C^* = \frac{TCM}{Q}$$ ***Equation 4.3***

Table 4.3. Hydraulic conditions for stage 1 of the three SE tests.

TEST ID	Q (m^3/s)	C* (mg/l)	T_{inj}	T_{travel}	T
SE2_130	0.002	130	13 min 53 s	28 s	14 min 21 s
SE5_110	0.005	110	5 min 33 s	14 s	5 min 47 s
SE2_560	0.002	560	1 min 23 s	28 s	1 min 51 s

The following steps were followed to carry out stage 1 of the SE tests:

I. Switch on the clear-water system and set the desired flow rate.
II. Start the injection of the mixture: a certain volume at a constant injection flow rate and constant concentration during a certain time (T_{inj}).
III. Once the desired volume of mixture has been injected, stop the injection pump (Figure 4.14).
IV. Wait a time interval equal to T_{travel} and switch off the system.
V. Collect the particles trapped at the sieve. This corresponds to the mass of particles evacuated through overflow during the stage 1 of the test (noted ME1).
VI. Characterize the sediment deposition pattern and location.

SE tests stage 2: the erosion rate

Stage 2 of each SE test pursued to estimate the capacity of erosion of sediments that settled in the previous stage. This case represents a real situation that occurs in subsequent CSOs: a first rain event has a higher pollutant load due not only to wastewater but especially because of wash-off and stormwater (runoff) contributions. Subsequent CSOs will also be loaded but it is expected that sediment concentrations will be relatively lower. In order to reduce the number of factors influencing the process, it was decided to use clean water during this second stage to ensure that no further settling would take place and that only solid matter already in the DSM-flux will be entrained and resuspended to be transported towards the outlet and (maybe) evacuated. In this stage 2, the duration of the events wasn't pre-stablished. The end of the tests was determined by the time when no more particles seemed to leave the device and the remaining deposited sediments seemed stationary. These assessments were done by means of

regular visual observations of the overflow during the test and by visually comparing photos of the sediments taken periodically every hour or half an hour.

The following steps were followed to carry out stage 2 of the SE tests:

I. Switch on the system again with the same flow rate (of clear water) as the previous stage (Table 4.3).
II. Regularly observe the overflow and register the evolution of the deposited sediments pattern.
III. When no more particle seems to leave the device and the remaining sediments seem stationary, switch off the system.
IV. Collect the particles trapped at the sieve. This corresponds to the mass of particles evacuated during the stage 2 of the test (noted ME2).
V. Collect the particles remaining in the DSM-flux. This corresponds to the mass of particles remaining at the device at the end of the stage 2 of the test (MR2).

It should be noted that the total injected mass (and corresponding inflow concentration) can then be evaluated M=ME1+ME2+MR2.

The granulometry analysis

In order to determine if there is a separation of the particle sizes at the DSM-flux, optical granulometry analyses were carried out with a particle size analyser. This type of instrument uses the theory of light scattering and adsorption (theory of Mie) to determine the size of the different particles of the sample from light attenuation when they are passed through a laser beam. The Mie theory is based on the hypothesis that particles are spherical, which is the case for the glass beads used in this study. To use the Mie equations, the refractive index of the material and the absorption part of that refractive index must be known. These parameters were not specified by the glass beads manufacturer so standard average values suggested by the particle size analyser manufacturer were used: 0 for the absorption and 1.52 for the refractive index. It should be noticed that the results obtained with this equipment are volume-based, e. g., the D50 diameter represents the diameter exceeded by 50% of the sampling volume. Further information about the operation of the Mastersizer 2000 particle size analyser can be found in its user manual (Malvern Instruments, 2007).

Five different samples were analysed for each of the SE tests. These samples are mixtures of material collected at different locations and stages of the tests, as follows:

- Sample Edsm – Material entering the DSM-flux = ME1+ME2+MR2
- Sample TrapS1 – Material trapped at the DSM-flux during stage 1 = ME2+MR2
- Sample EvacS1 – Material evacuated from the DSM-flux at stage 1 = ME1
- Sample TrapS2 – Material trapped at the DSM-flux during stage 2 = MR2
- Sample EvacS2 – Material evacuated from the DSM-flux at stage 2 = ME2

For the samples with material from different sources, the mixtures where made proportionally with reference to the total collected mass at that location and stage.

4.1.2.2. Retention and erosion rates resulting from the SE tests

Results of the three SE tests are presented in Table 4.4. As explained in section 4.1.1, the total collected mass (TCM) was considered as the initial mass entering the DSM-flux so retention and erosion rates were estimated with reference to this value (Equation 4.6 and Equation 4.7).

$$TCM = ME1 + ME2 + MR2 \qquad \textit{Equation 4.4}$$

$$MR1 = ME2 + MR2 \qquad \textit{Equation 4.5}$$

$$Retention\ Rate = \frac{ME2 + MR2}{ME1 + ME2 + MR2} = \frac{MR1}{TCM} \qquad \textit{Equation 4.6}$$

$$Erosion\ Rate = \frac{ME2}{ME2 + MR2} = \frac{ME2}{MR1} \qquad \textit{Equation 4.7}$$

Table 4.4. Results of the SE tests.

TEST ID	Q (m^3/s)	C* (mg/l)	ME1 (g)	ME2 (g)	MR2 (g)	MR1 (g)	TCM (g)	Retention rate (%)	Erosion rate (%)
SE2_130	0.002	130	93.0	8.1	99.4	107.5	200.5	53.6	7.5
SE5_110	0.005	110	126.2	42.7	1.1	43.9	170.0	25.8	97.4
SE2_560	0.002	560	41.4	12.1	33.0	45.0	86.4	52.1	26.8

When comparing the results of the tests carried out under the lower flow conditions with two different concentrations of particles (tests SE2_130 and SE2_560), it seems that the retention rate doesn't depend on the concentration of particles injected. Indeed, for the same flow conditions, the percentage of particles trapped at the DSM-flux in stage 1 is the same for both concentrations: around 50% for these tested conditions (Table 4.4).

The results issued from the tests carried out with similar concentrations of particles but different flow conditions (tests SE2_130 and SE5_110) show that the retention rate is, as expected, higher under the lower flow conditions: 53.6% *versus* 25.8% for the tested conditions.

Concerning the erosion rates, an interesting result is observed when comparing tests SE2_130 and SE2_560: although the former test has a higher deposition load at the beginning of stage 2 (MR1 of 107.5 g *versus* 45 g), the latter test presents a higher erosion rate (26.8% *versus* 7.5%). This would indicate an unexpected tendency: that, under the same flow conditions, the erosion rate is lower as the available mass load is higher. This result can actually be explained by the fact that, in both cases, despite the initial deposition load, the amount of material entrained is approximately the same: ME2 around 10 g (8.1 g for SE2_130 and 12.1 g for SE2_560). Thus, this means that the erosion mass load is constant for a given water discharge even with different available deposited sediment loads. This result might seem opposed to what has been observed, for example, in the stormwater retention basin managed by DEEP laboratory and OTHU in Chassieu (France), where the erosion capacity increases as the amount of cumulated sediments is larger. However, the reason behind this tendency is more related to the roughness (and thus, the volume or shape) of the deposited materials rather than to the quantity (mass load) (Dey *et al.*, 2011). As no topography of the sediment's relief was done at the end of these tests, it is not possible to determine if the roughness was similar or not in both cases. The absence of this topography data and its evolution during the tests also prevent the study from any information regarding the motion of material within the device. If there were dead zones where particles settle and are never entrained, maybe particles that were initially entrained in other regions of the device could reach these dead zones and thus settle down again, without being able to finally leave the device. This would mean that even if there is a higher entrainment of material because there is more material available (common tendency), it may not exit the device and won't be considered in the erosion rate computation, as it is estimated in this PhD work. These results were confirmed by the repetition of these two tests. Further tests under different flow conditions or with different initial deposition loads would give more information about this phenomenon and evaluate its robustness.

Finally, from tests SE5_110 and SE2_560 it is observed that with a similar deposition load in stage 1 (MR1 around 45 g), a higher flow rate implies a higher erosion rate (97.4% *versus* 26.8%), as it was expected.

4.1.2.3. Main deposition areas

For each of the three SE tests, whose characteristics are specified in Table 4.1 and results in Table 4.4, a deposition map was created for the sediments state at the end of stage 1 in order to identify the preferential areas of settling. Figure 4.16 (a), (b) and (c) show photos of the deposition areas at the end of stage 1 for tests SE2_130, SE5_110 and SE2_560 respectively and Figure 4.17 (a), (b), and (c) show the corresponding deposition maps.

Deposition during stage 1 under lower flow conditions (tests SE2_130 and SE2_560, Figure 4.17 (a) and (c)) is quite homogeneous from the downstream 2/3 length of the stabilization area until 1/10 length of the overflow area upstream the end wall of the device. Less deposition is observed close to the walls, especially in the right side of the device, revealing a slight asymmetric behaviour. This result is in agreement with the slight asymmetry observed at the velocity fields and turbulence quantities (Figure 4.7 (a) and Figure 4.10). At the end wall, a strip with no sediments is observed. Velocity and turbulence measurements weren't done in this strip area but maybe, as it was seen at the laterals of the stabilization zone (Figure 4.9), a vortex is formed in the XZ plane (it was XY plane for the laterals of the stabilization zone) probably induced by the impact of the flow with the end wall, as represented in Figure 4.15. This would create a recirculation area near the bottom that could avoid the material to be settled, entraining it upstream. This type of vortex is described by Gisonni and Hager (1997) for a short side-weir with an end wall.

Figure 4.15. Possible vortex structure formed at the bottom of the end wall of the DSM-flux device that could explain the absence of sediments in that area.

At the upstream 1/3 length of the stabilization zone, the deposition layer draws a quasi-symmetric parabolic profile showing two main areas without sediments downstream the dissipation zone, at both sides of the symmetry axis of the device. This result reveals that downstream the baffle blocks, there are two streams with higher velocities and turbulence

which avoid settling and/or entrain resuspension of material. These two streams are clearly observed at the <uv> velocity field figure obtained under the same flow conditions at VT tests (Figure 4.7 (a)), where normalized velocity magnitudes are higher at these two areas (1-1.3 *versus* 0.1-0.3 at the laterals and center). It is also observed from Figure 4.10 (a) that these two areas correspond to higher values of TKE (0.8-0.9 versus 0.1-0.2, range of values for the rest of the device). This result is shown on Figure 4.24, where the maximum TKE regions clearly correspond to those of lowest deposition.

The deposition maps from tests SE2_130 and SE2_560 confirm that the injection concentration doesn't have much influence on the settling and resuspension mechanisms. However, the magnitude of the flow rate does have an important influence, at it is observed when comparing the deposition maps from tests SE2_130 and SE5_110 (Figure 4.17 (a) and (b)). Indeed, a more limited deposition area is observed at the end of stage 1 under the higher flow conditions (test SE5_110). The two parabolas observed under lower flow conditions reach, in this case, the middle length of the stabilization area and their wakes extend until the upstream cross-section of the lateral weirs (beginning of overflow). Wider strips with no deposited sediment are also observed along the walls. The end wall band with little settled material is also wider than under the lower flow conditions. The asymmetry is even more evident in this case as we observe less deposition area at the right side bringing to light higher velocities or higher turbulence energy. However, this is not so clearly observed on the velocity field and TKE figures (Figure 4.7 (b) and Figure 4.10 (b) respectively), where asymmetry among left and right side variables remains limited.

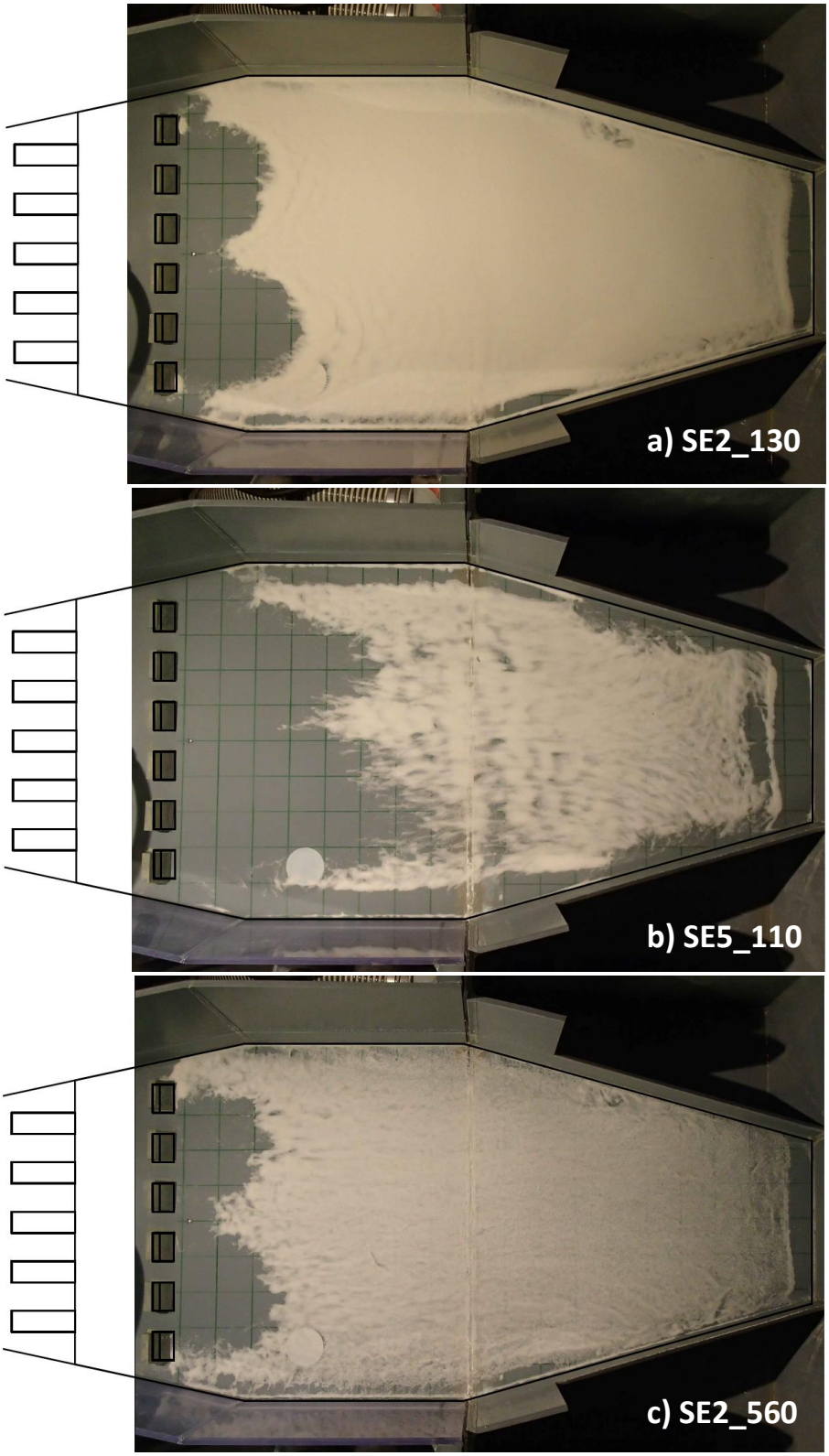

Figure 4.16. Photos of the deposition areas (corresponding to MR1 mass load) at the DSM-flux small-scale physical model at the end of stage 1 for (a) SE2_130, (b) SE5_110 and (c) SE2_560 tests.

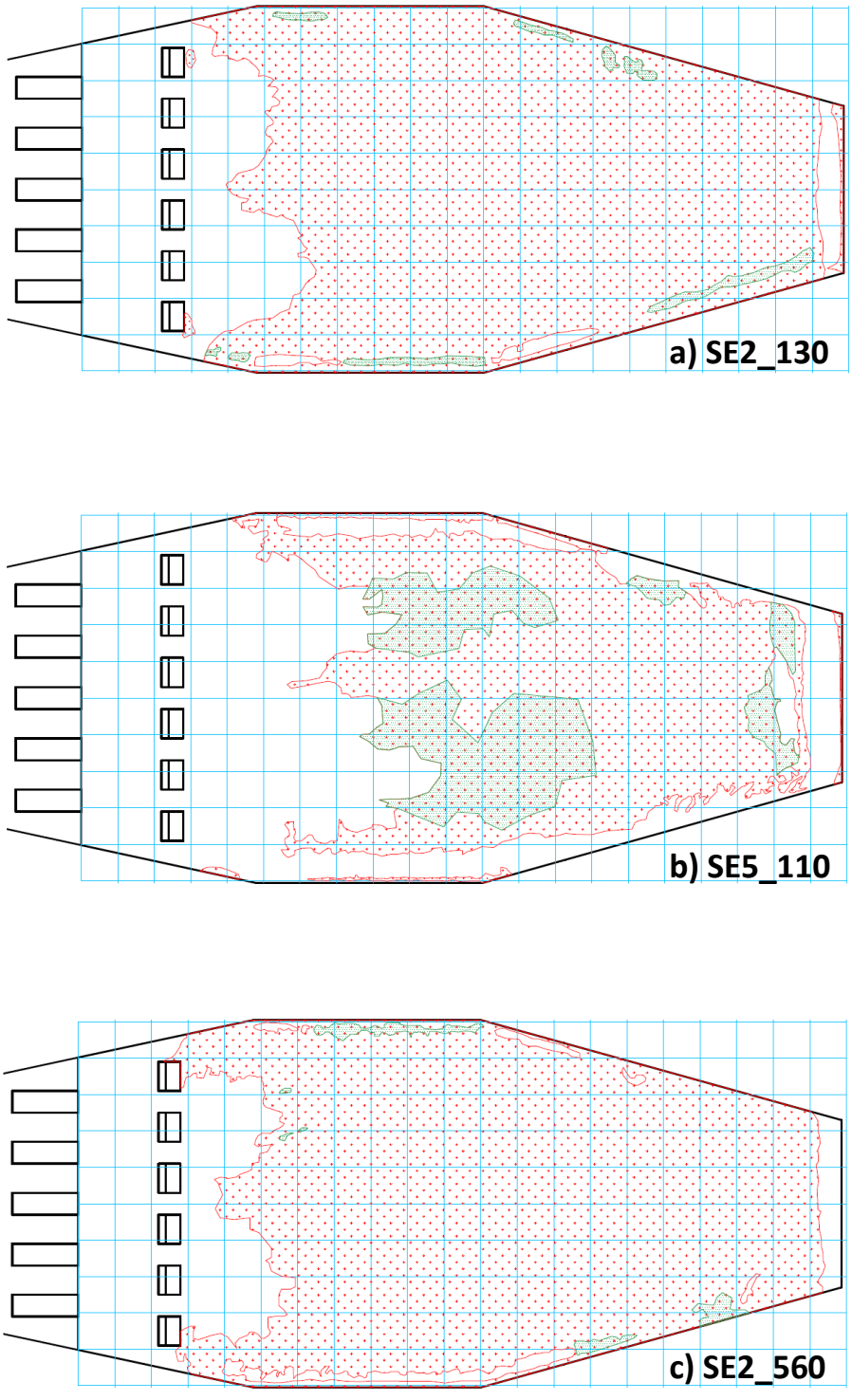

Figure 4.17. Deposition maps at the DSM-flux small-scale physical model at the end of stage 1 (corresponding to MR1 mass load) for (a) SE2_130, (b) SE5_110 and (c) SE2_560 tests. Zones where sediments settled are hatched in red with a grass pattern. Zones hatched in green with a dot pattern represent areas were the deposition layer was finer, so the bottom of the device was visible. This might be either because less settling had taken place there or because some erosion had already occurred. A 5 cm spaced grid, also drawn at the small-scale model, is included in the deposition maps for reference purposes.

4.1.2.4. Main entrainment areas

For each of the SE tests, a second deposition map was made for the sediments state at the end of stage 2 and photos were taken at different intervals of time during this stage in order to investigate the time evolution of the deposition areas and identify the preferential zones where erosion occurs under by comparison with the deposition maps at the end of stage 1 (Figure 4.16 and Figure 4.17) for the same tested flow conditions. Figure 4.18, Figure 4.19 and Figure 4.20 show the evolution of the sediments settled in the stage 1 (t = 0), during stage 2, and the deposition maps at the end of stage 2, for tests SE2_130, SE5_110 and SE2_560 respectively.

Similarly as for stage 1, Figure 4.21 (a), (b) and (c) show the photos of the deposition areas at the end of stage 2 for tests SE2_130, SE5_110 and SE2_560 respectively and Figure 4.22 (a), (b), and (c) show the corresponding deposition maps. In order to be able to better compare deposition at the end of stage 1 and stage 2, deposition maps from both instants of the test have been superposed at Figure 4.23.

A common observation from all figures is that erosion starts mainly in the layers next to the side walls and at the two eroded areas with parabolic shape downstream from the dissipation zone. These two areas extend downstream with time creating small riddles (under the lower flow conditions) or entraining the material settled downstream (higher flow conditions). More erosion is observed at the right side of the device, as expected from the slight asymmetries detected in the velocity field and turbulence analysis. Under the highest flow conditions tested in this study (which are relatively low for the design capacity of the device: 1/3 Q_{max}) it is observed that almost all the sediment is entrained within the first half hour of this stage 2 (Figure 4.22 (b)). This indicates that after a small rain event, where deposition occurs, the DSM-flux should be cleaned out because a subsequent event could probably wash off all the sediments.

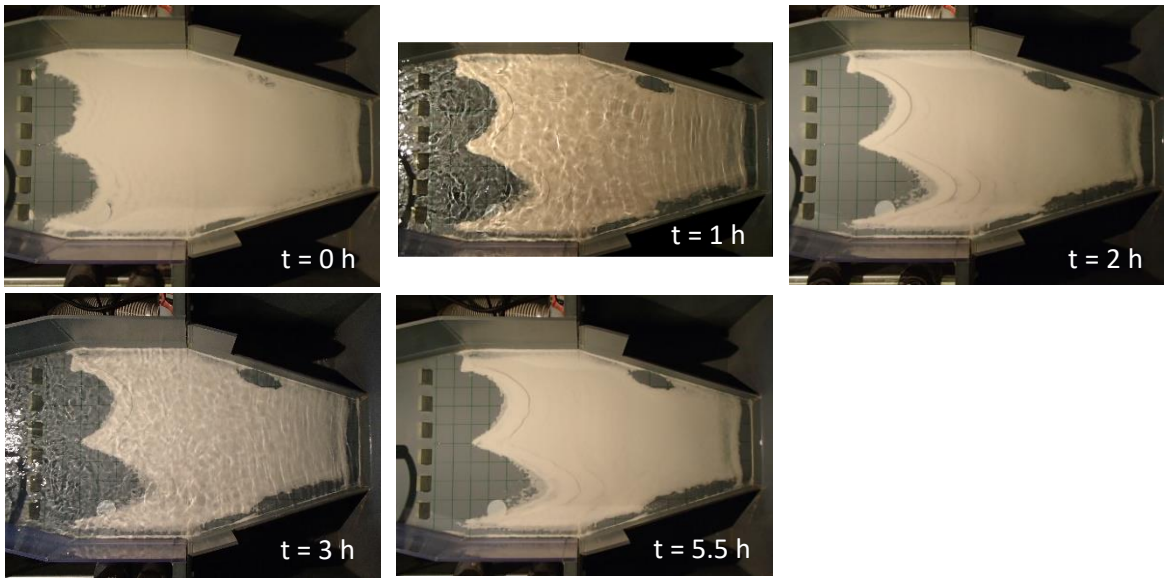

Figure 4.18. Photos showing the evolution of the material settled in stage 1 for the SE2_130 test.

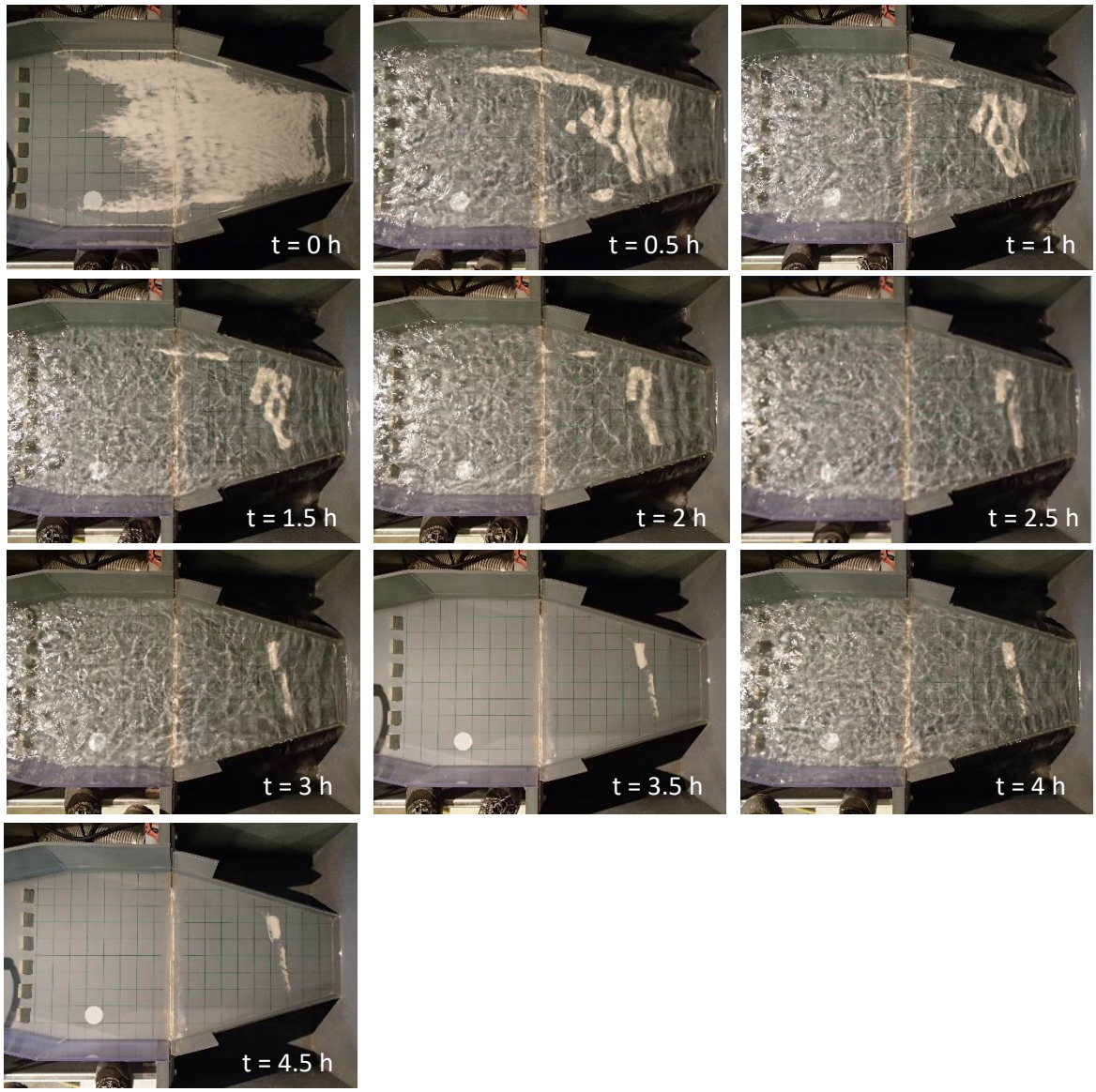

Figure 4.19. Photos showing the evolution of the material settled in stage 1 for the SE5_110 test.

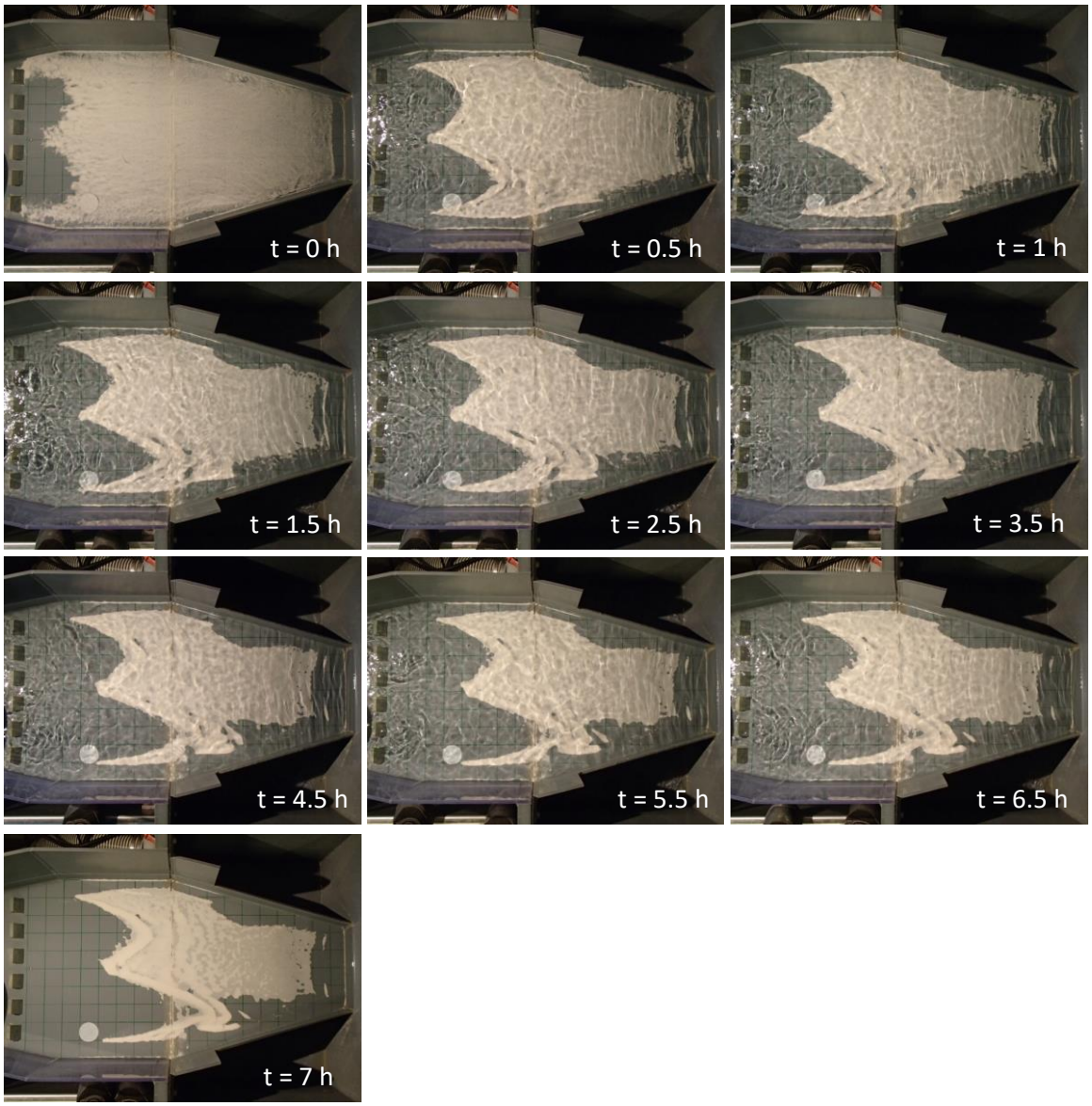

Figure 4.20. Photos showing the evolution of the material settled in stage 1 for the SE2_560 test.

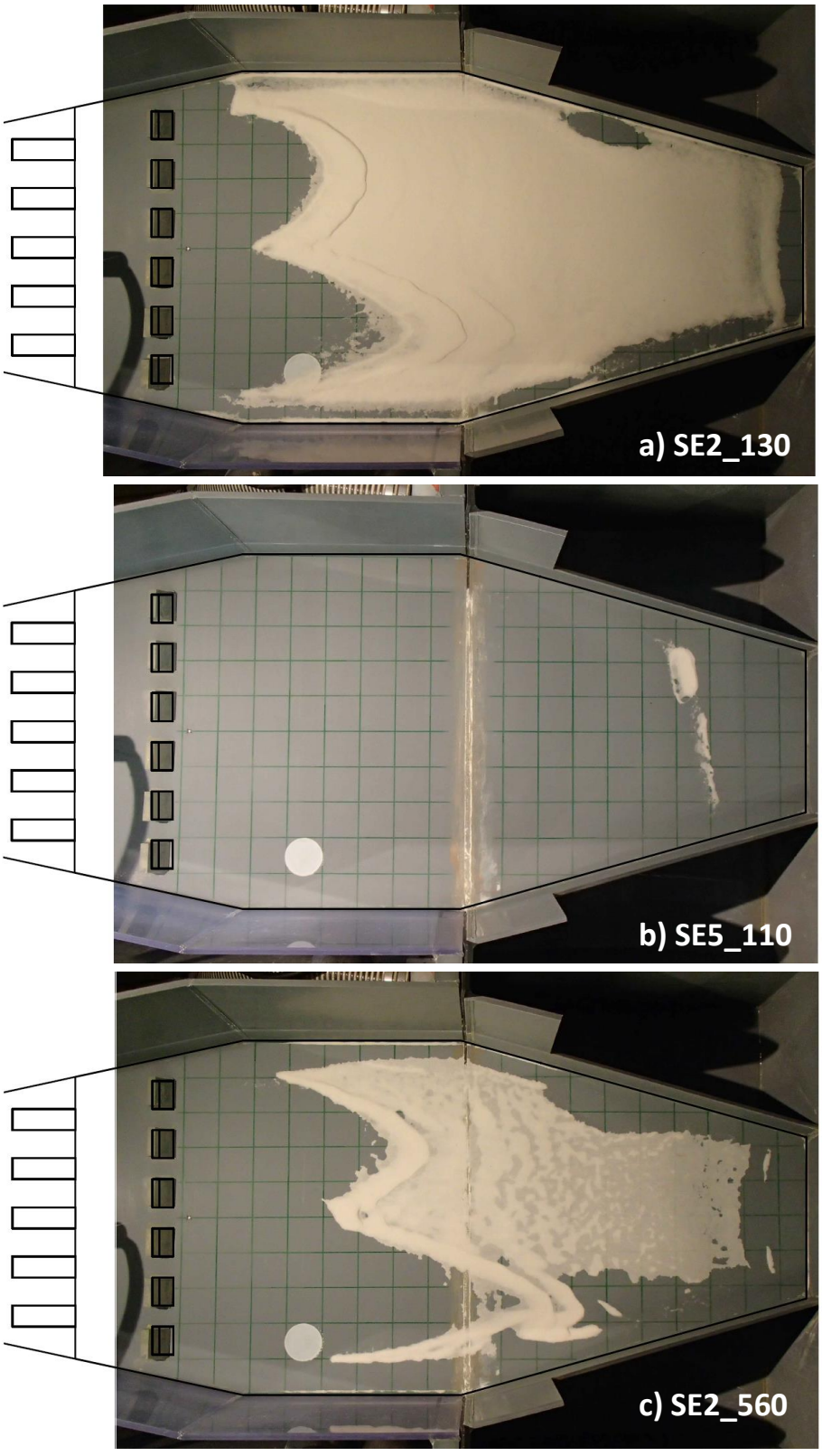

Figure 4.21. Photos of the deposition areas (corresponding to MR2 mass load) at the DSM-flux small-scale physical model at the end of stage 2 for (a) SE2_130, (b) SE5_110 and (c) SE2_560 tests.

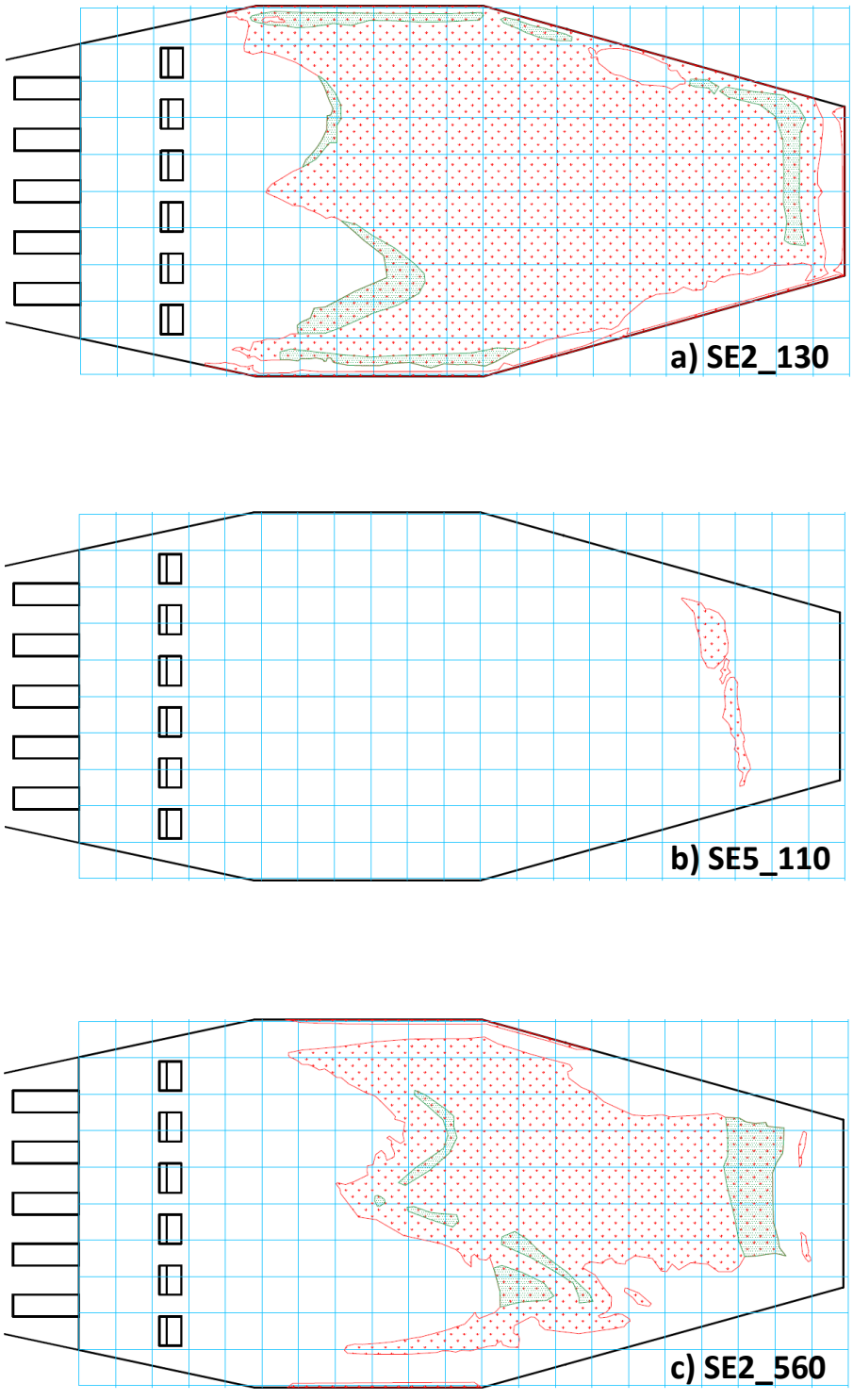

Figure 4.22. Deposition maps (corresponding to MR2 mass load) at the DSM-flux small-scale physical model at the end of stage 2 for (a) SE2_130, (b) SE5_110 and (c) SE2_560 tests. The legend for the colors of the hatched zones is the same as for the stage 1 (Figure 4.17) and the 5 cm space grid is also represented for reference.

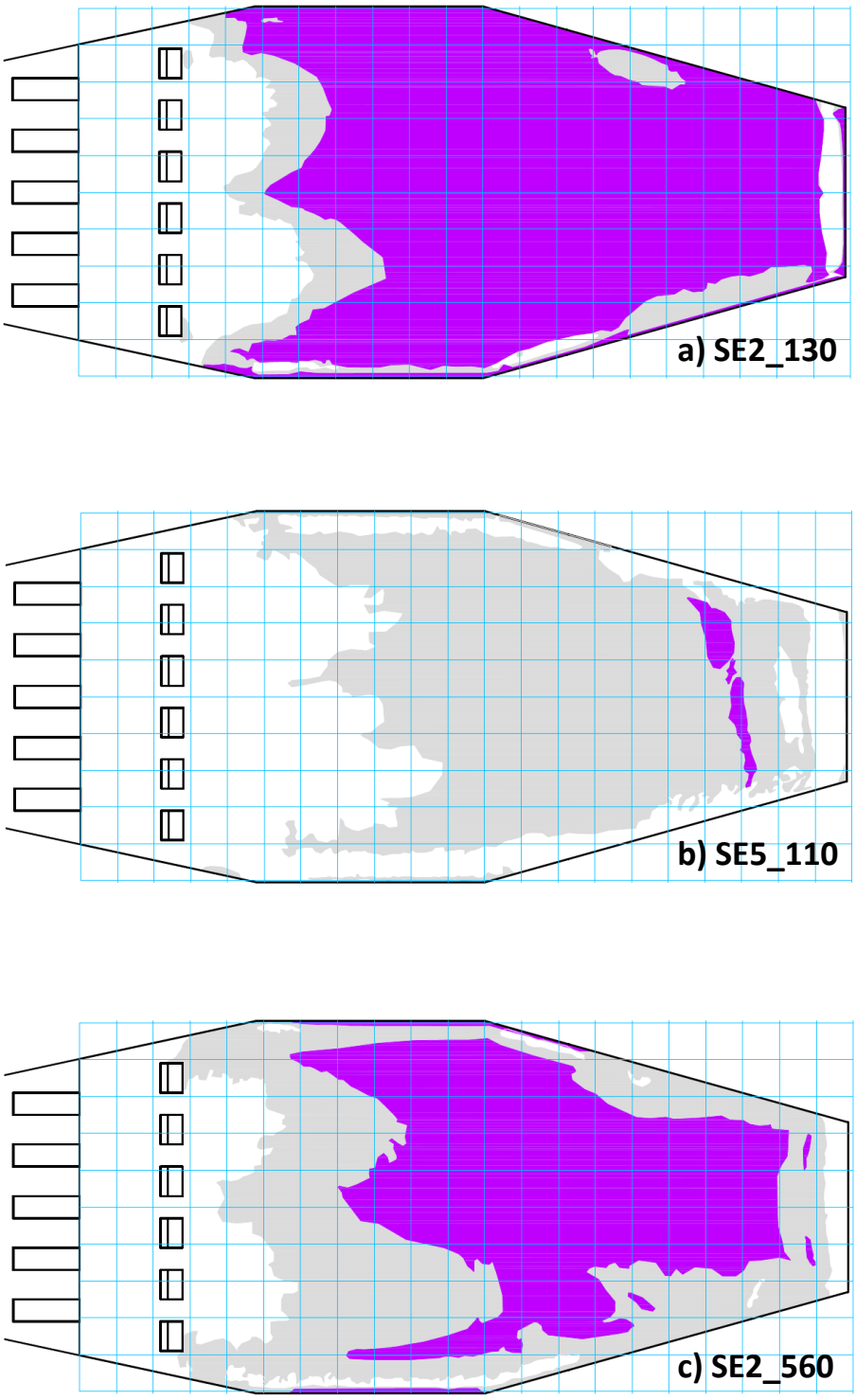

Figure 4.23. Superposition of depositions maps at the end of stage 1 (grey) and stage 2 (purple) for (a) SE2_130, (b) SE5_110 and (c) SE2_560 tests.

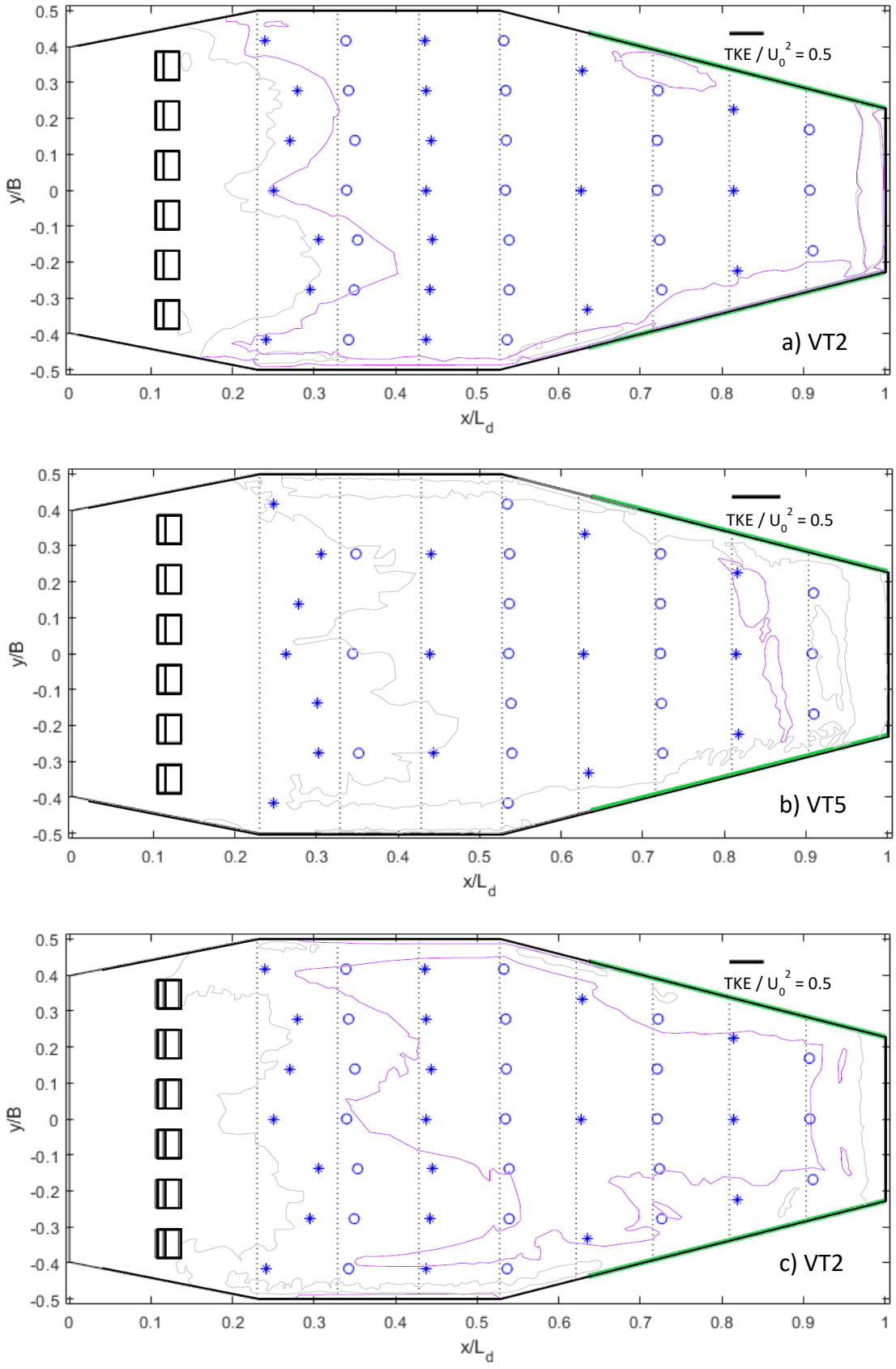

Figure 4.24. Superposition of deposition maps from Figure 4.23 (grey and violet curves) and TKE values (blue dots and asterisks) from (a) VT2, (b) VT5 and (c) VT2 tests, at depths z/H_0 = 0.125, 0.111 and 0.125 respectively, from Figure 4.10.

4.1.2.5. Assessment of particles segregation

As indicated in section 4.1.1, five different samples were analyzed for each of the SE tests in order to determine if there is a separation of the particle sizes at the DSM-flux:

- Sample Edsm – Material entering the DSM-flux = ME1+ME2+MR2
- Sample TrapS1 – Material trapped at the DSM-flux during stage 1 = ME2+MR2
- Sample EvacS1 – Material evacuated from the DSM-flux at stage 1 = ME1
- Sample TrapS2 – Material trapped at the DSM-flux during stage 2 = MR2
- Sample EvacS2 – Material evacuated from the DSM-flux at stage 2 = ME2

Figure 4.25, Figure 4.26 and Figure 4.27 show the volume-based particle size distribution curves for the five samples from tests SE2_130, SE5_110 and SE2_560 respectively. Table 4.5 presents the characteristic diameters D10, D50 and D90 for each sample of each test. It is observed that differences among the curves are minimal. For all tests, granulometry curves from samples Edsm and EvacS1 are almost identical, meaning that the size distribution of particles evacuating the DSM-flux during stage 1 is the same as the distribution of particles entering the DSM-flux. For tests SE2_130 and SE2_560 it seems that granulometric curves TrapS1, EvacS2 and TrapS2 are almost the same, which means that there is no separation of particle sizes during stage 2 either. From these two tests it is also observed that the granulometric curves for Edsm and EvacS1 are slightly different from curves TrapS1, EvacS2 and TrapS2: sizes are slightly smaller in the Edsm and EvacS1 curves. This would mean that the finest sizes are evacuated at stage 1, the bigger sizes being trapped at the DSM-flux. This pattern is not observed for a higher flow discharge (SE5_110), where all distributions seem almost the same. This would mean that under higher flow conditions, this slight separation doesn't occur. As these differences are very small, it is concluded from these results that there is no significant effect of particle sizes separation in the DSM-flux.

Table 4.5. Characteristic diameters from granulometric curves of Figure 4.25, Figure 4.26 and Figure 4.27.

	SE2_130			SE5_110			SE2_560		
	D10 (µm)	D50 (µm)	D90 (µm)	D10 (µm)	D50 (µm)	D90 (µm)	D10 (µm)	D50 (µm)	D90 (µm)
Entering DSM-flux (Edsm)	145	226	350	154	228	338	176	250	356
Trapped stage 1 (TrapS1)	159	235	349	165	236	339	189	261	358
Evacuated stage 1 (EvacS1)	142	220	339	155	228	333	174	247	351
Trapped stage 2 (TrapS2)	157	234	348	149	228	-	197	271	372
Evacuated stage 2 (EvacS2)	162	242	359	157	233	344	189	261	361

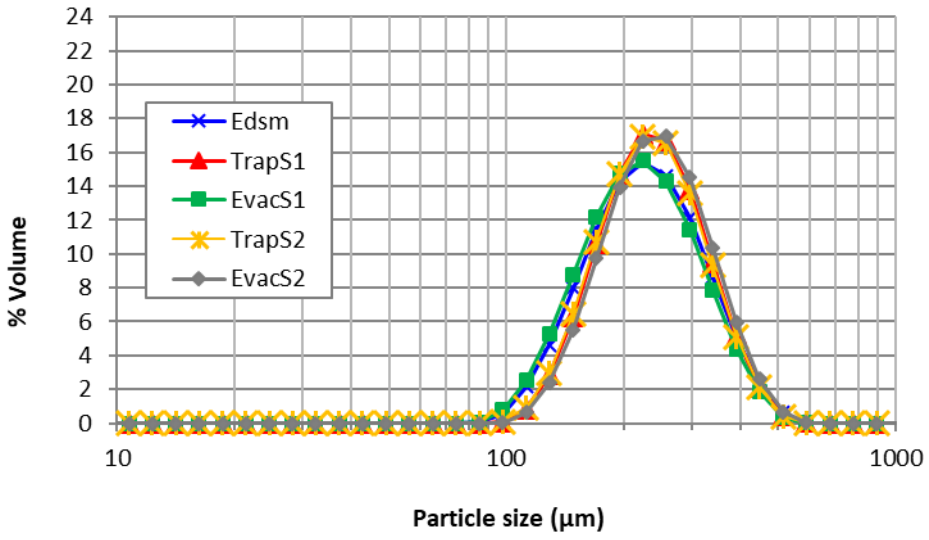

Figure 4.25. Particle size distribution of samples from test SE2_130.

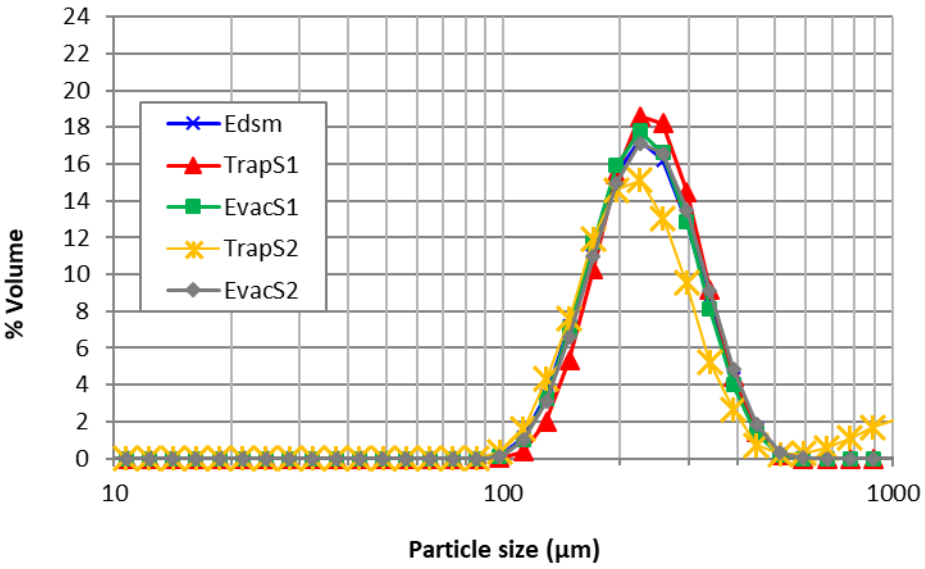

Figure 4.26. Particle size distribution of samples from test SE5_110.

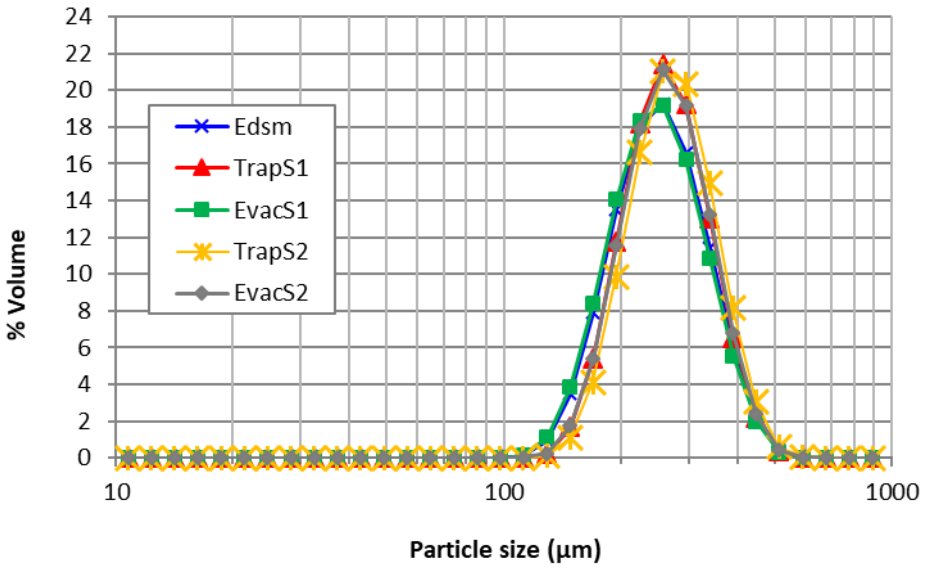

Figure 4.27. Particle size distribution of samples from test SE2_560.

4.1.3. Conclusions of Section 4.1

The main insights from this section are:

- The mean flow in the device is mainly 1D in the stabilization area, once influence of the hydraulic jump decreases, and 2D further downstream with a flow directed away from the centre axis towards the weir crests, especially in the near-surface area.
- A very slow flow region is observed for the lower discharge on both sides of the device.
- Two large-scale eddies are observed in the cross-section planes of the stabilization area, clockwise at the right side and anticlockwise at the left side.
- TKE is highly influenced by the hydraulic jump upstream and becomes quite homogeneously distributed further downstream. The patterns of deposition are thus expected to take place in the whole region except near the high TKE regions in the most upstream measured section (x/L_d=0.23 and $y/B=\pm0.25$).
- Flow and TKE patterns are considered symmetric, which might lead to a better distribution of the flow and suspended particles.
- The concentration of particles for a given flow does not seem to influence much the device retention efficiency. However, the magnitude of the flow rate does have an important influence: the higher the flow rate, the less deposition and more erosion.
- For the low flow conditions, the percentage of particles trapped by the DSM-flux is around 50% and it is reduced by half for a flow rate only slightly higher. It is thus possible that the DSM-flux is only able to retain the fine particulate pollutants (D50 between 100 and 300 µm) if the flow rates are relatively low.
- It seems that the erosion mass load is constant for a given water discharge even with different available deposited sediment loads. This unexpected result could be explained by the fact that only mass loads of the sediments were measured, and not the reliefs or evolution of the sediments volume. The material entrained but not overflowed is not considered in the erosion rate computation, the way it is computed in this PhD work, and this could explain the difference with other studies in the literature. If it is confirmed that part of the sediments previously deposited can be entrained but remain in the device, it would be a positive result for the retention function of the device.
- Some correlations are observed between hydrodynamic variables and deposition/erosion phenomena:
  - Deposition areas fairly correspond with the relatively low near-bottom TKE values regions.

  - Erosion starts mainly in the bands next to the side walls and in both eroded areas with parabolic shape downstream from the dissipation zone. These two areas extend downstream with time creating small riddles (under the lower flow conditions) or entraining the material settled downstream (higher flow conditions).

- For the lower flow conditions, almost all the sediment is remains in the device when a subsequent event with no pollutant charge impacts the sediments previously deposited. However, for a slightly higher flow rate, almost all the sediments are entrained. This indicates that after a rain event where deposition occurs, the DSM-flux should be cleaned out because a subsequent event could wash off all the sediments. The maintenance frequency must be addressed in the future. Another option would be to install a sediment trap at the bottom of the device covered with a grid of a specific opening so that it doesn't influence the flows dynamics, but it lets the particles enter the trap.
- Particle separation is not significant at the DSM-flux, at least for the fine range between 100 and 300 µm.

4.2. NUMERICAL ASSESSMENT OF THE HYDRODYNAMICS AT A LARGER SCALE

The DSM-flux hydrodynamics were assessed on the small-scale physical model for the range of hydraulic conditions allowed by the experimental set-up. Thanks to the tests carried out with glass beads (SE tests), some potential relationships between hydrodynamic variables and deposition/entrainment mechanisms were identified. On the other hand, the SE tests allowed to have an idea of the retention capabilities of the DSM-flux, but only for a few simple configurations.

As already introduced in Section 3.2, the DSM-flux will probably operate at overflow channels larger than the inflow pipe of the small-scale physical model used in this PhD work and, accordingly, the prototype device will usually have larger dimensions than the experimental device. As it was done in Section 3.2 for the monitoring methodology, in this Section 4.2 the hydrodynamics of the DSM-flux at small- and large-scale are assessed numerically by means of CFD simulations. The results of these simulations will firstly allow to assess the numerical options (flow equations, turbulence models, near-wall treatment, discretization schemes, etc) selected for the model by comparing numerical results with the experimental results at small-scale; and then, the scaling of the model will allow to study the hydrodynamics at a larger-scale and the possible scale effects that might appear. Subsequent simulations with particles once the hydrodynamics have been validated will also allow to forecast the retention efficiency of the device for different rain/concentration scenarios. Results related to CFD simulations of particles motion at large scale are not presented in this manuscript. However, the overall methodology and results of the hydrodynamics assessment are presented in the following subsections.

4.2.1. Materials and methods for the assessment of the hydrodynamics at a larger scale

To assess numerically the hydrodynamics of the DSM-flux at different scales and the possible scale effects on the flow, it is crucial to implement a numerical model that represents as best as possible the real physics. For that purpose, in Section 3.2 three different small-scale numerical models, described in detail in Section 2.1.2, were tested under similar conditions as the HQR tests and the results were compared to the experimental data. Results from Section 3.2.2 showed that for the three models the experimental HQR was well reproduced, suggesting that this relationship (and in particular the resolution of the free surface at the

downstream area) is not significantly sensitive to the different numerical options implemented in the models.

In this section, a similar methodology was followed to compare the experimental and numerical hydrodynamic data in order to identify the numerical options that better reproduces the physics of the DSM-flux flow. The three small-scale models implemented (Table 2.1) and simulated in Section 3.2 are the ones used in this part of the study. It is reminded that models SM-A and SM-B have the same numerical options except for the near-wall treatment. Also, to be able to apply the Enhanced-Wall Treatment (EWT) the mesh of SM-B was refined, so the size (and shape) of the computational mesh also differ. These two models will allow to study the effect of both, near-wall treatment and mesh size on the simulated flow. SM-C is identical to SM-B except for the mesh size (and quality), which is finer than for SM-B. Comparison between these two models will allow to study exclusively the effect of the mesh size on the results. As for the HQR validation, no calibration of equation parameters or unknown input values was performed.

Figure 4.28 presents a flowchart with the methodology initially planned (black and red lines) and finally followed (black lines) for this part of the study. As will be observed in the following sections, the three small-scale numerical models initially considered weren't able to reproduce accurately enough the velocity fields and turbulent quantities measured in the physical model. Further numerical options could not be tested within the time of this PhD work, so the model could not be validated. However, some flow patterns were quite well reproduced, and some useful insights issued from the analysis. As further investigation is needed to better reproduce the real physics of the flow, the subsequent steps described in Figure 4.28 (highlighted in red) concerning the scaling of the selected numerical model and the assessment of the hydrodynamics at a larger-scale model, were not carried out. Only an analysis of the hydrodynamics of the large-scale models tested in Sections 3.2.3 and 3.2.4 (and described in detail in Section 2.2.1) was performed as a preliminary test to determine the design of the field prototype and is presented in the following sections. The results issued from these analyses are considered only in relative terms (comparison among them) and being aware that a validation will be needed in the future. Furthermore, no simulation was done with solid matter as initially planned (red lines) because, for results to be reliable, the flow field must be validated. Thus, no direct assessment of the retention capabilities at the large-scale numerical model could be carried out in this PhD work.

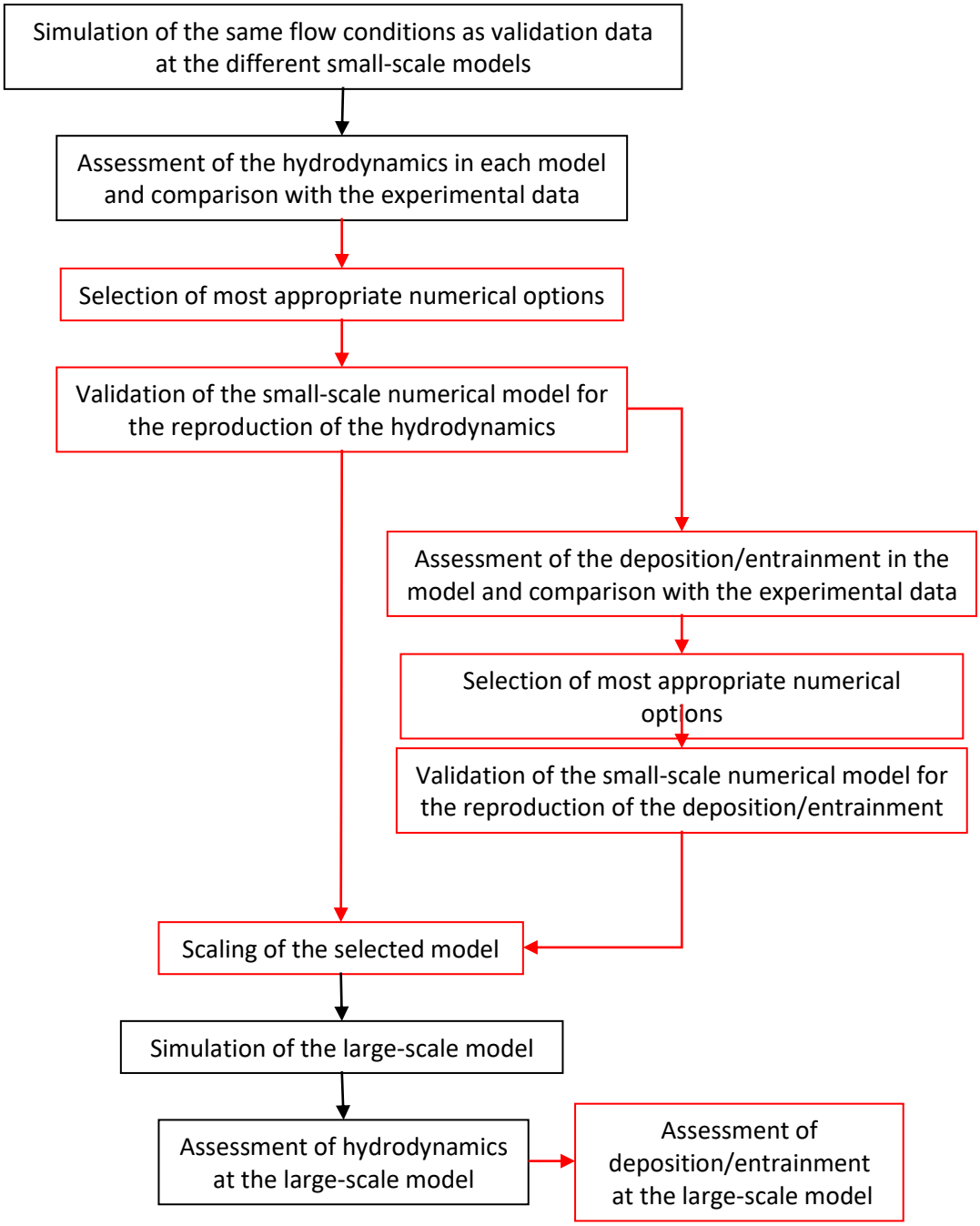

Figure 4.28. Methodology to assess the hydrodynamics and retention capabilities at large-scale. Parts in red could not be performed within the time of this PhD work.

Simulations for the assessment of the DSM-flux hydrodynamics at different scales

To determine which of the three numerical models considered in this study reproduces better the real hydrodynamics of the DSM-flux, simulations were performed under the two extreme flow rates tested on the small-scale physical model for the VT tests (Table 4.1): for 0.002 and

0.009 m^3/s. The characteristics of the simulations were already presented in Section 3.2.1. (Table 3.3), as well as the convergence criteria.

Similar to the averaging of the water levels and flow rates values presented in Section 3.2.1, simulated data for the velocity fields and turbulent quantities was recorded every 50 iterations for an interval between 50000 and 60000 iterations after convergence. The recording frequency was determined by the number of required samples, which was selected according to the capacity of the computer memory, and by the interval length, which was determined based on the residuals oscillation, which are recorded for each iteration. Velocity residuals seemed to vary pseudo-periodically within a certain range and it was decided to cover at least six pseudo-periods to be able to have a good representation of the range of variation. However, as it was not obvious to determine the variation period of the solution, the convergence of the cumulated mean was monitored in order to check if the interval and/or number of samples was enough to obtain the real mean values. All numerical data presented in Section 4.2.2 correspond to these averaged values. An analysis of their variability (standard deviation) and the averaged variables convergence is presented in Appendix 7.3.9.

4.2.2. Comparison of the small-scale numerical model hydrodynamics with the VT tests data

Similar to the figures in Section 4.1.1.2, Figure 4.29, Figure 4.30, Figure 4.31 and Figure 4.32 present the <uv> velocity fields for the two sampling depths specified in Figure 4.1: the near-bottom (Figure 4.29 and Figure 4.31) and the near-surface (Figure 4.30 and Figure 4.32) regions, for the lower (Figure 4.29 and Figure 4.30) and the higher (Figure 4.31 and Figure 4.32) flow rates. For each figure, (a) corresponds to the experimental data (already presented in the corresponding Figure 4.7 and Figure 4.8), and (b) and (c) correspond to the numerical data from SM-A and SM-B models, respectively. As it will be observed in next section, models SM-B and SM-C present similar solutions so model SM-C is not included in the figures for simplification. Data have been normalized by the bulk velocity U_0 at the stabilization zone estimated as the discharge of the device divided by the cross-section with the water depth H_0 obtained experimentally. The vertical component of these velocity fields is not considered in this comparison because it is relatively less significant, as observed from the experimental data presented in Section 4.1.1.2.

Under the lower flow conditions (Figure 4.29 and Figure 4.30), none of the numerical models is able to properly reproduce the experimental velocity fields. In general, numerical <uv> velocities are considerably higher than the experimental values, especially in model SM-A and in the near-surface region for both models (it should be noticed that the graphical scales can differ between experimental and numerical data). On the near-bottom region, (Figure 4.29), model SM-A presents two recirculation areas covering both laterals of the stabilization zone that are not observed in the experimental velocity field. The main flow enters the stabilization area from the centre and then is divided in two streams that form a clockwise recirculation at the right side of the device and an anticlockwise recirculation at the left side. In model SM-B there are also two recirculation areas but, in this case, they are located in the centre of the device. The main flow is divided in two streams when entering the stabilizations area that follow the laterals of the stabilization area, directing the flow upstream at the symmetry axis of the device. Velocities in the laterals of the device are relatively high compared to the centre, which is opposite to what is observed with the experimental data. In both numerical models, differences in magnitude between velocities at the stabilization area and velocities at the overflow area are significantly greater than at the physical model, where they seem more homogeneous (at least within the central part of the device). Also, in both numerical models, velocity vectors at the cross-section next to the end wall are directed towards upstream (indicating counter-current flow), which is not observed in the experimental data. In the near-surface region (Figure 4.30), model SM-A still presents two recirculation areas covering both lateral ends of the stabilization zone contrary to the experimental field, although these areas are narrower at this sampling depth. Model SM-B reproduces better the experimental results although velocities at the lateral ends of the stabilization zone are higher than velocities at the symmetry axis of the device, which is not the case in the experimental results. In both models, the main flow downstream the hydraulic jump is less aligned with the X-axis than in the experimental data. Despite the mismatch with the experimental data, both numerical results present a symmetric flow.

Under the higher flow conditions (Figure 4.31 and Figure 4.32), flow patterns are well reproduced by none of the models. In the near-bottom region, (Figure 4.31), model SM-A contains again two recirculation areas covering both lateral ends of the stabilization zone that are not observed with the experimental data. This confines the two main streams in the centre of the device whereas in the experimental data the two main streams are observed closer to the lateral walls. The general flow pattern in Model SM-B is similar to that of model SM-A, except that velocities in SM-B data are lower at the lateral recirculation areas and higher at the

symmetry axis of the device. Differences in velocities magnitudes between the stabilization and the overflow area seem smaller than under lower flow conditions. In the near-surface region, (Figure 4.32), computed <uv> velocities are considerably higher than the experimental values. Both models present similar flow patterns: velocities near the lateral walls of the stabilization area are significantly smaller than in the rest of the device, which is not observed on the physical model, where velocities seem more homogeneously distributed. As under low flow conditions, both numerical results present a quite symmetric flow, despite a slight imbalance observed for model SM-B.

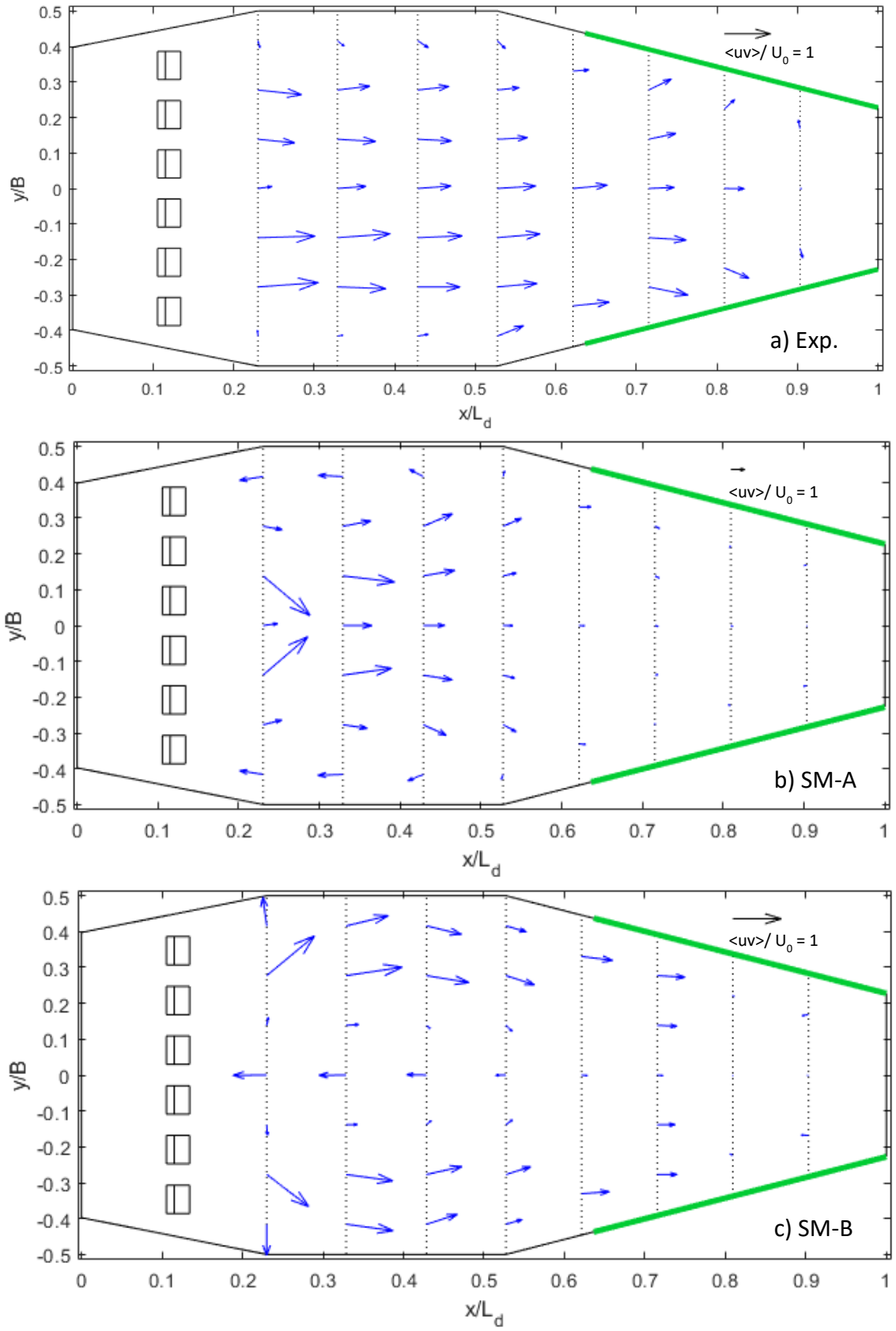

Figure 4.29. <uv> velocity fields (a) at the DSM-flux small-scale physical model for VT2 data (copy from Figure 4.7 (a)), (b) at the numerical model SM-A for Sim SM-A1 data and (c) at the numerical model SM-B for Sim SM-B1 data, in the near-bottom region ($z/H_0 = 0.125$).

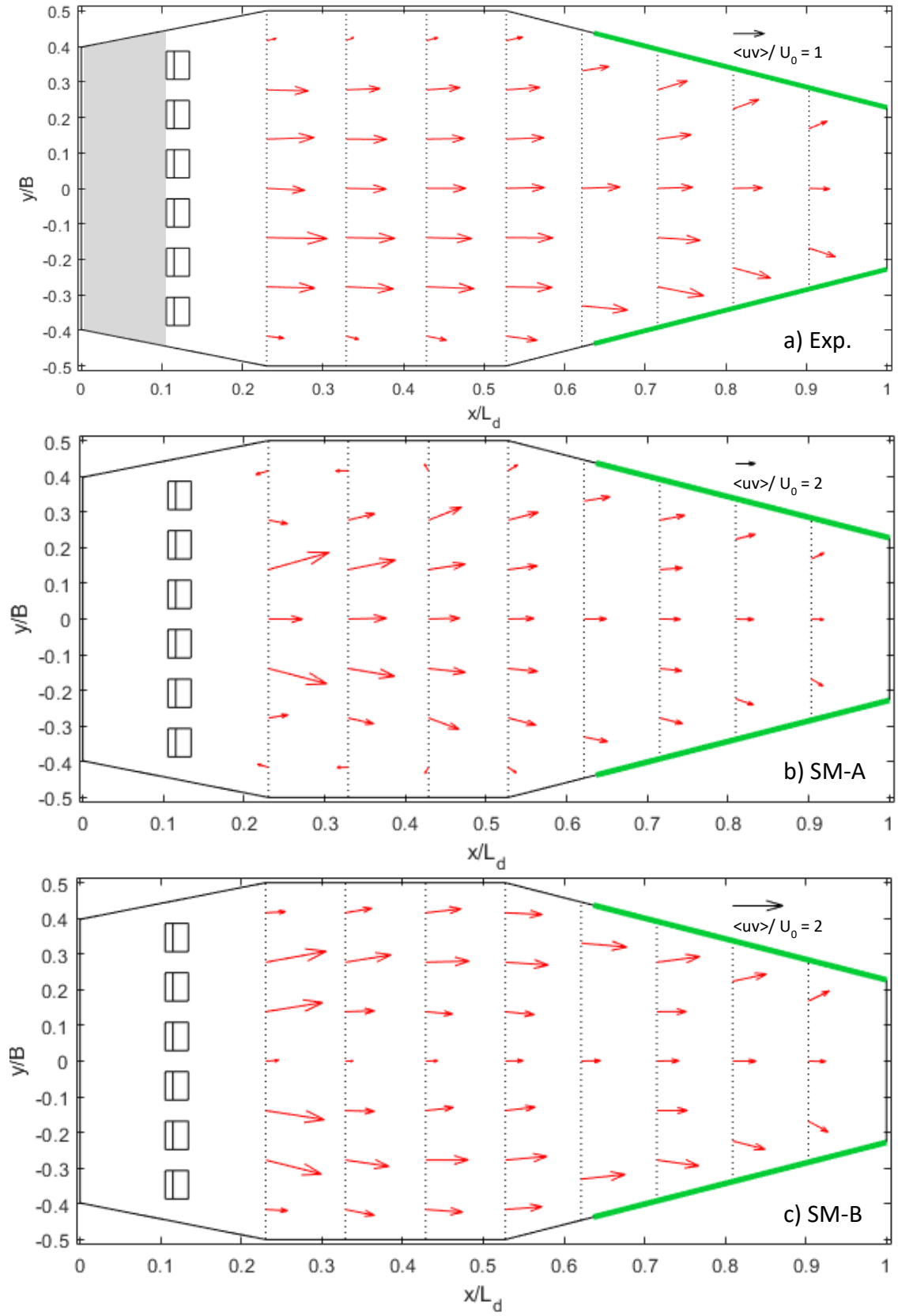

Figure 4.30. <uv> velocity fields (a) at the DSM-flux small-scale physical model for VT2 data (copy from Figure 4.8 (a), (b) at the numerical model SM-A for Sim SM-A1 data and (c) at the numerical model SM-B for Sim SM-B1 data, in the near-surface region ($z/H_0 = 0.694$).

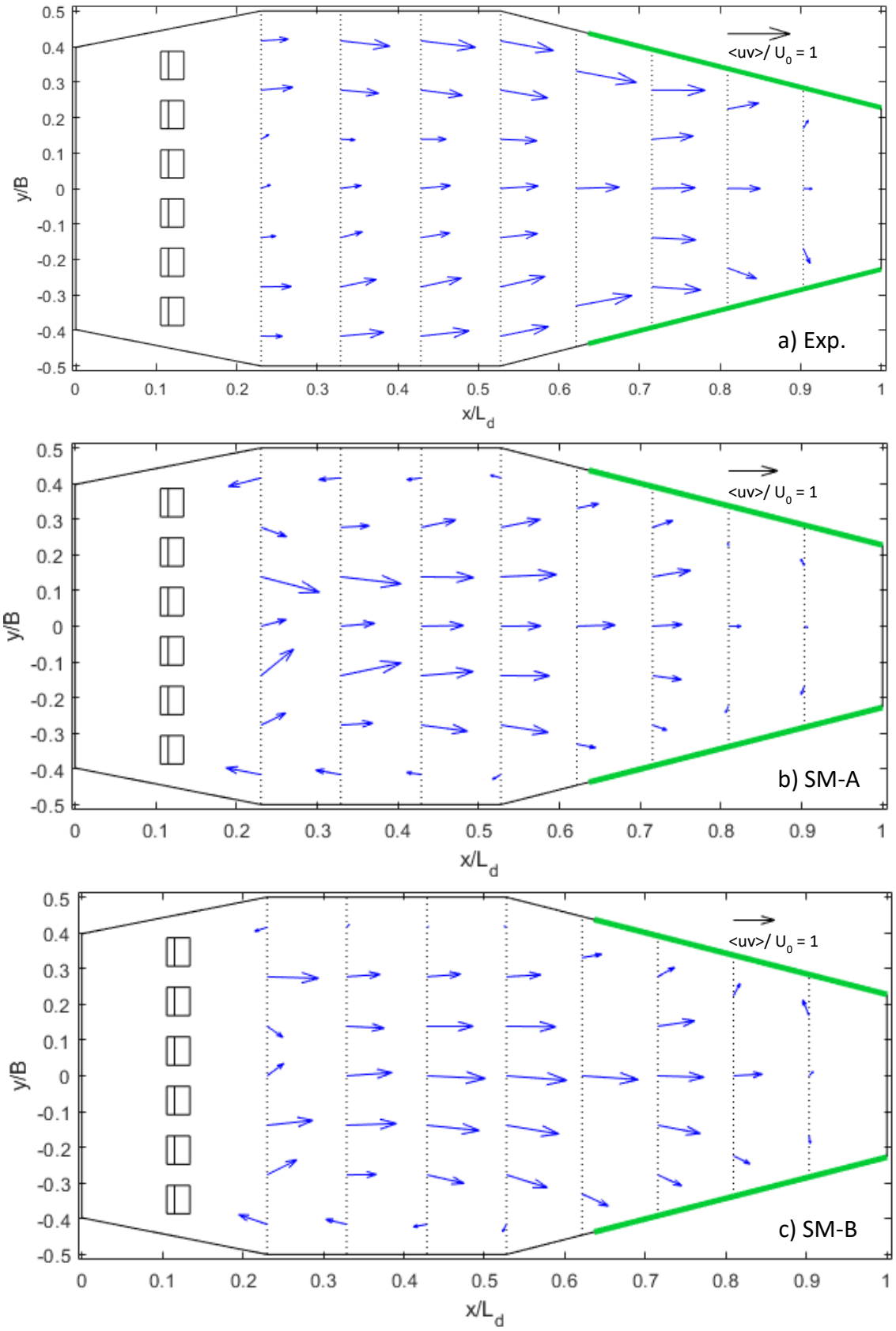

Figure 4.31. <uv> velocity fields (a) at the DSM-flux small-scale physical model for VT9 data (copy from Figure 4.7 (c), (b) at the numerical model SM-A for Sim SM-A5 data and (c) at the numerical model SM-B for Sim SM-B3 data, in the near-bottom region ($z/H_0 = 0.098$).

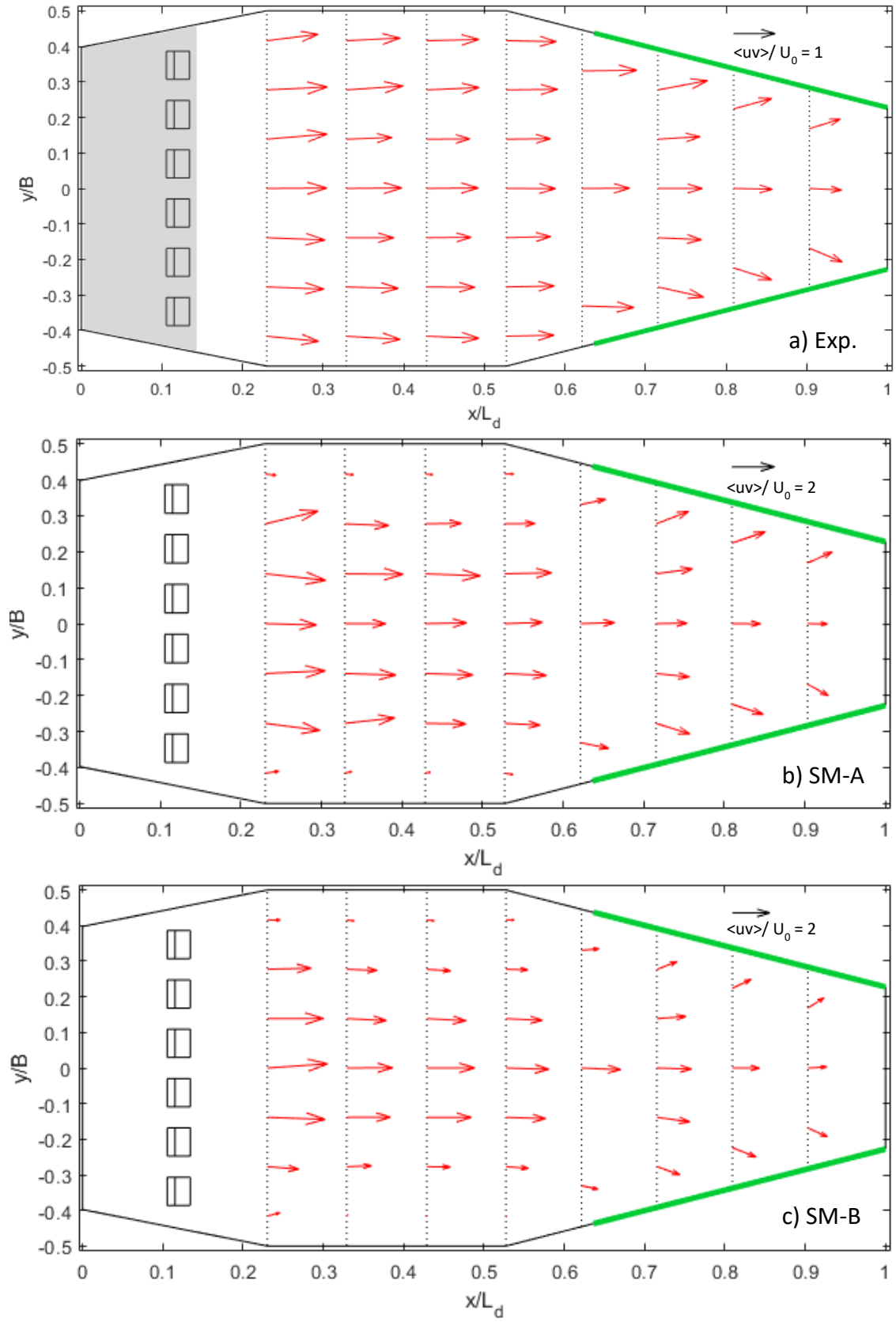

Figure 4.32. <uv> velocity fields (a) at the DSM-flux small-scale physical model for VT9 data (copy from Figure 4.8 (c), (b) at the numerical model SM-A for Sim SM-A5 data and (c) at the numerical model SM-B for Sim SM-B3 data, in the near-surface region (z/H₀ = 0.783).

TKE values have been only compared in the near-bottom region to see if the quasi-symmetric parabolic profile showing two main areas with high TKE downstream the dissipation zone, at both sides of the symmetry axis of the device, is reproduced by the models. Figure 4.33 and Figure 4.34 present the normalized TKE values for the lower and higher flow conditions, respectively. It is observed that both models fairly reproduce the characteristic double-parabola pattern at section $0.23L_d$. Indeed, Figure 4.35 and Figure 4.36 present the deposition areas issued from stages 1 (grey) and 2 (violet) of tests SE2_130 and SE2_560, respectively superposed with the TKE values presented in Figure 4.33 for the lower flow conditions. TKE values under lower flow conditions are significantly higher in model SM-A compared to the experimental and SM-B data. This difference is not noticeable under higher flow conditions. However, in this case, the position of the two parabolas in the numerical models is closer to the centre than in the experimental results. This is coherent with the flow patterns observed in Figure 4.31.

For a more quantitative estimation, normalized RMSE (Equation 4.8) values have been computed for each velocity component and TKE values and for each model, in order to quantify the errors in the modelling of the velocity fields and turbulence.

$$Normalized\ RMSE = \frac{\sqrt{\frac{1}{n}\sum_{i=1}^{n}\left(X_{i-num} - X_{i-exp}\right)^2}}{U_0} \qquad \textit{Equation 4.8}$$

In Equation 4.8, $X_{i\text{-}num}$ is the numerical variable, $X_{i\text{-}exp}$ the experimental variable and U_0 is the bulk velocity at the stabilization area obtained from experimental data. For the TKE, the normalization uses U_0^2 instead of U_0. Similarly to Section 3.3, errors relative to the local values can be extremely high (specially for <v> and <w> velocities) and indicators such as the MARE give extremely high global values which, in some cases, are not representative of the level of global correlation between numerical and experimental data. The normalization of the RMSE then conducts to a reference for comparison with other cases. Normalized RMSE has been computed by section and by sampling depth for each flow condition. Figure 4.37 and Figure 4.38 (resp. Figure 4.39 and Figure 4.40) present the results under lower flow conditions, for the near-bottom and near-surface regions respectively (resp. higher flow conditions).

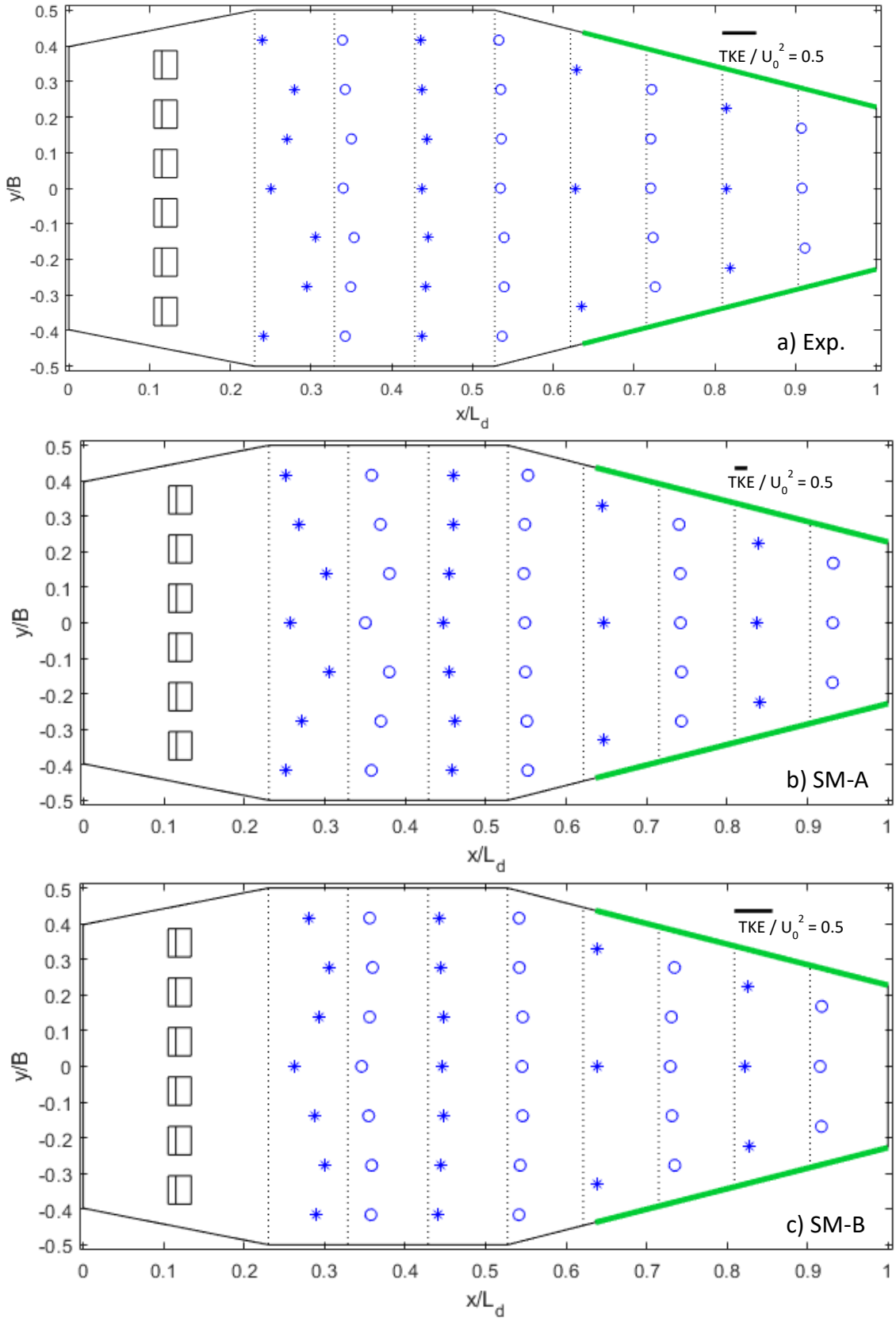

Figure 4.33. TKE values (a) at the DSM-flux small-scale physical model for VT2 data (copy from Figure 4.10 (a), (b) at the numerical model SM-A for Sim SM-A1 data and (c) at the numerical model SM-B for Sim SM-B1 data, in the near-bottom region (z/H₀ = 0.125).

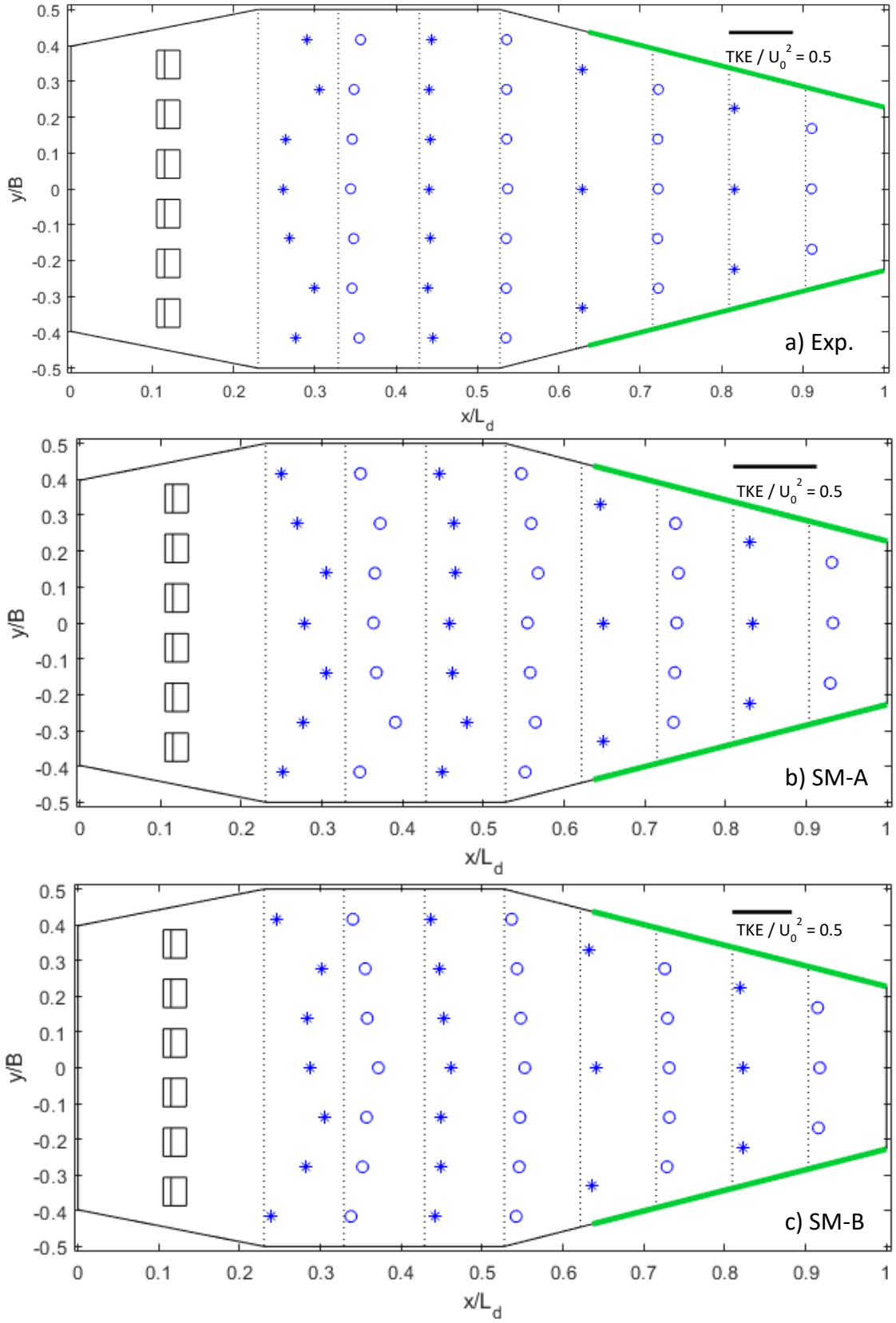

Figure 4.34. TKE values (a) at the DSM-flux small-scale physical model for VT9 data (copy from Figure 4.10 (c), (b) at the numerical model SM-A for Sim SM-A5 data and (c) at the numerical model SM-B for Sim SM-B3 data, in the near-bottom region ($z/H_0 = 0.098$).

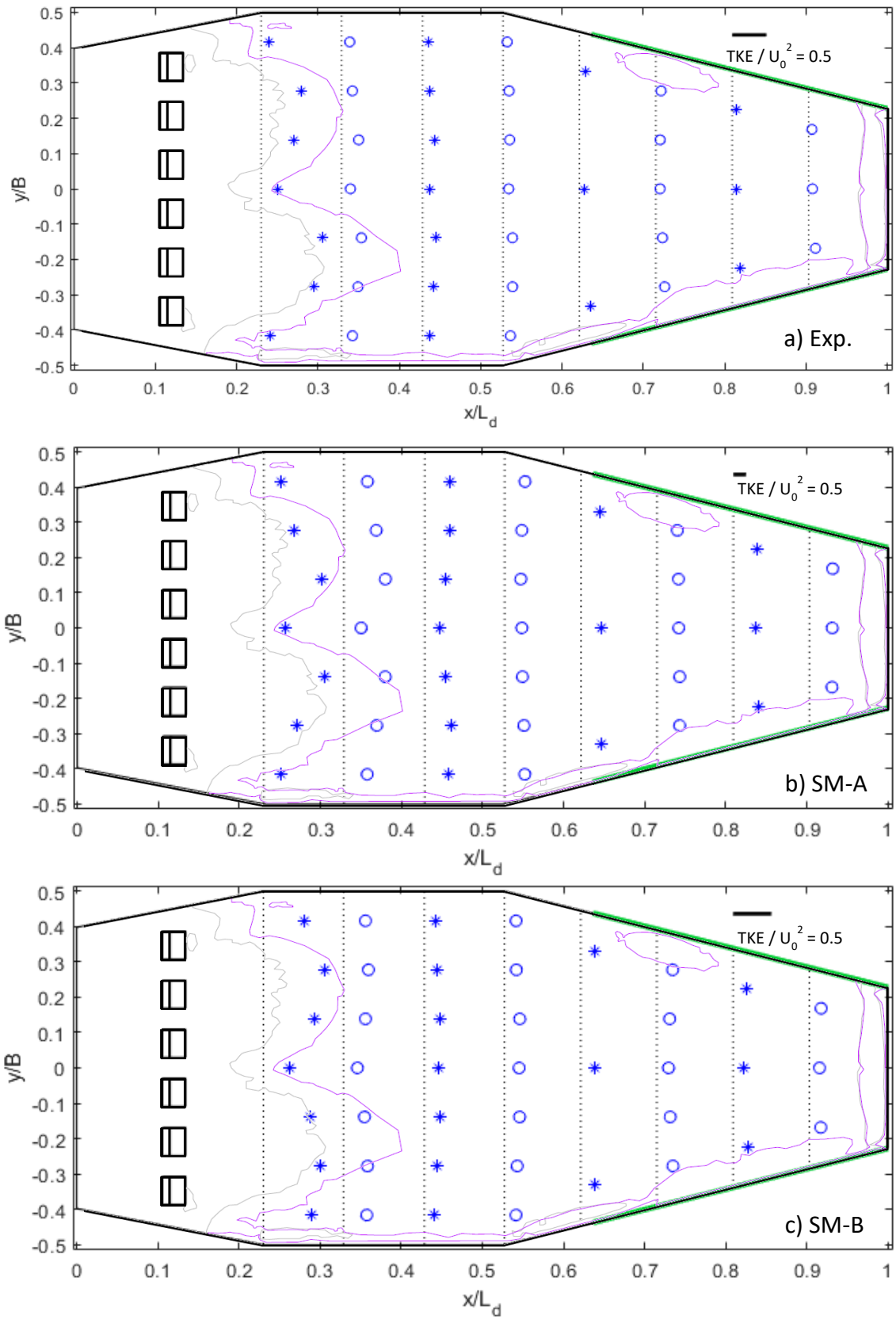

Figure 4.35. Superposition of deposition maps from test SE2_130 (Figure 4.23 (a)) and TKE values (a) at the DSM-flux small-scale physical model for VT2 data (copy from Figure 4.10 (a)), (b) at the numerical model SM-A for Sim SM-A1 data and (c) at the numerical model SM-B for Sim SM-B1 data, in the near-bottom region ($z/H_0 = 0.125$).

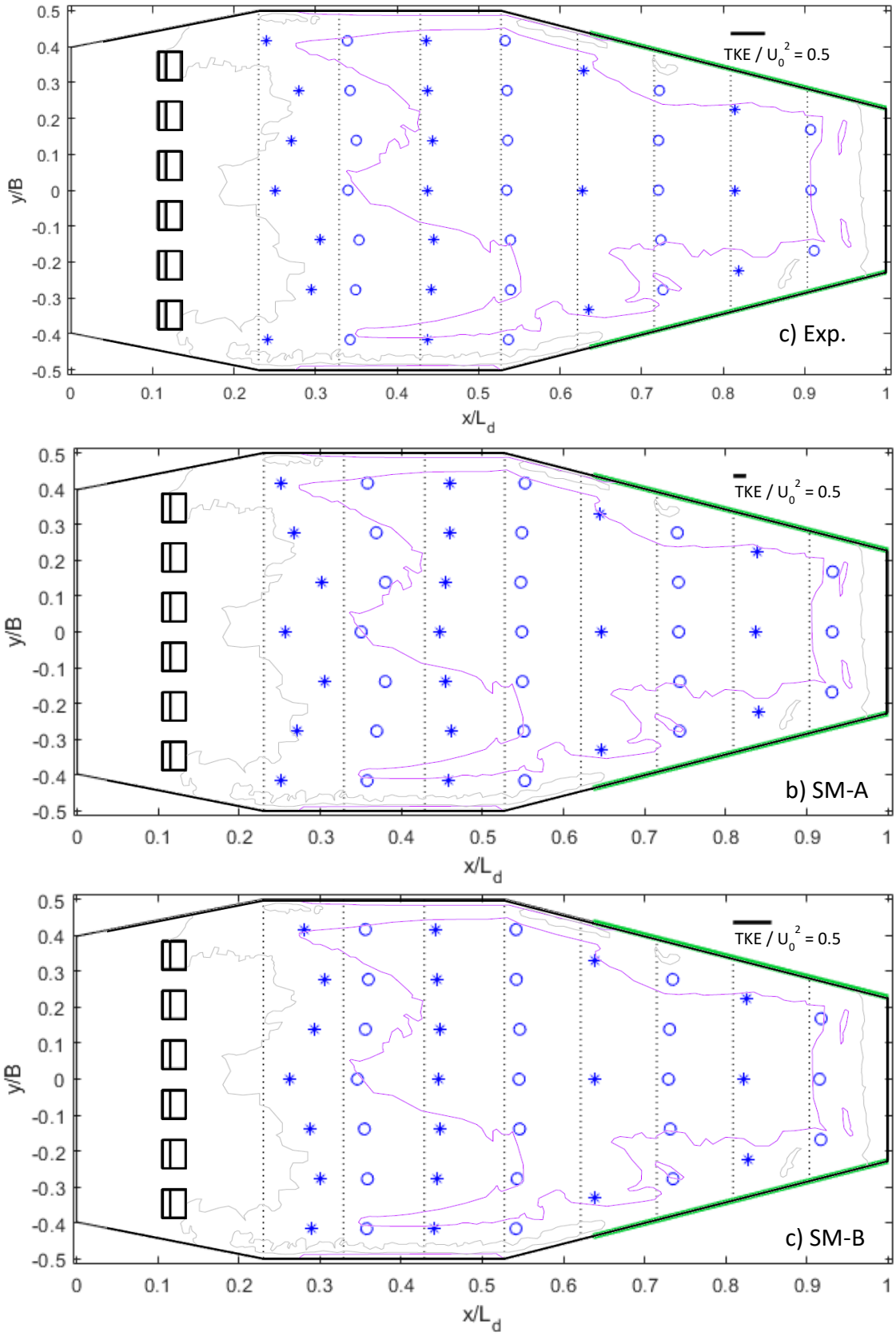

Figure 4.36. Superposition of deposition maps from test SE2_560 (Figure 4.23 (c)) and TKE values (a) at the DSM-flux small-scale physical model for VT2 data (copy from Figure 4.10 (a)), (b) at the numerical model SM-A for Sim SM-A1 data and (c) at the numerical model SM-B for Sim SM-B1 data, in the near-bottom region ($z/H_0 = 0.125$).

It is observed that, in general, normalized RMSE are higher at the section(s) immediately downstream the dissipation area. Also, normalized RMSE are relatively higher at lower flow conditions than at higher flow conditions. Global values for all points show that under higher flow conditions, normalized errors are especially high for <u> velocity, the rest of the variables having global errors lower than 35% of the bulk velocity for both models. Under lower flow conditions, this is only true for <w> velocity. Under lower flow conditions, SM-B presents lower RMSE values for both sampling depths, especially for normalized <u> and <v> velocities and TKE quantities. Under higher flow conditions, RMSE values from both models are not significantly different at any of the sampling depths.

It is not easy to globally evaluate these errors, as the criteria to validate or accept a model depends on many factors (objectives of the study, complexity of the flow, type of experimental data, measurements accuracy, etc). However, some studies are cited here to have an idea of the goodness of fit of these data in other case studies of open channel flows. For example, Momplot *et al.* (2017) compared experimental velocities measured by 2D-PIV (Particle Image Velocimetry) with results from a CFD model implemented in ANSYS-Fluent. They studied horizontal velocities at the bifurcation of an open channel operating under a subcritical regime and steady conditions. From the data presented in the paper, a normalized error has been estimated as the MAE computed by the authors for the <uv> velocity magnitude at the area of study divided by the bulk velocity at the upstream channel of the bifurcation. Normalized MAE for a relative depth of $z/H = 0.33$ is 0.4 and at $z/H = 0.75$ is 0.5. These values have been estimated for this case study in Table 4.6, with models SM-A and SM-B. We can see that for model SM-B under lower flow conditions and both models under higher flow conditions in the near-bottom region, values are comparable.

Table 4.6. Normalized MAE estimated between experimental data from VT tests and numerical data from SM-A and SM-B.

	Low flow conditions		**High flow conditions**	
	$MAE_{expSM-A}$	**$MAE_{expSM-B}$**	**$MAE_{expSM-A}$**	**$MAE_{expSM-B}$**
Near-bottom	0.9	0.4	0.4	0.4
Near-surface	1.5	0.5	0.8	0.7

Mignot *et al.* (2012) compared experimental velocities measured by ADV with results from a CFD model implemented in ANSYS-CXF. They studied 2D velocities at different depths and cross-sections at the junction of an open channel operating under a subcritical regime and steady conditions. Differences between numerical and experimental <u> velocities are given

related to the measured <u> velocity for different cross-sections upstream and downstream the junction. Despite that normalized <u> velocities from numerical and experimental data are also presented, these are given with contour graphs, which makes more difficult to estimate the normalized errors. However, from these graphs, it can be estimated that maximum normalized errors are between 0.3 and 0.6 the bulk velocity at the downstream channel.

Dufresne *et al.* (2007) compared experimental velocities and TKE quantities measured by 2D-PIV and ADV, respectively, with results from a CFD model implemented in ANSYS-Fluent. They studied 2D velocities and TKE at the cross-sections of a storm-water. The paper shows contours and vector graphs for comparison at one of the tests, but it only gives values of local errors at a few points of maximum velocity or TKE. From the data supplied in the publication, normalized errors for the maximum velocity and TKE points are estimated to 3-9 and 10, respectively.

Some other studies (Bayon *et al.*, 2016; Castillo *et al.*, 2014a; Cook *et al.*, 2002; Javan and Eghbalzadeh, 2013) have compared numerical and experimental velocity data for hydraulic jump cases. However, these comparisons are only done for a few velocity profiles and data is difficult to compare with the results of the DSM-flux models.

Regarding these results, it seems that none of the numerical combinations considered reproduces satisfactorily the experimental velocity fields and TKE values. Despite that in some cases differences seem to be equivalent to the ones from other studies in the literature (that considered to satisfactorily reproduce the experimental hydrodynamics), these values are still high. Besides, some flow patterns do not correspond qualitatively to those observed in the experimental model, like the recirculation areas.

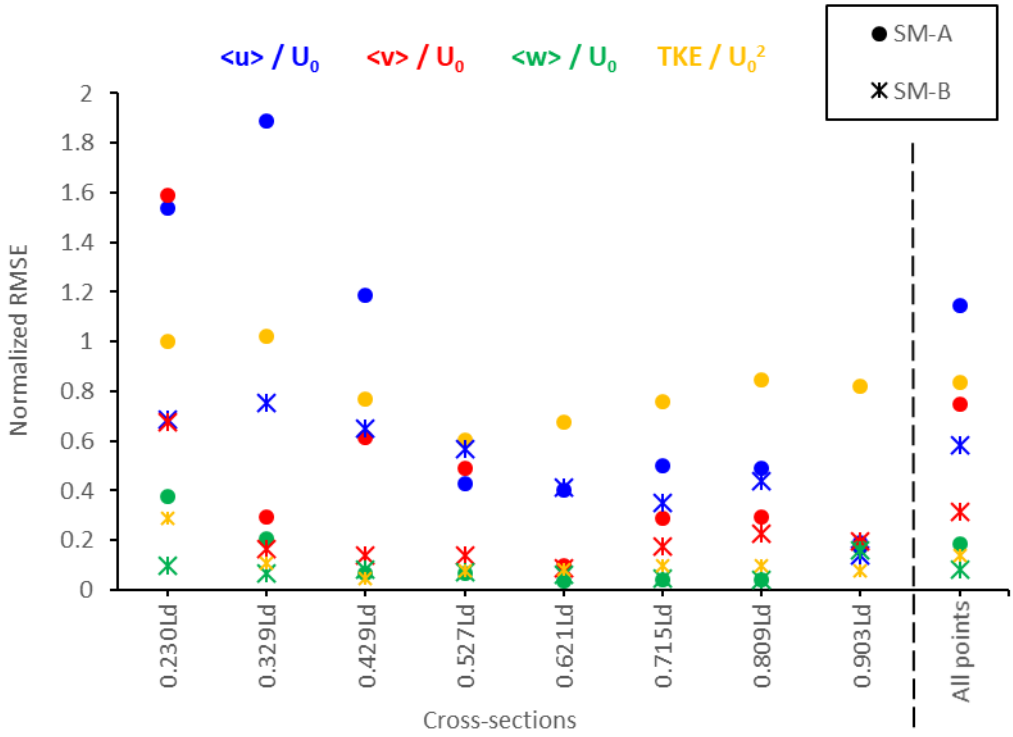

Figure 4.37. Normalized RMSE under the lower flow conditions (VT2, SM-A2, SM-B2) in the near-bottom region ($z/H_0 = 0.125$).

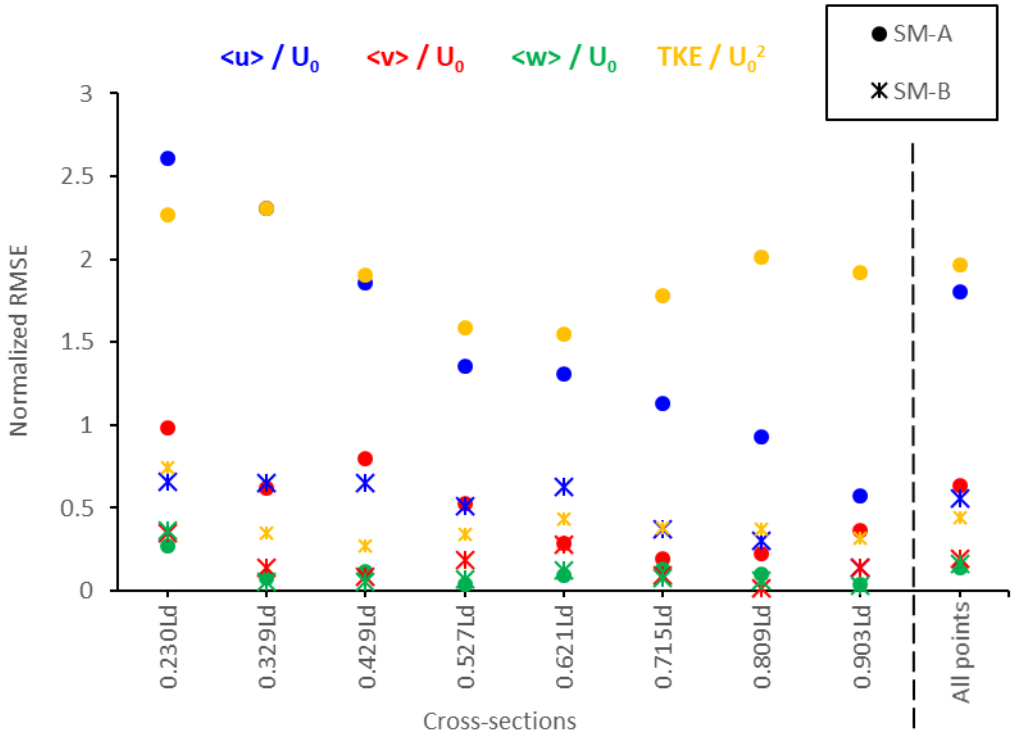

Figure 4.38. Normalized RMSE under the lower flow conditions (VT2, SM-A2, SM-B2) in the near-surface region ($z/H_0 = 0.694$).

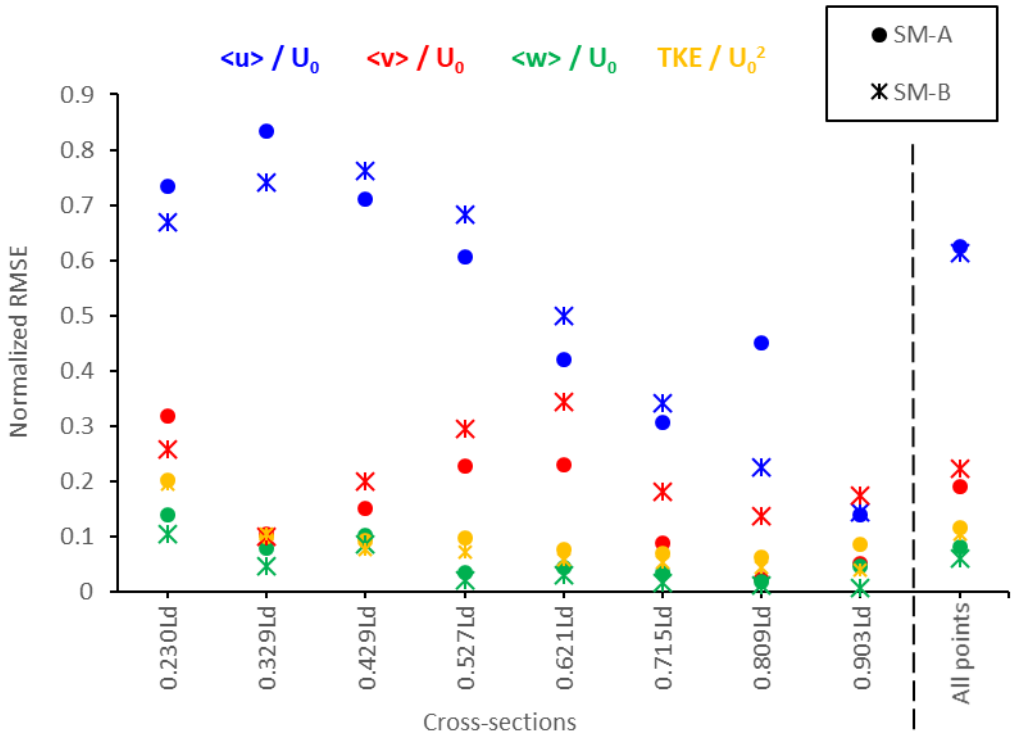

Figure 4.39. Normalized RMSE under the higher flow conditions (VT9, SM-A9, SM-B9) in the near-bottom region ($z/H_0 = 0.098$).

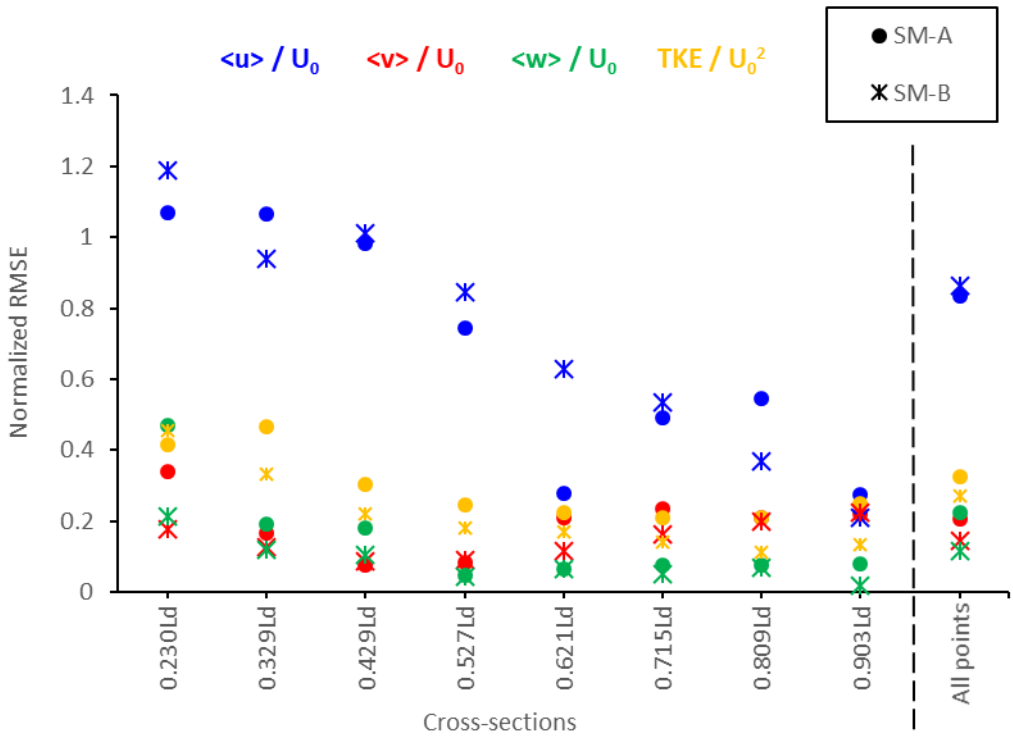

Figure 4.40. Normalized RMSE under the higher flow conditions (VT9, SM-A9, SM-B9) in the near-surface region ($z/H_0 = 0.783$).

Effects of the computational mesh on the small-scale numerical model hydrodynamics

The differences between the models SM-A and SM-B lie on the near-wall treatment (SWF for SM-A and EWT for SM-B) and the computational meshes (finer and of better quality in model SM-B). From the analysis of the previous section, it is clear that results from both models are not alike. The different near-wall treatment could influence the different results in the near-bottom region between both models under lower flow conditions. However, under higher flow conditions, these differences are not noticeable. It is thus believed that differences between both models are mainly due to the different computational meshes. This means that velocity fields and turbulence quantities would be sensitive to the size of the meshes, which was not the case for the HQR, as shown in Section 3.2.2.

In order to further analyse the sensitivity of the numerical results to the computational mesh size, and also to see if a better match with the experimental data was possible, results from models SM-B and SM-C, which are identical models except from the resolution of the mesh, were compared for the same simulation conditions.

Similar figures to the ones in the previous subsection for the flow patterns are included in the Appendices 7.3.5 and 7.3.6 (for the lower flow condition) and Appendices 7.3.7 and 7.3.8 (for the higher flow condition). In these figures, (a) corresponds to the experimental data (already presented in the corresponding Figure 4.7 and Figure 4.8), and (b) and (c) correspond to the numerical data from SM-C and SM-B, respectively.

Flow patterns from models SM-B and SM-C appear to be quite similar. The only noticeable differences under the lower flow rates are that (i) near the bottom (Appendix 7.3.5), model SM-C presents higher velocities at the symmetry axis of the device as well as near the lateral walls of the stabilization area, which diverges even more from experimental data than SM-B solution; and (ii) in the near-surface region (Appendix 7.3.6), there is a recirculation at the central part of the device at model SM-C that is not predicted by model SM-B, which makes velocities at that zone relatively lower, diverging even more from experimental data. Under higher flow rates, the only difference is that, in the near-bottom region (Appendix 7.3.8), velocities at the symmetry axis are slightly lower using the SM-C model.

As the main differences between results from models SM-B and SM-C lie on the magnitudes, a more detailed visual comparison "point by point" has been made between both models and the experimental data, for each velocity component and TKE values in Figure 4.41 and Figure 4.42, for lower flow conditions, and in Figure 4.43 and Figure 4.44 for higher flow conditions. It’s difficult to deduce common trends but, in general, it could be said that dispersion is higher

in the sections close the hydraulic jump, for all the components. TKE and <w> velocity values seem in general quite close but that's not the case for <u> velocity, which seems to present the higher discrepancies.

Normalized RMSE values have also been calculated for model SM-C to compare them to those of model SM-B. Figure 4.45 and Figure 4.46 present the results under lower flow conditions, for the near-bottom and near-surface regions respectively. Similarly, Figure 4.47 and Figure 4.48 present the results under higher flow conditions, for the near-bottom and near-surface regions respectively. The most significant differences are observed for the normalized <u> velocity component, whose RMSE is higher for the model SM-C than for the model SM-B at the lower flow conditions (but still lower than for model SM-A) and at higher flow conditions, RMSE is higher for the model SM-B than for model SM-C.

Regarding results of all these analyses, it can be concluded that, despite that the velocity fields and turbulence quantities don't match between models SM-B and SM-C, divergences are not significant, and it seems that the main patterns and overall values are close enough to think that a finer computational mesh wouldn't change significantly these results. Furthermore, it has been proved that a finer computational mesh like that of SM-C doesn't reproduce a velocity field and turbulence quantities closer to the experimental data.

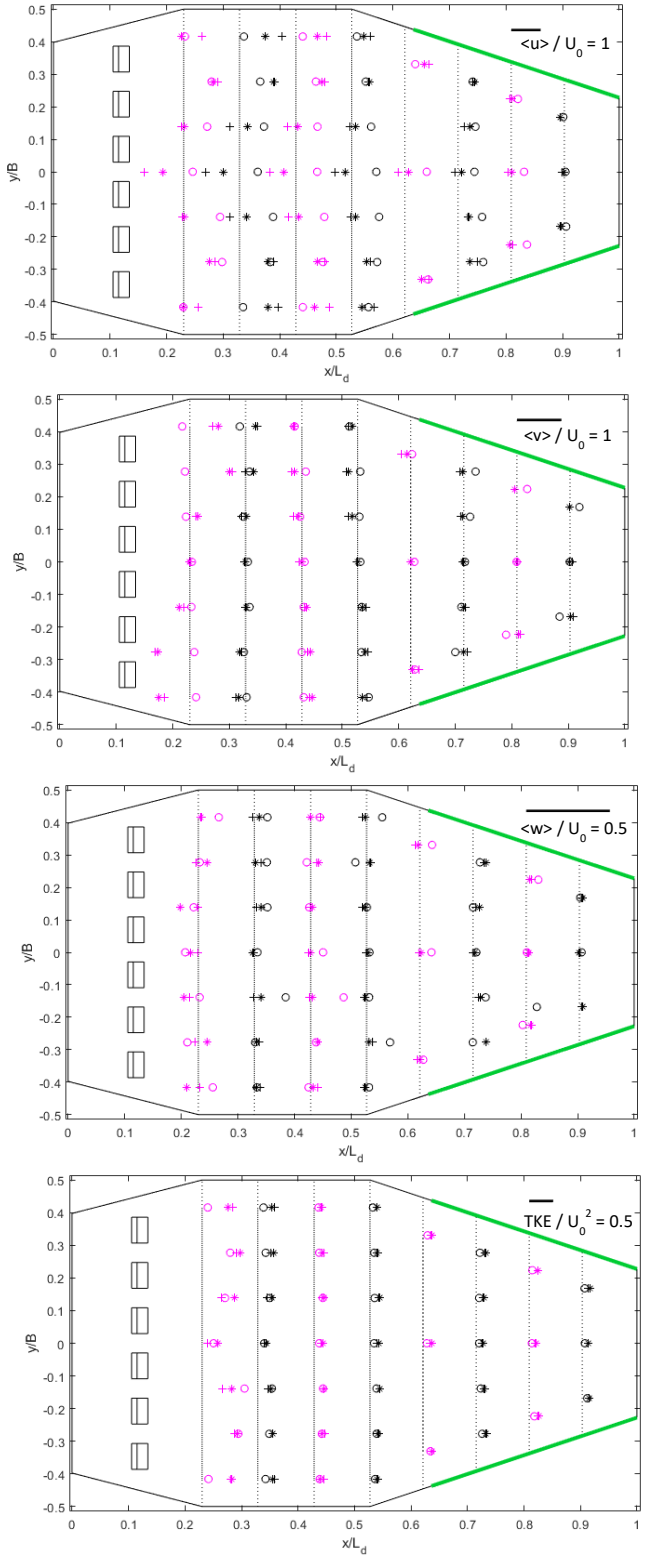

Figure 4.41. Normalized <u>, <v>, <w> and TKE at the DSM-flux small-scale physical model for VT2 data in dots (presented in Figure 4.7 (a)), at the numerical model SM-C for Sim SM-C1 data in asterisks and at the numerical model SM-B for Sim SM-B1 data in crosses, all in the near-bottom region ($z/H_0 = 0.125$). Two different colours are used to distinguish data from two consecutive sections.

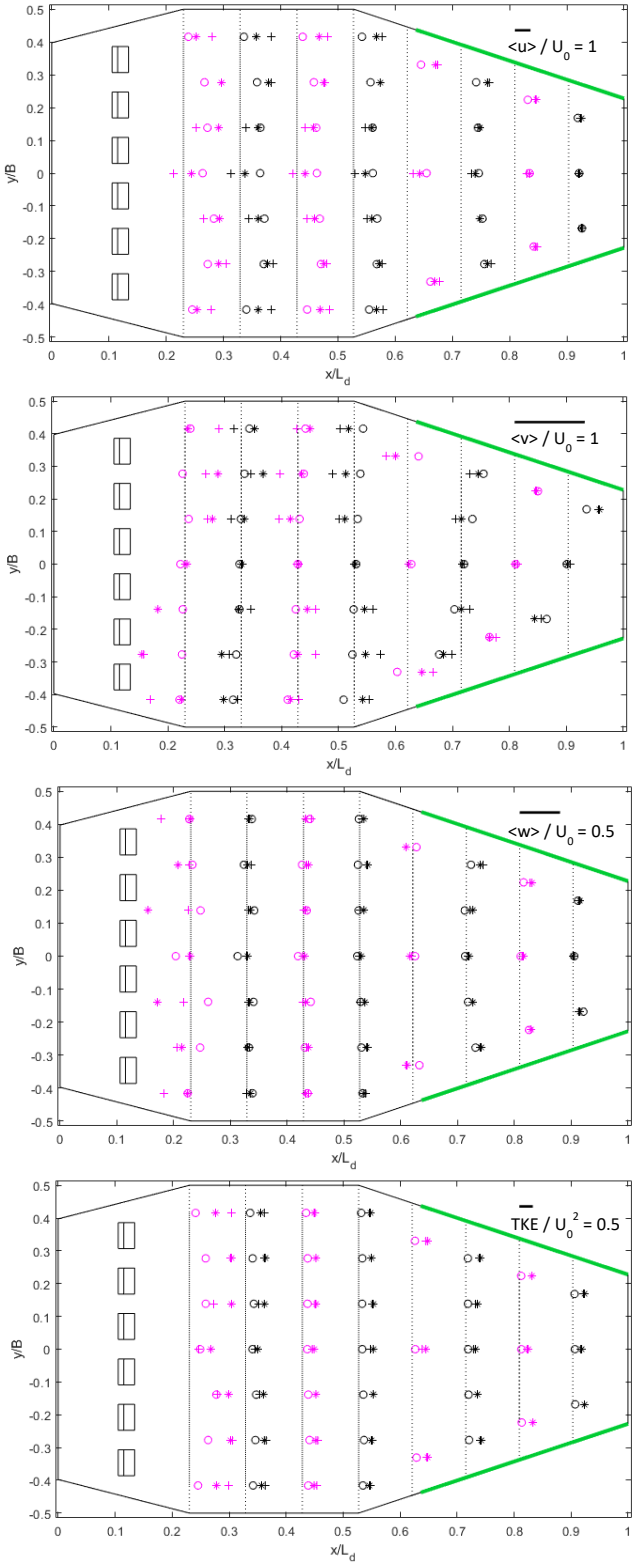

Figure 4.42. Normalized <u>, <v>, <w> and TKE at the DSM-flux small-scale physical model for VT2 data in dots (presented in Figure 4.8 (a)), at the numerical model SM-C for Sim SM-C1 data in asterisks and at the numerical model SM-B for Sim SM-B1 data in crosses, all in the near-surface region ($z/H_0 = 0.694$). Two different colours are used to distinguish data from two consecutive sections.

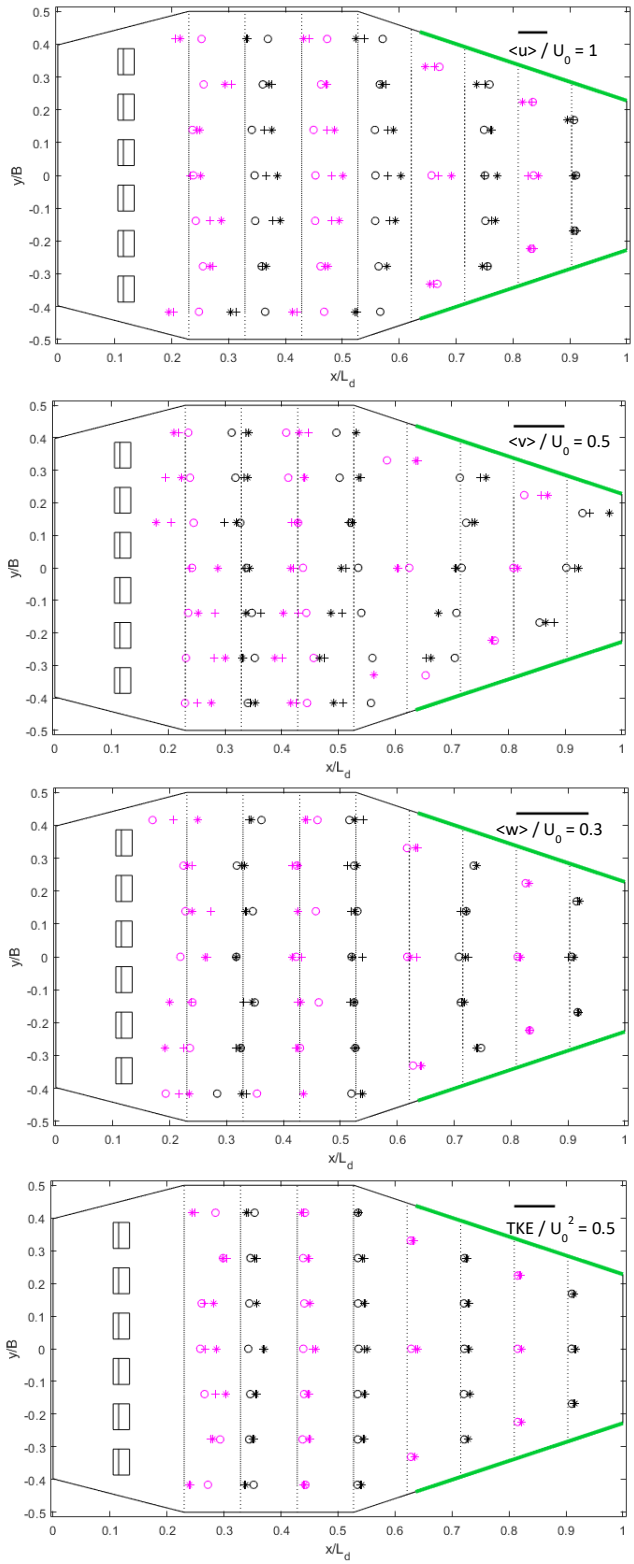

Figure 4.43. Normalized <u>, <v>, <w> and TKE at the DSM-flux small-scale physical model for VT9 data in dots (presented in Figure 4.7 (c), at the numerical model SM-C for Sim SM-C2 data in asterisks and at the numerical model SM-B for Sim SM-B3 data in crosses, all **in the near-bottom region ($z/H_0 = 0.098$).** ***Two different colours are used to distinguish data from two consecutive sections.***

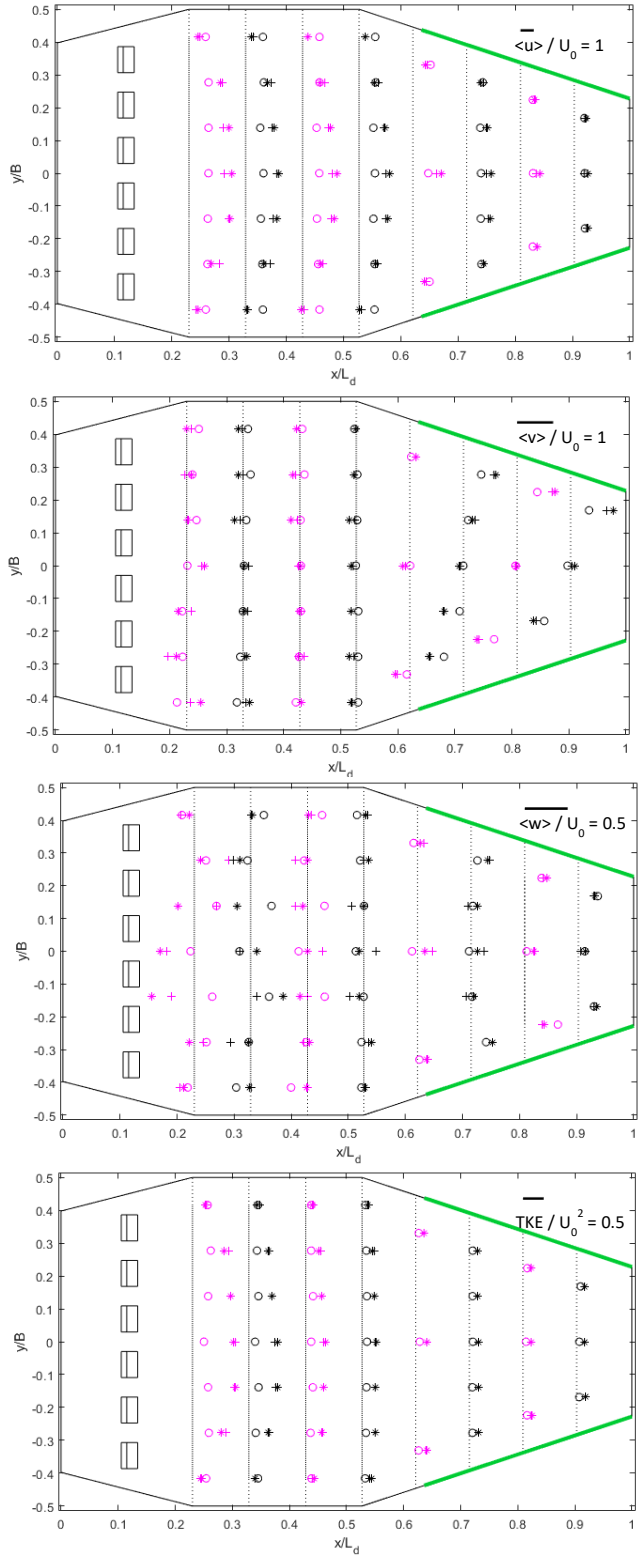

Figure 4.44. Normalized <u>, <v>, <w> and TKE at the DSM-flux small-scale physical model for VT9 data in dots (presented in Figure 4.8 (c), at the numerical model SM-C for Sim SM-C2 data in asterisks and at the numerical model SM-B for Sim SM-B3 data in crosses, all in the near-surface region ($z/H_0 = 0.783$). Two different colors are used to distinguish data from two consecutive sections.

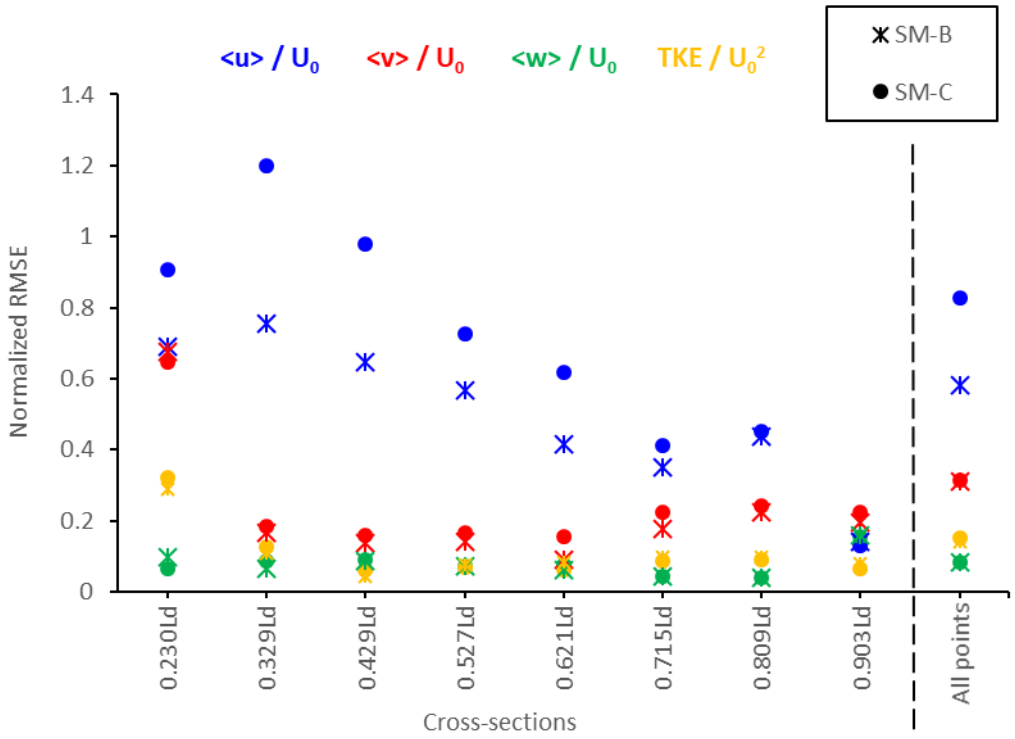

Figure 4.45. Normalized RMSE under the lower flow conditions (VT2, SM-B2, SM-C2) in the near-bottom region ($z/H_0 = 0.125$).

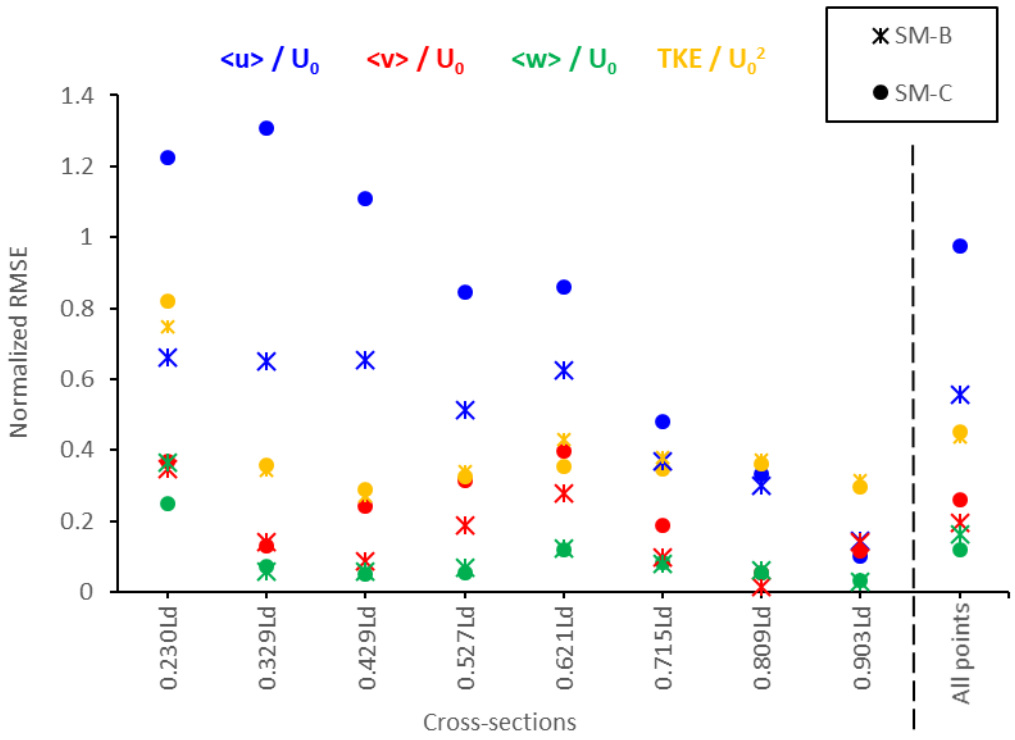

Figure 4.46. Normalized RMSE under the lower flow conditions (VT2, SM-B2, SM-C2) in the near-surface region ($z/H_0 = 0.694$).

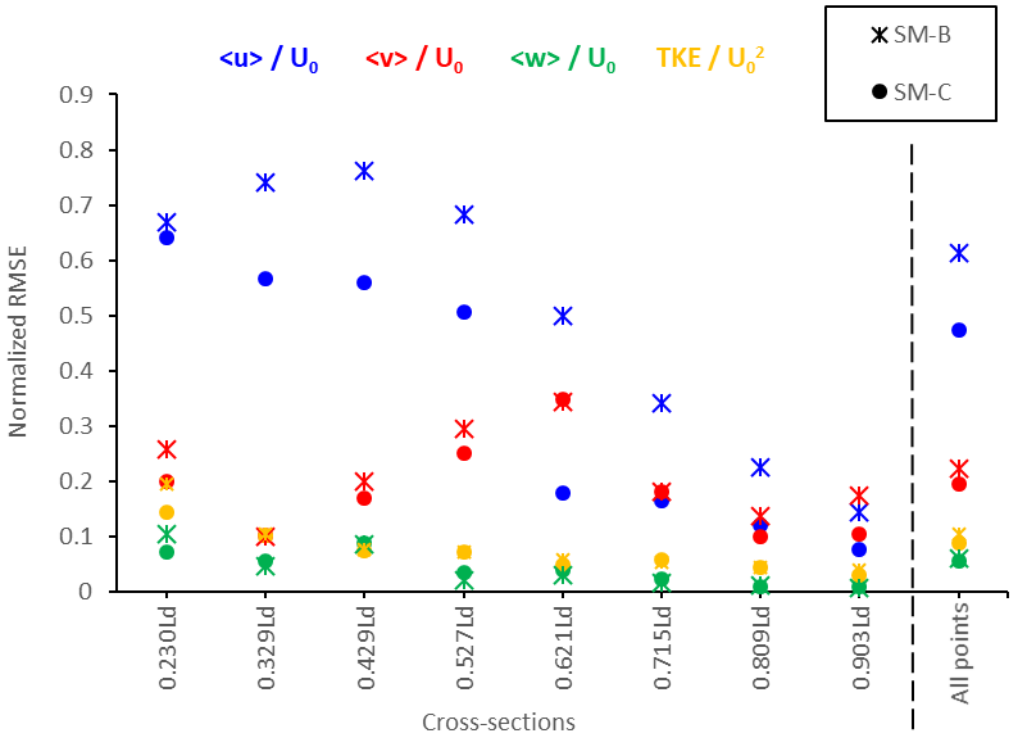

Figure 4.47. Normalized RMSE under the higher flow conditions (VT9, SM-B9, SM-C9) in the near-bottom region ($z/H_0 = 0.098$).

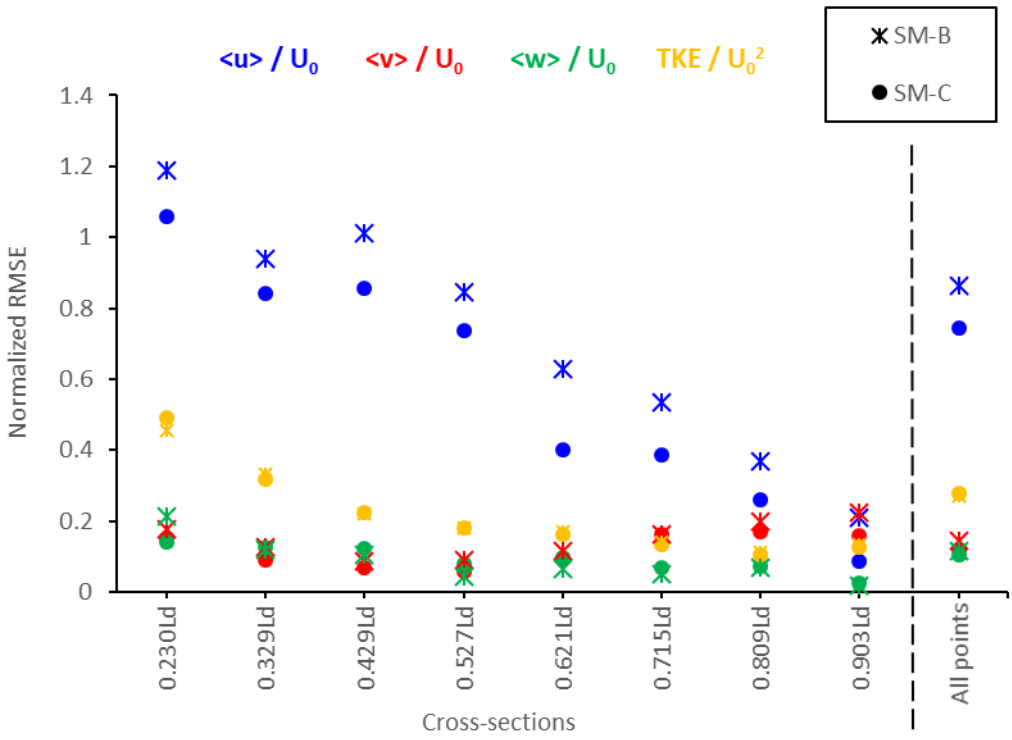

Figure 4.48. Normalized RMSE under the higher flow conditions (VT9, SM-B9, SM-C9) in the near-surface region ($z/H_0 = 0.783$).

Variability and uncertainty

The details of the variability and uncertainties analysis for the model SM-C are presented in Appendix 7.3.9 . This analysis cannot explain the discrepancies observed between experimental and numerical results. However, due to the difficulty encountered in obtaining numerical results, this analysis was performed by direct comparison between the three different models, and not in a systematic way, based notably on the GCI criteria. From the point of view of a work document, appropriate procedures are presented and discussed in the Appendix 7.3.9 , in order to be used for future works on this subject.

Final remarks and hints for the improvement of the numerical model performance

From the point of view of proposing advices for future works on this subject, we discuss here some proposals to improve the calculations. It has been observed in the small-scale physical model (Section 4.1.1.2) the existence of large-scale eddies in the cross-section planes of the stabilization area which, with a clockwise sense in the right part of the flow and anticlockwise in the left, make the flow go towards the walls at the surface and towards the centre at the bottom. Despite the mismatch of the numerical velocity fields with the experimental data, numerical models give further information about phenomena that can't be validated with the experimental data obtained in this PhD work. For example, there are other vortex structures that are formed at the dissipations area, out of the domain of the experimental tests. These recirculation areas are not only in the longitudinal profile plane (XZ), as is usual with hydraulic jumps, but they are also seen in the horizontal planes (XY) at different depths. Also, it has already mention in Section 4.1.2 the possibility of the formation of a recirculation zone at the end wall due to the flow impingement to the wall, as illustrated by Gisonni and Hager (1997). In fact, under lower flow conditions there is one vector from the experimental data at the section next to the end wall that is pointing upstream. Maybe the vortex exists but in between measurement points, so that it can be "observed" from the current data.

All this large-eddy structures manifest the complexity of the flow and questions the validity of the mathematical models used for its representation. An important part of the deviations could be due to the poor reproduction of the hydraulic jump. In their study for validation of a hydraulic jump model with experimental data, Castillo *et al.* (2014a) conclude that they have doubts about the suitability of using k-ε turbulence model to solve hydraulic jumps and Javan and Eghbalzadeh (2013) state that standard k-ε model could be the cause of the differences between measurements and computation results because it assumes an isotropic eddy-viscosity, which is not an accurate assumption for hydraulic jumps. They also conclude that the

use of wall functions for submerged hydraulic jumps, as it is the case in the DSM-flux, may not be appropriate as these functions should be applied to boundary layers of fully-developed flows, which is not the case in a hydraulic jump. Castillo *et al.*, suggests trying k-ω models that have proven satisfactory results in reproducing recirculation zones in detention basins, as it is the case in Yan *et al.* (2011) study. Castillo *et al.* (2014b) also uses a variant of the k-ω model, the SST k-ω model, to reproduce the impingement jet of an overflow nappe of a weir. They find good agreement with the validation data, which unfortunately didn't include velocity measures. Another study using the SST k-ω model to reproduce a free-falling nappe of a spillway into a plunge pool is validated with velocity measurements with acceptable results in some locations but Castillo and Carrillo (2015) concludes that further improvement must be done in the modelling of hydrodynamics including combination effects of velocities and air entrainment.

In addition to the turbulent model, different authors have highlighted the difficulties of modelling air entrainment in flows, which is a crucial phenomenon in hydraulic jumps (Castillo *et al.*, 2014a; Javan and Eghbalzadeh, 2013). Bayon *et al.* (2016) and Valero *et al.* (2014) include an additional model to reproduce the air entrainment in their studies with free hydraulic jumps. However, Witt *et al.* (2015) suggest that by adapting properly the mesh size to an estimated scale of the bubbles in the flow, there is no need to use extra air-entrainment models. They are satisfied with the level of similitude between the numerical obtained from the simulation of a free hydraulic jump and experimental data for this classical case study issued from the literature. (Bayon *et al.*, 2016; Valero *et al.*, 2014; Witt *et al.*, 2015) used all one of the variants of the k-ε turbulence model. A final remark is that, all the studies modelling hydraulic jumps cited here have carried out unsteady simulations, which wasn't the case in this PhD work.

In regard of these literature review, it is believed that the complexity of the flow (with air entrainment, vortex structures in the three directions, flow separation, *etc*.) might be better modelled with more sophisticated turbulence models, as the RSM. Another option is to consider LES simulations, if computational resources allow it.

As explained in Versteeg and Malalasekera (2007), the main drawback of the two-equation turbulent models is the assumption of eddy-viscosity isotropy, which makes them incapable of capturing the subtler relationships between turbulent energy production and turbulent stresses caused by anisotropy of the normal stresses. Thus, these models fail to represent the effects on turbulence of extra strains and body forces. Secondary flows in long non-circular

channels (as the ones that might occur at the DSM-flux), which are driven by anisotropic normal Reynolds stresses, can also not be predicted due to these deficiencies in the treatment of normal stresses within the k–ε model. To improve results in cases with significant anisotropy, a more complete and more complex model should be used: the RSM (Launder *et al.*, 1975). In this model, the hypothesis of isotropic eddy viscosity is no longer considered, and Reynolds stresses are directly modelled by developing transport equations for each of them.

RSM is less used in studies out the domain of research applications due to its computational cost and numerical instabilities (Andersson *et al.*, 2011; Versteeg and Malalasekera, 2007). However, it describes physics more accurately than the two-equation models and it's recommended for highly anisotropic flows, which could be the case of the DSM-flux flow. Despite its lower popularity, RSM has been successfully applied in some free surface flow problems with recirculation areas (Dufresne *et al.*, 2009; Momplot *et al.*, 2017).

A last suggestion for future work is to increase the experimental data with other types of methods, like the PIV. This technique has the advantage of being non-intrusive and it gives results with a higher resolution. More dense velocity fields and TKE contours could help to verify the hypothesis about the recirculation areas and improve the knowledge of the flow hydrodynamics. To apply this technique, a modification of the physical model must be done in order to make the walls of the device transparent.

4.2.3. Application for the large-scale numerical simulation

Previous section show that the virtual hydrodynamics reproduced by the numerical models implemented in this PhD work do not match with enough accuracy the experimental data. Thus, different numerical settings (flow equations, turbulence model, numerical schemes, etc) must be investigated in the future to try to better reproduce the flow in the device. In spite of this, the velocity fields and TKE contours from the simulations of flows in the large-scale models carried out in Section 3.2 are presented and discussed in this section because the current design of the DSM-flux field prototype was proposed based on these results. Obviously, the reliability of these results, particularly regarding velocity and TKE fields, is questionable. Indeed, the current design of the field prototype was initially based on the respect of HQR and the decreasing of velocity in the rectangular part of the DSM-flux in order to allow the sedimentation. Additional tests and simulations with various design strategies (*e.g.* to integrate a shaped invert trap) should be carried out once the numerical models will be completely validated. Even if the hydrodynamics is not accurately reproduced, it is believed

that the relative results among the different large-scale numerical models will give valuable insights on the retention capacity of the different designs.

The three large-scale numerical models are presented in Section 2.2.1. It is reminded that the main differences between the three models lie on the geometry. LM-A corresponds to the initial design, proportional to the small-scale with a scale factor of 2.67. LM-B corresponds to a first alternative design where extra baffle blocks are added, and their dimensions are adapted to some Momplot's (2014) recommendations. LM-C is a second alternative design which included the modifications of model LM-B in addition to an increase of the weirs height. The rest of numerical options are the same for the three models and are listed in (Table 2.4).

Regarding of this context, only the lowest (0.05 m^3/s) and the highest (0.18 m^3/s) flow conditions have been analysed. Although deposition will mainly occur at lower flow rates, it is believed that if hydraulic conditions for higher flow rates are modified in the direction to support deposition, even if it doesn't occur at that particular flow rate, deposition might be guaranteed until a higher limit. As explained in Section 3.2.4, the decision of testing different designs of the device was motivated because the velocities and TKE observed at the near-bottom region in the stabilization and overflow areas were considered too high for deposition to happen. Figure 4.49 and Figure 4.50 present the contours of velocity magnitudes (Velocity = square root ($u^2 + v^2 + w^2$)) at 0.9 cm from the bottom of the device, for the lower and the higher flow conditions tested in Section 3.2, respectively. Similarly, Figure 4.51 and Figure 4.52 present the contours of TKE magnitudes at 1 cm from the bottom of the device, for the lower and the higher flow conditions tested in Section 3.2, respectively.

At each figure, contours are presented for the three different models. The analysis of the initial design (LM-A) shows that, under lower flow conditions (Figure 4.49), velocities are relatively small at the overflow area and at the laterals of the device, which could lead to the deposition of material in these areas. However, at the higher flow conditions (Figure 4.50), high velocities appear at the centre of the stabilization area and at the central part of the entry of the overflow area, which could not only avoid deposition but also entrain the previously deposed material. Concerning the TKE values, estimations of the threshold for deposition from different studies with particles of characteristics closely enough to the ones expected at the DSM-flux show values about 10^{-5} (Yan *et al.*, 2011) or 10^{-4} (Dufresne, 2008). Thus, even the TKE values under the lower flow conditions (Figure 4.51) would be too high for these particles to settle.

The construction and monitoring of the DSM-flux field prototype has two main purposes: (i) to validate the monitoring methodology, and (ii) to assess the retention capacity of the device,

both under realistic operating conditions. In order to guarantee a minimum of retention in the field prototype so that the retention capacity of the device can be studied, it was decided to modify the initial design in order to (i) reduce the velocities, especially at higher flow rates and (ii) reduce the TKE magnitudes. Two alternative designs were suggested: model LM-B, where the number of dissipation blocks was increased and their height adapted according to some indications given in Momplot (2014), and model LM-C, which includes not only the modification of model LM-B concerning the dissipators but also an increase of the weir crest height.

Comparison of results between the initial model LM-A and the two alternative models LM-B and LM-C shows that, under lower flow conditions (Figure 4.49), velocities are quite similar in the three models. Slightly lower velocities are observed in the bottom of the weirs for models LM-B and LM-C and model LM-C presents lower velocities in the centre of the stabilization area. This is positive result if sediments are to be deposed in the stabilization area. Under higher flow conditions (Figure 4.50), the high velocities at the centre of the stabilization area and at the central part of the entry of the overflow area decrease in model LM-B and disappear in model LM-C. It is observed that model LM-C dissipated better the kinetic energy at the dissipation zone as velocities are downstream from this area are in general lower. Also, velocity field is more symmetric at LM-C model. Concerning the TKE values at lower flow conditions (Figure 4.51), it is observed that values do not vary significantly in model LM-B and they even increase at the overflow area for the LM-C model. However, under higher flow conditions (Figure 4.52), TKE values are lower in model LM-C at the overflow area and downstream part of the stabilization area, although they are higher at the lateral of the stabilization zone. As for the velocities, TKE contour at model LM-C seems more symmetric, which favours a better flow and suspended particles distribution in the device. Due to the slightly better conditions presented by model LM-C, especially in terms of velocity reduction (kinetic energy dissipation), this was the design selected for the DSM-flux field prototype.

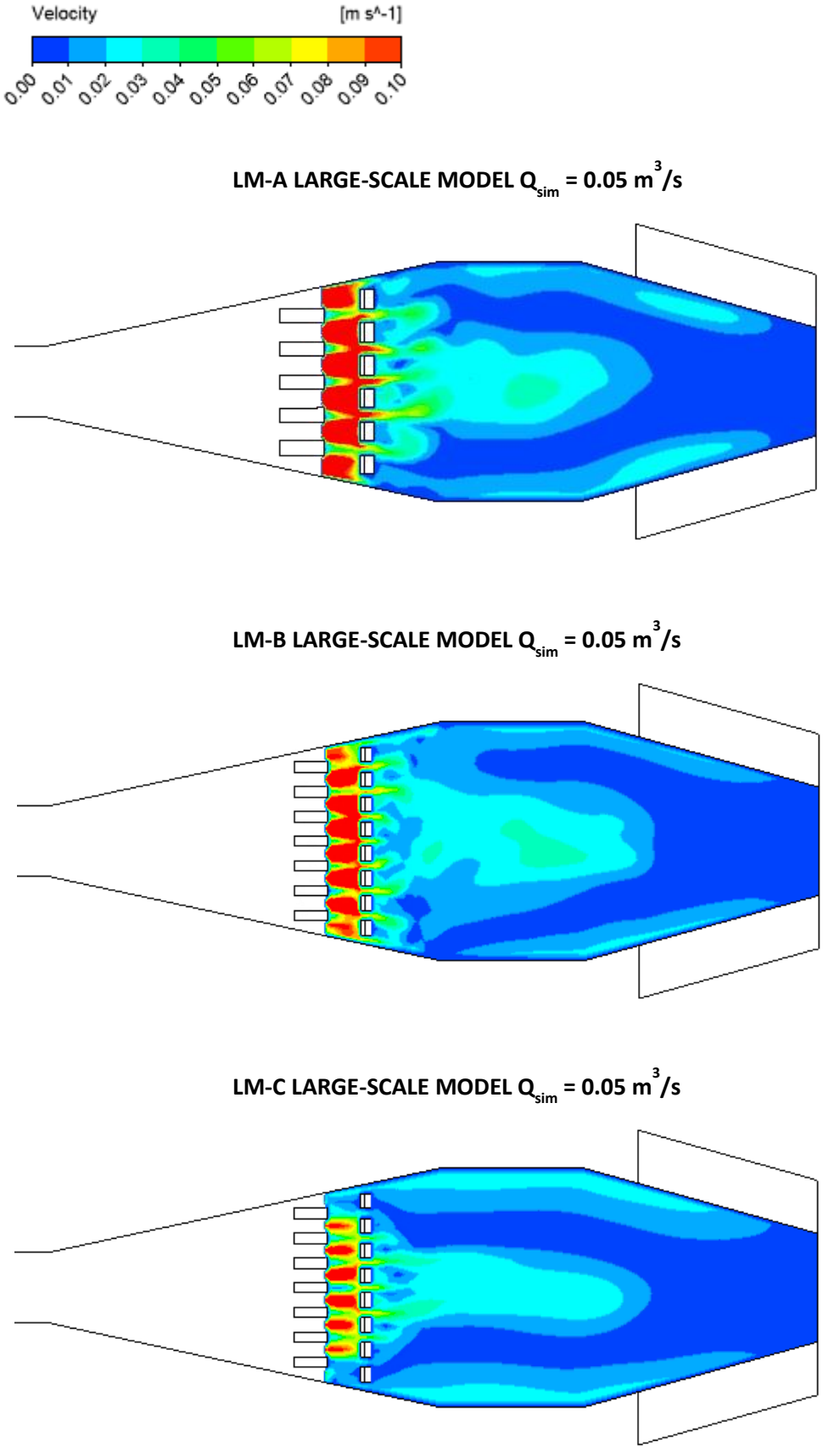

Figure 4.49. Velocity contours in the near-bottom region of the large-scale models, at depth z/H_0 = 0.2.

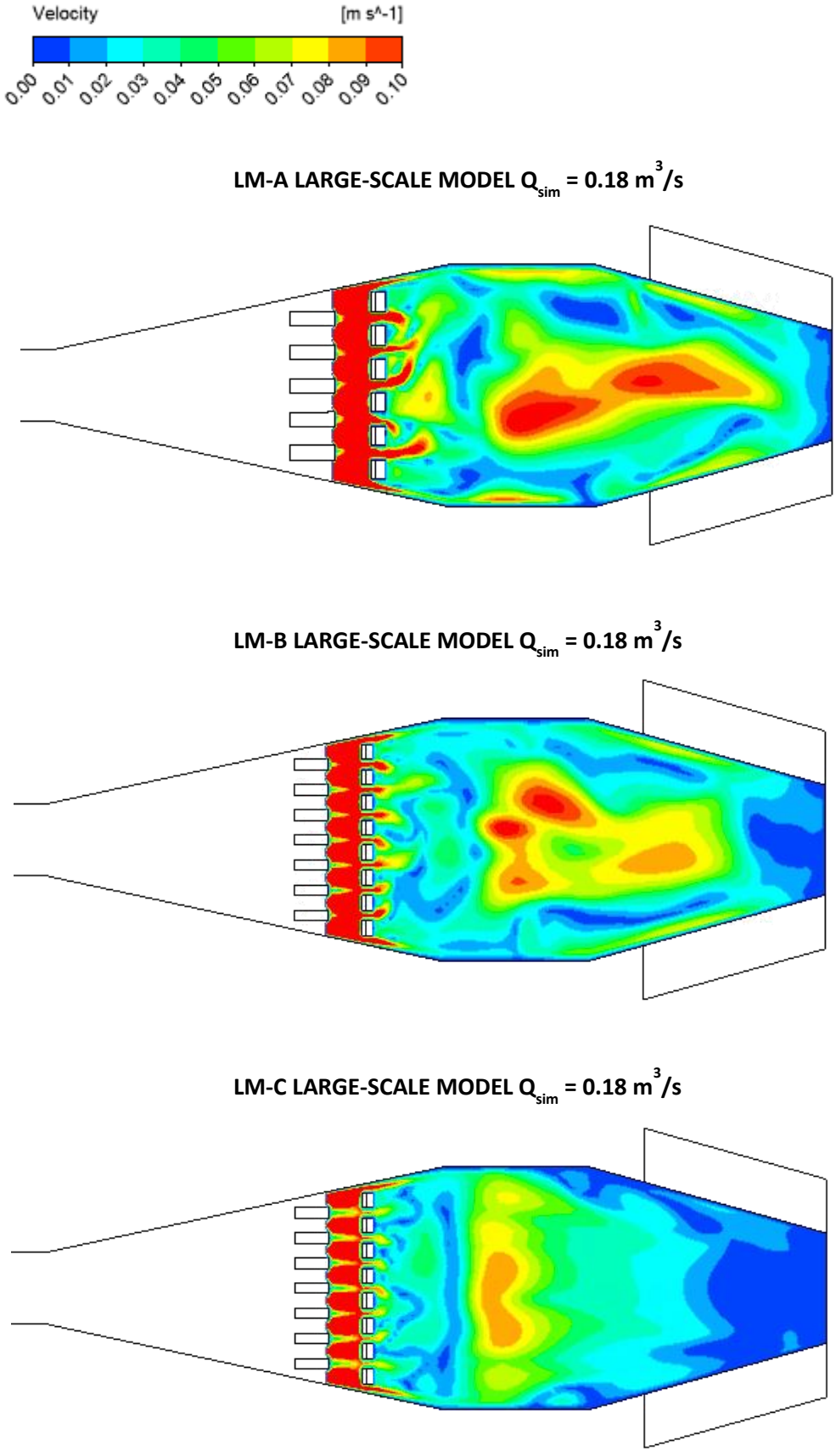

Figure 4.50. Velocity contours in the near-bottom region of the large-scale models, at depth z/H_0 = 0.065.

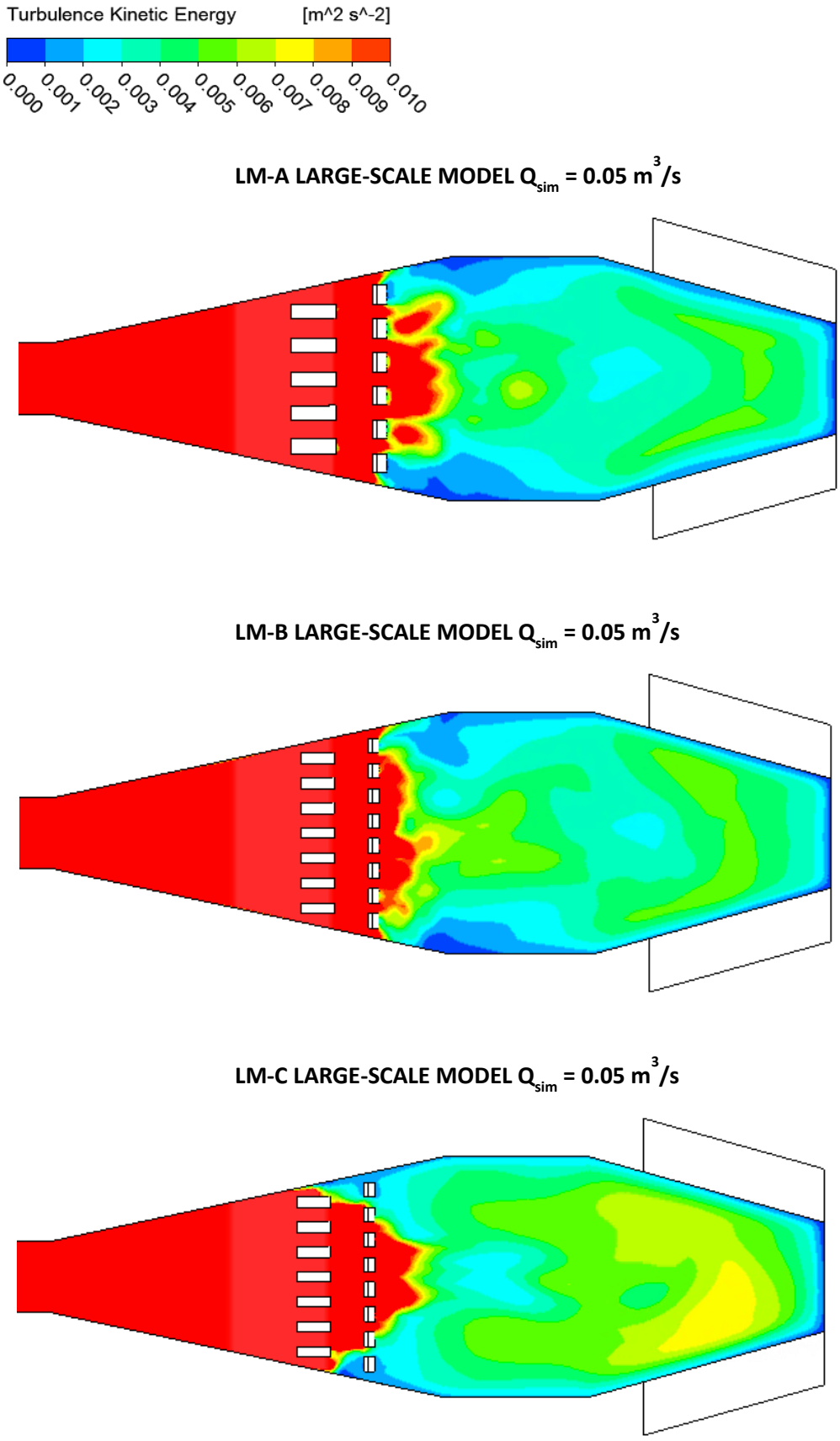

Figure 4.51. TKE contours in the near-bottom region of the large-scale models, at depth z/H_0 = 0.2.

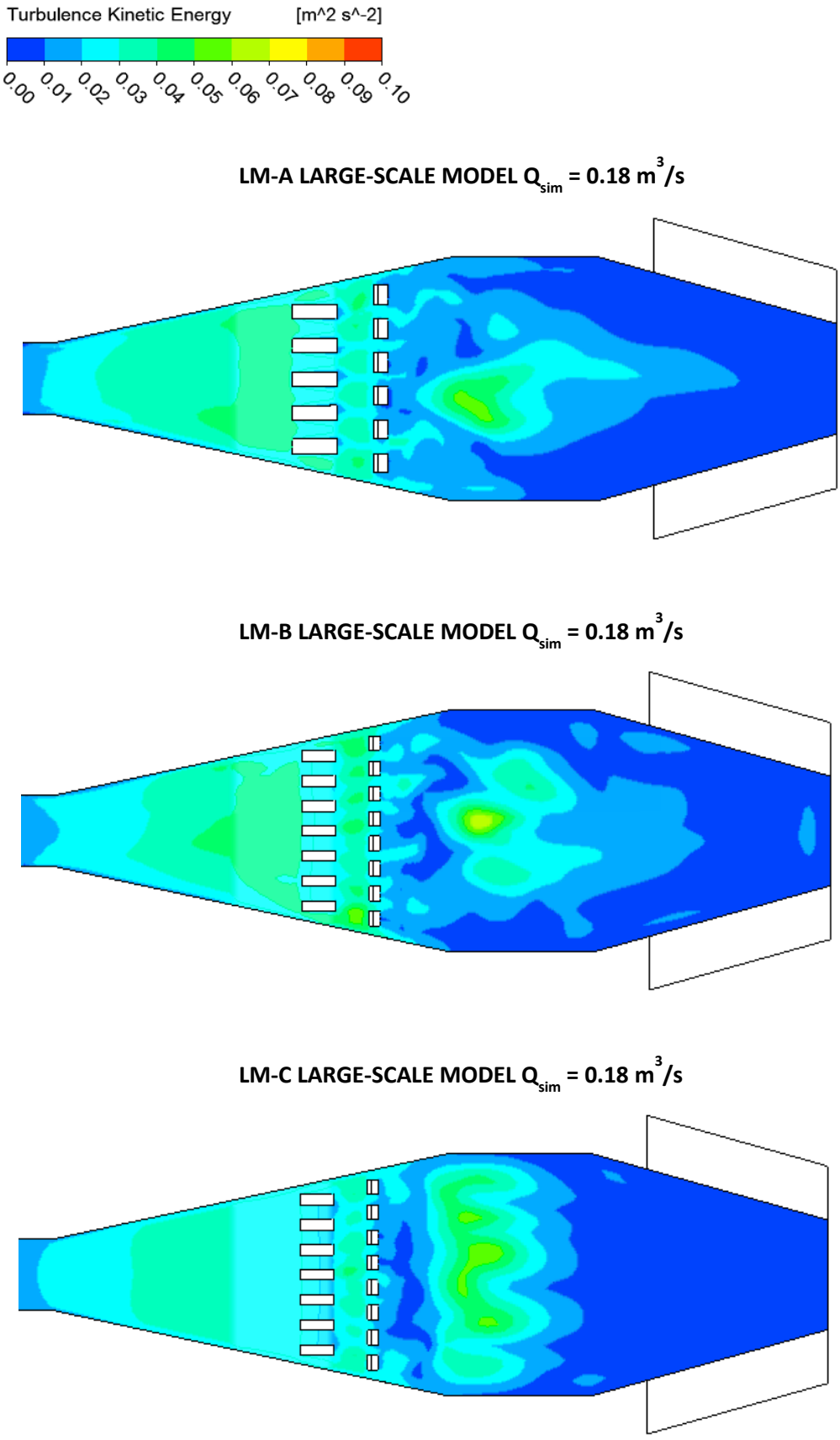

Figure 4.52. TKE contours in the near-bottom region of the large-scale models, at depth z/H_0 = 0.065.

4.2.4. Conclusions of Section 4.2

The main insights from this section are:

- Three small-scale numerical models were implemented in order to analyse the DSM-flux hydrodynamics for two different flow conditions. The differences between the models lie in a different discretization of the spatial domain (different computational mesh in size and quality terms) and a different near-wall treatment. None of the models appears to reproduce accurately enough the experimental velocity fields: significant differences are observed not only in the magnitude but also in the direction of the velocity vectors. TKE contours seem to match better the experimental results: the numerical models reproduce the characteristic double-parabola profile downstream the dissipation zone and present lower values in the rest of the device. However, deviations are still noticeable, especially for the higher flow rate and in the near-surface region.
- Differences were also significant between the numerical results of the models with different wall treatment and coarser mesh. Thus, either the different wall treatment or the different computational mesh (or both) have non-negligible influence on the velocity fields and TKE results.
- The effect of computational meshes was investigated for the two models having the same wall treatment and computational meshes with the better quality and more resolution, although different by a factor of 1.7. No significant differences were found in the velocity vectors directions between meshes with a difference of resolution of 1.7 times. Differences were mainly noticeable in terms of magnitudes, but the model with the highest mesh resolution did not reproduce better the experimental data. Thus, it is believed that the mesh resolution is not the main reason why the numerical results do not properly reproduce the experimental velocity fields and TKE values.
- Further investigation is needed to test other numerical options in order to reproduce better the hydrodynamics at the DSM-flux using the numerical models. It is believed that the complexity of the flow (with air entrainment, vortex structures in the three directions, flow separation) might better be modelled with more advanced turbulence models, as the RSM or k-ω SST, if solving RANs equations. Another option is to consider other numerical approaches, like Large Eddie Simulation (LES), Smooth Particle Hydrodynamics (SPH) or even Detached Eddie Simulation Numerical Solution (DES), if computational resources allow it.
- At a larger-scale (prototype scale), a model with a slightly modified design from the original one seems to dissipate better the kinetic energy and presents lower velocities at the

downstream part of the device, which are favourable for settling. For this reason, this design was selected to build the field prototype. However, a validation of this model needs to be carried out in future work.

4.3. OBSERVATION OF HYDRODYNAMICS AND RETENTION CAPABILITIES AT THE FIELD

The last stage to answer to question 2 of this PhD work (Figure 1.6) is the study of the hydrodynamics and retention capabilities of the DSM-flux field prototype under real operating conditions, in order to (i) estimate its retention efficiency and (ii) collect data to validate the large-scale numerical model. However, such analyses are challenging to be carried out directly *in situ* because the access to the facility during rain events is forbidden for security reasons.

Despite the difficulty to measure with, for example, an ADV probe, some other methods could be used to obtain velocity field data for numerical model validation. For example, Zhu *et al.* (2017) investigate the capabilities of common video-cameras to estimate surface velocity fields in a stormwater detention basin, like it is done with the PIV technique, called in this case LSPIV (large-scale PIV). Muste *et al.* (2014) developed this technique to measure velocity fields in shallow waters obtaining promising results in laboratory experiments for low-velocity flows. As the DSM-flux field prototype is already equipped with a video-camera, this methodology could be implemented at the field site in the future, when the technique will be more consolidated and validated for flows with higher velocity.

Other event-based methods to obtain data for validation and efficiency assessment at the field prototype are, for example, (i) the estimation of the TSS event mass load retained at the device by means of a balance-based method, and (ii) the monitoring of the evolution of deposition areas after each event by means of visual observations or, more accurately, by topographic reliefs obtained, for example, by photogrammetry techniques for 3D reconstruction, like the SFM technique applied by Regueiro-picallo *et al.* (2017) to determine the accumulation of sediments in a full scale physical model of a wastewater pipe. These event-based methods were planned to be implemented in the DSM-flux field prototype. However, the Sathonay-Camp experimental site was flooded several times during this PhD work due to the combination of extreme events and a misfunctioning of the sewer network downstream the site, whose backflow effects reached the DSM-flux chamber. These floods damaged some of the equipment, like the automatic samplers, that had to be replaced, and also caused the closure of the site for extended periods of time. These facts impeded applying field measurement methodologies, but their planning and preparation was developed during this PhD work, so they are described in the next section, to be applied in future studies. To conclude this part of the study, some preliminary data from the field prototype is presented and discussed in the last section.

4.3.1. Materials and methods for the assessment of the retention capabilities at the field

The efficiency of removal of a certain pollutant at a retention facility during a certain period of time T can be estimated with Equation 4.9 (Yan *et al.*, 2014):

$$Efficiency = 100 \cdot \frac{\int_{t=0}^{t=T} C_i \cdot Q_i \cdot dt - \int_{t=0}^{t=T} C_o \cdot Q_o \cdot dt}{\int_{t=0}^{t=T} C_i \cdot Q_i \cdot dt} \qquad \textit{Equation 4.9}$$

where C_i and C_o are the pollutant concentrations at the inlet and the outlet of the device, respectively, Q_i and Q_o are the discharge rates at the inlet and the outlet of the device, respectively and T is the period of time considered.

These efficiencies depend on the type of treatment that is carried out in the facility as well as on the inflow characteristics, pollutant types and particles characteristics as well as in the facility design and its management. Besides, the efficiency term has different meanings depending on the method used to calculate it and the period of time considered for the estimation (event, multi-event or annual) as reminded by Sebastian (2013). For a CSO, the event efficiency can be estimated by Equation 4.10:

$$Event\ Efficiency \approx 100 \cdot \frac{EMC_i \cdot V_i - EMC_o \cdot V_o}{EMC_i \cdot V_i} \qquad \textit{Equation 4.10}$$

where EMC_i and EMC_o are the event mean concentrations at the inlet and the outlet of the device, respectively, obtained by means of sampling strategies; and V_i and V_o are the CSO volumes at the inlet and the outlet of the device, respectively.

Chocat *et al.* (2007) give a general overview of the pollutant removal efficiencies of some facilities used for Urban Wet Weather Effluents (UWWEs). It is obvious that the facilities including a chemical or biological treatment will have a higher removal efficiency than the facilities only storing water. Extensive retention basins can have efficiencies up to 60-90 % in TSS removal. Lamella settlers can reach efficiencies up to 85% if reagents are added to the flow. Hydrodynamic separators have shown a medium-low efficiency in pollutant removal of UWWEs.

As explained in Section 2.2.2, the Sathonay-Camp experimental site is equipped with two automatic samplers (Liquistation CSP44 from Endress+Hauser) with sampling points located (a) at the entry of the device and (b) at the overflow area, near the turbidimeter (Figure 2.16). The

idea is to calculate the EMC at the entry and the overflow area of the device and use the CSO volume estimated by means of the HQR to compute Equation 4.10. The methodology to obtain the EMC is described in detail by Bertrand-Krajewski *et al.* (2000) and it basically consists of weight-averaging the concentration of TSS measured for different samples taken during the event according to the equivalent CSO volume represented by the sample in the event (Equation 4.11):

$$EMC = \frac{\sum_{i=1}^{n} C_i \cdot V_i}{\sum_{i=1}^{n} V_i} \qquad \textit{Equation 4.11}$$

where n is the total number of samples, C_i is the measured concentration of sample i and V_i is the measured volume of CSO represented by sample i. For a pQVcF sampling strategy (Table 1.4), V_i would be directly the volume of the sample.

Automatic samplers at the Sathonay-Camp experimental site allow a maximum of 12 samples of a maximum of 0.7 l per event. Ideally, these samples should cover the whole duration of the event and be able to catch all the hydrodynamics of the pollutants, as first-flush phenomena. A first analysis of the hydrographs recorded at the Sathonay-Camp experimental site (Table 3.9) shows that (i) there are two types of hydrographs: single-peak and double-peak events, (ii) most of the events are quite "symmetric", the peak discharges Q_{peak} and relative "valleys" between both peaks for double-peak events, being situated at the middle duration of the event, (iii) durations of events are quite heterogeneous but, as it was said in Section 3.3.2, 95% of the events have a duration of less than 2.5 h, so this could be considered the maximum duration as a first estimation.

Fully representative sampling strategies need some time to be adjusted according to the characteristics of each site. For the Sathonay-Camp experimental site it was decided to follow in the first time the cVcF sampling strategy (described in Table 1.4), as it is the simplest method to apply when hydrology of the site is still not well known and there is a lack of data. The shape of the recorded hydrographs (without long tails) suggests that a regular sampling frequency would be appropriate in this case. The sampling frequency would be determined by dividing the total discharge event duration by 12. Total duration could be considered as 2.5 h but, a more detailed analysis of the durations of the registered events shows that 60% of the events have a duration of less than one hour, so we could use this duration to increase the sampling frequency. As the DSM-flux measures flow rates, a pQVcF strategy (described in Table 1.4) was also considered, as it represents better the EMCs (Bertrand-Krajewski *et al.*, 2000). However, the DSM-flux HQR should be firstly improved (for the higher flow rates) to be

sure about the magnitude of the flow rates. Once this correction will be done, it would also allow checking if the capacity of the sampling bottles is enough to apply this strategy.

The sampling strategy can be improved in time by, for example, the information given by the turbidimeter. Turbidity data, even before correlation with the pollutants, will give information about the turbidity dynamics and then, the sampling frequency could be adapted to the pollutographs. For example, if pollutants concentrations vary faster at the beginning of the event, the sampling frequency can be increased for the first samples.

Other type of strategies that could be considered would be the dynamic strategies, as the one applied by Hofer *et al.* (2013) to a CSO in Graz, Austria. This methodology consists of programming different sampling strategies according different types of events. Either manually or automatically, the samplers change from one strategy to the other in relation with the weather forecast. Results from Hofer *et al.* (2013) are promising but, as they highlight, a good quality weather forecast (close enough to the site) and some historical knowledge about the flow dynamics in the sewer is essential for its application and success.

Concerning the pollutants, the plan was to monitor at least TSS and COD, as these pollutants will also be correlated to the turbidity data in order to establish the continuous monitoring methodology for quality. BOD5 was also planned to be monitored. Due to the increasing concern about micropollutants (Section 1.1), it was planned to monitor, at a second stage, at least the following components: 6 metals, 16 PAHs, 22 pesticides, 9 Polybrominated Diphenyl Ether (PBDEs), 8 Alkylphenols (Aps) and Alkylphenolethoxylates (APEOs), 2 Chlorobenzenes and 1 volatile organic halogenated compound (VOHC). However, this list could be increased according to the analysis offered by the different laboratories of analysis where the samples will be sent. To be able to analyse all these components, different sampling bottles were acquired, made of plastic or glass, that would be changed according to the objectives of each campaign. As the automatic samplers are not refrigerated, samples must be collected as soon as possible after the event and stored in appropriate temperature and light conditions. However, the fact that the experimental site is underground helps to keep the samples isolated from extreme temperature conditions until they are collected.

From a practical point of view, the identification of the beginning of the event is relatively simple in the present study case because, as explained in Section 3.3.2, there is no flow in the system during dry weather. Thus, the automatic samplers are programmed to start the sampling a few seconds after the water level in the distribution chamber reaches the invert of the 0.4 outflow pipe that conveys the water to the DSM-flux. The suction tube for the sampling

point at the overflow area is attached to the turbidity support in order to measure as close as possible to the turbidimeter to be able to relate both data accurately. The sampling at the entry of the DSM-flux is more challenging, as velocities in this part of the device are usually higher than the values recommended but the automatic sampler's manufacturers. Thus, a special support was designed to create a relatively calm area for the tube to be able to suction the water. This support consisted in a hinge-like element partly perforated and with an adjustable angle that would be placed in the symmetry axis of the device so that perturbations to the flow are as low as possible. The suction tube of the sampler is then placed inside. Figure 4.53 presents a schematic of the element. The support was tested in the small-scale physical model and it appeared that a strong fixation should be conceived in the field as the flow pressure, even if lowered by the perforations and the adjustable of the angle, was non-negligible. However, this element will only be installed for research purposes during the campaigns to assess the device efficiency. The rest of the time, it will be removed as it is not used for the calibration of the turbidimeter or, in the long term, for the monitoring of the CSO pollution. An optimisation of this design could be done when the numerical models will be validated, and its performance can be monitored with the video-camera installed on site.

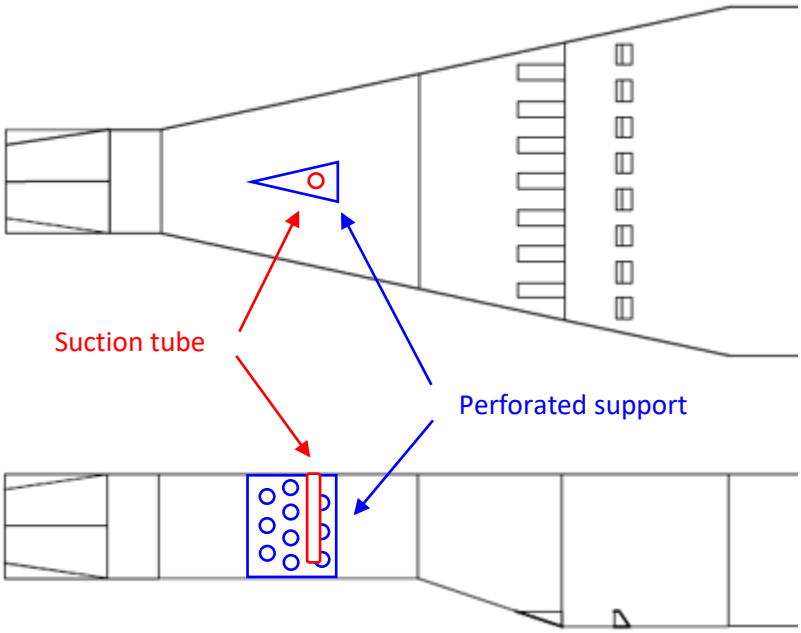

Figure 4.53. Schematic of the design of the support for the upstream suction tube of the automatic samplers.

Finally, concerning the monitoring of the evolution of the sediments, as explained in Section 2.2.2, the video camera (ExCam-IPM1145(-L) from Samcon) is placed above the entry of the DSM-flux, with a view angle that covers the whole device. This video camera is activated when

water enters the 0.4 m diameter outflow pipe of the distribution chamber simultaneously with a light spot. It was planned to use this camera not only to record the flow passing through the DSM-flux during a CSO event (in order to study the real hydrodynamics from visual observations), but also to monitor the deposition areas in the DMS-flux to register their evolution and plan maintenance interventions as the deposited volume exceeds a threshold value. It must be highlighted that, for these visual inspections, the water remaining in the device must be evacuated through the drainage orifice design for that purpose. As introduced in this section other methodologies, as the photogrammetry, could be used to quantify the sediments volume and lead to a more quantitative monitoring of the deposition. Also, it would be interesting to characterise the sediments that are retained by the DSM-flux to evaluate their quality and ecotoxicity and thus, find a way to either get rid of them or reuse them in other applications. As already mentioned, these video-camera images have the potential for surface velocimetry measurement (LSPIV) on the field as well. Unfortunately, the video-camera was only operating during the last months of this PhD work and no velocimetry measurements could be performed.

4.3.2. Some preliminary data

Figure 4.54 presents a photo of the overflow area of the DSM-flux field prototype taken the 14th of June of 2018, also showing the turbidity probe and its support. It is observed that a certain amount of sediments has been settled at the centre of the device, from the downstream part of the stabilization zone to more or less the middle of the overflow area. This photo proves that the DSM-Flux is able to intercept solid matter. From a visual inspection, sediments consist not only on the finest particles, but it seems that there are also greater size particles like sands or even some fine gravels. Other solid materials like toilet wet wipes are also present, specially attached to the turbidimeter support. Concerning the deposition area, more sediments are located at the overflow area than at the stabilization zone, which wasn't the behaviour planned for the design of the device. As it is observed from Table 3.9, this photo was taken after a serial of consecutive days of CSOs so these sediments probably do not correspond to a single event deposition so that the sediments might have been affected by the dynamics of the subsequent events. Unfortunately, the lighting associated to the video-camera was not installed at this time, making it impossible to evaluate the previous state of the device (from previous images) and there is no information about the last removal operation by the municipal operators. Thus, two hypotheses are left to be verified in future observations: either

the deposition is actually located mainly at the overflow zone (it was observed from SE tests that for relatively low flow rates fine material settled all over the downstream part of the stabilization area and at the overflow area (Figure 4.17 (a) and (c))) or/and the sediments have moved downstream due to entrainment by the subsequent events (it was also observed at the SE tests that the deposition areas were eroded from the upstream part of the stabilization area but that these particles didn't necessarily leave the device, some cumulated at the end of the stabilization area forming small ripples (Figure 4.18, Figure 4.19 and Figure 4.20).

Regarding the photo from Figure 4.54, it is clear that the sensitivity of the DSM-flux HQR to the presence of different thicknesses of sediments at the overflow area must be assessed either experimentally or numerically. However, from Section 3.3.2 results, it is observed, at least for the lower flow rates, that if sediments were present during the recorded events (which highly probable as sediments were observed during each intervention), these sediments did not significantly impact the estimation of the flow rates by means of the DSM-flux HQR. A good example is event number 41 (from the Appendix 7.2.1), which was occurred less than 30 hours before the photo from Figure 4.54 was taken.

Figure 4.54. Sediments at the DSM-flux field prototype. Photo taken the 14th of June of 2018.

Finally, the analysis of the few videos registered from Sathonay-Camp experimental site reveals that the small floating material are sometimes directed towards the lateral walls of the device before arriving to the overflow area and, instead of remaining close to the walls and leave the device through the weirs, they turn back and flow upstream close to the walls. This opens the question about the lateral recirculation zones numerically simulated for some configurations (Figure 4.29, Figure 4.30 and Figure 4.31) but not observed on the small-scale physical model. This discrepancy is definitely among the most interesting questions that will have to be analysed in future studies.

Chapter 5

5. CONCLUSIONS AND PERSPECTIVES

5.1. CONCLUSIONS

In this PhD work, two questions were addressed:

(i) Is the DSM-flux a robust monitoring device that provides reliable and accurate flow data?

(ii) Is the DSM-flux capable to efficiently retain particulate pollutants?

To answer these questions, a multiscale approach was considered in order to evaluate the DSM-flux behaviour with 2 different scales (small/large) and associated numerical modelling approaches, analysed under different operating conditions (laboratory/real site-specific). The main conclusions of this work are described in this section.

Concerning the first question, **the DSM-flux can be considered as a robust monitoring device that enables to get accurate and reliable flow data** according to the results of this PhD work. The monitoring methodology obtained experimentally, which is based on a stage-discharge relationship, has proven to measure accurately discharges and event volumes, independently of the hydrodynamic characteristics and complexity of the inflow. Indeed, at a small scale, uncertainties for the higher flow rates are estimated to 15% and the volumes of the tested events were measured with uncertainties lower than 2%. It is considered that uncertainties depend mainly on the water level gauge accuracy. It is believed that the homogeneity of the free surface at the sampling area - and its relatively stability, at least for the lower flow rates – observed during the tests will contribute to keep the uncertainties lower. At a larger scale, the monitoring methodology has proven to be still valid without significant scale effects, which exhibits the capabilities for a standardization of the method. Numerical simulations have shown that flow rates obtained by means of the DSM-flux HQR and water levels gauged with an uncertainty of 1 cm can be considered reliable as discharges fall within a 95% of confidence interval. This is still valid if the accuracy of the water level gauges improves up to 2 mm but only for the lower flow rates. It is also valid for small variations in the weirs height, which can be interesting from an operational point of view to increase the height and favour the retention function, for example. Finally, the monitoring of a prototype installed in the field confirmed the validity of the methodology under realistic operating conditions, at least for the flow rates ranged between 1 and 60 l/s and combined sewer overflow (CSO) events with discharge peaks lower than 150 l/s. Indeed, discharge rates of 80% of the events registered during this PhD work were reproduced with Nash-Sutcliffe coefficients higher than 0.5 and CSO volumes of almost half of the registered events were reproduced with relative differences

lower than 20%, which have been considered satisfactory values regarding the type of challenges addressed.

However, some aspects need further investigation. Significant deviations in flow rate values were observed at the field for the flow rates higher than 60 l/s between the DSM-flux methodology and a second one used for the verification. Some concerns arose about the reliability of the second methodology, based on a CFD approach, that did not allow to determine if the cause of the differences was (i) the non-reproducibility of the DSM-flux stage-discharge relationship under the field conditions or (ii) other field factors that influenced the representativeness of the numerical model used for the development of the second methodology in relation with the configuration of the site. Due to technical limitations, it was not possible to carry out a second verification in the framework of this PhD work and hence, it remains as a priority action to be developed in future work. On the other hand, the significant amount of sediments found in the prototype after the events, that were partly located at the overflow area of the device, highlighted the necessity of analyzing the sensitivity of the monitoring methodology to the presence of sediments in the sampling area. Regarding the field results, they do not seem to have a significant influence, at least on the lower flow rates, but a rigorous analysis at the laboratory should be carried out.

Concerning the second question, the conclusions are slightly less definite. It could be said that **the DSM-flux can retain efficiently a certain type of pollutants (fine light-weighted) under a certain type of flows (low steady)**, but this statement needs further specifications. According to the results of this PhD work, it has been proven that a small-scale device is able to retain up to 50 % of mass of the fine light-weighted particles conveyed in a steady flow of 2 l/s. This percentage of trapped particles varies depending on the flow rate. For the particles tested (D50 between 100 and 300 µm), the DSM-flux retention efficiency is reduced by half for a flow rate of 5 l/s. It is thus possible that the DSM-flux is only able to retain the fine particulate pollutants if the flow rates are relatively low. It has also been proven that, if a relatively low discharge flows without particles into the device, the DSM-flux is able to keep part of the sediments previously deposed. However, under this same assumption, if this discharge is slightly higher, almost all the sediments escape the device after 3 hours with the same flow rate. This indicates that after a certain number of rain events (maximum number to be assessed in the future) where deposition occurs, the DSM-flux should be cleaned out to avoid significant pollution peaks in the receiving waters due to the remobilization of the deposited sediments. Furthermore, it was observed that the deposition areas take place quite homogeneously over the whole downstream part of the device except near the high TKE

regions in the measured section next to the hydraulic jump. Erosion starts mainly in the bands next to the side walls and in both eroded areas with parabolic shape downstream from the dissipation zone. These two areas extend downstream with time creating small riddles (under the lower flow conditions) or entraining the material settled downstream (higher flow conditions).

This performance of the device could not be validated in a device with a larger scale. The numerical options that produced results fitting satisfactorily the experimental data for the study of the stage-discharge relationship did not reproduce the experimental velocity fields accurately enough for the settings to be validated. The similar results obtained using the same numerical options in two different computational mesh resolutions suggested that the mismatching with experimental data was not due to an insufficient discretization of the domain. Thus, other numerical options must be tested. As the numerical options could not be validated, it was not possible to assess numerically the retention capabilities under other conditions, for example, different flow rates or particles. Although the settling and entrainment of material cannot be monitored directly in the field, some protocols have been prepared, based on the first data and observations, to be able to assess the retention efficiency of the prototype under real operating conditions. Due to technical problems during the first months of operation, these analyses could not be carried out in the framework of this PhD work, but the experimental site has been already equipped and it is prepared for the future campaigns.

Apart from the scientific questions addressed, the installation of the first prototype of the DSM-flux in an existing combined sewer system has also highlighted its potential as a pre-calibrated, pre-design and multifunction device for monitoring complex flows. Indeed, the DSM-flux has some advantages compared to current measurement methods: (i) it aims at measuring CSO discharges directly in the overflow channel; (ii) only one water level measurement is needed to obtain discharge values; (iii) it is a pre-calibrated device that can be installed downstream from the existing CSO structure; (iv) its performance is independent of the inlet hydraulic conditions; and (v) it has additional functions apart from measuring CSO volumes, such as measuring total suspended solids (TSS) loads and reducing the particulate pollutants by sedimentation.

5.2. PERSPECTIVES

Several action lines have been identified to develop further the questions addressed in this PhD work and to improve the knowledge of the performance of this novel device. Based on the experience acquired during this study and keeping the same multiscale approach, suggestions are made about which would be the most appropriate systems to apply the different action lines.

Future work concerning the monitoring methodology

Results from the simulations at the large-scale models show that the stage-discharge relationship seems to overestimate the flow rates above a certain (Q, h) value. Data from the prototype, although not confirmed yet, seem to exhibit the same tendency. Several hypotheses about the reasons behind these differences observed using the numerical model were already discussed in Section 3.2.3 and some future work was suggested. Firstly, it should be confirmed that these deviations are not due to a numerical inaccuracy. This could be done with a mesh sensitivity analysis of the large-scale model mesh, which is relatively coarse. Also from a numerical point of view, it should be evaluated if the iteration-average free surface levels computed represent the time-averaged levels of an oscillating free surface. This must be done with unsteady simulations using URANS.

On the other hand, it is necessary to guarantee the representativeness and accuracy of the second technique used to characterize the flow rate and assess the performances of the DSM-flux HQR at the field. Either a proper fixing of the opening of the gate that could have failed at the distribution chamber is assured, or the DSM-flux inflow pipe is left completely open and a new model of the distribution chamber with a full opening is implemented to obtain a new distribution chamber HQR.

If the deviations at a large scale are confirmed, a study of the effect of the scale on the DSM-flux HQR should be carried out. Several numerical models of different scales could be implemented and the DSM-flux HQR could be adapted for the higher flow rates range as a function of the scale. This will also allow to determine the limits of performance of the device.

Another sensitivity analysis should be done concerning the influence of the presence of sediment deposits on the DSM-flux HQR. As a starting point, homogeneous layers of different thicknesses of sediment deposits could be placed and fixed at the overflow area of the device (fixed bed tests). This analysis could be carried out either experimentally or numerically.

However, if scale effects are confirmed, it would be more convenient to do the analysis numerically to be able to test different scales.

Future work concerning the assessment of the device retention efficiency

The difficulties to assess the suspended solids dynamics in the field prototype makes essential the use of a numerical model as a tool to reproduce the suspended solids transport, especially its sedimentation and erosion, for the study of a wide variety of flow conditions and types of suspended matters. Firstly, the numerical models must be improved and validated for the analysis results to increase their credibility. The numerical settings tested in this PhD work did not reproduce accurately enough the experimental data so other options are suggested. One option is to try other turbulence models, as already discussed in Section 4.2.4. More advanced models than the RNG k-ε model, might represent better the effects of turbulence, as for example the RSM, which is recommended for anisotropic and swirling flows as expected for the DSM-flux. Another type of turbulence model could be the two-layers models, as the SST k-ω model, that adapt the equations according to the value of the local Reynolds number. The presence of the baffle blocks in combination with the downstream influence of the weirs and end wall could create a low Reynolds region close to the bottom of the device that could be better modelled with this kind of turbulence equations.

Apart from the turbulence models, another option is to continue investigating different meshing strategies, particularly those that allow a higher resolution near the walls. Indeed, the near-wall treatment was satisfactorily applied at this study but the resolution of the mesh at the near-wall region was in its limits, with y^+ of around 5. The application of turbulence models like the SST k-ω requires y^+ of 1 or lower, which means that discretization of the near-wall region must be higher. The meshing strategies used in this study were very time consuming due to the relatively complex geometry of the device and did not allow further discretization near the walls. This was because the number of elements increases rapidly with a structured mesh type and the computing resources started to be compromised. The assessment of the performance of unstructured meshes, for example, or of hybrid meshes combining structured and unstructured zones, could represent an advantage to gain computational resources and be able to study more precisely different near-wall treatments or turbulence models.

In relation with the computational mesh and the use of models to represent different phenomena, the air-entrainment at the hydraulic jump was identified as another possible reason of the mismatch between numerical and experimental velocity fields. Different authors suggest implementing air-entrainment models to reproduce the phenomenon, but these are

still poorly validated. A more detailed study of the hydraulic jump including measuring the air entrainment as Bayon *et al.* (2016) did, could give more insight to this question and evaluate the option of incorporating these types of models to the software by means of user defined functions. Other authors like Witt *et al.* (2015) suggest that it is better to adapt the mesh size to the size of the bubbles rather than using the air-entrainment models. This approach could also be studied if the meshing strategies allow to modify the meshes more easily and if it is possible to characterize the bubbles produced at the hydraulic jump. However, this numerical strategy may also be time consuming due to huge sizes required for the computational meshes. A multiphase Euler-Euler approach, such as the Eulerian-granular numerical approach, could also be performed to account for air entrainment across the hydraulic jump. Another strategy could be to start simulations with high downstream crest height, imposing a subcritical regime, and examine the capability of the code as and when the downstream depth is decreased by modifying the height of this downstream crest up to its designed value.

Further experimental tests at the physical model would allow to increase the knowledge of the hydrodynamics of the flow (for example, to confirm the existence or not of large-scale eddies next to the end wall) and to get a larger database for calibration. PIV tests are suggested because (i) they provide a higher resolution of the data with a better global view of the velocity field and (ii) they allow to study unsteady velocity fields and swirls. The application of the PIV in the physical model would need a modification of the model walls to make them transparent for the laser beams. Different planes, especially in the XZ direction, would provide a better idea of the possible large-eddies formed in the device as well as determine the vertical distribution of the velocities downstream the dissipation area, which was not studied in detail with the ADV campaigns. These results would help evaluating the convenience of testing other numerical approaches, like the LES, instead of RANS.

Once the numerical options will be validated, further investigations can be carried out to analyse the retention capabilities of the device, particularly by injecting particles in the numerical flows. For this type of simulations, specific boundary conditions must be defined to determine the behaviour of a particle when impacting the wall. This is an additional numerical setting that will have to be tested and validated with experimental data. Some of the suggested conditions are related to the determination of a threshold values of shear stress or TKE that leads to particles entrainment, as it was initially applied by Yan (2013), then by Isenmann (2016). Although the results from the 3 SE tests will contribute to this validation process, it is recommended to make some more tests following the same methodology, with other types of particles (different sizes and densities) and different flow conditions. It would

also be interesting to add an additional step to these tests which would consists in doing a topographic survey of the sediments distribution. A low-cost technique is suggested for this purpose: the Structure For Motion photogrammetry-based method. This technique has proven satisfactory results in sediments surveys in conduits by Regueiro-picallo *et al.* (2018). Its results are comparable to laser techniques, but with the advantage of only needing a relatively good quality camera and not needing to modify or to adapt the physical model experimental set-up. The accuracy of this technique depends on different factors (resolution of the images, algorithms used for the 3D reconstruction, number of frames samples (pictures)) but it has been estimated to 0.1 mm (Regueiro-picallo *et al.*, 2018) for measurement distance of 1 m (James and Robson, 2012). Special attention should be given for the sediments of fine particles as the ones tested in this PhD work, as the thickness of the sediments of these tests was estimated to only a few millimetres. This technique could also be applied at the prototype to evaluate more accurately the deposition zones and volumes after an event, if needed.

Additional tests that could be carried out at the physical model would imply the simulation of unsteady flows representing the hydrographs registered at the field in order to study the influence of a varying flow rate on the deposition and entrainment of sediments, especially concerning the event efficiencies.

Event efficiencies are planned to be estimated at the field prototype for a certain number of events. As already introduced in Section 4.3.2, an initial protocol is suggested based on the results of this PhD work. Apart from estimating the efficiency of the device, the analysis of the samples collected during these campaigns will allow to increase the knowledge about the characterization of the CSOs pollutants. In order to complete the monitoring of the quality of the CSOs, the turbidimeter must be calibrated for the Sathonay-Camp experimental site to assess its performance under real operating conditions and confirm that measurements are possible and reliable by estimating the uncertainties of the method. The convenience of its position (at a point which is representative of the concentration of the overflows) must be validated by improving the knowledge of the settling and resuspension mechanisms at the overflow area with further experimental or numerical tests including the injection of particles.

Finally, a validated numerical model will allow to investigate further design options for the device as, for example, the integration of a sediment trap at the bottom of the stabilization zone to collect the sediments. Other scales of the numerical model could also be used to analyse possible scale effects on the sediment transport and determine relationships between the device efficiency and the inflow discharge rates (and pollution concentrations), if

necessary, including scale factors, similar to what it has been suggested for the monitoring methodology.

Chapter 6

6. REFERENCES

Ahm, M., Thorndahl, S., Nielsen, E.J., Rasmussen, R.M., 2016. Estimation of combined sewer overflow discharge: a software sensor approach based on local water level measurements. Water Sci. Technol. 74, 2683–2696. https://doi.org/10.2166/wst.2016.361

AIAA, 1998. Guide for the Verification and Validation of Computational Fluid Dynamics Simulations.

Andersson, B., Andersson, R., Håkansson, L., Mortensen, M., Sudiyo, R., Van Wachem, B., 2011. Computational fluid dynamics for engineers. Cambridge University Press.

ANSYS, 2016a. ANSYS ICEM CFD Help Manual v17.2.

ANSYS, 2016b. ANSYS CFX-Solver Modeling Guide v17.2.

ANSYS, 2015a. ANSYS Fluent Theory Guide v16.2.

ANSYS, 2015b. ANSYS Fluent User's Guide v16.2.

ANSYS, 2015c. ANSYS Fluent Meshing Guide v16.2.

AU, (Agence d'Urbanisme), 1998. Plan de Prévention des Risques d'inondation. Bassin versant du ruisseau du Ravin. [in French].

Babaali, H., Shamsai, A., Vosoughifar, H., 2014. Computational Modeling of the Hydraulic Jump in the Stilling Basin with Convergence Walls Using CFD Codes. Arab. J. Sci. Eng. 40, 381-395. https://doi.org/10.1007/s13369-014-1466-z

Bagheri, S., Kabiri-Samani, R.A., Heidarpour, M., 2014. Discharge coefficient of rectangular sharp-crested side weirs, Part I: Traditional weir equation. Flow Meas. Instrum. 35, 109-115. https://doi.org/10.1016/j.flowmeasinst.2013.11.005

Barth, T., Jespersen, D., 1989. The design and application of upwind schemes on unstructured meshes, in: 27th Aerospace Sciences Meeting. p. 366.

Bayon, A., Valero, D., García-Bartual, R., Vallés-Morán, F.J., López-Jiménez, P.A., 2016. Performance assessment of OpenFOAM and FLOW-3D in the numerical modeling of a low Reynolds number hydraulic jump. Environ. Model. Softw. 80, 322–335. https://doi.org/10.1016/j.envsoft.2016.02.018

Becouze-Lareure, C., 2010. Caractérisation et estimation des flux de substances prioritaires dans les rejets urbains par temps de pluie sur deux bassins versants expérimentaux. [in French]. INSA Lyon (Lyon, France).

Becouze-Lareure, C., Thiebaud, L., Bazin, C., Namour, P., Breil, P., Perrodin, Y., 2016. Dynamics of toxicity within different compartments of a peri-urban river subject to combined sewer overflow discharges. Sci. Total Environ. 539, 503–514. https://doi.org/10.1016/j.scitotenv.2015.08.128

Bertrand-Krajewski, J.-L., 2012. Short introduction to sediment transport. Lecture for Urban Hydrology. LGCIE, INSA de Lyon, France.

Bertrand-Krajewski, J.-L., Barraud, S., Kouyi, G.L., Torres, A., Lepot, M., 2008. On-line monitoring of particulate pollutant loads in urban sewer systems: Stakes, methods, example of application. [in French]. Houille Blanche 49–57. https://doi.org/10.1051/lhb:2008039

Bertrand-Krajewski, J.-L., Laplace, D., Joannis, C., Chebbo, G., 2000. Mesures en hydrologie urbaine et assainissement. [in French], 1st ed. Technique & Documentation.

Biswas, R., Strawn, R.C., 1998. Tetrahedral and hexahedral mesh adaptation for CFD problems. Appl. Numer. Math. 26, 135–151. https://doi.org/10.1016/S0168-9274(97)00092-5

Borghei, M.S., Kabiri-Samani, R.A., Nekoee, N., 2006. Oblique weir equation using incomplete self-similarity. Can. J. Civ. Eng. 33. https://doi.org/10.1139/l06-071

Borghei, M.S., Parvaneh, A., 2011. Discharge characteristics of a modified oblique side weir in subcritical flow. Flow Meas. Instrum. 22, 370–376. https://doi.org/10.1016/j.flowmeasinst.2011.04.009

Borghei, M.S., Vatannia, Z., Ghodsian, M., Jalili, R.M., 2003. Oblique rectangular sharp-crested weir. Proc. Inst. Civ. Eng. - Water Marit. Eng. 156, 185–191. https://doi.org/10.1680/wame.2003.156.2.185

Carstea, E.M., Bridgeman, J., Baker, A., Reynolds, D.M., 2016. Fluorescence spectroscopy for wastewater monitoring: A review. Water Res. 95, 205–219. https://doi.org/10.1016/j.watres.2016.03.021

Castillo, L.G., Carrillo, J.M., 2015. Experimental and numerical analysis of velocities in plunge pools of free falling spillways, in: E-Proceedings of the 36th IAHR World Congress, 28 June – 3 July 2015, The Hague, the Netherlands.

Castillo, L.G., Carrillo, J.M., García, J.T., Vigueras-Rodríguez, A., 2014a. Numerical Simulations And Laboratory Measurements In Hydraulic Jumps. 11th Int. Conf. Hydroinformatics 2014, New York, USA.

Castillo, L.G., Carrillo, J.M., Sordo-Ward, Á., 2014b. Simulation of overflow nappe impingement jets. J. Hydroinformatics 16, 922. https://doi.org/10.2166/hydro.2014.109

Celik, I.B., Ghia, U., Roache, P.J., Freitas, C.J., Coleman, H., Raad, P.E., 2008. Procedure for Estimation and Reporting of Uncertainty Due to Discretization in CFD Applications. J. Fluids Eng. 130, 078001-1/078001-4. https://doi.org/10.1115/1.2960953

Chanson, H., 1999. The Hydraulics of Open Channel Flow: An Introduction. Butterworth-Heinemann.

Chebbo, G., 1992. Solides des rejets urbains par temps de pluie: caractérisation et traitabilité. [in French]. ENPC (Paris, France).

Chen, H.C., Patel, V.C., 1988. Near-wall turbulence models for complex flows including separation. AIAA J. 26, 641–648.

Chocat, B., Barraud, S., Bertrand-Krajewski, J.-L., 2007. Les eaux pluviales urbaines et les rejets urbains de temps de pluie. [in French]. Tech. l'ingénieur. Gest. des eaux par les Collect. Territ. W6800, 1–17.

Cook, C.B., Richmond, M.C., Serkowski, J.A., Ebner, L.L., 2002. Free-surface computational fluid dynamics modeling of a spillway and tailrace: Case study of the Dalles project. Hydrovision.

Dey, S., Papanicolaou, A., 2008. Sediment threshold under stream flow: A state-of-the-art review. KSCE J. Civ. Eng. 12, 45–60. https://doi.org/10.1007/s12205-008-8045-3

Dey, S., Sarkar, S., Solari, L., 2011. Near-Bed Turbulence Characteristics at the Entrainment Threshold of Sediment Beds. J. Hydraul. Eng. 137, 945–958. https://doi.org/10.1061/(ASCE)HY.1943-7900.0000396

Díaz García, S., 2015. Análisis de los efectos hidráulicos asociados a la colocación de una compuerta inflable sobre un aliviadero mediante modelación física y numérica (CFD). [in Spanish]. Ing. del agua 19, 89–104. https://doi.org/10.4995/ia.2015.3623

Dufresne, M., 2008. La modélisation 3D du transport solide dans les bassins en assainissement: du pilote expérimental à l'ouvrage réel. [in French]. Université Louis Pasteur Strasbourg 1 (Strasbourg, France).

Dufresne, M., Terfous, A., Ghenaim, A., Poulet, J., 2009. CFD Modeling of Solid Separation in Three Combined Sewer. J. Environ. Eng. 135, 776–787. https://doi.org/10.1061/(ASCE)EE.1943-7870.0000017

Dufresne, M., Vazquez, J., Terfous, A., Poulet, J., 2007. Three-dimensional flow measurements and CFD modelling in a storm-water tank, in: NOVATECH'2007, Lyon, France.

Emiroglu, E.M., Kaya, N., Agaccioglu, H., 2010. Discharge Capacity of Labyrinth Side Weir Located on a Straight Channel. J. Irrig. Drain. Eng. 136, 37–46. https://doi.org/10.1061/(asce)ir.1943-4774.0000112

Erpicum, S., Tullis, P.B., Lodomez, M., Archambeau, P., Dewals, J.B., Pirotton, M., 2016. Scale effects in physical piano key weirs models. J. Hydraul. Res. 54, 692–698. https://doi.org/10.1080/00221686.2016.1211562

EUPC, (European Union Parliament and Council), 2013. DIRECTIVE 2013/39/EU OF THE EUROPEAN PARLIAMENT AND OF THE COUNCIL of 12 August 2013 amending Directives 2000/60/EC and 2008/105/EC as regards priority substances in the field of water policy, Official Journal of the European Union. The European Parliament and the Council.

EUPC, (European Union Parliament and Council), 2006. Regulation (EC) no 166/2006 of the European Parliament and of the Council of 18 January 2006 concerning the establishment of a European Pollutant Release and Transfer Register and amending Council Directives 91/689/EEC and 96/61/EC, Official Journal of the European Union. The European Parliament and the Council.

EUPC, (European Union Parliament and Council), 2000. DIRECTIVE 2000/60/EC OF THE EUROPEAN PARLIAMENT AND OF THE COUNCIL of 23 October 2000 establishing a framework for Community action in the field of water policy, Official Journal of the European Communities. The European Parliament and the Council.

Fach, S., Sitzenfrei, R., Rauch, W., 2009. Determining the spill flow discharge of combined sewer overflows using rating curves based on computational fluid dynamics instead of the standard weir equation. Water Sci. Technol. 60, 3035–3043. https://doi.org/10.2166/wst.2009.752

Gilard, O., Gendreau, N., Breil, P., Tschudy, E., 1997. Inondabilite du ruisseau du Ravin et de son bassin versant. Expertise Complementaire. [in French]. Lyon.

Gisonni, C., Hager, W.H., 1997. Short sewer sideweir. J. Irrig. Drain. Eng. 123, 354–363.

Goring, D.G., Nikora, V.I., 2002. Despiking Acoustic Doppler Velocimeter Data. J. Hydraul. Eng. 128, 117–126.

Graf, W.H., 2000. Hydraulique fluviale: écoulement et phénomènes de transport dans les canaux à géométrie simple, 2nd ed. PPUR presses polytechniques.

Gruber, G., Bertrand-Krajewski, J.-L., De Beneditis, J., Hochedlinger, M., Lettl, W., 2005a. Practical aspects, experiences and strategies by using UV/VIS sensors for long-term sewer monitoring, in: 10th International Conference on Urban Drainage, 21-26 August 2005, Copenhagen, Denmark. https://doi.org/10.2166/wpt.2006020

Gruber, G., Winkier, S., Pressi, A., 2005b. Continuous monitoring in sewer networks an aproach for quantification of pollution loads from CSOs into surface water bodies. Water Sci. Technol. 52, 215–223. https://doi.org/10.1016/j.solmat.2004.08.011

Guerber, F., Tabuchi, J., 1992. La dépollution des rejets urbains par temps de pluie : une approche globale. [in French]. La Houille Blanche 6, 443–447.

Habibzadeh, A., Asce, S.M., Wu, S., Ade, F., Rajaratnam, N., Asce, F., Loewen, M.R., 2011. Exploratory Study of Submerged Hydraulic Jumps with Blocks. J. Hydraul. Eng. 137, 2–6. https://doi.org/10.1061/(ASCE)HY.1943-7900.0000347

Habibzadeh, A., Loewen, M.R., Rajaratnam, N., 2014. Mean flow in a submerged hydraulic jump with baffle blocks. J. Eng. Mech. 140, 1–15.

Habibzadeh, A., Loewen, M.R., Rajaratnam, N., 2012. Performance of Baffle Blocks in Submerged Hydraulic Jumps. J. Hydraul. Eng. 138, 902–908. https://doi.org/10.1061/(ASCE)HY.1943-7900.0000587

Hager, H.W., 2010. Wastewater Hydraulics - Theory and Practice, 2nd ed. Springer.

Hirsch, C., 2007. Numerical computation of internal and external flows: The fundamentals of computational fluid dynamics. Elsevier.

Hirt, C.W., Nichols, B.D., 1981. Volume of fluid (VOF) method for the dynamics of free boundaries. J. Comput. Phys. 39, 201–225.

Hofer, T., Gamerith, V., Muschalla, D., Gruber, G., 2013. A sampling approach for storm events with focus on micropollutants at combined sewer overflows, in: NOVATECH'2013, Lyon, France.

House, A.M., Ellis, B.J., Herricks, E.E., Hvitved-Jacobsen, T., Seager, J., Lijklema, L., Aalderink, H., Clifforde, T.I., 1993. Urban Drainage -- Impacts on Receiving Water Quality. Water Sci. Technol. 27, 117–158.

IPCC, (Intergovernmental Panel on Climate Change), 2014. Climate change 2014. Synthesis report., Climate Change 2014: Synthesis Report. Contribution of Working Groups I, II and III to the Fifth Assessment Report of the Intergovernmental Panel on Climate Change. Geneva, Switzerland. https://doi.org/10.1017/CBO9781107415324

Isel, S., Dufresne, M., Fischer, M., Vazquez, J., 2014. Assessment of the overflow discharge in complex CSO chambers with water level measurements -- On-site validation of a CFD-based methodology. Flow Meas. Instrum. 35, 39–43. https://doi.org/https://doi.org/10.1016/j.flowmeasinst.2013.11.003

Isenmann, G., 2016. Approche Euler-Lagrange pour la modélisation du transport solide dans les ouvrages de décantation. [in French]. Université de Strasbourg (Strasbourg, France).

Issa, R.I., 1986. Solution of the implicitly discretised fluid flow equations by operator-splitting. J. Comput. Phys. 62, 40–65.

James, M.R., Robson, S., 2012. Straightforward reconstruction of 3D surfaces and topography with a camera : Accuracy and geoscience application. J. Geophys. Res. 117, 1–17. https://doi.org/10.1029/2011JF002289

Jarman, D.S., Faram, M.G., Butler, D., Tabor, G., Stovin, V.R., Burt, D., Throp, E., 2008. Computational fluid dynamics as a tool for urban drainage system analysis : A review of applications and best practice, in: 11th International Conference on Urban Drainage, Edinburgh, Scotland UK.

Javan, M., Eghbalzadeh, A., 2013. 2D numerical simulation of submerged hydraulic jumps. Appl. Math. Model. 37, 6661–6669. https://doi.org/10.1016/j.apm.2012.12.016

JCGM, (Joint Committee for Guides in Metrology), 2008. Evaluation of measurement data - Guide to the expression of uncertainty in measurement. International Organization for Standardization.

Jesson, M., Sterling, M., Bridgeman, J., 2013. Despiking velocity time-series — Optimisation through the combination of spike detection and replacement methods. Flow Meas. Instrum. 30, 45–51. https://doi.org/10.1016/j.flowmeasinst.2013.01.007

Joannis, C., Vazquez, J., Zug, M., 2009. Modélisation et métrologie des déversoirs d'orage. [in French]. Tech. l'ingénieur Gest. des eaux par les Collect. Territ. W6902, 1–18.

Jongen, T., 1992. Simulation and modeling of turbulent incompressible fluid flows. EPFL (Lausanne, Switzeland). https://doi.org/10.5075/epfl-thesis-1758

Kabiri-Samani, R.A., 2010. Analytical Approach for Flow over an Oblique Weir. Sci. Iran. 17, 107–117.

Kader, B.A., 1981. Temperature and concentration profiles in fully turbulent boundary layers. Int. J. Heat Mass Transf. 24, 1541–1544.

Launay, M., Dittmer, U., Steinmetz, H., 2016. Contribution of combined sewer overflows to micropollutant loads discharged into urban receiving water, in: NOVATECH'2016, Lyon, France.

Launder, B.E., Reece, G.J., Rodi, W., 1975. Progress in the development of a Reynolds-stress turbulence closure. J. Fluid Mech. 68, 537–566.

Launder, B.E., Spalding, D.B., 1972. Mathematical models of turbulence. Academic press.

Lepot, M., Torres, A., Hofer, T., Caradot, N., Gruber, G., Aubin, J.B., Bertrand-Krajewski, J.L., 2016. Calibration of UV/Vis spectrophotometers: A review and comparison of different methods to estimate TSS and total and dissolved COD concentrations in sewers, WWTPs and rivers. Water Res. 101, 519–534. https://doi.org/10.1016/j.watres.2016.05.070

Lipeme Kouyi, G., 2004. Expérimentations et modélisations tridimensionnelles de l'hydrodynamique et de la separation particulaire dans les déversoirs d'orage. [in French]. Université de Strasbourg 1 (Strasbourg, France).

Lipeme Kouyi, G., Arias, L., Barraud, S., Bertrand-Krajewski, J.-L., 2010. CFD Modelling of flows in a large stormwater detention and settling basin, in: NOVATECH 2010, Lyon, France.

Lipeme Kouyi, G., Bret, P., Didier, J.-M., Chocat, B., Billat, C., 2011. The use of CFD modelling to optimise measurement of overflow rates in a downstream-controlled dual-overflow structure. Water Sci. Technol. 64, 521–527. https://doi.org/10.2166/wst.2011.162

Lipeme Kouyi, G., Vazquez, J., Gallin, Y., Rollet, D., Sadowski, G.A., 2005. Use of 3D modelling and several ultrasound sensors to assess overflow rate. Water Sci. Technol. 51, 187–194.

Madoux-Humery, A.S., Dorner, S., Sauvé, S., Aboulfadl, K., Galarneau, M., Servais, P., Prévost, M., 2013. Temporal variability of combined sewer overflow contaminants: Evaluation of wastewater micropollutants as tracers of fecal contamination. Water Res. 47, 4370–4382. https://doi.org/10.1016/j.watres.2013.04.030

Malvern Instruments, 2007. Mastersizer 2000 User Manual.

Maté Marín, A., Lipeme Kouyi, G., Rivière, N., 2017. Uncertainty analysis of the DSM-flux stage-discharge relationship to measure CSOs: comparison of GUM and Monte Carlo approaches, in: 14th IWA/IAHR International Conference on Urban Drainage, 10-15 September 2017, Prague, Czech Republic.

Maté Marín, A., Rivière, N., Lipeme Kouyi, G., 2018. DSM-flux: A new technology for reliable Combined Sewer Overflow discharge monitoring with low uncertainties. J. Environ. Manage. 215. https://doi.org/10.1016/j.jenvman.2018.03.043

MDDELCC, (Ministère du Développement Durable de l'Environnement et de la Lutte contre les Changements Climatiques), 2014. Regulation respecting municipal wastewater treatment works, Environment Quality Act (chapter Q-2, r. 34.1). Ministère du Développement Durable de l'Environnement et de la Lutte contre les Changements Climatiques.

MEDDE, (Ministère de l'écologie du développement durable et de l'energie), 2015a. Arrêté du 21 juillet 2015 relatif aux systèmes d'assainissement collectif et aux installations d'assainissement non collectif, à l'exception des installations d'assainissement non collectif recevant une charge brute de pollution organique inférieure ou ég, Journal Officiel de la République Française. Ministère de l'écologie, du développement durable et de l'energie.

MEDDE, (Ministère de l'écologie du développement durable et de l'energie), 2015b. Note technique du 7 septembre 2015 relative à lamise en oeuvre de certaines dispositions de l'arrêté du 21 juillet 2015. [in French]. NOR : DEVL1519953N. MINISTÈRE DE L'ÉCOLOGIE, DU DÉVELOPPEMENT DURABLE ET DE L'ÉNERGIE.

MEDDE, (Ministère de l'écologie du développement durable et de l'energie), 2015c. Arrêté du 27 juillet 2015 modifiant l'arrêté du 25 janvier 2010 relatif aux méthodes et critères d'évaluation de l'état écologique, de l'état chimique et du potentiel écologique des eaux de surface pris en application des articles R. 212-10, R. 212-11 et , Journal Officiel de la République Française. Ministère de l'écologie, du développement durable et de l'energie.

Mehdizadeh, A., Firoozabadi, B., Sherif, S.A., 2010. Particle Trajectory Study in Submerged Flows With Baffles Using ν[sup 2]−f and k−ε Turbulence Models. J. Fluids Eng. 132, 051105/1-10. https://doi.org/10.1115/1.4001557

Melching, S.C., 2006. Wastewater Quality Monitoring and Treatment. John Wiley & Sons, Ltd, pp. 119–144. https://doi.org/10.1002/9780470058725.ch8

Mignot, E., Bonakdari, H., Kouyi, G.L., Bessette, A., Rivière, N., 2012. Experiments and 3D simulations of flow structures in junctions and of their influence on location of flowmeters, in: 12th International Conference on Urban Drainage, 11-16 September 2011, Porto Alegre/Brazil. https://doi.org/10.2166/wst.2012.319

MJC, (Ministry of Justice of Canada), 2015. Wastewater Systems Effluent Regulations. SOR/2012-139. Ministry of Justice of Canada.

Momplot, A., 2014. Modélisation tridimensionnelle des écoulements en réseau d'assainissement: Evaluation des modèles RANS à travers l'étude des écoulements au droit d'ouvrages spéciaux. INSA-Lyon (Lyon, France).

Momplot, A., Lipeme Kouyi, G., Mignot, E., Rivière, N., Bertrand-Krajewski, J.L., 2017. Typology of the flow structures in dividing open channel flows. J. Hydraul. Res. 55, 63–71. https://doi.org/10.1080/00221686.2016.1212409

Momplot, A., Visiedo, R., Volte, E., Cournoyer, B., Lipeme Kouyi, G., 2014. Best CSOs monitoring and management: the OMMD technology, in: 13th International Conference on Urban Drainage, 7-12 September 2014, Sarawak, Malaysia.

Moriasi, D.N., Arnold, J.G., Liew, M.W. Van, Bingner, R.L., Harmel, R.D., Veith, T.L., 2007. Model Evaluation Guidelines for Systematic Quantification of Accuracy in Watershed Simulations. Trans. ASABE 50, 885–900. https://doi.org/10.13031/2013.23153

Muste, M., Hauet, A., Fujita, I., Legout, C., Ho, H., 2014. Capabilities of Large-scale Particle Image Velocimetry to characterize shallow free-surface flows. Adv. Water Resour. 70, 160–171. https://doi.org/10.1016/j.advwatres.2014.04.004

Muste, M., Lee, K., Bertrand-Krajewski, J.-L., 2012. Standardized uncertainty analysis for hydrometry: a review of relevant approaches and implementation examples. Hydrol. Sci. J. 57, 643–667. https://doi.org/10.1080/02626667.2012.675064

Nash, J.E., Sutcliffe, J. V, 1970. River flow forecasting through conceptual models part I --- A discussion of principles. J. Hydrol. 10. https://doi.org/10.1016/0022-1694(70)90255-6

Nortek, 2015. ADV Vectrino Comprehensive Manual.

OME, (Ontario Ministry of Environment), 1994. Guideline F-5 - Levels of treatment for municipal and private sewage treatment works discharging to surface waters, Ontario Water Resources Act, RSO 1990, Section 53. Ontario Ministry of Environment.

Orszag, S.A., Yakhot, V., Flannery, W.S., Boysan, F., Choudhury, D., Maruzewski, J., 1993. Renormalization Group Modeling and Turbulence Simulations, in: International Conference on Near-Wall Turbulent Flows, Tempe, AZ.

Ozen, M., 2014. ANSYS Meshing Workshop [WWW Document]. URL https://www.ozeninc.com/wp-content/uploads/2014/11/MESHING_WORKSHOP_2014.pdf (accessed 2.11.18).

Pandey, R., Mittal, K.S., Choudhary, M.K., 2016. Flow Characteristics of Sharp Crested Rectangular Weir: A Review. Int. J. Innov. Res. Sci. Eng. Technol. 3, 171–178.

Passerat, J., Ouattara, K.N., Mouchel, J.-M., Rocher, V., Servais, P., 2011. Impact of an intense combined sewer overflow event on the microbiological water quality of the Seine River. Water Res. 45, 893–903. https://doi.org/https://doi.org/10.1016/j.watres.2010.09.024

Peakall, J., Warburton, J., 1996. Surface tension in small hydraulic river models - the significance of the Weber number. J. Hydrol. (New Zealand) 35, 199–212.

Phillips, J.P., Chalmers, T.A., Gray, L.J., Kolpin, W.D., Foreman, T.W., Wall, R.G., 2012. Combined Sewer Overflows: An Environmental Source of Hormones and Wastewater Micropollutants. Environ. Sci. Technol. 46, 5336–5343. https://doi.org/10.1021/es3001294

Ramamurthy, S.A., Qu, J., Vo, D., 2006. Nonlinear PLS Method for Side Weir Flows. J. Irrig. Drain. Eng. 132, 486–489. https://doi.org/10.1061/(ASCE)0733-9437(2006)132:5(486)

Rammal, M., 2016. Comparaison de différents scenarii de production de matières en suspension dans un réseau unitaire sur la base d'un modèle hydrodynamique adapté. [in French]. Ecole des Ponts ParisTech - Université Paris Est (Paris, France).

Regueiro-picallo, M., Anta, J., Suárez, J., Puertas, J., Jácome, A., Naves, J., 2018. Characterization of sediments during transport of solids in circular sewer pipes. Water Sci. Technol. in press, 1–8. https://doi.org/10.2166/wst.2018.055

Regueiro-picallo, M., Naves, J., Anta, J., Suárez, J., 2017. Monitoring accumulation sediment characteristics in full scale sewer physical model with urban wastewater. Water Sci. Technol. 76, 115–123. https://doi.org/10.2166/wst.2017.118

Rehbock, T., 1929. Wassermessung mit sharfkantigen uberfallwehren. [in German]. Zeitschrift des vereins Dtsch. ingenieure 73, 817–826.

Roache, P.J., 1997. Quantification of Uncertainty in Computational Fluid Dynamics. Annu. Rev. Fluid Mech. 29, 123–160. https://doi.org/10.1146/annurev.fluid.29.1.123

Rodi, W., 2017. Turbulence Modeling and Simulation in Hydraulics: A Historical Review. J. Hydraul. Eng. 143, 03117001. https://doi.org/10.1061/(ASCE)HY.1943-7900.0001288

Sabarots Gerbec, M., Badano, N.D., Menéndez, A.N., 2014. Estudio de optimización hidraúlica del vertedero Gatun mediante modelación CFD. [in Spanish], in: Xxv Congreso Latinoamericano De Hidráulica, Agosto 2014, Santiago, Chile.

Sebastian, C., 2013. Bassin de retenue des eaux pluviales en milieu urbain: performance en matière de piégeage des micropolluants. [in French]. INSA-Lyon (Lyon, France).

Smith, D.C., 1988. Outlet Structure Design for Conduits and Tunnels. J. Waterw. Port, Coastal, Ocean Eng. 114, 503–515. https://doi.org/{10.1061/(ASCE)0733-950X(1988)114:4(503)}URL

Tao, W., Bays, J.S., Meyer, D., Smardon, R.C., Levy, Z.F., 2014. Constructed wetlands for treatment of combined sewer overflow in the US: A review of design challenges and application status. Water (Switzerland) 6, 3362–3385. https://doi.org/10.3390/w6113362

Truchot, C.M., Chocat, B., Cathelain, M., Mares, A., Mouchel, M.J., 1994. La pollution due aux rejets urbains par temps de pluie: impacts sur les milieux récepteurs. [in French]. La Houille Blanche 97–105. https://doi.org/10.1051/lhb/1994012

UN, (United Nations), 2018. World Urbanization Prospects: The 2018 Revision. Key Facts. https://doi.org/doi.org/10.1017/CBO9781107415324.004

UN, (United Nations), 2017a. The United Nations World Water Development Report 2017: Wastewater, The Untapped Resource. World Water Assessment Programme. Paris.

UN, (United Nations), 2017b. World Population Prospects: The 2017 Revision, Key Findings and Advance Tables. (No. ESA/P/WP/248.). New York.

US-EPA, (United States Environmental Protection Agency), 1994. Combined Sewer Overflow (CSO) Control Policy. FRL-4732-7. United States Environmental Protection Agency.

Valero, D., Bung, ; D B, Crookston, B.M., Asce, M., 2018. Energy Dissipation of a Type III Basin under Design and Adverse Conditions for Stepped and Smooth Spillways. J. Hydraul. Eng. 144. https://doi.org/10.1061/(ASCE)HY.1943-7900.0001482

Valero, D., García-Bartual, R., Marco, J., 2014. Optimisation of Stilling Basin Chute Blocks Using a Calibrated Multiphase RANS Model, in: 5th International Junior Researcher and Engineer Workshop on Hydraulic Structures, 28-30 August 2014, Spa, Belgium.

Versini, A.P., Hannouche, A., Joannis, C., Chebbo, G.A., 2015. Guide technique - Comment estimer les incertitudes affectant les mesures de concentrations et de flux polluants en réseau d'assainissement. [in French]. Agence Nationale de la Recherche.

Versteeg, H.K., Malalasekera, W., 2007. An introduction to computational fluid dynamics: the finite volume method, 2nd ed. Pearson Education.

Viviano, G., Valsecchi, S., Polesello, S., Capodaglio, A., Tartari, G., Salerno, F., 2017. Combined Use of Caffeine and Turbidity to Evaluate the Impact of CSOs on River Water Quality. Water, Air, Soil Pollut. 228. https://doi.org/10.1007/s11270-017-3505-3

Volte, E., Visiedo, R., Lipeme Kouyi, G., 2013. Construction for monitoring and controling the flow and the quality of effluents in a discharge manifold. WO2013083932A1.

Voulgaris, G., Trowbridge, J.H., 1998. Evaluation of the acoustic Doppler velocimeter (ADV) for turbulence measurements. J. Atmos. Ocean. Technol. 15, 272–289.

Wahl, T.L., Goring, D.G., Nikora, V.I., 2003. Discussions and closures of '"Despiking Acoustic Doppler Velocimeter Data"' by Derek G. Goring and Vladimir I. Nikora January 2002, Vol. 128, No. 1, pp. 117–126. J. Hydraul. Eng. 129, 484–487.

Walters, D.K., Wolgemuth, N.M., 2009. A new interface-capturing discretization scheme for numerical solution of the volume fraction equation in two-phase flows. Int. J. Numer. methods fluids 60, 893–918.

Weyrauch, P., Matzinger, A., Pawlowsky-Reusing, E., Plume, S., Seggern, von D., Heinzmann, B., Schroeder, K., Rouault, P., 2010. Contribution of combined sewer overflows to trace contaminant loads in urban streams. Water Res. 44, 4451–4462. https://doi.org/https://doi.org/10.1016/j.watres.2010.06.011

Witt, A., Gulliver, J., Shen, L., 2015. Simulating air entrainment and vortex dynamics in a hydraulic jump. Int. J. Multiph. Flow 72, 165–180. https://doi.org/10.1016/j.ijmultiphaseflow.2015.02.012

Wolfshtein, M., 1969. The velocity and temperature distribution in one-dimensional flow with turbulence augmentation and pressure gradient. Int. J. Heat Mass Transf. 12, 301–318.

Wu, S., Rajaratnam, N., 1995. Effect of baffles on submerged flows. J. Hydraul. Eng. 121, 644-652.

Yan, H., 2013. Experiments and 3D modelling of hydrodynamics, sediment transport, settling and resuspension under unsteady conditions in an urban stormwater detention basin. INSA-Lyon (Lyon, France).

Yan, H., Lipeme Kouyi, G., Bertrand-Krajewski, J.-L., 2011. Modélisation numérique 3d des écoulements turbulents à surface libre charges en polluants particulaires dans un bassin de retenue- décantation des eaux pluviales. La Houille Blanche 5, 39–43. https://doi.org/10.1051/lhb/2011051

Yan, H., Lipeme Kouyi, G., Gonzalez-Merchan, C., Becouze-Lareure, C., Sebastian, C., Barraud, S., Bertrand-Krajewski, J.L., 2014. Computational fluid dynamics modelling of flow and particulate contaminants sedimentation in an urban stormwater detention and settling basin. Environ. Sci. Pollut. Res. 21, 5347–5356. https://doi.org/10.1007/s11356-013-2455-6

Zhang, X., Yuan, L., Yan, P., Li, J., He, X., 2015. Rectangular sharp-crested weir calibration for low head and clinging flow regime. Irrig. Sci. 33, 131–139. https://doi.org/10.1007/s00271-014-0453-1

Zhu, X., Miguet, S., Lipeme Kouyi, G., 2017. Application of Large Scale Particle Image Velocimetry to measure surface velocity field in a stormwater detention basin and to validate CFD model, in: 14th IWA/IAHR International Conference on Urban Drainage, 10-15 September 2017, Prague, Czech Republic.

Chapter 7

7. APPENDICES

Structure of the appendices:

7.1. APPENDICES OF CHAPTER 2

- 7.1.1. The small-scale DSM-flux dimensions
- 7.1.2. The small-scale physical model experimental set-up
- 7.1.3. The small-scale numerical models and computational meshes
- 7.1.4. The initial large-scale DSM-flux dimensions
- 7.1.5. The modified large-scale DSM-flux dimensions
- 7.1.6. The computational mesh of the large-scale numerical models

7.2. APPENDICES OF CHAPTER 3

- 7.2.1.The Sathonay-Camp experimental site hydrographs

7.3. APPENDICES OF CHAPTER 4

- 7.3.1. <u'v'> Reynolds stresses at the near-bottom region of the physical model
- 7.3.2. <u'v'> Reynolds stresses at the near-surface region of the physical model
- 7.3.3. <u'w'> Reynolds stresses at the near-bottom region of the physical model
- 7.3.4. <u'w'> Reynolds stresses at the near-surface region of the physical model
- 7.3.5. <uv> velocity fields at the near-bottom region of the small-scale numerical model under low flow conditions
- 7.3.6. <uv> velocity fields at the near-surface region of the small-scale numerical model under lower flow conditions
- 7.3.7. <uv> velocity fields at the near-bottom region of the small-scale numerical model under higher flow conditions
- 7.3.8. <uv> velocity fields at the near-surface region of the small-scale numerical model under higher flow conditions
- 7.3.9. Variability and uncertainties of velocity and turbulence data

APPENDICES OF CHAPTER 2

7.1.1. The small-scale DSM-flux dimensions

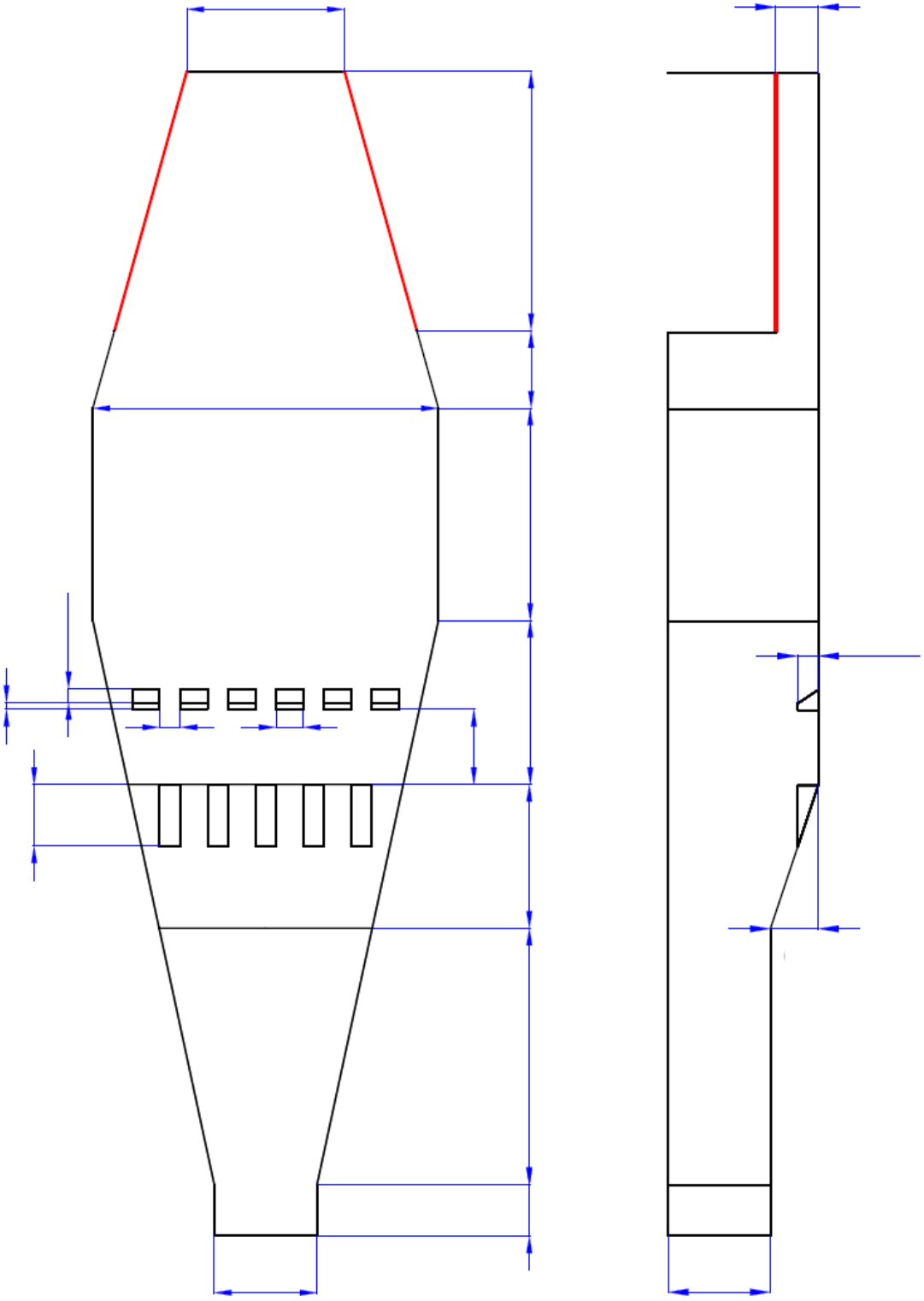

Dimensions have been removed from the public version for confidentiality reasons. Contact the author for further information. Weir crests in red.

7.1.2. The small-scale physical model experimental set-up

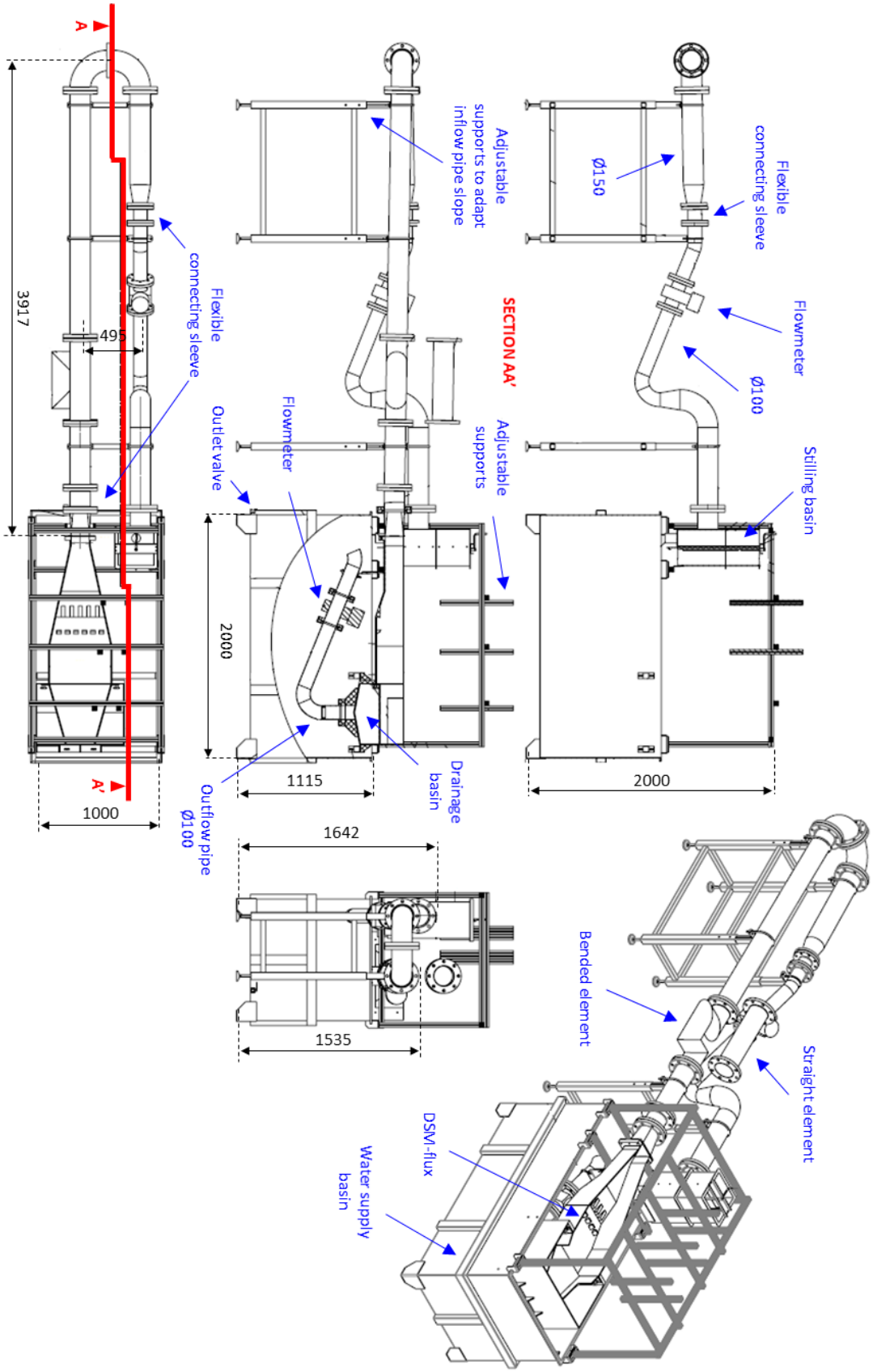

Dimensions in millimetres.

7.1.3. The small-scale numerical models and computational meshes

Horizontal view of the acceleration and dissipation areas

Model SM-A

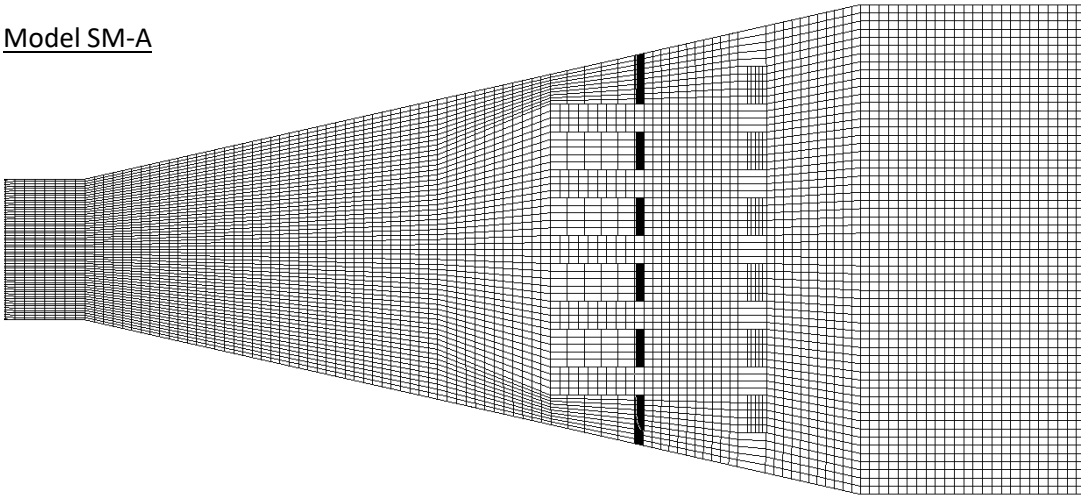

Model SM-B

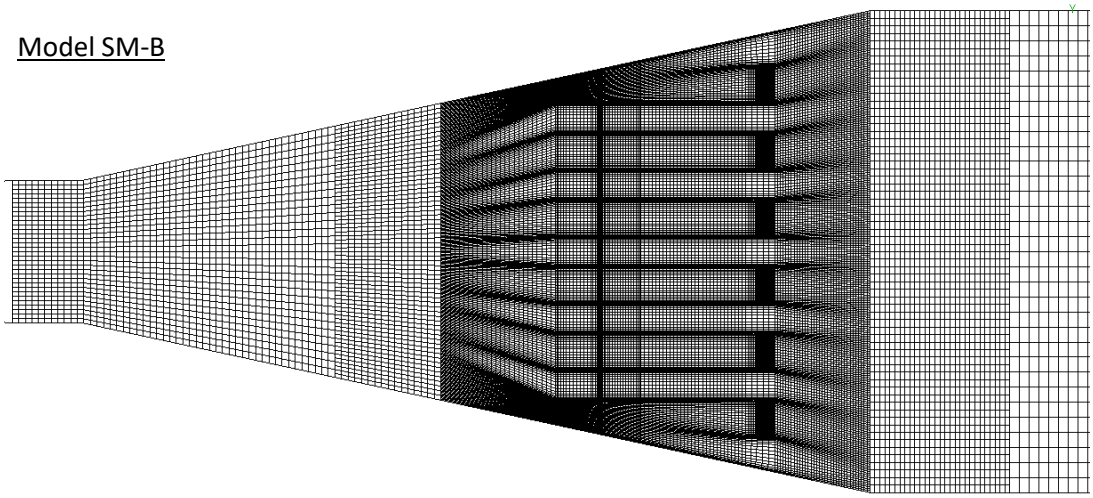

Model SM-C

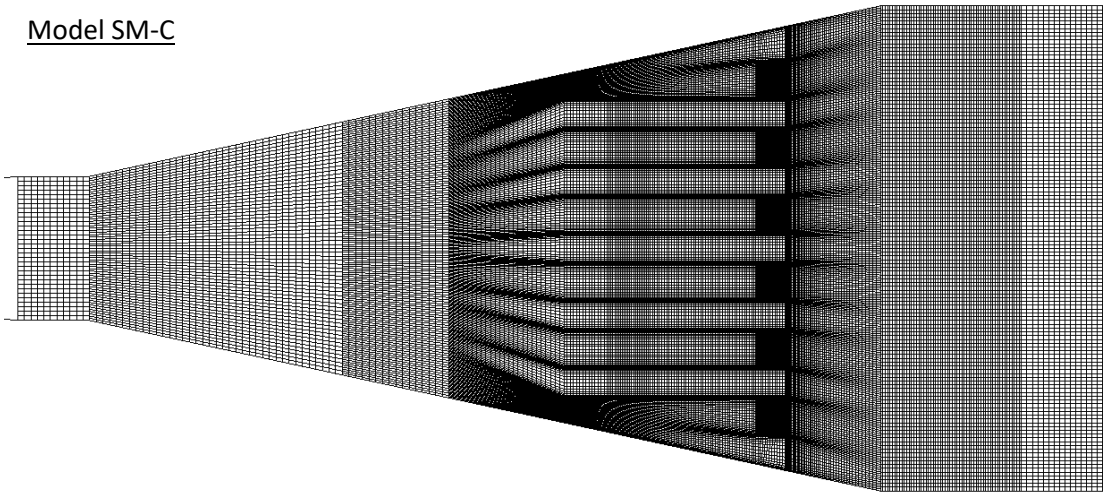

Profile view of the dissipators

Inlet

Model SM-A

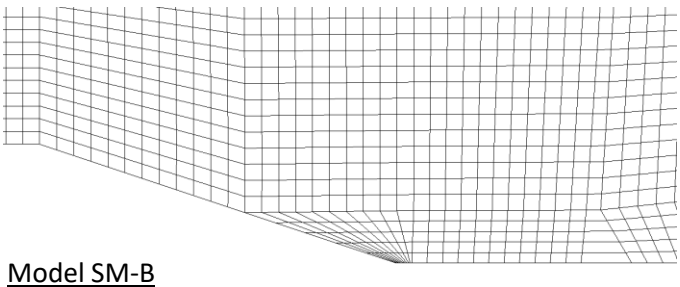

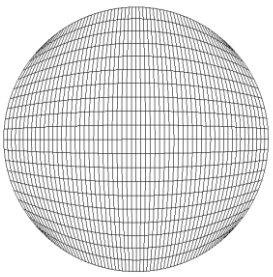

Model SM-B

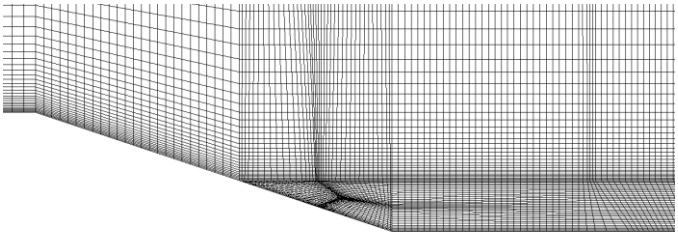

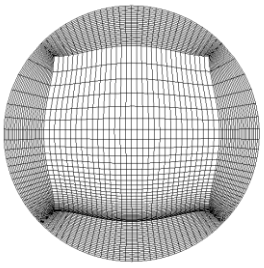

Model SM-C

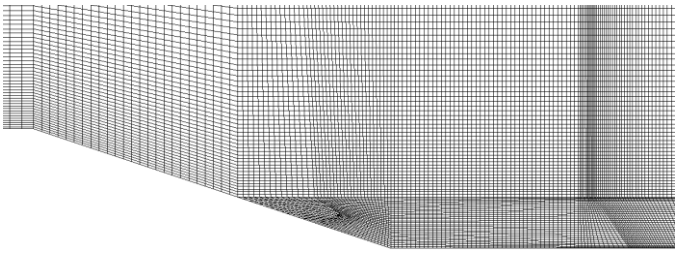

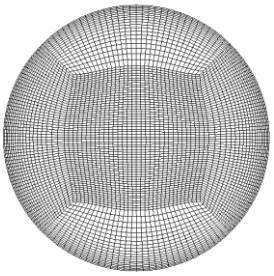

Cross-section at half length of the transition

Model SM-A

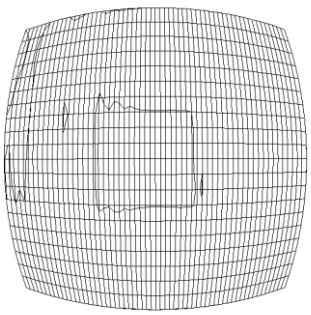

Model SM-B

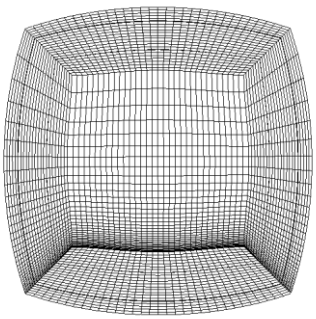

Model SM-C

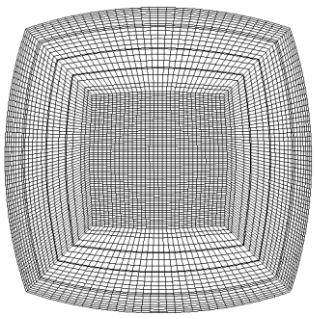

Profile view of the dissipators

Model SM-A

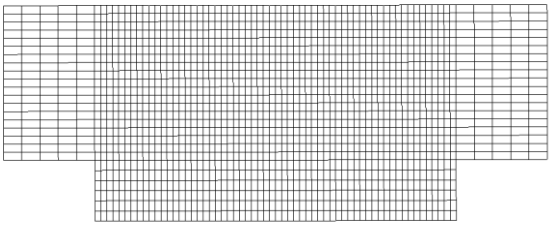

Model SM-B

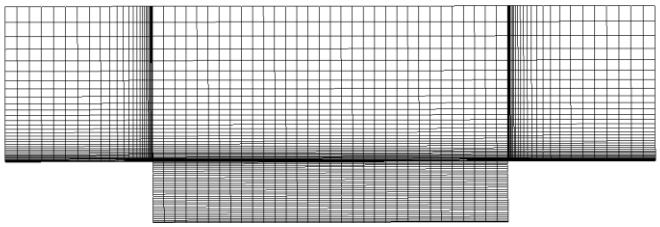

Model SM-C

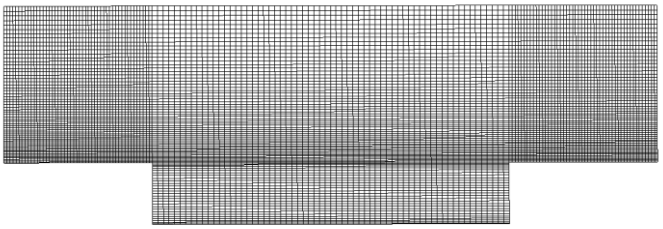

Horizontal view of the overflow area and outlets

Model SM-A

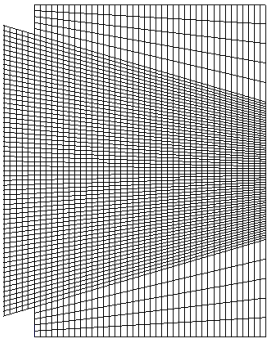

Model SM-B

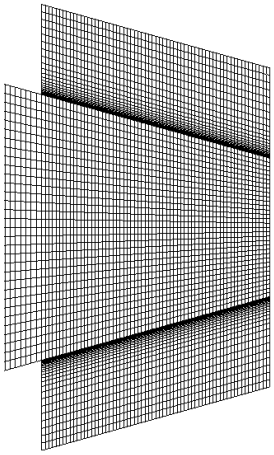

Model SM-C

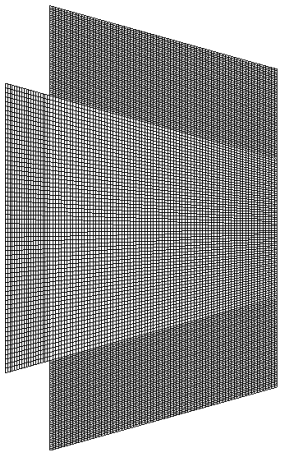

7.1.4. The initial large-scale DSM-flux dimensions

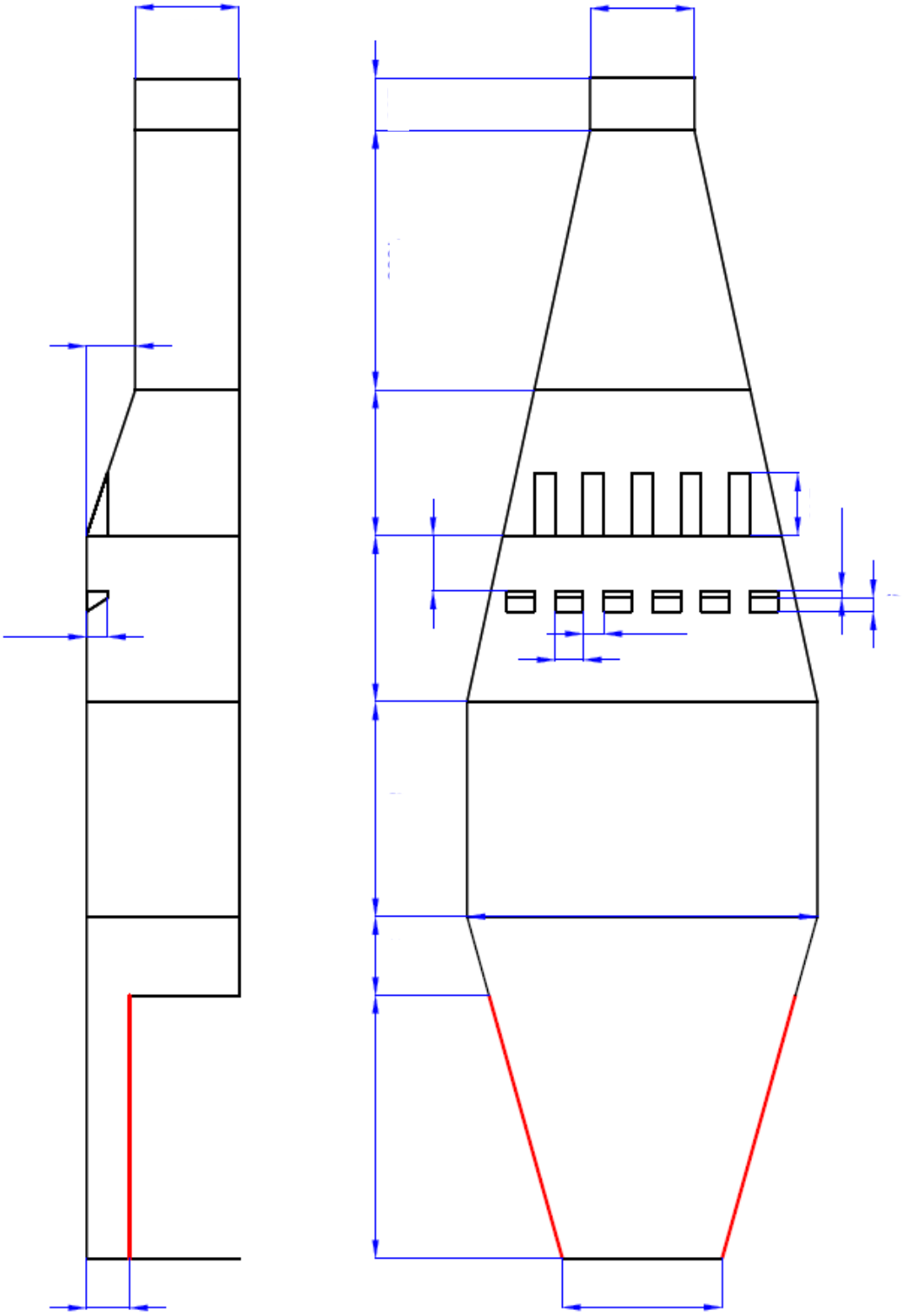

Dimensions have been removed from the public version for confidentiality reasons. Contact the author for further information. Weir crests in red.

7.1.5. The modified large-scale DSM-flux dimensions

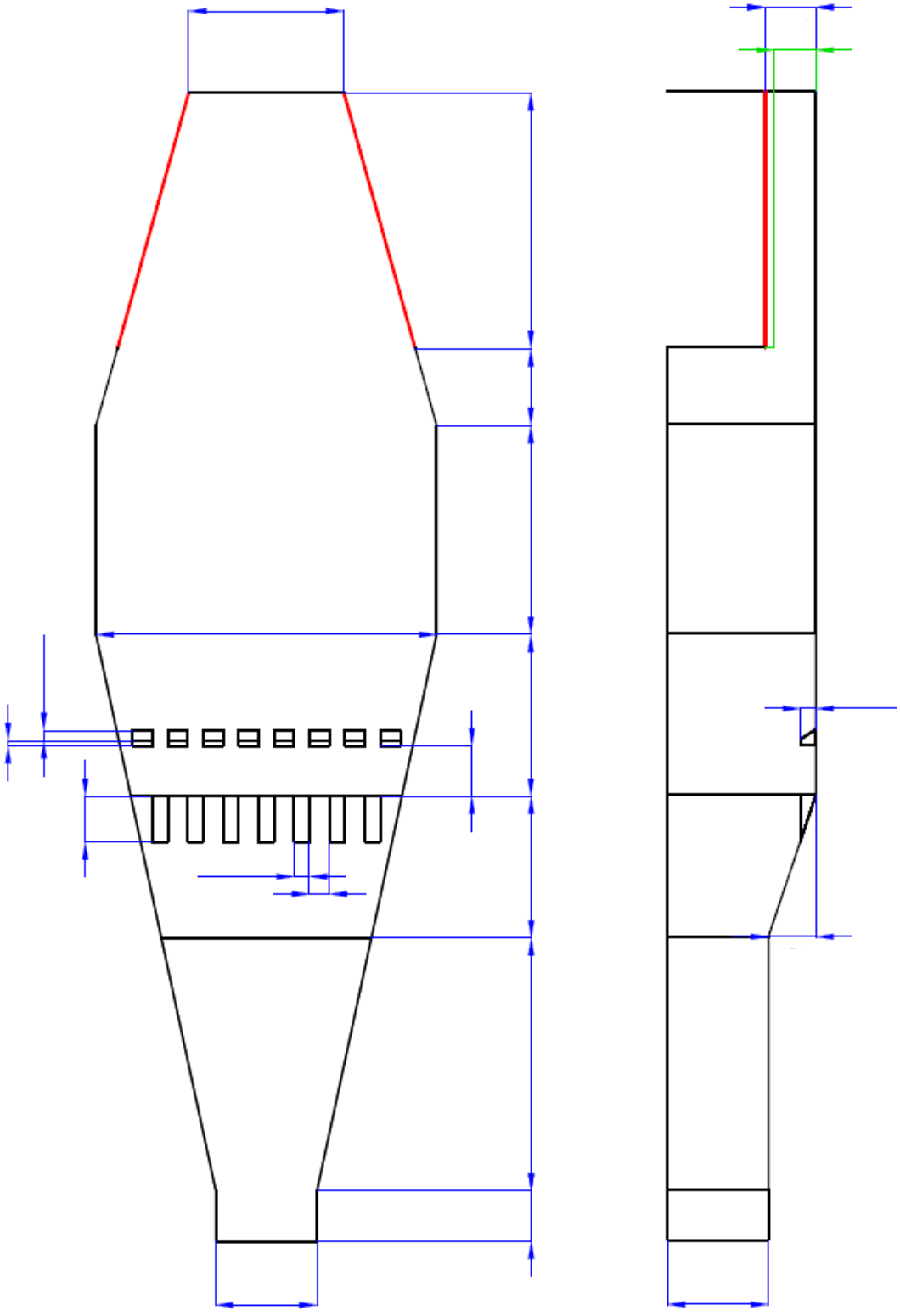

Dimensions have been removed from the public version for confidentiality reasons. Contact the author for further information. Weir crests in red for the field prototype (alternative design 2). Indicated in green the weir height for alternative design 1.

7.1.6. The computational mesh of the large-scale numerical models

Horizontal view of the acceleration and dissipation areas

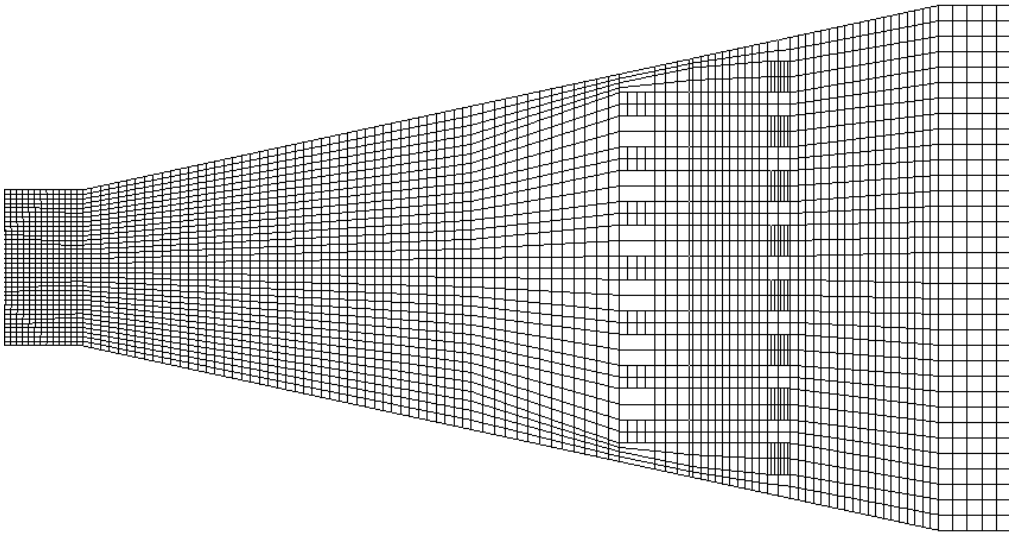

Profile view of the dissipators

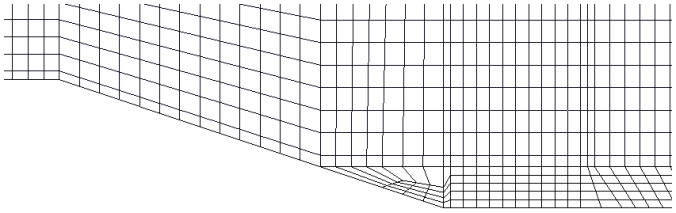

Horizontal view of the overflow area and outlets

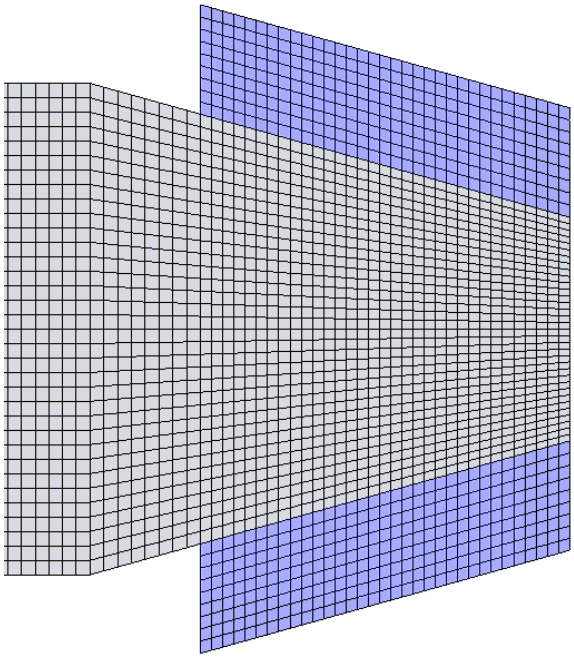

Cross-section of the connection with the inflow pipe: manhole (left) or transition (right)

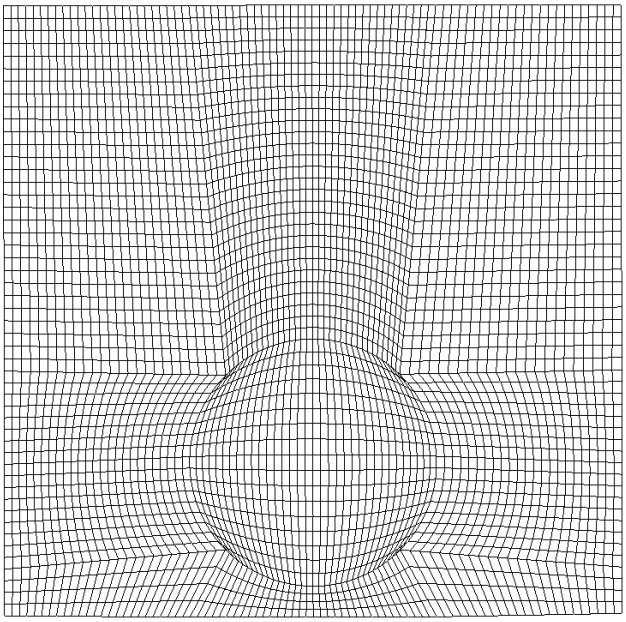

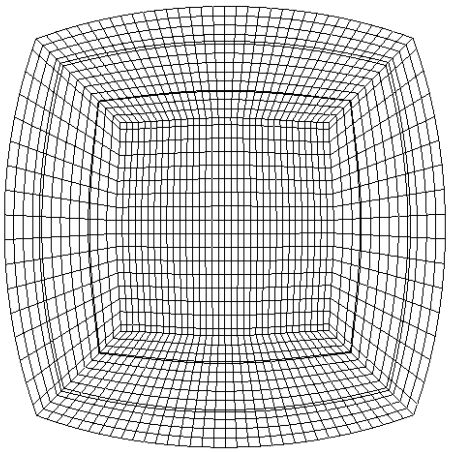

Inlet (model LM-A)

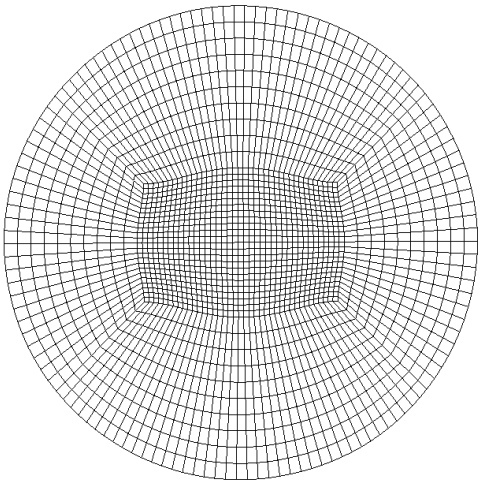

Inlet (models LM-B and LM-C)

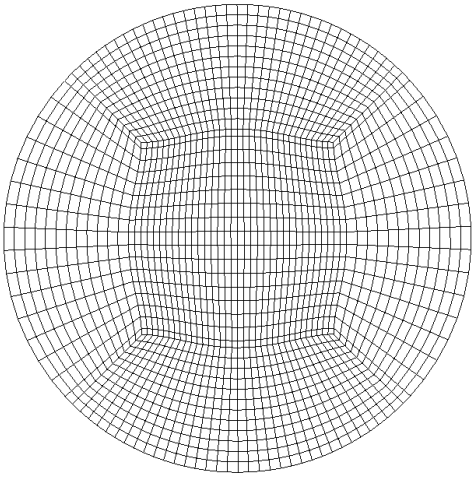

Cross-section at the overflow area

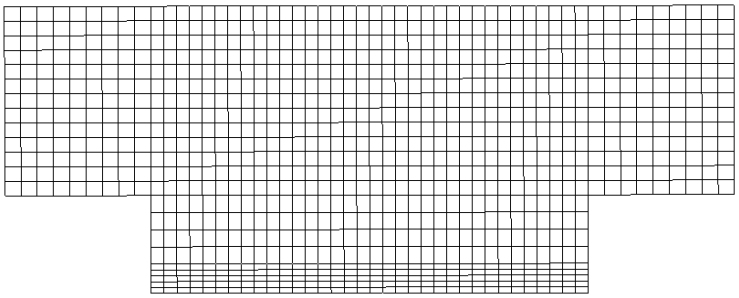

APPENDICES OF CHAPTER 3

7.2.1. The Sathonay-Camp experimental site hydrographs

EVENT 1

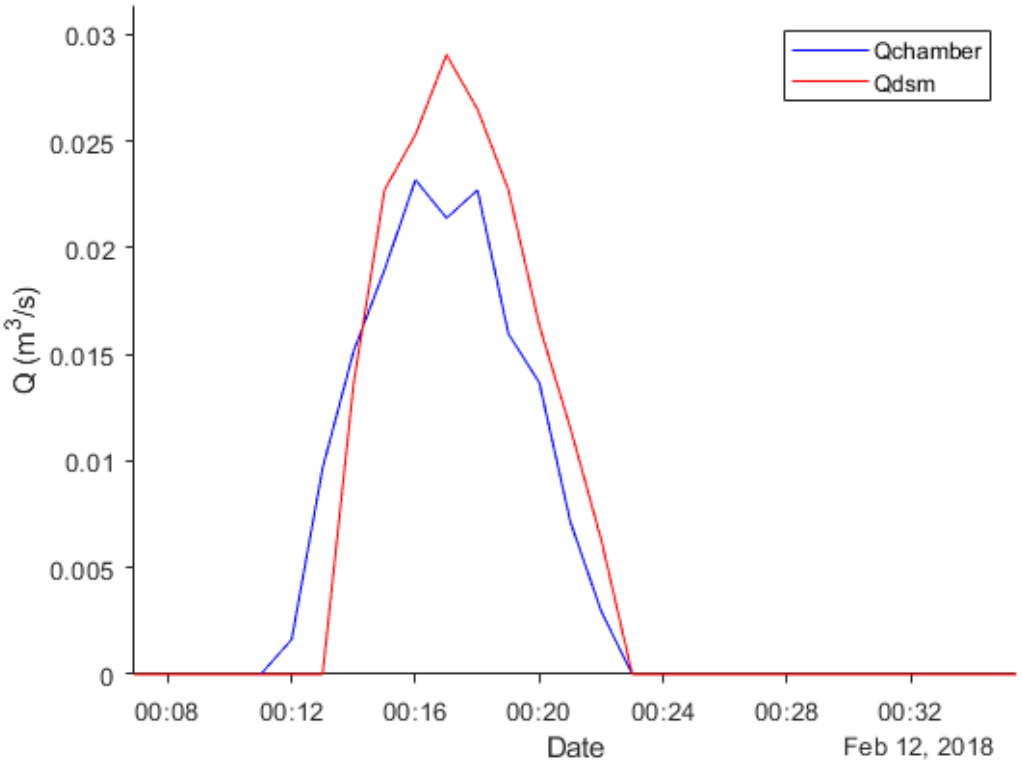

EVENT 2

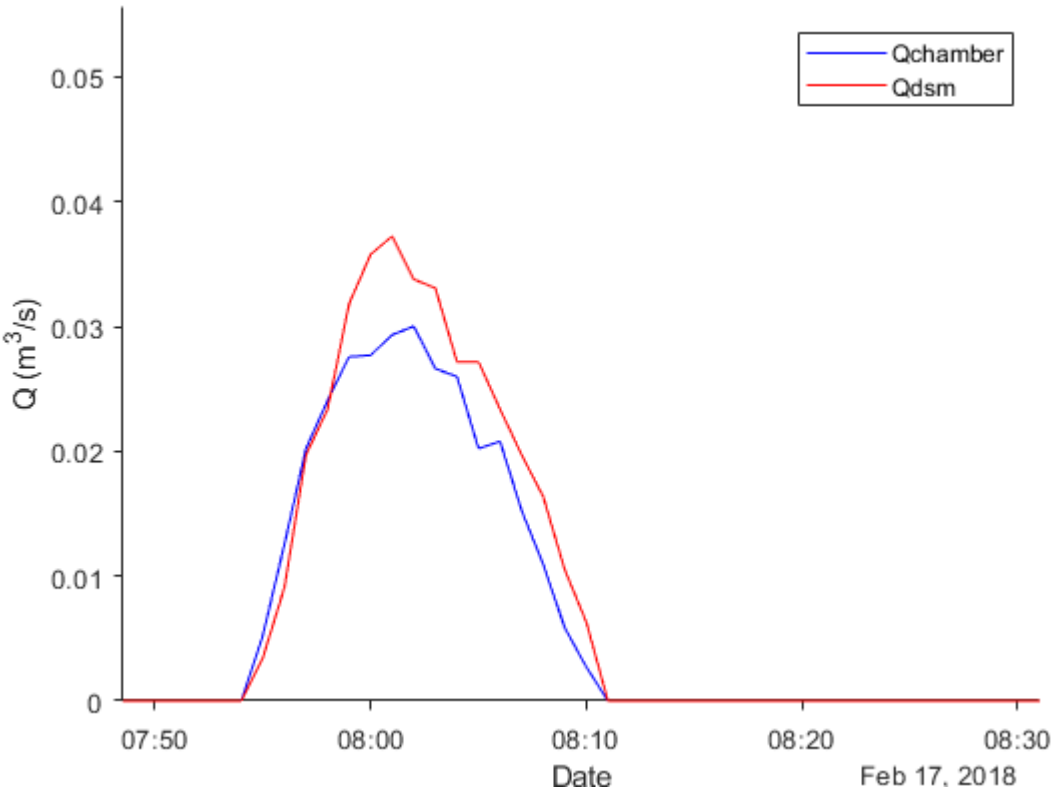

EVENT 3

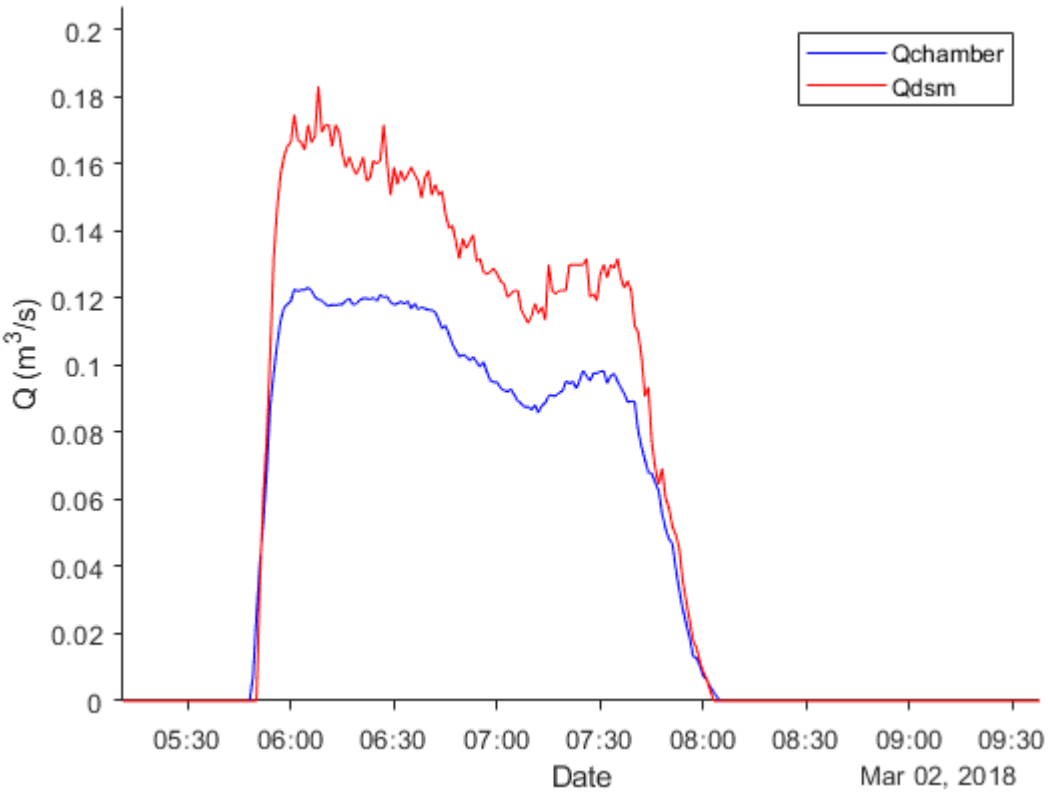

EVENT 4

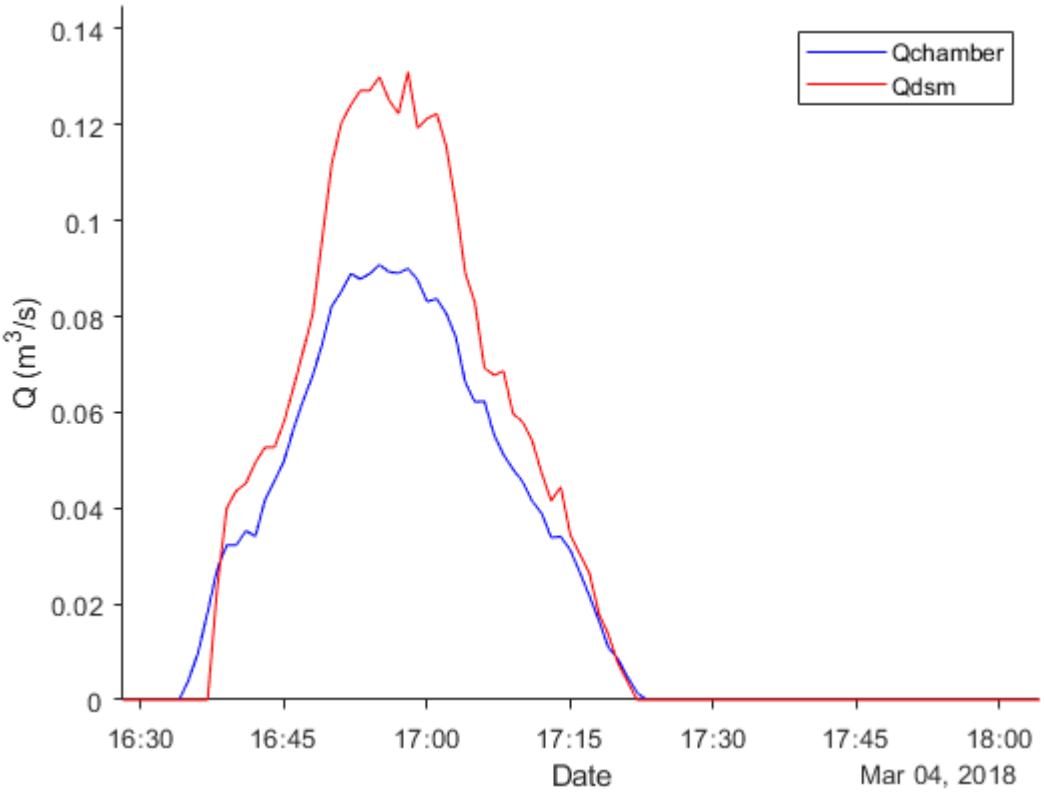

EVENTS 5, 6 AND 7

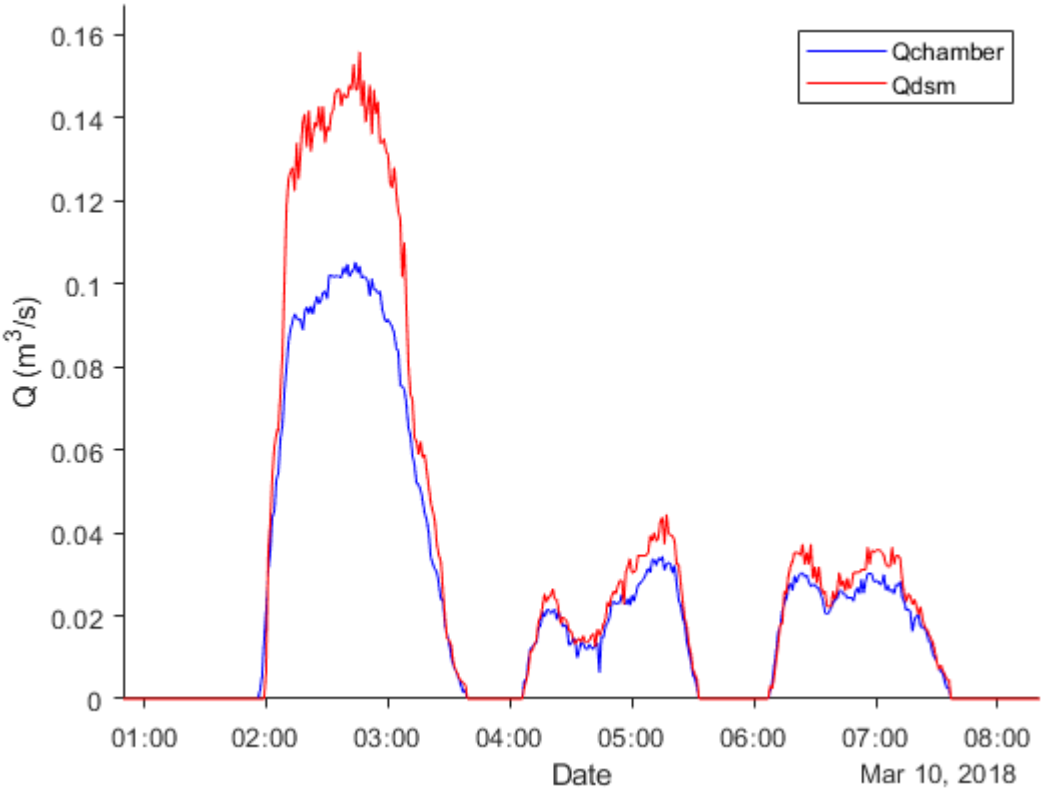

EVENTS 8 AND 9

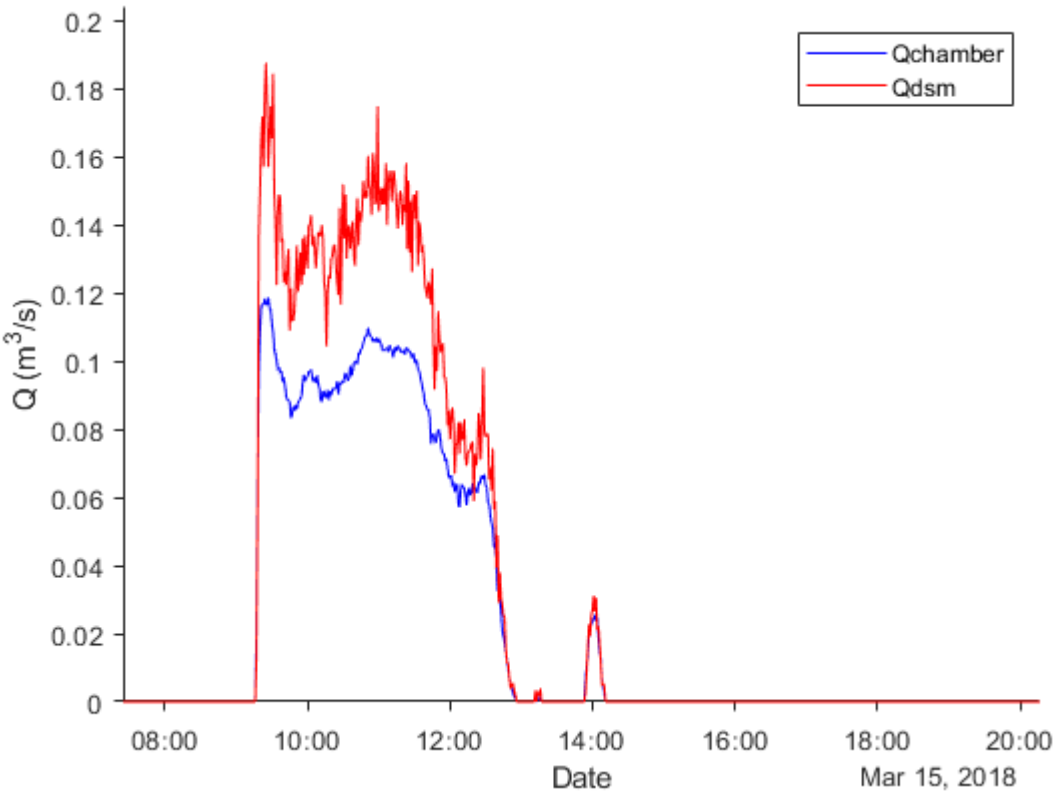

EVENT 10

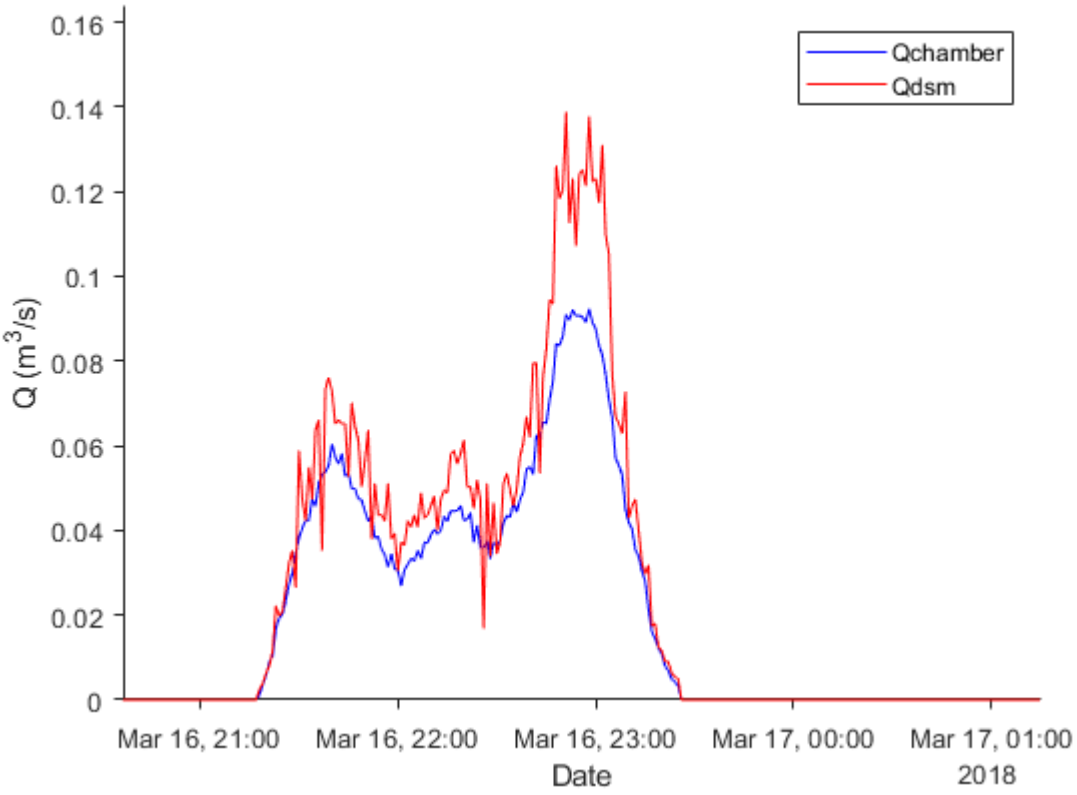

EVENT 11

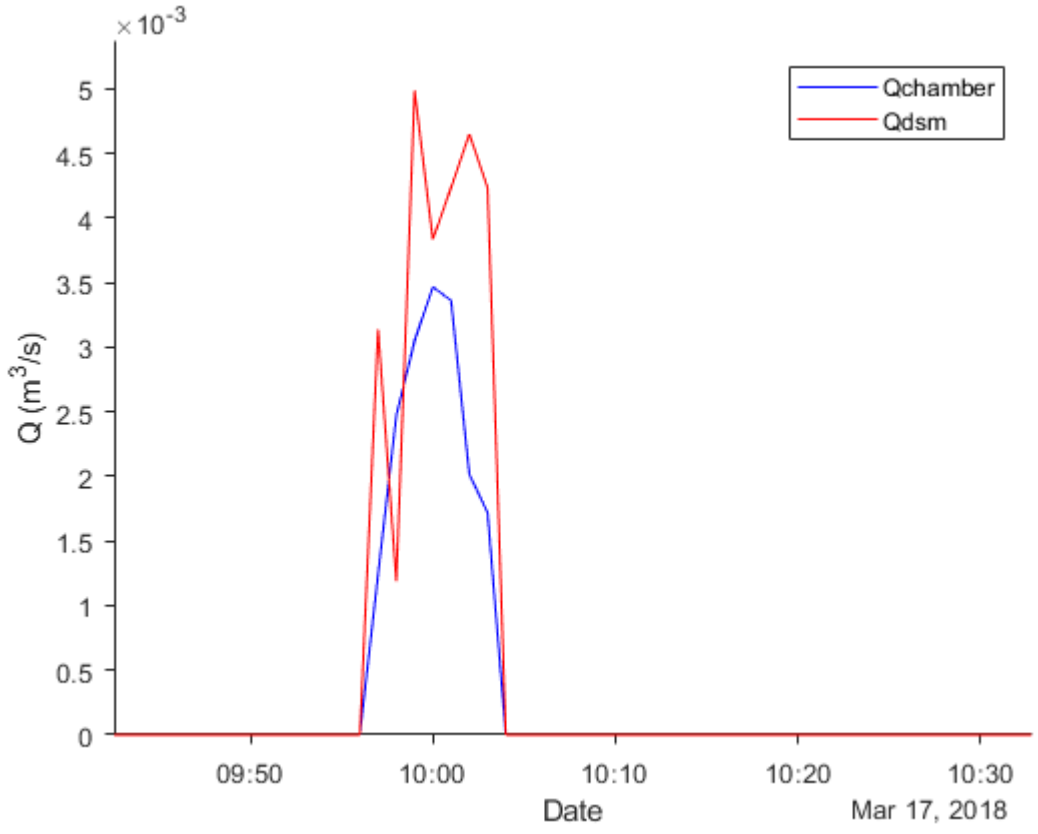

EVENT 12

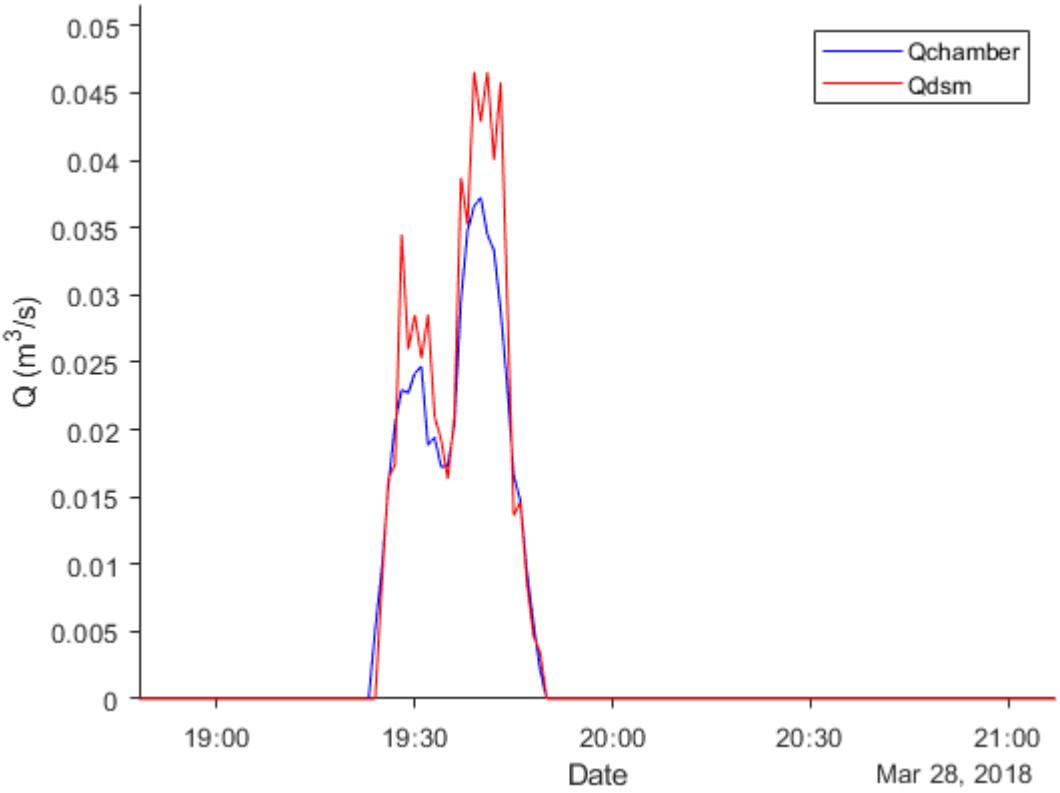

EVENT 13

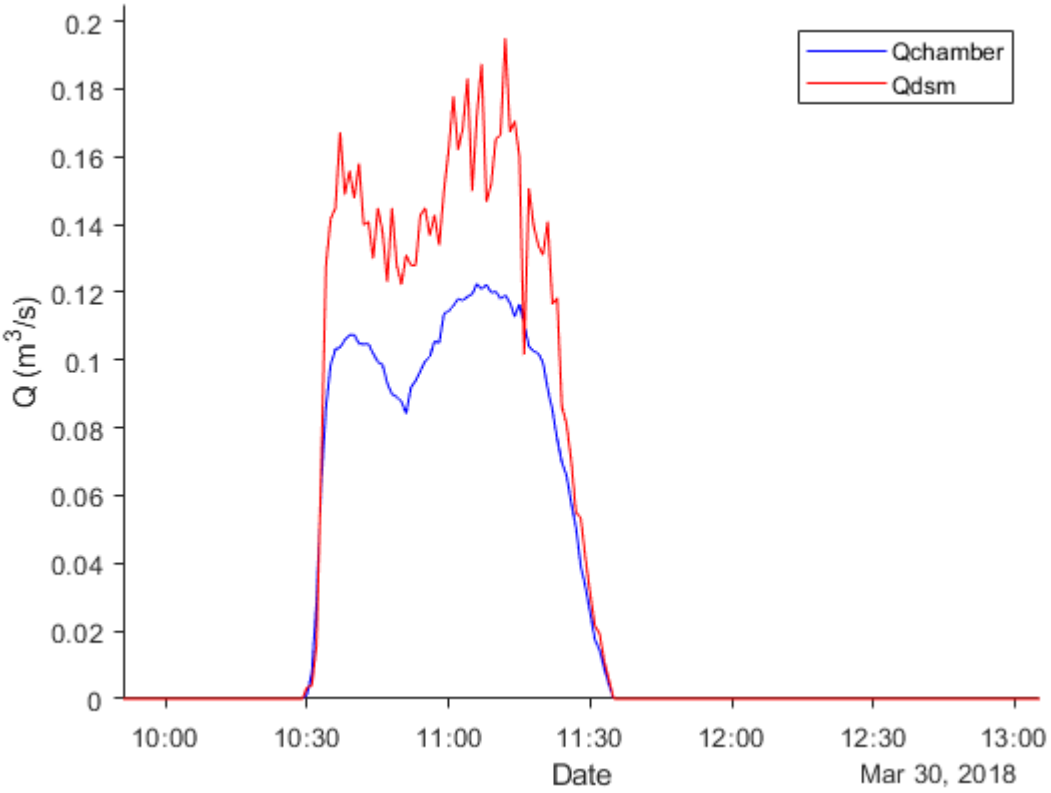

EVENTS 14 AND 15

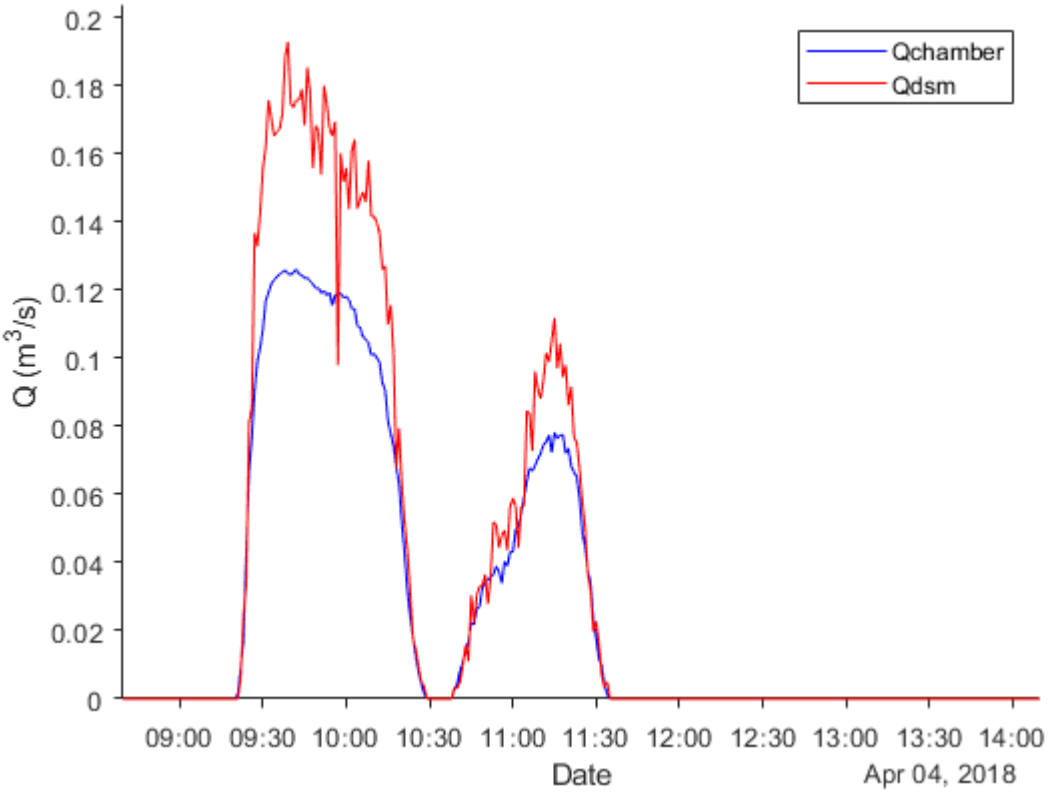

EVENT 16

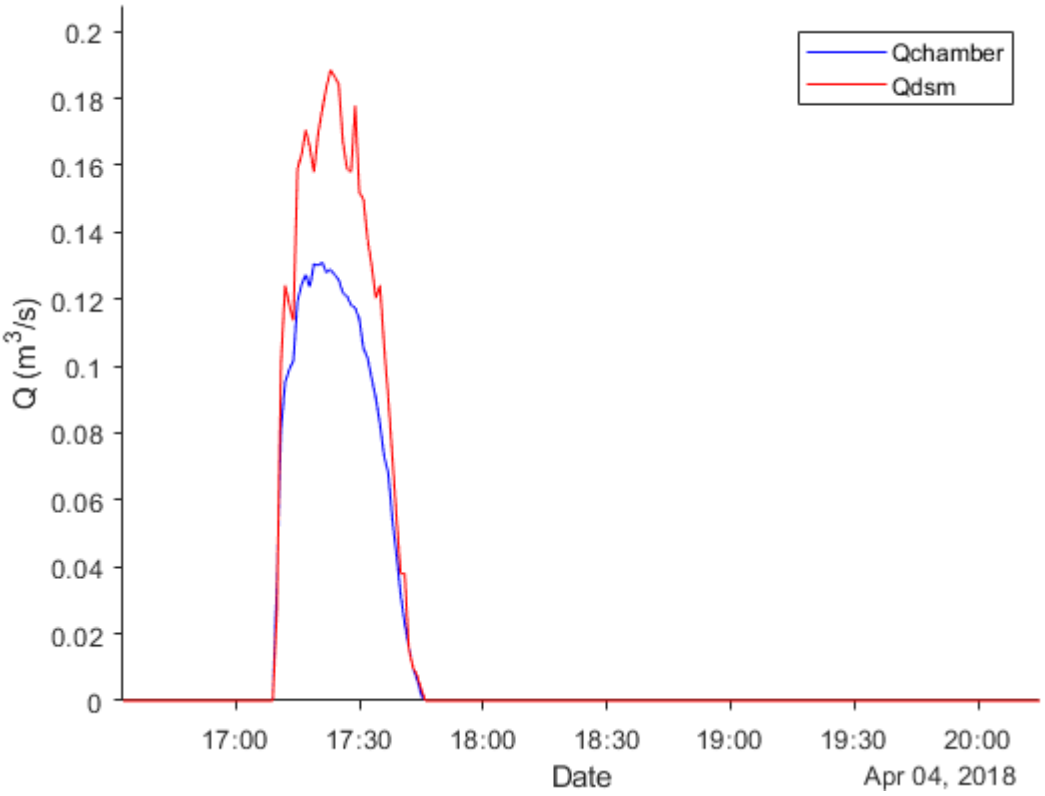

EVENT 17

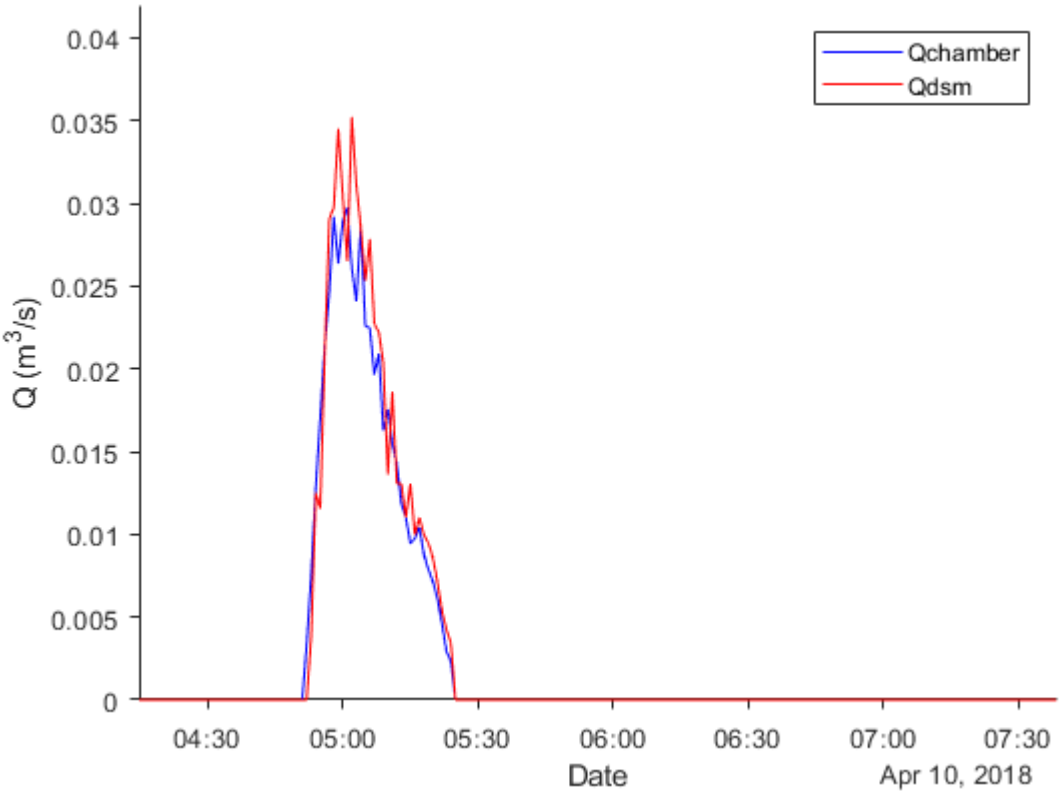

EVENT 18

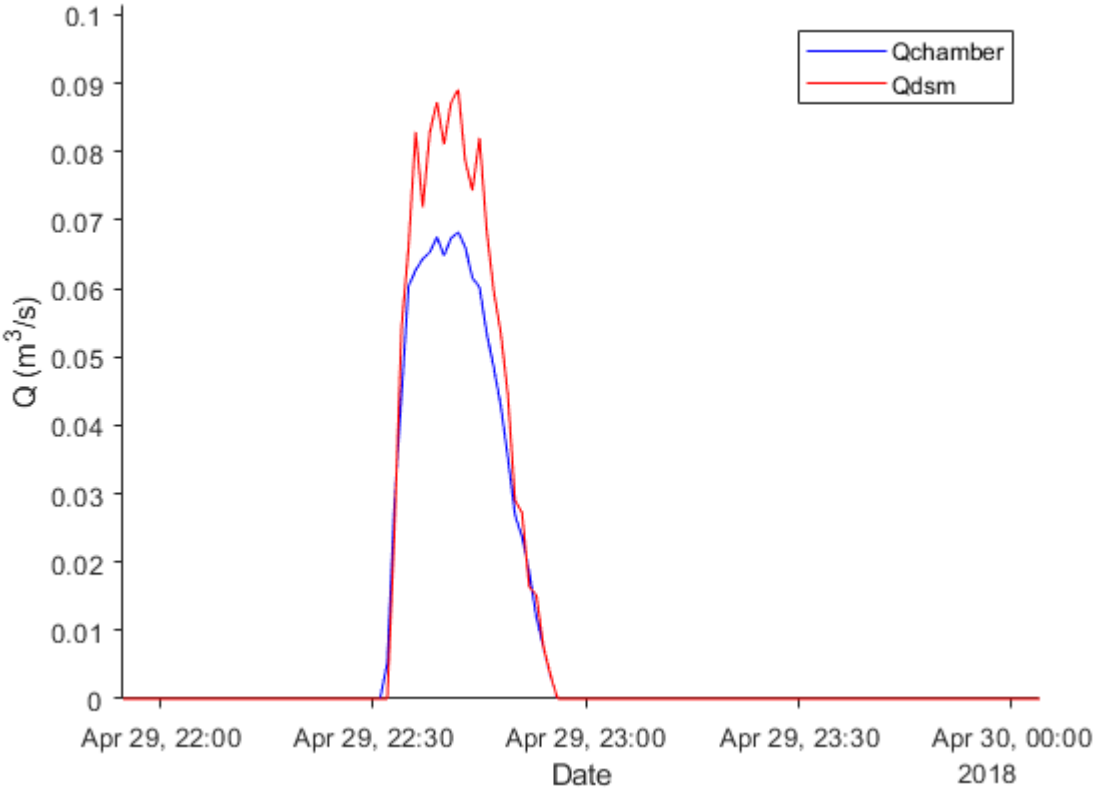

EVENT 19

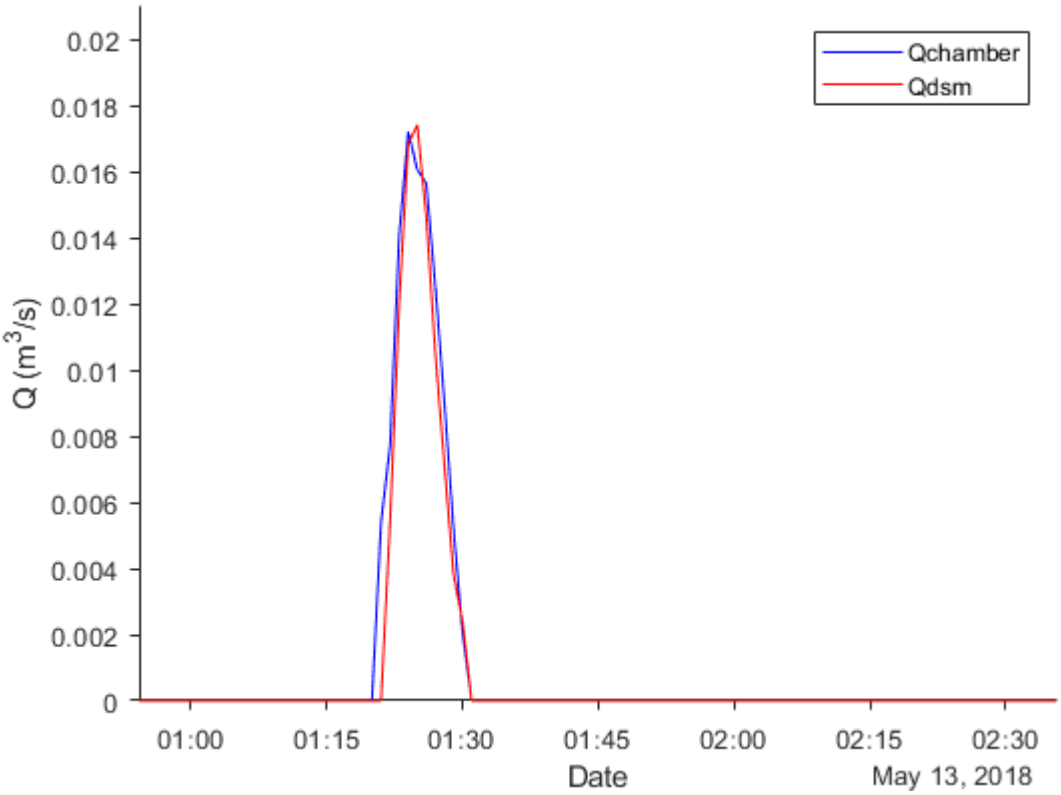

EVENTS 20 AND 21

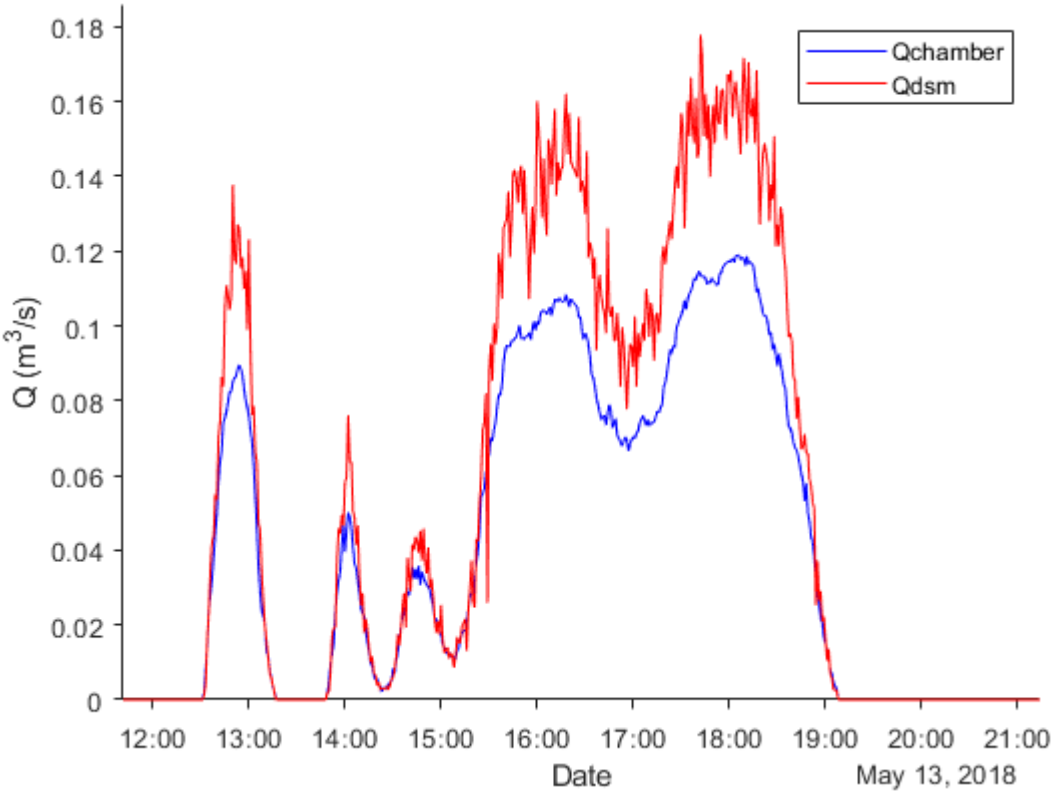

EVENTS 22 AND 23

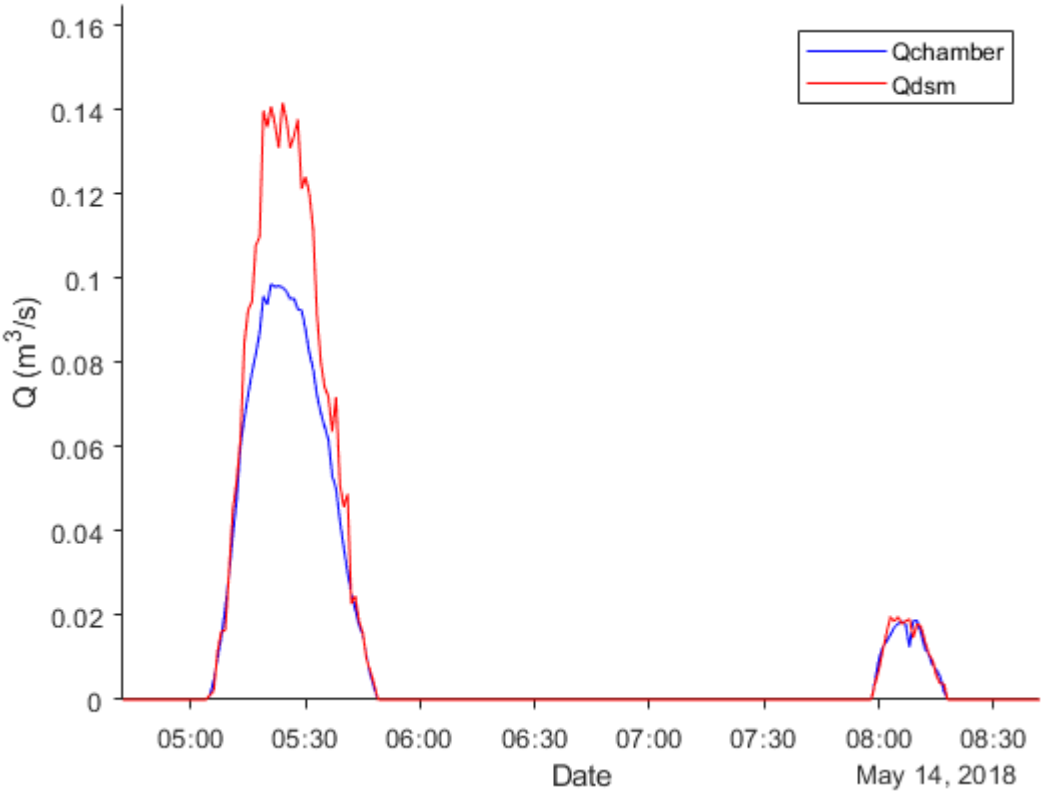

EVENT 24

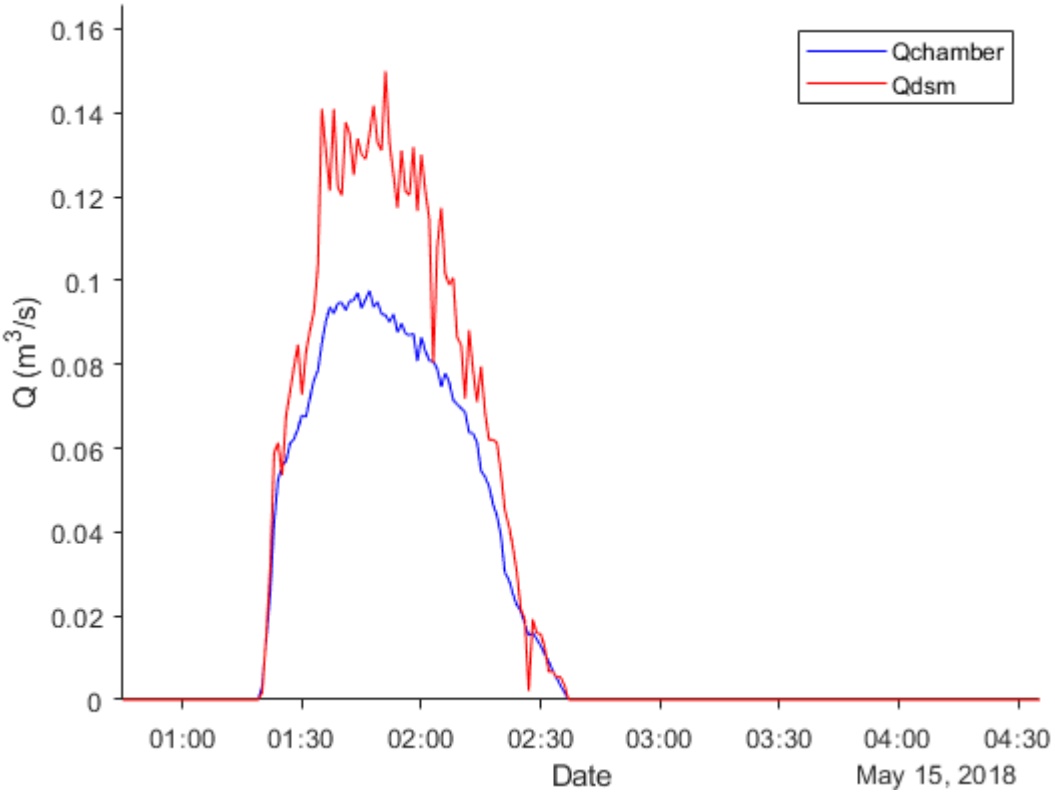

EVENTS 25 AND 26

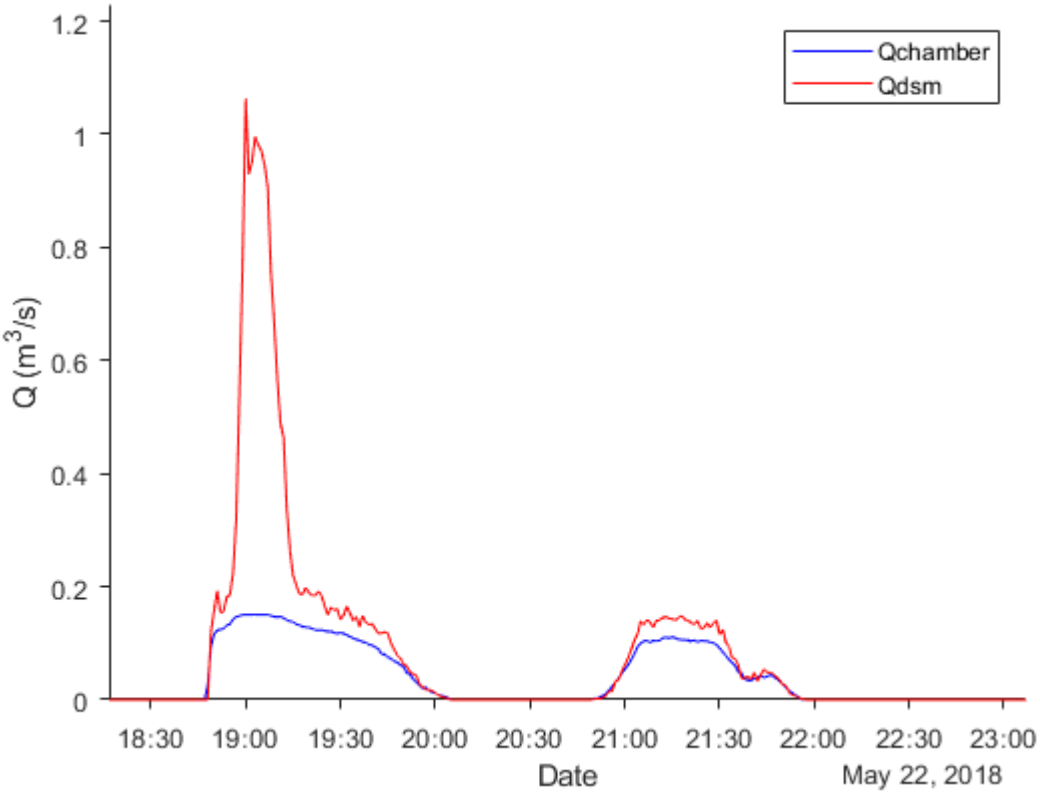

EVENTS 27, 28 AND 29

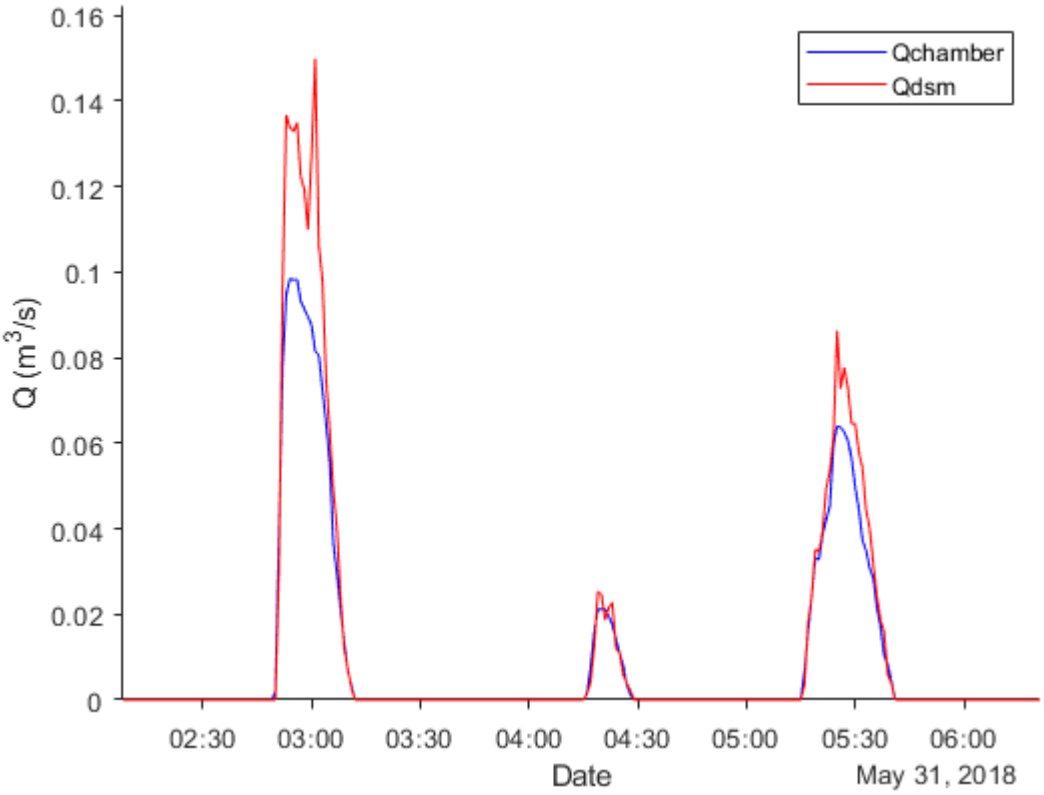

EVENTS 30 AND 31

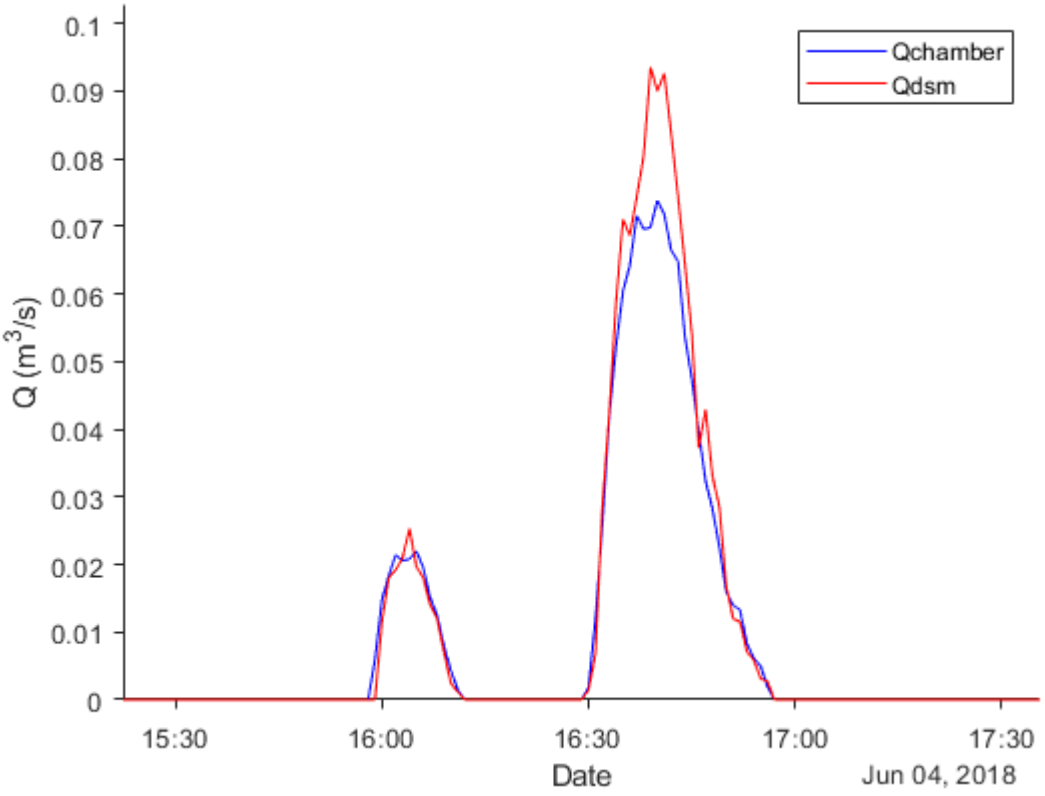

EVENT 32

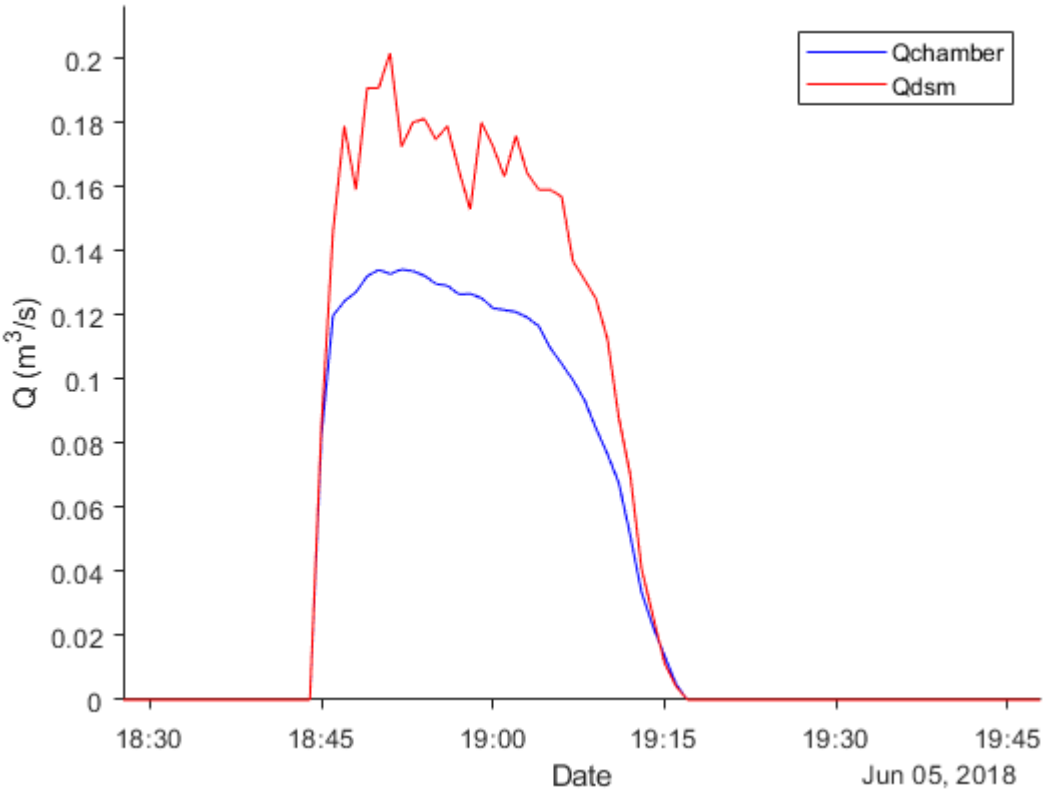

EVENTS 33 AND 34

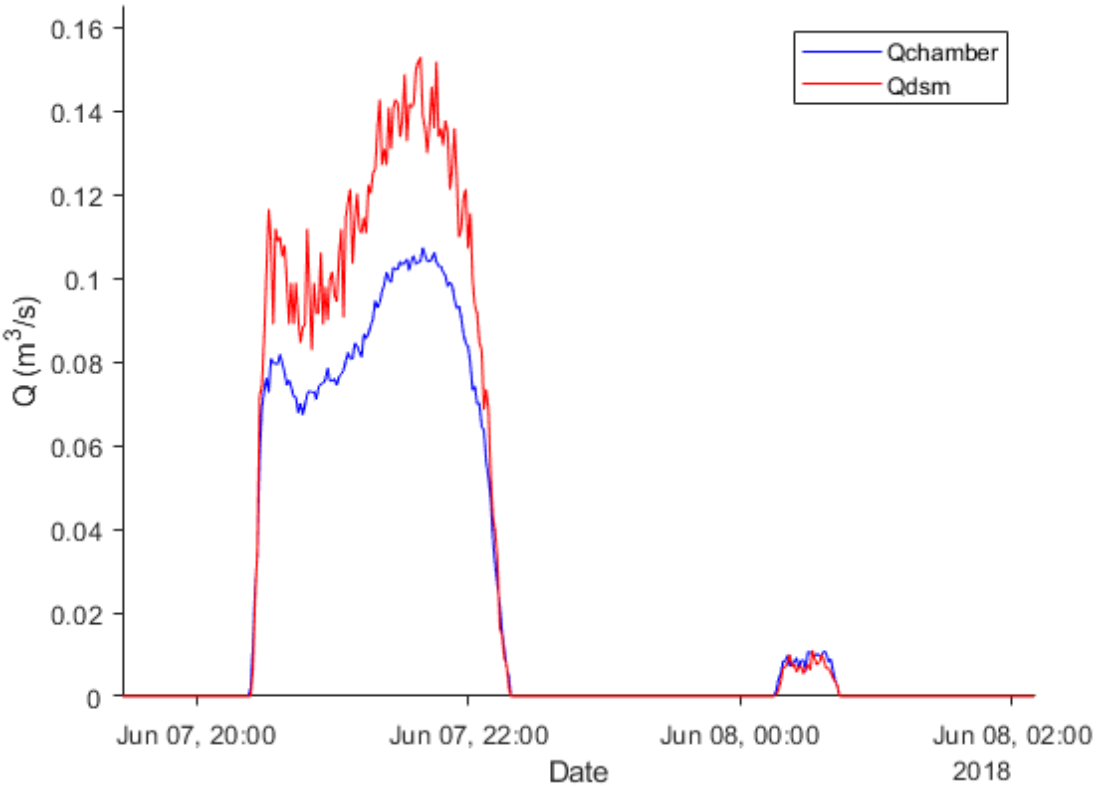

EVENT 35

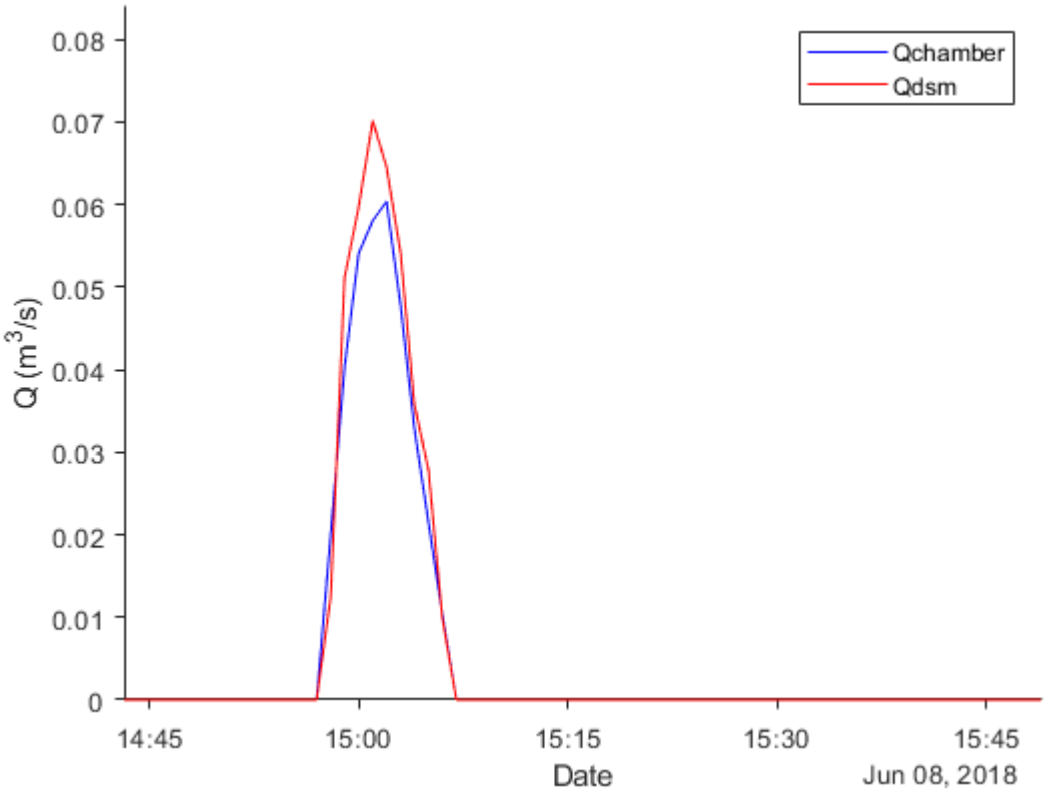

EVENT 36

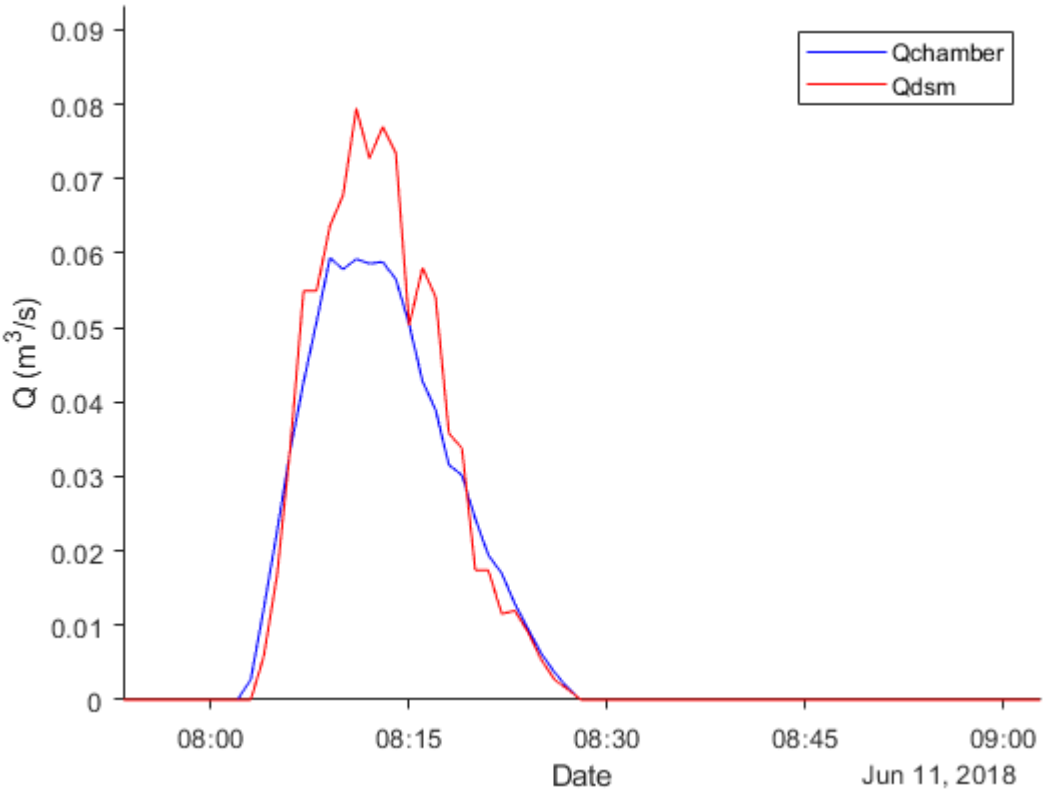

EVENT 37

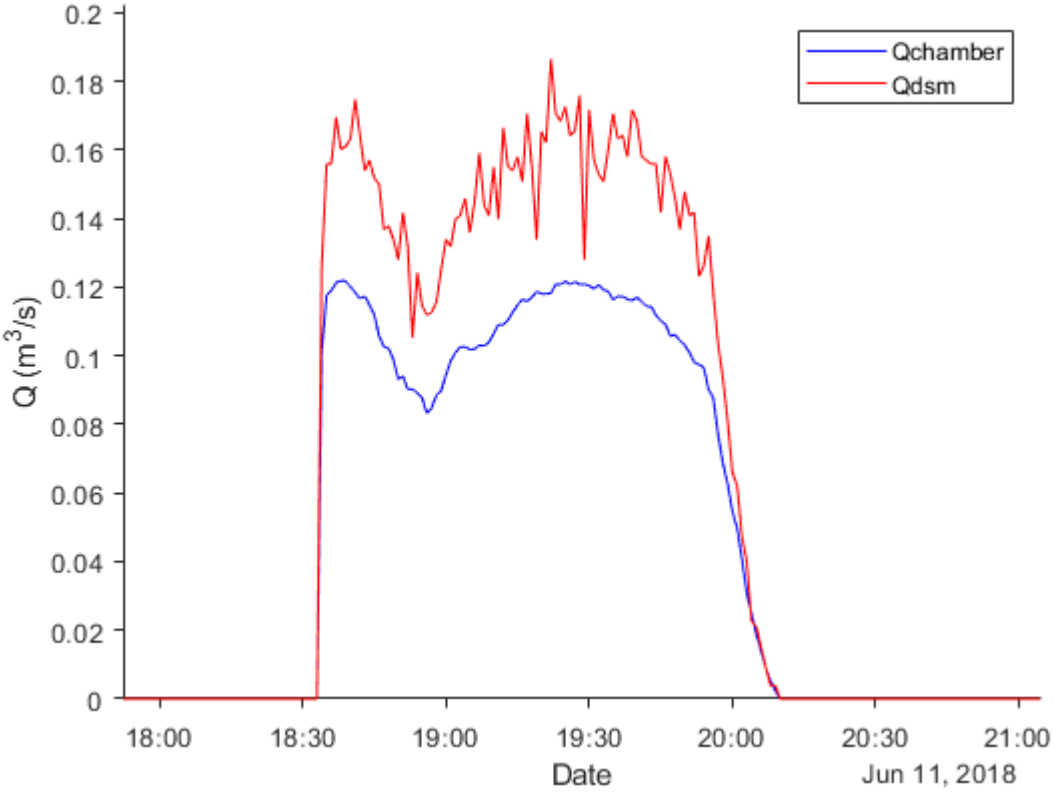

EVENTS 38, 39 AND 40

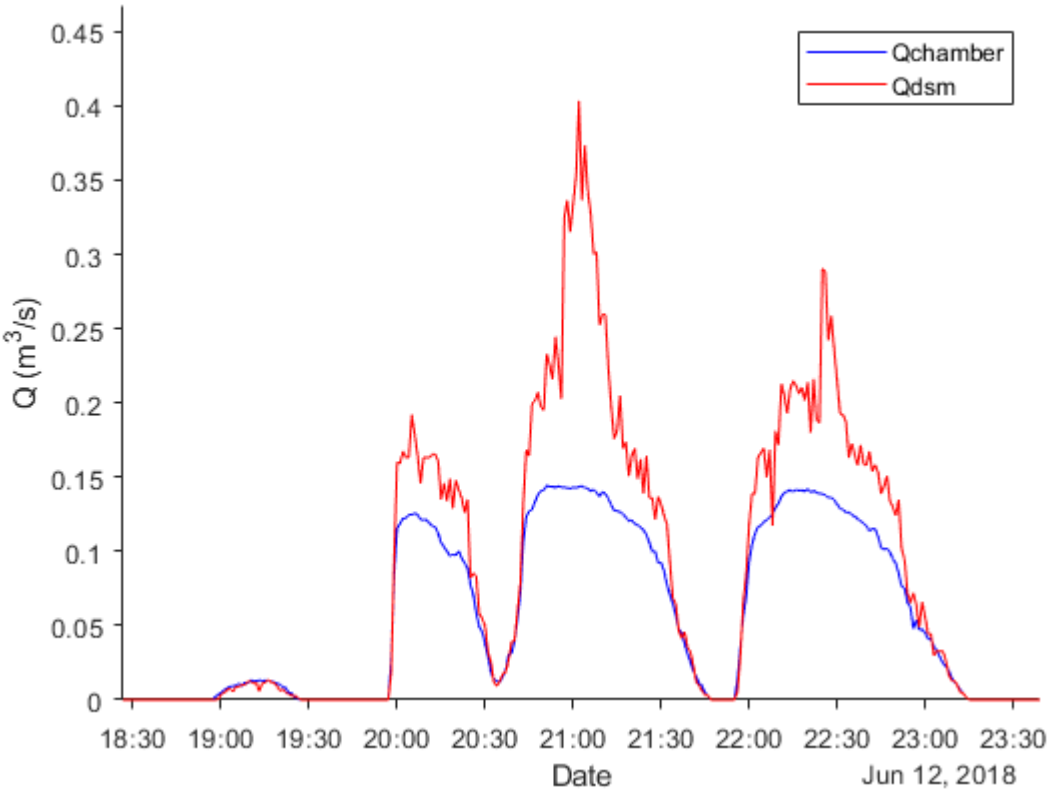

EVENT 41

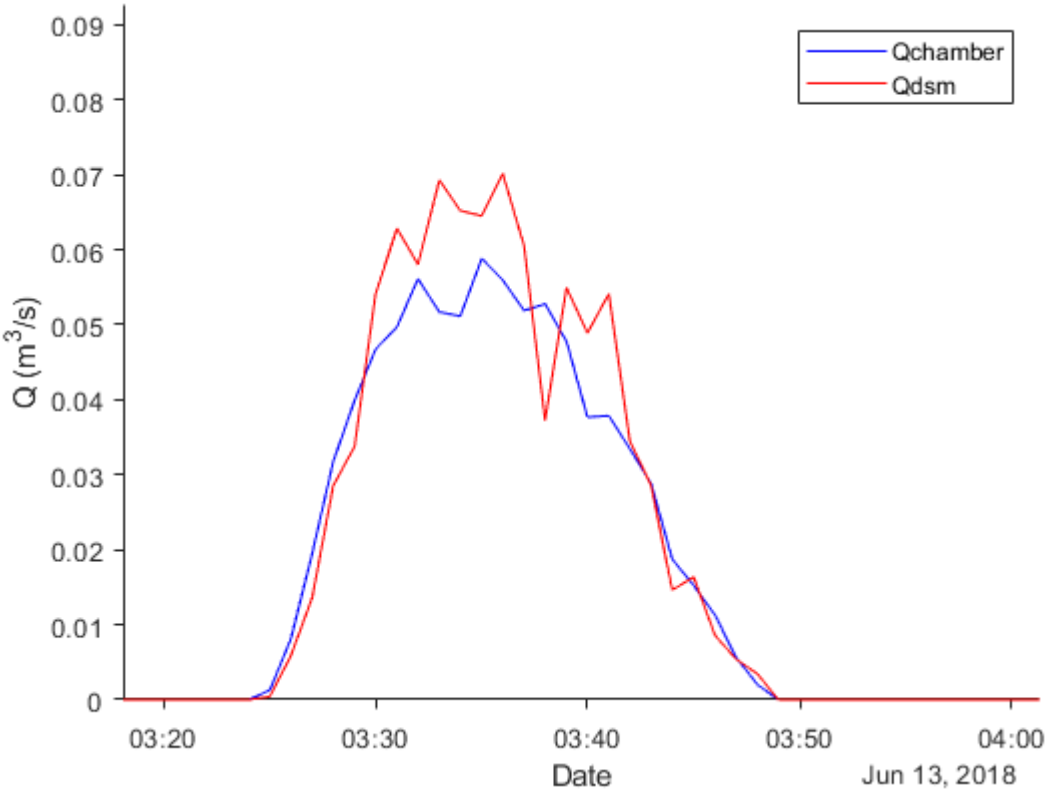

APPENDICES OF CHAPTER 4

7.3.1. <u'v'> Reynolds stresses at the near-bottom region of the physical model

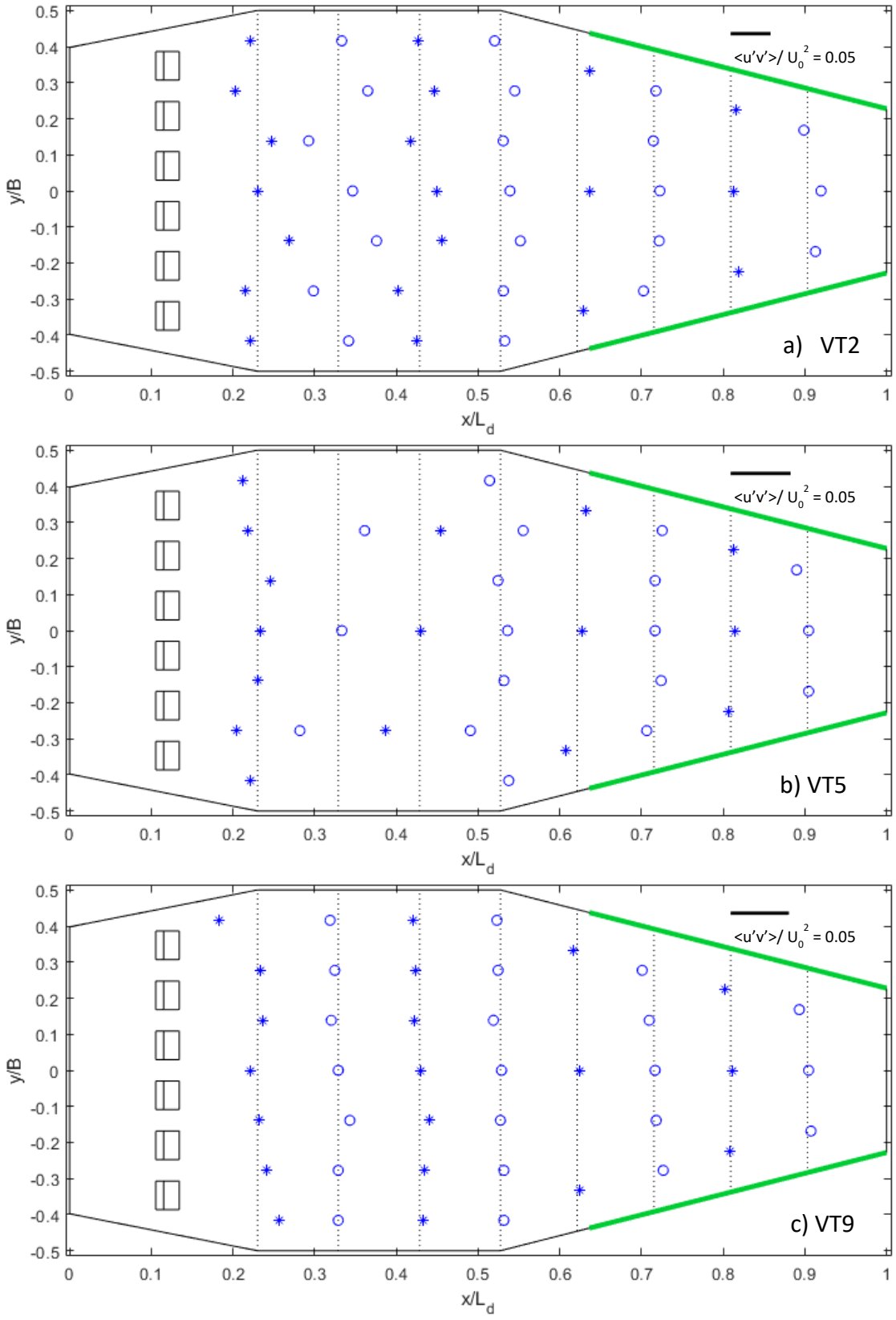

<u'v'> Reynolds stresses at the DSM-flux small-scale physical model for (a) VT2, (b) VT5 and (c) VT9 tests, in the near-bottom region, at depths z/H₀ = 0.125, 0.111 and 0.098 respectively. Two different markers are used to distinguish data from consecutive sections.

7.3.2. <u'v'> Reynolds stresses at the near-surface region of the physical model

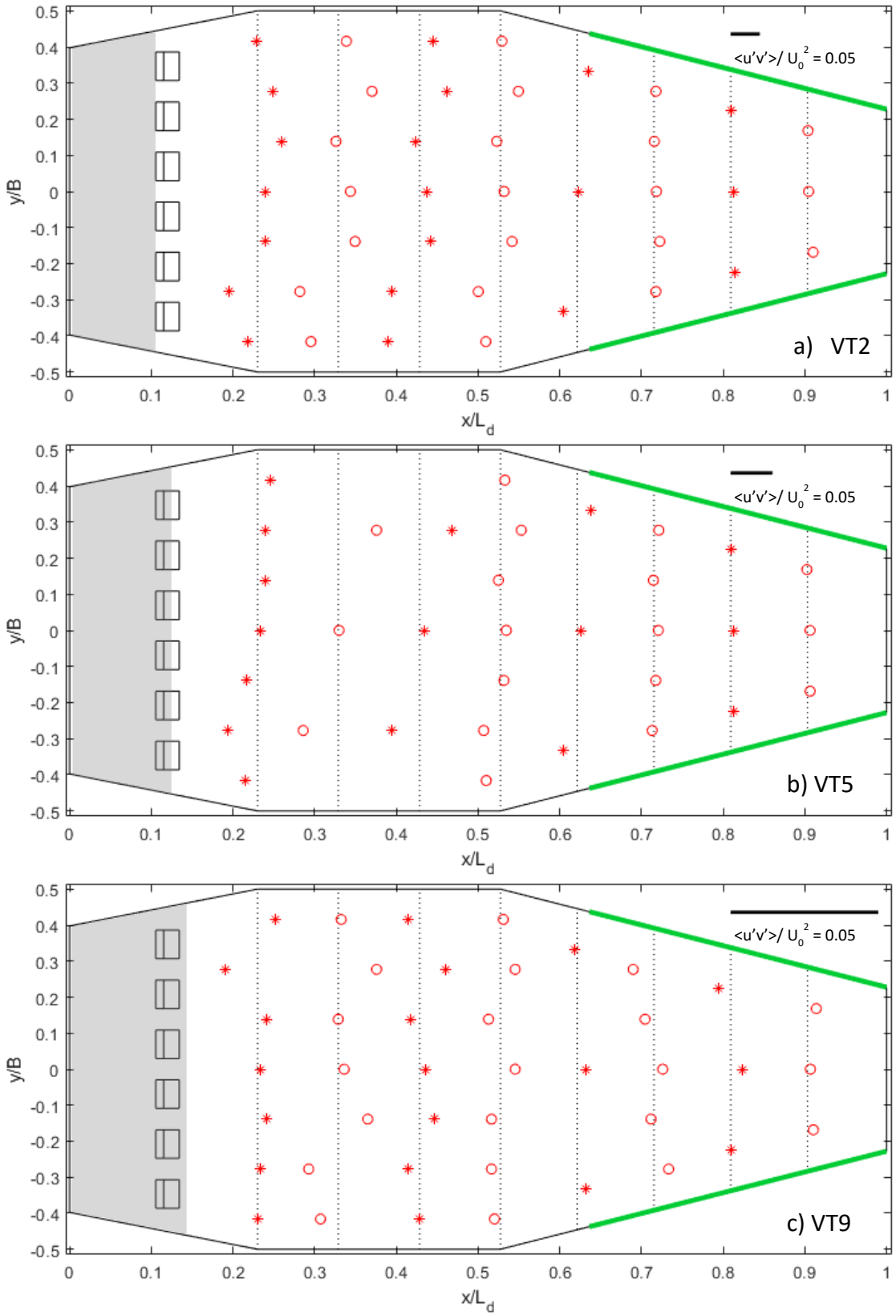

<u'v'> Reynolds stresses at the DSM-flux small-scale physical model for (a) VT2, (b) VT5 and (c) VT9 tests, in the near-surface region, at depths z/H_0 = 0.694, 0.741 and 0.783 respectively. Grey hatched area corresponds to the hydraulic jump recirculation area. Two different markers are used to distinguish data from consecutive sections.

7.3.3. <u'w'> Reynolds stresses at the near-bottom region of the physical model

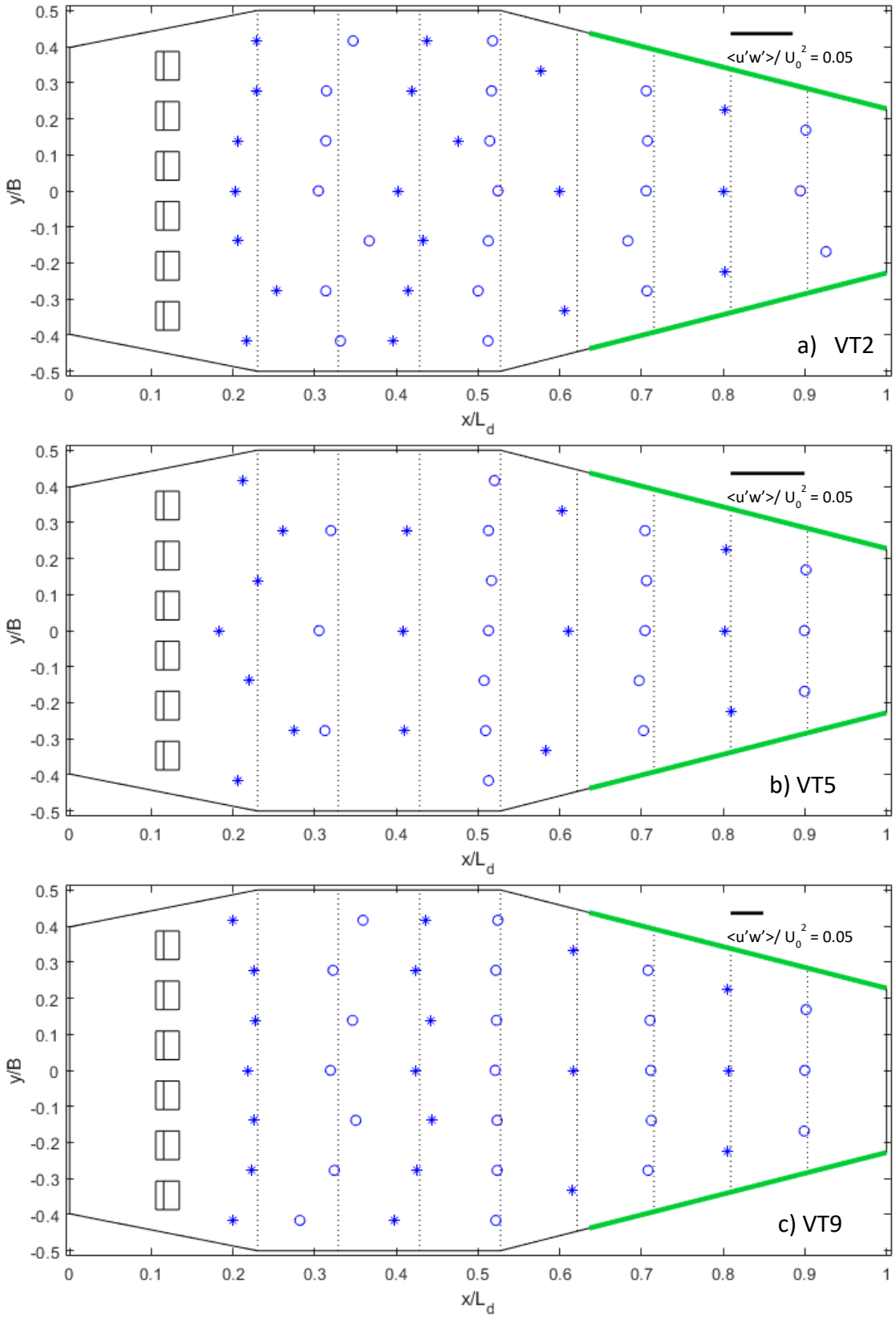

<u'w'> Reynolds stresses at the DSM-flux small-scale physical model for (a) VT2, (b) VT5 and (c) VT9 tests, in the near-bottom region, at depths z/H_0 = 0.125, 0.111 and 0.098 respectively. Two different markers are used to distinguish data from consecutive sections.

7.3.4. <u'w'> Reynolds stresses at the near-surface region of the physical model

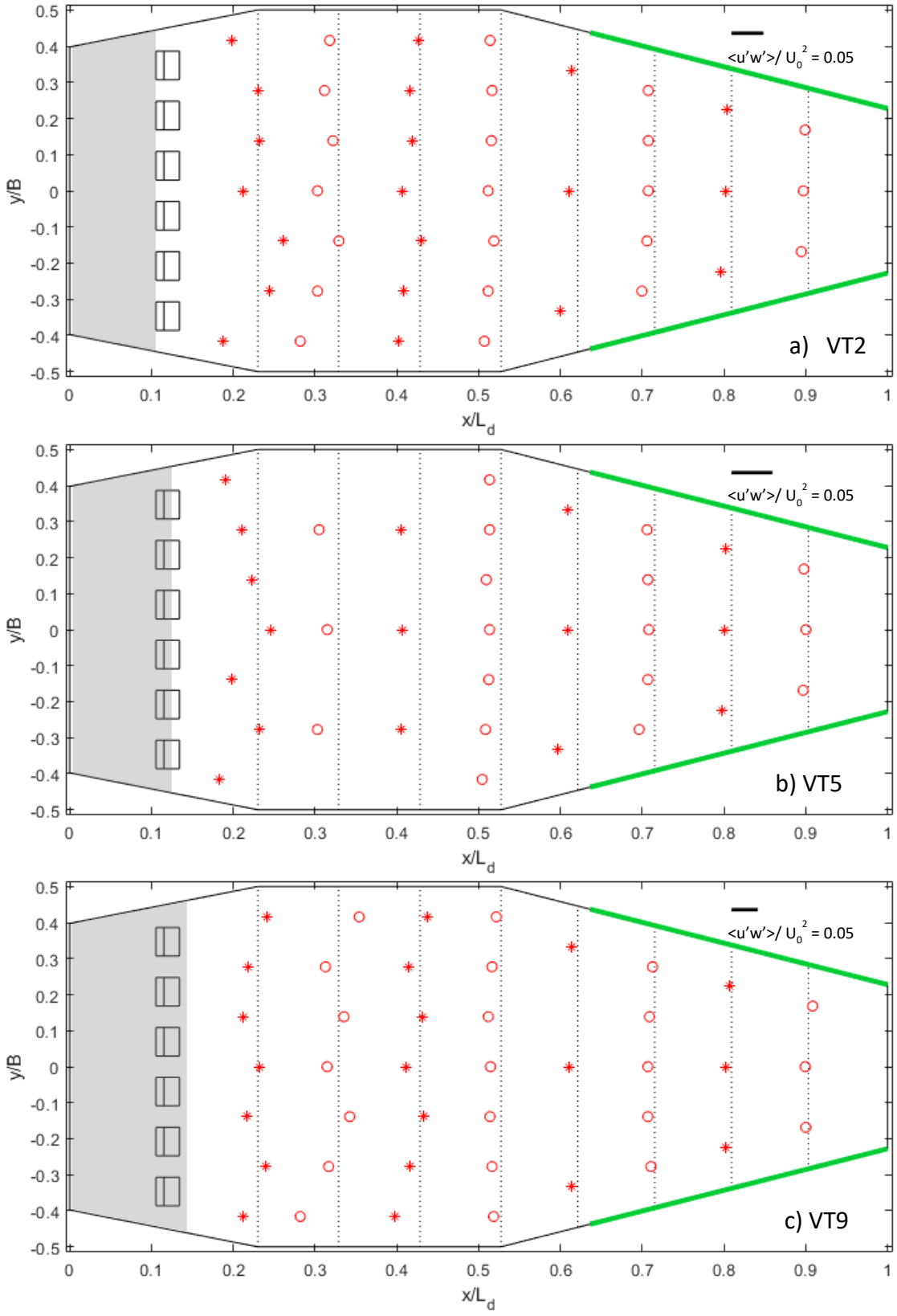

<u'w'> Reynolds stresses at the DSM-flux small-scale physical model for (a) VT2, (b) VT5 and (c) VT9 tests, in the near-surface region, at depths z/H_0 = 0.694, 0.741 and 0.783 respectively. Grey hatched area corresponds to the hydraulic jump recirculation area. Two different markers are used to distinguish data from consecutive sections.

7.3.5. <uv> velocity fields at the near-bottom region of the small-scale numerical model under low flow conditions

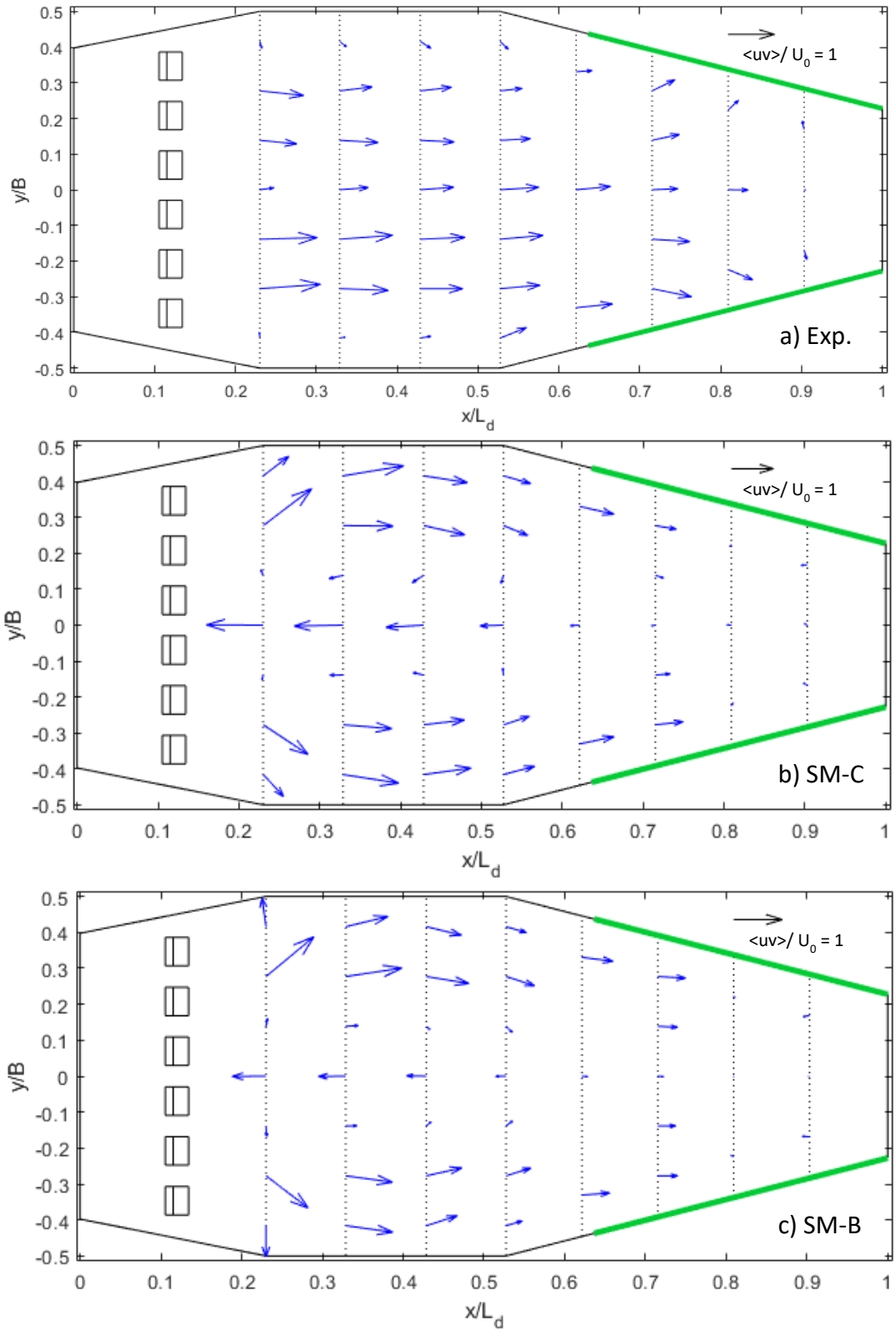

<uv> velocity fields (a) at the DSM-flux small-scale physical model for VT2 data (copy from Figure 4.7a), (b) at the numerical model SM-C for Sim SM-C1 data and (c) at the numerical model SM-B for Sim SM-B1 data, in the near-bottom region (z/H₀ = 0.125).

7.3.6. <uv> velocity fields at the near-surface region of the small-scale numerical model under lower flow conditions

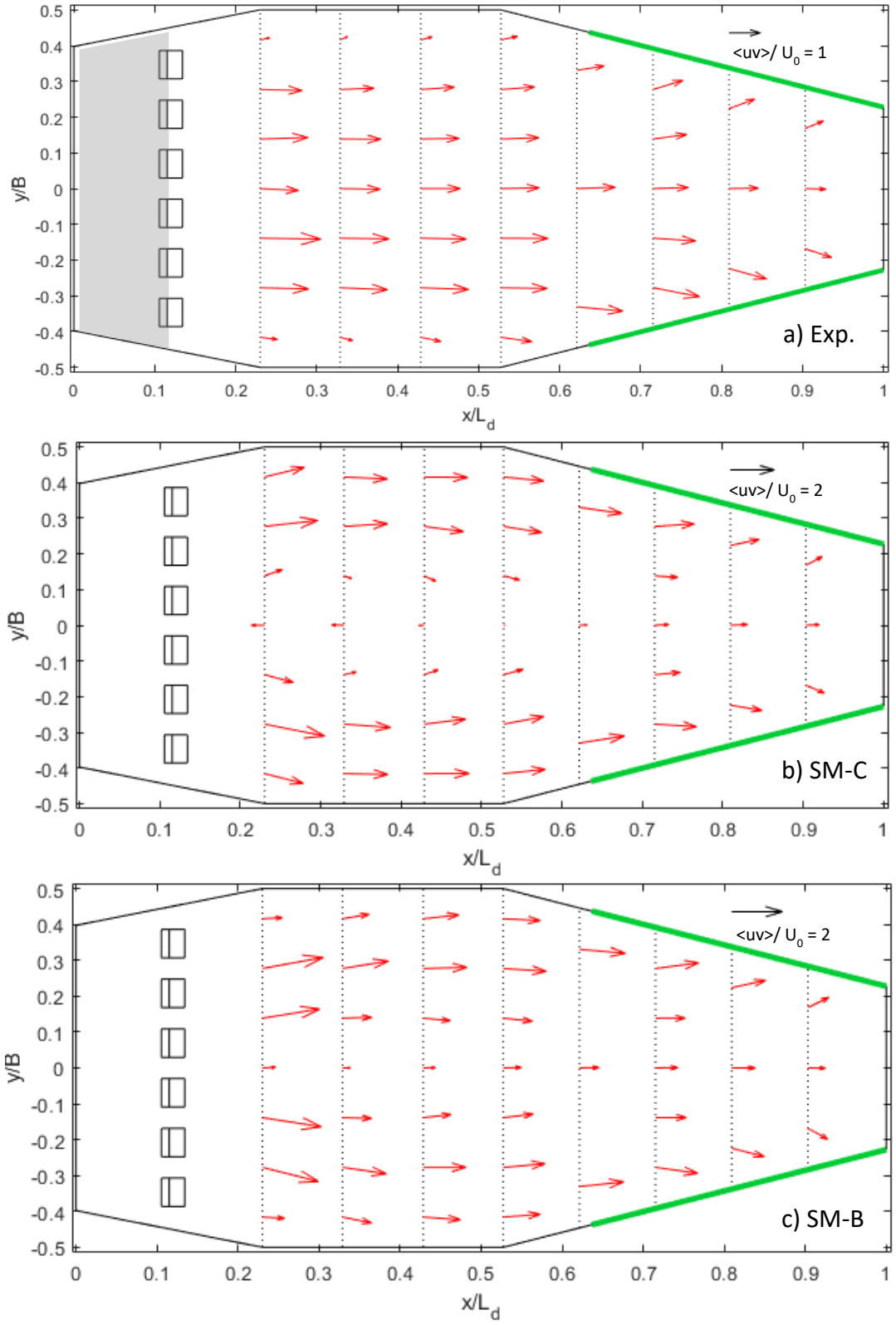

<uv> velocity fields (a) at the DSM-flux small-scale physical model for VT2 data (copy from Figure 4.8a), (b) at the numerical model SM-C for Sim SM-C1 data and (c) at the numerical model SM-B for Sim SM-B1 data, in the near-surface region ($z/H_0 = 0.694$).

7.3.7. <uv> velocity fields at the near-bottom region of the small-scale numerical model under higher flow conditions

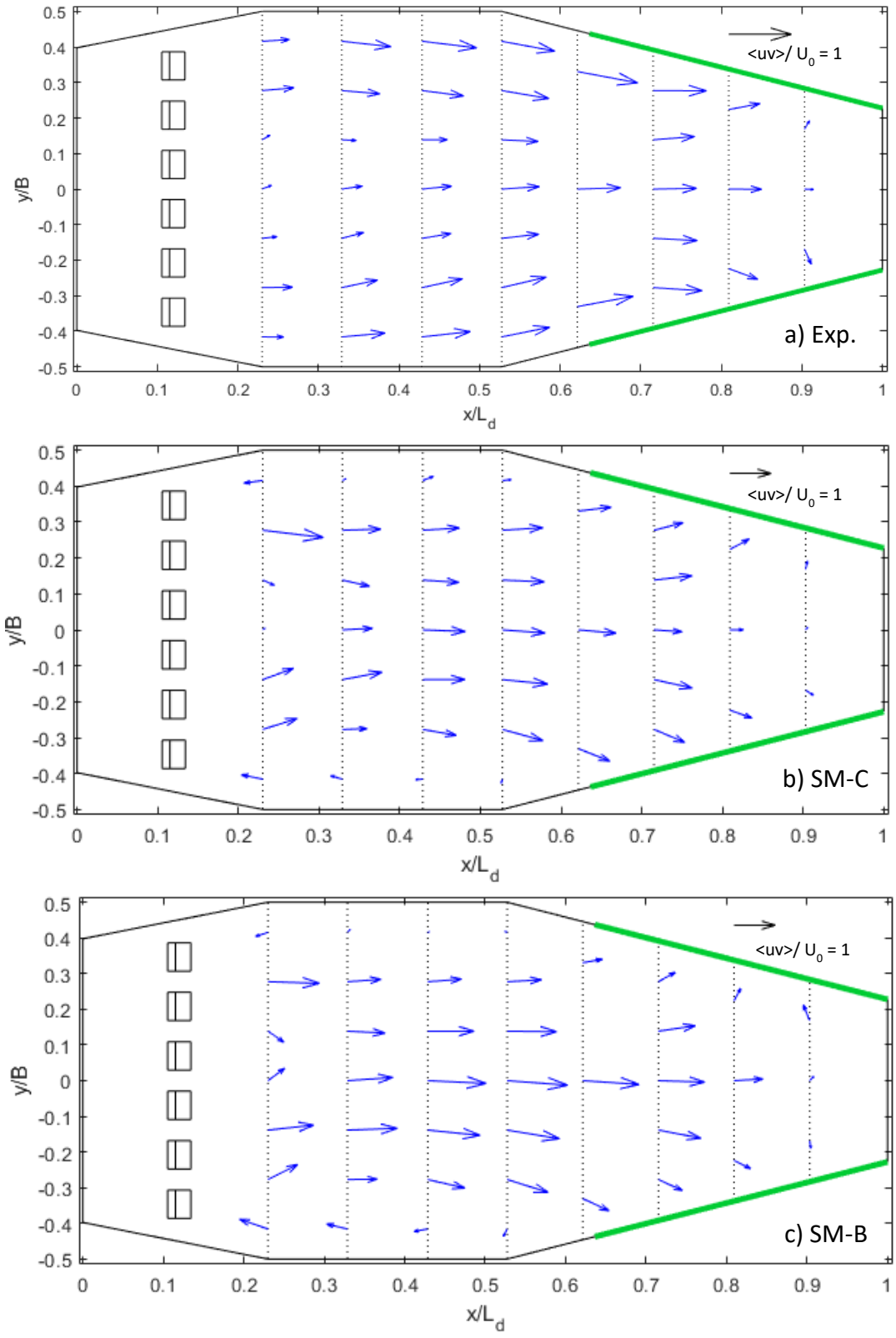

<uv> velocity fields (a) at the DSM-flux small-scale physical model for VT9 data (copy from Figure 4.7c), (b) at the numerical model SM-C for Sim SM-C2 data and (c) at the numerical model SM-B for Sim SM-B3 data, in the near-bottom region (z/H₀ = 0.098).

7.3.8. <uv> velocity fields at the near-surface region of the small-scale numerical model under higher flow conditions

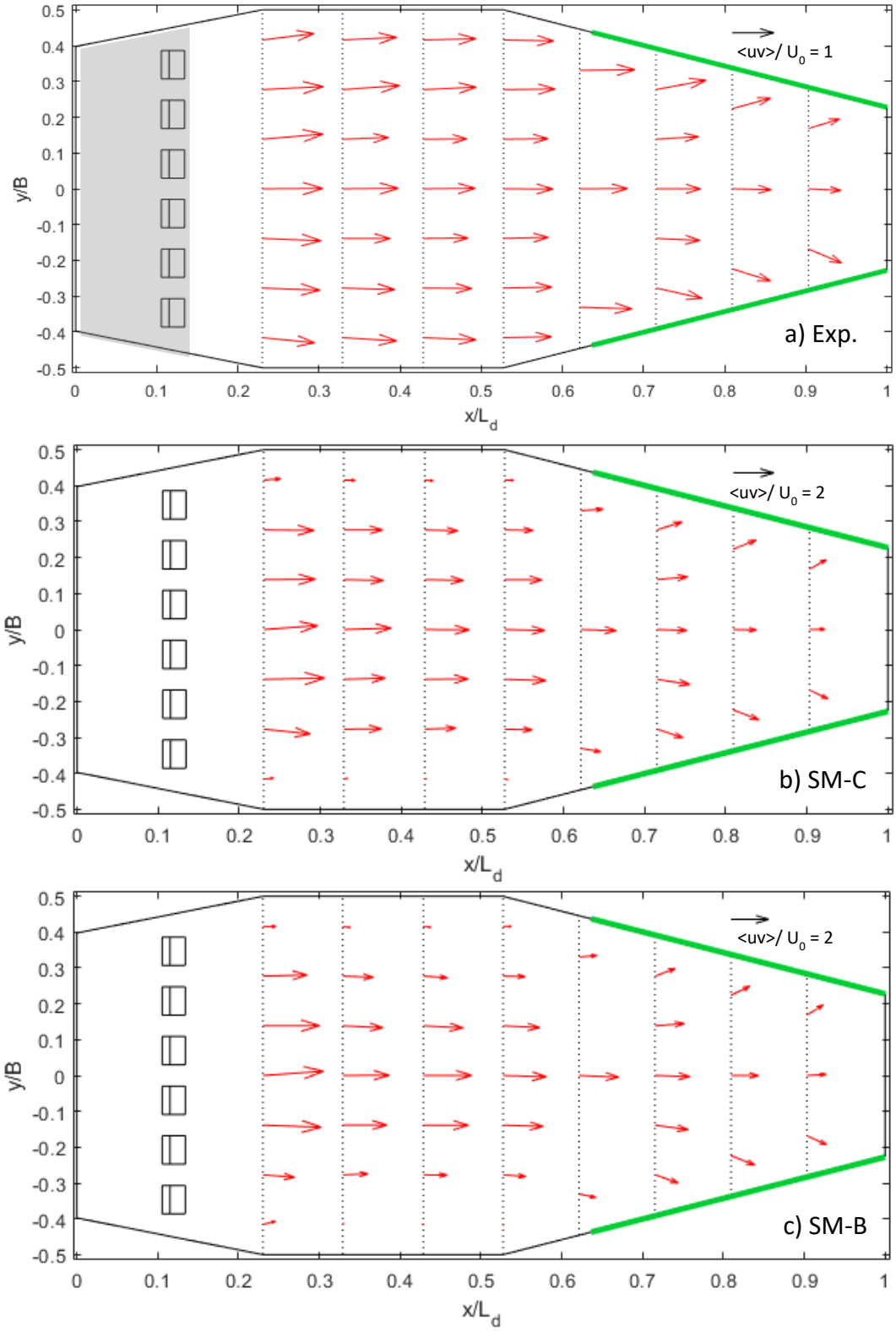

<uv> velocity fields (a) at the DSM-flux small-scale physical model for VT9 data (copy from Figure 4.8c), (b) at the numerical model SM-A for Sim SM-A5 data and (c) at the numerical model SM-B for Sim SM-B3 data, in the near-surface region (z/H₀ = 0.783).

7.3.9. Variability and uncertainties of velocity and turbulence data

From Figure 7.1 to Figure 7.8 (lower flow conditions) and from Figure 7.9 to Figure 7.16 (higher flow conditions) the results of the variability analysis for model SM-C are present. Error bars correspond to two times the standard deviation, which is an estimation of the uncertainty for normal-distributed data (a hypothesis of this study). In this case, around 1000 samples were considered for the computations, from an interval of approximately 50.000 iterations. In order to check if the interval and/or number of samples was enough to obtain the real mean values, the convergence of the cumulated mean was monitored. Some variables of some points didn't achieve this convergence, meaning that either the interval considered (and thus, the pseudo-period estimated for the variation of the solutions) wasn't long enough, or the number of samples taken should have been higher to represent better the dynamics. However, a great percentage of cases converged, so the analysis was found relevant.

In general, uncertainties are higher in the upstream points, especially for the normalized <w> velocity and TKE values. Normalized <w> velocity and TKE uncertainty at the overflow area are relatively low, especially under higher flow conditions, where error bars are almost covered by the dots in the graphics. Under lower flow conditions, it is observed that most of the experimental values are within the error bars of the numerical uncertainty for normalized <v> and <w> velocities. However, this is not the case for normalized <u> velocities, that are randomly above or below the error bars, especially at the near-surface region and upstream at the near-bottom region. And neither is the case for the TKE, where experimental values are clearly lower than the numerical values including the uncertainties (below the error bars). Under higher flow conditions, these patterns are similar for the near-bottom region. However, at the near-surface region, normalized <v> velocities at the overflow area are out of the error bars for more points than under lower flow conditions, and normalized <u> velocity and TKE divergences are greater, showing almost all experimental points out of the numerical data error bands.

Uncertainties for model SM-B are a bit lower than those of model SM-C under lower flow conditions. This might be the cause that there are slightly more experimental data out of the numerical data error bands. Under higher flow conditions, uncertainties seem similar in magnitude between both models but still it seems that there are slightly more experimental data out of the numerical data error bands in model SM-B than in SM-C. However, these differences are really subtle.

Concerning the estimation of uncertainties in the numerical results, using a statistical point of view, a more detailed analysis should be carried out to account for all the possible sources. In general, errors in numerical data should be considered as the combination of three components (ANSYS CXF v16, Eça, 2014): the round-off error, the iteration error and the discretization error (including the truncation error). Eça (2014) states that "*procedures for numerical error estimation assume the discretization error to be dominant. In practical CFD applications this is usually the case. Double-precision arithmetic makes the round-off error suitably small and in principle one should be able to reduce the iterative error to the level of the round-off error"*. In this PhD work, double-precision was used for all the simulations and the convergence criteria were well respected, so it could be supposed that the numerical error mainly depends on the discretization error. There are different methods in the literature to estimate spatial discretization error but the Grid Convergence Index (GCI) based on Richardson Extrapolation is one of the most commonly used and recommended by the American Society of Mechanical Engineers (ASME, 2008).

Uncertainty of the experimental data should also be estimated in future work. The sources of uncertainty in ADV experimental data are mainly the accuracy of the ADV, the mispositioning or misalignment of the probe (Peltier *et al.*, 2013) and the noise cause by the turbulence, especially in bubbly flows (Mori *et al.*, 2007; Frizel, 2000).

These analyses couldn't be done within the time of this PhD work, but they are strongly recommended as the addition of these errors in both sets of data will increase the criteria to accept and validate the numerical models.

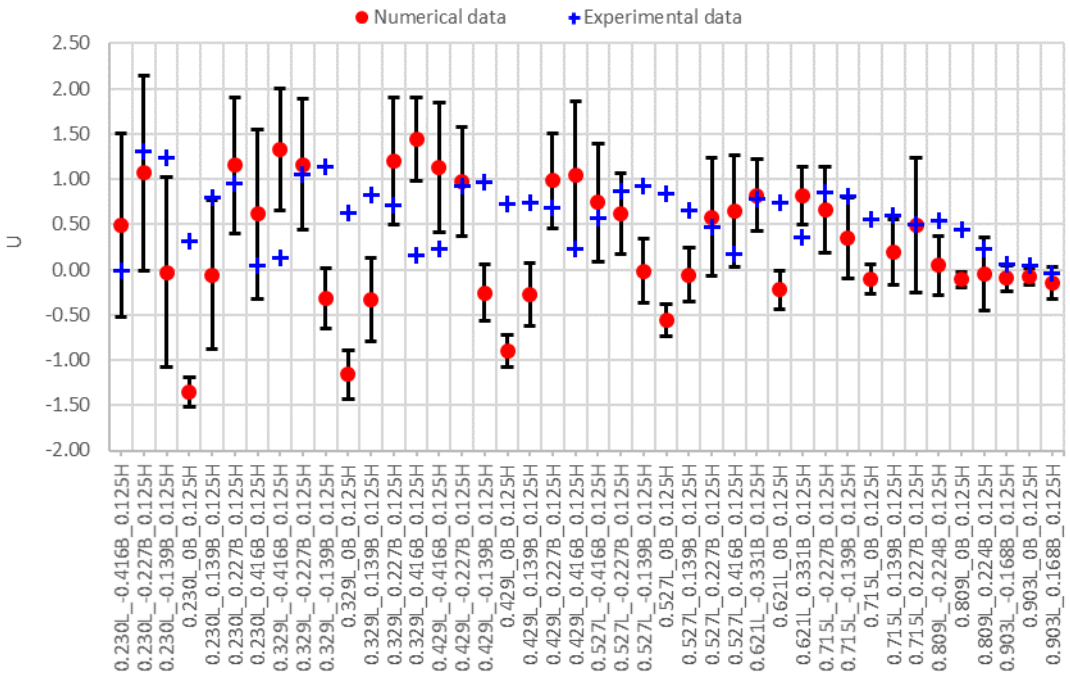

Figure 7.1. Normalized <u> velocity under the lower flow conditions in the near-bottom region ($z/H_0 = 0.125$). Points are organized from upstream to downstream in the direction of the X axis.

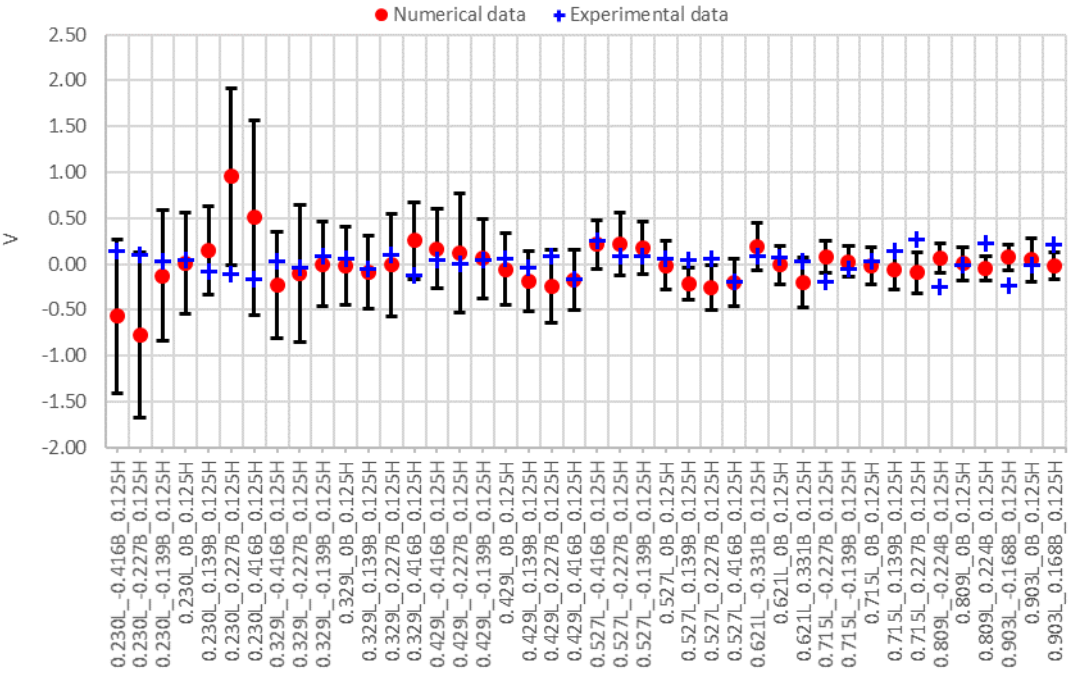

Figure 7.2. Normalized <v> velocity under the lower flow conditions in the near-bottom region ($z/H_0 = 0.125$). Points are organized from upstream to downstream in the direction of the X axis.

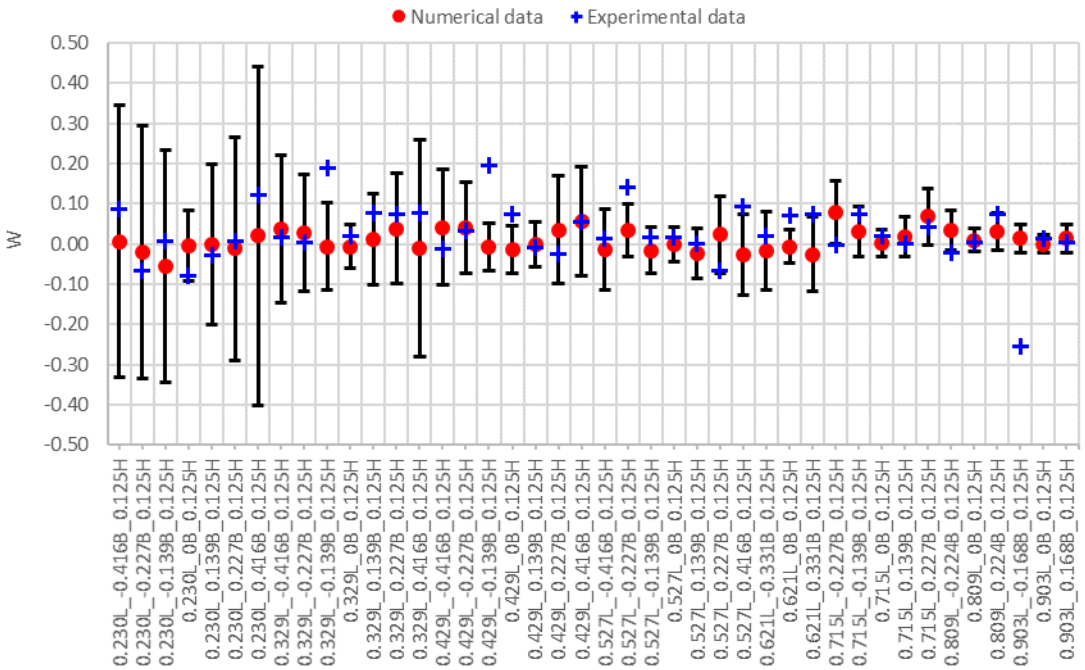

Figure 7.3. Normalized <w> velocity under the lower flow conditions in the near-bottom region ($z/H_0 = 0.125$). Points are organized from upstream to downstream in the direction of the X axis.

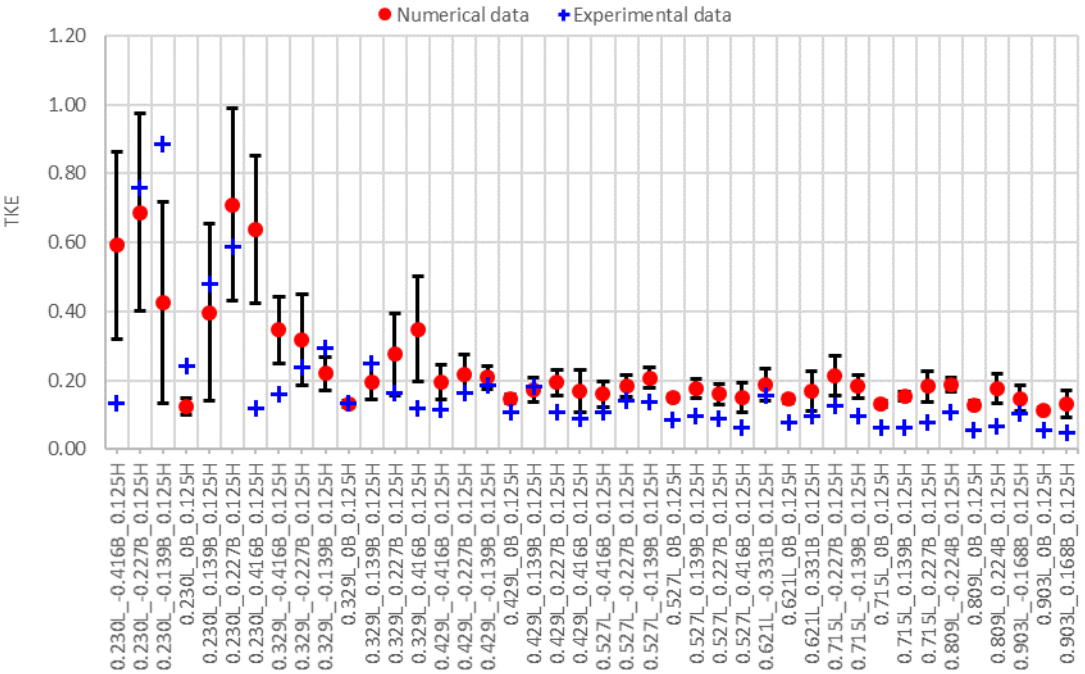

Figure 7.4. Normalized TKE under the lower flow conditions in the near-bottom region ($z/H_0 = 0.125$). Points are organized from upstream to downstream in the direction of the X axis.

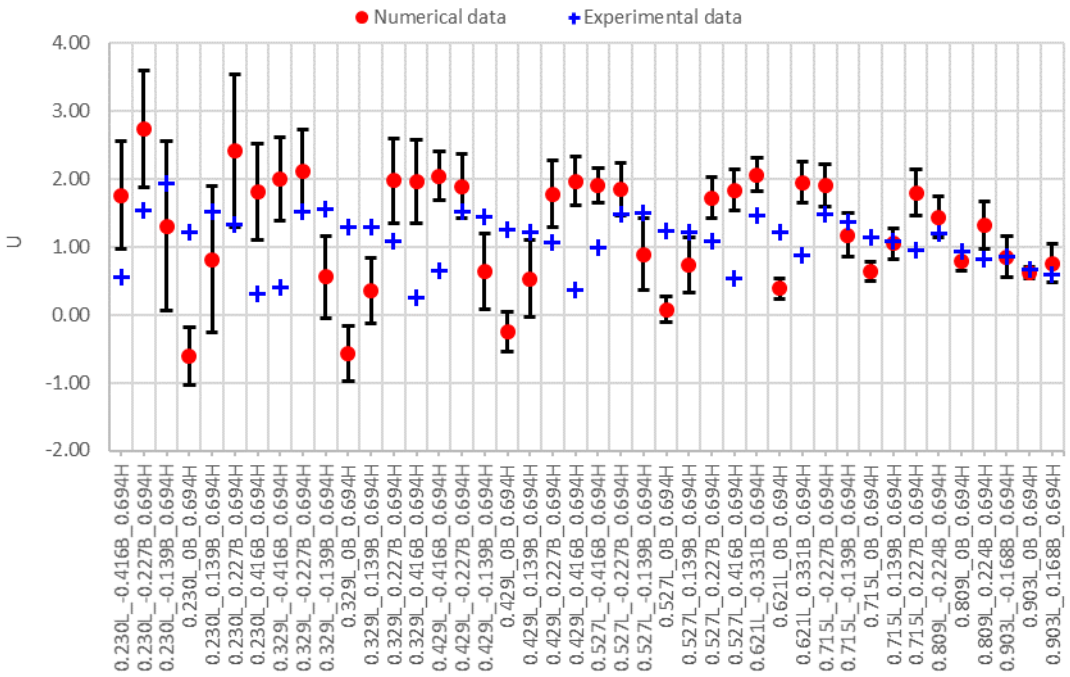

Figure 7.5. Normalized <u> velocity under the lower flow conditions in the near-surface region (z/H_0 = 0.694). Points are organized from upstream to downstream in the direction of the X axis.

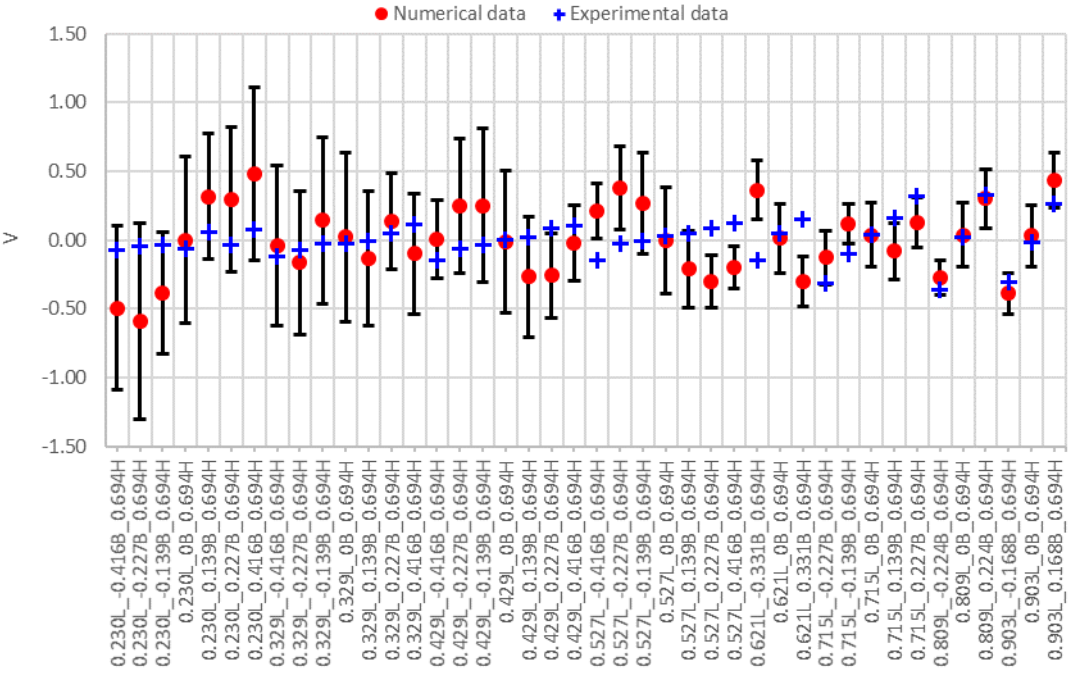

Figure 7.6. Normalized <v> velocity under the lower flow conditions in the near-surface region (z/H_0 = 0.694). Points are organized from upstream to downstream in the direction of the X axis.

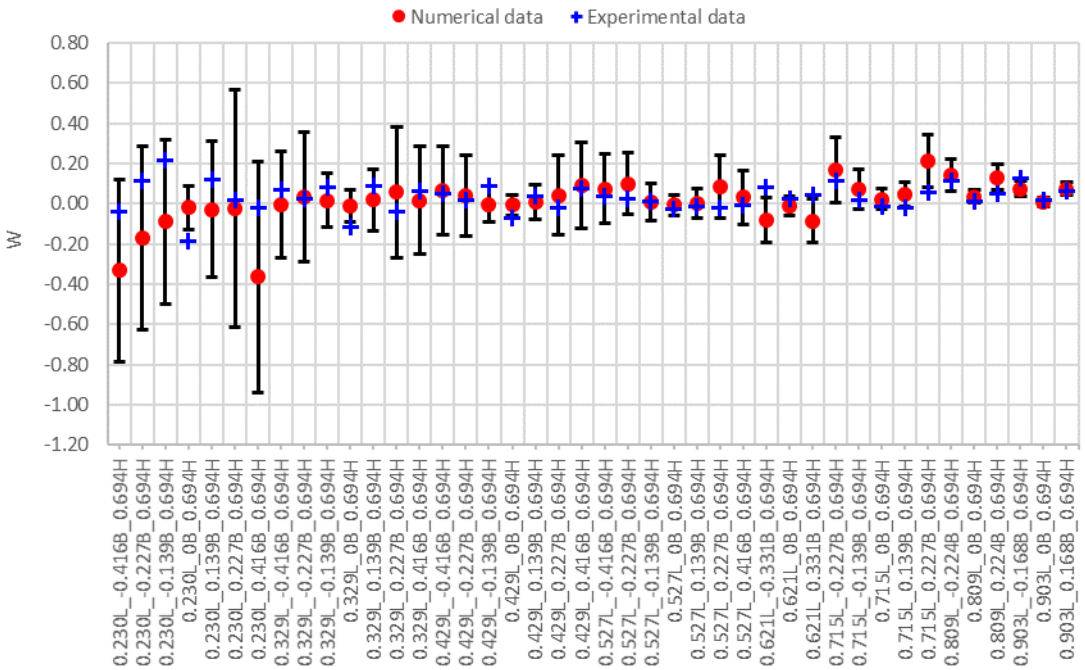

Figure 7.7. Normalized <w> velocity under the lower flow conditions in the near-surface region ($z/H_0 = 0.694$). Points are organized from upstream to downstream in the direction of the X axis.

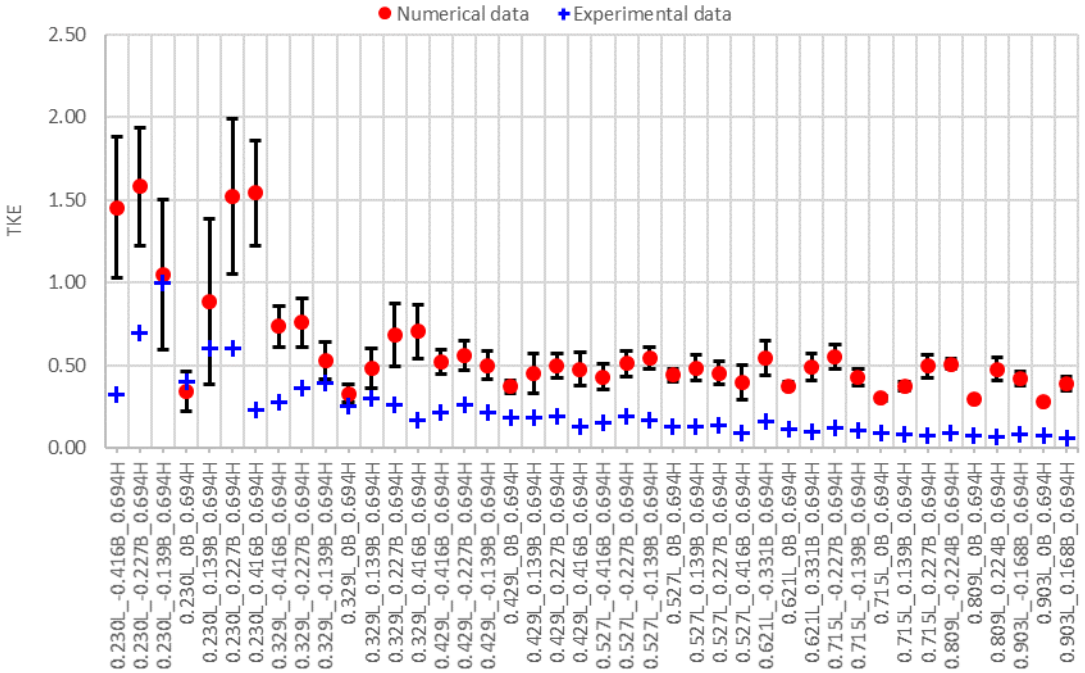

Figure 7.8. Normalized TKE under the lower flow conditions in the near-surface region ($z/H_0 = 0.694$). Points are organized from upstream to downstream in the direction of the X axis.

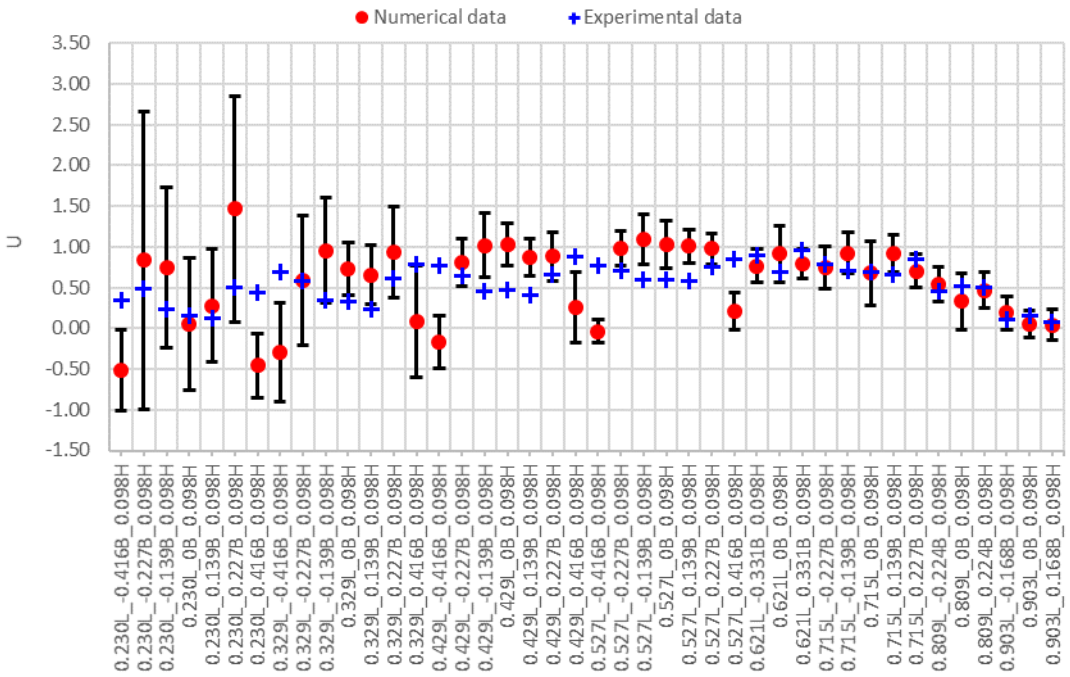

Figure 7.9. Normalized <u> velocity under the higher flow conditions in the near-bottom region (z/H_0 = 0.098). Points are organized from upstream to downstream in the direction of the X axis.

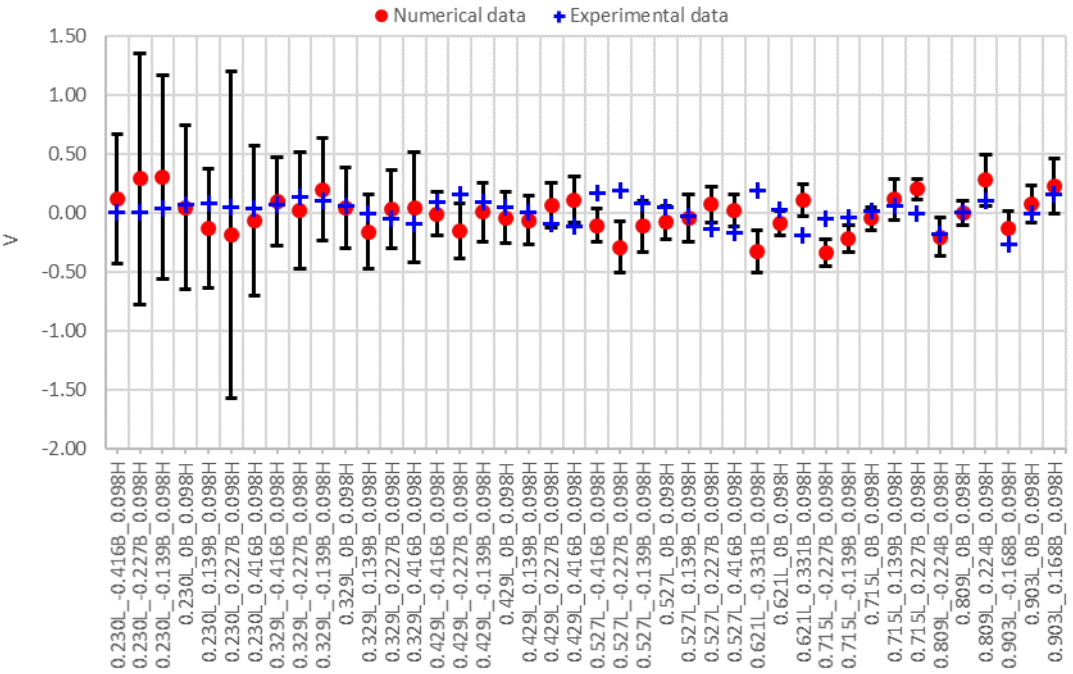

Figure 7.10. Normalized <v> velocity under the higher flow conditions in the near-bottom region (z/H_0 = 0.098). Points are organized from upstream to downstream in the direction of the X axis.

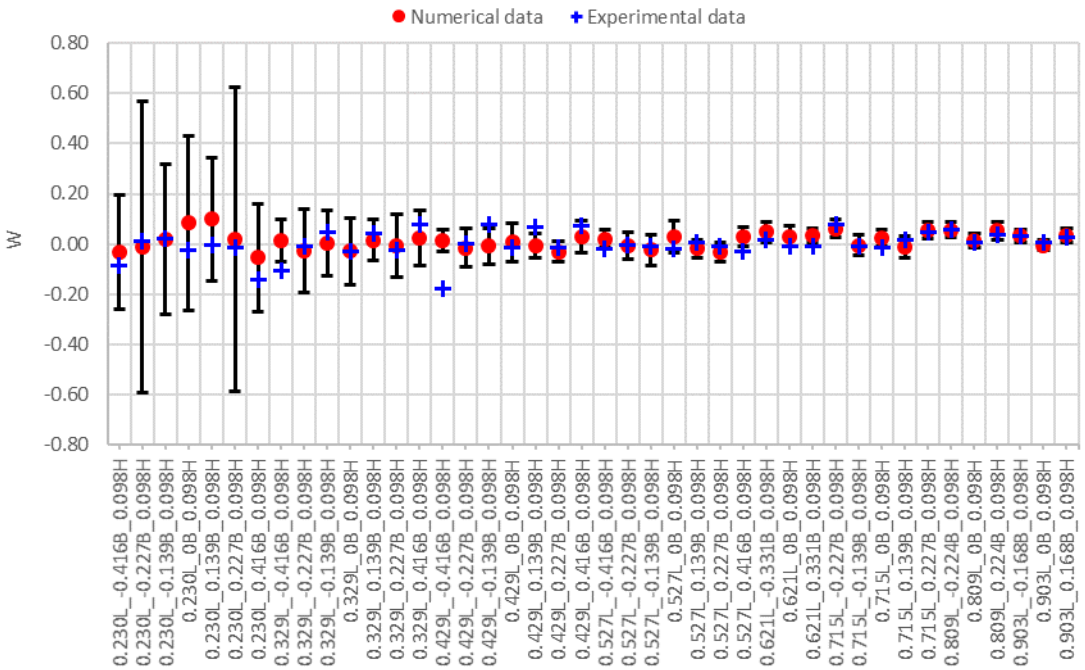

Figure 7.11. Normalized <w> velocity under the higher flow conditions in the near-bottom region ($z/H_0 = 0.098$). Points are organized from upstream to downstream in the direction of the X axis.

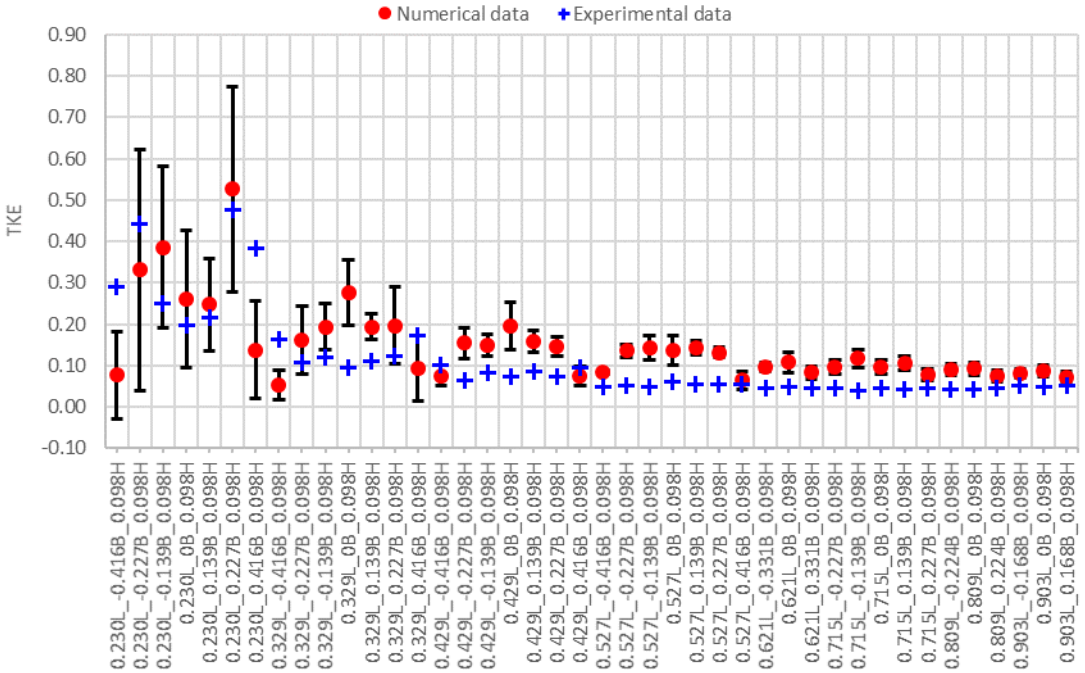

Figure 7.12. Normalized TKE under the higher flow conditions in the near-bottom region ($z/H_0 = 0.098$). Points are organized from upstream to downstream in the direction of the X axis.

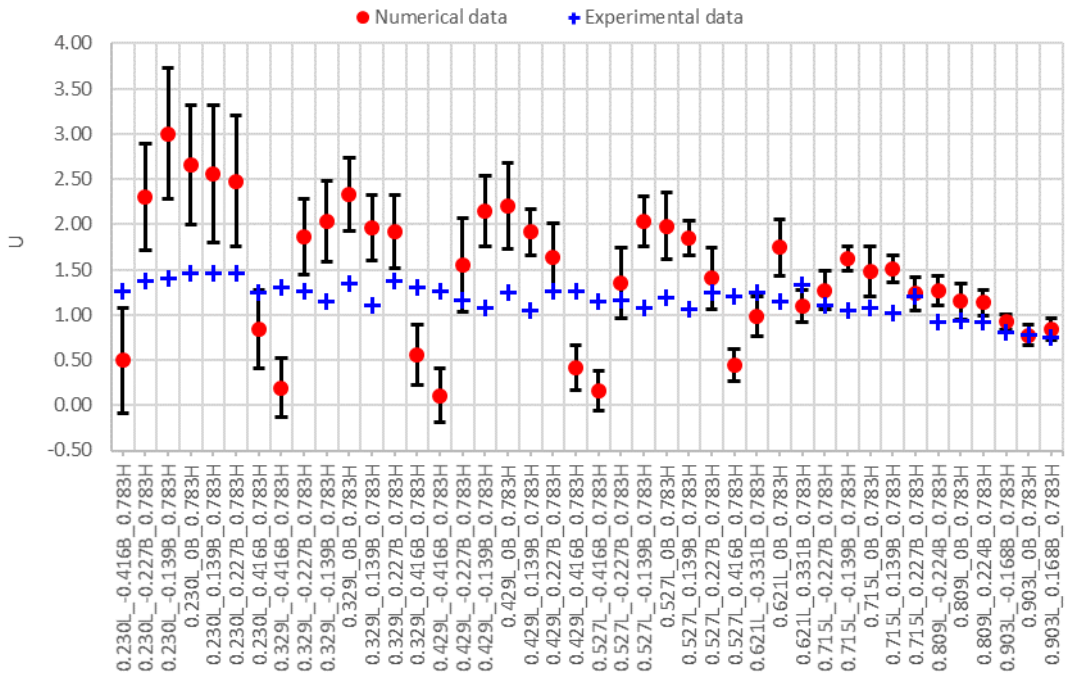

Figure 7.13. Normalized <u> velocity under the higher flow conditions in the near-surface region (z/H_0 = 0.783). Points are organized from upstream to downstream in the direction of the X axis.

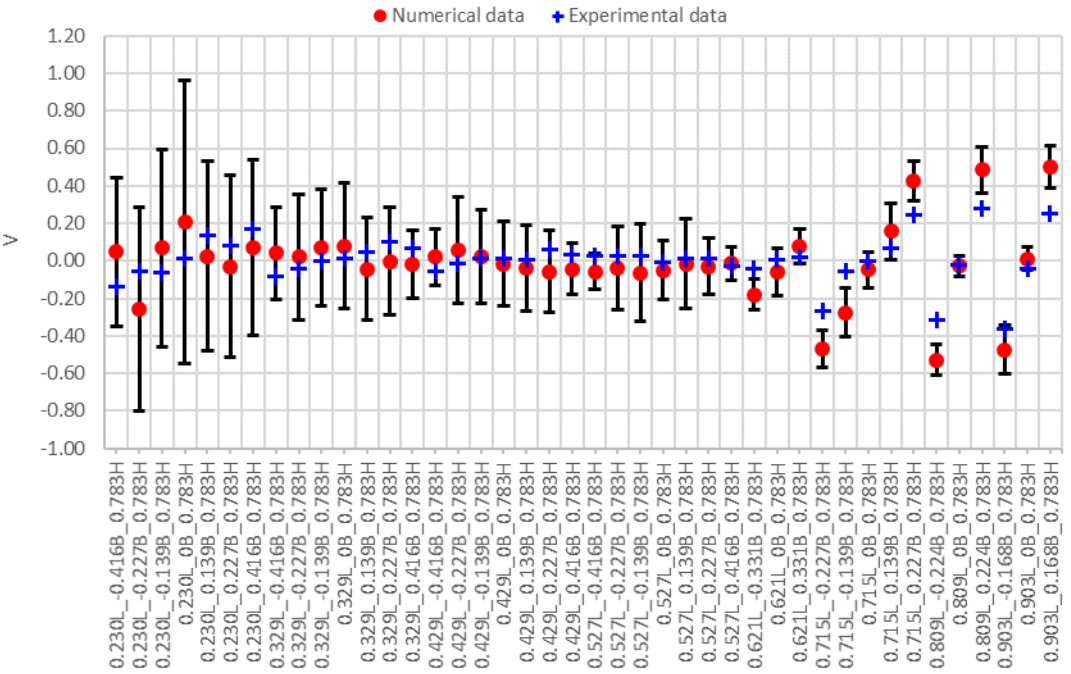

Figure 7.14. Normalized <v> velocity under the higher flow conditions in the near-surface region (z/H_0 = 0.783). Points are organized from upstream to downstream in the direction of the X axis.

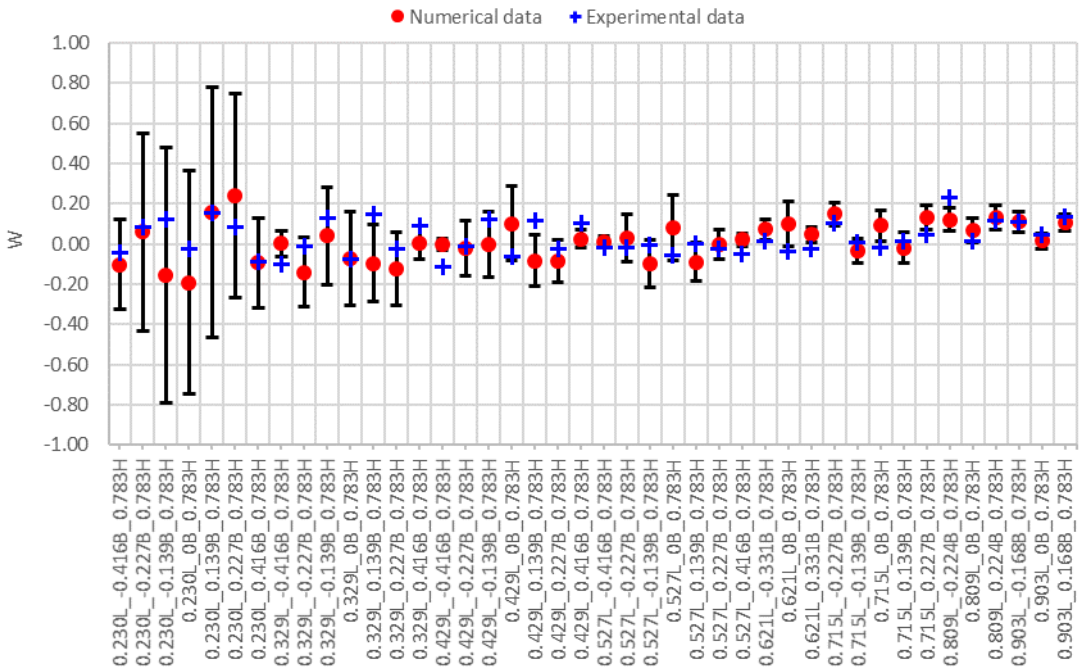

Figure 7.15. Normalized <w> velocity under the higher flow conditions in the near-surface region ($z/H_0 = 0.783$). Points are organized from upstream to downstream in the direction of the X axis.

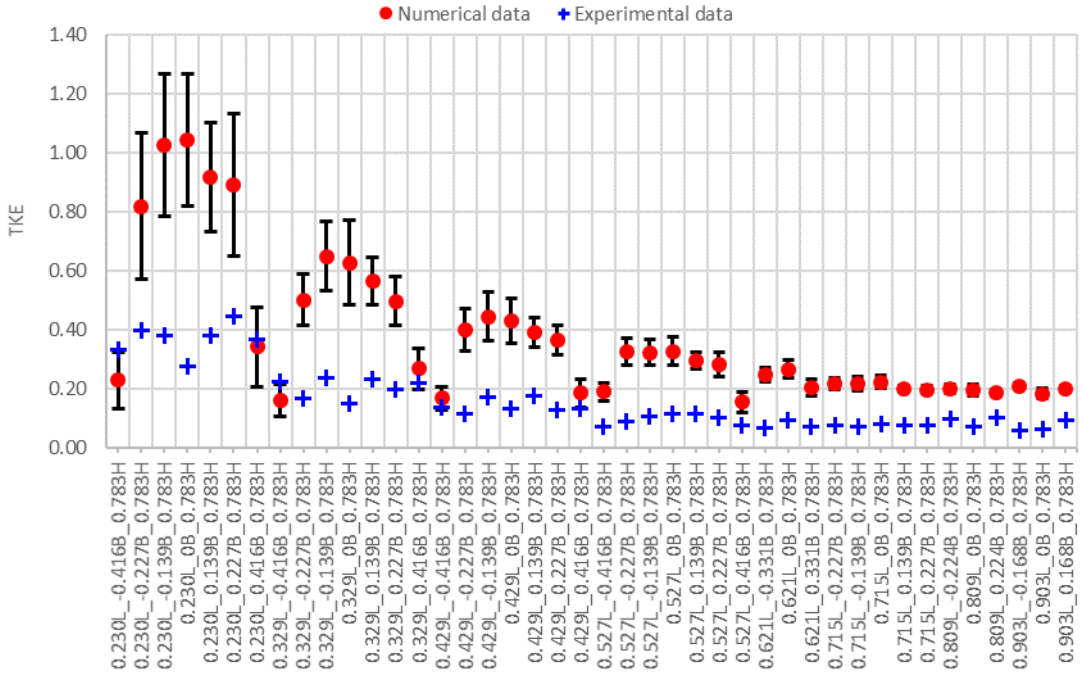

Figure 7.16. Normalized TKE under the higher flow conditions in the near-surface region ($z/H_0 = 0.783$). Points are organized from upstream to downstream in the direction of the X axis.

RÉSUMÉ ÉTENDU EN FRANÇAIS

INTRODUCTION

CONTEXTE : LE CONTRÔLE DE LA POLLUTION DES EAUX URBAINES

Le contrôle de la pollution des milieux aquatiques provoquée par les contaminants chimiques et biologiques véhiculés dans les eaux urbaines (eaux usées et eaux pluviales) est crucial pour la protection des ressources en eau, dans un contexte de changements globaux (demande en eau croissante, croissance démographique, urbanisation croissante, changement climatique). En effet, la disponibilité des ressources en eau est fortement liée à la qualité de l'eau : la pollution des sources d'eau, comme les masses d'eau réceptrices des effluents urbains, peut interdire l'utilisation de ces dernières et contribuer à la pénurie d'eau (ONU, 2017A). L'urbanisation accélérée et l'expansion des systèmes municipaux de distribution d'eau potable et d'assainissement contribuent à la production croissante d'effluents urbains et à leur importance croissante dans le cycle de l'eau. De nos jours, la population urbaine est estimée à 55% de la population mondiale et les Nations Unies estiment que d'ici 2050, la population urbaine représentera 68% de la population mondiale totale (ONU, 2018). Donc la gestion des effluents urbains s'avère un défi majeur.

Les rejets urbains par temps de pluie (RUTP) comprennent tous les effluents d'eau rejetés par les systèmes d'assainissement lors d'un évènement pluvieux, y compris les rejets des réseaux unitaires et d'eaux pluviales non traités, ainsi que les effluents traités des stations d'épuration (STEP). La pollution provenant des RUTPs est, en général, plus difficile à contrôler que les effluents urbains produits par temps sec, qui comprennent principalement les eaux usées permanentes domestiques et industrielles. Les raisons sont les suivantes : i) les RUTPs sont des flux irréguliers et difficilement prévisibles, ii) les pluies qui les déclenchent sont très variables et iii) il existe un manque de connaissances sur cette source de pollution, car l'intérêt d'étudier et de traiter ce type d'effluents a commencé plus tard que l'intérêt pour les effluents urbains par temps sec, comme ceux des STEPs (Guerber et Tabuchi, 1992). En outre, prendre en compte la pollution des RUTP nécessite une connaissance globale du bassin versant urbain (environnement naturel, climatologie, caractéristiques du bassin, données sur l'urbanisme, etc.), ce qui n'est pas toujours facile à obtenir, comme le rappellent Guerber et Tabuchi (1992).

Néanmoins, les impacts potentiels des RUTPs sur les écosystèmes et les usages de l'eau sont divers et leurs conséquences ne sont pas négligeables (Truchot *et al.*, 1994). En effet, les RUTPs ont souvent un impact significatif sur la morphologie des rivières (érosion du lit, dépôts

solides), sur la composition biochimique des milieux aquatiques (désoxygénation et chocs anoxiques, hyper-eutrophisation des nutriments, toxicité des micropolluants, risques pour la santé associés à la pollution bactériologique), sur la perception de ces milieux aquatiques (pollution visuelle et olfactive) ainsi que sur les utilisations de cette eau (eau potable, pisciculture, activité nautique) (House *et al.*, 1993; Truchot *et al.*, 1994). La maîtrise et la minimisation de ces impacts et de leurs conséquences nécessitent une meilleure connaissance et un meilleur contrôle des flux de polluants émis par les RUTPs, en particulier par ceux provenant des rejets non traités des déversoirs d'orage (DOs).

L'IMPORTANCE DES REJETS DES DOs COMME SOURCE DE POLLUTION

En effet, pendant les temps de pluie où il se produit des orages avec des pics de débit importants, les DOs évacuent les excédents d'eau qui ne peuvent pas être traités par les STEPs et ces effluents arrivent directement dans les milieux naturels sans aucun traitement. Les rejets des DOs représentent une source majeure de pollution pour les masses d'eau réceptrices, car ces débordements atteignent généralement les milieux récepteurs avec des concentrations de polluants significatives. Plusieurs études ont mis en évidence le rôle important des rejets des DOs en tant que chemins d'accès aux eaux réceptrices urbaines de divers contaminants, tels que les micropolluants organiques (Becouze-Lareure *et al.*, 2016; Launay *et al.*, 2016), en particulier ceux fortement éliminés par la WWTP (Phillips. *et al.*, 2012; Viviano *et al.*, 2017; Weyrauch *et al.*, 2010), micropolluants inorganiques (Becouze-Lareure *et al.*, 2016; Weyrauch *et al.*, 2010), nutriments (Becouze-Lareure *et al.*, 2016; Viviano *et al.*, 2017), d'hormones (Phillips *et al.*, 2012) ou de bactéries (Passerat *et al.*, 2011; Weyrauch *et al.*, 2010), entre autres. Ces études montrent l'importance de la contribution des rejets des DOs à la fois aux masses annuelles de polluants dans les eaux réceptrices et à leurs concentrations maximales de polluants pendant les orages, ainsi que leurs impacts sur ces masses d'eau.

Le rétablissement de la qualité des masses d'eau réceptrices nécessite des stratégies d'atténuation des impacts des RUTPs, incluant les rejets des DOs. Ces stratégies peuvent être classées soit en actions préventives, soit en actions correctives et sont expliquées en détail par Chocat *et al.* (2007). Toutes les stratégies nécessitent une meilleure compréhension de la dynamique des écoulements dans les systèmes d'assainissement, ainsi qu'un contrôle en continu et une surveillance fiable des volumes et des masses de polluants déversés. Des données fiables et précises sont non seulement nécessaires avant la mise en œuvre de ces

stratégies (à des fins de conception, par exemple), mais elles sont également nécessaires une fois que ces stratégies sont opérationnelles pour évaluer leurs performances.

De plus, au cours des dernières décennies, plusieurs autorités environnementales et gouvernements au monde ont encouragé les responsables des systèmes de drainage urbain à renforcer le contrôle des rejets des DOs (MDDELCC, 2014; MJC, 2015; US-EPA, 1994; OME, 1994) et à fournir des données fiables sur leur pollution. Depuis 2006, le Règlement Européen n° 166/2006 (UE, 2006) concernant la création d'un registre européen des rejets et des transferts de polluants oblige les États membres de l'Union européenne à notifier chaque année les rejets dans l'eau de tout polluant spécifié à l'annexe II du règlement dont la valeur seuil applicable spécifiée dans la présente annexe est dépassée. Ce règlement oblige les gestionnaires des systèmes d'assainissement urbain à mettre en œuvre des méthodes de surveillance fiables pour obtenir des données précises sur les rejets des DOs, du moins dans les cas les plus importants. Par exemple, en France, l'arrêté ministériel DEVL1429608A (MEDDE, 2015a) impose que les gestionnaires des réseaux d'assainissement urbain doivent (i) identifier et localiser tous les points de rejet (DOs) de leurs reseaux, (ii) quantifier le nombre de rejets et leur fréquence annuelle (iii) d'autosurveiller les DOs avec certaines caractéristiques de rejets, (iv) d'évaluer la qualité des eaux réceptrices dans certains cas spécifiques et (v) de transférer toutes ces données aux autorités environnementales nationales correspondantes, qui informeront chaque année la Commission Européenne.

Par conséquent, des données fiables et précises de volumes et masses rejetés par les DOs sont nécessaires pour des raisons environnementales, techniques et règlementaires. Le principal défi en matière de surveillance des DOs est que ces structures hydrauliques n'ont pas été conçues à l'origine pour la surveillance et la métrologie. En conséquence, ils présentent souvent une hydrodynamique complexe et les incertitudes associées aux processus de mesure traditionnels, si estimées, sont en général très élevées.

LA SURVEILLANCE ET LA MESURE DES REJETS DES DOs

La surveillance des flux de polluants est réalisée en mesurant conjointement les débits et les concentrations de polluants des rejets des DOs. Il existe de nos jours différentes méthodes de mesure de débits et concentrations de polluants des rejets de DOs. La revue bibliographique effectuée dans le document original en version anglaise de ce rapport de thèse a permis d'observer que les méthodes de mesure du type « relation hauteur d'eau-débit » (relation QH) présentent globalement les incertitudes les plus faibles lors de la mesure des débits. Si elle est

appliquée à l'aval du DO, la modélisation 3D fournit des résultats très satisfaisants, mais les HQR obtenues dépendent du site, car les géométries des DOs ne sont pas normalisées. Les dispositifs pré-étalonnés ou les canaux préconçus disponibles peuvent être installés dans les conduites de déversement en aval des DOs complexes, mais uniquement dans des conditions hydrauliques spécifiques, par exemple, une distance en amont appropriée avant la mise en œuvre du dispositif ou l'absence d'influence de l'aval, entre autres. En ce qui concerne les concentrations de polluants, le contrôle de la qualité des rejets des DOs est plus représentatif s'il est effectué directement au canal de déversement, simultanément aux débits et dans des conditions hydrauliques assurant un mélange homogène des polluants dans la section de mesure. Les techniques basées sur l'optique présentent les principaux avantages de fournir des résultats immédiats et continus, bien que l'établissement de relations entre les variables optiques et les paramètres du polluant nécessite un étalonnage sur site avec une méthode basée sur l'échantillonnage qui peut augmenter considérablement les incertitudes sur les valeurs de concentration résultantes. Seuls quelques polluants ont été corrélés de manière satisfaisante avec les variables optiques, mais les recherches continuent d'être en mesure d'augmenter cette liste.

LE DSM-flux

Le DSM-flux est un nouveau dispositif de mesure qui a été conçu pour répondre à certaines des caractéristiques préférables des dispositifs de surveillance des rejets des DOs énumérés à la section précédente. Le Dispositif pour la Surveillance et la Maîtrise des flux polluants (DSM-flux), dont le concept du design a été proposé par (Volte *et al.*, 2013), est un nouveau dispositif pré-étalonné et préconçu pour surveiller et contrôler la quantité et la qualité des rejets des DOs. Le DSM-flux a été conçu pour mesurer les débits et volumes déversés, ainsi que les concentrations et masses de polluants. De plus, grâce à sa conception, ce dispositif réduit également la pollution particulaire par sédimentation et atténue les effets de l'érosion sur les eaux réceptrices en dissipant de l'énergie cinétique de l'écoulement par turbulence.

Le DSM-flux est un canal ouvert rectangulaire avec une géométrie originale dont les dimensions sont fonction du diamètre interne du tuyau d'arrivée auquel le dispositif est connecté. Il est composé de quatre zones principales dont le but principal est de permettre au dispositif de fonctionner correctement sous différents régimes d'écoulement à différents endroits. Ces zones sont, d'amont en aval : la zone d'accélération, qui permet d'assurer un régime torrentiel à l'entrée du dispositif ; la zone de dissipation d'énergie, qui réduit l'énergie

cinétique de l'écoulement par turbulence et améliore le mélange de particules en suspension dans la section ; la zone de stabilisation, où le régime d'écoulement devient fluvial et les vitesses sont réduites pour favoriser la décantation de matière en suspension ; et la zone de déversement, où un double seuil à paroi mince assure un niveau d'eau stable pour réaliser des mesures ainsi que des conditions favorables pour l'échantillonnage. La figure 1 montre une vue 3D schématisée du dispositif.

Cette nouvelle technologie a été conçue pour offrir certains avantages par rapport à d'autres solutions de surveillance : sa méthodologie de mesure est indépendante de la géométrie des DOs en amont, elle est facile à installer sur site et ses caractéristiques hydrodynamiques fournissent les conditions appropriées pour une surveillance précise et fiable en continu ainsi qu'un échantillonnage de qualité.

OBJECTIFS DE THÈSE ET STRATEGIE GÉNÉRALE

Le DSM-flux a été conçu dans le but principal de surveiller les rejets des DOs et les flux de polluants. Sa conception initiale a été optimisée au laboratoire DEEP dans le cadre de la thèse de Momplot (2014) au moyen de tests expérimentaux et de simulations numériques, mais aucun test n'a été réalisé sur un prototype au terrain, dans des conditions de fonctionnement réelles. L'actuel travail de doctorat prend le relais du travail de Momplot (2014) et traite des aspects qui n'ont pas pu être abordés dans son travail ou qui nécessitent d'une évaluation plus approfondie.

L'objectif principal de ce travail de doctorat est d'évaluer la capacité du DSM-flux à surveiller les rejets des DOs et donc à protéger les eaux réceptrices en fournissant des données plus fiables et en réduisant les quantités de polluants particulaires rejetées. En d'autres termes, cette étude a pour objectif de confirmer que le DSM-flux fonctionne tel qu'il a été prévu lors de sa conception et de répondre ainsi à ces deux questions principales :

(i) Le DSM-flux, est-il un dispositif de surveillance robuste fournissant des données fiables et précises ?

(ii) Le DSM-flux, est-il capable de retenir efficacement les polluants particulaires ?

Pour répondre à ces questions, une approche systémique multi-échelle a été envisagée afin d'évaluer le comportement du flux DSM sur 3 systèmes de nature différente (physique / virtuelle), analysés dans différentes conditions de fonctionnement (laboratoire / virtuel / réel)

et à deux échelles différentes (petite /grande). La raison pour laquelle une approche systémique multi-échelles a adopté est que chacun des systèmes a ses forces et ses faiblesses pour répondre aux questions et on pense que l'étude des 3 systèmes et des 2 échelles, ainsi que de leurs relations, fournira la réponse la plus générique et la plus réaliste possible dans les limites (de temps et de ressources) de ce travail de doctorat.

L'objectif final étant d'analyser les performances du dispositif fonctionnant dans des conditions réalistes et à une échelle habituelle, chacune des questions a été abordée selon une stratégie commune, qui se divise en trois étapes principales, comme schématisé à la Figure 2. Chaque étape correspond aux analyses réalisées sur un des 3 systèmes : modèle physique réduit, modèle numérique et prototype au terrain.

L'originalité de ce travail de thèse réside dans le fait que les questions abordées ont été étudiées selon cette approche systémique multi-échelles où les résultats obtenus dans un dispositif d'une certaine échelle ont été reproduits sur un modèle équivalent mais de nature différente. Ensuite, le dispositif a été mis à l'échelle et les principaux mécanismes hydrodynamiques ont été étudiés dans un appareil plus grand, mettant en évidence non seulement les relations entre différentes échelles (lois de similitude et effets d'échelle), mais également entre des systèmes de nature différente. Toutes ces informations contribueront à la connaissance du comportement de DSM-flux et à l'amélioration et optimisation de sa conception.

RÉSULTATS PRINCIPAUX QUESTION 1 : Le DSM-flux, est-il un dispositif de surveillance robuste fournissant des données fiables et précises ?

ÉTAPE 1 : ANALISES SUR LE MODÈLE PHYSIQUE RÉDUIT

L'objectif de cette étape est de déterminer la méthodologie de mesure du DSM-flux et d'analyser sa fiabilité et robustesse. Le DSM-flux a été conçu avec une configuration spécifique qui permet la mesure des débits (entre autres objectifs indiqués à l'introduction) au moyen d'une mesure de niveau d'eau. Ainsi, l'établissement de la méthode de mesure se traduit par la détermination d'une relation hauteur d'eau-débit appropriée et par estimer ses limites d'incertitude.

Les résultats et conclusions principaux de cette partie sont les suivants :

Les principales conclusions de cette section sont les suivantes :

- Une méthodologie de mesure du type « relation hauteur d'eau-débit » (relation QH) simple à utiliser a été créé spécifiquement pour le DSM-flux au moyen d'essais sur un modèle physique à petite échelle.
- Il a été prouvé que la relation QH du DSM-flux est robuste pour de multiples conditions d'écoulement d'entrée au dispositif concernant différents régimes d'écoulement et champs de vitesse avec différentes caractéristiques de symétrie. Pour tous les cas testés, les valeurs de quatre indicateurs différents (RMSE, MAE, MARE et NSE) utilisées pour évaluer la qualité et la robustesse des modèles étalonnés avec des données expérimentales ont été estimées. En conditions de déversement libre aéré, les valeurs de RMSE et MAE étaient inférieures à 0.0004 m^3/s dans tous les cas, pour des débits compris entre 0.0041 et 0.0102 $m^3/$ s. Les valeurs du MARE étaient inférieures à 7% et le NSE (coefficient de Nash-Sutcliffe) dépassait 0,85 dans presque tous les cas. Dans le cas de conditions de flux extrêmes avec un obstacle à l'entrée, les valeurs des indicateurs statistiques sont toujours acceptables dans le contexte de la surveillance des DOs.
- La méthode du « Guide pour l'expression de l'incertitude de mesure » a été appliqué pour estimer les incertitudes associées à cette méthode de mesure et, pour des débits plus élevés, les incertitudes étaient inférieures à 15%. En ce qui concerne les volumes d'eau, pour les quatre événements typiques reproduits dans le modèle physique à petite échelle, les incertitudes étaient inférieures à 2%.
- Au vu des résultats sur le modèle réduit, le flux DSM apparaît comme une bonne alternative par rapport aux méthodes actuelles pour la surveillance fiable des rejets des DOs car la méthode de mesure est indépendante des conditions hydrauliques en amont du dispositif

et les incertitudes associées aux mesures de débit et de volume sont relativement faibles, en particulier lors de grands déversements.

La figure 3 montre la relation QH obtenue pour la mesure de débits au DSM-flux, avec les bandes de confiance de 95% et les points d'étalonnage et validation.

ÉTAPE 2 : SIMULATIONS AU MODÈLE NUMÉRIQUE ET MISE EN ÉCHELLE

La relation QH du DSM-flux s'est révélé être une méthodologie robuste pour la mesure avec précision les débits et les volumes des rejets des DOs à petite échelle. Cependant, le dispositif fonctionnera probablement dans des canaux de déversement plus grands que celui utilisé au modèle physique à petite échelle, car les conduites de déversement des DOs sur le terrain ont généralement des diamètres supérieurs à 0.15 m. L'utilisation de la relation QH dans un dispositif plus grand n'est pas toujours directe. Lors de la mise à l'échelle d'une structure hydraulique tenant compte la similitude de Froude pour l'écoulement (comme considéré dans cette thèse), les nombres de Reynolds et de Weber ne sont pas conservés, ce qui peut entraîner un comportement différent de l'écoulement à différentes échelles. Ces différences sont communément appelées « effets d'échelle » et, dans le cas de la méthode de mesure de débits du DSM, elles pourraient entraîner des relations différentes entre les débits et les niveaux d'eau en fonction de l'échelle de du dispositif. Les performances de la relation QH du DSM-flux à deux échelles différentes et les effets d'échelle possibles affectant cette relation ont été évalués numériquement au moyen de simulations CFD.

Les résultats et conclusions principaux de cette section sont les suivantes :

- La relation QH du DSM-flux est robuste à petite échelle, même en dehors de sa plage d'étalonnage au modèle physique réduit.
- La relation QH du DSM-flux semble robuste à grande échelle, en particulier pour les débits testés allant jusqu'à 0.1 m^3/s, avec des effets d'échelle pas significatifs.
- La relation QH du DSM-flux ne semble pas être influencée de manière significative par des modifications légères de son design original du rapport w / L.
- Une mise à l'échelle du dispositif DSM-flux préservant une similitude géométrique semble produire des vitesses et des valeurs d'énergie cinétique turbulente (TKE) qui, a priori, pourraient compromettre le dépôt de matériel en suspension au dispositif. Si cette fonction doit être assurée, il est recommandé d'augmenter le nombre de dissipateurs, d'adapter leur hauteur et d'augmenter les hauteurs des crêtes des seuils de la zone de déversement. La

relation QH du DSM-flux restera valable pour des débits et des niveaux d'eau relativement faibles. De nouvelles relations de conception dépendant, par exemple, de la taille du dispositif et des limites de validité de la relation QH actuelle doivent être établies pour ces cas.

- La relation QH du DSM-flux présente des divergences plus importantes à grande échelle pour des débits et des niveaux d'eau relativement élevés. Cependant, ces différences sont inférieures aux incertitudes habituelles trouvées sur le terrain. Des investigations supplémentaires sont nécessaires pour déterminer les raisons de ces divergences. Une relation modifiée pour les débits et les niveaux d'eau élevés doit être établie pour assurer la fonction de surveillance du dispositif dans cette plage de fonctionnement à des échelles plus grandes.

La figure 4 montre la relation QH obtenue au modèle physique pour le dispositif à grande échelle, avec les bandes de confiance de 95% correspondant à différentes précisions de l'instrument de mesure des hauteurs et les points solution du modèle numérique testé.

ÉTAPE 3 : VALIDATION DE LA MÉTHODE SUR LE PROTOTYPE AU TERRAIN

Les conclusions précédentes ont été établies au moyen d'essais de laboratoire, dans lesquels les conditions diffèrent de la réalité, les modèles étant simplifiés et, sur le terrain, d'autres facteurs peuvent influer sur les phénomènes qui nous intéressent. Dans ce cas, et du point de vue de la question 1 de ce travail de thèse, les facteurs suivants pourraient influencer la reproduction de la relation QH du DSM-flux sur le terrain: (i) le fait que le fluide réel n'est pas simplement de l'eau propre, comme dans le laboratoire mais qu'il transporte également des matières solides de différentes tailles et matériaux, (ii) le fait que les événements réels à mesurer sont des événements dynamiques non permanents, qui n'ont pas été testés à plus grande échelle, et (iii) le fait que les dispositifs réels installées sur le terrain n'ont pas une configuration idéale: il existe de petits défauts de construction et d'autres imprécisions susceptibles de modifier le comportement du flux par rapport aux modèles. Afin de valider la méthodologie de surveillance dans des conditions de fonctionnement réalistes et d'évaluer simultanément les effets d'échelle possibles à plus grande échelle, un prototype de terrain installé à Sathonay-Camp (France) a été surveillé pendant 4 mois et ses débits ont été comparés aux mesures faites avec une méthode de mesure indépendante, développée dans le cadre de cette étude spécifiquement pour cette validation.

Les principales conclusions de cette section sont les suivantes :

- Une seconde méthodologie de surveillance, basée également sur une relation QH mais indépendante à celle du DSM-flux, a été développée sur le site expérimental de Sathonay-Camp afin de comparer ces valeurs de débit à celles obtenues avec la relation QH du DSM-flux, avec l'objectif de valider la méthodologie de mesure du DSM-flux dans des conditions de fonctionnement réelles. La nouvelle méthode de surveillance a été établie numériquement et consistait en une relation QH entre les niveaux d'eau enregistrés dans une chambre de répartition en amont du DSM-flux et les débits acheminés vers le DSM-flux par le tuyau de connexion entre la chambre et le dispositif. La relation QH résultante pour la chambre a deux plages de fonctionnement différentes et son ajustement aux données numériques a été très bon.
- Les débits mesurés à l'aide des deux méthodes de surveillance sont similaires pour les débits les plus faibles mais diffèrent considérablement pour les débits les plus élevés, les débits mesurés au DSM-flux étant supérieurs à ceux obtenus au niveau de la chambre de répartition. Ces différences augmentent à mesure que la magnitude des déversements augmente. Les écarts (tant pour les volumes déversés que pour les débits) sont significatifs, en particulier pour les événements avec des pics de débit supérieurs à 0.15 m^3/ s. Des erreurs d'installation (augmentation de l'ouverture de la vanne d'entrée de la conduite de connexion, infiltration de l'eau de ruissellement des rues) ou des imprécisions dans les méthodes de mesure pour des débits plus élevés peuvent expliquer ces écarts.
- En dépit des différences pour les valeurs de débit plus élevées, les coefficients d'évaluation pour la plupart des événements enregistrés sont satisfaisants, avec une valeur NSE supérieure à 0.5 pour 83% des événements.
- Les volumes déversés ont également été estimés pour les deux méthodologies de mesure et comparés. Des différences relatives sont perceptibles (seuls 15% des événements présentent des différences de volume inférieures à 10%), mais les aspects techniques susmentionnés (vanne) font douter de leur pertinence. Il est nécessaire d'obtenir à l'avenir une seconde technique sûre et précise pour caractériser le débit et mieux évaluer les performances de la relation QH du DSM-flux au terrain. En raison de limitations techniques, il n'a pas été possible d'effectuer cette deuxième vérification dans le cadre de ce travail de thèse.

La figure 5 montre les hydrogrammes de deux évènements enregistrés au site de Sathonay-Camp où les débits sont mesurés par la méthode du DSM-flux (rouge) et par la méthode de la chambre de répartition (bleu). Pour les événements de relativement faibles débits comme ceux-ci, le calage entre les deux méthodes est très satisfaisant.

RÉSULTATS PRINCIPAUX QUESTION 2 : Le DSM-flux, est-il capable de retenir efficacement les polluants particulaires ?

ÉTAPE 1 : ANALISES SUR LE MODÈLE PHYSIQUE RÉDUIT

Du fait de sa conception, le flux DSM a la capacité de retenir des polluants particulaires par sédimentation. Cependant, le mouvement des matières solides, en particulier des particules les plus fines, entraînées par des écoulements relativement faiblement chargés, est principalement dirigé par les forces agissant dans le fluide. Ainsi, pour l'étude du transport solide dans le DSM-flux, ainsi que pour l'étude du début (entraînement) et la fin (décantation) du mouvement de la matière solide, il est essentiel de bien connaître la dynamique de l'écoulement dans le dispositif.

Le champ de vitesse et les quantités de turbulence correspondantes sont étudiés dans le modèle physique à petite échelle en fonction d'un débit constant entrant afin de mieux comprendre le comportement de l'écoulement dans le dispositif en régime permanent. Bien que les CSO soient des phénomènes non-permanents, ces résultats donneront un premier aperçu de l'hydrodynamique de l'écoulement du dispositif dans ses conditions hydrauliques les plus simples et permettront de mieux relier ces variables aux mécanismes des dépôts.

L'efficacité d'un dispositif de rétention de conception spécifique dépend notamment des caractéristiques d'entrée de l'écoulement, des types de polluants et du type de particules, ainsi que de la conception et de la gestion des installations, telles que l'état du dispositif avant l'événement. Pour caractériser pleinement un tel dispositif, plusieurs combinaisons doivent être étudiées mais, dans le cadre de cette thèse, seules quelques configurations seront abordées. Cette partie de l'étude est consacrée à trois objectifs : (i) évaluer la capacité de rétention du DSM-flux en cas d'eaux polluées et déterminer les zones de dépôts potentiels ; (ii) estimer le taux d'érosion des sédiments déposés au dispositif lors d'un événement ultérieur peu pollué et déterminer les zones potentielles d'entraînement de particules ; et (iii) déterminer si le DSM-flux contribue à une séparation granulométrique entre les masses de matière retenues et celles déversées. Les mêmes configurations d'écoulement que celles utilisées pour l'évaluation des champs de vitesses et de la turbulence ont été sélectionnées afin d'étudier les relations potentielles entre l'hydrodynamique du dispositif et les mécanismes de sédimentation et d'entraînement.

Les résultats et conclusions principaux de cette partie du travail sont les suivants :

- L'écoulement moyen dans le dispositif est principalement 1D dans la zone de stabilisation, une fois que l'influence du ressaut hydraulique a diminué, et 2D en aval, avec un écoulement dirigé de l'axe central vers les crêtes de déversement, en particulier près de la surface.
- Une région d'écoulement très lente est observée pour le débit inférieur des deux côtés du dispositif.
- On observe deux tourbillons à grande échelle dans les sections transversales de la zone de stabilisation, dans le sens horaire à droite et dans le sens antihoraire à gauche.
- L'énergie cinétique turbulente (TKE) est fortement influencée par le ressaut hydraulique en amont et se répartit de manière assez homogène en aval du dispositif. Les cartographies de dépôt devraient donc se produire dans l'ensemble de la région aval, sauf près des sections à TKE élevé plus en amont.
- Les modèles d'écoulement et de TKE sont considérés comme symétriques, ce qui pourrait conduire à une meilleure distribution de l'écoulement et des particules en suspension.
- La concentration de particules pour un débit donné ne semble pas influer beaucoup sur l'efficacité de rétention du dispositif. Cependant, la magnitude du débit a une influence importante : plus le débit est élevé, moins il y a des dépôts et l'érosion est plus importante.
- Pour les conditions de faible débit, le pourcentage de particules piégées par le DSM-flux est d'environ 50% mais elle est réduite de moitié pour un débit légèrement supérieur. Il est donc possible que le DSM-flux ne puisse retenir les polluants particulaires fins (D50 compris entre 100 et 300 µm) que si les débits sont relativement faibles.
- Il semble que la masse entrainée soit constante pour un débit d'eau donné, même avec différentes masses de sédiments déposées disponibles. Ce résultat inattendu pourrait s'expliquer par le fait que seules les masses des sédiments ont été mesurées, et non les reliefs ou l'évolution du volume des sédiments. Le matériau entraîné mais non déversé n'est pas pris en compte dans le calcul du taux d'érosion, comme il est calculé dans ce travail de thèse, ce qui pourrait expliquer la différence avec d'autres études dans la littérature. S'il est confirmé qu'une partie des sédiments précédemment déposés peut être entraînée mais reste dans le dispositif, le résultat serait positif pour la fonction de rétention du dispositif.
- Quelques corrélations ont été observées entre les variables hydrodynamiques et les phénomènes de dépôt / érosion :

  - Les zones de dépôt correspondent assez bien aux régions de valeurs TKE proches du fond, relativement basses.
  - L'érosion commence principalement dans les bandes adjacentes aux murs latéraux et dans les deux zones érodées de forme parabolique en aval de la zone de dissipation. Avec le temps, ces deux zones s'étendent en aval, créant de petites énigmes (dans des conditions de faible débit) ou entraînant la matière déposée en aval (conditions de débit plus élevées).
- Dans les conditions de faible débit, la quasi-totalité des sédiments reste dans le dispositif lorsqu'un événement ultérieur dépourvu de charge polluante affecte les sédiments déposés précédemment. Cependant, pour un débit légèrement plus élevé, presque tous les sédiments sont entraînés. Cela indique qu'après un événement pluvieux où des dépôts se produisent, le DSM-flux doit être nettoyé car un événement ultérieur pourrait laver tous les sédiments. La fréquence de maintenance doit être abordée à l'avenir. Une autre option consisterait à installer un piège à sédiments en bas du dispositif recouvert d'une grille d'une ouverture spécifique, de manière à ne pas influencer la dynamique des flux, mais à laisser les particules entrer dans le piège.
- La séparation des particules n'est pas significative au niveau du DSM-flux, du moins pour la plage fine comprise entre 100 et 300 µm.

La figure 6 montre (a) les cartographies de dépôt (gris) et d'entrainement ultérieur (violet) superposées à les données de TKE au fond (point et étoiles bleus). On observe la corrélation à l'amont, où les zones de TKE plus élevé ne sont pas couvertes par les dépôts (forme de double parabole). Les champs de vitesses au fond (b, bleu) et en surface (c, rouge) pour ce même débit (2 l/s) sont aussi présentés.

ÉTAPE 2 : SIMULATIONS AU MODÈLE NUMÉRIQUE ET MISE EN ÉCHELLE

L'hydrodynamique du DSM-flux a été évaluée sur le modèle physique à petite échelle pour la gamme de conditions hydrauliques permises par la configuration expérimentale. Grâce aux tests réalisés avec des billes de verre, certaines relations potentielles entre les variables hydrodynamiques et les mécanismes de dépôt / entraînement ont été identifiées. Par ailleurs, ces tests ont permis d'avoir une idée des capacités de rétention du flux DSM, mais seulement pour quelques configurations simples.

Comme il a déjà été expliqué, le DSM-flux fonctionnera probablement dans des canaux de déversement plus grands que celui du modèle physique à petite échelle et, par conséquent, le

dispositif prototype aura généralement des dimensions plus grandes que le dispositif expérimental. L'hydrodynamique du DSM-flux à petite et grande échelle est évaluée numériquement au moyen de simulations CFD. Les résultats de ces simulations permettront d'abord d'évaluer les options numériques (équations d'écoulement, modèles de turbulence, traitement près des parois, schémas de discrétisation, etc.) sélectionnées pour le modèle en comparant les résultats numériques aux résultats expérimentaux à petite échelle ; et ensuite, la mise à l'échelle du modèle permettra d'étudier l'hydrodynamique à plus grande échelle et les effets d'échelle possibles qui pourraient apparaître. Des simulations ultérieures avec des particules une fois que l'hydrodynamique aura été validée permettront également de prévoir l'efficacité de rétention de l'appareil pour différents scénarios pluie / concentration. Les résultats liés aux simulations CFD du transport des particules à grande échelle ne sont pas présentés dans ce manuscrit. En effet, ils n'ont pas pu être réalises à cause de la non validation du modèle.

Les principales conclusions de cette section sont les suivantes :

- Trois modèles numériques à petite échelle ont été implémentés afin d'analyser l'hydrodynamique du DSM-flux pour deux conditions d'écoulement différentes. Les différences entre les modèles résident dans une discrétisation différente du domaine spatial (maille de calcul différente en termes de taille et de qualité) et dans un traitement différent près de la paroi. Aucun des modèles ne semble reproduire assez précisément les champs de vitesse expérimentaux : des différences significatives sont observées non seulement dans la magnitude, mais également dans la direction des vecteurs de vitesse. Les contours TKE semblent mieux correspondre aux résultats expérimentaux : les modèles numériques reproduisent le profil caractéristique de la double parabole en aval de la zone de dissipation et présentent des valeurs plus faibles dans le reste de l'appareil. Cependant, des écarts sont encore perceptibles, en particulier pour les débits plus élevés et les zones proches de la surface.
- Les différences étaient également significatives entre les résultats numériques des modèles avec un traitement de paroi différent et un maillage plus grossier. Ainsi, soit le traitement de paroi différent, soit le maillage de calcul différent (ou les deux) ont une influence non négligeable sur les champs de vitesse et les résultats TKE.
- L'effet des maillages de calcul a été étudié pour les deux modèles ayant le même traitement de paroi et des maillages de calcul similaires, offrant une meilleure qualité et une résolution supérieure, mais différents de taille avec un facteur 1.7. Aucune différence significative n'a été trouvée dans les directions des vecteurs de vitesse entre les mailles

avec une différence de résolution de 1.7. Les différences étaient principalement perceptibles en termes de magnitudes, mais le modèle avec la résolution de maille la plus élevée ne reproduisait pas mieux les données expérimentales. Ainsi, on pense que la résolution du maillage n'est pas la raison principale pour laquelle les résultats numériques ne reproduisent pas correctement les champs de vitesse expérimentaux et les valeurs TKE.

- Des recherches supplémentaires sont nécessaires pour tester d'autres options numériques afin de mieux reproduire l'hydrodynamique au DSM-flux à l'aide des modèles numériques. La complexité du flux (entraînement de l'air, structures de vortex dans les trois directions, séparation du flux) pourrait être mieux modélisée avec des modèles de turbulence plus avancés, tels que RSM ou k-ω SST, si les équations RAN sont résolues. Une autre option consiste à envisager d'autres approches numériques, telles que la LES, la SPH ou même la DES, si les ressources de calcul le permettent.
- À plus grande échelle (échelle du prototype), un modèle légèrement modifié par rapport au modèle d'origine semble mieux dissiper l'énergie cinétique et présente des vitesses plus faibles au niveau de la partie aval du dispositif, qui favorisent la décantation. Pour cette raison, cette conception a été choisie pour construire le prototype de terrain. Cependant, une validation de ce modèle doit être effectuée dans les travaux futurs.

La figure 7 montre un exemple des champs de vitesses expérimentaux (a) et numériques (b et c) pour 2 l/s au fond du dispositif, issus des deux modèles les plus différents testés.

ÉTAPE 3 : OBSERVATION DE L'HYDRODYNAMIQUE OU SES EFFETS AU TERRAIN

La dernière étape pour répondre à la question 2 de ce travail de doctorat est l'étude de l'hydrodynamiques et de la capacité de rétention du prototype au terrain fonctionnant dans des conditions de réelles, afin de (i) estimer son efficacité de rétention et (ii) collecter des données pour valider le modèle numérique à grande échelle. Cependant, de telles analyses sont difficiles à effectuer directement sur place car l'accès aux installations en temps de pluie est interdit pour des raisons de sécurité.

Malgré la difficulté de mesurer avec, par exemple, une sonde ADV, d'autres méthodes pourraient être utilisées pour obtenir des données de champ de vitesse pour la validation de modèle numérique. Par exemple, Zhu *et al.* (2017) étudient les capacités des caméras vidéo courantes pour estimer les champs de vitesse de surface dans un bassin de rétention d'eaux pluviales, comme cela est fait avec la technique PIV, appelée dans ce cas LSPIV (PIV à grande échelle). Le prototype de terrain du DSM-flux étant déjà équipé d'une caméra vidéo, cette

méthodologie pourrait être mise en œuvre sur le site à l'avenir, lorsque la technique sera davantage consolidée et validée pour les flux à plus grande vitesse.

D'autres méthodes basées sur l'évènement peuvent s'appliquer pour obtenir des données de validation et d'évaluation de l'efficacité sur le prototype de terrain, par exemple, (i) l'estimation de la masse évènementielle du solides en suspension conservée sur le dispositif au moyen d'une méthode basée sur le bilan de masse à l'entrée et en sortie, et (ii) le suivi de l'évolution des zones de dépôt après chaque événement au moyen d'observations visuelles ou plus précisément de reliefs topographiques obtenus, par exemple, par des techniques de photogrammétrie pour la reconstruction 3D. Il était prévu que ces méthodes soient implémentées dans le prototype de terrain du DSM-flux. Cependant, le site expérimental de Sathonay-Camp a été inondé à plusieurs reprises au cours de cette thèse en raison de la combinaison d'événements extrêmes et du dysfonctionnement du réseau d'assainissement en aval du site, dont les effets de refoulement ont atteint la chambre du DSM-flux. Ces inondations ont endommagé certains équipements, tels que les préleveurs automatiques, qui ont dû être remplacés, et ont également entraîné la fermeture du site pendant de longues périodes. Ces faits ont entravé l'application des méthodologies de mesure sur le terrain, mais leur planification et leur préparation ont été développées au cours de ce travail de doctorat. Elles sont donc décrites dans ce travail de thèse, pour être appliquées dans les études futures.

Pour conclure cette partie de l'étude, quelques données préliminaires du prototype de terrain sont présentées et discutées ici :

La figure 8 présente une photo de la zone de déversement du prototype prise le 14 juin 2018, montrant également la sonde de turbidité et son support. On constate qu'une certaine quantité de sédiments s'est déposée au centre du dispositif, depuis la partie aval de la zone de stabilisation jusqu'au peu près la moitié de la zone de déversement. Cette photo prouve que le DSM-Flux est capable d'intercepter des matières solides. D'après une inspection visuelle, les sédiments sont constitués non seulement des particules les plus fines, mais il semble également y avoir des particules de plus grande taille telles que des sables ou même des graviers fins. D'autres matériaux solides tels que des lingettes humides pour la toilette sont également présents, spécialement attachés au support du turbidimètre. En ce qui concerne la zone de dépôt, plus de sédiments se trouvent dans la zone de déversement que dans la zone de stabilisation, ce qui n'était pas le comportement prévu pour la conception du dispositif. Cette photo a été prise après une série de jours consécutifs de déversements. Ces sédiments

ne correspondent donc probablement pas à un dépôt d'événement unique, de sorte que les sédiments pourraient avoir été affectés par la dynamique des événements ultérieurs.

En ce qui concerne cette photo, il est clair que la sensibilité de la relation QH du DSM-flux à la présence d'épaisseurs différentes de sédiments dans la zone de débordement doit être évaluée de manière expérimentale ou numérique. Cependant, d'après le bon calage obtenu pour les faibles débits, il parait que cette influence n'est pas trop significative.

Enfin, l'analyse des quelques vidéos enregistrées sur le site expérimental de Sathonay-Camp révèle que les petits matériaux flottants sont parfois dirigés vers les parois latérales de du dispositif avant d'arriver à la zone de déversement et, au lieu de rester près des murs et de quitter le DSM-flux à travers les déversoirs, ils font demi-tour et remontent le long de l'écoulement, près des murs. Cela pose la question des zones de recirculation latérale simulées numériquement pour certaines configurations mais non observées sur le modèle physique à petite échelle. Cette divergence est sans aucun doute l'une des questions les plus intéressantes à analyser dans les prochaines études.

CONCLUSIONS GÉNÉRALES ET PERSPECTIVES

Dans cette thèse, deux questions ont été posées :

(i) Le DSM-flux, est-il un dispositif de surveillance robuste fournissant des données fiables et précises ?

(ii) Le flux DSM est-il capable de retenir efficacement les polluants particulaires ?

Pour répondre à ces questions, une approche systémique multi-échelles a été envisagée afin d'évaluer le comportement du DSM-flux à 2 échelles différentes (petite / grande) et les approches de modélisation numérique associées, analysées dans différentes conditions de fonctionnement (laboratoire / site réel). Les principales conclusions de ce travail sont décrites dans cette section.

Concernant la première question, **le DSM-flux peut être considéré comme un dispositif de surveillance robuste permettant d'obtenir des données de flux précises et fiables** vu les résultats de cette thèse. La méthodologie de mesure obtenue expérimentalement, qui repose sur une relation hauteur d'eau-débit, s'est révélée capable de mesurer avec précision les débits et les volumes d'événements, indépendamment des caractéristiques hydrodynamiques et de la complexité de l'écoulement d'entrée. En effet, à une petite échelle, les incertitudes pour les débits plus élevés sont estimées à 15% et les volumes des événements testés ont été mesurés avec des incertitudes inférieures à 2%. On considère que les incertitudes dépendent principalement de la précision de la mesure du niveau d'eau. On pense que l'homogénéité de la surface libre au niveau de la zone d'échantillonnage - et sa stabilité relative, du moins pour les débits plus faibles - observée lors des tests contribueront à maintenir les incertitudes plus basses. À plus grande échelle, la méthodologie de surveillance s'est avérée toujours valable sans effets d'échelle significatifs, ce qui montre la capacité de standardisation de la méthode. Aussi à grande échelle, des simulations numériques ont montré que les débits obtenus à l'aide de la relation QH du DSM-flux et les niveaux d'eau mesurés avec une incertitude de 1 cm peuvent être considérés comme fiables, car les débits se situent dans un intervalle de confiance de 95%. Cela reste valable si la précision des mesures de niveau d'eau s'améliore jusqu'à 2 mm mais uniquement pour les débits inférieurs. Cela vaut également pour les petites variations de la hauteur des crêtes des seuils, ce qui peut être intéressant du point de vue opérationnel pour augmenter la hauteur et favoriser la fonction de rétention, par exemple. Enfin, la surveillance d'un prototype installé sur le terrain a confirmé la validité de la méthodologie dans des conditions de fonctionnement réalistes, du moins pour les débits compris entre 1 et 60 l/s et pour des déversements de DOs avec des pics de débit inférieures à

150 l/s. En effet, les débits de 80% des événements enregistrés au cours de cette thèse ont été reproduits avec des coefficients de Nash-Sutcliffe supérieurs à 0.5 et les volumes de déversement de près de la moitié des événements enregistrés ont été reproduits avec des différences relatives inférieures à 20%, valeurs considérées comme satisfaisantes au regard du type de défis abordés.

Cependant, certains aspects nécessitent des analyses plus approfondies. Des écarts importants dans les valeurs de débit ont été observés sur le terrain pour les débits supérieurs à 60 l/s entre la méthodologie DSM-flux et une seconde utilisée pour la vérification. La fiabilité de la seconde méthodologie, basée sur une approche CFD, a suscité certains doutes sur sa fiabilité qui n'ont pas permis de déterminer si la cause des différences était (i) la non-reproductibilité de la relation QH du DSM-flux dans des conditions de terrain ou (ii) d'autres facteurs de terrain qui ont influencé la représentativité du modèle numérique utilisé pour le développement de la deuxième méthodologie en relation avec la configuration du site. En raison de contraintes techniques, il n'a pas été possible de procéder à une seconde vérification dans le cadre de ce travail de doctorat et, par conséquent, cela reste une action prioritaire à développer dans les travaux futurs. D'autre part, la quantité importante de sédiments retrouvée dans le prototype après les événements, en partie situés dans la zone de déversement du dispositif, a mis en évidence la nécessité d'analyser la sensibilité de la méthode de mesure à la présence de sédiments dans la zone d'échantillonnage. Lors des observations sur le terrain, ils ne semblent pas avoir d'influence notable, du moins sur les débits plus faibles, mais une analyse rigoureuse en laboratoire devrait être effectuée.

En ce qui concerne la deuxième question, les conclusions sont légèrement moins précises et évidentes. On pourrait dire que **le DSM-flux à petite échelle peut retenir efficacement un certain type de polluants (fins et légers) sous un certain type d'écoulement (faible débit et constant),** mais cette déclaration nécessite des spécifications plus détaillées. D'après les résultats de cette thèse, il a été prouvé qu'un appareil de petite taille est capable de retenir jusqu'à 50% de la masse des particules fines de faible densité véhiculées dans un débit constant de 2 l/s. Ce pourcentage de particules piégées varie en fonction du débit. Pour les particules testées (D50 compris entre 100 et 300 µm), l'efficacité de rétention du DSM-flux est réduite de moitié pour un débit de 5 l/s. Il est donc possible que le DSM-flux ne puisse retenir les polluants particulaires fins que si les débits sont relativement faibles. Il a également été prouvé que si un débit relativement faible s'écoulait sans particules dans le dispositif, le DSM-flux est capable de conserver une partie des sédiments précédemment déposés. Cependant, dans la même hypothèse, si ce débit est légèrement supérieur, presque tous les sédiments

s’échappent de l’appareil au bout de 3 heures avec le même débit en permanent. Cela indique qu'après un certain nombre d'événements pluvieux (nombre maximum à évaluer dans le futur) où les dépôts se produisent, le DSM-flux doit être nettoyé pour éviter des pics de pollution importants dans les eaux réceptrices du fait de la remobilisation des sédiments déposés. En outre, il a été observé que les zones de dépôt se disposent de manière assez homogène sur toute la partie aval du dispositif, sauf près des régions à TKE élevée dans la section mesurée à côté du ressaut hydraulique. L'érosion commence principalement dans les bandes adjacentes aux murs latéraux et dans les deux zones érodées de forme parabolique en aval de la zone de dissipation. Avec le temps, ces deux zones s’étendent en aval, créant de petites rides (dans des conditions de faible débit) ou entraînant la matière déposée en aval (conditions de débit plus élevées).

Cette performance du dispositif n'a pas pu être validée dans un appareil à plus grande échelle. Les options numériques qui ont produit des résultats correspondant de manière satisfaisante aux données expérimentales pour l'étude de la relation QH ne reproduisaient pas les champs de vitesse expérimentaux avec suffisamment de précision pour que les modèles puissent être validés. Les résultats similaires obtenus en utilisant les mêmes options numériques dans deux résolutions de maillage de calcul différentes suggéraient que l'inadéquation avec les données expérimentales n'était pas due à une discrétisation insuffisante du domaine. Ainsi, d'autres options numériques doivent être testées : des modèles de turbulence RSM ou k-ω SST sont recommandés, ou même d’autres approches numériques plus exigeants en temps de calcul pourraient s’envisager si les ressources le permettent. Ces options numériques n'ayant pas pu être validées, il n'a pas été possible d'évaluer numériquement les capacités de rétention dans d'autres conditions, par exemple des débits ou des particules différents. Bien que le dépôt et l’entraînement du matériel ne puissent pas être surveillés directement sur le terrain, certains protocoles ont été préparés, sur la base des premières données et observations des événements enregistrés, afin de pouvoir évaluer l’efficacité de rétention du prototype dans des conditions de fonctionnement réelles. En raison de problèmes techniques rencontrés au cours des premiers mois d'exploitation, ces analyses n'ont pas pu être effectuées dans le cadre de cette thèse mais le site expérimental est déjà équipé et préparé pour les futures campagnes.

Outre les questions scientifiques abordées, l'installation du premier prototype du DSM-flux dans un réseau d’assainissement unitaires existant a également mis en évidence son potentiel en tant que dispositif pré-étalonné, préconçu et multifonction pour la surveillance d’écoulements complexes. En effet, le DSM-flux présente certains avantages par rapport aux

méthodes de mesure actuelles: (i) il vise à mesurer les rejets de DOs directement dans le canal de déversement; ii) une seule mesure du niveau d'eau est nécessaire pour obtenir les valeurs de débit; (iii) il s'agit d'un appareil pré-étalonné pouvant être installé en aval d'un DO déjà existant; (iv) sa performance est indépendante des conditions hydrauliques d'entrée; et (v) il a des fonctions supplémentaires en plus de la mesure des volumes déversés, telles que la mesure de la masse total de solides en suspension et la réduction des polluants particulaires par sédimentation.

Figure 1

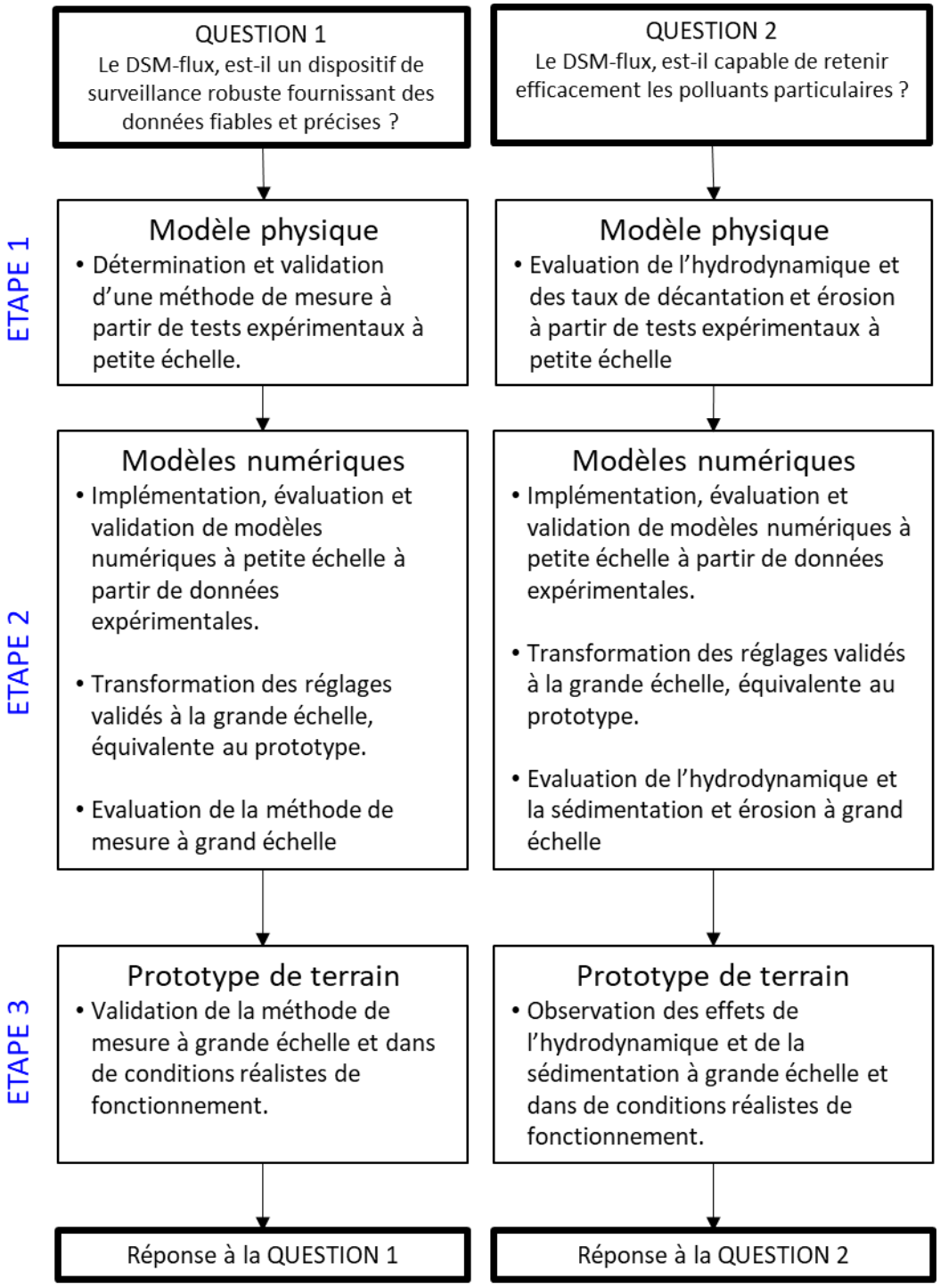

Figure 2

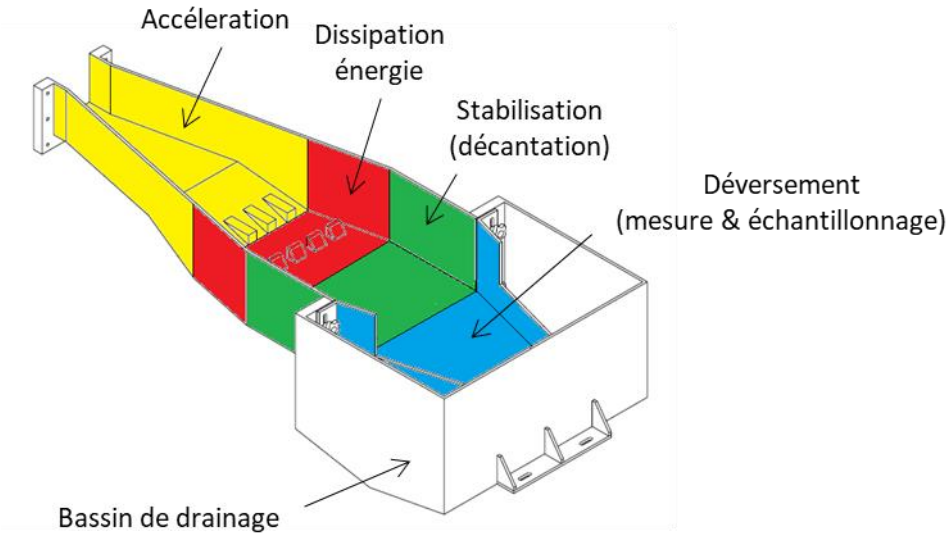

Figure 3

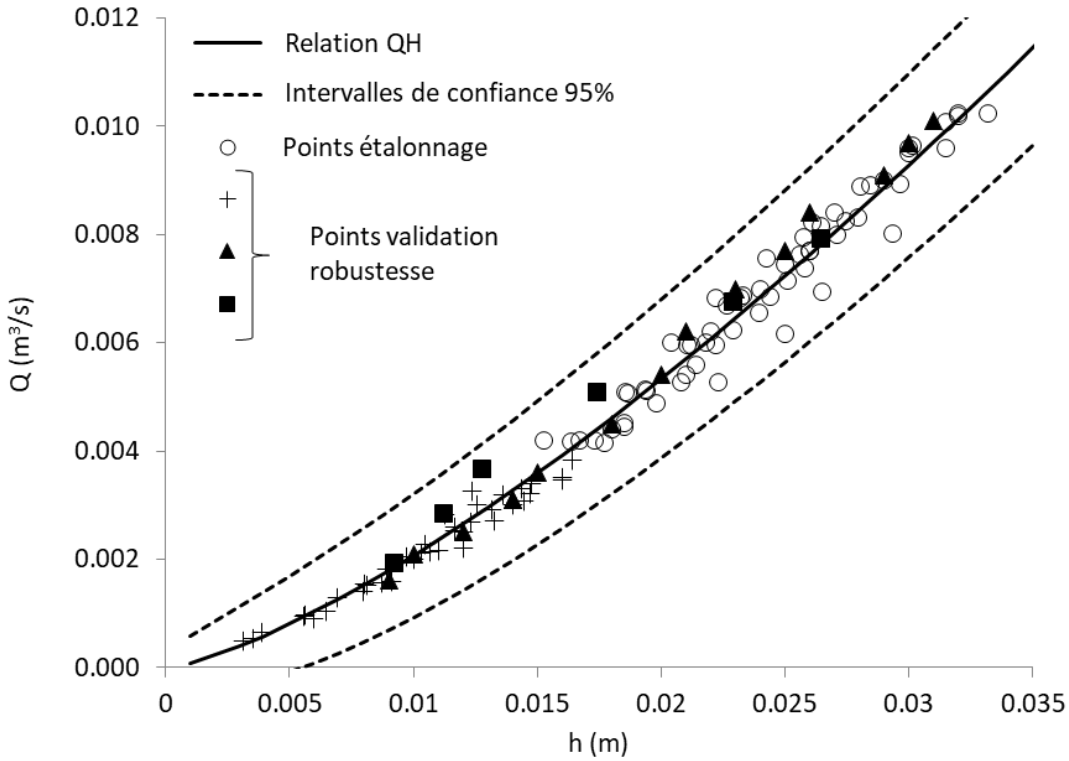

Figure 4

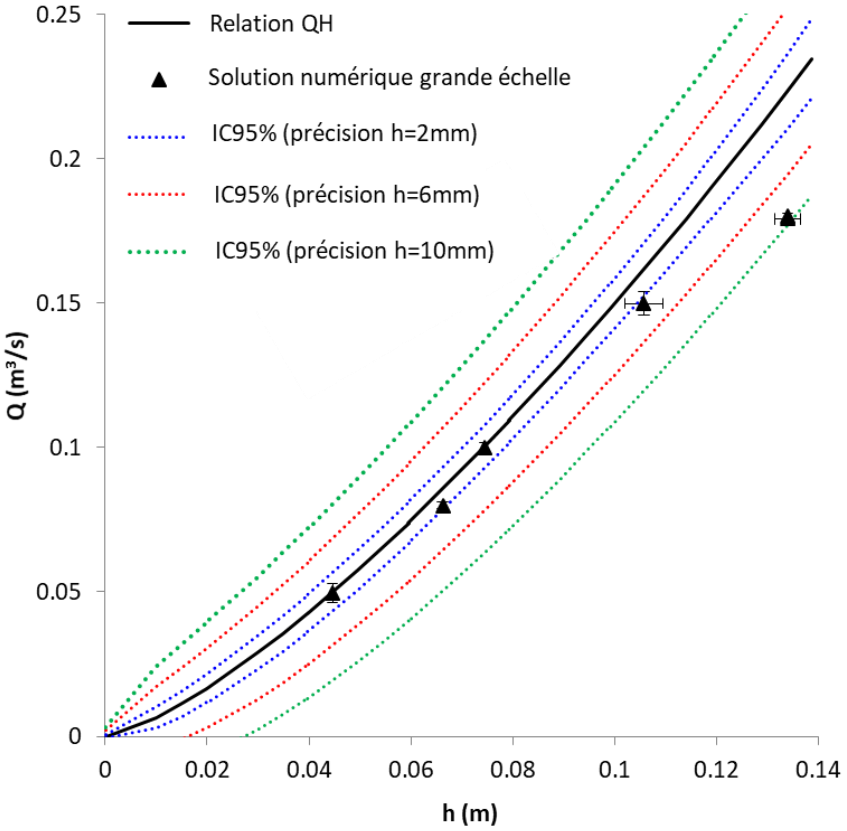

Figure 5

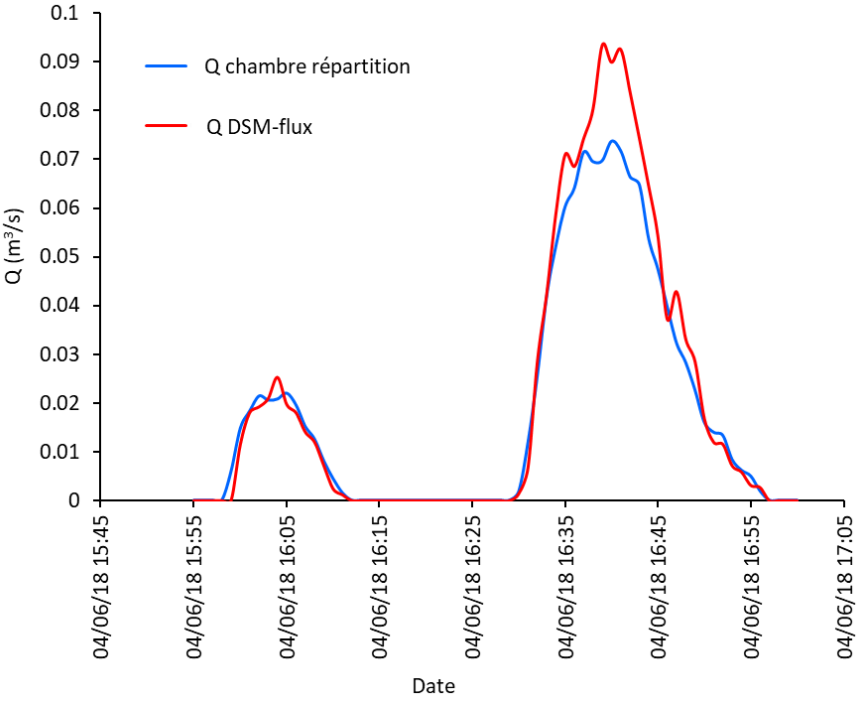

Figure 6

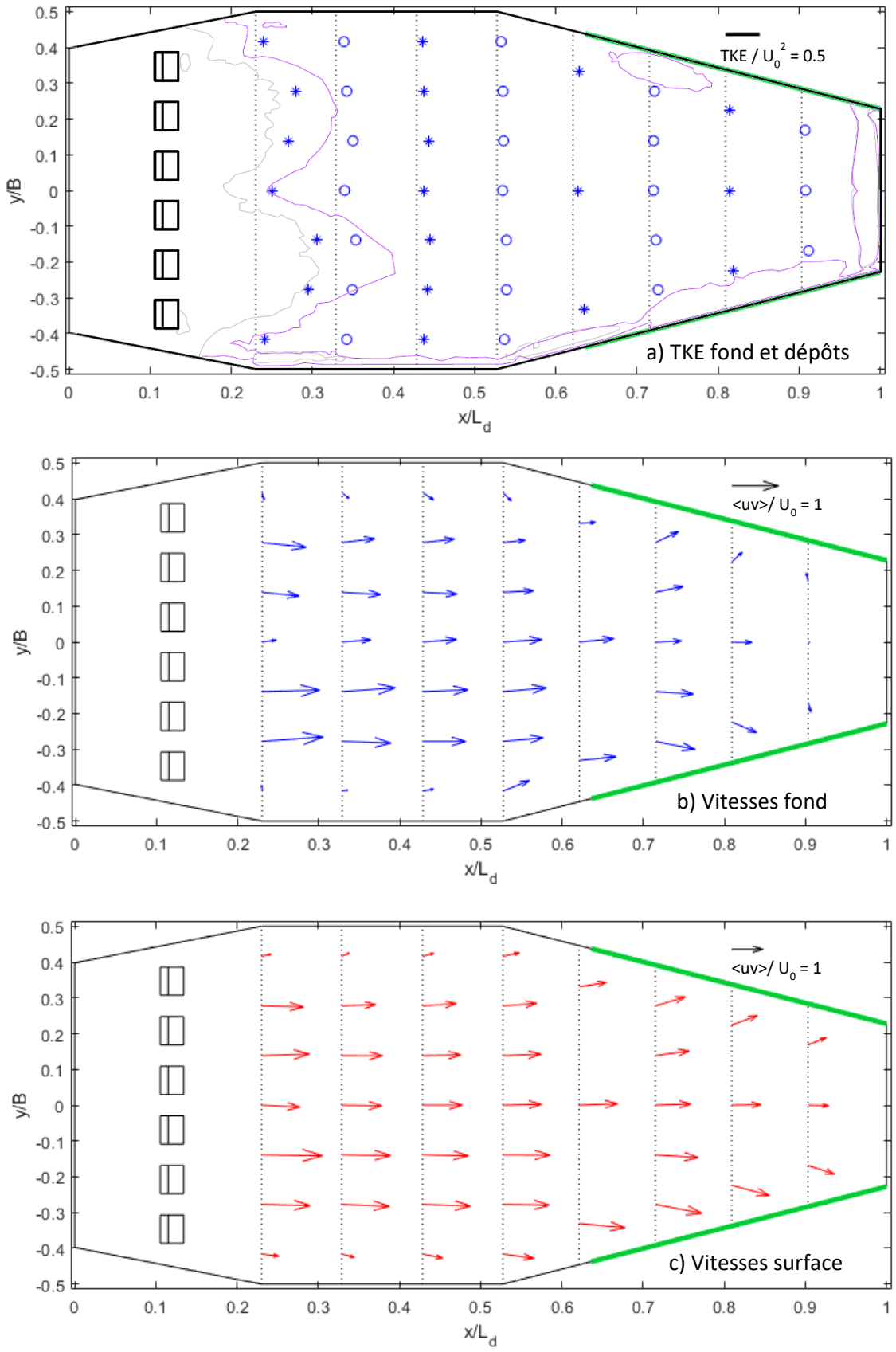

Figure 7

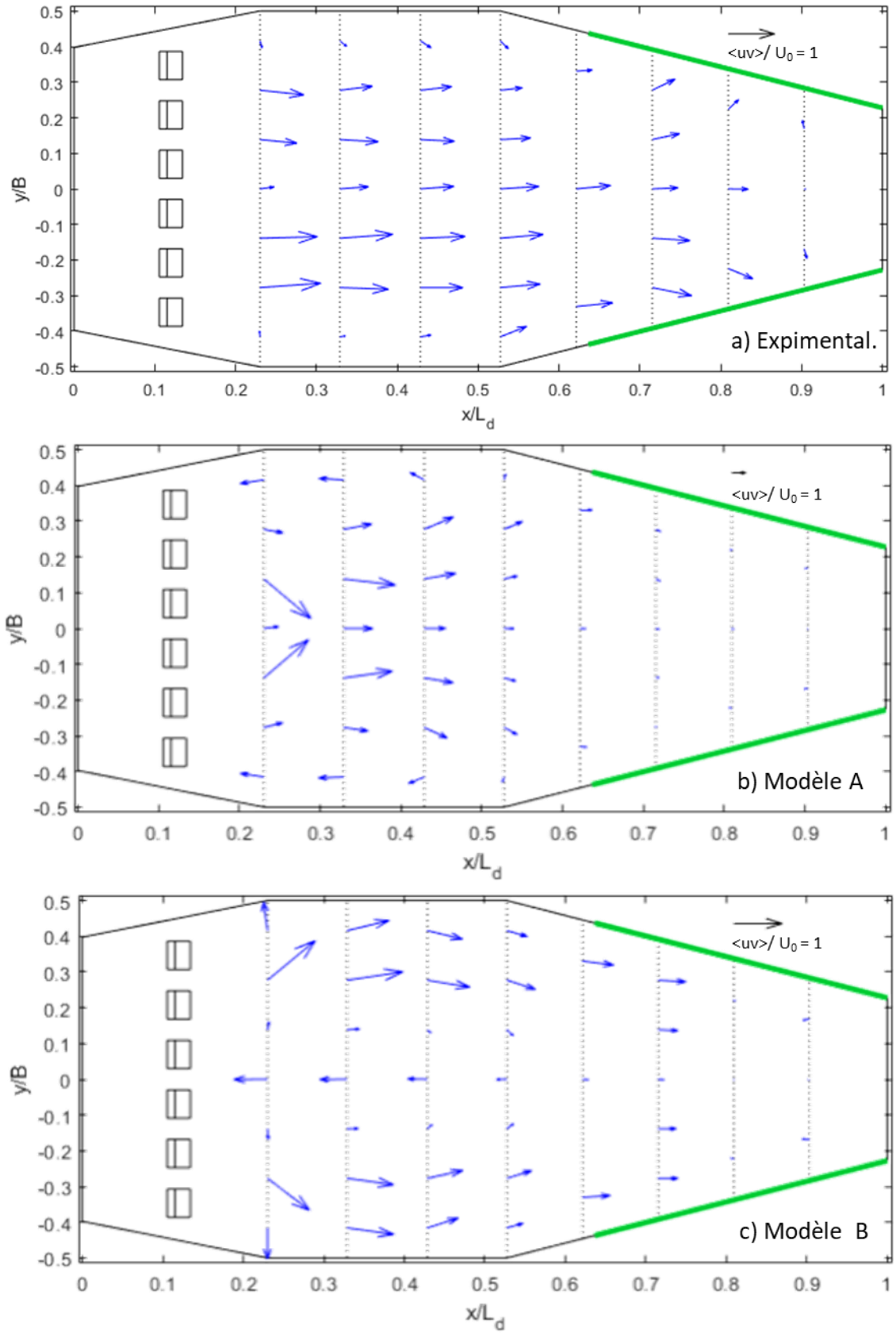

Figure 8

FOLIO ADMINISTRATIF

THESE DE L'UNIVERSITE DE LYON OPEREE AU SEIN DE L'INSA LYON

NOM : MATE MARIN DATE de SOUTENANCE : 12/02/2019

Prénoms : Ainhoa

TITRE : MULTISCALE APPROACH TO ASSESS THE DSM-flux CAPACITY TO MITIGATE IMPACTS ON THE RECEIVING WATERS. QUANTIFICATION OF OVERFLOW RATES AND INTERCEPTION OF PARTICULATE POLLUTANTS FROM COMBINED SEWER OVERFLOWS.

Approche multi-échelle pour évaluer la capacité du DSM flux à protéger les milieux aquatiques. Quantification des flux d'eau rejetés par les déversoirs d'orage et interception des polluants particulaires.

NATURE : Doctorat Numéro d'ordre : 2019LYSEI008

Ecole doctorale : Ecole Doctorale ED162 MECANIQUE, ENERGETIQUE, GENIE CIVIL, ACOUSTIQUE

Spécialité : Génie Civil

RESUME :

Au cours des dix dernières années, les gouvernements de l'Union Européenne ont été encouragés à collecter des données sur le volume et la qualité de tous les effluents d'eaux urbaines ayant un impact environnemental significatif sur les milieux aquatiques récepteurs. Les méthodes de surveillance de ces flux nécessitent des améliorations, en particulier pour les déversoirs d'orage, structures complexes responsables en grande partie de la dégradation de la qualité des milieux récepteurs. Le DSM-flux (Dispositif pour la surveillance et maîtrise des flux d'eaux et polluants des réseaux d'eaux pluviales et unitaires) est un nouveau dispositif préconçu et pré-étalonné qui garantit les conditions hydrauliques appropriées permettant de mesurer les débits et volumes déversés ainsi que les concentrations et masses de polluants qui y sont transportées. Dans cette thèse, une relation permettant de mesurer le débit au passage du DSM-flux a été construite grâce à une étude expérimentale sur modèle physique réduit, puis validée pour plusieurs configurations d'écoulement à l'amont du dispositif. Quelles que soient les conditions hydrauliques en amont, les incertitudes relatives sont inférieures à 15% et 2% pour les débits et les volumes étudiés, respectivement. La méthode de mesure a été validée in situ sur un dispositif à grande échelle construit sur le terrain et fonctionnant en conditions réelles, ce qui montre la robustesse de la méthode. De plus, grâce à sa conception originale, le DSM-flux favorise l'interception d'une fraction des polluants particulaires. L'hydrodynamique de ce dispositif de mesure a été analysée ainsi que les conditions qui engendrent la décantation des polluants particulaires. En fonction des conditions d'écoulement, il retient 50% de la masse totale des matières solides fines en suspension transitant par le dispositif. Sa capacité de rétention a été aussi observée sur le terrain et une méthodologie a été élaborée pour quantifier son efficacité de rétention lors d'études futures.

MOTS-CLÉS : DSM-flux, CFD, ADV, CSO, reliable monitoring, retention efficiency, multiscale approach

Laboratoire (s) de recherche : Déchets Eaux Environnement Pollution (DEEP)

Directeur de thèse : Gislain LIPEME KOUYI // Nicolas RIVIERE

Président de jury : Sylvie GILLOT

Composition du jury : Benjamin DEWALS, Gilles BELAUD, Ronan PHILIPPE, Gislain LIPEME KOUYI, Nicolas RIVIERE, Emmanuel MIGNOT, Regis VISIEDO